# Halodifluoromethyl Moieties as Unconventional Halogen Bond Donors in Drug Discovery and Peptide Design

**Dissertation**

der Mathematisch-Naturwissenschaftlichen Fakultät

der Eberhard Karls Universität Tübingen

zur Erlangung des Grades eines

Doktors der Naturwissenschaften

(Dr. rer. nat.)

vorgelegt von

Sebastian Vaas

aus Offenbach am Main

Tübingen

2023

Gedruckt mit Genehmigung der Mathematisch-Naturwissenschaftlichen Fakultät der Eberhard Karls Universität Tübingen.

| | |
|---|---|
| Tag der mündlichen Qualifikation: | 21.09.2023 |
| Dekan: | Prof. Dr. Thilo Stehle |
| 1. Berichterstatter: | Prof. Dr. Frank M. Böckler |
| 2. Berichterstatter: | Prof. Dr. Dirk Schwarzer |

# Acknowledgment

I would like to thank everyone who has contributed to this work in a variety of ways over the past few years, espacially the following people.

First and foremost, I want to thank **Prof. Dr. Frank M. Böckler** for his guidance and supervision throughout my research. Under his mentorship, I had the opportunity to delve into this fascinating project.

I am grateful to **Prof. Dr. Dirk Schwarzer** for being my second superviser and member of my doctoral viva.

I would like to thank **Prof. Dr. Harald Groß** for participating in my doctoral viva as an examiner and for his help with CD spectroscopy.

To **Jun.-Prof. Dr. Matthias Gehringer**, I am grateful for being an examiner in my viva and for engaging in highly beneficial discussions.

Many thanks to **Prof. Dr. Thilo Stehle** for granting access to the SLS beamline.

A special note of appreciation goes to **Dr. Dieter Schollmeyer** from the Johannes Gutenberg-Universität Mainz for his expertise in performing the X-ray measurements and data processing of the small molecule crystals.

I would like to thank **Prof. Dr. Michael Lämmerhofer**, **Dr. Bernhard Drotleff**, and **Matthias Olfert** for their contribution to the micorosomal assay by performing MS experiments and data analysis.

Within the Department of Chemistry, my thanks go to **Dr. Markus Kramer**, **Paul Schuler**, **Priska Kolb**, and **Dominik Brzecki** for their diligent work in running all NMR experiments. I also want to thank **Dr. Dorothee Wistuba**, **Dr. Peter Haiss**, **Claudia Krause**, and **Dr. Norbert Grzegorzek** for their efforts in performing the mass spectrometry.

A heartfelt thanks to my group colleagues **Dr. Markus O. Zimmermann**, **Theresa Klett**, **Jason Stahlecker**, **Marc U. Engelhardt**, **Larissa Ernst**, and **Janosch Rheinganz** for their support and advice in completing this thesis, which I greatly appreciate. Your presence has made this journey not only productive but also enjoyable.

Many thanks to the current and former group members, especially **Martin Schwer**, **Jian Xin**, **Susanne Hennig**, **Dr. Marcel Dammann**, **Dr. Andreas Lange**, **Dr. Johannes Heidrich**, **Dr. Christoph Ernst**, **Dr. Tamer M. Ibrahim** for the lively exchange of ideas and for fostering a pleasant working atmosphere on the 8th floor.

I would also like to express my deepest gratitude to my wife and my family. Your unwavering support, understanding, and encouragement have been a constant source of strength throughout this endeavor. Your love and belief in me have been the driving force behind my perseverance, and I am immensely grateful for having you by my side.

# List of Publications and Posters

## Publications

**S. Vaas**, M. O. Zimmermann, D. Schollmeyer, J. Stahlecker, M. U. Engelhardt, J. Rheinganz, B. Drotleff, M. Olfert, M. Lämmerhofer, M. Kramer, T. Stehle, F. M. Boeckler. Principles and Applications of $CF_2X$ Moieties as Unconventional Halogen Bond Donors in Medicinal Chemistry, Chemical Biology and Drug Discovery. *J. Med. Chem.* **2023**, *66* (15), 10202–10225. doi: 10.1021/acs.jmedchem.3c00634

**S. Vaas**, M. O. Zimmermann, T. Klett, and F. M. Boeckler. Synthesis of Amino Acids Bearing Halodifluoromethyl Moieties and Their Application to p53-Derived Peptides Binding to Mdm2/Mdm4. *Drug Des. Dev. Ther.* **2023**, *17*, 1247–1274. doi: 10.2147/DDDT.S406703

## Posters

**S. Vaas**, M. O. Zimmermann, T. Klett, M. U. Engelhardt, M. Dammann, B. Drotleff, M. Lämmerhofer, F. M. Böckler: Synthesis and Evaluation of Fragments containing Halodifluoro Methyl Groups as Novel XB Donors. Poster presented at 4th International Symposium on Halogen Bonding, 2020 Nov 2-5, Stellenbosch, South Africa.

M. Dammann, M. U. Engelhardt, **S. Vaas**, M. O. Zimmermann, F. M. Böckler: HEFLibs (Halogen Enriched Fragment Library): Screening and Hit Validation. Poster presented at 4th International Symposium on Halogen Bonding, 2020 Nov 2-5, Stellenbosch, South Africa.

M. U. Engelhardt, M. O. Zimmermann, F.-M. Siemers, M. Dammann, **S. Vaas**, F. M. Böckler: Employing Machine Learning to establish QM-derived Scoring Functions for the Assessment of Halogen-π-Interactions. Poster presented at 4th International Symposium on Halogen Bonding, 2020 Nov 2-5, Stellenbosch, South Africa.

# List of Abbreviations

| | |
|---|---|
| 2xYT | 2x Yeast extract tryptone broth |
| 4PL | Four parameter logistic regression |
| AA | Amino acid |
| ABCN | 1,1'-Azobis(cyclohexanecarbonitrile) |
| ABL1 | ABL proto-oncogene 1, non-receptor tyrosine kinase |
| Abu | α-Aminobutyric acid |
| Ac | Acetyl |
| ACN | Acetonitrile |
| AHA | Acetohydroxamic acid |
| Ala | Alanine |
| AMP-PCP | β,γ-Methyleneadenosine 5'-triphosphate disodium salt |
| API | Active pharmaceutical ingredient |
| APS | Ammonium persulfate |
| Asp | Aspartic acid |
| BCR | BCR activator of RhoGEF and GTPase |
| β-ME | 2-Mercaptoethanol |
| Boc | *tert*-Butoxycarbonyl |
| BSA | Bovine serum albumin |
| BSSE | Basis set superposition error |
| CCDC | Cambridge Crystallographic Data Centre |
| CCP4 | Collaborative Computational Project Number 4 |
| CD | Circular dichroism |
| ChB | Chalcogen bond |
| CML | Chronic myelogenous leukemia |
| COOT | Crystallographic Object-Oriented Toolkit |
| CuAAC | Copper(I)-catalyzed alkyne-azide cycloaddition |
| CV | Column volume |
| Dab | 1,4-Diaminobutyric acid |
| DAST | Diethylaminosulfur trifluoride |
| DBDMH | 1,3-Dibromo-5,5-dimethylhydantoin |

*Continued on next page*

| | |
|---|---|
| DCE | 1,2-Dichloroethane |
| DCM | Dichloromethane |
| DHP | 3,4-Dihydropyran |
| DIPEA | *N*,*N*'-Diisopropylethylamine |
| DMAP | Dimethylaminopyridine |
| DMF | *N*,*N*-Dimethylformamide |
| DMS | Dimethyl sulfide |
| DMSO | Dimethyl sulfoxide |
| DNA | Deoxyribonucleic acid |
| DTT | Dithiothreitol |
| EDCI | 1-Ethyl-3-(3-dimethylaminopropyl)carbodiimide |
| EDTA | Ethylenediaminetetraacetic acid |
| EI | Electron ionization |
| ELISA | Ezyme-linked immunosorbent assay |
| ESI | Electronspray ionization |
| ESP | Electrostatic potential |
| EWG | Electron-withdrawing group |
| FA | Formic acid |
| FAM | 5(6)-Fluorescein |
| FBDD | Fragment-based drug discovery |
| FDA | Food and Drug Administration |
| Fmoc | 9-Fluorenylmethoxycarbonyl |
| FP | Fluorescence polarization |
| Glu | Glutamic acid |
| GSH | Glutathione |
| HBTU | 3-[Bis(dimethylamino)methyliumyl]-3*H*-benzotriazol-1-oxide hexafluorophosphate |
| HEPES | 4-(2-hydroxyethyl)-1-piperazineethanesulfonic acid |
| HOBt | 1*H*-1,2,3-Benzotriazol-1-ol |
| HPLC | High-performance liquid chromatography |
| IPTG | Isopropyl β-D-1-thiogalactopyranoside |
| ITC | Isothermal titration calorimetry |

*Continued on next page*

| | |
|---|---|
| JNK1 | c-Jun N-terminal kinase 1 |
| JNK3 | c-Jun N-terminal kinase 3 |
| LB | Lysogeny broth |
| LC | Liquid chromatography |
| Leu | Leucine |
| LTMP | Lithium tetramethylpiperidide |
| mCPBA | *meta*-Chloroperoxybenzoic acid |
| MDM2 | Mouse double minute 2 homolog |
| MDM4, MDMX | Mouse double minute X homolog |
| MFS | Minimal final solubility |
| MIS | Minimal instant solubility |
| MOE | Molecular Operating Environment |
| MOPS | 3-(*N*-Morpholino)propanesulfonic acid |
| MS | Mass spectrometry |
| MWCO | Molecular-weight cutoff |
| N/A | Not available, not applicable |
| NBS | *N*-Bromosuccinimide |
| Nle | Norleucine |
| NMM | *N*-Methylmorpholine |
| NMR | Nuclear magnetic resonance |
| p53 | Tumor protein p53 |
| PBS | Phosphate-buffered saline |
| PDB | Protein data bank |
| PE | Petroleum ether |
| PEG | Polyethylene glycol |
| Phe | Phenylalanine |
| PMP | *p*-Methoxyphenyl |
| PMSF | Phenylmethylsulfonyl fluoride |
| PPI | Protein-protein interaction |
| ppm | Parts per million |
| Pra | Propargylglycine |
| Pro | Proline |

*Continued on next page*

| | |
|---|---|
| PTSA | *p*-Toluenesulfonic acid |
| RC | Regenerated cellulose |
| RP | Reversed-phase |
| rt, RT | Room temperature |
| SD | Standard deviation |
| SDS-PAGE | Sodium dodecyl sulfate-polyacrylamide gel electrophoresis |
| SEC | Size-exclusion chromatography |
| Ser | Serine |
| SPPS | Solid-phase peptide synthesis |
| STAMP | Specifically Targeting the ABL Myristoyl Pocket |
| STD | Saturation transfer difference |
| T3P | Propanephosphonic acid anhydride |
| TBTA | Tris((1-benzyl-4-triazolyl)methyl)amine |
| TEMED | Tetramethylethylenediamine |
| TEV | *Tobacco etch virus* |
| TFA | Trifluoroacetic acid |
| THF | Tetrahydrofuran |
| THP | 2-Tetrahydropyranyl |
| Thr | Threonine |
| TIPS | Triisopropylsilane |
| TLC | Thin-layer chromatography |
| TMEM16A | Transmembrane protein 16A |
| TRIS | Tris(hydroxymethyl)aminomethane |
| Trp | Tryptophane |
| Tyr | Tyrosine |
| UV | Ultraviolet |
| VEGFR | Vascular endothelial growth factor receptor |
| XB | Halogen bond |
| XDS | X-ray Detector Software |

# Table of Contents

# 1 General Introduction

## 1.1 The Halogen Bond

Large biomolecules such as proteins, DNA, and RNA interact with each other and with smaller endogenous and exogenous ligand molecules. These interactions are essentially driven by intermolecular attractive and repulsive forces. In contrast to the stronger covalent, ionic and metallic bonds, these are relatively weaker non-covalent interactions such as van der Waals forces, hydrogen bonds, π-effetcs and hydrophobic interactions, or halogen bonds. A halogen bond (XB) is based on attractive interactions between an electron donor (B) and an electron-deficient region of the halogen (X), the σ-hole, which results from the anisotropic electron distribution of the halogen.[5] This is explained by the circumstance that the three unshared electron pairs have an approximate $s^2 p_x^2 p_y^2 p_z^1$ configuration and form a belt of negative charge around the central region (Figure 1). Appropriate halogens for XB are chlorine, bromine, and iodine with increasing size of

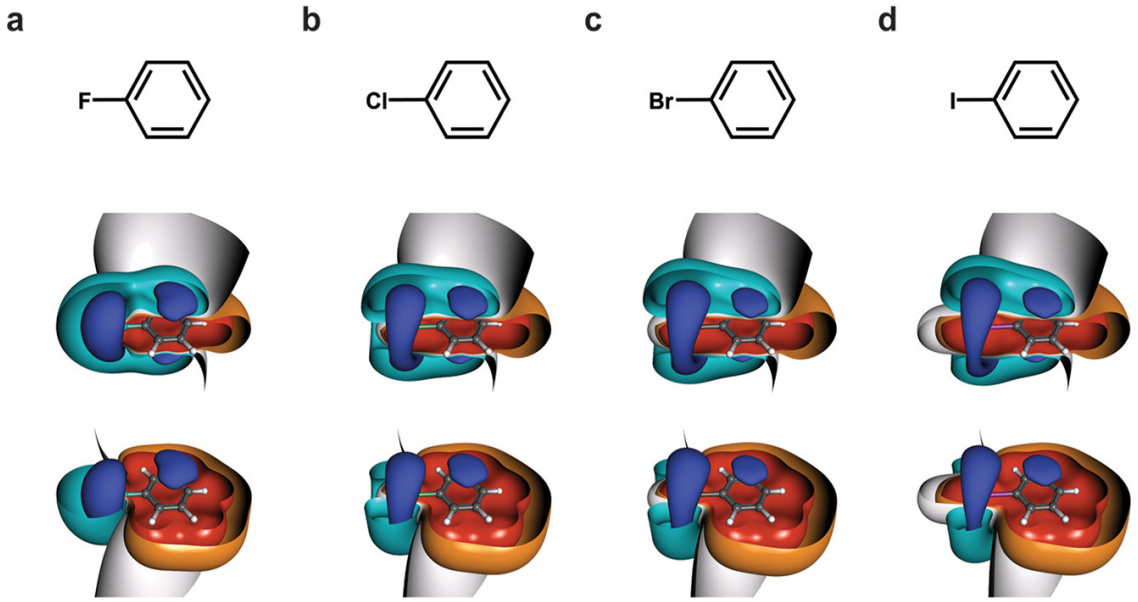


**Figure 1:** Structural formulas and electrostatic potential (ESP) isosurfaces of halobenzenes (MP2/TZVPP). Negative ESP isosurfaces at an energy of −0.012 au are colored in dark blue and at an energy of −0.006 au in cyan. Positive ESP isosurfaces at 0.012 au are colored in red and at an energy of 0.006 au in orange. The isosurfaces at 0.000 au, indicating the boundaries for the transition between negative and positive ESPs, are shown as gray surfaces: **(a)** fluorobenzene, no σ-hole on the halogen; **(b)** chlorobenzene; **(c)** bromobenzene; **(d)** iodobenzene, increasing σ-hole (positive charge) on the halogen opposite the R−X bond, plus belt of negative electrostatic potential. All pictures were prepared with MOLCAD.[1,2] Figure adopted from Wilcken *et al.* (2013).[3]

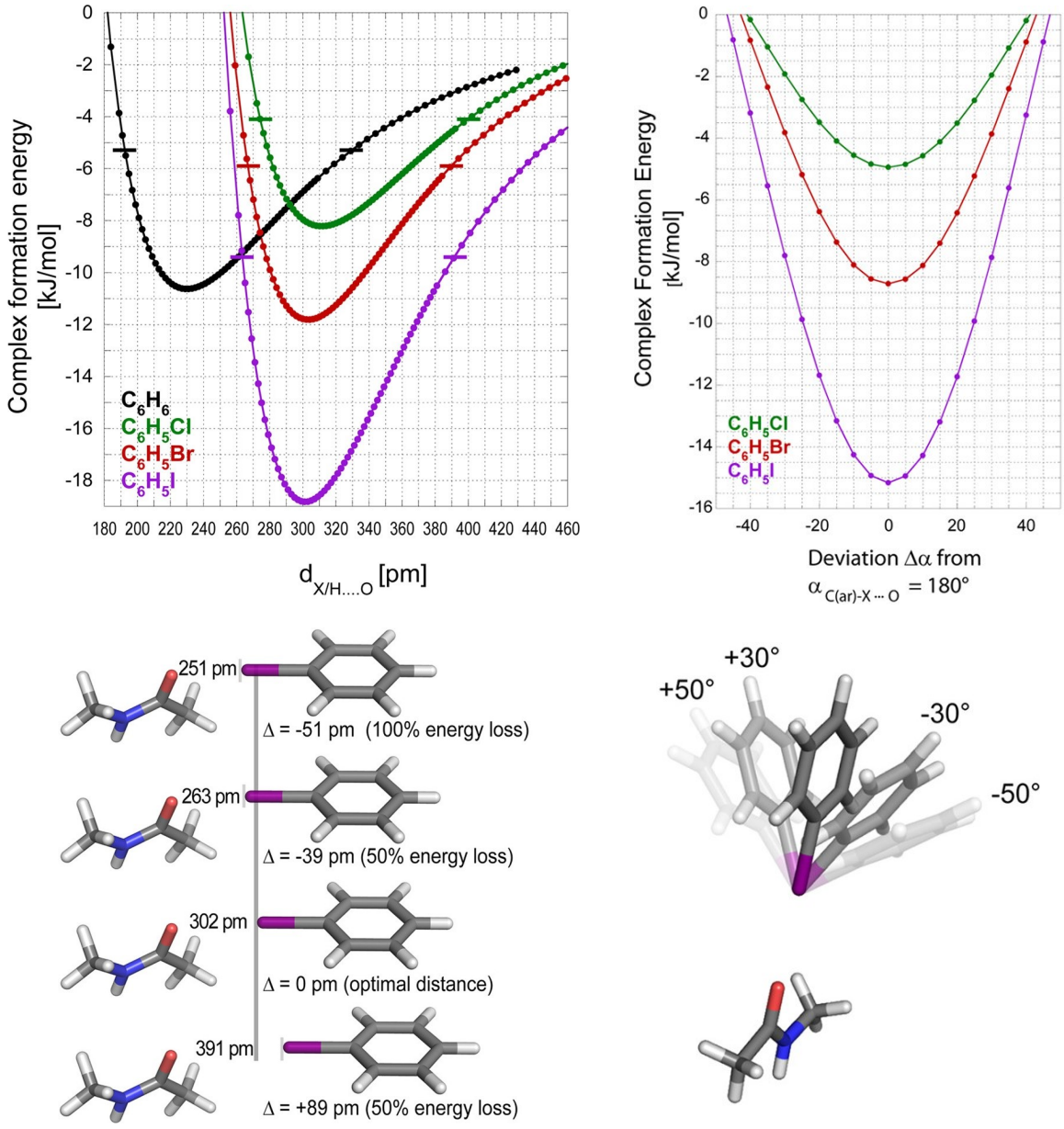


**(a)** Distance dependency.

**(b)** Angle dependency.

**Figure 2:** Dependencies of the complex-formation energies ΔE (kJ mol$^{-1}$) of the backbone model system *N*-methylacetamide and benzene ($C_6H_6$, black curve), chlorobenzene ($C_6H_5Cl$, green curve), bromobenzene ($C_6H_5Br$, brown curve), or iodobenzene ($C_6H_5I$, purple curve). **(a)** Distance-dependency: Characteristic distances for iodobenzene are shown below, illustrating how different scaffold placements affect the complex-formation energy. **(b)** σ-Hole angle dependency: Characteristic angles for iodobenzene illustrate how deviations from optimal σ-hole angle impair complex formation energies. Structural depictions were prepared with PyMOL. Figures were adopted and modified from Wilcken *et al.* (2012 and 2013).[3,4]

the σ-hole, while fluorine lacks a positively charged σ-hole. The XB interaction is strongly directed along the C−X···B axis, with the best interaction energies found at an C−X···B angle of 180° with a deviation of up to 30° and an X···B distance of 3–4 Å (Figure 2).[6,7]

Since halogens are rather atypical in biological macromolecules, the occurrence of halogens as electron acceptors is mainly limited to the corresponding ligands. Electron donors in proteins are typically the backbone carbonyl of the main chain[7–10] and oxygen or nitrogen atoms of electron-rich side chains (e.g., aspartate, glutamate)[11], serine, histidine[12], or sulfur in methionine[13]. Depending on the angle and distance, the complex formation energies for XBs are in the range of 4–50 kJ mol$^{-1}$.[3,6,9] For contextualization, Wilcken *et al.* set up a computed model system with chlorobenzene, bromobenzene, and iodobenzene in complex with the carbonyl oxygen of *N*-methylacetamide as a simulated protein backbone (Figure 2a). The calculated complex formation energies were –8.2, –11.8, and –18.8 kJ mol$^{-1}$ (X···O distance: 302, 304, and 312 pm), respectively.[6] As a comparison, the hydrogen bond of an $H_2O$ dimer has an energy of about 17–21 kJ mol$^{-1}$.[14] However, it should be noted that the values from various sources are difficult to compare due to different calculation methods. Halogen bonds are best described theoretically using high-level quantum chemical methods such as coupled cluster (CCSD-(T)) and perturbation theory (MP2) calculations involving basis sets such as completeness-optimized basis sets (CBS) or karlsruhe basis sets (e.g., TZVPP).[15–17] Much larger molecular systems can be studied with quantum mechanical/molecular mechanical (QM/MM) calculations or semiempirical studies.[18–20] If necessary, the basis set superposition errors (BSSEs) can be corrected using the procedure of Boys and Bernardi.[21] Besides the quality of geometry, the strength of the halogen bond depends on the chemical environment and is therefore tuneable. Substituent-mediated inductive and mesomeric effects, as well as scaffold effects, can influence the electron density at the halogen and thus the size and the shape of the σ-hole.[8] Strong electron withdrawing groups (EWG) such as nitro, nitrile or fluorine substituents withdraw electron density from the halogen, leading to potentially stronger halogen bonds. Negative and positive charges have an even stronger effect. Negative charges in the system can increase the electron density to such a degree that the σ-hole is marginalized, while positive charges have a strong tuning effect. Besides halogen bonds, chalcogen bonds (ChB, Ch = O, S, Se, Te) are another notable class of attractive interactions with nucleophiles that are important in biological systems.[22,23] ChBs are also highly dependent on the angle and distance. Unlike halogens, the concerned elements of group 16 of the periodic table usually form two covalent bonds and have two σ-holes. In particular, ChB interactions of sulfur in methionine side chains,[24] but also of selenomethionines[25] are known.

## 1.2 Halogens in Biologically Active Agents

A wide variety of natural and synthetically produced bioactive agents are known that contain halogens. Halogenated natural products (NPs) have a broad range of biological activity, e.g. against cancer, bacteria and fungi, and are consequently of interest for research

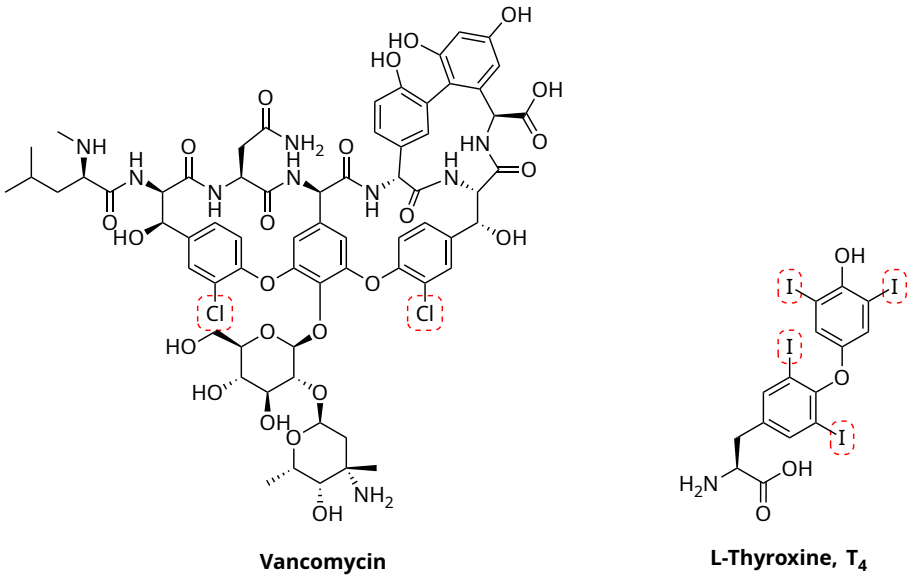


**Figure 3:** Vancomycin contains two chlorine atoms and L-thyroxine ($T_4$) contains four iodine atoms.

and an important source of potential medical agents. A chlorine-containing antibiotic approved for treatment is for example vancomycin (Figure 3), a natural antibacterial glycopeptide with activity against methicillin-resistant *Staphylococcus aureus* (MRSA).[27] Other well-known examples are the tyrosine-based thyroid hormones triiodothyronine ($T_3$) and thyroxine ($T_4$), produced and released by the thyroid gland (Figure 3 and 4).[28–30] These iodine-containing hormones play an important role in the regulation of metabolism in the human organism.

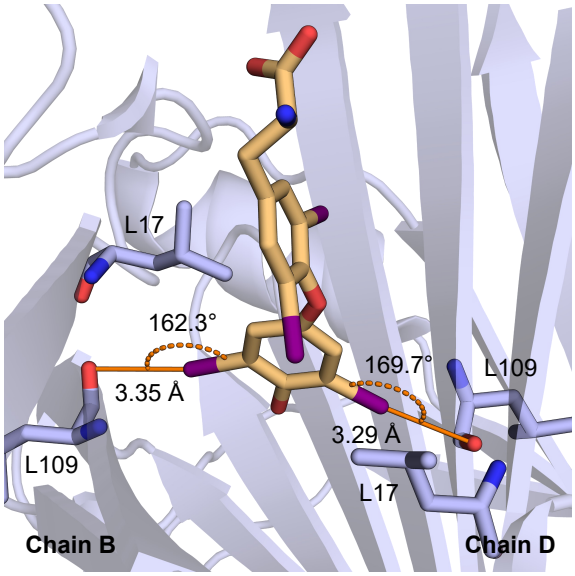


**Figure 4:** L-Thyroxine is complexed by concurrent binding to two β-sheets from different subunits of transthyretin involving two halogen bonds (PDB ID: 1SN0).[26] The backbone oxygens of two L109s are addressed by one iodine atom each.

Over 5000 halogenated NPs are described in the literature.[31,32] These NPs contain mainly chlorine and bromine, while fluorine and iodine are less common.[33–35] The distribution of halogens in approved medicinal products is divergent: In 2020, 16 FDA-approved drugs out of 53 (30 %), including biopharmaceutical products, were halogen-containing drugs, 13 contained flourine, one of them contained additionally bromine, another one additionally chlorine and bromine.[36] Three others contained chlorine and/or bromine. Fourteen approved drugs out of 50 (28 %) in 2021 were halogen-containing drugs, eight contained fluorine, four contained chlorine and two contained a combination of the two halogens.[37] None possessed iodine. Nevertheless, a significant proportion of all recently approved drugs contain halogens, with fluorine predominating. The incorporation of fluorine has the potential to improve metabolic stability, alter physicochemical properties, and increase binding affinity.[38] This is based on the following properties of the fluorine atom: the relatively small size of fluorine (van der Waals radius of 1.47 Å), comparable to hydrogen (van der Waals radius of 1.20 Å), the strong electron-withdrawing property of fluorine, the greater stability of the C−F bond compared to the C−H bond, and the greater lipophilicity of fluorine compared to hydrogen.[38] The heavier halogens exhibit similar proporties with the additional feature that they are more polarizable because of their seize and they are capable of engaging in XB formation.[39,40] It is also worth mentioning the halogen's tendency of the van der Waals radii[41] and their electronegativity according to Pauling (in parenthesis): Fluorine: 1.47 Å (4.0), chlorine: 1.74 Å (3.2), bromine: 1.85 Å (3.0), and iodine: 1.98 Å (2.7). Therefore, halogens are an important tool for positively influencing the properties of active ingredients.

## 1.3 Compounds containing Halodifluoromethyl Moieties

The synthesis and evalution of $CF_2X$-bearing (X = Cl, Br, I) compounds with implication on XB in drug design is a central component of the present work. Therefore, the preparation of $CF_2X$ groups and their relevance and prevalence in the previous literature is elaborated in the following sections. Fluorine-stabilized halogens (Cl, Br, I) attached to $sp^3$-hybridized C atoms exhibit different spatial behavior than aromatically bonded, highly directional halogens. Shindo *et al.* investigated bromodifluoro- and chlorodifluoroacetamides for theirs applicability as a warhead for covalently binding inhibitors.[42] Both had far too low reactivity for use as warheads under physological conditions, but that in turn makes this $CF_2X$ feature interesting for use as a Lewis base in XB. As shown in Figure 5 on the following page, the absence (number of "linker atoms": LA = 0) or choice of different linkers (LA ≥ 1) correlating with different rotational degrees of freedom (number of "rotation axes": RA) and geometries enables new potential and previously understudied protein-peptide and protein-ligand interaction capabilities.

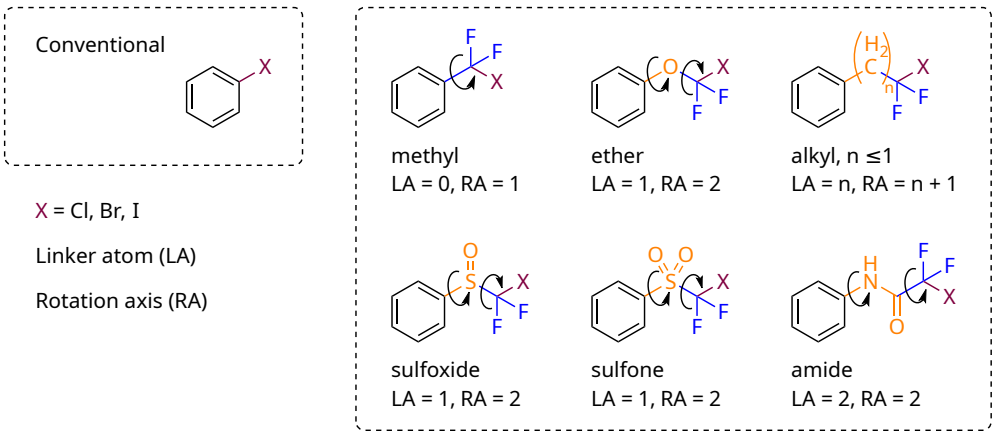


**Figure 5:** Overview regarding possible $CF_2X$-bearing structures with benzene as general scaffold pattern. The abbreviation "LA" indicates the number of linker atoms and "RA" the rotatable bond axes.

### 1.3.1 General Synthesis

A compound with $CF_2X$ (X = Cl, Br, I) group rarely represents the desired final product. In organic synthesis the $CF_2X$ unit is an important building block for further synthesis steps using the non-fluorine halogen as leaving group. The $CF_2X$ unit is especially a precursor for trifluoromethyl ($CF_3$), difluoromethyl ($CF_2H$) and difluoromethylene ($CF_2$) building blocks or for $^{18}$F-labeling of trifluoromethylated ($CF_2{}^{18}F$) compounds[43]. In general, besides some reactions with $CF_2Cl$- and $CF_2I$-containing compounds as starting material, mainly syntheses with $CF_2Br$ units are described resulting from the trade-off between stability and reactivity of the halogenated substances. Consequently, most of the studies are focused on the accessibility of the brominated analog. Scheme 1 on the next page lists some selected examples of reaction mechanisms by which $CF_2Br$ is accessible.

Reaction (a)[44–47] describes the photo- or heat-induced radical bromination of a $CF_2H$ group, for which in turn there are numerous methods to generate this difluoromethylated functionality.[48] Suitable brominating agents include bromine and *N*-bromosuccinimide. Halogen exchange reaction (b)[49,50] by substitution of one fluorine atom of a $CF_3$ group into a bromine is a second possible route. In 2021, Dorian *et al.* presented an iron-mediated halogen exchange reaction using boron tribromide as a brominating agent. Starting from $CF_2Br$-alkynes, Diels-Alder and other transformation reactions (c)[51–53] are possible. Apart from the generation of phenyl derivatives, numerous heterocycles are reported: benzoxazoles[54,55], 1,2,4-oxadiazoles[54], 1,3-imidazolines, 1,3-oxazolines[56,57], and pyrazole[58] to mention some. $CF_2Br$-alkynes themselves are prepared from ethynyllithium derivatives with dibromodifluoromethane ($CF_2Br_2$) (d)[59,60] and other reagents[61]. In 2014, the group of Inoue described the bromodifluoromethylation (e)[62] of aromatic Grignard reagents bearing electron-withdrawing groups (EWG) with $CF_2Br_2$. Example (f)[63]

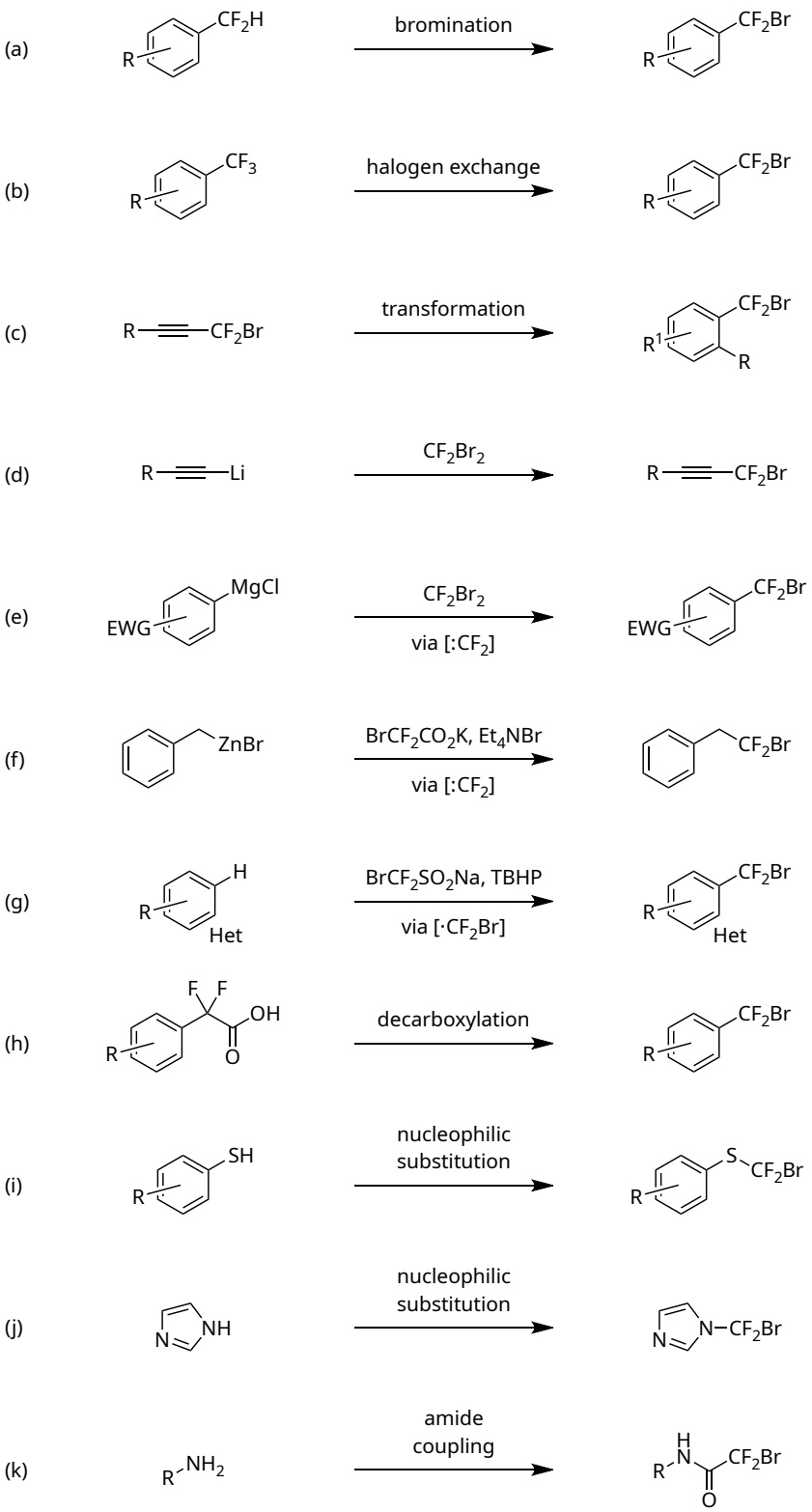


**Scheme 1:** Overview of selected synthesis methods described in the literature for the preparation of organic compounds with $CF_2Br$ moiety.

shows the chemical reaction of a presented study by Dilman and coworkers reported in 2013 using potassium bromodifluoroacetate ($BrCF_2CO_2K$) to prepare $CF_2Br$ moiety from organozinc reagents via postulated difluorocarbene-mediated mechanism. Previously, in 2013, the same research group demonstrated a similar reaction with the alternative reagent (bromodifluoromethyl)trimethylsilane by treating the resulting reaction solution with bromine to obtain $CF_2Br$ and with iodine to produce a $CF_2I$ group.[64] In 2016, Qing *et al.* reported sodium bromodifluoromethanesulfinate[65,66] ($BrCF_2SO_2Na$) as a bromodifluoromethylating agent, as shown in (g)[67], and demonstrated the incorporation of $CF_2Br$ via radical reaction mechanism using benzofuran, benzo[*b*]thiophene and 2*H*-chromen-2-one derivatives as examples. Gouverneur and coworkers devised a method for the synthesis of a $CF_2Br$ group via a radical decarboxylation halogenation as part of their research on $^{18}$F-labeling of $CF_3$ groups. First, a Barton ester is formed.[68] Photo- or heat-induced, depending on whether the reaction takes place on a benzyl[69] or on an ether[43], a radical adduct is generated *in situ*. With a suitable radical scavenger, in this case bromotrichloromethane ($BrCCl_3$) as simultaneous solvent, the bromine derivative is subsequently formed. The same research group described the preparation (i)[43] of thioether using thiolates as starting material. Example (j) shows the nucleophilic substitution of $CF_2Br_2$ using benzimidazole, indazole[70] or pyrazole[71,72] under basic conditions forming an N−C bond. Method (k)[42,73–75] produces amides and can achieved from commercially available reagents like bromodifluoroacetic acid ($BrF_2CCO_2H$), bromodifluoroacetyl chloride ($BrF_2CCOCl$) or bromodifluoroacetic anhydride ($(BrF_2CCO)_2O$) with amines. Many more syntheses leading to further diverse chemical structures are described in the literature.

### 1.3.2 Active Pharmaceutical Ingredients

Only a few active pharmaceutical ingredients (APIs) with $CF_2X$ moiety are described in the literature.[73,74,76–80] As shown in Figure 6 on the facing page, the presented examples are limitied to $CF_2Cl$ groups. Asciminib (Novartis) is an FDA-approved (2021) allosteric inhibitor of ABL1 and is used to treat chronic myelogenous leukemia (CML) by inhibiting the BCR-ABL fusion protein through binding to the myristoyl pocket of the kinase domain.[76,77] The binding mode was elucidated by the crystal structure of the ABL1 kinase protein (T334I_D382N) in complex with asciminib and nilotinib (PDB: 5MO4). In the structure, the chlorine atom forms a halogen bond with the oxygen of the backbone of Leu448 at an angle of 178.3° and a distance of 3.3 Å (for more details, see Section 3.1.4.3). Padsevonil (UCB Pharma) is a drug candidat in phase III (2019) with selective affinity for both presynaptic synaptic vesicle 2 (SV2) proteins and postsynaptic central benzodiazepine receptor (cBZR) sites on the γ-aminobutyric acid ($GABA_A$) receptor and intended as a therapeutic agent for the treatment of epilepsy.[78] Compounds **A** and **B** from Figure 6 are inhibitors of the vascular endothelial growth factor receptor (VEGFR) family, showing $IC_{50}$ values of

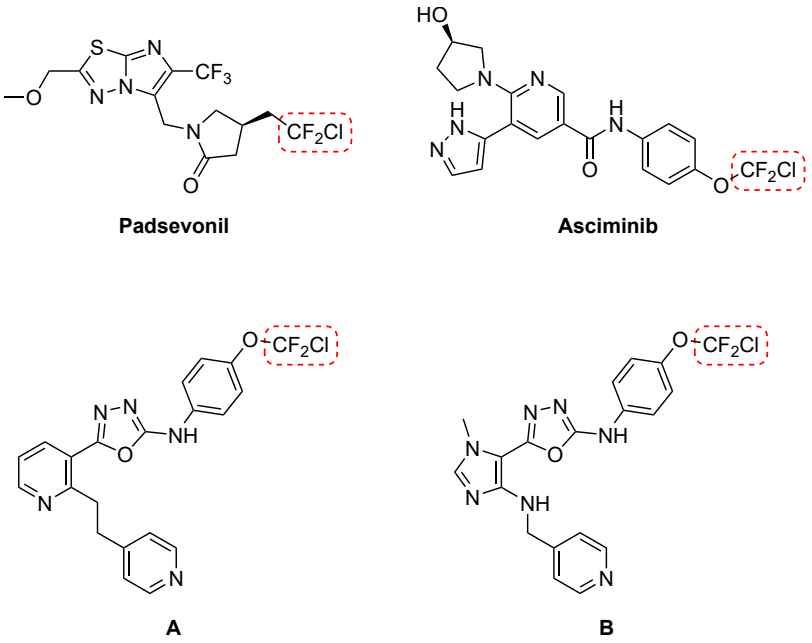


**Figure 6:** Active pharmaceutical ingredients containing $CF_2Cl$ moiety: Padsevonil (UCB Pharma) is an inhibitor of SV2 and $GABA_A$. Asciminib (Novartis) inhibits ABL1 and is used in the treatment of CML by inhibiting the BCR-ABL fusion protein. **A** and **B** are active against both VEGFR-1 and VEGFR-2.

96 nM and 63 nM, respectively, in cell-based ELISA assays for VEGFR-2.[79,80] In enzymatic assay for VGEFR-1 and VGEFR-2, $IC_{50}$ values ranged from 31 nM to 770 nM. The binding modes of these three compounds are not described in the literature. Moreover, Xu *et al.* synthesized and tested in 2011 antifungal active 1,2,4-triazole derivatives with $CF_2Cl$ acetamide moiety. In 2017, Truong *et al.* reported 2-acylaminocycloalkylthiophene-3-carboxylic acid arylamides substituted with $CF_2X$ acetamides as inhibitors of the calcium-activated chloride channel Transmembrane Protein 16A (TMEM16A).[74] These acetamides are accessible by route (k) of Scheme 1 on page 7.

Of particular interest is the preparation of the required $CF_2Cl$ synthons. The synthesis of the padsevonil building block is described in UCB Pharma's patent application, as shown in method (l)[81] of Scheme 2 on the following page. Starting from 4-(2,2-difluorovinyl)pyrrolidin-2-one, the reaction mixture is heated in concentrated hydrochloric acid, resulting in addition of HCl to the difluorovinyl double bond and hydrolysis of the γ-lactam. Step 2 and 3, treating with thionyl chloride and DIPEA, leads to ring closure again. A preparation protocol of the $CF_2Br$ derivative in 62 % aqueous hydrobromic acid is also known.[82] The synthesis of the asciminib synthon 4-(chlorodifluoromethoxy)aniline is described in several sources.[83] The route (m)[84] starts by chlorination of the difluoromethoxy group of phthalimide-protected 4-(difluoromethoxy)aniline with chlorine, followed by removal of the protecting group with hydrazine hydrate. Another method (n)[85] descibes the direct fluorination of (trichloromethoxy)benzene by hydrogen fluoride with the catalyst Fluorad FX-8 at high

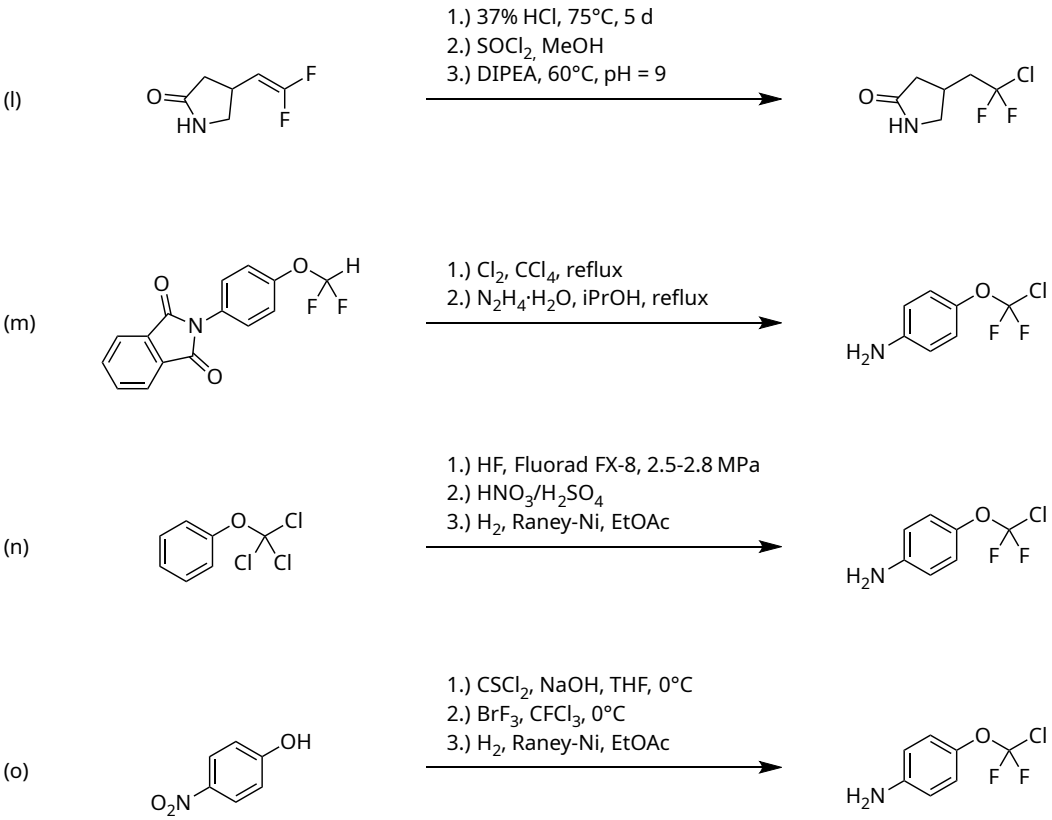


**Scheme 2:** Intermediate syntheses of padsevonil (l) and asciminib (m), (n), (o).

pressure, followed by nitration with $HNO_3$ in *para* position and reduction of the nitro group with $H_2$/Raney-Ni. In 2008, the working group of Rozen established route (o)[86]. The 4-nitrophenol chlorothioformate was formed from 4-nitrophenol using thiophosgene and NaOH as a base. Subsequently, 1-(chlorodifluoromethoxy)-4-nitrobenzene was prepared with $BrF_3$ as fluorinating agent. The authors didn't reduce the nitro group of this derivative, but stated that the reduction of 1-(chlorodifluoromethoxy)-3-nitrobenzene could be obtained by using NaSH in MeOH. However, the reduction of the 4-nitro derivative in concern with $H_2$/Raney-Ni has already been described in method (n).

### 1.3.3 Amino Acids and Peptides

Halogenated amino acids and peptides have been the subject of interest in recent research.[87,88] Several reviews address the occurrence of natural halogenated amino acids in microbial organisms, their bioactive features, or the potential of biomimetic engineering in peptide-based drug development and self-assembly. While a wide range of chlorine-, bromine- and iodine-substituted aromatic amino acids in nature are described, the known aliphatic halogenated amino acids are essentially limited to chlorine derivatives due to reactivity of the halogens in aliphatic compounds. In addition, numerous synthetically accessible halogenated amino acids have been described in the literature.[89,90]

Halogenation of amino acid side chains is an effective tool for modulating the binding selectivity and increasing the binding affinity of peptides.[91] This modification also affects the physicochemical properties of the peptides, such as catabolic stability, lipophilicity, and membrane permeability, as mentioned in Section 1.2 on page 3.[92]

Peptides for therapeutic applications are often derived from natural sources or are protein mimetics modified to improve properties such as stability and affinity. These modifications include e.g. the use of D-amino acids instead of L-amino acids, modification of the peptide backbone, attaching of lipids or polymers, protection of peptide termini, bridging and cyclization to chemically constrained peptides, and incorporation of unnatural building blocks, for instance halogenated amino acids.[93–95]

Thus, $CF_2X$-modified examples of amino acids[96–100] and carbohydrates[101–105] are also reported in the literature. Besides proteins, there are other biopolymers that consist of monomeric units, e.g fatty acids, carbohydrates and nucleobases, which are covalently bonded to form larger molecules or attached to proteins and peptides. As described in Section 1.3.1 on page 6, in previous literature, the $CF_2Br$ group served as an intermediate for $CF_2$ building blocks. In this work, the synthesis routes for new $CF_2X$-containing amino acids and their application in drug design are described. Exemplary synthesis strategies of $CF_2X$-containing alanine and proline derivatives from previous literature are described below (Scheme 3).

In 1998, Amii *et al.* presented a method for synthesizing 3-bromo-3,3-difluoroalanine Schiff bases **p-2** from gycine Schiff bases **p-1** using commercially available $CF_2Br_2$.[96] The starting material **p-1** was treated with lithium 2,2,6,6-tetramethylpiperidide (LTMP)

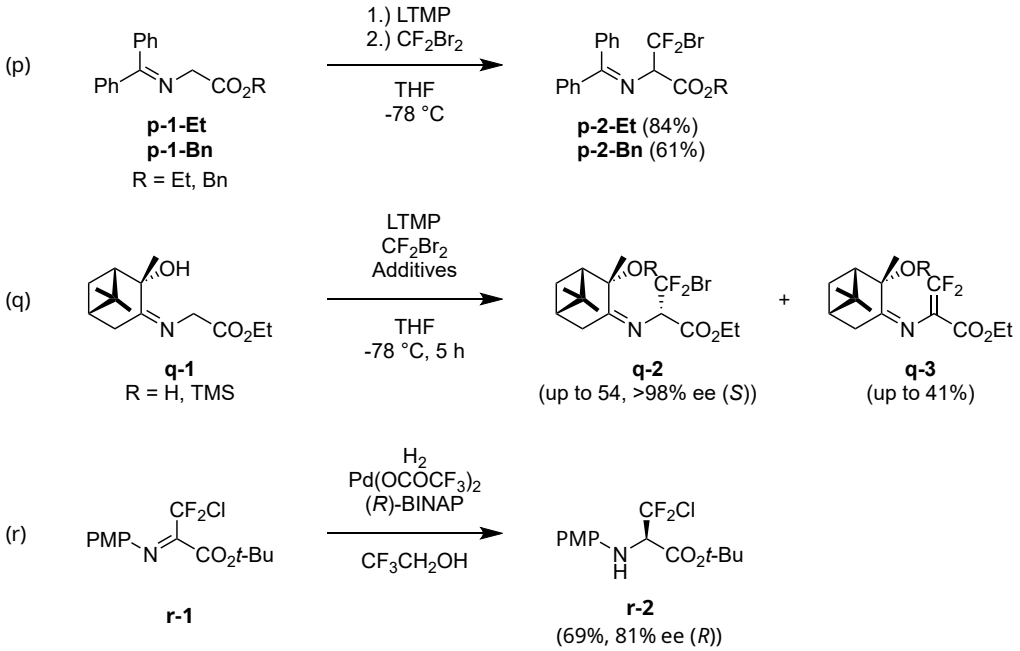


**Scheme 3:** Synthesis of $CF_2X$-bearing alanine derivatives (X = Cl, Br).

in THF at −78 °C followed by $CF_2Br_2$ yielding an enantiomer mixture of **p-2-Et** (84 %) or **p-2-Bn** (61 %). Depending on the further use of the amino acid, it may be essential to obtain an enantiomerically pure substance. Katagiri *et al.* reported in 2001 an efficient synthesis of optically pure 3-bromo-3,3-difluoroalanine derivatives employing a chiral auxiliary strategy.[97] The diastereoselective nucleophilic alkylation of hydroxypinanone glycinate Schiff base **q-1** with $CF_2Br_2$ was optimized using different additives and reaction conditions. The best yield of L-alanine derivatives was achieved with three equivalents trimethylsilyl trifluoromethanesulfonate (TMSOTf) resulting in a mixture of 54 % (>98 % d.e.) **q-2** with R = H and trimethylsilyl (TMS) group, but no side product **q-3**. TMS and the auxiliary can be removed by treatment with 1 N aqueous hydrochloric acid. A different approach is displayed in route (r)[106]: A basic protocol for the synthesis of haloacetimidoyl iodides, followed by homologation reaction obtaining **r-1** was published by Watanabe and coworkers.[107,108] The authors described a catalytic asymmetric method for hydrogenation of **r-1** using hydrogen pressure, a catalytic amount of $Pd(OCOCF_3)_2$ and (*R*)-BINAP in 2,2,2-trifluoroethanol to obtain the (*R*) enantiomer of **r-2** with 69 % (81 % ee) yield. Taking into account the optical purity of the asymmetric hydrogenation route, the data indicate that the overall yield is comparable to the Suzuki method (q). However, the enantiomeric purity is significantly lower.

In 2018, Tolmachova *et al.* disclosured a synthesis route (s)[100] obtaining *trans*-3-$CF_2$X-3-hydroxyprolines (X = Cl, Br), as shown in Scheme 4. Compounds **s-1**[109,110] were reacted with ethyl isocyanoacetate under basic conditions. The reaction gave an *anti*- and *syn*-diastereomers mixture (9:1) of **s-2-Cl** and in case of **s-2-Br** only the *anti* derivatives. The intermediates **s-2** were treated with 6 N HCl, followed by hydroganation with hydrogen

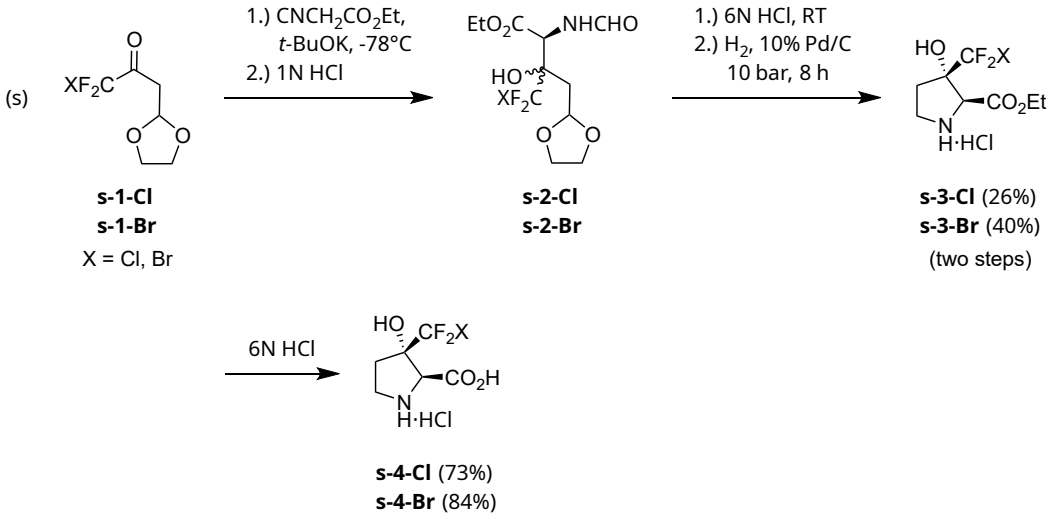


**Scheme 4:** Synthesis of $CF_2$X-bearing proline derivatives (X = Cl, Br).

and catalyst Pd/C to afford **s-3-Cl** and **s-3-Br** with 26 % and 40 % yields, respectively, over two steps. The ester groups were hydrolyzed and the *trans* diastereomers **s-4-Cl** (73 %) and **s-4-Br** (84 %) were isolated by crystallization from ethanol.

# 2 Objective of the Thesis

The major objective of this thesis is the evaluation and the implementation of $CF_2X$ groups (X = Cl, Br, I) as unconventional XB donors in medicinal chemistry and drug discovery. The aim is to assess these moieties for their suitability as an additional tool for drug development and optimization. Based on the spatial behavior of this chemical moiety and its XB capability, we expect potential for promising molecular interactions with target proteins. Substance analogs with $CF_2H$ moieties as potential HB donors and $CF_3$ groups as references are important comparators. The project is divided into three sections and grouped into two parts: Part A, the study of $CF_2X$-containing small molecules (Section 3.1 on page 17 and Section 3.2 on page 64), and Part B, the study of $CF_2Cl$/$CF_2Br$-bearing amino acids and peptides (Section 3.3 on page 78).

Part A elaborates the syntheses of two sets of fragment series containing $CF_2X$ ether and acetamide moieties (X = H, F, Cl, Br, I) to investigate their properties with respect to XB using X-ray crystallography and *in silico*-aided methods. Another aspect is the stability of these fragments. An enlarged series of fragments, which may be expanded into a library in the future, is screened and studied at JNK1 and JNK3 by using biophysical methods such as saturation transfer difference NMR, isothermal titration calorimetry, and protein crystallization. In addition to library screening, a second strategy is evaluated to generate XB hits from the decoration of ligands of the protein database crystal structures with a $CF_2Br$ unit and to rotate this group to find suitable XB interactions. Based on these results, further test fragments were synthesized and also tested against JNK1 and JNK3.

In Part B, the syntheses of amino acids with $CF_2X$-bearing aryl and alkyl side chains are elaborated. For this purpose, amino acids derived mainly from phenylalanine and lysine are prepared, incorporated into MDM2- and MDM4-binding peptide sequences, and evaluated by fluorescence polarization assays and computational methods.

# 3 Results and Discussion

## 3.1 Principles and Applications of $CF_2X$ Moieties as Unconventional Halogen Bond Donors in Medicinal Chemistry, Chemical Biology and Drug Discovery

Parts of this Section 3.1 were published in:

**S. Vaas**, M. O. Zimmermann, D. Schollmeyer, J. Stahlecker, M. U. Engelhardt, J. Rheinganz, B. Drotleff, M. Olfert, M. Lämmerhofer, M. Kramer, T. Stehle, F. M. Boeckler. Principles and Applications of $CF_2X$ Moieties as Unconventional Halogen Bond Donors in Medicinal Chemistry, Chemical Biology and Drug Discovery. *J. Med. Chem.* **2023**, *66* (15), 10202–10225. doi: 10.1021/acs.jmedchem.3c00634[111]



### 3.1.1 Abstract

From monitoring the PDB, we identified the allosteric BCR-ABL inhibitor asciminib as a first example for halogen bonding (XB) through a $CF_2Cl$ group. As an orthogonal principle to the established (hetero)aryl halides, we herein highlight the usefulness of $CF_2X$ (X = Cl, Br, or I) moieties from a variety of perspectives. We establish synthesis pathways leading to tool compounds bearing $CF_2X$ moieties attached to an ether or amide linker and study their chemical and metabolic stability, their logP and solubility, as well as the role of XB in their small molecular crystal structures. Employing QM techniques, we analyze the observed interactions, provide insights into the conformational degrees of freedom, and highlight flexibilities and preferences in the potential interaction space. To foster their use in molecular design, we characterize their highly tuned XB donor capacities and its interaction strength dependent on geometric parameters. Implementation of structurally diversified $CF_2X$ acetamides as a subset into our halogen-enriched fragment library (HEFLib) and biophysical evaluation by STD NMR and ITC, revealed a 1,3,4-thiadiazole pattern binding to JNK1 and JNK3. The crystal structure of fragment **30** with JNK3 exhibits a highly interesting binding mode, featuring an XB of $CF_2Br$ toward the P-loop, as well as chalcogen bonds within **30** and toward the gate keeper methionine. Thus, we suggest that utilizing unexplored chemical space combined with the chance to establish unconventional binding modes, provides excellent opportunities for patentable chemotypes opening new avenues for therapeutic intervention.

### 3.1.2 Introduction

Halogen bonds (XB) are highly directional interactions between the electropositive region on the halogen (X = Cl, Br, I), the σ-hole, and a nucleophilic interaction partner (B), typically an atom containing one or more nonbonding electron pairs, a π-system, or an anion.[112] Aryl halides with an $sp^2$-hybridized carbon-halogen ($C(sp^2)-X$) moiety or ethynyl halide species ($C(sp)-X$) form halogen bonds, which are well studied in organocatalysis[113–116], crystal engineering[117–119], biological systems[120–122], and medicinal chemistry[3,123,124].

In comparison, the use of alkyl halides with an $sp^3$-hybridized carbon-halogen ($C(sp^3)-X$) moiety is often limited by their reactivity, when X can serve as a leaving group for substitution, elimination, and radical reactions. It is also typically perceived that the smaller the s-part of the hybridization, the weaker will be the potential strength of the XB.[125] As a consequence, strong electron-withdrawing groups (EWGs) are required as XB-tuning substituents modulating the electron density at the halogen atom and, thus, improving the XB strength. Ideal EWGs will not only enhance the formation of XBs, but also substantially diminish the reactivity as a prerequisite to utilize this chemistry in different applications. From a design perspective, stabilized $C(sp^3)-X$ moieties help to overcome the limitations of in-plane XBs formed by (hetero)aryl halides and facilitate an orthogonal spatial behavior.

One embodiment of such an ideal EWG is fluorine. Halodifluoromethyl ($C(sp^3)F_2X$) groups are considered to be much less reactive than ($C(sp^3)H_2X$) groups, based on the strong electron-withdrawing properties of both fluorine atoms and their shielding of the carbon atom. In addition, fluorine atoms are small in size and weight, while being able to engage in their own intermolecular contacts, such as orthogonal multipolar interactions.[126]

Numerous synthetic methods have been described in the literature as these $CF_2X$ groups are suitable intermediates for the preparation of trifluoromethyl ($CF_3$)[62,67,127], difluoromethyl ($CF_2H$)[62] and difluoromethylene ($CF_2$)[55,62,67,128] building blocks or for $^{18}$F-labeling of trifluoromethylated compounds[43,45,69,129,130]. α,ω-Dihalo-perfluorinated alkanes or α-halo-perfluorinated alkanes have been widely used as XB tool compounds for studies regarding anion recognition[117,131–134], catalysis and synthesis[135–142], crystal engineering[143–150], host-guest complexes[151–155], materials[156–164], probes for molecular recognition[165–169], self-assembly[170–176], and supramolecular architecture[177–183].

Still, their use to target biological systems in medicinal chemistry, chemical biology, and drug discovery has been rather unexplored. Some halodifluoroacetamide ($-NHCO-CF_2X$) containing agents have been reported with respect to their antifungal activity[73], as well as compounds targeting the calcium-activated chloride channel Transmembrane Protein 16A (TMEM16A)[74]. We recently reported halodifluoroacetamide-containing peptides that bind to E3 ubiquitin-protein ligase MDM2 and MDM4, which are negative regulators of the p53 tumor suppressor (see Section 3.3 on page 78).[184] The epilepsy drug candidate (phase III,

2019) padsevonil with 2-chloro-2,2-difluoroethyl ($-CH_2-CF_2Cl$) moiety has selective affinity for both presynaptic synaptic vesicle 2 (SV2) proteins and postsynaptic central benzodiazepine receptor (cBZR) sites on the γ-aminobutyric acid ($GABA_A$) receptor.[78] Inhibitors of Vascular Endothelial Growth Factor (VEGF) receptors with $CF_2Cl$ ether ($-O-CF_2Cl$) group have been published[79,80], as well as asciminib, an FDA-approved (2021) allosteric inhibitor of ABL1 kinase, targeting the fusion protein BCR-ABL in chronic myeloid leukemia (CML)[76,77]. Except for the example of asciminib, so far, no structural evidence for a $CF_2X\cdots B$ interaction is present in the PDB. Interestingly, the existence of this particular halogen bond was not even highlighted in the corresponding publication.[76]

To the best of our knowledge, $CF_2X$ groups are virtually absent from systematic methods for the exploration of therapeutics beyond these examples. We previously developed our Halogen-Enriched Fragment Library (HEFLib), which consists of about 200 halogenated fragments, to explore the potential of XB in fragment-based approaches.[6,124,185] So far, this library contains exclusively chlorine, bromine, or iodine bound to (hetero)aromatic systems. As a tool for a more systematic exploration of protein binding environments suitable for recognizing $CF_2X$ moieties, we have started to integrate $CF_2X$-bearing fragments in our HEFLibs approach, as outlined herein.

### 3.1.3 Study Design

The protein crystal structure of asciminib with ABL1 kinase mutant T334I_D382N (PDB ID: 5MO4), solved by Wylie *et al.*,[76] revealed an XB interaction between the chlorine atom of the $CF_2Cl$ ether group of asciminib (**20c**) and the backbone carbonyl oxygen of L448 with an almost ideal $C(sp^3)-Cl\cdots O$ angle of 178.3° and a $Cl\cdots O$ distance of 3.3 Å deep in the allosteric myristate binding pocket (Figure 7 on the following page). Based on this structure, we calculated the XB complex formation energies of asciminib and other halogen-substituted derivatives of asciminib at the MP2/TZVPP level of theory, as shown in Table 2 on page 21. The structure of *N*-methylacetamide, as a shortened XB acceptor in the model system, was derived from the peptide bond of L448 in the protein crystal structure of the ABL1 kinase. All atoms of the $CF_2X$ moiety, as well as all hydrogen atoms were optimized for **20a**–**e**, while the scaffold of asciminib and the *N*-methylacetamide was fixed. The complex formation energy of asciminib (**20c**) was $-11.2\,kJ\,mol^{-1}$ (3.3 Å; 178.3°) by using the original coordinates of the $CF_2Cl$ moiety. For reasons of comparability, the $CF_2Cl$ group was relaxed like the modified $CF_2X$ systems, yielding a very similar complex formation energy of $-10.4\,kJ\,mol^{-1}$ at the same distance of 3.3 Å, but with a slightly decreased σ-hole angle of 172.0°. The halogen is almost in plane with the peptide bond (dihedral angle $\delta_{C_\alpha-C=O\cdots Cl}$ = 32.0°) at a bond angle $\alpha_{C=O\cdots Cl}$ of 124.7°, which represents a reasonably good interaction geometry (see the sphere in Figure 7 on the following page).

The best interaction geometries (about −15 kJ mol$^{-1}$) can only be formed perpendicular to the plane of the peptide bond. However, the hydrophobic residues A452, V487, and M491 prevent the formation of such an even more favorable interaction geometry.

The $CF_2Br$-substituted ether **20d** gave a complex formation energy of −15.4 kJ mol$^{-1}$ (3.1 Å) and the iodine derivative **20e** showed −24.0 kJ mol$^{-1}$ (2.9 Å). For the heavier halogens, a shortened interaction distance and an increased interaction strength was revealed, while the σ-hole angle is always close to the optimum. Based on the inability to present a σ-hole toward the backbone carbonyl oxygen (no XB), the $CF_3$ ether **20b** gave much lower interaction energies (−1.6 kJ mol$^{-1}$, 3.6 Å). Due to the smaller size of the hydrogen atom and the reduced length of its bond to the C(sp$^3$) atom, the hydrogen bond (HB) of the

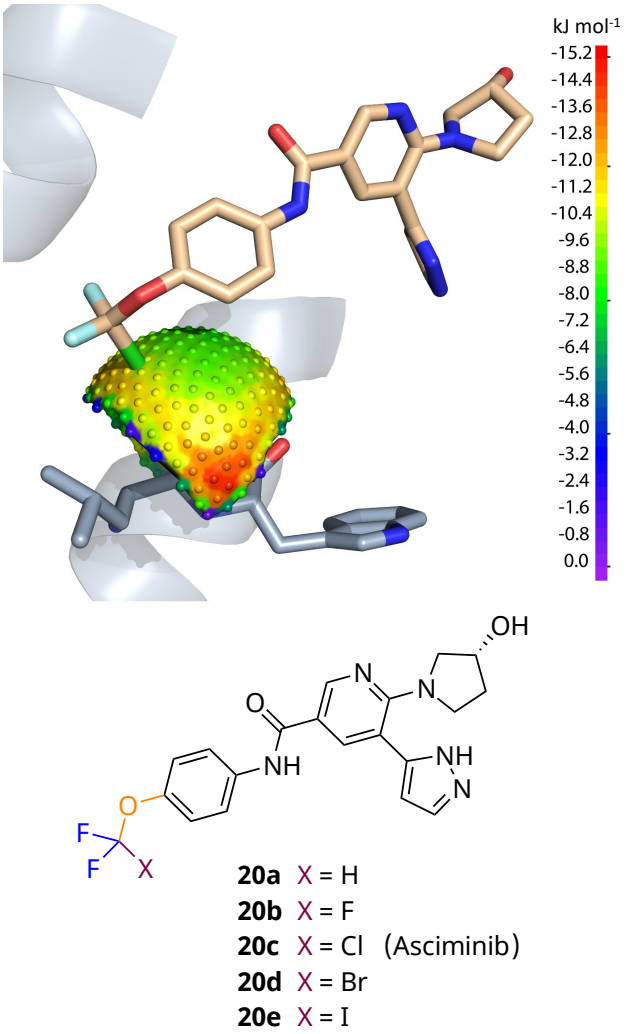


**Figure 7:** XB interaction of asciminib (**20c**) targeting the backbone oxygen of L448 in the myristoyl pocket of ABL1 (T334I_D382N) kinase (PDB ID: 5MO4). The sphere around the backbone carbonyl illustrates by color gradient the direction-dependent interaction energies calculated from using the (chlorodifluoromethoxy)benzene fragment of asciminib at the MP2/TZVPP level of theory. Structural derivatives (**20a**,**b**,**d**, and **20e**) of asciminib (**20c**) are presented herein.

**Table 2:** Calculated complex formation energies ΔE (MP2/TZVPP level in comparison to MP2/QZVPP and M06-2X-D3/TZVPP), interaction distance X···O, and σ-hole angle C−X···O of asciminib (**20c**, $CF_2Cl$) and analogs (**20a**,**b**,**d**,**e**, $CF_2X$ with X = H, F, Br, I) with *N*-methylacetamide, derived from the peptide bond of L448 in the protein crystal structure of ABL1 (T334I_D382N) kinase (PDB ID: 5MO4).

| Compound | X | ΔE (kJ mol$^{-1}$) | | | X···O (Å) | C−X···O (°) |
|---|---|---|---|---|---|---|
| | | MP2/ TZVPP | MP2/ QZVPP[b] | M06-2X-D3/ TZVPP[b] | | |
| **20a** | H | −7.3 | −7.2 | −7.7 | 3.8 | 155.1 |
| **20b** | F | −1.6 | −1.5 | −1.5 | 3.6 | 144.9 |
| **Asciminib (5MO4)**[a] | Cl | −11.2 | −11.2 | −10.5 | 3.3 | 178.3 |
| **Asciminib (20c)** | Cl | −10.4 | −10.4 | −9.7 | 3.3 | 172.0 |
| **20d** | Br | −15.4 | −15.3 | −14.9 | 3.1 | 174.6 |
| **20e** | I | −24.0 | −24.9 | −24.4 | 2.9 | 175.1 |

[a] The $CF_2Cl$ moiety of asciminib was not optimized in this reference calculation.
[b] Single point calculation based on MP2/TZVPP geometry.

$CF_2H$ derivative **20a** is weaker (7.3 kJ mol$^{-1}$, 3.8 Å) than any of the halogen bonds. Comparison with larger basis sets (MP2/QZVPP) or DFT-methods recommendable for halogen bonding (M06-2X-D3/TZVPP) was performed and is illustrated in Table 2. It shows rather good consistency of the reported complex formation energies.

We have shown that all these compounds are synthetically accessible (see Section 3.1.4.3 on page 27). The backbone oxygen of L448 can be addressed by $C(sp^3)F_2$−X ethers with significant XB contributions, while it cannot be targeted by an aromatic $C(sp^2)$−X based on the asciminib scaffold. This finding strengthened our interest in investigating $CF_2X$ groups with respect to the strength of their fluorine-tuned XB interactions and their unconventional interaction geometries.

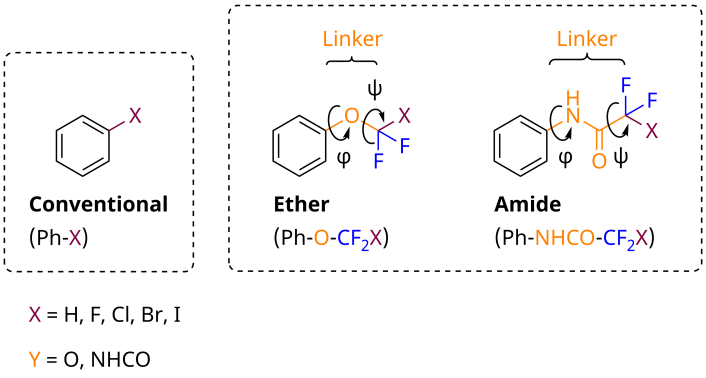


**Figure 8:** General molecular structures of Ph−X and Ph−Y−$CF_2X$ (X = H, F, Cl, Br, I; Y = O, NHCO) with dihedral angles (φ, ψ). The axis of rotation is defined as the middle of the three axes forming the dihedral angle.

Besides halodifluoromethoxy moieties (−O−$CF_2X$), we have subsequently also extended our studies of model systems to halodifluoroacetamide moieties (−NHCO−$CF_2X$). In contrast to aryl halides, both Ph−Y−$CF_2X$ patterns (Y = O, NHCO) have two axes of rotation and consequently two dihedral angles ($\varphi$, $\psi$), as illustrated in Figure 8 on the previous page. However, the amide is an easily synthetically accessible linker, providing an elongated distance between the $CF_2X$ function and the attached scaffold. Based on the resonance effects of the amide bond, this linker behaves rigidly, not increasing the conformational degrees of freedom, while providing complementary, asymmetric capabilities for molecular interactions, e.g., HB donors or acceptors. The novel spatial interaction possibilities of $CF_2X$-bearing ether and amide molecules raise the question of their individual conformational isomerism and dynamics, which we investigated using *in silico* conformational analysis and comparative data analysis of small molecule crystal structures. Using computational and experimental methods, we evaluate further properties of $CF_2X$ moieties, related to their applicability in medicinal chemistry, such as stability, solubility, electro-

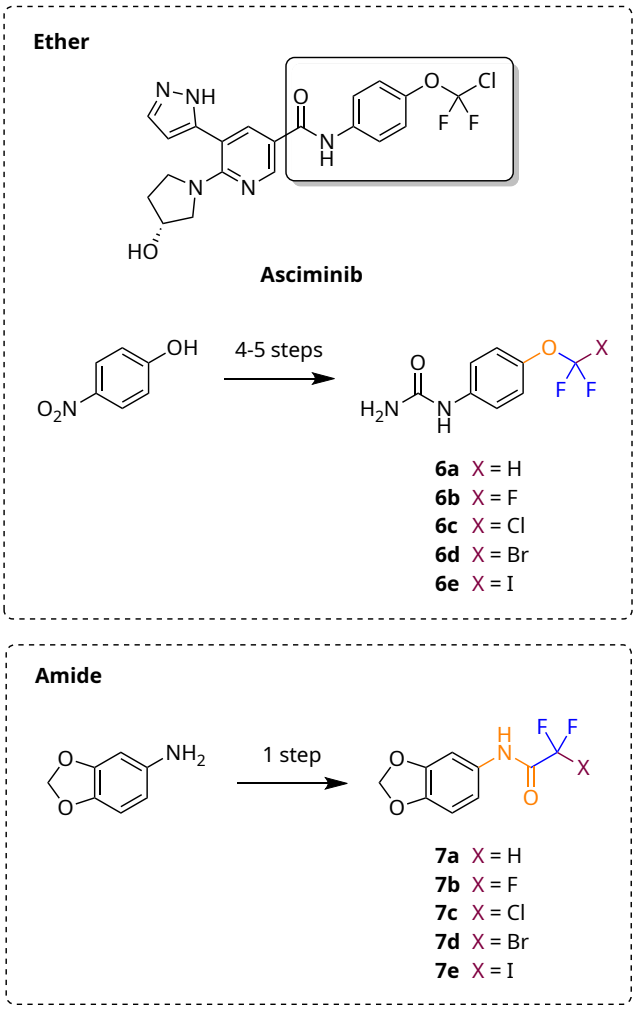


**Figure 9:** 1-(4-(Difluorohalomethoxy)phenyl)urea (**6a**–**e**) and *N*-(benzo[*d*][1,3]dioxol-5-yl)-2,2-difluoro-2-haloacetamide (**7a**–**e**) derivatives for experimental studies.

static properties ($V_{max}$), and their impact on XB strength. In the second pivotal part of this study (Section 3.1.10 on page 54 ff.), we implemented $CF_2X$-containing acetamides into a halogen-enriched fragment library (HEFLib), which we assessed by biophysical screening methods against c-Jun N-terminal kinases 1 and 3 (JNK1 and JNK3).

For our experimental studies using small molecule crystallization and conformational analysis, we have designed two series of ether- and amide-containing molecules (Figure 9 on the preceding page) each with $CF_2X$ units (X = H, F, Cl, Br, I), of which the hydrogen derivatives are enabled to form HBs and the chlorine, bromine, and iodine derivatives are enabled to form XBs. In the case of $CF_2H$, the fluorine atoms significantly increase the polarization of the C−H bond, leading to improved HB.[186] Herein, we do not focus on HBs, but we will use it for the purpose of comparing it to XBs. It was important to choose molecular patterns where all desired derivatives with X = H, F, Cl, Br, or I are synthetically accessible, solid compounds, and capable of forming crystals. As shown in Figure 9, we synthesized $CF_2X$ ether fragments (**6a**–**e**) derived from the structure of the BCR-ABL inhibitor asciminib. Depending on the starting compound, we obtained our desired urea derivatives in up to five synthesis steps. To obtain a similar series of acetamides (**7a**–**e**), we acetylated benzo[*d*][1,3]dioxol-5-amine with the appropriate reagents in one-step syntheses. Apart from $CF_2X$, both chemical patterns have comparable structural elements in different arrangements: a central benzene ring, at least one phenolic ether and an amide substructure. None of the chemical functions is considered particularly reactive.

### 3.1.4 Chemistry

#### 3.1.4.1 Test Fragments for Evaluation of $CF_2X$ Moieties

The required $CF_2H$, $CF_3$ and $CF_2Cl$ ether derivatives of 4-aniline (**5a**–**c**) and 4-nitrobenzene were commercially available. Synthesis methods of $CF_2Cl$[84–86] and $CF_2Br$[43] ethers were described in the literature. For $CF_2Br$ ether and its precursor syntheses, we adapted the methods of Khotavivattana *et al.* (2015) and Zhou *et al.* (2016).[43,187] Regarding $CF_2I$ ether, a new synthesis method had to be established as described below. To our knowledge, only one synthesis method to obtain $CF_2I$ ether has been reported in the literature, but this method was not practical for our applications. Guo *et al.* (2000) described the reaction of nucleophiles such as alcoholates with difluorodiiodomethane ($CF_2I_2$) in DMF at room temperature to their corresponding carbamates as major products and the formation of $CF_2I$ ether moieties as a minor product with low yields of 0–15 %.[188] Moreover, $CF_2I_2$ is a relatively expensive reagent.

Two methods to synthesize intermediate **3** were performed, as shown in Scheme 5 on the following page. The first approach required ethyl 2-bromo-2,2-difluoroacetate as reagent forming an ester intermediate **2**, followed by hydrolysis, all under basic conditions

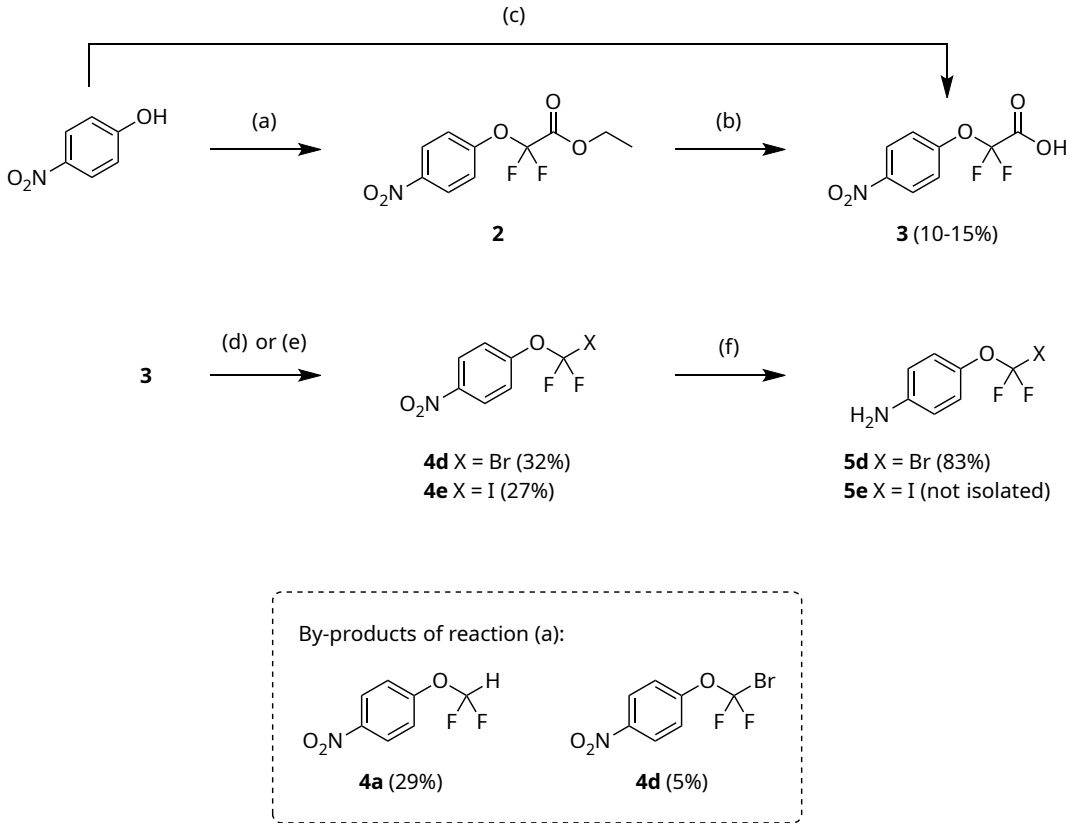


**Scheme 5:** Synthesis of phenylamine derivatives containing $CF_2X$ ether moiety. Reagents and conditions: (a) Ethyl bromodifluoroacetate, $K_2CO_3$, DMF, argon atmosphere, rt, 13 h; (b) 6 M aq. NaOH/$Et_2O$ (1:1), rt, 3 h, 15 % (2 steps); (c) (1) NaH, 1,4-dioxane, argon atmosphere, rt, 30 min; (2) potassium 2-bromo-2,2-difluoroacetate **1a**, 1,4-dioxane, argon atmosphere, 80 °C, 20 h, 10 %; (d) X = Br: (1) $(COCl)_2$, DMF (cat.), DCM, rt, 3 h; (2) DMAP, sodium-*N*-hydroxy-2-thiopyridone, $BrCCl_3$, argon atmosphere, 120 °C, 2 h, 32 %; (e) X = I: (1) $(COCl)_2$, DMF (cat.), DCM, rt, 3 h; (2) $CHI_3$, DMAP, sodium-*N*-hydroxy-2-thiopyridone, toluene, argon atmosphere, 120 °C, 2 h, 27 %; (f) $SnCl_2 \cdot 2\,H_2O$, aq. HCl, EtOH, argon atmosphere, rt, 16 h.

(step (a) / (b)).[43] The synthesis route with potassium 2-bromo-2,2-difluoroacetate (**1b**) led directly to intermediate **3** (step (c)).[187] Low yields were characteristic of these reactions with 4-nitrophenol. The direct methoxy formation of **3** gave 10 % yield. The two-step synthesis with the more elaborate workup of **3** via intermediate **2** gave 15 % yield. Interestingly, during the first step (a), intermediates **4a** (29 %) and **4d** (5 %) were formed with significant yields, relative to the major product **3**, which was not described in literature. Considering the yield of intermediate **4d** from **3** (32 %), as well as time and material, it was cheaper and easier to isolate **4d** as a by-product from step (a). The reason for the formation of **4a** and **4d** was probably the partial hydrolysis in the first step, followed by decarboxylation, which was intercepted by hydrogen and bromine sources.

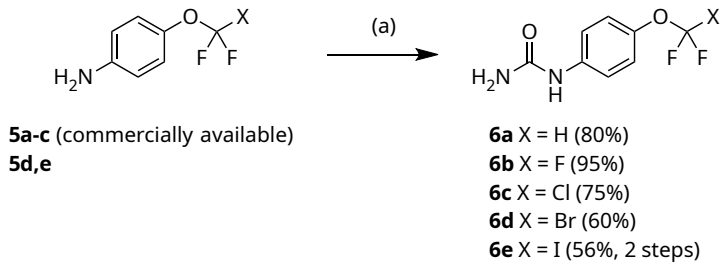


**Scheme 6:** Synthesis of phenylurea derivatives containing $CF_2X$ ether moiety. Reagents and conditions: (a) KCN, 10 % acetic acid, rt, 3 h, 56–95 %.

The syntheses of **4d** and **4e** from **3** were carried out via Barton decarboxylation halogenation to form a Barton ester intermediate, which was decarboxylated in a subsequent step under heat by a radical mechanism. In the presence of a suitable reagent, the radical was scavenged by a halogen source. For bromination reactions, the solvent bromotrichloromethane ($BrCCl_3$) also acted as a radical scavenger yielding 32 % of **4d** (step (d)). For the iodination reaction, the commercially unavailable analog iodotrichloromethane ($ICCl_3$) was not an option. Instead, two equivalents of iodoform ($CHI_3$) in toluene were successfully established as an iodine source for $CF_2I$ ether synthesis with a yield of 27 % for **4e** (step (e)). The subsequent reduction reactions of the nitro group to the amine functionality (**5d**,**e**) were carried out using $SnCl_2$ under acidic conditions and argon atmosphere (step (f)). Derivatives **5a**–**e** were reacted in 10 % acetic acid with potassium cyanide to give their corresponding urea derivatives **6a**–**e** with yields ranging from 56 to 95 % (Scheme 6).

Acetamide ($-NHCO-CF_2X$) compounds **7a**–**d** were obtained under basic conditions from their halogenated acetic anhydrides, with yields of 69–78 % (step (a) in Scheme 7). Since 2,2-difluoro-2-iodoacetic anhydride was not commercially available, the iodine derivative **7e** was prepared from potassium 2,2-difluoro-2-iodoacetate (**1b**) in a yield of 24 %, using propanephosphonic acid anhydride (T3P) as a coupling agent (step (b)).

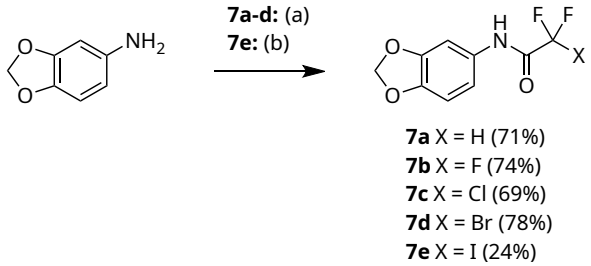


**Scheme 7:** Synthesis of *N*-(benzo[*d*][1,3]dioxol-5-yl)acetamide derivatives. $X^1$ = H, F, Cl, Br; $X^2$ = I. Reagents and conditions: (a) $X^1$: $(X^1F_2CCO)_2O$, NMM, THF, rt, 18 h, 69–78 %; (b) $X^2$: potassium 2,2-difluoro-2-iodoacetate **1b**, T3P (≥50 % solution in EtOAc), DIPEA in DMF, rt, 5 h, 24 %.

Reagents potassium 2-bromo-2,2-difluoroacetate **1a** (99 %) and potassium 2,2-difluoro-2-iodoacetate **1b** (80 %) used in the reactions (c) of Scheme 5 on page 24 and (b) of Scheme 7 on the preceding page were obtained from their corresponding ethyl esters by hydrolysis with KOH.

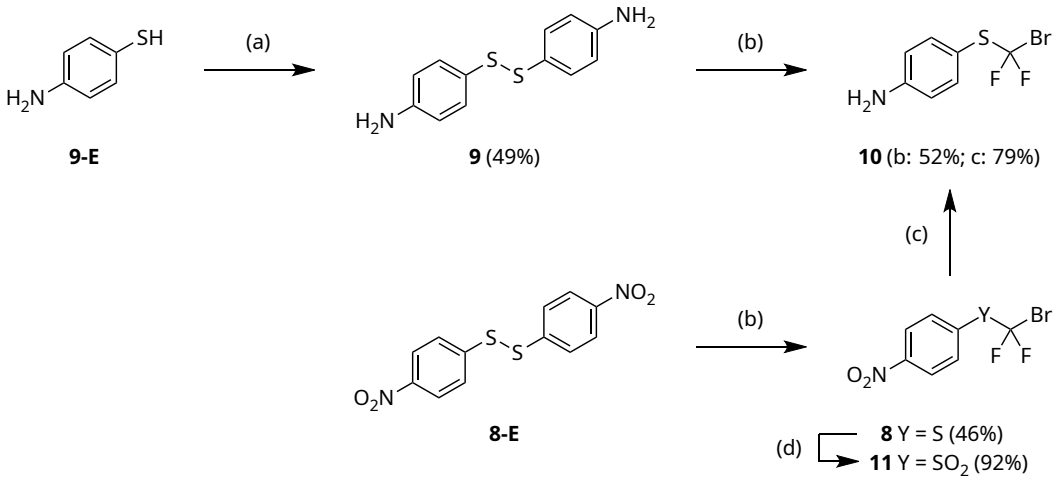


**Scheme 8:** Synthesis of thioether and sulfone derivatives containing $CF_2Br$ moiety. Reagents and conditions: (a) DMSO, rt, 24 h, 49 %; (b) $Na_2HPO_4$, $Na_2S_2O_4$, $CF_2Br_2$, DMF/$H_2O$ (5:1), rt, 18 h, 46–52 %; (c) $SnCl_2 \cdot 2\,H_2O$, aq. HCl, EtOH, argon atmosphere, rt, 16 h, 79 %; (d) mCPBA, DCM, rt, 18 h, 92 %.

Solely for our stability tests in Section 3.1.5 on page 31 ff., we synthesized sulfone and thioether derivatives, as shown in Scheme 8. Bromodifluoromethyl sulfides ($-S-CF_2Br$) can be prepared from their corresponding thiols according to the literature.[189,190] However, this is subject to limitations with regard to further protic functionalities such as amines. As shown in Scheme 8, bromodifluoromethylsulfane groups were prepared from their corresponding disulfides. For this purpose, the appropriate thiols were first oxidized (**9**). Then, sulphur dioxide radical anion precursor sodium dithionite produced the electrophilic bromodifluoromethyl radical which was captured by disulfides (**9**, 1,2-bis(4-nitrophenyl)-disulfane) obtaining bromodifluoromethyl sulfanes (**8** and **10**).[43,191] Intermediate **8** was also oxidized to sulfone ($-SO_2-CF_2Br$) derivative **11**.[190]

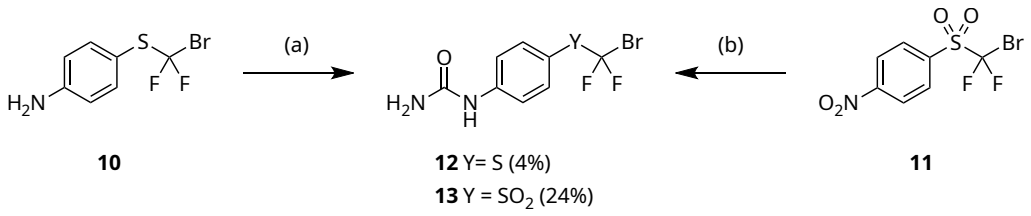


**Scheme 9:** Synthesis of 4-phenylurea derivatives. Y = S, $SO_2$. Reagents and conditions: (a) KCN, 10 % acetic acid, rt, 3 h; (b) (1) $SnCl_2 \cdot 2\,H_2O$, aq. HCl, EtOH, argon atmosphere, rt, 16 h; (2) KCN, 10 % acetic acid, rt, 3 h.

As shown in Scheme 9 on the facing page, thioether derivative **10** was reacted in 10 % acetic acid with potassium cyanide to give its corresponding urea derivative **12** with extremely low yield of 4 %. The two-step synthesis (reduction and urea formation) of compound **13** from intermediate **11** gave a yield of 24 %.

### 3.1.4.2 Fragment Library

The assessment of the small fragment library presented in this work includes mostly $CF_2X$ acetamides (Section 3.1.10 on page 54 ff.). All tested acetamide and non-acetamide fragments are summarized in Table 11 on page 55. For amide synthesis, inexpensive and diverse fragment structures were acquired. Two General Procedures **D** and **I** using acetic anhydrides were established and applied depending on the solubility of the substance to be reacted (Scheme 10; see also the General Procedures of Section 6.3.1 on page 137 and page 139) except for $CF_2I$-containing fragments, whose corresponding anhydride was not commercially available. Due to different reactivities and omitted reaction optimization, yields could vary. Acetamide fragments bearing $CF_2I$ moiety were prepared according to General Procedure **H** from potassium 2,2-difluoro-2-iodo-acetate **1b** using coupling reagent T3P (see Section 6.3.1 on page 139).

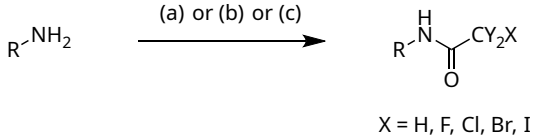


**Scheme 10:** Synthesis of acetamides containing $CF_2X$ moiety. $X^1$ = H, F, Cl, Br; $X^2$ = I. Reagents and conditions: (a) $X^1$, General Procedure **D**: corresponding acetic anhydride, NMM, THF, 18 h, rt; (b) $X^1$, General Procedure **I**: corresponding acetic anhydride, $Et_3N$, DCM, 18 h, rt; (c) $X^2$, General Procedure **H**: **1b**, T3P in EtOAc, DIPEA, DCM, argon atmosphere, rt, 1 h.

### 3.1.4.3 Asciminib Derivatives (20a–e)

Asciminib is a protein kinase inhibitor for the treatment of Philadelphia chromosome-positive chronic myeloid leukemia (Ph+ CML) that was approved for medical use in the United States in October 2021.[192] This agent is an antineoplastic drug from the new class of STAMP inhibitors, the abbreviation for "Specifically Targeting the ABL Myristoyl Pocket".[193] In wild-type ABL1, the myristoyl pocket is an allosteric binding site for the myristoylated *N*-terminus, which is absent in the BCR-ABL fusion protein, leading to mis-regulation with constitutive activity. Asciminib binds to this allosteric site with inhibitory activity.[77]

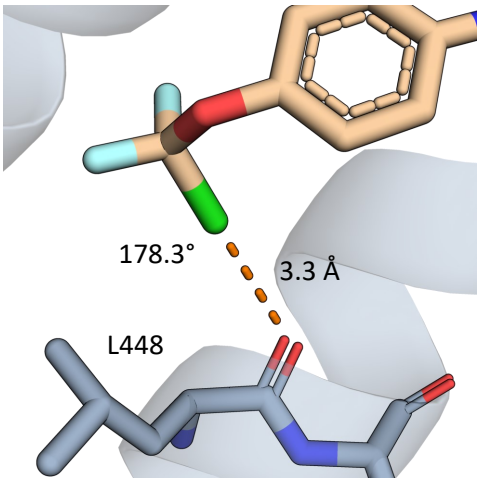


**Figure 10:** Binding geometry of the $-O-CF_2Cl$ moiety of ascminib (**20c**) in ABL1 kinase (T334I_D382N) in complex with asciminib and nilotinib. PDB ID: 5MO4.

**Table 3:** Comparision between calculated complex formation energies ΔE of **20a**–**e** in PDB ID: 5MO4 with *in silico* halogen substitution.

| Compound | X | ΔE (kJ mol$^{-1}$) |
|---|---|---|
| **20a** | H | −7.3 |
| **20b** | F | −1.6 |
| **20c** | Cl | −10.4 |
| **20d** | Br | −15.4 |
| **20e** | I | −24.0 |

As described in Section 3.1.3 on page 19, the binding of asciminib involves a $-O-CF_2Cl$ group that forms a halogen bond with the oxygen of the backbone of L448, depicted in Figure 10 on the next page (PDB ID: 5MO4).[76] The angle of 178.3° formed in the crystal structure is almost ideal. The chlorine-oxygen distance of 3.3 Å is favorable in terms of interaction distance, but still leaves space for the theoretical substitution of chlorine by spatially larger atoms such as bromine and iodine. As shown in Table 3, calculations of the XB complex formation energy ΔE at the MP2/TZVPP level of theory showed a value of −10.4 kJ mol$^{-1}$ for chlorine, a substitution by bromine −15.4 kJ mol$^{-1}$ and a value of −24.0 kJ mol$^{-1}$ for iodine. Accordingly, the halogen bond appears to contribute significantly to the binding of the molecule. An elaborated synthesis procedure (Scheme 11 on the next page) for the preparation of brominated and iodinated asciminib derivatives, which might have better affinities due to the higher strength of the halogen bond, is presented below.

The development and a four-step synthetic pathway of asciminib with an overall yield of 42.5 % were described by Schoepfer *et al.* in 2018.[77] To reduce the total number of required synthesis steps, the synthesis sequence of the individual reaction steps was amended. Thus, the amide coupling of **5a**–**e** was not done in the first step, but in a later stage as illustrated in Scheme 11 on the facing page. As a result, the number of synthesis steps could be reduced from a total of 20 to as few as 13 steps. Intermediate **15** was prepared from methyl 5-bromo-6-chloronicotinate (**14**) with (*R*)-pyrrolidin-3-ol hydrochloride via $S_NAr$ reaction. Subsequent Suzuki coupling with 1-(tetrahydro-2*H*-pyran-2-yl)-5-(4,4,5,5-tetramethyl-1,3,2-dioxaborolan-2-yl)-1*H*-pyrazole provided **16a** followed by ester hydrolysis to afford the pivotal intermediate **17a**. The fragments **5a**–**e** were attached via coupling reagents to obtain **18a**–**e**, followed by a deprotection step with TFA to provide the desired

test compounds **20a**–**e**. An alternative synthesis pathway (Method B) involved additional protection of the alcohol group of **16a** with THP to form **16b** and subsequent hydrolysis to obtain the pivotal intermediate **17b**. Test compounds **20a**–**e** were obtained by treating the acid chloride of **17b** with **5a**–**e** and THP deprotection without isolating **19a**–**e** separatly.

The comparison between the yields in the final reaction steps gave higher yields for method B (acid chloride) compared to method A (coupling reagent EDCI) as shown in Table 4 on the next page. An exception was **20e**, where method A gave the better yields. However, it should be noted that the incoorperation reactions of $CF_2X$ ether moiety were mostly performed only once. Furthermore, method B required an additional THP protection step. The overall yield of **17a** (Method A) starting from **15** was 76.5 %, while for **17b** (Method B) it was 65.7 %, which had an influence on the overall yield.

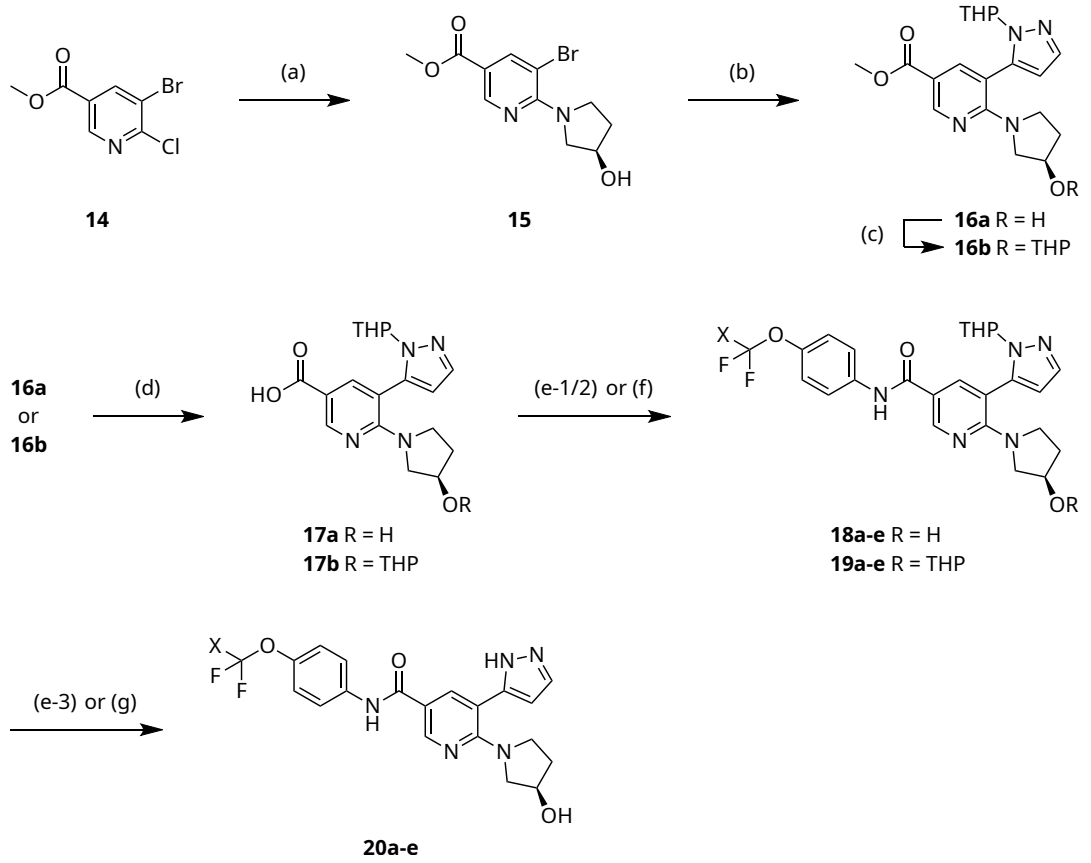


**Scheme 11:** Synthesis of Asciminib derivatives. X = H, F, Cl, Br, I; R = H, THP. Reagents and conditions: (a) (*R*)-Pyrrolidin-3-ol hydrochloride, DIPEA, *i*-PrOH, 70 °C, 14 h, 96 %; (b) 1-(tetrahydro-2*H*-pyran-2-yl)-5-(4,4,5,5-tetramethyl-1,3,2-dioxaborolan-2-yl)-1*H*-pyrazole, $K_3PO_4$, $Pd(PPh_3)_2Cl_2$, toluene, argon atmosphere, 95 °C, 36 h, 79 %; (c) DHP, PTSA, DCM, 40 °C, 48 h, 88 %; (d) NaOH, MeOH/$H_2O$ (3:1), rt, 16–19 h, 77–97 %; (e-1/2) (1) **17b**, DMF, $(COCl)_2$, DCM, 0 °C to rt, 3 h; (2) **5a**–**e**, $Et_3N$, THF, 0 °C to rt, 16 h; (e-3) **19a**–**e**, TFA, DCM, 0 °C to rt, 3 h, 10–69 %; (f) **17a**, **5a**–**e**, EDCI · HCl, HOBt · $H_2O$, DMAP, DIPEA, THF, 45 °C, 48 h, 27–67 %; (g) **18a**–**e**, TFA, DCM, 0 °C to rt, 4 h, 31–51 %;

**Table 4:** Comparision between yields of **5a**–**e** incooperation and THP deprotection step to obtain the final products **20a**–**e**. X = H, F, Cl, Br, I and reactions (e)–(g) as shown in Scheme 11 on the preceding page. Yields in %.

| | | Method A | | | Method B |
|---|---|---|---|---|---|
| Compound | X | (f) | (g) | (f) and (g) | (e) |
| **20a** | H | 22.2 | 33.9 | 7.5 | 29.6 |
| **20b** | F | 66.6 | 50.8 | 33.8 | 69.2 |
| **20c** | Cl | 30.6 | 30.8 | 9.4 | 19.7 |
| **20d** | Br | 26.8 | 51.3 | 13.7 | 39.4 |
| **20e** | I | 30.5 | 43.1 | 13.1 | 10.3 |

As later described in Section 3.1.7 on page 40 and Section 5.3 on page 118, an attempt was made to form small molecule crystals from **20a**–**e**. However, the asciminib derivatives precipitated as amorphous solids. All attempts to evaluate the derivatives **20a**–**e**, particularly asciminib (**20c**), for binding affinity and inhibitory properties failed. Among others, the ADP-Glo Kinase Assay from Promega, the Kinase HotSpot Profiling Assay from Reaction Biology, and the cell-based InCELL Pulse ABL1 Target Engagement Assay from Eurofins did not provide useful measurement results. Whether this was due to the assay conditions, the assay design not being optimized for the new allosteric binding mode, or inappropriate ABL1 constructs could not be determined beyond doubt, but was attempted to be ruled out in advance. However, despite the lack of evaluation capabilities in this instance, it has been demonstrated that there are certainly practical applications for the $-O-CF_2X$ group. $-O-CF_2Br$ and $-O-CF_2I$ moieties are synthetically accessible and can be incorporated into active pharmaceutical agents.

### 3.1.5 Chemical and Metabolic Stability

Since the chemical and metabolic stability of a ligand is of particular importance in drug discovery, we performed an initial evaluation of these unconventional $CF_2X$-bearing moieties using a glutathione (GSH) and microsomal stability assay (MSA) under aqueous conditions (pH 7.4). A distinction always had to be made between reactions related to the function under study and those occurring elsewhere in the molecule, as far as this was possible. While glutathione nucleophilically substitutes reactive substances, microsomes essentially contain phase I enzymes, primarily cytochromes P450 (CYPs), catalyzing monooxygenase reactions.

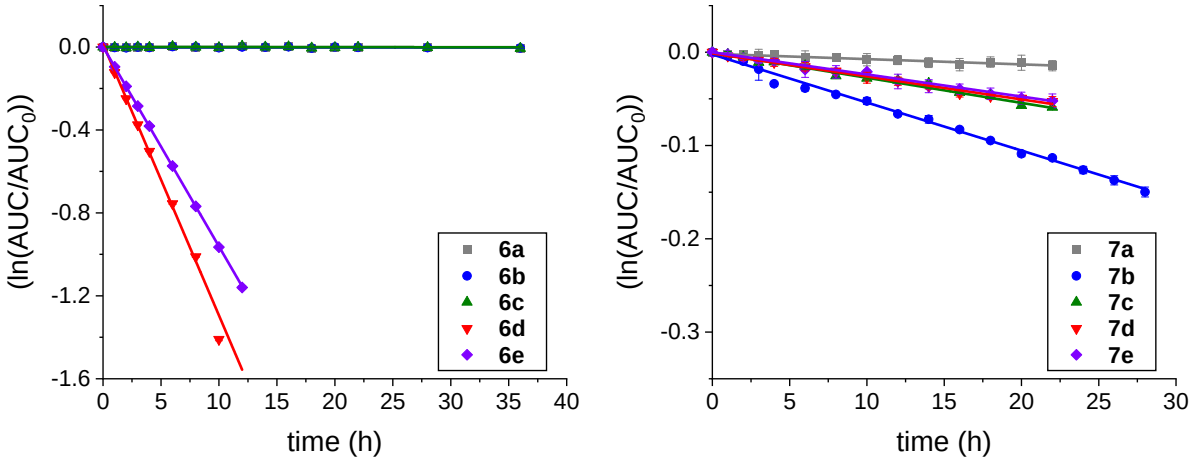


**(a)** GSH: **6a–e** **(b)** GSH: **7a–e**

**Figure 11:** Glutathione stability assay in 10 mM PBS buffer (pH 7.4) containing 10 % (v/v) ACN at 37 °C. Each measurement was performed in triplicate. **(a)** Compounds **6a–e** ($-O-CF_2X$). **(b)** Compounds **7a–e** ($-NHCO-CF_2X$).

A graphical representation of the chemical stability assay (GSH assay) is shown in Figure 11. As summarized in Table 5, the stabilities in the GSH assay vary considerably. With the exception of **6d**,**e**, the half-life $t_{1/2}$ of all compounds amounts to several days.

**Table 5:** Glutathione stability assay of compounds **6a–e** and **7a–e** measured at concentrations of 250 µM with 5 mM GSH and 100 µM internal standard, at 37 °C in 10 mM PBS (pH 7.4) containing 10 % (v/v) ACN. Each measurement was performed in triplicate.

| | Ether **6a–e** | | Amide **7a–e** | |
|---|---|---|---|---|
| X | **6** | $t_{1/2}$ (h) | **7** | $t_{1/2}$ (h) |
| H | **a** | >1200 | **a** | >1200 |
| F | **b** | >1200 | **b** | 130 |
| Cl | **c** | >1200 | **c** | 260 |
| Br | **d** | 5.3 | **d** | 280 |
| I | **e** | 7.2 | **e** | 290 |

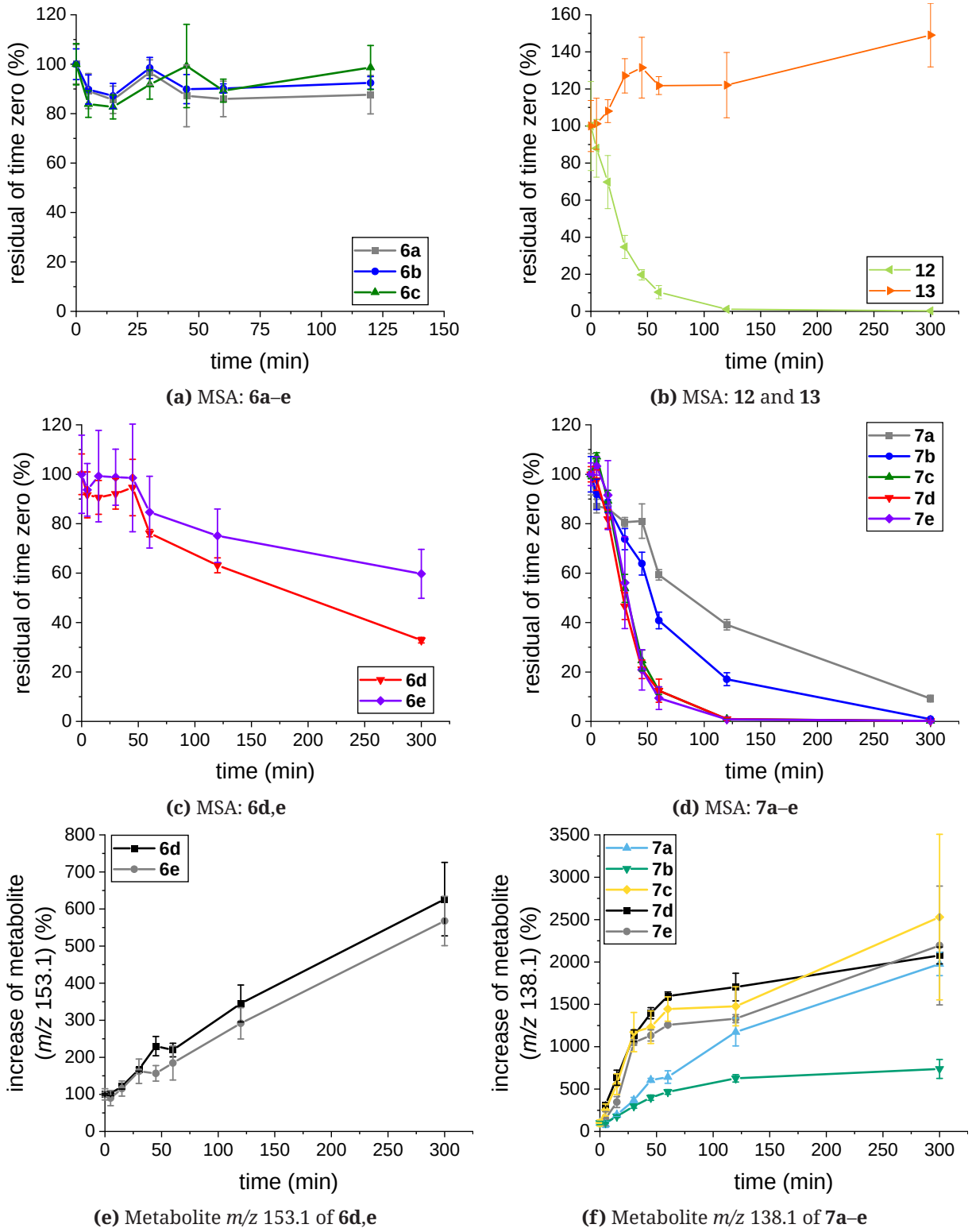


**(a)** MSA: **6a–e**

**(b)** MSA: **12** and **13**

**(c)** MSA: **6d**,**e**

**(d)** MSA: **7a–e**

**(e)** Metabolite *m/z* 153.1 of **6d**,**e**

**(f)** Metabolite *m/z* 138.1 of **7a–e**

**Figure 12:** Microsomal stability assay in 100 mM in potassium phosphate buffer (pH 7.4) at 37 °C. X = H, F, Br, Cl, I. **(a,c)** Compounds **6a–e** (−O−$CF_2$X). **(b)** Compounds **12** (−S−$CF_2$Br) and **13** (−$SO_2$−$CF_2$Br). **(d)** Compounds **7a–e** (−NHCO−$CF_2$X). **(e)** Metabolite *m/z* 153.1 of **6d**,**e** corresponds to [M+H−$OCF_2$X]. **(f)** Metabolite *m/z* 138.1 of **7a–e** corresponds to [M+H−$COCF_2$X].

The half-lives $t_{1/2}$ derived from curve fits of the obtained data of **6d** and **6e** are 5.3 and 7.2 hours, respectively. The resulting $t_{1/2}$ values for amides **7b**–**e** range from 130 to 290 hours, while all other compounds (**6a**–**c** and **7a**) are even more stable, exceeding 1200 hours. In particular, the HB donors **6a** and **7a** as well as the XB donors **6c** and **7c**–**e** are characterized by GSH half-lives of at least 10 days.

In the MSA (Figure 12 on the preceding page), amides **7a**–**e** showed a metabolite with *m/z* = 138.1 in small amounts, corresponding to amide cleavage and a loss of the respective $COCF_2X$ group. While the thioether **12** with $CF_2Br$ moiety was rapidly degraded, the analogous sulfone **13** was stable. Ethers **6a**–**c** were stable in the MSA, whereas ethers **6d**,**e** lost their $CF_2X$ group, which was accompanied by an increase in the corresponding phenolic metabolite (*m/z* 153.1). Due to the structural similarity of **6d**,**e** to acetaminophen (paracetamol), a comparable meachnism involving reactive NAPQI-like intermediates is possible (Scheme 12).[194] In the human organism, acetaminophen is inactivated mainly by sulfation and glucuronidation. A small amount is *N*-hydroxylated by CYP3A4 / CYP2E1 and subsequently dehydrated to toxic *N*-acetyl-*p*-benzoquinone imine (NAPQI). The imine is detoxified and inactivated by glutathione conjugation.

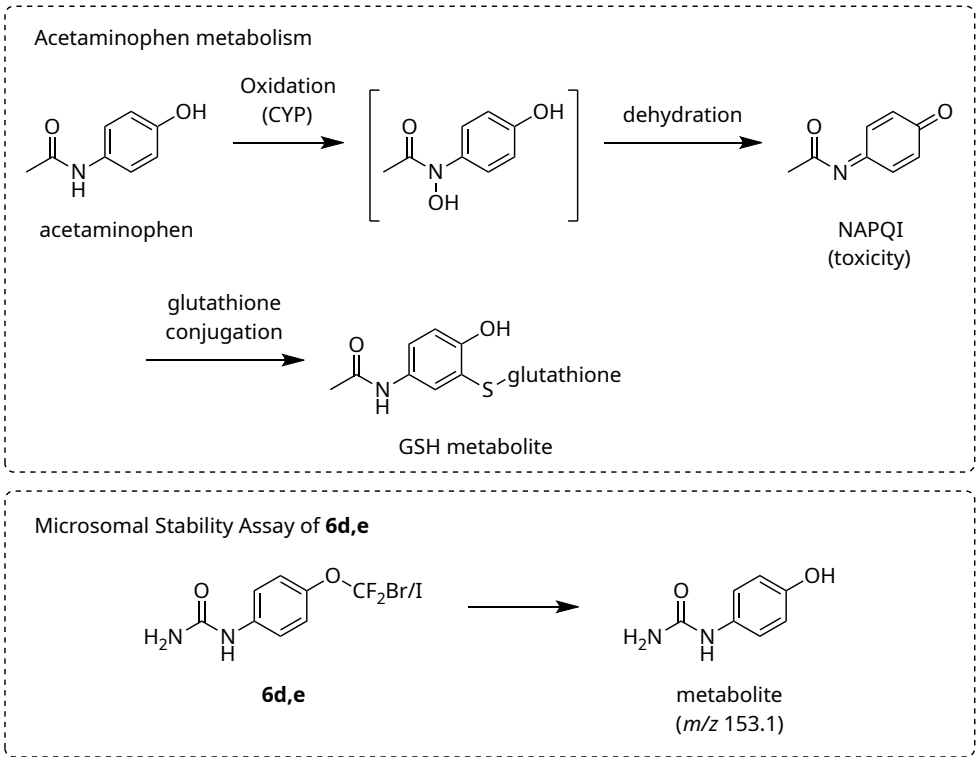


**Scheme 12:** Acetaminphen (paracetamol) cytochrome P-450 metabolism pathway (phase I) and glutathione conjugation (phase II). Observed metabolite *m/z* 153.1 in the microsomal stability assay of **6d**,**e**.

### 3.1.6 LogP and Solubility

As an indicator for the hydrophilicity / lipophilicity of a compound, the logP was calculated using Schrödinger QikProp (Table 6).[195,196] The logP is defined as the logarithm of the partition coefficient (ratio of organic-to-aqueous phase concentrations). Smaller or more negative values highlight higher hydrophilicity, whereas larger values indicate a higher lipophilicity.[197] This property is a key characteristic of drug molecules, affecting their absorption, distribution, metabolism, and excretion.[198] Although it can be an indicator of solubility, it is not the only criterion determining solubility.

**Table 6:** LogP values for model compounds, including **6a**–**e** and **7a**–**e**, calculated using Schrödinger QikProp.

| 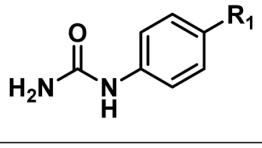 | amide 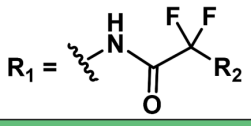 | ether (**6a**-**e**) 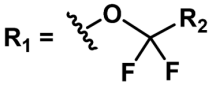 | 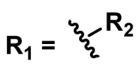 |
|---|---|---|---|
| $R_2$ = H | 0.005 | 0.838 | 0.641 |
| $R_2$ = F | 0.244 | 1.014 | 0.669 |
| $R_2$ = Cl | 0.525 | 1.301 | 0.671 |
| $R_2$ = Br | 0.591 | 1.39 | 0.636 |
| $R_2$ = I | 0.668 | 1.471 | 0.629 |

| 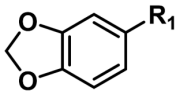 | amide (**7a**-**e**) 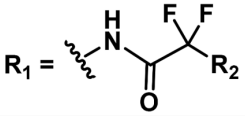 | ether 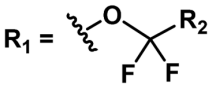 | 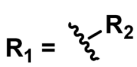 |
|---|---|---|---|
| $R_2$ = H | 1.631 | 2.821 | 1.500 |
| $R_2$ = F | 1.878 | 2.947 | 1.652 |
| $R_2$ = Cl | 2.169 | 3.322 | 2.107 |
| $R_2$ = Br | 2.239 | 3.472 | 2.263 |
| $R_2$ = I | 2.315 | 3.582 | 2.330 |

For our compounds, the logP values of **6c**–**e** range from 1.301 to 1.471, with the respective value increasing from Cl < Br < I. The logP values of **7c**–**e** range from 2.169 to 2.315 following a similar trend for the different halogens than before. We virtually generated all different combinations of the phenylurea scaffold (substituted in position 4) in the upper part of Table 6 or the benzo[*d*][1,3]dioxole scaffold (substituted in position 5) in the lower part

of Table 6 with the substituents being hydrogen or any of the halogens (F, Cl, Br, I) either directly attached to the scaffold (as a representation of the arylhalides) or attached to 2,2-difluoroacetamide or difluoromethoxy as a linker. Independent of whether hydrogen or any halogen is attached, the amides always gave lower logP values by 1.18 ± 0.08 for the benzo[*d*][1,3]dioxoles and by 0.80 ± 0.03 for the phenylurea derivatives. Based on the higher polarity of the amide linker and its capability to donate and accept hydrogen bonds, this systematic difference is unsurprising.

We also compared the arylhalides with each linker and found that the amides very often closely match the logP of the respective arylhalides (ΔlogP ~ 0.08 ± 0.26) with 1-phenylurea (ΔlogP ~ 0.64) and 1-(4-fluorophenyl)urea (ΔlogP ~ 0.43) being outliers. The ether linker was always profoundly more lipophilic than the simple respective arylhalide. For the phenylurea scaffold the difference was ΔlogP ~ 0.55 ± 0.27, for the benzo[*d*][1,3]dioxole scaffold, the difference was even larger with ΔlogP ~ 1.26 ± 0.05.

For the amides, the change from hydrogen to fluorine increased the logP by 0.24 ± 0.01, for the ether linker, by 0.15 ± 0.04. Halogen exchange from fluorine to chlorine produced a stronger increase (0.29 ± 0.01 for the amides and 0.33 ± 0.06 for the ether linkers), than exchange of chlorine to bromine (0.09 ± 0.04) or bromine to iodine (0.09 ± 0.02). In summary, the lipophilicity of the compounds increases slightly from $CF_2H$ to $CF_3$ to $CF_2Cl$, but then only marginally to $CF_2Br$ and $CF_2I$. It should be noted that the statistical fit of the logP (octanol/water) model in QikProp was reported to have a coefficient of determination $r^2$ = 0.93 and an RMSD = 0.50. Thus, there are certain statistical limitations of the model and the interpretation of smaller effects discussed before should be taken with caution.

In addition, it appears reasonable that the model cannot properly recognize the anisotropic nature of the electron distribution around chlorine, bromine, and iodine, as illustrated by the ESP plots in Figure 14 on page 37. (Alternative mapping of positive and negative ESP onto the 0.001 au contour of the electronic density can be found in Figure 14 on page 37.) The size of the positive potential (orange/red surfaces, oriented toward above the aromatic ring in the ether model structures and oriented toward the right side away from the plane in the amide model structures) increases from $CF_2Cl$ to $CF_2Br$ to $CF_2I$, while it is not visible in $CF_3$. This positive potential (highlighted by green arrows) is the "electrostatic embodiment" of the σ-hole, piercing though the negative electrostatic potential typically found equatorially around the halogen chlorine, bromine, and iodine. The electron withdrawing effects of the geminal fluorine atoms foster the size and range of the positive potentials. From this electrostatic visualization it is difficult to estimate, how strong the influence of these electrostatic features will be on logP and solubility, however, it is plausible that they could favor iodine over bromine over chlorine over fluorine.

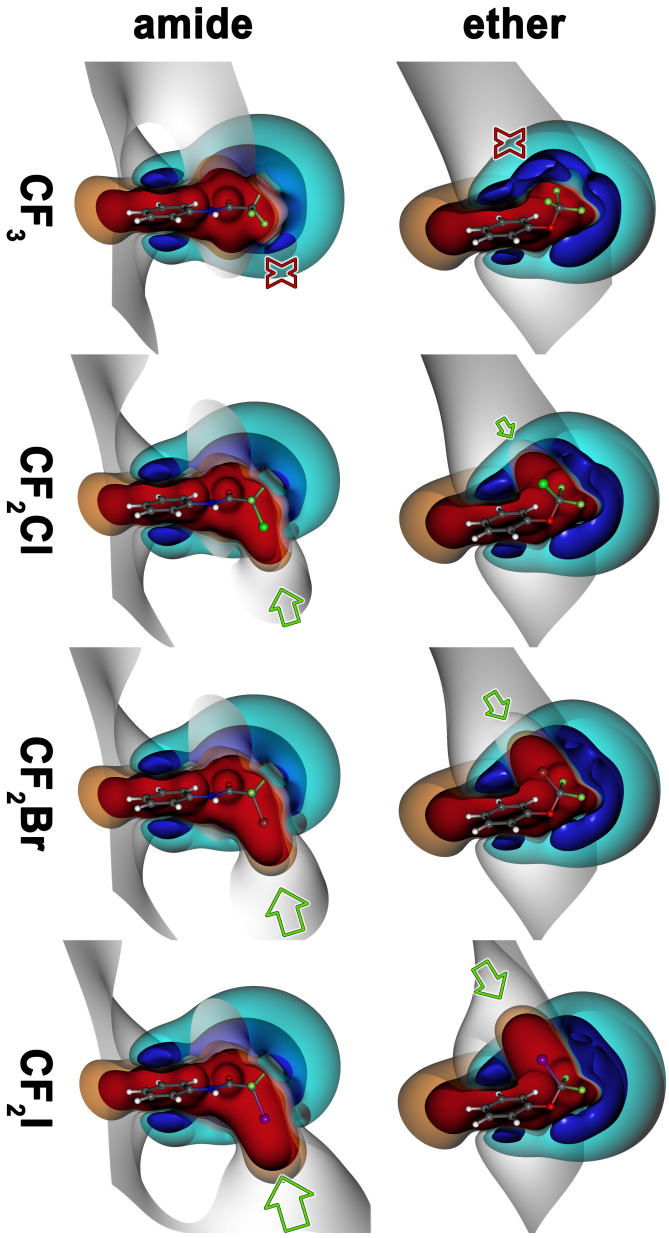


**Figure 13:** ESP isosurface depictions of model compounds (2,2-difluoro-2-halomethoxybenzenes = "ether" or 2,2-difluoro-2-halo-*N*-phenyl-acetamides = "amide") bearing different functional moieties ($CF_3$, $CF_2Cl$, $CF_2Br$, $CF_2I$) calculated at the MP2/TZVPP level of theory. Negative ESP isosurfaces at an energy of −0.01 au are colored in dark blue and at an energy of −0.005 au in cyan. Positive ESP isosurfaces at +0.01 au are colored in red and at an energy of +0.005 au in orange. The isosurfaces at 0.000 au, indicating the boundaries for the transition between negative and positive ESPs, are shown as gray surfaces. Increasing positive potentials representing the σ-hole on the halogen opposite the C−X bond are visible from $CF_3$ to $CF_2Cl$ to $CF_2Br$ to $CF_2I$. They are highlighted by increasing green arrows, while red crosses mark the position where $CF_3$ lacks a similar σ-hole. Structures are shown as balls and sticks. All pictures were prepared with MOLCAD.[1,2]

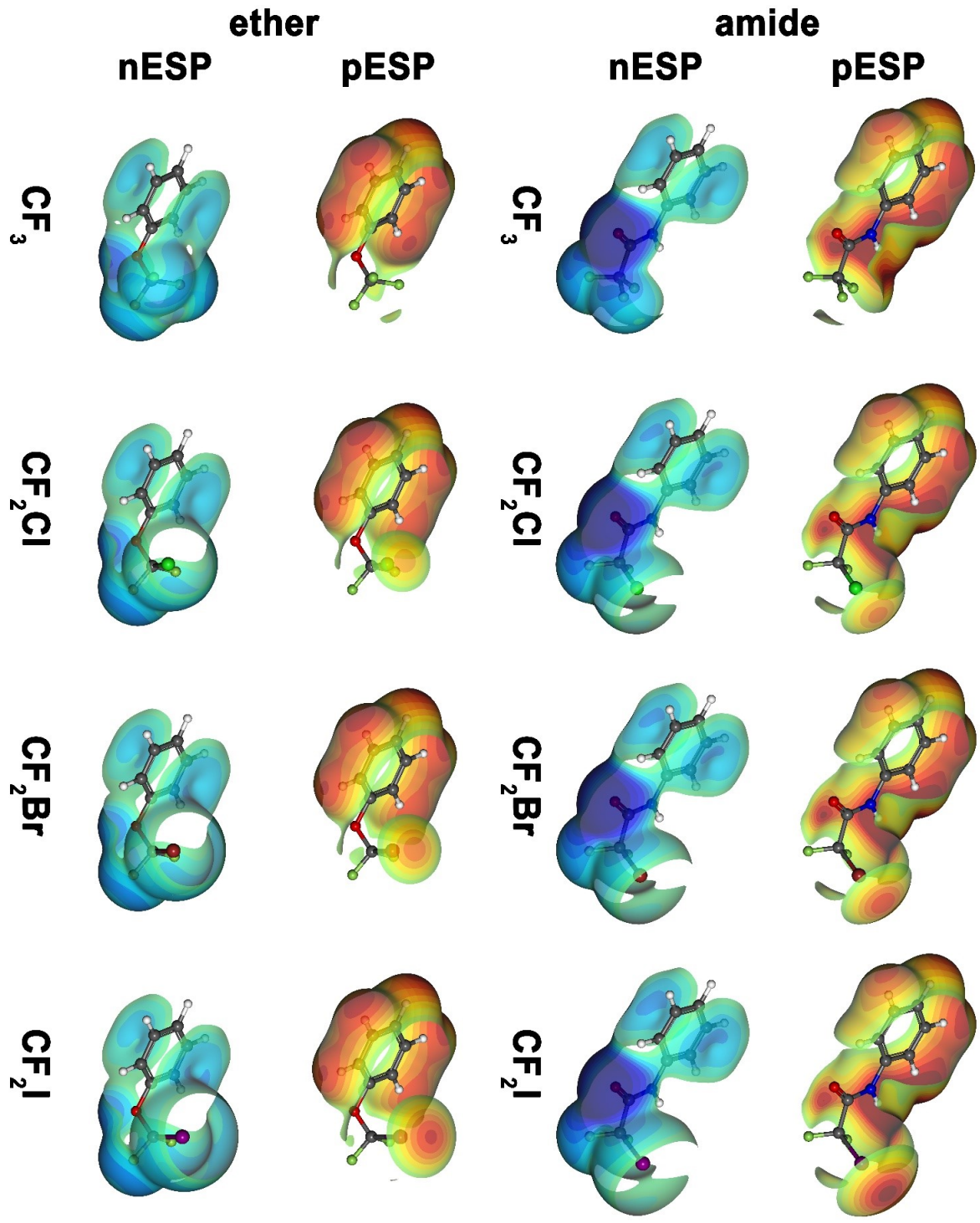


**Figure 14:** Positive (pESP) and negative electrostatic potentials (nESP) of model compounds (2,2-difluoro-2-halo-methoxybenzenes = "ether" or 2,2-difluoro-2-halo-*N*-phenyl-acetamides = "amide") bearing different functional moieties ($CF_3$, $CF_2Cl$, $CF_2Br$, $CF_2I$) mapped onto the 0.001 au contour of the electronic density obtained at the MP2/TZVPP level of theory.

To investigate this more deeply, we measured the kinetic solubility of **6a**–**e** and **7a**–**e** with a turbidimetric assay in the concentration range of 0.43 mM to 5 mM in a buffer (50 mM HEPES, 100 mM NaCl, pH 7.4) containing 5 % (v/v) DMSO to mimic typical assay conditions. The occurrence of precipitates was monitored in a time-dependent manner over approximately 1 hour by measuring light scattering between 600 nm and 800 nm in a 96 well plate, freshly shaken before each measurement cycle. The concentration-dependent absorption spectra for all compounds, measured at the beginning (3 minutes), an intermediate cycle (25 minutes) and at the end (53 minutes) can be found in the literature.[111] The highest concentration up to which no scattering is observed is reported as "minimal instant solubility" (MIS) based on the first measurement cycle and as "minimal final solubility" (MFS) based on the last measurement cycle. These results were compared to logS predictions also done by QikProp.

For the phenylurea scaffold bearing an ether linker, MIS and MFS were identical for **6a**, **6d** and **6c** with values of 5 mM, 5 mM, and 4 mM, respectively. $CF_3$-bearing **6b** had an MIS of 3.2 mM and an MFS of 2.6 mM, while the $CF_2I$-bearing **6e** had also an MIS of 3.2 mM, but an MFS of 2 mM. For **6a** ($CF_2H$) and **6d** ($CF_2Br$) no evidence of precipitation was found at the highest concentration tested. Thus, the actual solubility could be even significantly higher. Predictions by QikProp suggest solubilities of about 46 mM for **6a**, 28 mM for **6b**, 10 mM for **6c** and **6d**, and 8 mM for **6e**. Although the prediction is rather close to the measurement, the more limited solubility of $CF_3$ (**6b**) and the rather good solubility of the bromine derivative (**6d**) are somewhat surprising.

For the benzo[*d*][1,3]dioxole scaffold (**7a**–**e**), for all compounds except **7e** ($CF_2I$) an MIS value of 5 mM was determined. The same MFS of 5 mM was found for **7a**, **7c**, and **7d**. For the $CF_3$ derivative **7b**, the MFS decreased to 4 mM. The $CF_2I$ derivative **7e** had a slightly more limited solubility of 3.2 mM (MIS) and 2 mM (MFS). QikProp predicted always a clearly lower solubility than that for the ether compounds (**6a**–**e**). **7a** was suggested to have a 7 mM solubility. As the determined concentration of 5 mM was the maximal concentration available, the real solubility could be actually 7 mM or higher. For **7b**, a slightly reduced solubility of 4 mM was predicted and confirmed by the experimental assay. While the solubility for **7c**–**e** was predicted to be approximately the same (1.5 to 1.9 mM), the reduced solubility for chlorine (**7c**) and bromine (**7d**) cannot be confirmed by the experimental values (5 mM or higher). For the iodinated compound (**7e**) an MIS of 3.2 mM and an MFS of 2 mM were found, thus, the prediction of 1.6 mM is quite good. Based on the published statistical parameters of the QikProp logS model ($r^2$ = 0.91 and RMSE = 0.63 log units), the prediction is reasonably well in line with the experiment. Still, it cannot be used to differentiate small, but experimentally important differences. As a more general trend from the turbidimetric assay, we find slightly reduced solubility of the $CF_2I$-bearing compounds **6e** and **7e**. The results for the $CF_3$ groups (**6b**/**7b**) were more heterogeneous. Overall,

the tool compounds exhibited solubilities, that still allow the usage of typical biophysical fragment-screening techniques. As a consequence, we provide QikProp logP (o/w) and logS predictions, as well as MIS and MFS values determined by experiment for all fragment-sized compounds (**21**–**31**, **35**, **38**, **40**–**46**) reported in a subsequent Table A1 on page 230.

### 3.1.7 Small Molecule Crystals

We crystallized compounds **6a**–**e** (CCDC IDs: 2248877, 2232102–2232105) and **7a**–**e** (CCDC IDs: 2232106–2232110), which typically formed long, colorless needles or plates. The crystals were grown as described in Section 5.3 on page 118 via vapor diffusion or solvent evaporation. The crystal structure data sets are in Appendix A.7 on page 255. The crystallization experiments of asciminib derivatives (**20a**–**e**) led to formation of amorphous solids.

#### 3.1.7.1 $CF_2X$ Ether Moiety (6a–e)

As shown in Table 7, **6a**–**e** constituted different crystal systems and space groups. Common to all crystal structures **6a**–**e** is their self-assembly in stacks mediated by parallel-displaced π-π stacking of the aromatic rings, HB between the urea components (bidentate O1···H1N/H2NB contacts), and nonpolar contacts between the hydrophobic ether groups, with no solvent molecules in the crystal lattice (Figures A14–A18, A24 on page 255 ff.). **6a** and **6b** form both the symmetric orthorhombic space group $P2_12_12_1$. Because of the poor quality of **6a**, this data set should be taken with caution, but the crystal structure has essentially the same modification as **6b**. The chlorine derivative **6c** ($P2_1/n$) has a much more complicated superstructure, reflected in the high number of single molecules in the asymmetric monoclinic cell. 24 individual molecules arrange themselves in six different conformations (molecules A–F), which differ only very slightly (Figure 15a on the next page). A different self-assembly is presumably due to the larger van der Waals radius of the halogen and the longer C−Cl bond length (~1.7 Å) compared to C−F (~1.3 Å), which causes a change in self-assembly. The $CF_2Cl$ ether groups face each other with a

**Table 7:** Crystallographic data for **6a**–**e**.

| | **6a** | **6b** | **6c** | **6d** | **6e** |
|---|---|---|---|---|---|
| X | H | F | Cl | Br | I |
| crystal system | ortho-rhombic | ortho-rhombic | monoclinic | triclinic | monoclinic |
| space group | $P2_12_12_1$ | $P2_12_12_1$ | $P2_1/n$ | $P\bar{1}$ | $P2_1/n$ |
| a (Å) | 4.583 | 4.603 | 23.504 | 4.614 | 11.011 |
| b (Å) | 5.359 | 5.311 | 9.021 | 8.548 | 4.601 |
| c (Å) | 34.717 | 36.096 | 28.905 | 12.925 | 19.813 |
| α (°) | 90.0 | 90.0 | 90.0 | 75.698 | 90.0 |
| β (°) | 90.0 | 90.0 | 106.05 | 82.322 | 96.097 |
| γ (°) | 90.0 | 90.0 | 90.0 | 77.166 | 90.0 |
| cell volume ($Å^3$) | 852.80 | 882.43 | 5890.1 | 480.01 | 998.10 |
| Z | 4 | 4 | 24 | 2 | 4 |
| cal. density ($mg\,m^{-3}$) | 1.575 | 1.657 | 1.601 | 1.945 | 2.183 |

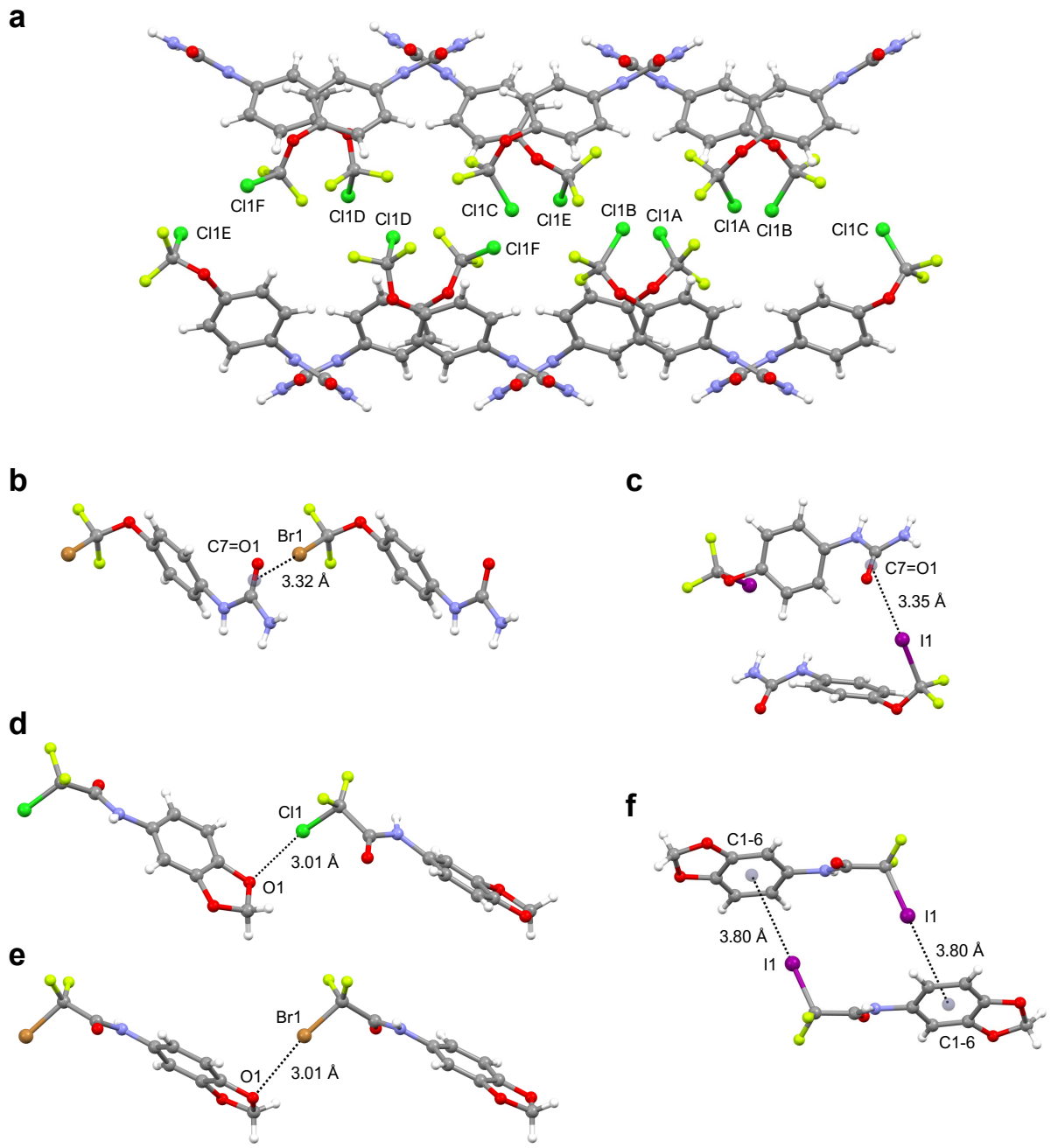


**Figure 15:** Crystal structures of **6c–e** and **7c–e**. **(a)** Crystal structure of **6c**. Shown is the arrangement of $2 \times 6$ single molecules A–F (single molecules with Cl1A–F atom). View along the *b* axis. **(b–f)** Overview of XB interactions between two single molecules: **(b)** Crystal structure of **6d** (Br1···(C7=O1), 3.32 Å). **(c)** Crystal structure of **6e** (I1···(C7=O1), 3.35 Å). **(d)** Crystal structure of **7c** (molecule A, Cl1···O1, 3.01 Å). **(e)** Crystal structure of **7d** (molecule A, Br1···O1, 3.01 Å). **(f)** Crystal structure of **7e** (I1···(C1-6), 3.80 Å); view along the *b* axis.

variety of six different XB interaction geometries in molecules A to F (see Figure A26 and Table A21 on pages 277–278): Distances between chlorine as an XB donor and fluorine as an XB acceptor range from 3.14 Å and 3.60 Å with σ-hole angles between 142.2° and 166.5°.

Besides fluorine, also chlorine can act as an XB acceptor, however, only at much weaker interaction geometries: Distances can be found at 3.524 Å and 4.281 Å, with σ-hole angles of 145.5° and 140.6°, respectively.

**6d** forms an asymmetric triclinic crystal system with space group $P\bar{1}$ and **6e** constitutes a monoclinic space group $P2_1/n$. While in the crystals of **6a**–**c** the polar urea and nonpolar halogenated methoxy groups have no spatial contact with each other, the lattice layers of **6d**,**e** shift toward each other in an effort to form an XB, preserving the displaced π-stacking (Figure A24c,d on page 275). Thus, the bromine and iodine atoms are involved in XB interactions, in which the electron-rich π cloud of the urea carbonyl C=O bond interacts as an XB acceptor (Figure 15b,c on the previous page: Br1···(C7=O1), 3.32 Å, 175.4°; I1···(C7=O1), 3.35 Å, 176.9°). Besides the modification change caused by XB, the differences in self-assembly between **6d** and **6e** can be explained by the different magnitudes of the van der Waals radii and C−X distances (C−Br, 1.95 Å; C−I, 2.15 Å). For **6d**,**e**, we calculated the complex formation energies of the XB interactions between two single molecules of the crystals and performed distance scans by varying the distance along the C8−X1 axes (MP2/TZVPP), as shown in Figure 16. Previously we rotated the XB donor molecule of **6e** 180° along its C8−I1 axis to reduce energy contributions of other molecular interactions. The XB of **6d** contributes −14.6 kJ mol$^{-1}$, and **6e** gives −22.8 kJ mol$^{-1}$ (Table 9 on page 45).

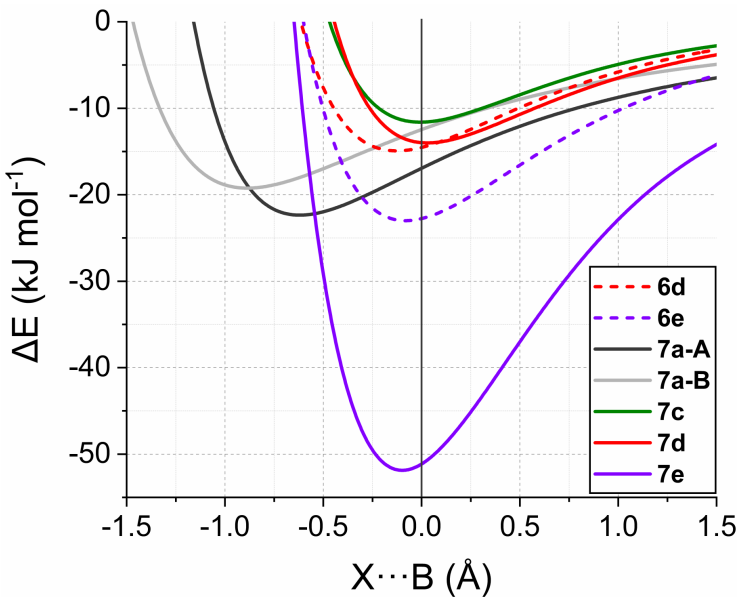


**Figure 16:** Calculated complex formation energies ΔE in kJ mol$^{-1}$ determined using a distance scan of **6d**,**e** along their C8−X1 axes and **7a**,**c**–**e** along their C9−H1/X1 axes. The XB donor of **6e** was rotated 180° along its C8−I1 axis to reduce energy contributions of other molecular interactions. The distance scan for **7e** includes a pair of two single molecules with two mutual XB contacts, doubling the interaction energy at least. The distances were varied with an increment of 0.1 Å of each step, whereby x = 0.0 Å corresponds to the original HB/XB distance found in the individual crystal structures.

Both deviate only slightly from the calculated energy minimum. It is important to note that we performed these calculations to support our analysis and interpretation of the interactions found in the crystal structures, but not for purposes of systematically comparing the interaction strength of the $CF_2X$ moieties.

#### 3.1.7.2 $CF_2X$ Acetamide Moiety (7a–e)

Common characteristics of crystals **7a**–**e** are parallel-displaced π-π stacking and HB between amides (O3···H1N, ~2.0 Å; Figures A19–A23 and A25 on page 265 ff.). Various weaker CH side contacts on the halogens are additionally present. No solvent molecules are integrated in the crystal lattices. As shown in Table 8, **7a** and **7b** assemble into asymmetric crystal systems with the triclinic space group $P\bar{1}$ and monoclinic C2/c, respectively. The cell of **7a** contains two independent molecules (molecules A and B), each forming an HB between the $CF_2H$ group and the amide oxygen of the other type of molecule (Figure 17 on the following page: O3B···H9A, 2.89 Å, −16.9 kJ mol$^{-1}$; O3A···H9B, 3.33 Å, −12.5 kJ mol$^{-1}$). It should be noted that these intermolecular interactions are likely dominated by the classical HBs (H1NA···O3B, 1.99 Å; H2NB···O3A, 2.96 Å). Thus, the $CF_2H$···O3A/B contact does not reach its full potential (see the curve optimum for both contacts in Figure 16 on the preceding page). In addition, neither the interaction partner of $CF_2Cl$ / $CF_2Br$ (O1 in the benzo[*d*][1,3]dioxole substructure), nor the interaction partner of $CF_2I$ (delocalized π-system of the aromatic ring) can be targeted by $CF_2H$.

**Table 8:** Crystallographic data for **7a**–**e**.

| | **7a** | **7b** | **7c** | **7d** | **7e** |
|---|---|---|---|---|---|
| X | H | F | Cl | Br | I |
| crystal system | triclinic | monoclinic | ortho-rhombic | ortho-rhombic | monoclinic |
| space group | $P\bar{1}$ | C2/c | $Pna2_1$ | $Pna2_1$ | $P2_1/n$ |
| a (Å) | 4.067 | 17.293 | 9.956 | 9.945 | 13.154 |
| b (Å) | 22.496 | 5.033 | 19.625 | 20.146 | 5.065 |
| c (Å) | 9.579 | 21.184 | 4.844 | 4.880 | 16.165 |
| α (°) | 90.793 | 90.0 | 90.0 | 90.0 | 90.0 |
| β (°) | 100.07 | 105.30 | 90.0 | 90.0 | 99.687 |
| γ (°) | 89.197 | 90.0 | 90.0 | 90.0 | 90.0 |
| cell volume (Å$^3$) | 862.62 | 1778.4 | 946.39 | 977.60 | 1061.6 |
| Z | 4 | 8 | 4 | 4 | 4 |
| cal. density (mg m$^{-3}$) | 1.657 | 1.742 | 1.752 | 1.998 | 2.134 |

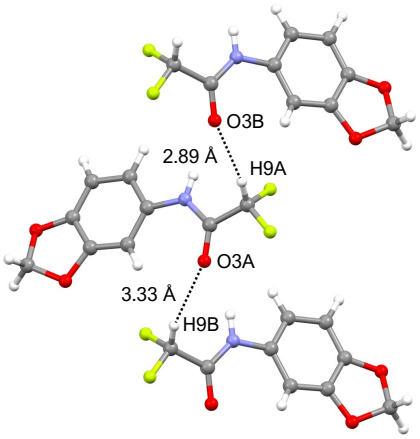


**Figure 17:** HB interactions of $CF_2H$ groups in the crystal structure of **7a** (O3B···H9A, 2.89 Å; O3A···H9B, 3.33 Å). View along the *a* axis.

The symmetric orthorhombic crystals ($Pna2_1$) of compounds **7c** and **7d** are isomorphic. Interestingly, the amides are disordered, with two variants (molecules A and B) flipped by 180° with respect to each other, each having an occupancy of 50 % (Figures A21 and A22 on page 269 ff.). The partitioned occupancy indicates that both nonsymmetric variants of the crystal molecules A and B are energetically equivalent. This also affects the respective locations of the fluorine atoms F1 and F2, while the heavier halogens Cl1 and Br1 remain largely fixed. The carbon atom C9, on the other hand, could not be meaningfully resolved into two positions. Hence, the C9−Cl1 and C9−Br1 bond vectors, which are important for forming the XB, have virtually the same orientation. Both structures are engaged in XBs targeting O1 of the benzo[*d*][1,3]dioxole structure as an XB acceptor (Figure 15d,e on page 41. Cl1···O1, 3.01 Å, 170.8°; Br1···O1, 3.01 Å, 171.9°).

Acetamide **7e** forms an asymmetric monoclinic crystal system with the space group $P2_1/n$ and is the only crystal structure in which the heavier halogen is oriented toward the delocalized π-electrons of the aromatic ring (Figure 15 on page 41: I1···C1-6(centroid), 3.80 Å, 175.0°). Comparison with the trifluoroacetamide **7b** shows that enabling HB (**7a**) and XB (**7c**–**e**) leads to very specific changes in the crystal lattice. As shown in Figure A25 on page 276, an HB network is maintained along the amides, and the individual molecules in **7a**,**c**,**d** alternately adopt a position more orthogonal to that of each other (Figure A25c–e). In **7e**, the lattice is rearranged so that two single molecules direct their iodine atom toward each other's parallel-aligned aromatic rings (Figure A25b). We performed a distance scan analogous to that for **6d**,**e** (Figure 16 on page 42). The XBs of **7c** and **7d** contribute $-11.7\,kJ\,mol^{-1}$ and $-14.1\,kJ\,mol^{-1}$, respectively (Table 9 on the facing page). The mutual iodine-π interactions of two single molecules of **7e** yield a total energy ΔE of $-51.3\,kJ\,mol^{-1}$. Artificially restricting this system to one XB only clarifies that only slightly less than half of the interaction energy could be attributable to one XB contact. Unlike the XB-capable deriva-

**Table 9:** Determined XB distances X···B, σ-hole angles C−X···B and calculated complex formation energies ΔE of **6d**,**e**, **7c**–**e** and asciminib (**20c**) (PDB ID: 5MO4).

| | XB donor | XB acceptor | X···B (Å) | C−X···B (°) | ΔE (kJ mol$^{-1}$) |
|---|---|---|---|---|---|
| **6d** | Br1 | (C7=O1)[c] | 3.321 | 175.4 | –14.6 |
| **6e** | I1 | (C7=O1)[c] | 3.348 | 176.9 | –22.8 |
| Asciminib (**20c**)[a] | Cl | O(L448)[d] | 3.27 | 178.3 | –11.2 |
| **7c**[b] | Cl1 | O1 | 3.009(6) | 170.8(3) | –11.7 |
| **7d**[b] | Br1 | O1 | 3.014(6) | 171.9(3) | –14.1 |
| **7e** | I1 | (C1-6)[c] | 3.797 | 175 | –51.3[e] |

[a] Based on the PDB ID: 5MO4.[76]
[b] Isomorphic crystal structures.
[c] Represents the centroids of the XB acceptor.
[d] Backbone oxygen of L448 in ABL1 (T334I_D382N).
[e] ΔE of a pair of two single molecules with two mutual XB contacts.

tives, **7a** cannot fully exploit the potential of HB because the ΔE minimum requires a closer acceptor-donor contact, which is not realized in the crystal lattice. So far, the computational efforts were intended to illustrate the importance of certain contacts observed in our small molecule crystal structures. In subsequent paragraphs, we analyze the optimal conformations and interaction geometries that allow to harness the full potential of $CF_2X$ moieties based on halogen bonding.

### 3.1.8 Conformational Analysis

In the next step, we used conformational analysis (gasphase) to investigate whether $CF_2X$ groups (X = H, Cl, Br, I) with ether or amide linker systems adopt preferred geometries and whether these are consistent with our experimental data. For this purpose, we used geometry-optimized model molecules (Figure 8 on page 21), which we rotated along their rotatable binding axes in increments of 10° steps to determine the relative energy changes $\Delta E$ in $kJ\,mol^{-1}$ from single point calculations. Because no optimizations were conducted after each rotation step with the dihedral angles ($\varphi$, $\psi$) being constrained, the resulting energies of geometries more distant to the starting point are typically higher than after constrained relaxation. This can slightly underestimate the number of good to excellent conformations and cause the plots to be not fully symmetric. As illustrated in Figure 18a,b on the facing page, the potential energy surface profiles of the ethers are very different compared to the amide. The red mark corresponds to the dihedral angles ($\varphi$, $\psi$) of the initial geometry-optimized conformations and gray areas are regions with high energy levels of $\Delta E > 100\,kJ\,mol^{-1}$, which we assumed to be highly improbable geometries. These disallowed surface areas ($\Delta E > 100\,kJ\,mol^{-1}$) of ether functionalities with X = Cl, Br, I vary from 25 to 27 % and equals 14 % for X = H. While there are only few areas of very low conformational energies (dark blue in Figure 18a) for X = Cl, Br, I, these favored conformational areas are significantly increased for $CF_2H$. Thus, the XB donors will form good interactions with acceptors in the binding site more selectively than the HB donor. Likewise, the higher conformational restrictions of the XB donors are likely to give them an entropic advantage.

Among the amide molecules (Figure 18b), the iodine derivative shows the highest maximum of $67.2\,kJ\,mol^{-1}$ relative to its geometry-optimized structure. It is evident that the rotational barriers are significantly lower, and more conformational degrees of freedom of the $CF_2X$ groups are possible, compared to the ether analogs (Figure 18a). The $CF_2H$ and $CF_2X$ groups show plots that are more similar for the amide linker. However, the preferred $\varphi$ angle of $CF_2H$ is located approximately between 120° and 180° (and between −120° and −180°), whereas the preferred $\varphi$ angle of $CF_2X$ is roughly 60° to 120° (or −60° to −120°).

To illustrate the agreement between this theoretical evaluation and our small molecular crystal structures, we annotated the plots with the experimentally determined conformations. Based on symmetry effects in these dihedral plots and alternatives to measure the $\psi$ angle due to the exact alignment of the 180° flipped phenyl ring, the same conformation found in a crystal structure could be annotated for positive or negative values of $\varphi$. This is illustrated for ether derivatives in Figure 18d and for amide derivatives in Figure 18e. The structure of the energy minima for the spherical-octahedral form for the spherical form of the X-ray diffraction of the $OCF_2X$ is shown as C1, C2, and C3 with the flipped versions ($\psi \pm 180°$) depicted as transparent sticks. Based on the coplanarity of the amide and the

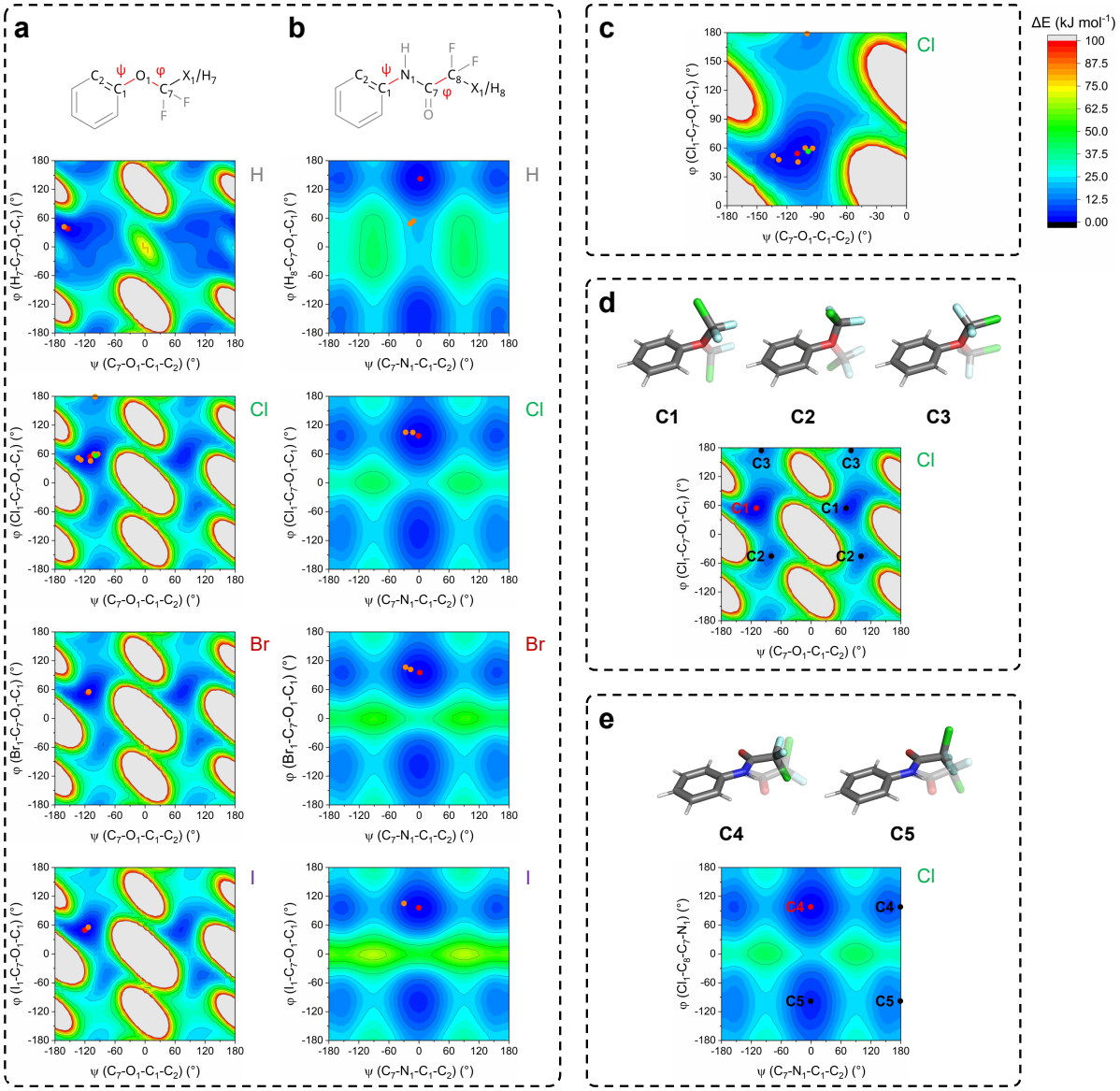


**Figure 18:** Conformational Analysis. **(a–e)** Contour maps of potential energy surfaces (PESs) of model molecules with general formula Ph−Y−$CF_2$X (Y = O, NHCO) as a function of dihedral angles φ and ψ in degree and ΔE in kJ mol$^{-1}$. Red mark: initial geometry-optimized conformation. Black marks: conformations at other ΔE minima. Orange marks: conformations found in the corresponding crystal structures of **6a**,**c**–**e** and **7a**,**c**–**e**. Green mark: conformation of asciminib (**20c**) found in ABL1 protein (T334I_D382N), PDB ID: 5MO4.[76] **(a)** PES contour maps of ethers (−O−), from top to down: X = H, Cl, Br, or I. **(b)** PES contour maps of amides (−NHCO−), from top to down: X = H, Cl, Br, I. **(c)** Detailed PES contour map of Ph−O−$CF_2$Cl with geometries of **6d** and asciminib (**20c**) found in PDB ID: 5MO4. **(d)** Corresponding Ph−O−$CF_2$Cl conformations of red and black marks in PES contour map. **(e)** Corresponding Ph−NHCO−$CF_2$Cl conformations of red and black marks in PES contour map. Structures of the energy minima C1−C3 in **(d)** and C4−C5 in **(e)** are shown as sticks. The flipped versions (ψ ± 180 kJ mol$^{-1}$) are depicted as transparent sticks.

phenyl ring, for $NHCOCF_2X$ only two ψ angles, 0° and 180°, can occur. The $C_X{-}X$ bonds in structures C4 and C5, representing the energy minima, are roughly orthogonal to the plane of the π-system (φ ~ ±90°). The flipped versions (ψ ± 180°) of C4 and C5 are again depicted as transparent sticks. For simplicity reasons, we provide all annotations in Figures 18a–c on the previous page in one quadrant (ether: φ = 0° to 180° and ψ = −180° to 0°; amide: φ = 0° to 180° and ψ = −90° to 90°) representing several possible geometrically or energetically equivalent crystal conformers.

Figure 18a–c on the preceding page also shows the geometric data of the small molecule crystal structures (orange mark) and of asciminib in ABL1 protein crystal structure 5MO4 (green mark) as dihedral angles of the ether- or amide-linked $CF_2X$ group. The torsion angles of the crystal data all coincide with the calculated data and are located in the dark blue areas representing low energy values. Interestingly, two deviating features can be observed: Molecule F in the crystal lattice of **6c** (single molecule with Cl1F atom in Figure 15a on page 41) is the only molecule showing an elongated conformation (φ = 179.3(9)°; ψ = −100(1)° corresponding to C3 in Figure 18d). This conformation is only a local minimum, compared to the global minimum represented by C1. Second, induced by the formation of an HB (Figure 17 on page 44), the torsion angles of **7a** (molecule A: φ = ±54(4)°; ψ = ±11.0(8)°; molecule B: φ = ±48(4)°; ψ = ±17.4(8)°) deviate significantly in their φ angle from the calculated energy minima. In summary, the crystal structures of molecules bearing chlorine, bromine, or iodine show excellent agreement with the PES minima (and their tolerances) obtained from QM calculations of the ether and amide model systems.

The hitherto discussed potential energy plots clearly highlight that despite preferential orientations of the halogens in $CF_2X$ groups, there is a significant degree of flexibility allowing these halogens to form XBs to various acceptors in the binding site. In contrast to the typically considered (hetero)arylhalide XB donors, $CF_2X$ groups allow for an orthogonal binding vector strongly deviating from linearity and a far greater "allowed conformational space". Thus, for $CF_2X$ groups, the calculation of XB strength should always be adjusted by the relative conformational energy. As mentioned before, the distribution of conformational energies in this "allowed space" versus the strength of XBs obtained from these conformations can play an important role in the enthalpy/entropy compensation of ligand binding.

As guidelines for the molecular design of such moieties, we have tried to visualize the "XB interaction space" with close to optimal conformational energies. Figure 19 on the next page illustrates the conformation-dependent orientation of the $C_X{-}X$ bond axes as elongated interaction vectors. Shown are the vectors of all determined geometries within Δφ,Δψ = ±90° (rotated in increments of 10°) and with ΔE equal to or less than 20 kJ $mol^{-1}$ in relation to the geometry-optimized minimum. From the graphics, it is evident that ethers (Figure 19a) and amides (Figure 19b) are capable of addressing different, linker-specific

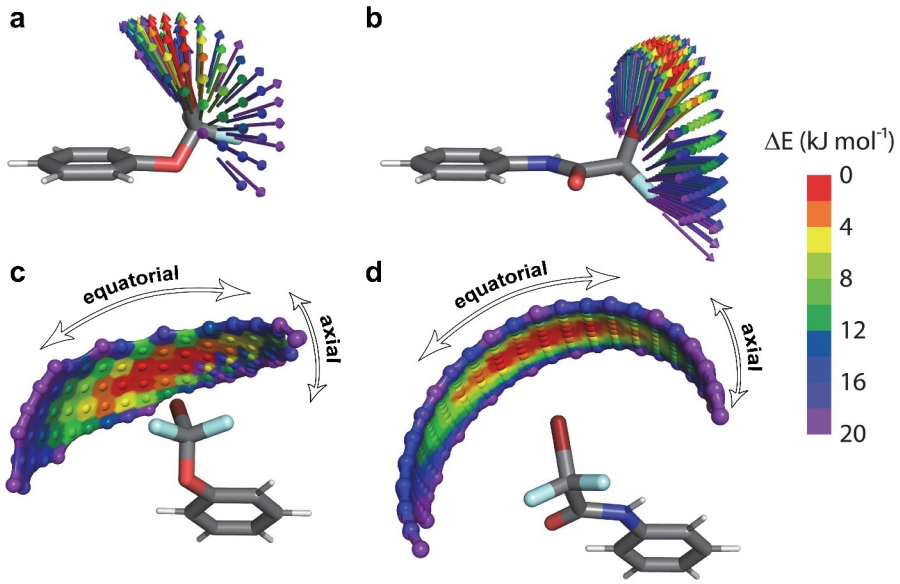


**Figure 19:** Visualization of the conformational flexibility of the $CF_2Br$ moiety attached to an ether as linker **(a,c)** or an amide as linker **(b,d)**. **(a,b)** Interaction vectors of 2.0 Å length are plotted in elongation of the $C_X{-}X$ bond within the boundaries of $\Delta\varphi,\Delta\psi = \pm 90°$. **(c,d)** Pseudointeraction points are depicted at a distance of 3.0 Å to the halogen and enclosed with a color-coded surface. Color coding of vectors and surfaces reflects a gradient between the conformational energy of the geometry-optimized minimum ($\Delta E = 0\,kJ\,mol^{-1}$) and an enhanced conformational energy of $\Delta E = 20\,kJ\,mol^{-1}$.

spatial segments representing the locations of potential XB acceptors in a protein binding site. In case of the ether linker, the interaction vectors always lean toward the normal vector of the aromatic ring, in case of the amide linker, the interaction vectors always project away from the π-surface of the aromatic ring. Still, this "axial variation" is small for both linkers, leading to rather slim segments that can be targeted, displayed as a color-coded surface of pseudointeraction points at a distance of 3.0 Å to the halogen in Figure 19c,d. In comparison, the "equatorial variation" (with respect to the $C_{ar}{-}N$ or $C_{ar}{-}O$ bond) is much larger for both linkers, yielding a substantial segment of potential interaction partners. Within these boundaries, the size of the surface of potential interaction partners does not differ quite significantly between the different linkers and the different halogens.

### 3.1.9 Complex Formation Energies and $V_{max}$

Since we have characterized the probable interaction space induced by suitable geometries of ether or amide linkers, we further investigated the XB strength dependent on the halogen, the type of linker, and the distance from the XB acceptor. We focused our theoretical view on this moiety only on the halogen bond. Hence, it should be noted that, obviously, interactions of the linker (HBs toward ether or amide), as well as interactions of the C−F bonds, such as orthogonal multipolar interactions, can strongly enhance the interaction energy of this moiety with particular amino acids in the binding site.[126,199–201]

As a model system for comparing XB and HB strength, we have used *N*-methylacetamide as a representative of the ubiquitously available backbone peptide bond.[4] We performed distance scans between the HB/XB donors of our model molecules (as shown in Figure 8 on page 21) and the oxygen of *N*-methylacetamide as the HB/XB acceptor (Figure 20 on page 52). The distance was changed in increments of 0.1 Å and the complex formation energies (ΔE) were calculated as single points for each increment. The $C_X$−X···O angle was fixed to 180°, and the X···O=C angle was fixed to 120°. As shown in Table 10 on the facing page, the results reveal highly tuned ΔE for ether and amide $CF_2X$ moieties with Cl (ΔE = −10.5 / −10.1 kJ mol$^{-1}$) < Br (ΔE = −13.7 / −14.3 kJ mol$^{-1}$) < I (ΔE = −20.1 / −21.6 kJ mol$^{-1}$). These results are quite similar to the computational analysis of the experimental small molecule crystal data already discussed (Table 9 on page 45).

Calculations were performed at the MP2/TZVPP level of theory as a standard. We often find for XB interactions that MP2 energies without correction of the basis set superposition error (BSSE) resemble benchmark calculations at the CCSD(T) level of theory with a complete basis set extrapolation (CBS) more closely than MP2 energies with BSSE. Still, MP2 is well known to overestimate the strength of interactions. Thus, in Table 10, we additionally report MP2/TZVPP energies with BSSE, MP2/QZVPP energies, as well as M06-2X/TZVPP energies with D3 dispersion correction. M06-2X has been shown to yield excellent geometries and energies for the XB18 and XB51 halogen bonding benchmark sets.[202]

As expected, the BSSE correction reduced the adduct formation energies (on average by 21.6 %). However, the consistency with the larger QZVPP basis set (+2.1 % on average) and, particularly, the comparison with the established M06-2X hybrid functional (−2.8 % on average) suggest that uncorrected MP2 values might only overestimate the adduct formation energy slightly and are not unreasonable to use for further discussions.

The respective average complex formation energies of the $CF_2X$ amides and ethers are increased by a factor of 1.60 for chlorine, 1.36 for bromine and 1.23 for iodine compared to the corresponding unsubstituted halobenzenes. This reflects the substantial polarization (tuning) effect by both fluorine atoms attached to the same $sp^3$ carbon atom onto the halogen X, as well as additional electron withdrawing effects from the linker oxygen or

**Table 10:** Calculated σ-hole and XB data of geometry-optimized model molecules with the general formula Ph−Y−R (Y = N/A, O, NHCO; R = $CF_2X$) and X = H, Cl, Br, I. The stated complex formation energies ΔE and the distance X···O correspond to the minima of distance scans between the HB/XB donor and the oxygen of *N*-methylacetamide as HB/XB acceptor. The $C_X$−X···O angle is equal to 180° and the X···O=C angle is equal to 120°. The $V_{max}$-values were calculated for an isodensity surface of 0.02 au. MP2/TZVPP calculations without BSSE are compared with BSSE-corrected MP2/TZVPP results, as well as with MP2/QZVPP and M06-2X-D3/TZVPP.

| Ph−Y−R | | | H | | Cl | | | Br | | | I | | |
|---|---|---|---|---|---|---|---|---|---|---|---|---|---|
| Y | R | QM method | ΔE (kJ mol$^{-1}$) | X···O (Å) | $V_{max}$ | ΔE (kJ mol$^{-1}$) | X···O (Å) | $V_{max}$ | ΔE (kJ mol$^{-1}$) | X···O (Å) | $V_{max}$ | ΔE (kJ mol$^{-1}$) | X···O (Å) |
| | −X | MP2/TZVPP | −10.8 | 2.3 | 0.116 | −6.4 | 3.0 | 0.149 | −10.3 | 3.0 | 0.182 | −17.0 | 3.0 |
| −O− | $-CF_2X$ | MP2/TZVPP | −20.3[a] | 2.1 | 0.133 | −10.5 | 2.9 | 0.160 | −13.7 | 3.0 | 0.202 | −20.1 | 3.0 |
| −O− | $-CF_2X$ | MP2/TZVPP[b] | −16.0 | | | −8.1 | | | −11.2 | | | −15.9 | |
| −O− | $-CF_2X$ | MP2/QZVPP | −19.8 | | | −11.0 | | | −13.9 | | | −21.0 | |
| −O− | $-CF_2X$ | M06-2X-D3/TZVPP | −18.7 | | | −10.1 | | | −12.9 | | | −19.6 | |
| −NHCO− | $-CF_2X$ | MP2/TZVPP | −14.9 | 2.1 | 0.141 | −10.1 | 2.9 | 0.169 | −14.3 | 2.9 | 0.200 | −21.6 | 2.9 |
| −NHCO− | $-CF_2X$ | MP2/TZVPP[b] | −11.1 | | | −7.8 | | | −11.6 | | | −16.8 | |
| −NHCO− | $-CF_2X$ | MP2/QZVPP | −14.1 | | | −10.6 | | | −14.7 | | | −23.0 | |
| −NHCO− | $-CF_2X$ | M06-2X-D3/TZVPP | −13.9 | | | −10.2 | | | −14.4 | | | −22.1 | |

[a] Additional weak secondary interactions between the aromatic ring and *N*-methylacetamide occur based on the ether geometry.
[b] BSSE corrected.

amide. Tuning of XBs is very often represented by the increase of the σ-hole.[203–210] As a useful descriptor of this improved anisotropic distribution of the electron density, the maximal positive electrostatic potential $V_{max}$, derived from plotting the ESP onto a specific electron isodensity surface, is provided. While most literature data is based on ESPs plotted onto an isodensity surface of 0.001 or 0.002 au, we have previously established reasons,

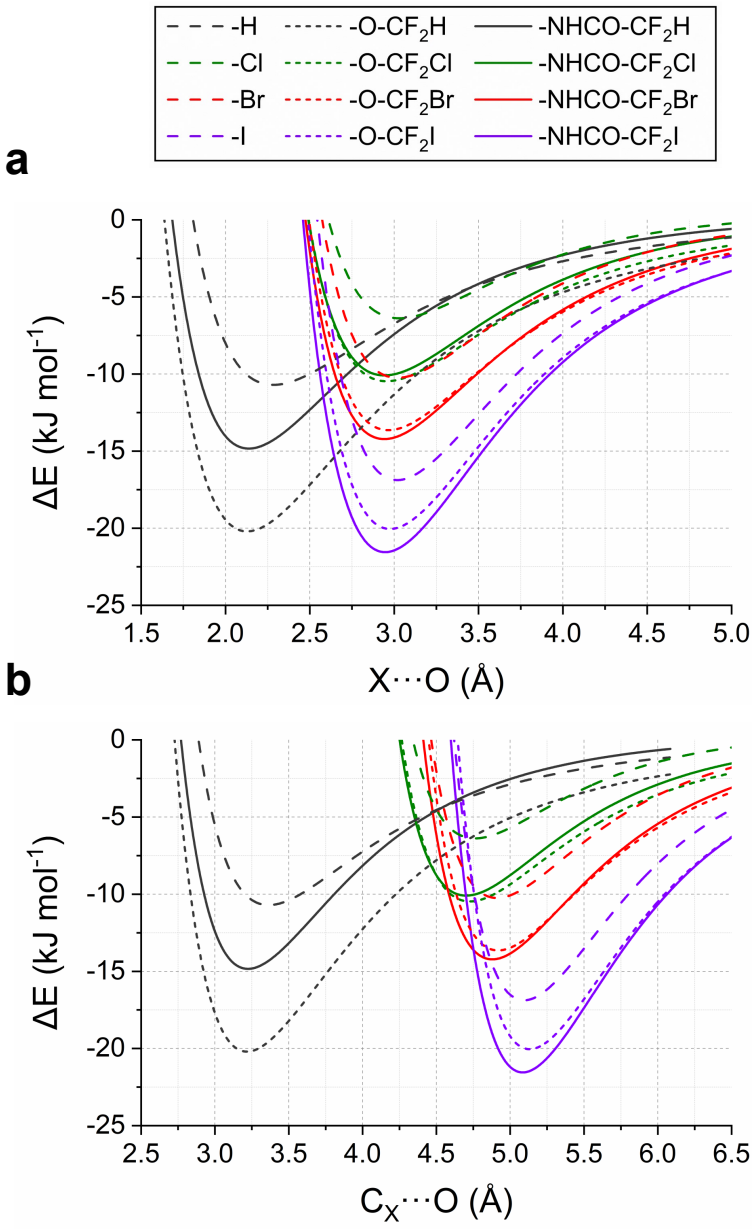


**Figure 20:** Calculated complex formation energies ΔE in kJ mol$^{-1}$ determined using a distance scan of model molecules with the general formula Ph−Y−R (Y = N/A, O, NHCO; R = $CF_2X$) along their $C_X$−X axes and the oxygen of *N*-methylacetamide as HB/XB acceptor. The $C_X$−X···O angle is equal to 180° and the X···O=C angle is equal to 120°. The distances were varied with an increment of 0.1 Å of each step. **(a)** Distance of X···O. **(b)** Distance of $C_X$···O.

why we use an isodensity surface of 0.02 au.[8] From the data in Table 10 on page 51, it can also be concluded that the $V_{max}$ values of the $CF_2X$ groups increase significantly by 7–22 % compared to the corresponding halobenzenes. While the absolute changes in $V_{max}$ and complex formation energies ΔE between Ph−X and Ph−O−$CF_2$X or Ph−NHCO−$CF_2$X, do not differ much for X = Cl, Br, or I, it should be noted that the strongest relative improvement is consistently found for chlorine.

In the case of HB, the complex formation energy is increased by a factor of 1.39 for the $CF_2H$ moiety with an amide linker and by a factor of 1.89 with an ether linker in comparison with the dispersion-based interaction of benzene. However, the HB minima are each about 0.8 to 0.9 Å closer to the acceptor (Figure 20a), so that $CF_2X$ moieties can be used to target more distant donors. This is even more pronounced based on the different $C_X$−X bond lengths, when considering the $C_X$···O distance (Figure 20b), instead of the X···O distance (Figure 20a).

### 3.1.10 Fragment Library

#### 3.1.10.1 Biophysical Fragment Screening on JNK1 and JNK3

To demonstrate the use of $CF_2X$ in targeting binding sites, we have synthesized a series of fragments bearing R−NHCO−$CF_2X$ with diversified scaffolds (R = organic scaffold; X = Cl, Br, I) as an addition to our HEFLibs concept.[6,211–214] The advantage of this fragment-based strategy is its focus on only a few relevant key interactions. Using STD NMR and ITC as primary and secondary biophysical screening techniques, respectively, we applied this small library of $CF_2X$-fragments to the c-Jun N-terminal kinases 1 and 3 (JNK1 and JNK3).[24,215] Here we focused on halogenated acetamides, because their synthesis is much simpler, faster, and cheaper, which facilitates the rapid establishment of a fragment library enriched in $CF_2X$ acetamides. In addition, the higher polarity of the amide linker in comparison to the ether linker, should be beneficial for the solubility of the resulting fragments. A small variety of diverse building blocks with few non-hydrogen atoms was purchased. Aside from aromatic amines with different aryl and heteroaryl scaffolds as starting materials (**7c**–**e**, **23**–**32**, **35**–**36**, **38**–**40**, and **42**–**45**), our test library includes amides prepared from acyclic primary (**22**) and cyclic secondary (**41**) alkyl amines. As acylation of imidazole[1,2-*a*]pyridine was easily achieved, we also included 2-chloro-2,2-difluoro-1-(imidazo[1,2-*a*]pyridin-3-yl)ethan-1-one (**21**) containing a carbonyl (R−CO−$CF_2Cl$) instead of an amide linker in our fragment library. The fragments **11** and **34** contain a sulfone (R−$SO_2$−$CF_2Br$).

Table 11 on the next page summarizes the results of the STD NMR screening and ITC validation measurements. Initially, 22 fragments (**7c**–**e**, **11**, **21**–**23**, **26**–**29**, and **34**–**45**) were tested for JNK3 binding by STD NMR. The $CF_2Cl$-containing 1,3,4-thiadiazole derivatives **23** and **29** were identified as hits and confirmed by ITC measurements as micromolar binders with affinities of 240 μM and 25 μM, respectively. To study the halogen influence on JNK3 binding, the matched molecular pairs of $CF_2Br$ (**24**, **30**) and $CF_2I$ (**25**, **31**) analogs were synthesized and added to our library. The unmodified educt of **29**–**31**, 5-(pyridin-4-yl)-1,3,4-thiadiazol-2-amine (**46**), was evaluated as a reference compound. For JNK1, all 23 listed fragments with the exception of **46** were screened by STD NMR, followed by individual ITC validation.

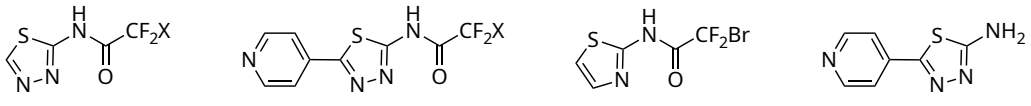


**23-25** **29-31** **35** **46**

X = Cl, Br, I

**Figure 21:** ITC validated STD NMR screening hits **23**–**25**, **29**–**31**, **35** and **46**.

The smaller 1,3,4-thiadiazole fragments **23**–**25** (12 heavy atoms) bound to JNK1 at a $K_d$ of 104–193 µM and on average slightly worse to JNK3 with a $K_d$ of 186–248 µM. The *N*-(5-(pyridin-4-yl)-1,3,4-thiadiazol-2-yl)acetamide derivatives **29**–**31** (18 heavy atoms) bound with higher affinity in the low two-digit range to JNK1 ($K_d$ = 10–20 µM) and JNK3 ($K_d$ = 13–23 µM). Although the heavier fragments had a 10-fold higher affinity, they exhibited a lower ligand efficiency (LE) due to the 50 % higher number of heavy atoms (**29**–**31**: 0.36–0.39 versus **23**–**25**: 0.42–0.46). In summary, the STD NMR signals of **23**–**25** indicated that the hydrogen atom of the thiadiazole ring is involved in protein binding. However, substitution by a pyridine (**29**–**31**) increased the binding affinity by approxi-

**Table 11:** Biophysical measurements using STD NMR and ITC against JNK1 and JNK3. Red colored dot (●): no binding event or not detectable. Green colored dot (●): detected binding event. Molecular weight (MW) in g mol$^{-1}$, HA is the number of heavy atoms, ITC is the measured $K_d$ in µM, and LE is the ligand efficiency as defined in equation 8 on page 123.

| | | | | | JNK1 | | | JNK3 | | |
|---|---|---|---|---|---|---|---|---|---|---|
| Entry | X | Spacer | MW | HA | STD | $K_d$ (µM) | LE | STD | $K_d$ (µM) | LE |
| **7c** | Cl | amide | 249.6 | 16 | ● | | | ● | >1000 | |
| **7d** | Br | amide | 294.1 | 16 | ● | >1000 | | ● | >1000 | |
| **7e** | I | amide | 341.1 | 16 | ● | | | ● | | |
| **11** | Br | sulfone | 316.1 | 16 | ● | | | ● | | |
| **21** | Cl | carbonyl | 230.6 | 15 | ● | >1000 | | ● | >1000 | |
| **22** | Cl | amide | 272.7 | 18 | ● | | | ● | | |
| **23** | Cl | amide | 213.6 | 12 | ● | 186 ± 0.3 | 0.44 | ● | 243 ± 3 | 0.42 |
| **24** | Br | amide | 258.0 | 12 | ● | 193 ± 15 | 0.43 | | 248 ± 70 | 0.42 |
| **25** | I | amide | 305.0 | 12 | ● | 104 ± 17 | 0.46 | | 186 ± 86 | 0.44 |
| **26** | Cl | amide | 283.7 | 17 | ● | | | ● | | |
| **27** | Cl | amide | 237.6 | 15 | ● | | | ● | | |
| **28** | Cl | amide | 281.6 | 18 | ● | | | ● | | |
| **29** | Cl | amide | 290.7 | 18 | ● | 20 ± 2 | 0.37 | ● | 23 ± 4 | 0.36 |
| **30** | Br | amide | 335.1 | 18 | ● | 15 ± 2 | 0.38 | | 17 ± 2 | 0.37 |
| **31** | I | amide | 382.1 | 18 | ● | 10 ± 0.3 | 0.39 | | 13 ± 5 | 0.38 |
| **34** | Br | sulfone | 292.1 | 13 | ● | | | ● | | |
| **35** | Br | amide | 257.1 | 12 | ● | >1000 | | ● | >1000 | |
| **36** | Br | amide | 295.0 | 16 | ● | | | ● | | |
| **38** | Br | amide | 308.1 | 17 | ● | | | ● | | |
| **39** | Br | amide | 286.5 | 14 | ● | | | ● | | |
| **40** | Br | amide | 331.1 | 19 | ● | | | ● | | |
| **41** | Br | amide | 337.1 | 19 | ● | | | ● | | |
| **42** | Br | amide | 308.1 | 16 | ● | | | ● | | |
| **43** | Br | amide | 382.2 | 21 | ● | | | ● | | |
| **44** | Br | amide | 363.1 | 21 | ● | | | ● | | |
| **45** | Br | amide | 268.0 | 14 | ● | | | ● | | |
| **46** | N/A | N/A | 178.2 | 12 | | 162 ± 20 | 0.44 | | | |

mately 10-fold. Interestingly, loss of the HB acceptor by exchange of the N3 atom in the thiadiazole ring of **24** into a carbon atom, yielding a thiazole ring (**35**), was accompanied by a significant reduction in affinity ($K_d > 1000\,\mu M$). The comparison of **29**–**31** to their educt **46** ($K_d = 162\,\mu M$) as a reference, showed that halodifluoroacetylation of the heteroaromatic amine increased the affinity between 8-fold and 15-fold for JNK1.

The results clearly show that halodifluoroacetylation contributes to affinity enhancement of **29**–**31**, but it is not necessarily unambiguous to draw conclusions from these matched molecular pairs about XB interactions. For both JNK1 and JNK3, a moderate increase of affinity was measured for **23** ($CF_2Cl$, $K_d^{JNK1} = 186\,\mu M$; $K_d^{JNK3} = 243\,\mu M$) ≈ **24** ($CF_2Br$, $K_d^{JNK1} = 193\,\mu M$; $K_d^{JNK3} = 248\,\mu M$) toward **25** ($CF_2I$, $K_d^{JNK1} = 104\,\mu M$; $K_d^{JNK3} = 186\,\mu M$). One-way ANOVA and Bonferroni's post hoc test revealed that this difference was only statistically significant between iodine (**25**) and both other halogens (**23**: $p = 0.028$; **24**: $p = 0.015$) for JNK1. A similar trend of affinities toward JNK1 and JNK3 was found for the extended 4-pyridine-substituted analogs: **29** ($CF_2Cl$, $K_d^{JNK1} = 20\,\mu M$; $K_d^{JNK3} = 23\,\mu M$) < **30** ($CF_2Br$, $K_d^{JNK1} = 15\,\mu M$; $K_d^{JNK3} = 17\,\mu M$) < **31** ($CF_2I$, $K_d^{JNK1} = 10\,\mu M$; $K_d^{JNK3} = 12\,\mu M$). Again, we find only a proper statistical difference ($p = 0.008$) based on a one-way ANOVA and Bonferroni's post hoc test for chlorine (**29**) and iodine (**31**). All relevant ITC runs, their parameters, and resulting $K_d$ values can be found in the Appendix (Table A2 and Figures A3–A7 on page 232 ff.). For optimal XBs, these differences could be more pronounced, but steric restrictions in the binding site and increased conformational energies can diminish the size of the trend. To elucidate the structural basis for the observed structure-activity relationship (SAR) and to clarify the role of the involved interactions, we conducted crystallization experiments with JNK3.

#### 3.1.10.2 Crystal Structure of JNK3 in Complex with Compound 30

The $CF_2Br$ acetamide derivatives **24** and **30** were soaked in JNK3 crystals by using a sitting-drop procedure. Thus far, soaking approaches of fragment **24** could not displace AMP-PCP, possibly due to the weaker affinity of 178 μM, but a JNK3 crystal was obtained with ligand **30** ($K_d$ = 17 μM) bound in the ATP binding pocket, as shown in Figure 23 on page 59. The JNK3 crystal structure was determined in space group $P2_12_12$ (18) with two chains in the asymmetric unit and a resolution of 1.86 Å (Table 12). The chain B and its bound ligand **30** were insufficiently resolved and therefore the following analysis focuses on chain A.

**Table 12:** Crystallographic data collection and refinement statistics of JNK3 in complex with **30**.

| | **30** |
|---|---|
| PDB ID | 8BZP |
| Wavelength (Å) | 0.92 |
| Space Group | $P2_12_12$ (18) |
| Cell Dimensions | |
| a,b,c (Å) | 109.80, 155.38, 43.96 |
| α,β,γ (°) | 90, 90, 90 |
| Resolution Range (Å) | 50–1.86 (1.97–1.86) |
| Redundancy | 13.42 (13.62) |
| Completeness (%) | 99.4 (99.9) |
| Mean I/σ (I) | 13.95 (1.05) |
| $R_{meas.}$ (%) | 11.4 (250.4) |
| CC1/2 (%) | 99.9 (54.9) |
| Wilson B ($Å^2$) | 45.7 |
| Resolution Included (Å) | 46.84–1.86 |
| $R_{work}/R_{free}$ (%) | 18.94 / 21.64 |
| Bond RMSD (Å) | 0.008 |
| Angle RMSD (°) | 0.936 |
| Ramachandran (%) | |
| outliers, allowed, favored | 0 / 1.67 / 98.33 |
| Rotamer Outliers (%) | 1.43 |
| All-Atom Clashscore | 2.47 |
| Average B Factor | |
| Overall ($Å^2$) | 46.2 |
| Protein ($Å^2$) | 45.6 |
| Ligand ($Å^2$) | 54.8 |
| Water ($Å^2$) | 48.6 |

Based on the electron density (see unbiased omit-map in Figure 23c), two conformations with different orientations of the $CF_2Br$ moiety (**30-A** and **30-B**) were built with 50:50 occupancy. The 4-pyridinyl-1,3,4-thiadiazole substructure is placed almost identically in both conformations, targeting the hinge region and gatekeeper M146 (Figure 23d). The N4 atom of pyridine forms a strong HB with the backbone N−H of M149 ($d_{\mathbf{30\text{-}A},N\cdots N}$ = 2.9 Å; $d_{\mathbf{30\text{-}B},N\cdots N}$ = 2.7 Å), whereas the C7−H and C8−H of pyridine form weaker HBs with the backbone oxygens of G147 ($d_{\mathbf{30\text{-}A},C\cdots O}$ = 3.2 Å; $d_{\mathbf{30\text{-}B},C\cdots O}$ = 3.1 Å) and M149 $d_{\mathbf{30\text{-}A},C\cdots O}$ = 3.9 Å; $d_{\mathbf{30\text{-}B},C\cdots O}$ = 3.6 Å). Numerous C−H···π contacts are formed with the top and bottom side of the aromatic rings of the ligand. The gatekeeper M146 is engaged in a chalcogen bond (ChB) with N3 of the thiadiazole ring system ($d_{\mathbf{30\text{-}A},S\cdots N}$ = 3.6 Å, $\alpha_{\mathbf{30\text{-}A},C-S\cdots N}$ = 156.4°; $d_{\mathbf{30\text{-}B},S\cdots N}$ = 3.5 Å, $\alpha_{\mathbf{30\text{-}B},C-S\cdots N}$ = 151.2°). A second ChB interaction is intramolecularly located between the sulfur atom of the thiadiazole and the oxygen atom of the amide ($d_{\mathbf{30\text{-}A},S\cdots N}$ = 3.0 Å, $\alpha_{\mathbf{30\text{-}A},C-S\cdots N}$ = 153.8°; $d_{\mathbf{30\text{-}B},S\cdots N}$ = 3.0 Å, $\alpha_{\mathbf{30\text{-}B},C-S\cdots N}$ = 156.6°). Intramolecular ChB of this type have already been described in the literature.[216] Nagao *et al.* calculated an *ab initio* geometry optimization at the HF/3-21G* level for a similar thiadiazole system (Figure 22).[217] They obtained a relative energy difference of −36.6 kJ mol$^{-1}$ for the closest S···O contact of a 2,2,2-trifluoro-*N*-(1,3,4-thiadiazol-2-yl)acetamide derivative. This suggests that the rotatability of the thiadiazole-amide bond is significantly constrained by the ChB interaction and that a conformation with close S···O contact is typically preferred over the 180°-flipped conformation. This is consistent with the observed electron density in our crystal structure.

In conformation **30-B** ($\psi_{\mathbf{30\text{-}B}}$ = 107.4°), the bromine forms an XB with the backbone oxygen of G76 ($d_{\mathbf{30\text{-}B},Br\cdots O}$ = 3.3 Å, $\alpha_{\mathbf{30\text{-}B},C-Br\cdots O}$ = 161.9°) located in the P-loop of JNK3 (Figure 23d on the next page). The side chain of K93 and the P-loop (G76 to S72) form a cavity around the bromine atom (distances of approximately 3.7–4.1 Å) and constrain the bromine in its effort to adopt a more ideal σ-hole angle than 161.9°. Simultaneously, the protonated side chain amine of K93 is engaged in a fluorine interaction ($d_{\mathbf{30\text{-}B},N\cdots F}$ = 2.8 Å). To elucidate the relevance of these interactions and compare both observed binding modes, we conducted model calculations at the MP2/TZVPP level of theory. The protein backbone

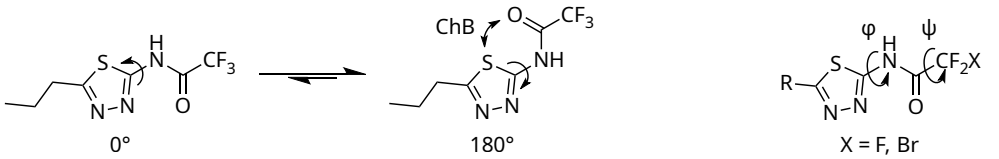


**(a)** Thiadiazole model of Nagao *et al.* **(b)** Torsion angles (φ, ψ)

**Figure 22:** Torsion of a thiadiazole model. **(a)** An *ab initio* geometry optimization at the HF/3-21G* level for a thiadiazole model with ΔE = −36.6 kJ mol$^{-1}$ at an angle of 180° relative to 0°. Adopted from Nagao *et al.*[217] **(b)** Torsion angle nomenclature: φ = S–C–N–C and ψ = X–C–C–N.

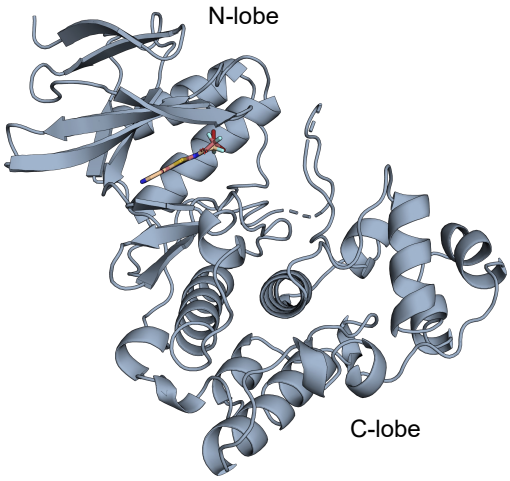


**(a)** 8BZP: JNK3 with fragment **30**.

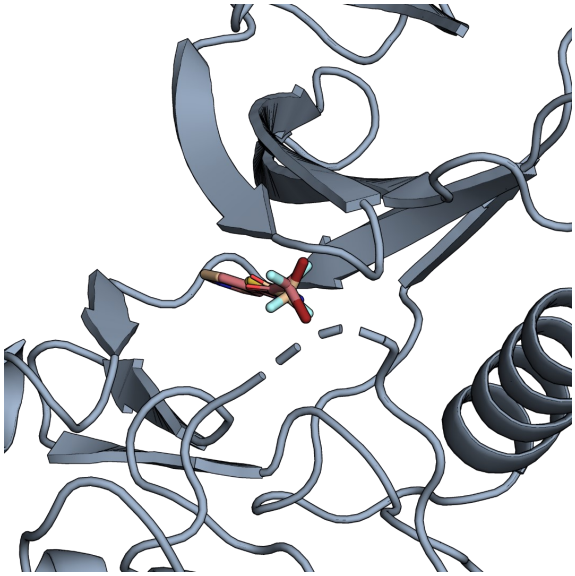

**(b)** 8BZP: Binding site of JNK3.

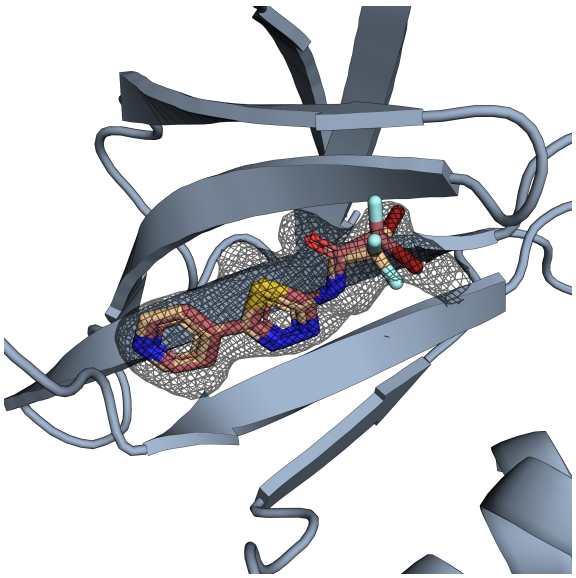

**(c)** Unbiased omit-map.

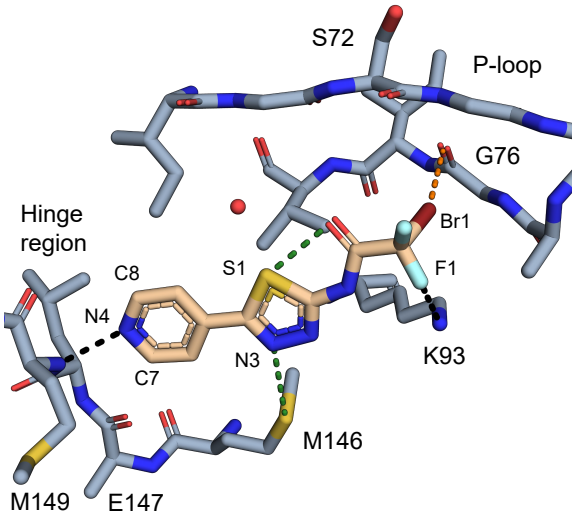


**(d)** Key interactions of **30-B**.

**Figure 23:** JNK3 crystallized with fragment **30** in the ATP binding site (PDB ID: 8BZP). **(a)** Total view of JNK3 (chain A) shown as gray cartoon in complex with **30**. **(b)** Focused view of the ATP binding site with two conformations of **30** (conformer **30-A** shown with carbon atoms in red and conformer **30-B** with carbon atoms in beige). **(c)** The unbiased omit-map is contoured in gray at 3σ. **(d)** The key interactions of conformation **30-B** are highlighted in detail. The fragment accepts a hydrogen bond (black dotted lines) from the backbone N−H of M149 localized in the hinge region and further two weaker hydrogen bonds (not indicated) from the backbone carbonyls of E147 and M149 to the adjacent C−H moieties of the pyridine N. The 1,3,4-thiadiazole ring forms an intramolecular ChB (green dotted lines) between its sulfur atom and the carbonyl oxygen of its amide. The nitrogen atom N3, accepts a second ChB from the side chain of the gatekeeper M146 (green dotted lines). **30-B** donates an XB (orange dotted lines) from its bromine atom toward the backbone carbonyl of G76 and accepts an HB contact (black dotted line) from the protonated side chain amine of K93 onto one of its fluorine atoms.

between the $C_\alpha$ of Q75 and the $C_\alpha$ of I77 including the interaction partner G76 was represented as 2-acetamido-*N*-methylacetamide, as was the protein backbone of the beginning P-loop between $C_\alpha$ of S72 and $C_\alpha$ of A74. The side chain of lysine K93 was capped to 1-propylammonium. Hydrogen atoms were added and optimized, while all other atoms were fixed to the coordinates of the crystal structure. Despite the not ideal σ-hole angle, we observe a good interaction energy for the XB of $-12.3\,\mathrm{kJ\,mol^{-1}}$. The proximal P-loop (most likely G73) yields a complex formation energy of $-10.4\,\mathrm{kJ\,mol^{-1}}$ for the $CF_2Br$ moiety. As expected, the charged HB between K93 and the fluorine atom exhibits the strongest complex formation energy with $-22.3\,\mathrm{kJ\,mol^{-1}}$.

The second conformation **30-A** ($\psi_{\mathbf{30\text{-}A}} = -64.7°$) is based on a $CF_2Br$ group, rotated approximately by 170°, orienting one fluorine atom in the described cavity and the bromine atom facing toward the empty phosphate pocket (Figure 23c). Possible key interactions stabilizing this binding mode could be HBs from the charged side chain of K93 to the electron-rich belts around the fluorine and bromine atoms ($d_{\mathbf{30\text{-}A},\mathrm{N\cdots F}} = 3.4\,$Å, $d_{\mathbf{30\text{-}A},\mathrm{N\cdots Br}} = 3.6\,$Å). From our model calculations, we have learned that the lysine contacts are slightly impaired with $-18.5\,\mathrm{kJ\,mol^{-1}}$ in comparison to conformation B. Likewise, the contacts to both stretches of backbone adjacent to the P-loop, S72–A74 and Q75–I77, give reduced interaction energies of $-5.1\,\mathrm{kJ\,mol^{-1}}$ and $-6.5\,\mathrm{kJ\,mol^{-1}}$, respectively. In addition, the conformational energy of B is more advantageous than that of A ($\Delta E = 11.4\,\mathrm{kJ\,mol^{-1}}$). Overall, conformation A shows surprisingly reasonable interaction energies, however, all calculations suggest that conformation B (Figure 23d) should be the stronger binder. It should be noted that the side chain of Q75 is not resolved in the crystal structure; however, it is possibly proximal to the $CF_2X$ moiety in both conformations. Thus, an influence of this residue on the binding mode in solution cannot be ruled out.

The protein crystal structure of JNK3 in complex with ligand **30** provides plausible explanations for the SAR of **23**–**25**, **29**–**31**, **35**, and **46** that were previously discussed. Compound **46** is not capable of forming the interactions of the halogenated acetamide group and binds substantially weaker to JNK1 ($K_d = 162\,\mu$M). The inability to form a ChB due to the absence of a suitable ChB donor atom (such as N3 in the thiadiazoles) most likely explains why thiazole **35** ($K_d > 1000\,\mu$M) was not detectable in the ITC experiments and emphasizes the importance of the ChB to the sulfur atom of gatekeeper M246 for the thiadiazole ligands. Compounds **23**–**25** showed only a minor trend of decreasing $K_d$ values in the series C ≈ Br > I ($K_d = 243\,\mu\mathrm{M} \approx 248\,\mu\mathrm{M} > 186\,\mu$M), while **29**–**31** ($K_d = 12$–$23\,\mu$M) bound better by a factor of approximately 10-fold to 15-fold. As stated before, the only significant difference is found for the exchange of chlorine (**29**) into iodine (**31**). The anchoring of fragments **29**–**31** in the hinge region by the pyridine ring as a hinge-binding motif likely plays an important role in the affinity boost compared to **23**–**25**.

As presented herein (Table 10 on page 51), the theoretically possible difference in interaction energy at an optimal XB geometry of each halogen shows that halogen exchange from chlorine to bromine could improve the ΔE by approximately $-4.2\,\mathrm{kJ\,mol^{-1}}$. Likewise, halogen exchange from bromine to iodine could strengthen the interaction by approximately $-7.3\,\mathrm{kJ\,mol^{-1}}$. Starting from a σ-hole angle $\alpha_{C-Br\cdots O}$ of 161.9° between bromine and the backbone oxygen of G76 located in the P-loop of JNK3, we astonishingly found that the bulkier iodine (**31**) can be accommodated with improved affinity in comparison to bromine (**30**). It remains speculative, whether some small degree of adaptability of the P-loop is a necessary prerequisite for this observed structure-affinity relationship. This example highlights that the heavier halogens will not necessarily always be the sweet spot for forming XBs just based on their potential to exhibit enlarged σ-holes. For $CF_2X$ moieties, the conformational strain, as well as strength and multitude of other interactions fixing the binding mode and limiting the formation of an optimal geometry, can be quite influential. In some binding sites and modes, an iodine will rise to the full potential of its possible XB strength. In other binding scenarios, an intermediately sized bromine or smaller chlorine might be enabled to form optimal XB interactions.

### 3.1.11 Conclusion

We have demonstrated that molecules containing $C(sp^3)F_2X$ moieties (X = Cl, Br, I) attached by linker systems such as ethers or amides are synthetically accessible, and that amide derivatives are particularly suitable for fragment-based drug discovery, providing the opportunity to identify highly interesting, unconventional XB-based binding modes in biological targets.

Starting from a PDB analysis fostering our interest in $CF_2X$ derivatives based on the crystal structure of Asciminib in ABL1 kinase [76], we have created a series of matched molecular pairs for two different linker systems (**6a**–**e** and **7a**–**e**). Using these tool compounds, we studied their chemical and metabolic stability, as well as their physicochemical properties, particularly with respect to solubility and logP. The polarization between fluorine and X = Cl, Br, or I and the role of the anisotropic electron distribution around X, as illustrated by ESP plots, certainly has an influence on stability and physicochemical properties. QikProp has been shown to provide reasonable predictions for quite a few solubilites. However, in some cases (**22**, **26**, **29**–**31**, **40**, **44** and **45**) solubility issues were predicted that were fortunately not observed in the turbidimetric assay. In some cases, solubility issues were predicted correctly (**42** and **43**). Thus, we recommend for compounds containing $CF_2X$ moieties to always confirm predictions of solubility with experimental evidence and to avoid taking solubility warnings as the main criterion to decide for or against the synthesis (or procurement) of a compound.

In crystallization experiments with our tool compounds, we have shown that the self-assembly of the $CF_2X$ derivatives in the crystalline solid-state is mainly driven by XBs and influenced by the size of the halogen. $CF_2X$ ether and amide groups adopt preferred geometries, capable of targeting potential XB acceptors that are not readily addressable with $C(sp^2)$−X moieties of (hetero)aryl halides, and they tend to strive in our crystal structures for the optimal XB angle and distance, unlike our analogous HB donor $CF_2H$ (**7a**). Using QM methods, we characterized the conformational flexibility of such $CF_2X$ ether and amide functions, finding good agreement with the experimental data from our small molecule crystals. We highlight clear conformational limitations, which are essential to consider, when using these moieties in molecular design. In addition, we find a reasonable degree of flexibility of these moieties to adapt to different XB acceptors in a binding site with low conformational strain, particularly in comparison with $C(sp^2)$−X moieties. We further characterized the potential XB strength of these $CF_2X$ donors in a distance-dependent manner. Compared to the respective halobenzenes, we find that the XB interactions are improved by approximately 3.5 to 4.5 kJ mol$^{-1}$, based on the tuning effects of the fluorine atoms and the linker functions.

The $CF_2X$ structural motif is underrepresented in drug discovery and has hardly been applied so far. Organic amines are readily available and suitable starting materials for the facile preparation of a structurally diverse fragment library featuring $CF_2X$ amides. We propose that unconventional or even rather unique binding modes could be explored based on such libraries, which are hardly accessible from conventional chemical space, allowing for the discovery of unclaimed, patentable chemotypes and the establishment of added therapeutic opportunities.

To demonstrate the usefulness and good applicability of this concept, we screened c-Jun N-terminal kinases 1 and 3 (JNK1 and JNK3), using STD NMR and validated hits by ITC, revealing several hits in the micromolar range. Particularly the 5-(pyridin-4-yl)-1,3,4-thiadiazole scaffold showed good binding to both kinases. The affinity of its bromine derivative (**30**) to JNK3 and JNK1 was 17 μM and 15 μM, respectively. We determined the crystal structure of **30** in complex with JNK3, elucidating that the $CF_2Br$ moiety interacts with the P-loop in a unique way, which has not been reported so far. It can concomitantly donate an XB with a distance of 3.3 Å and a σ-hole angle of 161.9° toward the backbone oxygen of G76 located in the P-loop, while accepting a hydrogen bond from the charged side chain of K93 onto one of its fluorine atoms. Overall, the interactions in the binding site are shifted from sites that traditionally receive most attention, such as the hinge and the back pocket, toward the sugar / phosphate binding site of ATP. Only the pyridine substructure forms an HB with the hinge. Thus, fragment **30** has good optimization potential by elaborating the hinge-binding motif and performing fragment growth and merging approaches.

Future studies will focus on expanding the fragment library, as well as developing further linker systems and other stable $C(sp^3)-X$ structures. The steadily expanding library will continue to be screened for additional binding fragments targeting therapeutically relevant proteins. Found hits are subjected to lead optimization.

## 3.2 Indazole-based Kinase Inhibitors Bearing $CF_2H$ or $CF_2X$ Methyl Moieties

### 3.2.1 Protein Data Base Scan

A PDB decoration scan was developed to find ligands with novel halogen bonding modes. The ligands were decorated with a $CF_2X$ methyl group and rotated along their $R_{ar}-C_{CF_2X}$ axis. In general, we decorated C atoms in aromatic systems with $CF_2Br$ units. The output in its scope and quality of a PDB decoration scan is decisively dependent on the selected parameters: σ-angle and distance between acceptor and donor atoms, tolorated level of clashes between decorated units, ligands and proteins. Other parameters include stepsize the rotation along the $C_{ar}-C_{CF_2X}$ axis. The runtime of the search depends mainly on the latter parameter and the number of data to be checked.

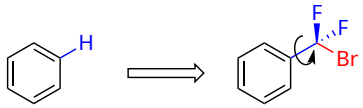


**Figure 24:** Exemplary substitution pattern leading to the decoration of a ligand with a $CF_2Br$ methyl group.

An exemplary PDB decoration scan was performed with 538 UniProt IDs (all kinases, MDM2, MDM4, HIV-1 protease and SARS-CoV-2 main protease) to find halogen bonding acceptor heteroatoms in proteins (method is described in Section 5.7.10). During the scanning 8975 files were checked, 80 474 positions for potential decorations were found and 2804 postitions with a σ-hole angle ≥150° and a donor-acceptor distance between 2.5 Å and 4.5 Å were decorated. Five hits referring to incompletely resolved and therefore not assigned to proteinogenic amino acids. The decorated $CF_2Br$ unit was rotated in 5 % increments and the position closest to the 180° σ-angle was recorded.

Figure 25 on the next page shows the distribution of hits among amino acids and their correlation with amino acid abundance in proteins divided into 1660 backbone heteroatom hits and 1139 side chain hits.[218] Further breakdown into nitrogen and oxygen backbone acceptor atoms can be found in the Appendix A.5 on page 242. From the graphs, it is evident that the hit rate of backbone heteroatoms correlates with the abundance of amino acids (ρ = 0.92). In the case of side chains, such a correlation is not entirely obvious (ρ = 0.57). The outlier glycine in Figure A11a on page 242 is noticeable. The hit rate of glycine is three times higher than its relative abundance in proteins. The mere absence of a space-occupying organic residue does not fully explain this. First, there is no similar correlation between smaller side chain size and increased hit rate for the other amino acids. Second, the heteroatoms of the backbone are unfavorably arranged for a halogen approaching

from the side of the nonexistent side chain. Rather, the lack of side chain allows glycine to adopt more possible torsion angles, which increases the statistical hit probability.

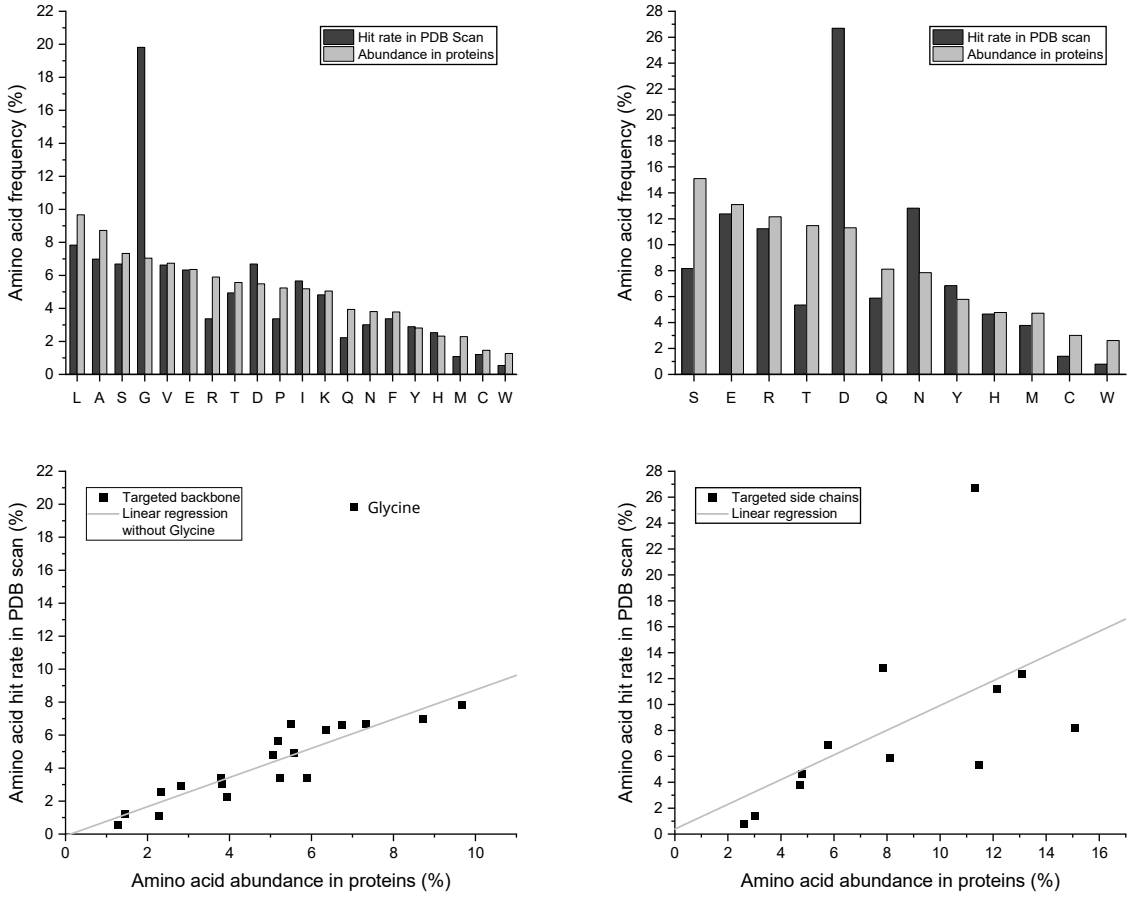


**(a)** Protein backbone.

**(b)** Protein side chain.

**Figure 25:** Correlation between targeted halogen bonding acceptor heteroatoms of protein backbones with a σ-hole angle ≥150° and abundance of amino acids in proteins. Number of targeted backbone amino acids n = 1660 (backbone N: n = 726 and backbone O: n = 934); number of targeted protein side chains n = 1139 and sum of targeted acceptor atoms n = 2799. **(a)** Comparison between halogen acceptor amino acids in protein backbone and abundance in proteins (ρ = 0.92). **(b)** Comparison between halogen acceptor side chains of amino acids and amino acid abundance in proteins. Abundance in proteins normalized to 100 % (ρ = 0.57).

### 3.2.2 Design and Development of Fragment Pattern Scaffold

The results presented in this scetion were obtained by performing a PDB scan of the entire database with a $CF_2Br$ unit decoration of unsubstituted aromatic C atoms and a rotation of 10° increments along the $C_{ar}-C_{CF_2Br}$ axis. The scan revealed numerous structures from which promising ones were selected. Protein clashes, distances, angles, and spatial accessibility of acceptor atoms were particularly important in the selection. Clashes within the decorated ligand were of secondary importance if the structure in question could be modified. An interesting clustering was observed for ligands in PDB crystal structures of kinases containing an indazole or pyrazole scaffold. Examples are shown in Table 13 and Figure 26.

**Table 13:** Selection of indazole- and pyrazole-based ligands found by PDB decoration scan.

| Entry | PDB ID | Protein | Acceptor AA | Acceptor atom | Distance X···O (Å) | σ-hole angle C−X···O (°) |
|---|---|---|---|---|---|---|
| (a)[219] | 3ZLY | MEK1 | S194 | O | 2.92 | 177.7 |
| (b)[220] | 2VTA | CDK2 | Q131 | O | 3.41 | 165.2 |
| (c)[221] | 3FI3 | JNK3 | S193 | O | 3.44 | 172.4 |
| (d)[222] | 5D9L | RSK2 | E197 | O | 3.58 | 160.5 |
| (e)[223] | 3LFS | CDK2 | E12 | O | 2.87 | 164.0 |
| (f)[224] | 4WRS | PIM1 | D131 | OD2 | 3.37 | 175.6 |

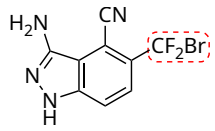


**(a)** 3ZLY, MEK1, S194

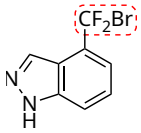


**(b)** 2VTA, CDK2, Q131

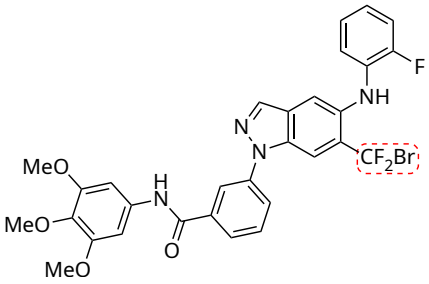


**(c)** 3FI3, JNK3, S193

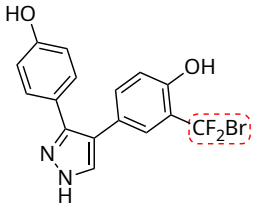


**(d)** 5D9L, RSK2, E197

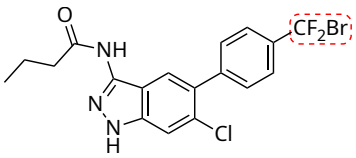


**(e)** 3LFS, CDK2, E12

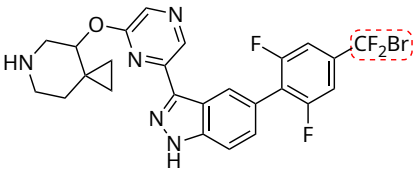


**(f)** 4WRS, PIM1, D131

**Figure 26:** $CF_2Br$-decorated ligand structures described in Table 13. **(a–f)** PDB ID, protein, targeted acceptor amino acid.

The decorated ligands of entries (a) to (d) (3ZLY, 2VTA, 3FI3, 5D9L) also have in common that they all target the same backbone oxygen. This backbone oxygen is conserved in the secondary structure of all kinases. The distances found vary from 2.92 Å to 3.58 Å and the σ-hole angles range from 160.5° to 177.7°, where 2.92 Å and 177.7° of ligand in 3ZLY is a nearly ideal geometry for halogen bonds. Note that these are not geometries of ligands converged in optimization calculations. As shown in Figure 27, the C−Br bonds of the ligands in 3ZLY and 2VTA are approximately orthogonal to their aromatic plane, i.e., in a more energetically favorable geometry. Furthermore, both ligands bind to the kinase hinge region.

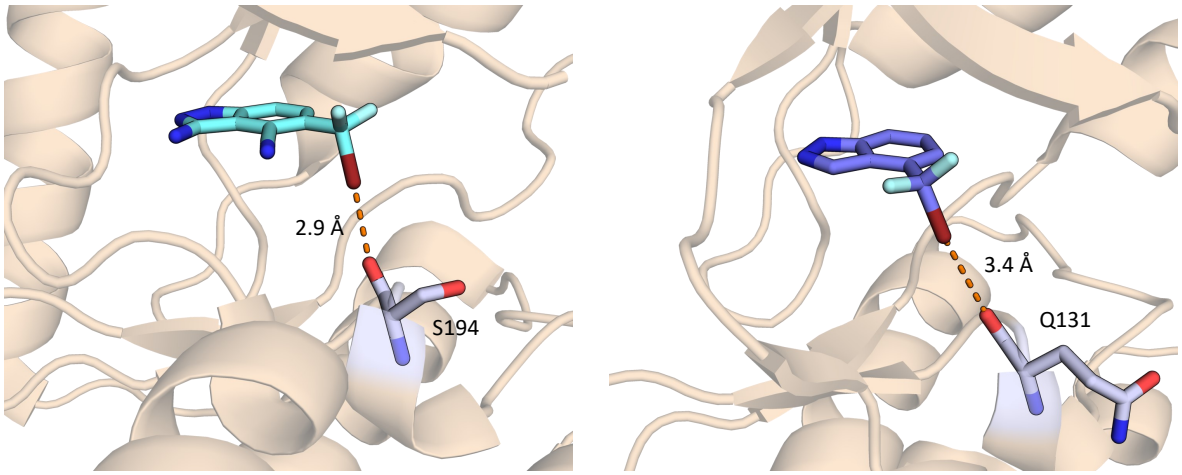


**(a)** PDB ID: 3ZLY (MEK1) **(b)** PDB ID: 2VTA (CDK2)

**Figure 27:** $CF_2Br$-decorated ligands with an indazole scaffold and presumed halogen-bonding interaction (orange dotted line) targeting a highly conserved backbone carbonyl oxygen in kinases. **(a)** 5-Bromodifluoromethyl decorated 3-amino-1*H*-inzadzole-4-carbonitrile targeting the backbone oxygen of S194 in MEK1. **(b)** 4-Bromodifluoromethyl decorated 1*H*-indazole targeting the backbone oxygen of Q131 in CDK2.

For the studies in this thesis, three scaffolds were derived from the findings to investigate possible XB interactions of an attached $CF_2Br$ group in kinases, but also HB interactions of a $CF_2H$ group. All three scaffold structures are shown in Figure 28 on the next page: 1*H*-indazol-3-amine, benzo[*d*]isoxazol-3-amine and imidazo[1,5-*a*]pyridin-3-amine. They are fragment-sized molecules with 13 or 14 heavy atoms and a molecular weight between 183.1 and 263.0 g mol$^{-1}$. In addition, these studies served to evaluate the PDB decoration scan for its suitability as a tool for structural optimization and enhancement. The synthesis and chemical accessibility of the aimed test compounds are discussed in Section 3.2.3 on page 69. The biophysical evaluation of the actually synthesized test compounds are described in Section 3.2.4 on page 73.

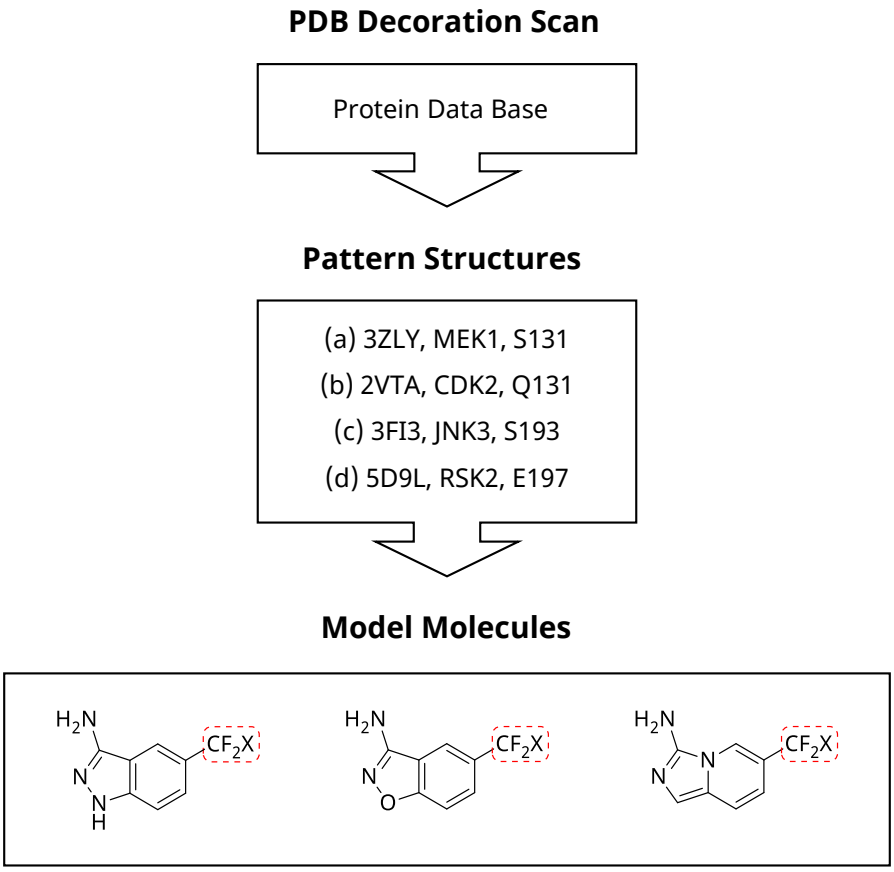


**Figure 28:** Workflow in the development of $CF_2X$-decorated model molecules with X = H, F, Br as ligands for hypothesis evaluation using JNK1 and JNK3 as target examples.

### 3.2.3 Synthesis of Kinase-binding Fragments based on PDB Scan

In this section, we discuss the synthesis pathway and challenges associated with the accessibility of test compounds derived from a PDB scan (Section 3.2.2 on page 66). As described in the introduction (Section 1.3.1 on page 6), numerous methods were described to generate $CF_2Br$ moieties, but also $CF_2H$ moieties. One approach was their synthesis by bromination of $CF_2H$ groups, which in turn could be prepared with fluorinating agents from their corresponding aldehydes. This had the advantage that the hydrogen variants also intended for testing were obtained as a preliminary stage. Trifluoromethylated compounds were synthesized as test references.

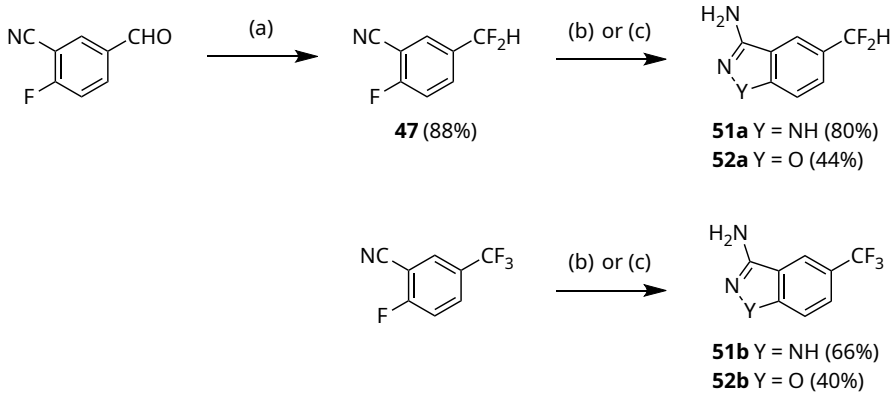


**Scheme 13:** Synthesis of indazole (Y = NH) and benzisoxazole (Y = O) derivatives. Reagents and conditions: (a) DAST, DCM, -10 °C to rt, argon atmosphere, 18 h; (b) $N_2H_4$, EtOH, 90 °C, 4 h; (c) AHA, *t*-BuOK, DMF, rt, 18 h.

As shown in Scheme 13 and Scheme 14 on the next page, **47** and **48** were synthesized from their corresponding aldehydes with the fluorination agent diethylaminosulfur trifluoride (DAST) yielding 88 % and 84 %.[225] In the next step, the ring closure reactions were carried out first, since experiments showed that $CF_2Br$ groups did not withstand the indazole cyclization reaction with hydrazine excess under reflux conditions. 2-Fluorobenzonitriles with $CF_2H$ und $CF_3$ moieties, on the other hand, could be converted with yields of 80 % for **51a** and 66 % for **51b** under the conditions mentioned.[226,227] The cyclization reactions to the benzisoxazoles were performed with acetohydroxamic acid (AHA) under basic conditions at room temperature to give **52a** and **52b** with moderate yields of 44 % and 40 %, respectively.[228]

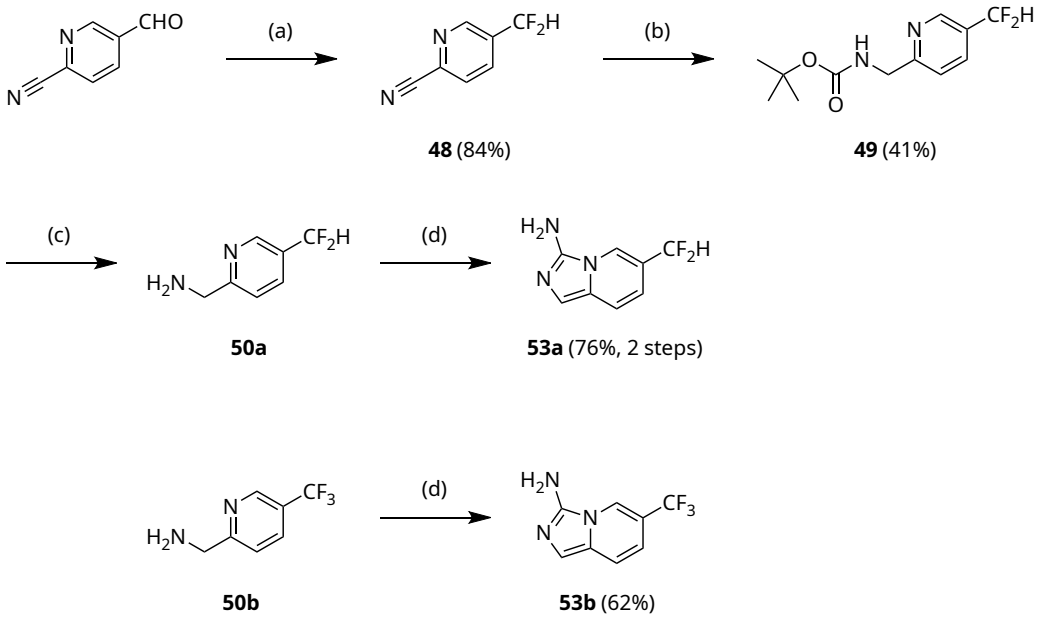


**Scheme 14:** Synthesis of imidazo[1,5-*a*]pyridin-3-amine derivatives. Reagents and conditions: (a) DAST, DCM, -10 °C to rt, argon atmosphere, 18 h; (b) $NaBH_4$, $Boc_2O$, $NiCl_2 \cdot 5\,H_2O$, MeOH, 0 °C to rt, 18 h; (c) TFA, DCM, rt, 24 h; (d) BrCN, $Et_3N$, toluene, rt, 30 min.

The synthesis of imidazo[1,5-*a*]pyridin-3-amines require more reaction steps. First, a reduction of **48** with sodium borohydride, di-*tert*-butyl dicarbonate and nickel(II) chloride was carried out to obtain the Boc-protected amine **49**.[229] Other reduction reactions tested, e.g. with lithium aluminum hydride, did not lead to the desired amine. Subsequently, **50a** was obtained by acid-catalyzed deprotection with TFA, then the free amine was reacted under basic conditions with bromocyanogen to give 76 % of the imidazo[1,5-*a*]pyridin-3-amine **53a**.[230] Purification of the intermediates was not required. The ring closure reaction of $CF_3$-bearing test compound **53b** was performed starting from the commercially available amine with a yield of 62 %.

The decisive bromination of the $CF_2H$-bearing compounds **51a**, **52a** and **53a** required the protection of the free amines with a protecting group. Bromination experiments of unprotected **51a** and **52a** did not lead to the desired products under different solvent and reagent conditions at room temperature and under heat. In some solvents such as benzene or tetrachloromethane, the reactants were even insoluble. Fmoc-protected intermediates showed poor dissolution properties, while Boc-protected substances were soluble in benzene and tetrachloromethane. The Boc-protected substances **54a**, **55a** and **56a** were prepared with yields ranging from 81 % to 86 %, as shown in Scheme 15 on the facing page.

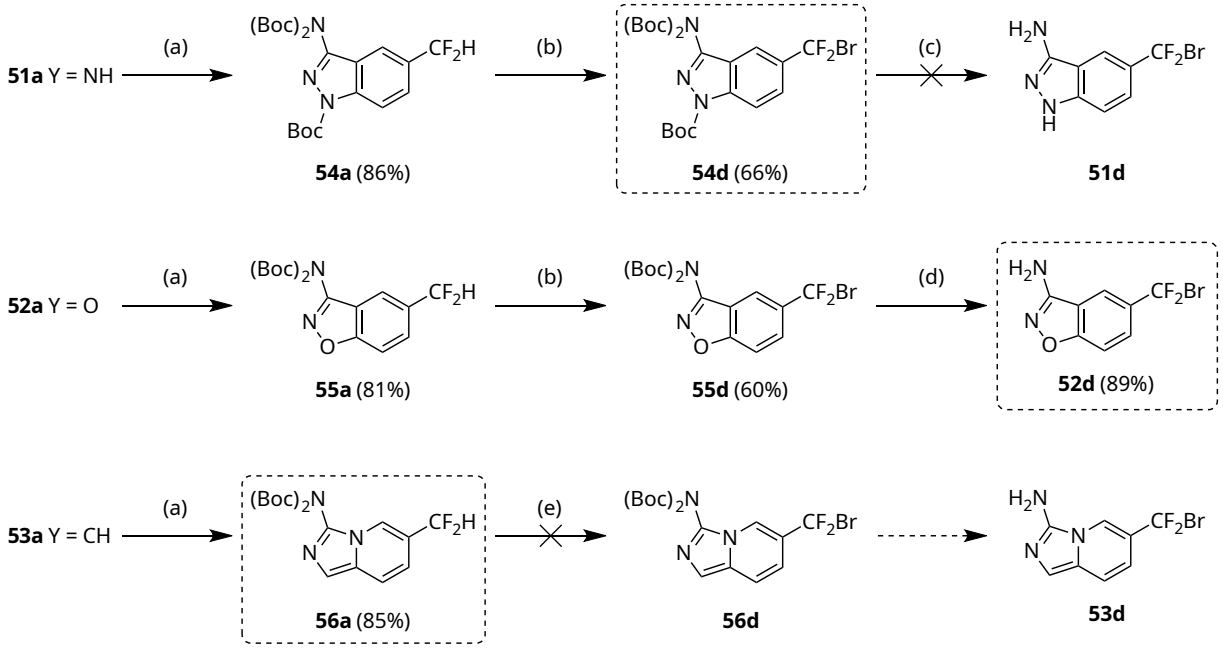


**Scheme 15:** Synthesis of imidazo[1,5-*a*]pyridin-3-amine derivatives. Dashed boxes: last synthetically accessible intermediates. Reagents and conditions: (a) $Boc_2O$, DMAP, THF, argon atmosphere, rt, 18 h, 81–86 %; (b) DBDMH, $CCl_4$, 300 W sun lamp, rt, 4–10 d, 60 –66 %; (c) different reagents and conditions, no desired product; (d) TFA, DCM, rt, 24 h, 89 %; (e) different reagents and conditions, no desired product.

The best results for obtaining $CF_2Br$-bearing **54d** and **55d** were achieved by bromination of **54a** and **55a** with 1,3-dibromo-5,5-dimethylhydantoin (DBDMH) in tetrachloromethane under illumination with a 300 W sun lamp and at ambient temperature. Alternatively, benzene could also be used as a solvent. For the bromination reaction, DBDMH was preferable to the more common reagent *N*-bromosuccinimide (NBS)[44,47] because fewer by-products and higher yields were obtained. After irradiation for 4 days, **54d** could be isolated with a yield of 66 % and **55d** could be isolated after 10 days with a yield of 60 %. Bromination of **56a** was not successful under any condition. As shown in scheme 16, position 1 of the imidazo[1,5-*a*]pyridine ring system showed high reactivity to bromination, while the $CF_2H$ group was never converted to a $CF_2Br$ group even with an excess of brominating reagent under different conditions.[231,232]

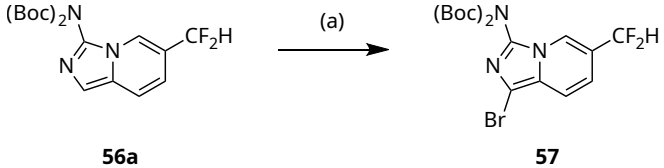


**Scheme 16:** By-product **57**. Reagents and conditions: (a) e.g., DBDMH, $CCl_4$, reflux, 18 h.

The successfully brominated intermediate **54d** and **55d** had to be deprotected in the final step. The benzisoxazole derivative **55d** was deprotected with 4 M HCl in 1,4-dioxane, obtaining test compound **52d** with a yield of 89 %. In contrast, deprotection of the acid-labile Boc protecting groups of **54d** with TFA or HCl in different solvents at different temperatures always led to non-specific degradation. In a deprotection experiment, **54d** was refluxed in aqueous HCl with two acid equivalents per Boc group, yielding up to 20 % of the $CF_2Cl$-bearing intermediate **51c**. However, **51c** was also not stable and decomposed over time.

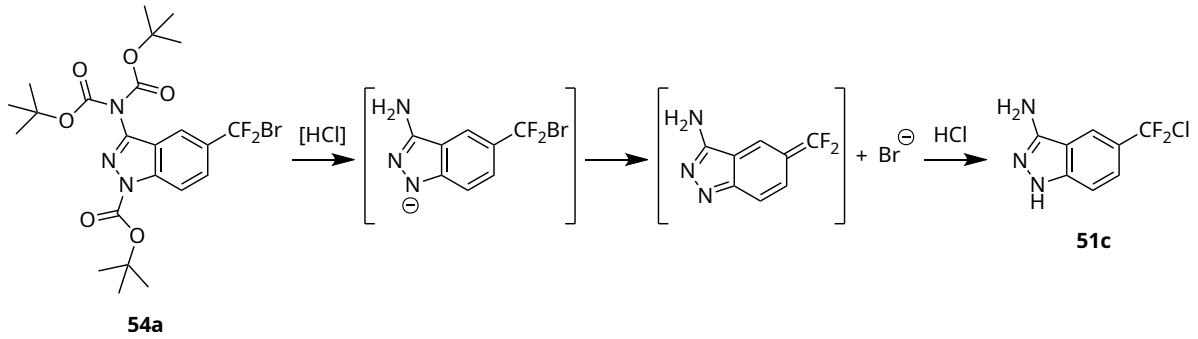


**Scheme 17:** Presumed reaction mechanism resulting in **51c** as by-product. First, elimination of a bromine atom. Second, addition of a chlorine atom.

This led to the hypothesis shown in Scheme 17. Due to mesomeric effects, the bromine atom was eliminated to form difluoromethylene and the chlorine atom was added. The fact that **51c** was not stable was probably also due to the elimination of chlorine, which was slower than that of bromine. Company UCB Pharma (UCB Biopharma SRL, Belgium) filed a patent in 2011 in which a homologous reaction was used to obtain a $CF_2Cl$ intermediate, as shown in Scheme 18.[81] This is an intermediate step in the synthesis of the antiepileptic drug padsevonil (Figure 6 on page 9).

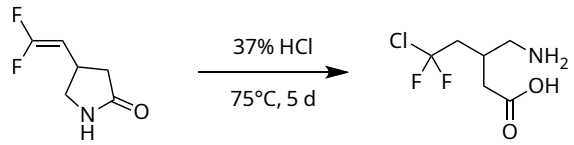


**Scheme 18:** Padesvonil intermediate synthesis.

### 3.2.4 Biophysical Assessment

Compounds **51a**, **52a** and **53a** with $CF_2H$ moiety as well as **51b**, **52b** and **53b** with $CF_3$ moiety (Figure 29) were evaluated using STD NMR and ITC against JNK1 and JNK3, respectively. The benzisoxazole with **52d** $CF_2Br$ moiety was tested only using ITC. Since the chlorine- and bromine-containing analogs with exception of **52d** were not synthetically accessible, as described in Section 3.2.3, only the compounds with $CF_2H$ and $CF_3$ group were investigated.

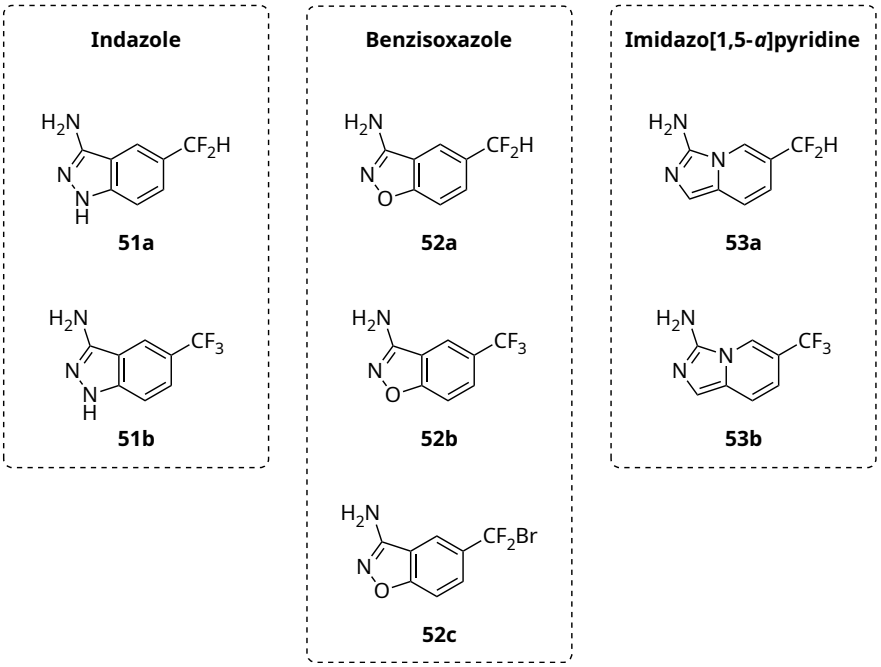


**Figure 29:** Test fragments: Indazole (**51a**,**b**), benzisoxazole (**52a**,**b**,**d**) and imidazo[1,5-*a*]pyridine (**53a**,**b**) derivatives.

As shown in Table 14 on the next page, only the imidazo[1,5-*a*]pyridines **53a** and **53b** were detectable by STD NMR according to our positive criterion (signal three-times larger than the background noise). No STD effect of hydrogen atoms was observed for all fragments, except for the C-1 hydrogen atoms of **53a** and **53b**, which could be due to the fact – based on the known literature [219,220] – that they bind to the hinge region with hydrogen bonds (Figure A2 on page 231). Since the other derivatives do not have a C−H moiety in this position and N−H is not visible in this NMR experiment, they inevitably remained negative in STD NMR. All other aromatic $^1$H nuclei also did not exhibit a positive STD signal (a signal intensity three times greater than the local noise in the difference spectrum).

Regardless of the STD NMR screening result, all fragments were measured by ITC against JNK1 and JNK3. The benzisoxazoles **52a**,**b**,**d** were confirmed as too weak or not binding. Apparently, the oxygen atom in the ring system has an adverse impact on the binding. A potential HB/XB cannot compensate for this. The positive STD signal of **53a** and **53b**

**Table 14:** Biophysical measurements using STD NMR and ITC against JNK1 and JNK3. Red colored dot (●): no binding event or not detectable. Green colored dot (●): detected binding event. Molecular weight (MW) in g mol$^{-1}$, HA is the number of heavy atoms, ITC is the measured $K_d$ in μM, and LE is the ligand efficiency as defined in equation 8 on page 123.

| | | | | | JNK1 | | | JNK3 | | |
|---|---|---|---|---|---|---|---|---|---|---|
| Compound | X | Spacer | MW | HA | STD | $K_d$ (μM) | LE | STD | $K_d$ (μM) | LE |
| **51a** | H | N/A | 183.2 | 13 | ● | 68 ± 20 | 0.45 | ● | 12 | 0.53 |
| **52a** | H | N/A | 184.1 | 13 | ● | >1000 | | ● | >1000 | |
| **53a** | H | N/A | 183.2 | 13 | ● | 92 ± 40 | 0.43 | ● | 109 | 0.40 |
| **51b** | F | N/A | 201.2 | 14 | ● | 61 ± 13 | 0.42 | ● | 100 | 0.43 |
| **52b** | F | N/A | 202.1 | 14 | ● | >1000 | | ● | >1000 | |
| **53b** | F | N/A | 201.2 | 14 | ● | 80 ± 24 | 0.41 | ● | >1000 | |
| **52d** | Br | N/A | 263.0 | 14 | | >1000 | | | >1000 | |

already indicated that an HB donor could be essential in this position; and indazoles (**51a**, **51b**) with N−H moiety bound more strongly than imidazo[1,5-*a*]pyridines (**53a**, **53b**) with C−H moiety.

In the case of JNK1, all $CF_2H$-bearing indazole (**51a**) and imidazo[1,5-*a*]pyridine (**53a**) derivatives bound in the same order of magnitude as their corresponding $CF_3$ analogs (**51b**) and **53b**). The indazole fragment **51a** bound at a $K_d$ of 68 μM and **51b** at a $K_d$ of 61 μM, while the imidazo[1,5-*a*]pyridine **53a** had a $K_d$ of 92 μM and **53b** a $K_d$ of 80 μM. Due to the difference in the number of heavy atoms (HA), a slightly increase in ligand efficiency (LE) of 5–7 % was detectable for $CF_2H$ (LE = 0.45 / 0.43) compared to $CF_3$ (LE = 0.42 / 0.41) derivatives.

For JNK3, more pronounced differences were observed between the $CF_2H$ and $CF_3$ variants. The $CF_2H$ indazole **51a** bound at $K_d$ of 12 μM and the $CF_3$ derivative **51b** gave a $K_d$ of 100 μM. This represented a 23 % increase in LE from 0.43 to 0.53 in favor of **51a**. For the $CF_2H$ imidazo[1,5-*a*]pyridine **53a**, a $K_d$ of 109 μM was determined, whereas the $CF_3$ analog **53b** was not determinable due to weak binding. For further investigation of the observed effect in JNK3, protein crystals were prepared in complex with **51a**, as detailed in the following Section 3.2.5.

### 3.2.5 Crystal Structure of JNK3 in Complex with Compound 51a

The $CF_2H$ indazole derivative **51a** was soaked into JNK3 crystals obtained by a sitting-drop procedure. The processing and refinement statistics are summarized in Table 15. The JNK3 crystal structure was solved in space group $P2_12_12$ (18) with two chains in an asymmetric unit and a resolution of 1.92 Å. Parts of the activation loop (A-loop) (Chain A: position 214–215, 221–228; chain B: position 214–224), P-loop (Chain A / B: position 71–75), and *C*-terminus of Chain B (position 376–382) were not solved. Ligand **51a** bound in the ATP binding site of chain A and chain B. The density of X-ray structural analysis permitted the determination of two 180° flipped ligand molecules in each ATP binding site (50:50 occupancy; Chain A: **51a-A**, **51a-B**; chain B: **51a-C**, **51a-D**; see Figure 30a,b on page 76).

**Table 15:** Crystallographic data for JNK3 in complex with **51a**.

| | **51a** |
|---|---|
| Wavelength | 0.92 |
| Space Group | $P2_12_12$ (18) |
| Cell Dimensions | |
| a,b,c (Å) | 110.07, 155.79, 43.83 |
| α,β,γ (°) | 90, 90, 90 |
| Resolution Range (Å) | 50–1.92 (2.04–1.92) |
| Redundancy | 8.06 (8.16) |
| Completeness (%) | 99.9 (99.9) |
| Mean I/σ (I) | 10.91 (1.08) |
| $R_{meas}$ (%) | 12.3 (208.4) |
| CC1/2 (%) | 99.8 (43.4) |
| Wilson B ($Å^2$) | 47.0 |
| Resolution Included (Å) | 46.97–1.92 |
| $R_{work}/R_{free}$ (%) | 20.19 / 23.17 |
| Bond RMSD (Å) | 0.01 |
| Angle RMSD (°) | 1.158 |
| Ramachandran (%) | |
| outliers, allowed, favored | 0 / 1.82 / 98.18 |
| Rotamer Outliers (%) | 3.96 |
| All-Atom Clashscore | 2.36 |
| Average B Factor | |
| Overall ($Å^2$) | 45.51 |
| Protein ($Å^2$) | 45.43 |
| Ligand ($Å^2$) | 45.86 |
| Water ($Å^2$) | 44.67 |

All four modes bind to the hinge region, as shown in Figure 30c–f. Indazole **51a** forms HBs with the backbone NH of M149 and the oxygens of Q147 and M149 (HB distances of 2.3–4.4 Å). Serveral CH–π contacts surround the top and bottom side of the aromatic system. The amine functions of **51a-A** and **51a-C** are on the solvent exposed side, whereas

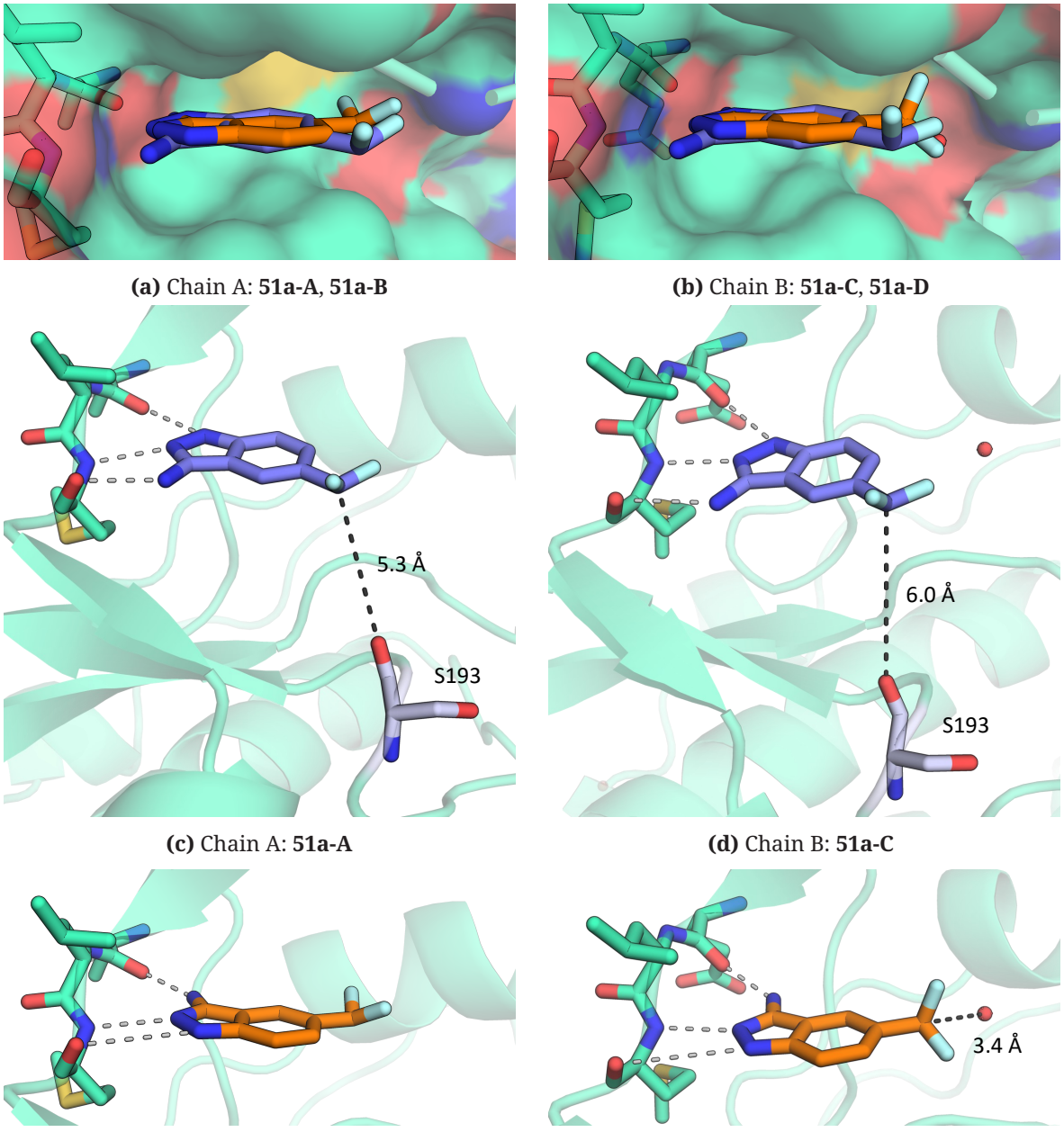


**(a)** Chain A: **51a-A**, **51a-B**

**(b)** Chain B: **51a-C**, **51a-D**

**(c)** Chain A: **51a-A**

**(d)** Chain B: **51a-C**

**(e)** Chain A: **51a-B**

**(f)** Chain B: **51a-D**

**Figure 30:** JNK3 crystallized with fragment **51a** in the ATP binding site. **(a,b)** Two binding modes were identified in chain A and B, respectively (Chain A: **51a-A** (blue), **51a-B** (orange); chain B: **51a-C** (blue), **51a-D** (orange)). **(c)** $CF_2H$ group of **51a-A** in chain A is facing the backbone oxygen of S193 ($C_H$···O: 5.3 Å). **(d)** $CF_2H$ group of **51a-C** in chain B is facing the backbone oxygen of S193 ($C_H$···O: 6.0 Å). **(e)** $CF_2H$ group of **51a-B** in chain A is without a potential interaction partner. **(f)** $CF_2H$ group of **51a-D** in chain B is facing a water oxygen ($C_H$···O: 3.4 Å).

ligands **51a-B** and **51a-D** are flipped around a 180° axis with the same amine deep in the pocket. Analogously, the $CF_2H$ groups of **51a-B** and **51a-D** are located deeper in the binding pocket. Further differences are found in the interaction partners of the $CF_2H$ moieties. Modes **51a-A** and **51a-C** are involved in a long-distance HB ($C_H \cdots O_{S193}$: 5.3 Å / 6.0 Å) with the HB-tuned $CF_2H$ group targeting the intended backbone oxygen of S193, as proposed in Section 3.2.2 on page 66. The spacing is sufficiently large for a halogen atom (X = Cl, Br, I). As shown in Figure 30, the $CF_2H$ groups clearly align toward S193. For this cause, a fluorine atom is inclined to the ring plane, respectively. Although the ΔE contribution may seem negligible due to the distance, it appears to be present based on the directional conformation. More obvious is the HB interaction of ligand mode **51a-D** with a water molecule (Figure 30f). The $CF_2-H$ bond is approximately in the plane of the aromatic indazole ring to engage in this HB interaction at a distance of 3.4 Å ($C_H \cdots O_{H_2O}$).

### 3.2.6 Conclusion

The ITC data and crystal structure show that a PDB decoration scan is a generally suitable tool for identifying protein binding ligands with $CF_2X$ moieties (X = H, Cl, Br, I). We found indazoles (**51a**,**b**) with $CF_2H$ moieties binding to JNK1 and JNK3, and derived from them also binding imidazo[1,5-*a*]pyridine derivatives (**53a**,**b**). The preparation of the desired indazoles **51d** and imidazo[1,5-*a*]pyridine **53d** with $CF_2Br$ groups (and indazole with $CF_2Cl$ **51c** group) in this specific example failed due to synthetic accessibility. Molecular instability caused by mesomeric properties (indazole) and deficiency of the brominability of the $CF_2H$ group (imidazo[1,5-*a*]pyridine) are possibly limiting factors. These are factors that must be considered in future synthesis strategies. With protected aromatic NH function or an oxygen atom instead, $CF_2Br$-bearing indazoles (**54d**) and benzisoxalzoles (**52d** and **55d**) are synthetically achievable, but lose their binding capability. Thus, a sterically undemanding NH or CH function as HB donor is mandatory for binding in these chemical pattern structures. Only JNK3 showed significantly better binding for $CF_2H$-bearing indazoles / imidazo[1,5-*a*]pyridines ($K_d$ = 12 μM / 109 μM) compared to those with $CF_3$ group ($K_d$ = 100 μM / >1000 μM). This could be due to differences in the binding pocket, but would need further investigation in the future.

## 3.3 Synthesis of Amino Acids Bearing $CF_2X$ Moieties and Their Application to p53-Derived Peptides Binding to MDM2/MDM4

Parts of this Section 3.3 were published in:

**S. Vaas**, M. O. Zimmermann, T. Klett, and F. M. Boeckler. Synthesis of Amino Acids Bearing Halodifluoromethyl Moieties and Their Application to p53-Derived Peptides Binding to Mdm2/Mdm4. *Drug Des. Dev. Ther.* **2023**, *17*, 1247–1274. doi: 10.2147/DDDT.S406703[184]



### 3.3.1 Abstract

Therapeutic peptides are a significant class of drugs in the treatment of a wide range of diseases. To enhance their properties, such as stability or binding affinity, they are usually chemically modified. This includes, among other techniques, cyclization of the peptide chain by bridging, modifications to the backbone, and incorporation of unnatural amino acids. One approach previously established, is the use of halogenated aromatic amino acids. In principle, they are thereby enabled to form halogen bonds. In this study, we focus on the $-R-CF_2X$ moiety (R = O, NHCO; X = Cl, Br) as an uncommon halogen bond donor. These groups enable more spatial variability in protein-protein interactions. The chosen approach via Fmoc-protected building blocks allows for the incorporation of these modified amino acids in peptides using solid-phase peptide synthesis. We demonstrate that a p53-derived peptide with Lys24Nle(εNHCOCF$_2$X) against MDM4 has an improved inhibition constant $K_i$ compared to the unmodified peptide. The decreasing $K_i$ value with increasing size of halogens (F > Cl > Br) indicates a formation of a halogen bond. By reducing the side chain length of Nle(εNHCOCF$_2$X) to Abu(γNHCOCF$_2$X) and through quantum mechanical calculations, we suggest that the observed affinity enhancement is related to halogen bond-induced intramolecular stabilization of the α-helical binding mode of the peptide or a direct interaction with His54 in human MDM4. Therapeutic peptides are a significant class of drugs in the treatment of a wide range of diseases. To enhance their properties, such as stability or binding affinity, they are usually chemically modified. This includes, among other techniques, cyclization of the peptide chain by bridging, modifications to the backbone, and incorporation of unnatural amino acids. One approach previously established, is the use of halogenated aromatic amino acids. In principle, they are thereby enabled to form halogen bonds. In this study, we focus on the $-R-CF_2X$ moiety (R = O, NHCO; X = Cl, Br) as an uncommon halogen bond donor.

These groups enable more spatial variability in protein-protein interactions. The chosen approach via Fmoc-protected building blocks allows for the incorporation of these modified amino acids in peptides using solid-phase peptide synthesis. We demonstrate that a p53-derived peptide with Lys24Nle(εNHCOCF$_2$X) against MDM4 has an improved inhibition constant $K_i$ compared to the unmodified peptide. The decreasing $K_i$ value with increasing size of halogens (F < Cl < Br) indicates a formation of a halogen bond. By reducing the side chain length of Nle(εNHCOCF$_2$X) to Abu(γNHCOCF$_2$X) and through quantum mechanical calculations, we suggest that the observed affinity enhancement is related to halogen bond-induced intramolecular stabilization of the α-helical binding mode of the peptide or a direct interaction with His54 in human MDM4.

### 3.3.2 Introduction

Halogenated amino acids and peptides have been the subject of interest in recent research.[87,88,121,122,233–243] Several reviews address the occurrence of natural halogenated amino acids in microbial organisms, bioactive features, e.g., in antimicrobial peptides, or the potential of biomimetic engineering in peptide-based drug development and self-assembly. While a wide range of chlorine-, bromine- and iodine-substituted aromatic amino acids in nature are described, the known aliphatic halogenated amino acids are essentially limited to chlorine derivatives due to reactivity of the halogens in aliphatic compounds. In addition, numerous synthetically accessible amino acids have been described in the literature, in particular derivatives of the proteinogenic amino acids phenylalanine, tyrosine, tryptophan, and histidine.[89,90]

Peptides for therapeutic applications are often derived from natural products or are protein mimetics modified to improve properties such as stability or affinity. These modifications include the use of D-amino acids instead of L-amino acids, modification of the peptide backbone, attaching of lipids or polymers, protection of peptide termini, bridging and cyclization to chemically constrained peptides, and incorporation of unnatural building blocks, for instance halogenated amino acids.[93,95,244]

Halogenation of amino acid side chains or drugs in general appears to be an effective tool for modulating binding selectivity and increasing binding affinity.[91] This modification affects also physicochemical properties of peptides, such as catabolic stability, lipophilicity, and membrane permeability.[92] In addition, chlorine, bromine, and iodine are able to engage in halogen bonding (XB). A halogen bond is a non-covalent bond based on attractive interactions between an electron donor (B) and an electron-deficient region of the halogen (X), the σ-hole, which results from the anisotropic electron distribution of the halogen.[5] This interaction is strongly directed along the C−X···B axis, with the best interaction energies found at an angle of 180° with a deviation of up to 30° and an X···B distance

of about 3–4 Å.[4,6] Electron donors in proteins are typically the backbone carbonyl of the main chain[8–10] and oxygen or nitrogen atoms of electron-rich side chains (eg, aspartate, glutamate),[11] serine, histidine,[12] or sulfur in methionine.[13]

As described, halogens bound to aromatic systems are particularly stable relative to aliphatic compounds. In this work, instead of this conventional approach, we establish amino acids with $CF_2Br$ ethers and $CF_2X$ acetamides (X = Cl, Br), where two electron-withdrawing fluorine atoms are used to stabilize the C−X bond. So far, amino acid-derived compounds with $sp^3$-hybridized $CF_2Br$ moiety have been described mainly as precursor for the synthesis of difluoromethylene building blocks.[97,98] Applications of such moieties to fragment-based drug discovery, their interactions in small molecule crystals and computational studies with respect to their use in molecular design are reported in Section 3.1 on page 17.

First, we performed bottom-up synthesis of Fmoc-protected phenylalanine with a $CF_2Br$ ether function in either *meta* or *para* position. In addition, we prepared the $CF_2X$ acetamides by one-step syntheses from Fmoc-protected lysine and 2,4-diaminobutyric acid. Fmoc-protection of the amine was necessary for its use in solid-phase peptide synthesis (SPPS). For evaluation, the synthesized amino acids were incorporated into 12-mer p53-derived peptides by automated SPPS.

The tumor suppressor protein p53 is an important oncologic target and is known to be implicated in most of all human cancers.[245,246] Rescuing p53 mutations and targeting the p53 regulatory network has been a focal point of our research.[6,7,201,213,247**?** –250] The proteins MDM2 and MDM4 are negative regulators of p53, and their interaction is a common model system for evaluating inhibition of protein-protein interactions (PPIs).[94] Both proteins bind to the same sequence in the intrinsically disordered *N*-terminus of p53 with their structurally very similar *N*-terminal domains.[251,252] The surface region of the binding site of MDM2 and MDM4 are small hydrophobic clefts[253,254] with limited molecular interaction capabilities. The critical amino acids Phe19, Trp23 and Leu26 (p53 numbering) involved in the binding are found in almost every peptide sequence described in literature.[255] Mutations of these amino acids lead to a drastic loss of binding affinity.[256] These properties hinder the substitution of these three amino acids by other proteinogenic and non-proteinogenic amino acids and complicate the introduction of new PPI contacts that could lead to stronger interactions. Therefore, in our study, we consider the enhancement of direct peptide-protein interactions, as well as the stabilization of the helix formation of the p53 peptide by forming an intramolecular interaction.

This PPI model was used to evaluate our p53-derived sequences containing the $CF_2X$-bearing amino acids by determination of $K_i$ values using a competitive fluorescence polarization (FP) assay[257] with an *N*-terminal fluorescein-labeled high-affinity peptide as probe.[248,255,258]

### 3.3.3 PDB Database Screening and Sequence Selection

Trying to rationalize possible applications of $CF_2X$-bearing amino acid side chains in PPI, we scanned HIV-1 protease, MDM2, and MDM4 Protein Data Bank (PDB) entries via aromatic C atom decoration of phenylalanine and tyrosine using a PyMOL/Python script. The attached substituents were rotated along its individual axes in five-degree steps. Hits with suitable C−X···B angle and X···B distance (B = N, O) were checked. Incidentally, the search was limited to the entries of resolved crystal structures deposited in the PDB.

Two selected findings are shown in Figure 31. Figure 31a shows a peptide phenylalanine decorated with a CF2Br unit in *para* position in a CA-p2 substrate/HIV-1 protease complex (PDB ID: 1A8K; peptide sequence: RVL-r-FEA-Ahx-$NH_2$),[259] with a σ-hole angle of 165.8 °C and a distance of 3.4 Å to the Pro81 backbone oxygen. Another decoration result was found in a PMI (N8A mutant)/MDM2 complex (PDB ID: 3LNZ; peptide sequence: TSFAEYWALLSP)[256] as shown in Figure 31b, where a peptide tyrosine was decorated in *meta* position. The $CF_2Br$ ether moiety intramolecularly targets a peptide threonine with a C−Br···O angle of 177.2° and an X···O distance of 3.0 Å. Suitable peptide decorations with direct interaction between peptide and MDM2/MDM4 were not found in contrast to intramolecular side chain interactions, which may be due to the nature of the binding pocket described in the introduction. Inspired by these results, the syntheses of halogenated

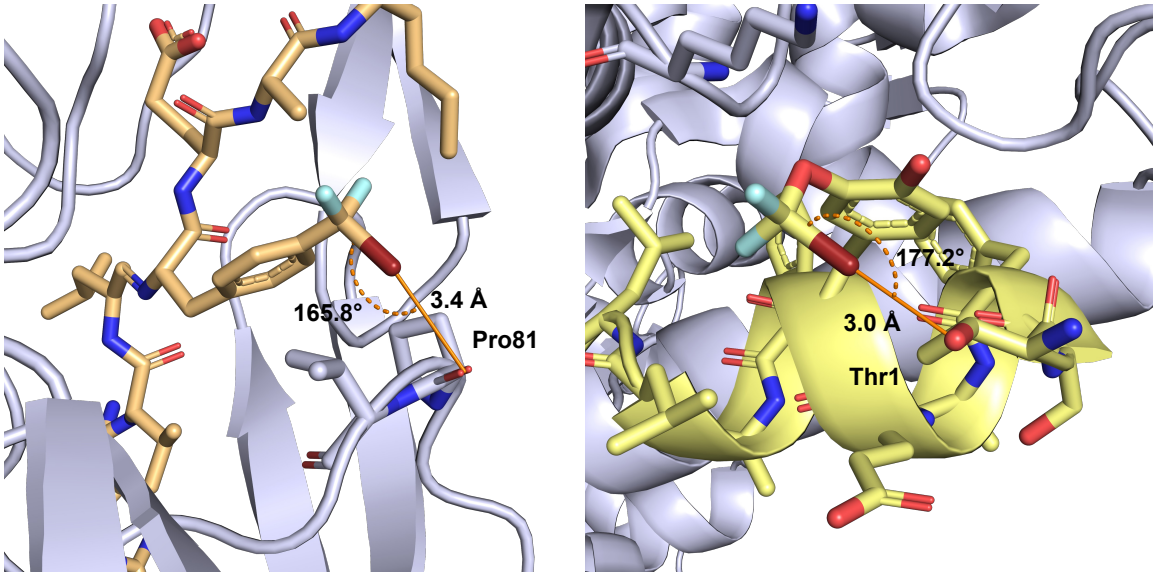


**(a)** 1A8K, HIV-1 Protease **(b)** 3LNZ, MDM2

**Figure 31:** PDB decoration scan of aromatic amino acids in peptides. **(a)** $CF_2Br$ methyl unit attached to a phenylalanine in *para* position targeting the backbone oxygen of Pro81 in a CA-p2 substrate/HIV-1 protease crystal structure (PDB ID: 1A8K). **(b)** $CF_2Br$ ether moiety attached to a tyrosine in *meta* position intramolecularly targeting a peptide threonine side chain in a 12-mer peptide inhibitor PMI (N8A mutant)/MDM2 crystal structure (PDB ID: 3LNZ).

Fmoc-protected phenylalanines were planned and performed as described. Due to chemical stability considerations, the synthesis of amino acids with a catechol substructure (as shown in Figure 31b) was omitted. In addition to the ether function, we also attempted to prepare a thioether and sulfone isostere.

As a second approach, non-aromatic amino acids were synthesized by acetylation of aminated alkyl side chains and their incorporation into the $^{17\text{-}28}$p53 *wild-type* sequence (ETFSDLWKLLPE) mutating Lys24Nle(εNHCOR) and Lys24Abu(γNHCOR) (with R = $CH_3$, $CF_2H$, $CF_3$, $CF_2Cl$ and $CF_2Br$). Due to the large number of degrees of freedom in the lysine side chain, computational decoration scans of PDB structures were not considered appropriate here. Besides the importance of being located in the sequence binding to MDM2/MDM4, the p53 sequence interacts with mitochondrial E3 ubiquitin protein ligase 1 (MUL1) resulting in ubiquitination of cytoplasmic p53 at Lys24 and subsequent proteasomal degradation.[260] Acetylated lysine is no longer expected to cross-link interchain with the *C*-terminal glycine of ubiquitin. Known mutation Lys24Arg in p53 abolishes ubiquitination by MUL1 and the somatic mutation Lys24Asn is implicated in sporadic cancer.[261] Therefore, we were interested in evaluating the p53 sequence by modifying the existing Lys24 via different substituted acetyl groups.

### 3.3.4 Amino Acid Synthesis

#### 3.3.4.1 Aromatic Amino Acids based on Phenylalanine with $CF_2Br$ Moiety

The amino acid precursors **71**–**75** containing $CF_2Br$ functionality were synthesized from methylbenzene derivatives as shown in Scheme 19. A brominatable methyl unit was mandatory to introduce the diethylacetamidomalonate function, which was subsequently converted to the amino acid function.

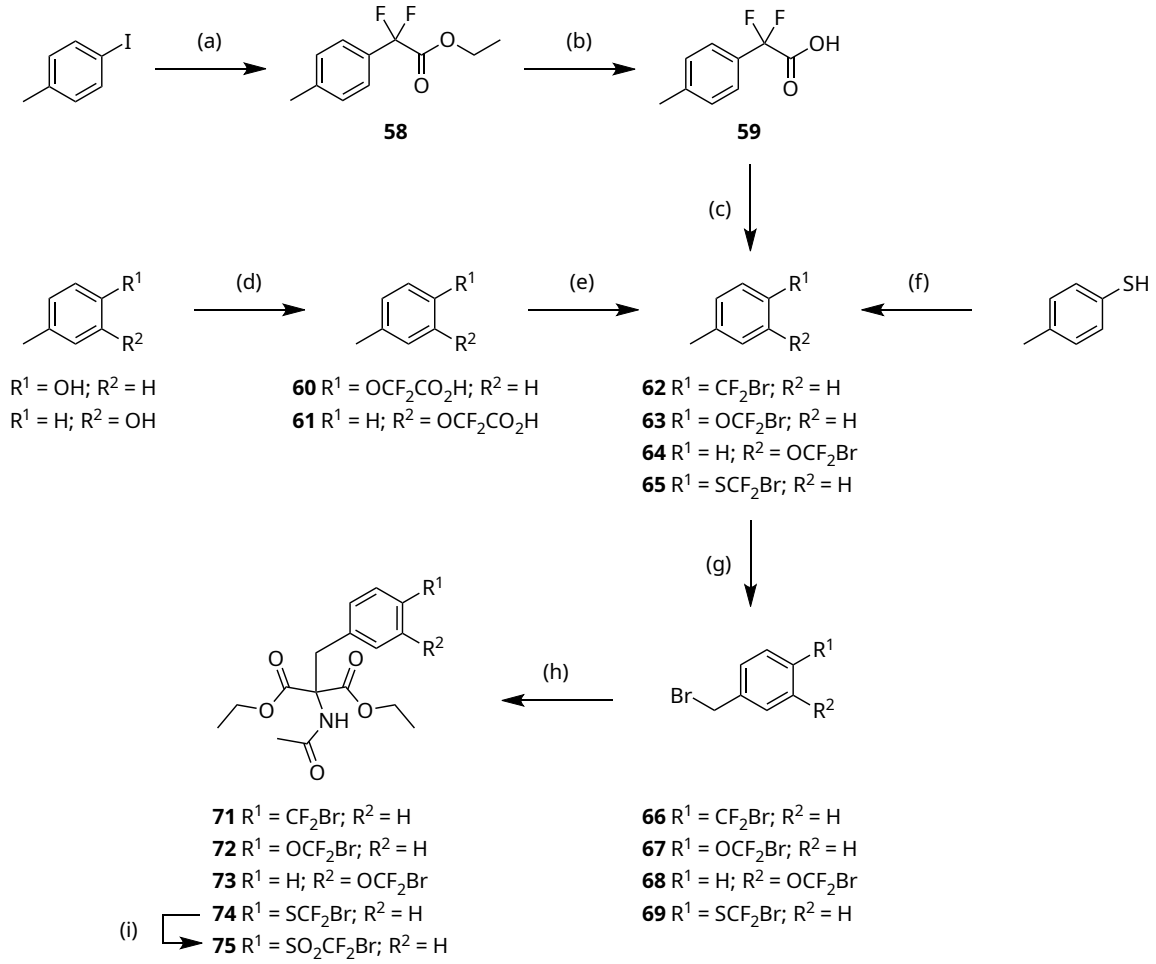


**Scheme 19:** Synthesis of 3-/4-methylbenzene derivatives containing $CF_2Br$ moiety as precursors for amino acid synthesis. Reagents and conditions: (a) Ethyl bromodifluoroacetate, act. $Cu^0$, argon atmosphere, 60 °C, 26 h; (b) 1 M aq. $K_2CO_3$/MeOH (1:1), rt, 18 h; (c) (1) $(COCl)_2$, DMF (cat.), DCM, rt, 3 h; (2) DMAP, sodium-*N*-hydroxy-2-thiopyridone, $BrCCl_3$, argon atmosphere, 300 W sunlamp, rt, 20 h; (d) (1) NaH, 1,4-dioxane, argon atmosphere, rt, 30 min; (2) potassium 2-bromo-2,2-difluoroacetate **1a**, 1,4-dioxane, argon atmosphere, 80 °C, 20 h; (e) (1) $(COCl)_2$, DMF (cat.), DCM, rt, 3 h; (2) DMAP, sodium-*N*-hydroxy-2-thiopyridone, $BrCCl_3$, argon atmosphere, 120 °C, 2 h; (f) (1) NaH, DMF, rt, 0 °C; (2) $CF_2Br_2$, DMF, 0 °C, 3 h; (g-1) NBS, ABCN, $CCl_4$ or benzene, argon atmosphere, reflux, 8 h; (g-2) diethylacetamidomalonate, $K_2CO_3$, KI, ACN, argon atmosphere, reflux, 18 h; (g-2) mCPBA, DCM, rt, 18 h.

Ethyl 2,2-difluoro-2-(*p*-tolyl)acetate (**58**) was synthesized by means of Ullmann coupling using hydrochloric acid activated copper(0) as catalyst.[69,262] The obtained ester was hydrolyzed under basic conditions to halogenate the free carboxylic acid (**59**) by Barton decarboxylation. The Barton decarboxylation requires the *in situ* generation of a Barton ester using acid chloride generated with oxalyl chloride and sodium-*N*-hydroxy-2-thiopyridone as reagent,[68] which is followed by a photoinduced radical decarboxylation. With a suitable radical trapping agent such as $BrCCl_3$, the introduction of a bromine is possible, as performed in our case to obtain **62** with a yield of 41 %.

*p*-Cresol and *m*-Cresol were elaborated to give bromodifluoromethoxylated derivatives using a reaction sequence with analogous intermediates.[43] The free carboxylic acids **60** and **61** were generated via nucleophilic substitution directly with the reagent potassium bromodifluoroacetate (**1a**) under basic conditions bypassing ester hydrolysis. In contrast to photolyzed Barton decarboxylation at methyl groups, this reaction with methoxy groups requires higher temperatures around 120 °C for 2 h and provided slightly higher yields with 51 % for **63** and 54 % for **64**.

The synthesis of bromodifluoromethyl sulfone had the advantage that it was directly obtained from the corresponding thiol in a one-step synthesis due to the higher nucleophilicity of thiolates compared to alcoholates. In the first step, sodium hydride was used to generate the thiolate, which was reacted with reagent $CF_2Br_2$ to obtain **65** with a yield of 63 %.

The $CF_2Br$ thioether moiety could be directly obtained from the corresponding thiol in a one-step synthesis, due to the higher nucleophilicity of thiolates compared to alcoholates. In the first step, sodium hydride was used to generate the thiolate, which was reacted with reagent $CF_2Br_2$ to obtain **65** with a yield of 63 %.[43,189] The synthesized compounds with $CF_2Br$ moieties (**62**–**65**) were all brominated at the methyl position and, without further purification, converted to the amino acid precursors **71**–**74**.[263] The yield of this two-step synthesis varied from 45 % for **71** to 77 % for **74**. In addition, **65** was oxidized with mCPBA to the sulfone derivative **75** with a yield of 73 %.[189]

Synthesizing amino acid functionality while maintaining the $CF_2Br$ moiety was a particular challenge. Two possible routes to obtain Fmoc-protected amino acids are shown in Scheme 20 on the next page. Route (a) presents a one-pot-synthesis under heat with harsh acidic conditions leading to ester hydrolysis, amide hydrolysis and decarboxylation, followed by subsequent Fmoc-protection of amine functionality and chiral column chromatography. The simplest reaction condition is refluxing in concentrated hydrochloric acid. This and different modulations of temperature, reaction time, acids, acid concentrations, organic solvents and organic solvent contents did not result in the desired products.

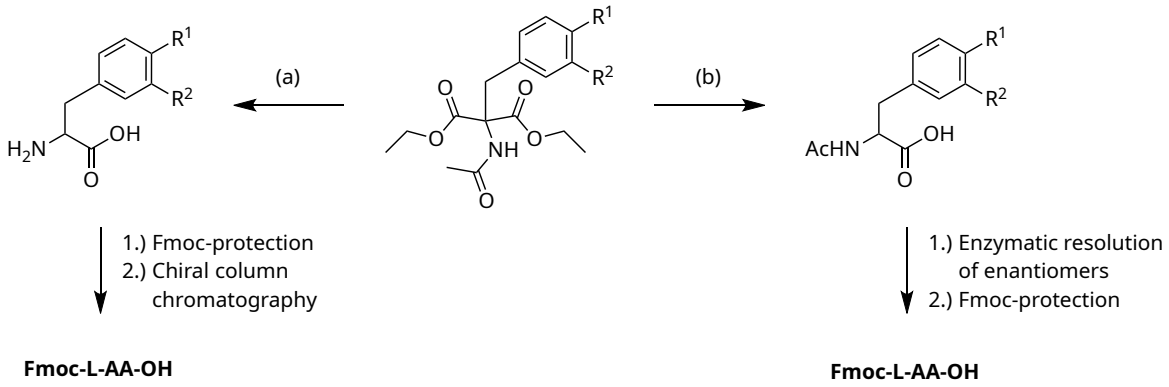


**Scheme 20:** Two possible routes to obtain Fmoc-protected amino acids. Route (a) presents acidic conditions and route (b) alkaline reaction conditions.

With bases such as NaOH, it is possible to generate amino acids according to route (b) while retaining the acetamido and $CF_2Br_2$ moiety (Scheme 20). This was achieved for **72** and **73**, while **71**, **74** and **75** also degraded with this method (Scheme 21). In principle, this method can be carried out in one step under heat, see **76** with a yield of 57 %. Alternatively, hydrolysis can be done first at room temperature under basic condition and decarboxylation in a second step without base under heat.

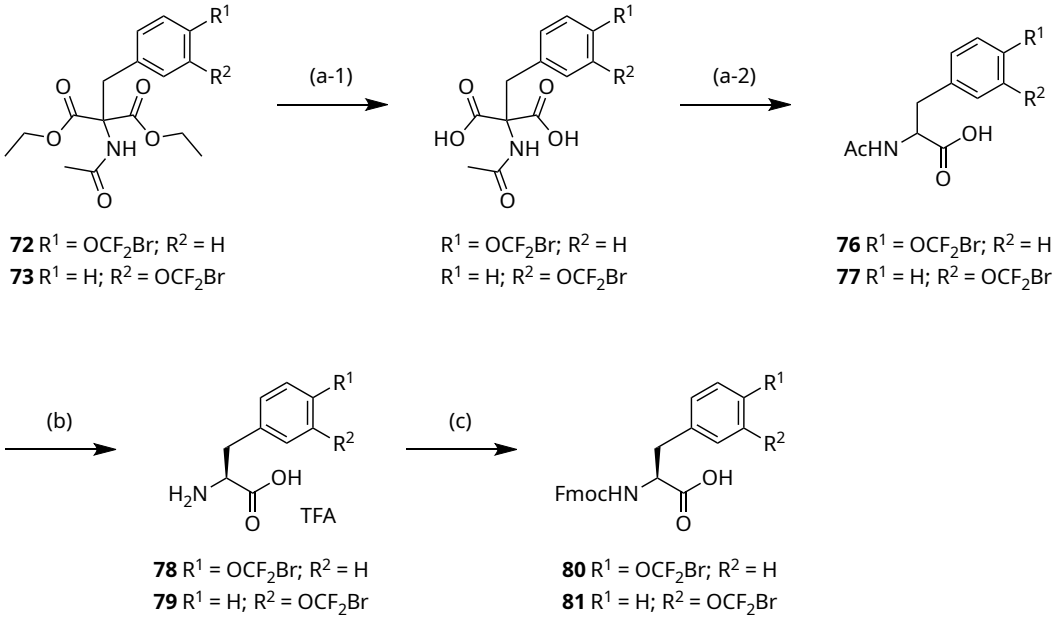


**Scheme 21:** Synthesis of Fmoc-protected amino acid derivatives containing $CF_2Br$ moiety. Reagents and conditions: (a-1/2) **72**, NaOH, MeOH/$H_2O$ (3:1), rt, 1 h, then 80 °C, 3 h; or: (a-1) **73**, NaOH, MeOH/$H_2O$ (3:1), rt, 4 h; (a-2) THF/$H_2O$ (3:1), 3 h, 70 °C; (b) **76**, 0.1 M phosphate buffer (pH 8), $CoCl_2$, Amano Acylase, rt, 6 h; or: **77**, 1 M aq. NaOH, pH 7.0–10, Amano Acylase, rt, 4 h; (c) Fmoc-Cl, $Na_2CO_3$, 1,4-dioxane, rt, 4 h.

The second method resulted in a higher yield of 93 % for the conversion of **73** to **77**. An additional advantage of this synthetic route (b) was that an enzymatic resolution of enantiomers was performed in the following step, which eliminated the need for separation via chiral column chromatography. Amano Acylase was used for acetamide cleavage of only the L-enantiomers, while the D-enantiomers were left acetylated. The yields were 10 % for **78** and 13 % for **79**, although it should be noted that the maximum yield could only be 50 %. In order to use the amino acids in peptide synthesis, they were Fmoc-protected in the final synthesis step (**80** and **81**).

### 3.3.4.2 Non-aromatic Amino Acids with $CF_2X$ Acetamide Moiety

Another method to obtain Fmoc-protected amino acids with $CF_2X$ moiety is to modify side chains with amine function by coupling with derivatives of acetic anhydride or other acetic acid-based reagents to their corresponding $CF_2X$ acetamides. The advantage is that the desired products can be achieved in a one-step synthesis due to the commercial availability of the reagents. Fmoc-L-Nle(εNHCOCH$_3$)-OH (**82a**) and Fmoc-L-Nle(εNHCOCF$_3$)-OH (**82c**) are commercially available and applicable for solid-phase peptide synthesis.

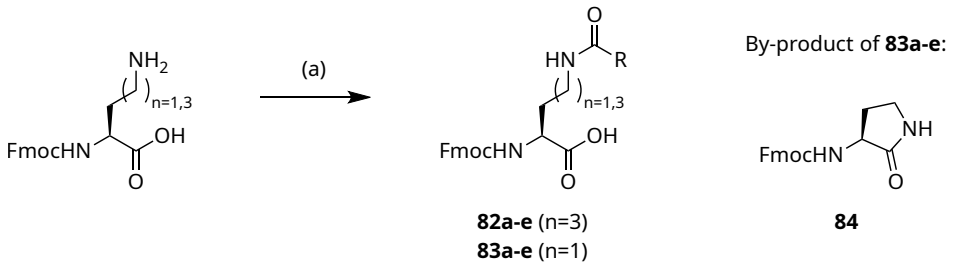


**Scheme 22:** Synthesis of Fmoc-protected L-norleucine (**82a**–**e**) and L-α-aminobutyric acid (**83a**–**e**) derivatives containing acetamide moiety. R = $CH_3$, $CF_2H$, $CF_3$, $CF_2Cl$, $CF_2Br$. Reagents and conditions: (a) NMM, corresponding anhydride $(RCO)_2O$, THF, argon atmosphere, 0 °C to rt, 2.5 h.

For the studies presented in this work, acetylated derivatives of Fmoc-protected L-norleucine with a side chain of four methylene groups and Fmoc-protected L-α-aminobutyric acid, a shorter variant with a side chain of two methylene groups, were synthesized as shown in Scheme 22. All derivatives were synthesized in THF with NMM as base through addition of the appropriate anhydride. Iodine derivatives were not synthesized because difluoroiodoacetic anhydride was not commercially available. As Table 16 on the next page shows, there were significant differences in the yields. In principle, the yields of acetylated lysine analogs **82b**,**d**,**e** were with >50 % higher than those of the shorter variants **83a**–**e** with <50 % yield, which made this synthesis method more suitable for the lysine derivatives.

**Table 16:** Comparison between yields of Fmoc-protected Nle and Abu derivatives. Synthesis procedures: see Section 6.3.7 on page 182.

| | | Yields (%) | | |
|---|---|---|---|---|
| Compound | R | Nle (**82**) | Abu (**83**) | By-product (**84**) |
| **a** | $CH_3$ | N/A[a] | 45.0 | N/A[b] |
| **b** | $CF_2H$ | 89.9 | 24.6 | 13.8 |
| **c** | $CF_3$ | N/A[a] | 21.6 | 64.4 |
| **d** | $CF_2Cl$ | 55.7 | 23.3 | 29.9 |
| **e** | $CF_2Br$ | 57.0 | 23.7 | 43.6 |

[a] Commercially available.
[b] Not detected.

Acetylation of L-α-aminobutyric acid instead tended to form the five-membered γ-lactam (**84**), which was confirmed by mass spectroscopy and NMR. The obtained yields of the by-product (14–64 %) were not consistent in relation to the halogenated main products (20–25 %). Seven-membered ε-lactam by-products of **82a**–**e** synthesis were not observed.

### 3.3.5 Peptide Synthesis

#### 3.3.5.1 Solid-Phase Peptide Synthesis

Solid-phase peptide synthesis (SPPS) was first described in 1962 by Bruce Merrifield, who later received the Nobel Prize for this discovery.[264] All peptides synthesized in this thesis were prepared using Fmoc method and SPPS, the most commonly used strategy for peptide synthesis today.[265,266] A polyethylene glycol (PEG)-based Rink amide resin was applied as the solid phase to provide *C*-terminal amides. Piperidine was used for Fmoc cleavage, HBTU as coupling reagent, NMM as base, and acetic anhydride / 2,6-lutidine as capping reagent after each cyclization coupling step. The peptides were treated with a solution of tifluoroacetic acid (TFA), water, triisopropyl silane (TIPS) and phenol (about 90/4.5/4.5/1-ratio) to remove all the side chains and to cleave the peptides from the resin (detailed procedure see Section 6.2.1 on page 135).

Chromatographic reversed-phase purification did not reveal any significant difference in the purity and yield of the peptides containing the $CF_2Br$ ether and $CF_2X$ amide moieties compared to the peptides prepared entirely from standard Fmoc-protected amino acids. Consequently, the modified amino acids can be exposed to strongly basic as well as strongly acidic conditions without any loss of the $CF_2X$ group or other peptide degradation. Even mild reducing agents such as TIPS, which acts as a hydride donor scavenger, do not appear to have any adverse effects.[267] All synthesized peptide sequences with detected high-resolution masses were listed in Table 18 on page 91 and Table 19 on page 92.

#### 3.3.5.2 Peptide Cyclization: Optimization of Copper(I)-catalyzed Alkyne-Azide Cycloaddition Reaction

To investigate the properties of the peptide helicity due to a potential intramolecular XB interaction, chemically constrained peptides were synthesized in addition to their linear peptide analogs. The exact experimental strategy and background are outlined in Section 3.3.7.3 on page 100. Numerous methodologies are described for generating peptides chemically constrained.[244] The triazole stapling method was chosen because of the commercial availability of amino acids and the bridging range provided (*i* and *i*+*n*).

A triazole stapeling method is demonstrated by Cantel *et al.* in 2008 through cyclization of L-norleucine($\varepsilon N_3$) and L-propargylglcyine at position *i* and *i+4*, mimicking the amide-stapled peptide inhibitor of parathyroid hormone-related peptide (PTHrP).[268] Kawamoto *et al.* described in 2012 further triazole-stapled peptides synthesized by copper(I)-catalyzed alkyne-azide cycloaddition (CuAAC) reaction. They used BCL9 α-helical peptides as a model varying the length and the L- and D-enantiomers of concerning amino acides to investigated helicity and protein binding affinity interaction with β-Catenin.[269]

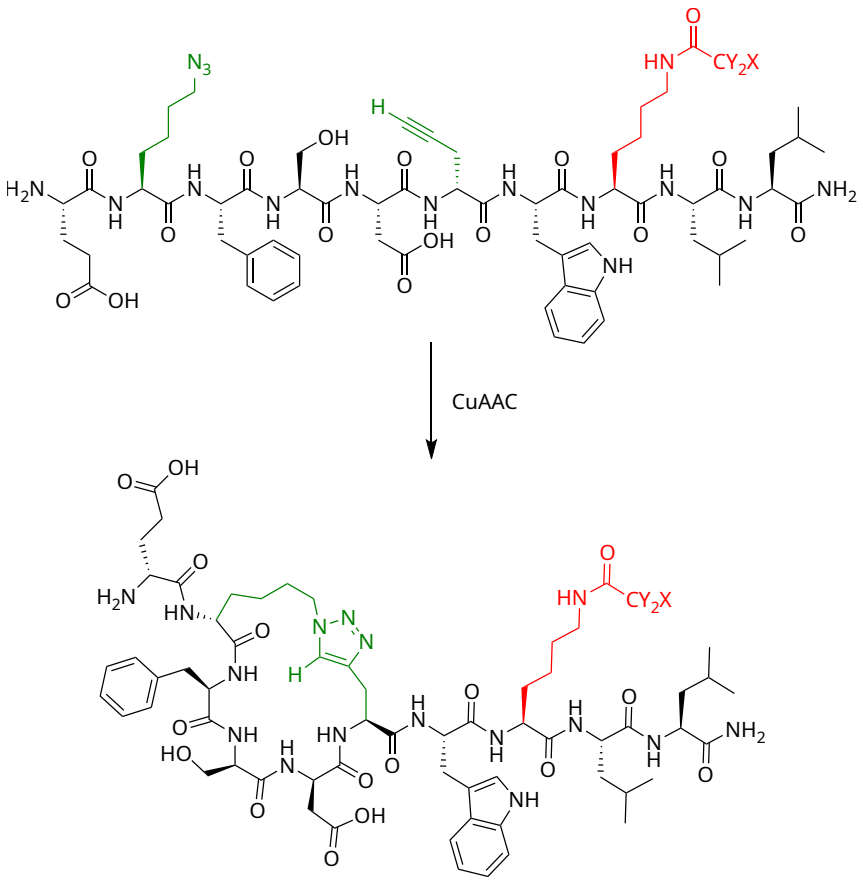


**Scheme 23:** Exemplary CuAAC reaction of a 10-mer test peptide.

A large number of experiments following the protocols of Cantel *et al.* and Kawamoto *et al.* did not lead to the desired result of a triazole-stapled peptide (Scheme 23). Increased and decreased equivalent combinations of copper and reducing agent (sodium ascorbate and TCEP) from 1 to 20 eq and varying solvent ratio of *t*-BuOH / $H_2O$ did not result in triazole-stapled peptides, but in undefinable white precipitation over the reaction time. In addition, the peptides showed very low solubility in this solvent mixture. The analysis was complicated by the fact that reactant and product had the same molecular mass and the retention shift of linear peptide to stapled peptide in analytical HPLC was not known at the outset.

However, some basic changes in the reaction conditions resulted in the desired product with negligible by-products according to HPLC. Acetonitrile is usually avoided for Cu(I)-catalyzed reactions because acetonitrile can coordinate on Cu(I). On the other hand, the peptides showed much higher solubility in ACN / $H_2O$ (2:1) mixture and this mixture could be directly injected into the semi-preparative C18 column for purification (see Section 6.1.3 on page 133) after the completion of the reaction. A different solvent mixture alone, however, did not yet lead to the successful reaction. Additionally base ($NaHCO_3$) leading to pH ≥ 7 and a commercially available ligand (TBTA) were added. In a 2004 study,

**Table 17:** Comparision between literature protocol[269] from Kawamoto *et al.* (2012) and optimized CuAAC procedure for the generation of triazole-stapled peptides.

| | Literature | Optimization |
|---|---|---|
| Solvent | *t*-BuOH / $H_2O$ (2:1) | **ACN / $H_2O$ (2:1)** |
| Peptide TPV-18 (with Nle(εNHCOCH$_3$)) | 1 mg mL$^{-1}$ | 8 mg mL$^{-1}$ |
| Precatalyst (Cu(II)$SO_4 \cdot 5\,H_2O$) | 4.4 eq | 1.0 eq |
| Reducing agent (sodium ascorbate) | 4.4 eq | 2.0 eq |
| Ligand (TBTA) | - | **1.0 eq** |
| Base ($NaHCO_3$) | - | **5.0 eq** |

Chan *et al.* described TBTA as a ligand that stabilized Cu(I), protected from disproportionation and increased the yield in a large number of copper(I)-catalyzed alkyne-azide cycloadditions.[270] If these changes were taken into account and the triazole stapling method was carried out under the conditions indicated in Table 17, the reaction was completed within 30 minutes or less. The successful CuAAC reaction was confirmed by NMR, as shown in Figure 32. Linear peptide had a propargyl hydrogen atom (TPV-18$_{linear}$: 2.60 ppm), while stapled peptide had a triazole hydrogen atom (TPV-18$_{stapled}$: 7.59 ppm). The cyclized peptides had also a about two-minute shorter retention time compared to their linear analogs.

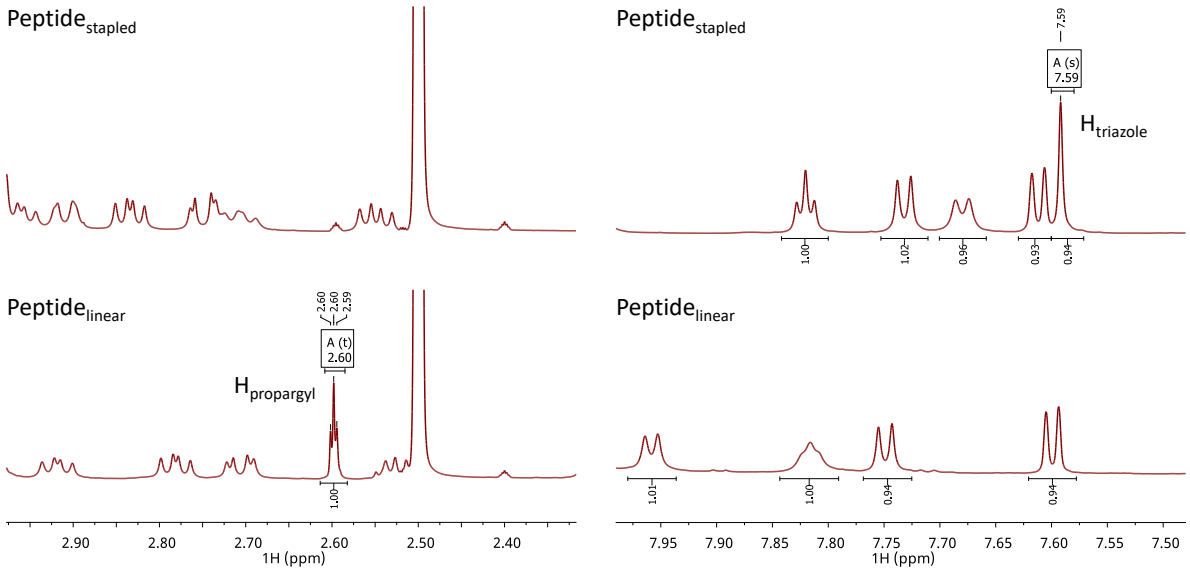


**(a)** Propargyl-H. **(b)** Triazole-H.

**Figure 32:** Linear vs. stapled peptide NMR control of TPV-18 (with Nle(εNHCOCH$_3$)). **(a)** Propargyl hydrogen atom in linear peptide. **(b)** Triazole hydrogen atom in peptide.

**Table 18:** Peptide overview: Incooperated aromatic amino acids with different ether moiety based on phenylalanine.

| Entry | Peptide sequence | x | $[M+xH]^{x+}$ (theor.) (*m/z*) | $[M+xH]^{x+}$ (*m/z*) | rel. Δm (ppm) |
|---|---|---|---|---|---|
| **TPV-1** | $H_2N$-TSFAE **Y** WALLSP-$CONH_2$ | 1 | 1383.6943 | 1383.6939 | 0.3 |
| **TPV-2** | $H_2N$-TSFAE **F** WALLSP-$CONH_2$ | 1 | 1367.6994 | 1367.7014 | 1.5 |
| **TPV-3** | $H_2N$-TSFAE **F(*m*-$OCF_2Br$)** WALLSP-$CONH_2$ | 1 | 1511.6016 | 1511.6020 | 0.3 |
| **TPV-4** | $H_2N$-TSFAE **F(*m*-$OCF_3$)** WALLSP-$CONH_2$ | 2 | 726.3445 | 726.3444 | 0.2 |
| **TPV-5** | $H_2N$-TSFAE **F(*m*-$OCH_3$)** WALLSP-$CONH_2$ | 2 | 699.3586 | 699.3593 | 0.9 |
| **TPV-1-FAM** | FAM-TSFAE **Y** WALLSP-$CONH_2$ | 2 | 871.3747 | 871.3750 | 0.4 |
| **TPV-2-FAM** | FAM-TSFAE **F** WALLSP-$CONH_2$ | 2 | 863.3772 | 863.3775 | 0.4 |
| **TPV-3-FAM** | FAM-TSFAE **F(*m*-$OCF_2Br$)** WALLSP-$CONH_2$ | 2 | 935.3283 | 935.3269 | 1.5 |
| **TPV-4-FAM** | FAM-TSFAE **F(*m*-$OCF_3$)** WALLSP-$CONH_2$ | 2 | 905.3684 | 905.3680 | 0.4 |
| **TPV-5-FAM** | FAM-TSFAE **F(*m*-$OCH_3$)** WALLSP-$CONH_2$ | 2 | 878.3825 | 878.3820 | 0.6 |

**Table 19:** Peptide overview: Incooperated non-aromatic amino acids with $CF_2X$ acetamide moiety.

| Entry | Peptide sequence | x | $[M+xH]^{x+}_{(theor.)}$ (*m/z*) | $[M+xH]^{x+}$ (*m/z*) | rel. Δm (ppm) | $t_R$ (min) |
|---|---|---|---|---|---|---|
| **$^{17-28}$p53** | $H_2N$-ETFSDLW **K** LLPE-$CONH_2$ | 2 | 738.8903 | 738.8889 | 1.9 | 7.34 |
| **TPV-6** | $H_2N$-ETFSDLW **Nle(εNHCOCH$_3$)** LLPE-$CONH_2$ | 2 | 759.8956 | 759.8947 | 1.1 | 8.22 |
| **TPV-7** | $H_2N$-ETFSDLW **Nle(εNHCOCF$_2$H)** LLPE-$CONH_2$ | 2 | 777.8862 | 777.8856 | 0.8 | 8.19 |
| **TPV-8** | $H_2N$-ETFSDLW **Nle(εNHCOCF$_3$)** LLPE-$CONH_2$ | 2 | 786.8814 | 786.8825 | 1.3 | 8.50 |
| **TPV-9** | $H_2N$-ETFSDLW **Nle(εNHCOCF$_2$Cl)** LLPE-$CONH_2$ | 2 | 794.8667 | 794.8650 | 2.1 | 8.64 |
| **TPV-10** | $H_2N$-ETFSDLW **Nle(εNHCOCF$_2$Br)** LLPE-$CONH_2$ | 1 | 1632.6755 | 1632.6754 | 0.1 | 8.66 |
| **TPV-11** | $H_2N$-ETFSDLW **Dab** LLPE-$CONH_2$ | 2 | 724.8746 | 724.8739 | 1.0 | 7.25 |
| **TPV-12** | $H_2N$-ETFSDLW **Abu(γNHCOCH$_3$)** LLPE-$CONH_2$ | 2 | 745.8799 | 745.8787 | 1.6 | 7.88 |
| **TPV-13** | $H_2N$-ETFSDLW **Abu(γNHCOCF$_2$H)** LLPE-$CONH_2$ | 2 | 763.8705 | 763.8686 | 2.5 | 7.95 |
| **TPV-14** | $H_2N$-ETFSDLW **Abu(γNHCOCF$_3$)** LLPE-$CONH_2$ | 2 | 772.8658 | 772.8645 | 1.7 | 8.22 |
| **TPV-15** | $H_2N$-ETFSDLW **Abu(γNHCOCF$_2$Cl)** LLPE-$CONH_2$ | 2 | 780.8510 | 780.8506 | 0.5 | 8.36 |
| **TPV-16** | $H_2N$-ETFSDLW **Abu(γNHCOCF$_2$Br)** LLPE-$CONH_2$ | 2 | 802.8258 | 802.8245 | 1.6 | 8.40 |
| **$^{17-26}$p53** | $H_2N$-E **T** FSD **L** W **K** LL-$CONH_2$ | 1 | 1250.6780 | 1250.6763 | 1.3 | 8.78 |
| **TPV-17$_{linear}$**<br>**TPV-17$_{stapled}$** | $H_2N$-E Nle(ε$N_3$) FSD **D-Pra** W **K** LL-$CONH_2$ | 1 | 1285.6688 | 1285.6663<br>1285.6667 | 1.9<br>1.6 | 6.89<br>5.57 |
| **TPV-18$_{linear}$**<br>**TPV-18$_{stapled}$** | $H_2N$-E **Nle(εN$_3$)** FSD **D-Pra** W **Nle(εNHCOCH$_3$)** LL-$CONH_2$ | 1 | 1327.6793 | 1327.6767<br>1327.6755 | 2.0<br>2.9 | 7.93<br>5.81 |
| **TPV-19$_{linear}$**<br>**TPV-19$_{stapled}$** | $H_2N$-E **Nle(εN$_3$)** FSD **D-Pra** W **Nle(εNHCOCF$_2$H)** LL-$CONH_2$ | 1 | 1363.6605 | 1363.6578<br>1363.6566 | 2.0<br>2.9 | 8.07<br>6.03 |
| **TPV-20$_{linear}$**<br>**TPV-20$_{stapled}$** | $H_2N$-E **Nle(εN$_3$)** FSD **D-Pra** W **Nle(εNHCOCF$_3$)** LL-$CONH_2$ | 1 | 1381.6497 | 1381.6484<br>1381.6475 | 2.0<br>2.6 | 8.61<br>6.63 |
| **TPV-21$_{linear}$**<br>**TPV-21$_{stapled}$** | $H_2N$-E **Nle(εN$_3$)** FSD **D-Pra** W **Nle(εNHCOCF$_2$Cl)** LL-$CONH_2$ | 1 | 1397.6215 | 1397.6197<br>1397.6185 | 1.3<br>2.2 | 8.79<br>6.82 |
| **TPV-22$_{linear}$**<br>**TPV-22$_{stapled}$** | $H_2N$-E **Nle(εN$_3$)** FSD **D-Pra** W **Nle(εNHCOCF$_2$Br)** LL-$CONH_2$ | 1 | 1441.5710 | 1441.5691<br>1441.5669 | 1.3<br>2.9 | 8.80<br>6.80 |

#### 3.3.5.3 Peptide Library

Table 18 on page 91 and Table 19 on the preceding page list all peptides studied in this thesis, which were derived in Section 3.3.3 on page 81. All synthesized peptides were confirmed by high-resolution mass spectroscopy (HR-MS). Tables 18 on page 91 contains peptides derived from sequence $H_2N$-TSFAE**Y**WALLSP-$CONH_2$ [256] whose Tyr6 (red) has been substituted by modified phenylalanine-derived amino acids. The experimental results of these peptides binding to MDM2 and MDM4 are discussed in Section 3.3.7.1 on page 96. All p53-derived peptides are included in Table 19 on the preceding page, and their experimental data, binding to MDM4 and CD spectroscopy findings, can be found from Section 3.3.7.2 on page 98 onward. The modified amino acid of $^{17\text{-}28}$p53 ($H_2N$-ETFSDLW**K**LLPE-$CONH_2$) was Lys24 (red) and in $^{17\text{-}26}$p53 ($H_2N$-E**T**FSD**L**W**K**LL-$CONH_2$) was additionally substituted Thr18 and Leu22 (green) for CuAAC cyclization.

### 3.3.6 Theoretical Basics of Biophysical Peptide Evaluation

#### 3.3.6.1 Fluorescence Polarisation Assay

The fluorescence polarisation (FP) assay is a well-established method for studying peptide-protein or protein-protein interactions (PPIs) and is suitable to high-throughput screening applications.[271,272] By exciting a fluorophore with linearly polarized light, the polarization of the emitted light is inversely proportional to the rate of molecular rotation. Since the free fluorophore in solution has a high tumbling rate during the fluorescence lifetime, the emitted light is largely depolarized. If a fluorescently labeled molecule, in this thesis a peptide, binds to a protein, the tumbling rate of this complex is significantly reduced, resulting in a higher polarization of the emitted light. Based on the different polarization values of a molecule in its unbound and bound states, the ratio of bound and unbound molecules can be derived from the observed polarization. Fluorescence polarization $P$ is defined by Equation 1,

$$P = \frac{I_{\parallel} - I_{\perp}}{I_{\parallel} + I_{\perp}} \tag{1}$$

where $I_{\parallel}$ denotes the intensity of emitted light polarized parallel to the excitation light, and $I_{\perp}$ is the intensity of the emitted light polarized prependicular to the excitation light. For fitting binding curves and displacement curves, the data are converted to anisotropy $A$ according to the following Equation 2:

$$A = \frac{I_{\parallel} - I_{\perp}}{I_{\parallel} + 2I_{\perp}} = \frac{2P}{3 - P} \tag{2}$$

Using these converted data, equations are fitted to sigmoidal curves describing multiple binding equilibria between the protein, the labeled probe, and a potential competitor. The curves obtained can be used to determine the $K_d$ value of labeled molecules. In this work, *N*-terminal carboxyfluorescein-labeled peptide FAM-LTFEHYWAQLTS-$CONH_2$ was measured as a known high-affine MDM2/MDM4 fluorescent probe.[248] The concentration of the probe in the competitive FP-assay with unlabeled test peptide should be as low as possible and not higher than twice the probe $K_d$ to avoid stoichiometric titrations.[272] The protein concentration for the competitive assay is determined in the range of 50 % to 80 %, the area of greatest magnitude of change, by direct titration of probe according to the following Equation 3:

$$Inhibition\% = 1 - \frac{FP - FP_{min}}{FP_{max} - FP_{min}} \tag{3}$$

In 2004, Nikolovska-Coleska *et al.* presented a modified Cheng-Prusoff equation, which more accurately computes the $K_i$ value for FP-based competitive binding assay conditions.[257] This new Equation 4 is defined as:

$$K_i = \frac{[I]_{50}}{\frac{[L]_{50}}{K_d} + \frac{[P]_0}{K_d} + 1} \tag{4}$$

Where $K_i$ denotes the inhibition constant of an inhibitor to the protein, $[I]_{50}$ is the concentration of the free inhibitor at 50 % inhibition, $[L]_{50}$ is the concentration of the free labeled ligand at 50 % inhibition, $[P]_0$ is the concentration of the free protein at 0 % inhibition, and $K_d$ is the dissociation constant of the protein-ligand complex.

#### 3.3.6.2 Circular Dichroism Spectroscopy

Local segments of proteins and peptides form a secondary structure: α-Helices and β-sheets or adopt random coils. Peptides are usually arranged as α-helices or random coils. Using circular dichroism (CD) spectroscopy, peptides can be analyzed for this secundary structure, or more precisely: for the fraction between α-helix and random coil. When circularly polarized light passes through an absorbing optically active medium such as peptides, the speeds between right and left polarizations differ, as do their wavelengths and the extent of their absorption. The difference between right and left polarization absorbtion is circular dichroism and is measured as ellipticity θ. α-Helices have a minimum at 222 nm and 208 nm, which are more distinct the larger the fraction of helices relative to other structures. A conversion for ellipticity at 222 nm normalized to peptide concentration and length is given by the following Equation 5 on the next page:

$$[\theta]_{222} = \frac{\theta_{222} \cdot M}{c \cdot l \cdot n} \tag{5}$$

Where $[\theta]_{222}$ denotes the mean residue weight ellipticity at 222 nm, $\theta_{222}$ is the measured ellipticity at 222 nm, $M$ ist the molecular weight of peptide, $c$ is the peptide concentration, $l$ is the cell path length and $n$ is the number of amino acid residues in the peptide.

Assuming that the helix content of a peptide is linearly related to its mean residue ellipticity as measured by CD at 222 nm, the maximum helix content is calculated according to Luo and Baldwin (1997) by Equation 6:[273]

$$[\theta]_{max} = \frac{-44000 + 250T}{1 - \frac{k}{n}} \tag{6}$$

Where $[\theta]_{max}$ is the maximum helicity, $T$ is the temperature in °C, $k$ is a finite length correction parameter with $k = 4$ and $n$ is the number of amino acid residues in the peptide. The relative amount of helicity is described by Equation 7:

$$Helicity\% = \frac{[\theta]_{222}}{[\theta]_{max}} \cdot 100 \tag{7}$$

### 3.3.7 Biophysical Evaluation of Peptides with MDM2 and MDM4

#### 3.3.7.1 Competitive FP-Assay of Peptides with $CF_2Br$ Ether Moiety

Prior to performing the competitive assays, direct titrations were carried out using 20 nM high-affinity probe FAM-LTFEHYWAQLTS-$CONH_2$ to determine the working concentrations of the proteins. For the competitive assay, a protein working concentration of 30 nM was determined for MDM2 and 60 nM for MDM4, and the $K_d$ values determined were 14.3 nM and 38.2 nM, respectively. The test peptides were TPV-3 ($CF_2Br$), TPV-4 ($CF_3$), and TPV-5 ($CH_3$) from Table 18 on page 91.

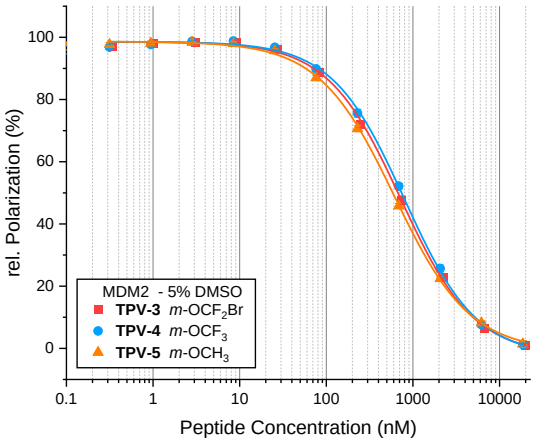


**(a)** MDM2 with 5 % (v/v) DMSO

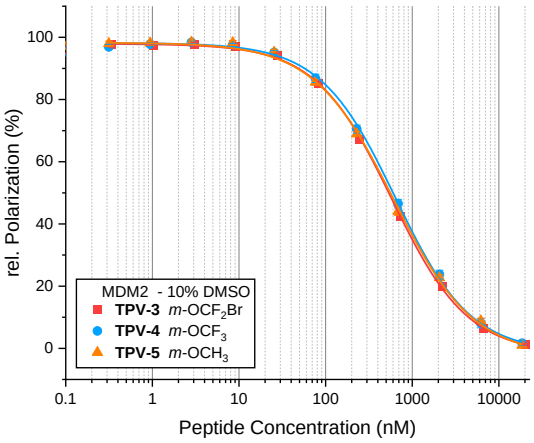


**(b)** MDM2 with 10 % (v/v) DMSO

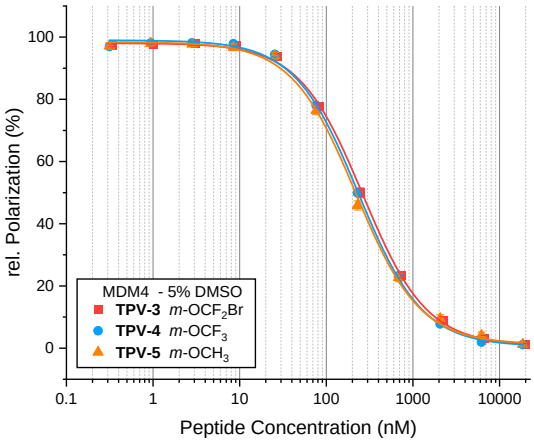


**(c)** MDM4 with 5 % (v/v) DMSO

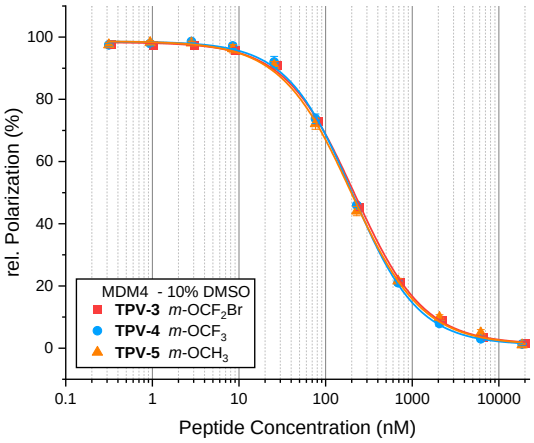


**(d)** MDM4 with 10 % (v/v) DMSO

**Figure 33: (a–d)** Relative fluorescence polarization (%) of competitive fluorescence polarization assay for TPV-3, TPV-4 and TPV-5 with 20 nM fluorescence-labeled probe and 30 nM MDM2 ($K_d$ = 14.3 nM) or 60 nM MDM4 ($K_d$ = 38.2 nM), measured in 5 % (v/v) or 10 % (v/v) DMSO. Measurement series are shown as mean ± SD (each measuring point as quadruplicate; number of measurement series: n = 3).

As described in Section 3.3.3 on page 81, modification of the 12-mer peptide in MDM2 crystal structure 3LNZ with a $CF_2Br$ ether moiety was expected to result in intramolecular XB bond with threonine side chain. This suggested that a peptide with the $CF_2Br$ ether moiety should have a stabilizing effect on the helical secondary structure, and thus on the overall bonding, compared to the $CF_3$ ether variant. For comparison, a peptide containing $CH_3$ ether moiety was also measured.

As shown in Figure 33 on the facing page and Table 20, all tested peptides bound to MDM2 and MDM4. Initially, a DMSO concentration of 5 % (v/v) was used. Very similar values were obtained with $K_i$ values ranging from 199 nM to 258 nM for MDM2 and slightly better with 71 nM to 82 nM slightly better for MDM4. Due to the very moderate solubility of the peptides, the measurements were repeated in 10 % (v/v) DMSO. As a result, all peptides displaced the probe more effectively, but again, no significant differences between peptides were observed in terms of inhibitory properties. The measured $K_i$ values measured rang from 171 nM to 189 nM for MDM2 and 55 nM to 65 nM for MDM4. Only at MDM2 TPV-3 displaced the probe better than TPV-4 (5 % (v/v) DMSO: 217 nM vs. 258 nM, and 10 % (v/v) DMSO: 171 nM vs. 189 nM). Figure 33 on the facing page notably illustrates by the nearly identical shape of the curve that all measured differences are not significant.

**Table 20:** Summary of competitive fluorescence polarization assay results of measured $IC_{50}$ and calculated $K_i$ values (nM) for TPV-3, TPV-4 and TPV-5 with 20 nM fluorescence-labeled probe and 30 nM MDM2 ($K_d$ = 14.6 nM) or 60 nM MDM4 ($K_d$ = 38.2 nM), measured in 5 % (v/v) or 10 % (v/v) DMSO. Values are shown as mean ± SD (each measuring point as quadruplicate; number of measurement series: n = 3).

| | | Phe6 | MDM2 | | | MDM4 | | |
|---|---|---|---|---|---|---|---|---|
| DMSO | Peptide | (*m*-OR) | $IC_{50}$ (nM) | $K_i$ (nM) | Ratio | $IC_{50}$ (nM) | $K_i$ (nM) | Ratio |
| 5 % | **TPV-3** | $CF_2Br$ | 736 ± 15 | 217 ± 4 | 1.00 | 258 ± 9 | 82 ± 3 | 1.00 |
| | **TPV-4** | $CF_3$ | 809 ± 28 | 258 ± 8 | 1.19 | 237 ± 7 | 75 ± 3 | 0.91 |
| | **TPV-5** | $CH_3$ | 676 ± 24 | 199 ± 7 | 0.92 | 221 ± 7 | 71 ± 3 | 0.87 |
| 10 % | **TPV-3** | $CF_2Br$ | 586 ± 11 | 171 ± 3 | 1.00 | 211 ± 3 | 65 ± 1 | 1.00 |
| | **TPV-4** | $CF_3$ | 64 ± 2 | 189 ± 1 | 1.11 | 203 ± 4 | 62 ± 2 | 0.95 |
| | **TPV-5** | $CH_3$ | 635 ± 13 | 186 ± 4 | 1.09 | 186 ± 5 | 55 ± 2 | 0.85 |

As shown in Figure 31b on page 81, we hypothesize that the putative XB interaction occurs on the solvent exposed side of the peptide. This may have a detrimental effect on peptide affinity. Experience with the solubilities of the modifications investigated had shown that these decrease in aqueous environments in the following order: $CH_3 > CF_3 > CF_2Br$. Accordingly, the $CF_2Br$ moiety was disadvantageous compared to the other two groups. Furthermore, the solubilizing hydroxy functionality contained in the original tyrosine was removed. The binding mode could not be revealed since the growth of MDM4/TPV-3 co-crystals were not successful.

### 3.3.7.2 Competitive FP-Assay of Peptides with $CF_2X$ Acetamide Moiety

This section is focused on the more decisive $^{17\text{-}28}$p53 peptide and its acetylated derivatives. For the competitive assay with the $^{17\text{-}28}$p53-derived peptides, a MDM4 working concentration of 30 nM was determined by direct titration using 20 nM high-affinity probe, and the probe $K_d$ determined was 11.5 nM.

Initially, peptides $^{17\text{-}28}$p53, TPV-6 to TPV-10 with modified Lys24Nle(εNHCOR) (R = $CH_3$, $CF_2H$, $CF_3$, $CF_2Cl$, $CF_2Br$; Table 19 on page 92) were measured by FP-displacement assay with MDM4. As shown in Figure 34a and Table 21 on the facing page, significant inhibitory

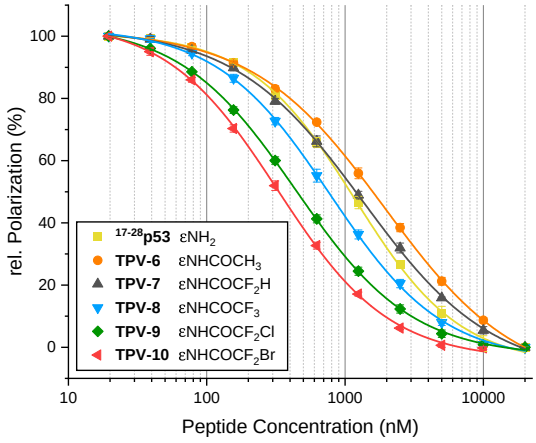


**(a)** $^{17\text{-}28}$p53 and TPV-6 to PV-10.

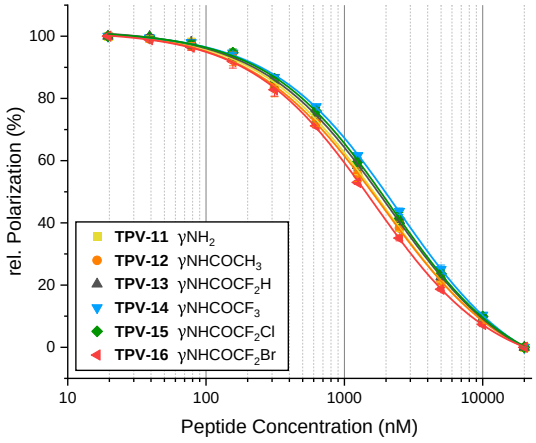


**(b)** TPV-11 to TPV-16.

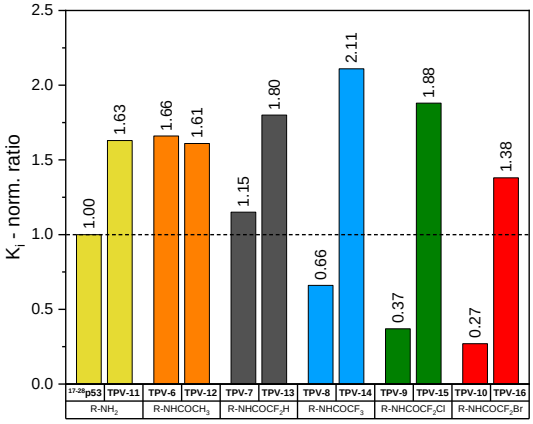


**(c)** Normalized $K_i$ values.

**Figure 34:** Relative fluorescence polarization (%) of competitive fluorescence polarization assay for $^{17\text{-}28}$p53 and TPV-6 to TPV-16 with 20 nM fluorescence-labeled probe and 30 nM MDM4 ($K_d$ = 11.5 nM) in 5 % DMSO. Measurement series are shown as mean ± SD (each measuring point as quadruplicate; number of measurement series: n = 3). **(a)** $^{17\text{-}28}$p53 with Lys and TPV-6 to TPV-10 with Nle derivatives in position 24. **(b)** TPV-11 with Dab and TPV-12 to TPV-16 with Abu derivatives in position 24. **(c)** Normalized $K_i$ values.

**Table 21:** Summary of competitive fluorescence polarization assay results of measured $IC_{50}$ and calculated $K_i$ values (nM) for $^{17\text{-}28}$p53 and TPV-6 to TPV-16 with 20 nM fluorescence-labeled probe and 30 nM MDM4 ($K_d$ = 11.5 nM) in 5 % (v/v) DMSO. Values are shown as mean ± SD (each measuring point as quadruplicate; number of measurement series: n = 3).

| Peptide | Xaa24 | $IC_{50}$ (nM) | $K_i$ (nM) | Ratio |
|---|---|---|---|---|
| **$^{17\text{-}28}$p53** | Lys | 1173 ± 39 | 307 ± 10 | 1.00 |
| **TPV-6** | Nle(εNHCOCH$_3$) | 1927 ± 47 | 509 ± 32 | 1.66 |
| **TPV-7** | Nle(εNHCOCF$_2$H) | 1347 ± 38 | 353 ± 19 | 1.15 |
| **TPV-8** | Nle(εNHCOCF$_3$) | 779 ± 24 | 202 ± 9 | 0.66 |
| **TPV-9** | Nle(εNHCOCF$_2$Cl) | 440 ± 8 | 112 ± 5 | 0.37 |
| **TPV-10** | Nle(εNHCOCF$_2$Br) | 326 ± 9 | 82 ± 3 | 0.27 |
| **TPV-11** | Dab | 1897 ± 48 | 500 ± 30 | 1.63 |
| **TPV-12** | Abu(γNHCOCH$_3$) | 1874 ± 53 | 494 ± 36 | 1.61 |
| **TPV-13** | Abu(γNHCOCF$_2$H) | 2096 ± 55 | 552 ± 12 | 1.80 |
| **TPV-14** | Abu(γNHCOCF$_3$) | 2447 ± 70 | 647 ± 34 | 2.11 |
| **TPV-15** | Abu(γNHCOCF$_2$Cl) | 2176 ± 65 | 577 ± 47 | 1.88 |
| **TPV-16** | Abu(γNHCOCF$_2$Br) | 1611 ± 30 | 423 ± 2 | 1.38 |

differences were observed. A $K_i$ value of 307 nM was measured for the *wild-type* sequence of $^{17\text{-}28}$p53. In relation to this, acetylated lysine (TPV-6) had a 1.66-fold higher $K_i$ value at 509 nM, and difluoroacetylated TPV-7 had a 1.15-fold higher $K_i$ value at 353 nM. For TPV-8 ($CF_3$), TPV-9 ($CF_2Cl$), and TPV-10 ($CF_2Br$), we observed an increase in inhibitory properties, as we would expect from an XB interaction. TPV-8 had a $K_i$ of 202 nM, TPV-9 112 nM and TPV-10 82 nM. All peptides displaced the probe better than the $^{17\text{-}28}$p53 peptide, the chlorine derivative by 3-fold and the bromine derivative by 4-fold. The difference was quite remarkable, considering that of the 215 atoms or 111 heavy atoms (110 heavy atoms in case of TPA-7) that constitute each of the peptides TPV-7 to TPV-10, only one halogen atom was exchanged for another atom.

However, it was not yet possible to ascertain from the trend of the $K_i$ whether an halogen bond was involved. To understand the mode of binding more clearly, peptides were tested which contained Lys24Dab and Lys24Abu(γNHCOR) derivatives with only two methylene units in the side chain instead of four methylene units like Lys/Nle derivatives. The measurements of corresponding peptides TPV-11 to TPV-16 are shown in Figure 34b on the preceding page. All peptides displaced the probe with $K_i$ 423 nM to 647 nM worse than the $^{17\text{-}28}$p53 peptide, as listed in Table 21. From this, we deduced that the side chain length was relevant for the interaction of the halogenated acetyl groups of TPV-8, TPV-9, and TPV-10, which led them to show better inhibition than $^{17\text{-}28}$p53. Figure 34c on the preceding page shows the normalized $K_i$ values of all tested peptides relative to $^{17\text{-}28}$p53.

### 3.3.7.3 Helicity of Chemically Constrained Peptides

For the purpose of studying the helicity and the influence of acetylations in position 24 on binding stabilization effects to MDM4, chemically-constrained peptides were prepared. The individual amino acids first had to be considered and their significance for the interaction with MDM4 elucidated. The sequence discussed is shown in Figure 35 and its side chains are colored according to their function. The blue-colored possess high significance for the binding-affinity to MDM4 and cannot be substituted without loss of bonding ability. The orange-colored side chains were relevant to the binding hypothesis discussed in Section 3.3.7.2 on page 98. The terminal black ones were left out of consideration, since

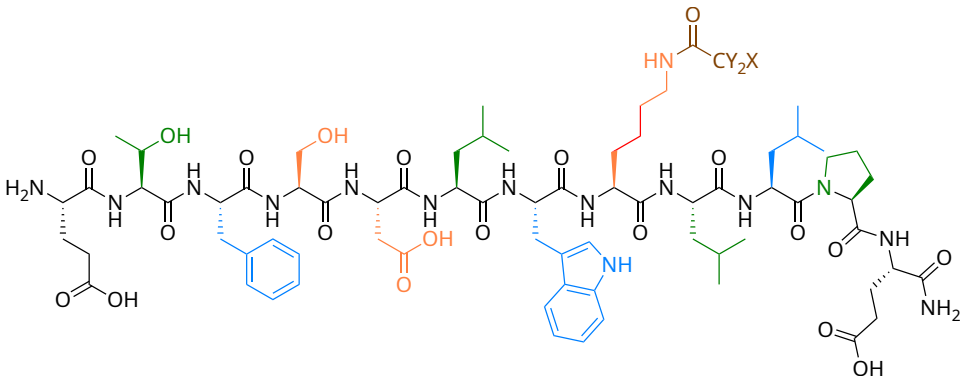


**(a)** Structure of acetylated $^{17\text{-}28}$p53.

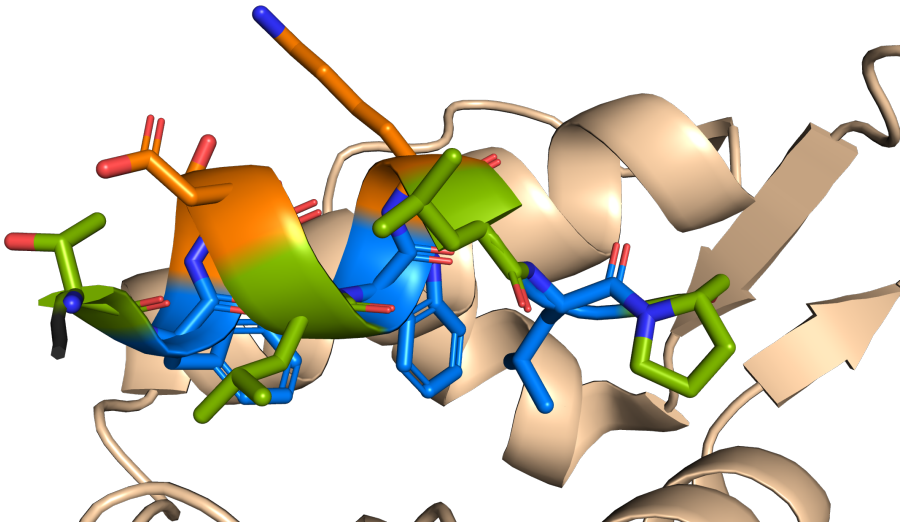

**(b)** $^{15\text{-}29}$p53/MDMX complex (PDB: 2Z5T).

**Figure 35: (a,b)** Consideration of the impact of individual amino acids in $^{17\text{-}28}$p53. Blue: high significance; orange: important for hypothesis; green: less important or dispensable and eligible for substitution; black: terminal amino acids not resolved in the crystal structure.

they were not completely resolved in crystal structures. The remaining green side chains were thus candidates for substitution by residues with ring closure capability obtaining cyclized peptides.

There are numerous methods available from which to select.[244] Decisive for the choice of stapling method is, among other aspects, the distance between the amino acids to be bridged. The biorthogonal Huisgen Cu(I)-mediated 1,3-dipolar cycloaddition reaction was selected using commercially available azido and alkynyl amino acids incorporated at

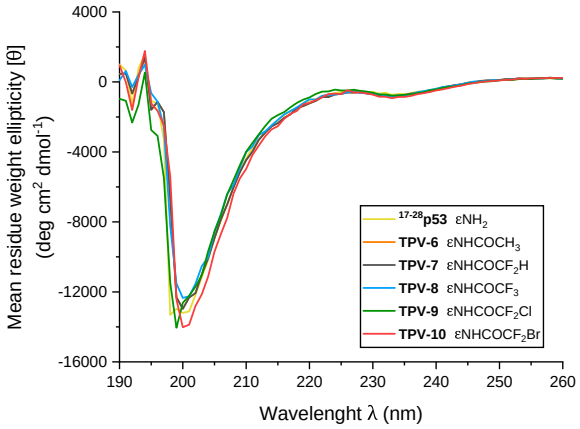


**(a)** Peptides $^{17\text{-}28}$p53 and TPV-6 to TPV-10.

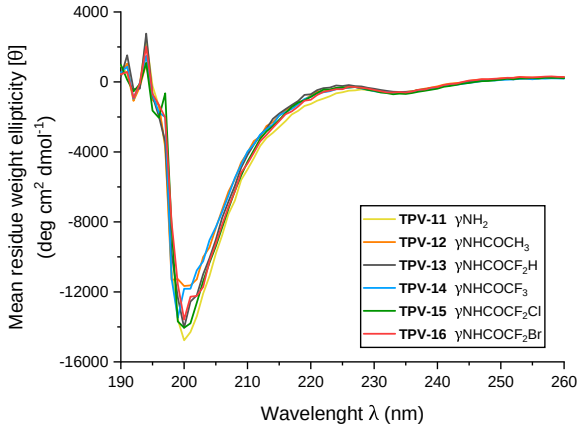


**(b)** Peptides TPV-11 to TPV-16.

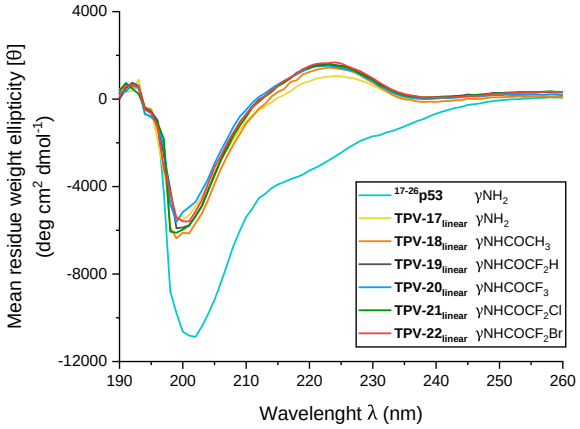


**(c)** Peptide $^{17\text{-}26}$p53 and linear peptides of TPV-17 to TPV-22.

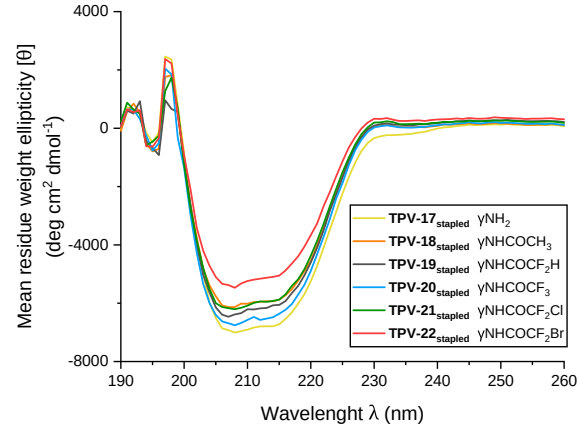


**(d)** Triazole-stapled peptides of TPV-17 to TPV-22.

**Figure 36:** CD spectra of 150 µM peptides in PBS (pH 7.4) at 20 °C. The spectra were averaged over 2 or 10 scans. The PBS-only basline was subtracted from each spectrum. The mean residue weight ellipticity [θ] were determined using eq 11 on page 125 as described in 5.5.4 on page 125. **(a)** $^{17\text{-}28}$p53 and its acetylated derivatives TPV-6 to TPV-10. Number of scans n = 2. **(b)** TPV-11 containing amino acid Dab24 and its acetylated derivatives TPV-12 to TPV-16. Number of scans n = 2. **(c)** $^{17\text{-}28}$p53, linear peptide TPV-17 and its acetylated unconstrained derivatives TPV-18 to TPV-22. Number of scans n = 10. **(d)** Triazole-stapled peptide TPV-17 and its acetylated triazole-stapled derivatives TPV-18 to TPV-22. Number of scans n = 10.

positions *i* and *i*+4, namely Thr18 and Leu22. Details of the optimized triazole stapling synthesis were described in Section 3.3.5.2 on page 88. Moreover, due to proline's helix-breaking properties, Pro27 and Glu28 were truncated. In terms of binding, they are dispensable according to the literature.[256]

Regrettably, both the linear and cyclized peptides TPV-17 to TPV-22 significantly forfeit their ability to displace the probe. The concentration of the peptides could also not be increased arbitrarily, since otherwise the intrinsic fluorescence of the peptides, especially that of the bromine variant TPV-22, superimposed the actual measurement. This effect could not be compensated by a weaker binding probe. However, this could be due to the fact that the stapling modifications impaired binding, which was expected at least for the linear peptides, or that the two truncated amino acids Pro27 and Glu28 contributed to the binding to an appreciable extent.

CD spectra were recorded to investigate the effect of acetylation on helicity in solution, as shown in Figure 36 on the previous page. As expected, the spectra of the unconstrained peptides did not show helicity but rather reflected formation of random coils with a minimum at about 200 nm and a maximum at about 220 nm (Figure 36 on the preceding page). Deviating from this, $^{17\text{-}26}$p53 had no maximum. In contrast, the CD spectra of the triazole-stapled peptides indicated helicity. Typical for helical structures are a minimum at 208 nm and at 222 nm.[273,274] In our case we observed a shift of local minimum from 222 nm toward 215 nm for the peptides measured. This is not an uncommon effect, observed with very short peptides.[275]

Using the Equations 11–13 described in Section 3.3.6.1 on page 93 with $[\theta]_{obs,215}$ instead of $[\theta]_{222}$, values for helicity in the range of 22 % to 29 % were obtained (Table 22). Either the basis of calculation from the literature was not adequate, or the measured values are exclusively the cyclic portion while the rest was random-coil, or there was a more complex equilibrium between full and partial helicity and non-helicity. The low helicity values of the triazole-stapled 10-mer peptides did not correlate with the measured $K_i$ values of the 12-mer peptide analogues against MDM4 (Table 21 on page 99), and the deviations between them were not significant enough to draw conclusions about the influence of

**Table 22:** Mean residue weight ellipticity $[\theta]$ (deg cm$^2$ dmol$^{-1}$) at $\lambda = 215$ and calculated helicity (%).

| Peptide | Xaa24 | $[\theta]_{obs,215}$ | Helicity (%) |
|---|---|---|---|
| **TPV-17$_{stapled}$** | Lys | –6726 | 29 |
| **TPV-18$_{stapled}$** | Nle(γNHCOCH$_3$) | –5875 | 25 |
| **TPV-19$_{stapled}$** | Nle(γNHCOCF$_2$H) | –6059 | 26 |
| **TPV-20$_{stapled}$** | Nle(γNHCOCF$_3$) | –6363 | 27 |
| **TPV-21$_{stapled}$** | Nle(γNHCOCF$_2$Cl) | –5875 | 25 |
| **TPV-22$_{stapled}$** | Nle(γNHCOCF$_2$Br) | –5053 | 22 |

the halogenated acetyl residues on the helicity in solution. Therefore, no conclusions about the binding mode of the peptides to MDM4 could be drawn based on the CD spectra. Measurement in complex with MDM4 was not practical because this protein itself has a high helix content and the equilibrium between binding and nonbinding peptides would have been difficult to determine. It is conceivable that the maximum helicity determined in the literature and its linear correlation are not applicable in every situation. Also the shift of the minima of the CD spectra from 222 nm to 215 nm is a deviation from the conventional literature. In conclusion, if the acetylations of the peptides have a stabilizing effect on secundary peptide structure, they were probably present only in helical form bound in complex with MDM4.

#### 3.3.7.4 Elucidation of the MDM4/TPV-10 Binding Mode

Crystal structures were necessary to elucidate the binding mode beyond doubt. In order to obtain MDM4/TPV-10 co-crystals, we screened crystalization conditions using Crystal Screening Kits from Jena Bioscience, Germany: JBScreen PACT++ HTS, JBScreen JCSG++ HTS and JBScreen Classic HTS II. However, no conditions could be found that result in the formation of crystals.

We have attempted to approach a plausible binding hypothesis *in silico* via known crystal structures deposited in the PDB, as we were not able to obtain a crystal structure of the best binding peptide TPA-6 with MDM4. Only a few appropriate MDM4/p53-peptide crystal structures were available. Deposited MDM4 crystal structures in complex with

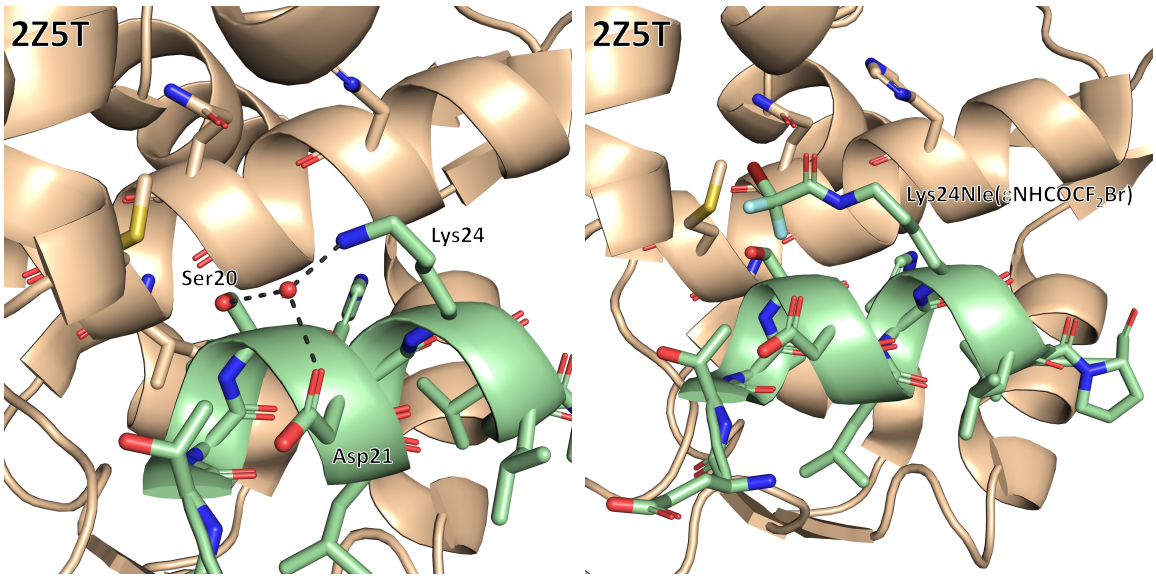


**(a)** 2Z5T. **(b)** Modified 2Z5T.

**Figure 37:** MDM4/$^{15\text{-}29}$p53 crystal structure (chain E and chain F of PDB ID: 2Z5T).[276] **(a)** A water molecule is coordinated by the side chains of Ser20, Asp21, and Lys24. **(b)** Illustration of modified Lys24Nle(εNHCOCF$_2$Br) in $^{15\text{-}29}$p53 peptide.

the p53 peptide were 3DAB and 3DAC (both human),[254] or structurally highly similar 2Z5S and 2Z5T (both *danio rerio*).[276] The crystal cells contain up to 4 MDM4/p53-peptide pairs in which not all Lys24 of the peptide are fully resolved. In 2Z5T (chain F), Lys24 in association with Ser20 and Asp21 forms a complex with a water molecule (Figure 37a on the preceding page).

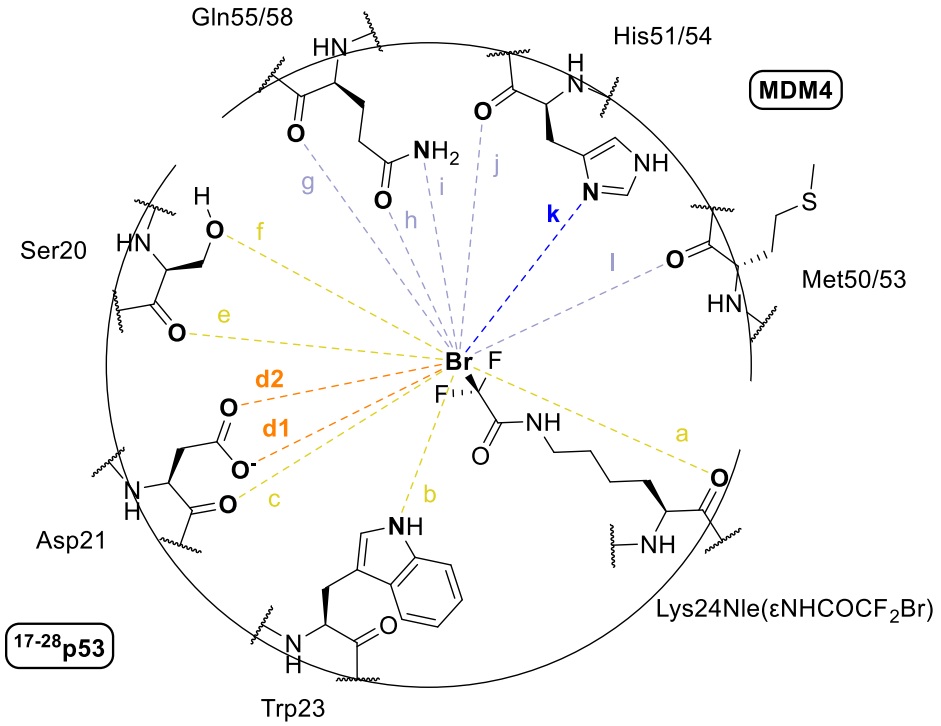


**(a)** Molecular interactions.

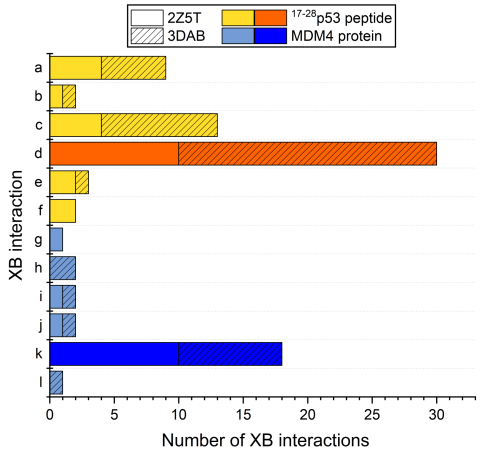


**(b)** Number of XB interactions.

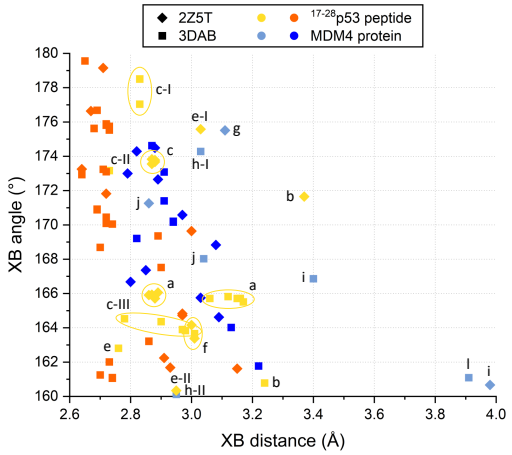


**(c)** Statistical distribution.

**Figure 38:** Statistical representation of the conformational analysis and subsequent geometry optimization process. **(a)** Schematic representation of all XB interactions found between the bromine atom and XB acceptors in $^{15\text{-}29}$p53 peptide and in MDM4 protein. **(b)** Number of matches of the respective XB acceptors. **(c)** Dependencies of the XB (C−Br···N/O) angle (°) to the XB (Br···N/O) distance (Å).

As shown in Figure 37b on page 103, we modified Lys24 of the p53 peptide in 2Z5T and in 3DAB, by attaching a $CF_2Br$ acetamide group. In a next step, we carried out a conformational analysis of the modified side chain to sufficiently cover the conformational space. After sorting out conformers involving clashes with the surrounding crystal structure, we performed a geometry optimization using TPSS-D3/def-SV(P).[277–280]

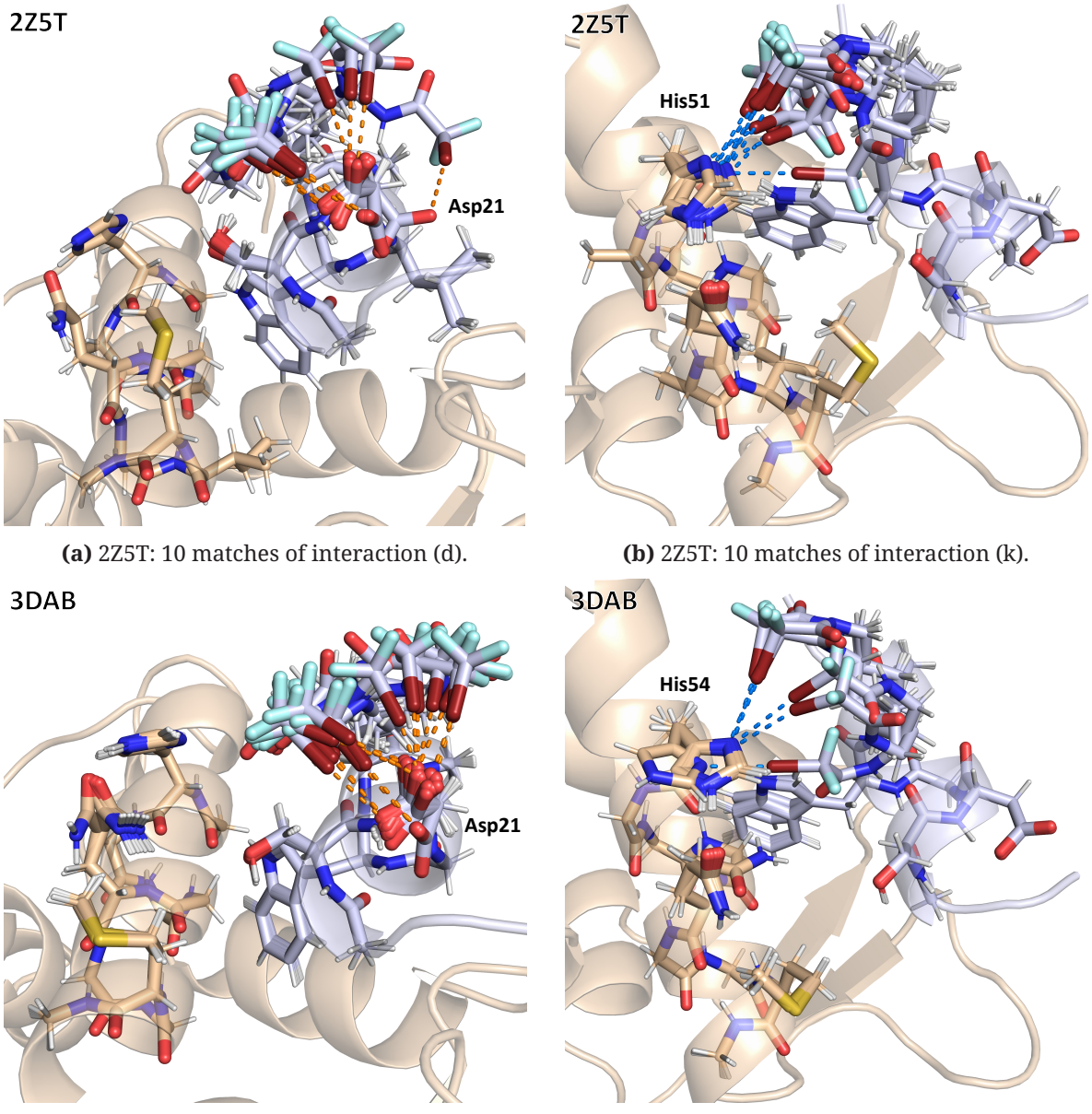


**(a)** 2Z5T: 10 matches of interaction (d).

**(b)** 2Z5T: 10 matches of interaction (k).

**(c)** 3DAB: 20 matches of interaction (d).

**(d)** 3DAB: 8 matches of interaction (k).

**Figure 39:** Final conformations after geometry optimization with Lys24Nle(εNHCOCF$_2$Br) in modified crystal structures of PDB IDs 2Z5T and 3DAB.[254,276] MDM4 protein in beige. $^{15\text{-}29}$p53 peptide in light blue. **(a)** 2Z5T: Ten XB matches (d) targeting intramolecularly the Asp21 side chain of $^{15\text{-}29}$p53 peptide. **(b)** 2Z5T: Ten XB matches (k) targeting the His51 side chain of MDM4 protein. **(c)** 3DAB: 25 XB matches (d) targeting intramolecularly the Asp21 side chain of $^{15\text{-}29}$p53 peptide. **(d)** 3DAB: Eight XB matches (k) targeting the His54 side chain of MDM4 protein.

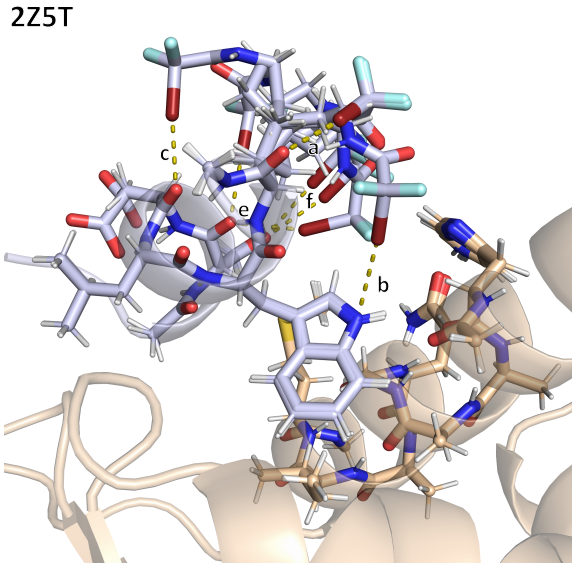


**(a)** 2Z5T: 10 matches of interaction (d).

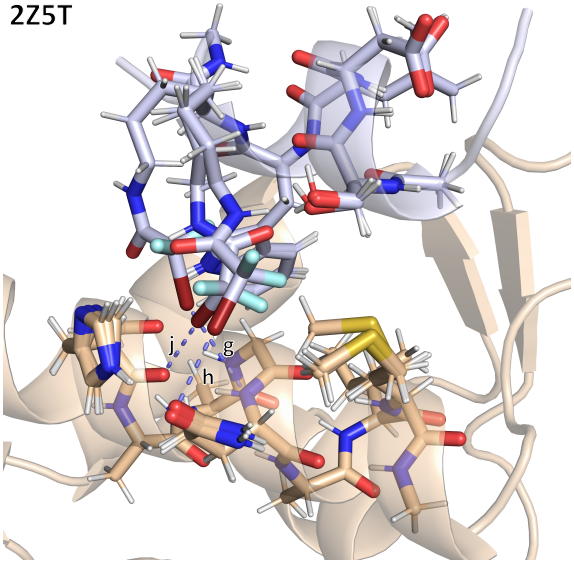


**(b)** 2Z5T: 10 matches of interaction (k).

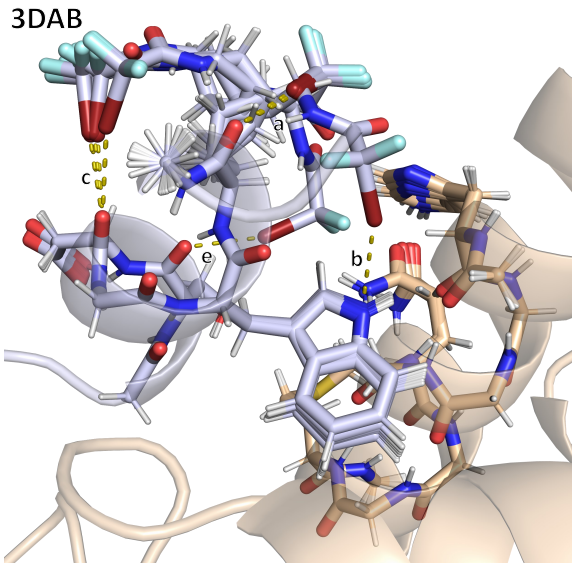


**(c)** 3DAB: 20 matches of interaction (d).

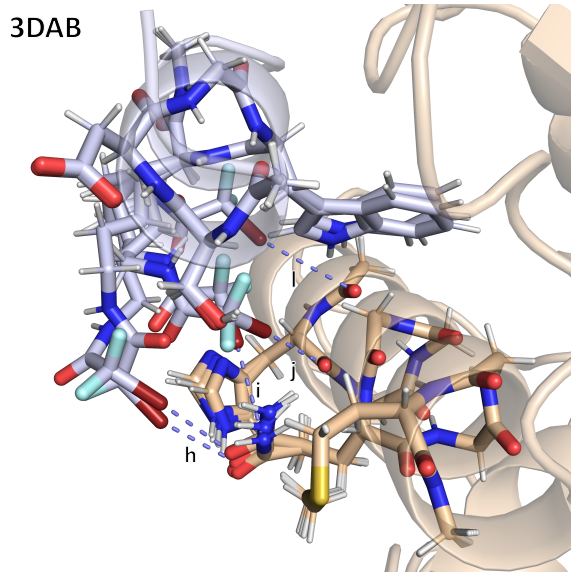


**(d)** 3DAB: 8 matches of interaction (k).

**Figure 40:** Final conformations after geometry optimization with Lys24Nle(εNHCOCF$_2$Br) in modified crystal structures of PDB IDs 2Z5T and 3DAB. MDM4 protein in beige. $^{15\text{-}29}$p53 peptide in light blue. SC: Side chain; BB: Backbone. **(a)** 2Z5T: 13 intramolecular XBs of the peptide not targeting the side chain of Asp21. Four XBs directed toward Asp21-BB (c) and four toward Lys24-BB (a) each have nearly identical geometry. **(b)** 2Z5T: Three XBs aimed against the protein, but not targeting the side chain of His51. **(c)** 3DAB: 16 intramolecular XBs of the peptide not targeting the side chain of Asp21. Four XBs directed toward Asp21-BB (c) and four toward Lys24-BB (a) each have nearly identical geometry. **(d)** 3DAB: Five XBs aimed against the protein, but not targeting the side chain of His54.

During optimization, heavy atoms of the peptide and protein backbone were kept frozen. Out of the 247 converged structures of 2Z5T, 36 structures yielded a halogen bond with a distance <4 Å and an interaction angle >160° (Figure 39 on the preceding page

and Table A7 on page 247). Only one of these halogen bonds already existed before the optimization process. In the case of 3DAB, 304 structures converged, with 54 halogen bonds using the thresholds as above (Figure 39 and Table A8). Further analysis of the data revealed binding modes with additional interactions, such as 33 H···F contacts of the fluorine atoms (<3.0 Å, >150°), 25 hydrogen bonds (HBs, <3.5 Å, >150°) of the amide O, and five HBs of the amide NH (<3.5 Å, >150°, Table A9) for 2Z5T as well as 50 interactions of fluorine atoms and three amide NH contacts in the case of 3DAB (Table A10). In some cases, combinations of these interactions can occur in the same structure. For 2Z5T, we found in 84 of the total 247 structures at least one intermolecular or intramolecular interaction from the $CF_2Br$ acetamide group toward MDM4 or the peptide itself, respectively. For 3DAB, 100 of the total 304 structures exhibited such positive results (intramolecular or intermolecular interactions). The remaining 163 (2Z5T) / 204 (3DAB) converged structures mostly started at a great distance from potential interaction partners and consequently found none during optimization. In summary, 49 % of the 184 positive results involve an XB, 39 % involve contact with at least one of the two fluorine atoms, 11 % involve an HB with the amide oxygen, and 4 % involve an HB with the amide NH.

We split the XBs into two groups as highlighted by color in Figure 38a on page 104: 23 (2Z5T) / 41 (3DAB) intramolecular XBs were found between the $CF_2Br$ and different XB acceptors in the peptide and 13 (2Z5T) / 13 (3DAB) XBs targeting the protein. Within the peptide, the bromine found six appropriate XB acceptors and five in MDM4. Interestingly, the XB acceptor Asp21 side chain in p53 stand out with 35 matches and the histidine side chain [His51 in zebrafish MDM4 (2Z5T) and His54 in human MDM4 (3DAB)] in MDM4 with 18 matches. Replacing the coordinated water molecule, the intramolecular XB aims at the potentially negatively charged carboxylic acid of Asp21 and thereby would conceivably stabilize helix formation (Figure 40a and 40c on the preceding page). Additional data from CD spectra (Figure 36 on page 101) indicate that no increased helicity was observed in solution and that this possible intramolecular binding would only be present if the peptide, which is intrinsically disordered in solution, adopts a helical structure in the binding site of MDM4. As shown in Figure 40b and 40d, the second proposed interaction possibility leading to affinity enhancement is an XB with the unprotonated Nδ of the His51/54 side chain in MDM4. In both proposals, the XB acceptor also aligns to the XB donor during optimization process (Figure 39). In contrast to the intramolecular contact, the interactions to MDM4 have a more concerted character, which is due to the longer distance to be bridged. Both described interactions are not or only with difficulty feasible using the shorter amino acid derivatives with Lys24Abu(γNHCOR). Since the distance to MDM4 was very long (>9 Å from Cα) a direct interaction with His51/54 of MDM4 was rather excluded, but an intramolecular contact with Asp21 is conceivable (>7 Å from Cα). Less frequently found XB interactions, which were labelled (a), (b), (c), (e), (f), (g), (h), (i), (j), and (l) in Figure 38 on page 104,

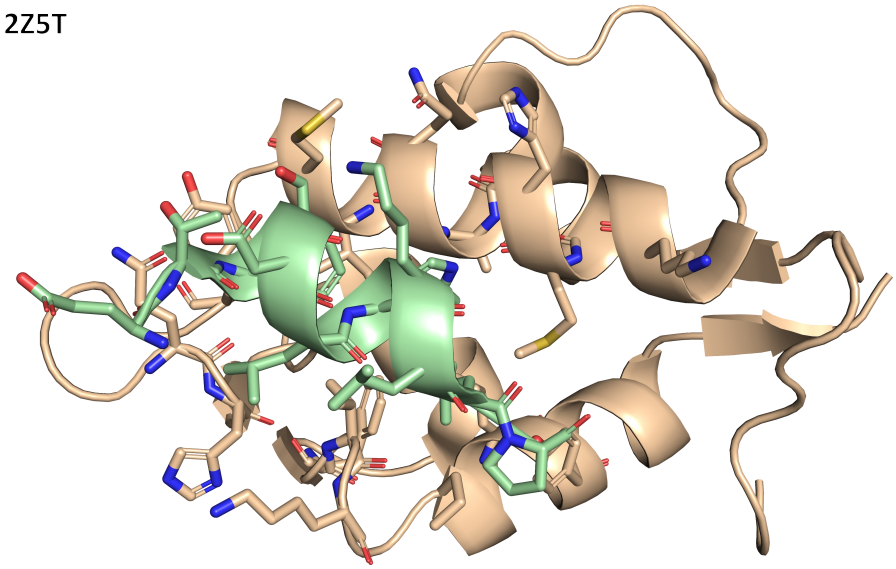


**(a)** 2Z5T: MDM4/$^{15\text{-}29}$p53 peptide.

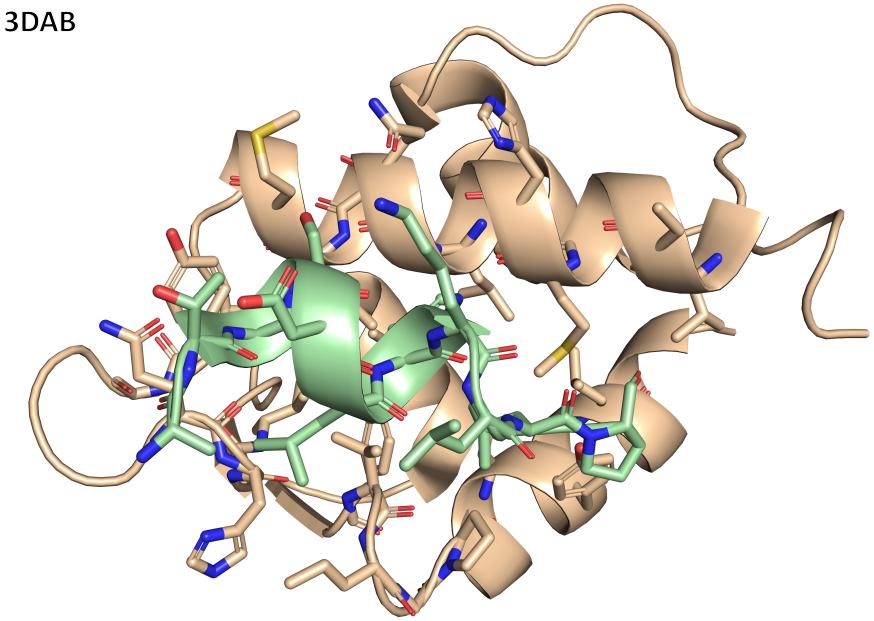


**(b)** 3DAB: MDM4/$^{15\text{-}29}$p53 peptide.

**Figure 41:** All amino acids within 12 Å around Lys24 of $^{15\text{-}29}$p53 peptide chains are depicted as sticks. Protein in beige, peptide in green. **(a)** Overview of chain E (MDM4) and chain F ($^{15\text{-}29}$p53 peptide) in 2Z5T. **(b)** Overview of chain C (MDM4) and chain D ($^{15\text{-}29}$p53 peptide) in 3DAB.

are depicted in Figure 40 on page 106 for comparison. In addition, all amino acids within 12 Å distance around Lys24 of the $^{15\text{-}29}$p53 peptide chain are shown as a reference for the putative interaction space in Figure 41 for zebrafish MDM4 (2Z5T) and human MDM4 (3DAB).

### 3.3.8 Conclusion

In summary, we have established two approaches to synthesize Fmoc-protected amino acids with a $CF_2X$ moiety for application in SPPS. First, bottom-up synthesis of phenylalanine-derived **80** and **81** with a $CF_2Br$ ether moiety in *para* or *meta* position was conducted. Then, we synthesized amino acids with an alkyl side chain (**82** and **83**) of variable length ($(CH_2)_n$, n =1,3) containing a terminal $CF_2X$ acetamide moiety (X = Cl, Br). Compared to the 7-step synthesis of ethers, the preparation of the acetamide derivatives from commercially available amines is considerably simpler with only one synthesis step and provides rapid generation of a wide range of building blocks for the SPPS.

The incorporation of Lys24Nle(εNHCOCF$_2$X) into $^{17\text{-}28}$p53-derived peptides shows decreasing $K_i$ values in the competitive FP-assay toward MDM4 in the order X = F > Cl > Br, indicating an XB interaction. This trend is not observed in measurements with shorter side chain Lys24Abu(γNHCOCF$_2$X) derivatives. The Lys24Nle(εNHCOCF$_2$Br) derivative shows a 4-fold stronger inhibition constant compared to the unacetylated amine of Lys24. Compared to the ether moiety, the amide increases the solubility significantly and enables the formation of hydrogen bonds as HB donor and HB acceptor in addition to its XB donor functionality. Cyclization experiments, CD spectra, and further *in silico* experiments using published protein crystal structures indicate an intramolecular interaction occurring in the MDM4-bound, helical state of the peptide. Herein, we found an XB interaction with the carboxylic acid group of Asp21. Likewise, a direct intermolecular XB between the unprotonated Nδ in His54 of human MDM4 and the $CF_2Cl$ or $CF_2Br$ moiety of the peptides could explain the increase in affinity.

Future studies should focus on the design of further amino acids bearing $CF_2X$ moieties, the identification of high-affinity peptide sequences containing these amino acids, and the investigation of their mode-of-action regarding XB.

# 4 Zusammenfassung (german)

Die in Arzneistoffen (engl. *active pharmaceutical ingredients*, APIs) enthaltenen Halogene Chlor, Brom und Iod (X = Cl, Br, I) sind üblicherweise kovalent an $sp^2$-hybridisierten, aromatischen Systemen ($C(sp^2)-X$) gebunden. Alkyl-gebundene Chlor-, Brom- und Iodatome ($C(sp^3)-X$) sind in der Regel nicht ausreichend chemisch stabil für Anwendungen in biologischen Systemen. Die vorliegende Dissertationsschrift beschäftigt sich nun mit der Analyse und Anwendung von unkonventionellen Halogenbindungen (XB), deren $C(sp^3)-X$-Bindung mittels zweier Fluorsubstituenten am Kohlenstoffatom ($R-CF_2-X$) stabilisiert wird, um sie für Anwendungen in der Wirkstoffentwicklung nutzbar zu machen. In der Literatur ist mit Asciminib ($-O-CF_2Cl$) bisher nur ein von der FDA zugelassener Wirkstoff beschrieben. Wir versprechen uns von $CF_2X$-Gruppen als zusätzliches Werkzeug in der molekularen Optimierung von Wirkstoffkandidaten die Möglichkeiten zur Entdeckung neuer und interessanter Proteinbindungsmodi. Analysiert wurden hierbei unter anderem die synthetische Zugänglichkeit solcher Verbindungen, deren chemische und metabolische Stabilität, physiko-chemische Eigenschaften wie Löslichkeiten, bevorzugte Konformationen sowie mittels computer-gestützten Methoden Halogenbindungseigenschaften wie $V_{max}$ und Komplexbildungsenergien ΔE. Praktisch angewandt wurden diese $CF_2X$-Gruppen durch Inkorporation in Fragment-Bibliotheken für Fragment-basierte Wirkstoffforschung (engl. *fragment-based drug discovery*, FBDD) und in Fmoc-geschützten Aminosäuren zur Festphasen-Peptidsynthese (engl. *solid phase peptide synthesis*, SPPS).

Diese Dissertationsschrift gliedert sich in drei thematisch abgrenzbare Teile (siehe Abschnitt 3.1, 3.2 und 3.3), wobei sich die ersten beide Teile mit niedermolekularen Verbindungen befassen und der dritte Teil Aminosäuren und Peptiden zum Thema hat.

Im ersten Teil (Abschnitt 3.1) werden Grundsätze und Anwendungen von $CF_2X$-Eigenschaften als unkonventionelle Halogenbindungsdonoren in der medizinischen Chemie, der chemischen Biologie und der Arzneimittelentdeckung eruiert. Hierzu wurden zunächst zwei Serien an Modellmolekülen synthetisiert: *1-(4-(Difluorohalomethoxy)phenyl)urea* (**6a**–**e**) und N-*(benzo[*d*][1,3]dioxol-5-yl)-2,2-difluoro-2-haloacetamide* (**7a**–**e**) mit der allgemeinen Formel $R-Y-CF_2X$ (R = organischer Rest; Y = Amid, Ether (Linker-System); X = H, F, Cl, Br, I).

In Kristallisationsexperimenten mit unseren Modellverbindungen haben wir gezeigt, dass die Selbstorganisation der $CF_2X$-Derivate im kristallinen Festkörper hauptsächlich von XBs angetrieben und von der Größe des Halogens beeinflusst wird. $CF_2X$ Ether- und Amidgruppen nehmen bevorzugte Geometrien an, die in der Lage sind, potenzielle XB-Akzeptoren anzusteuern, die mit $C(sp^2)-X$-Gruppen von (Hetero)arylhalogeniden nicht ohne weiteres adressierbar sind. Darüber hinaus neigen sie in unseren Kristallstrukturen dazu, nach dem optimalen XB-Winkel und -Abstand zu streben, anders als unser analoger

HB-Donor $CF_2H$ (**7a**). Mithilfe von Methoden der Quantenmechanik (QM) haben wir die Konformationsflexibilität solcher $CF_2X$ Ether- und Amidfunktionen charakterisiert und eine gute Übereinstimmung mit den experimentellen Daten unserer kleinen Molekülkristalle festgestellt. Hiebei zeigten sich eindeutige Konformationsbeschränkungen, die bei der Verwendung dieser chemischen Funktionen im Moleküldesign unbedingt zu berücksichtigen sind. Darüber hinaus finden wir ein angemessenes Maß an Flexibilität dieser chemischen Gruppen, um sich an verschiedene XB-Akzeptoren in einer Bindungsstelle mit geringer konformationeller Belastung anzupassen, insbesondere im Vergleich zu $C(sp^2)-X$-Strukturen. Wir haben die potentielle XB-Stärke dieser $CF_2X$-Donoren in einer abstandsabhängigen Weise weiter charakterisiert. Im Vergleich zu den entsprechenden Halogen-Benzolen stellen wir fest, dass die XB-Wechselwirkungen durch die Tuning-Effekte der Fluoratome und der Linkerfunktionen um etwa 3,5 bis 4.5 kJ $mol^{-1}$ verbessert werden.

Das Strukturmotiv $CF_2X$ ist in der Arzneimittelforschung unterrepräsentiert und wurde bisher kaum angewendet. Organische Amine sind leicht verfügbare und geeignete Ausgangsmaterialien für die einfache Herstellung einer strukturell vielfältigen Fragmentbibliothek mit $CF_2X$ Amiden. Wir schlagen vor, dass auf der Grundlage solcher Bibliotheken unkonventionelle oder sogar einzigartige Bindungsmodi erforscht werden könnten, die im konventionellen chemischen Raum kaum zugänglich sind, was die Entdeckung bisher nicht genutzter, patentierbarer Chemotypen und die Schaffung zusätzlicher therapeutischer Möglichkeiten erlauben würde.

Um die Nützlichkeit und gute Anwendbarkeit dieses Konzepts zu demonstrieren, haben wir die c-Jun N-terminalen Kinasen 1 und 3 (JNK1 und JNK3) mittels STD-NMR untersucht und die bindenden Fragmente mittels ITC validiert, wobei mehrere Treffer im Bereich der mikromolekularen Affinität gefunden wurden. Insbesondere das 5-(Pyridin-4-yl)-1,3,4-thiadiazol-Gerüst zeigte eine gute Bindung an beide Kinasen. Die Affinität seines Bromderivats (**30**) zu JNK3 und JNK1 betrug 17 µM bzw. 15 µM. Wir haben die Kristallstruktur von **30** im Komplex mit JNK3 bestimmt und dabei festgestellt, dass die $CF_2Br$ Gruppe auf einzigartige Weise mit der P-Schleife (engl. *P-loop*) interagiert, was bisher noch nicht berichtet wurde. Sie kann gleichzeitig eine XB mit einem Abstand von 3.3 Å und einem σ-Loch-Winkel (engl. *σ-hole angle*) von 161.9° zum Rückgrat-Sauerstoff von G76 im *P-loop* eingehen, während sie eine Wasserstoffbindung von der geladenen Seitenkette von K93 an eines ihrer Fluoratome akzeptiert. Insgesamt verlagern sich die Wechselwirkungen in der Bindungsstelle von Positionen, denen traditionell die meiste Aufmerksamkeit gewidmet wird, wie dem Scharnier (engl. *hinge region*) und der hinteren Tasche, zur Zucker- / Phosphat-Bindungsstelle von ATP. Nur die Pyridin-Substruktur bildet eine HB mit der *hinge region*. Daher hat das Fragment **30** ein gutes Optimierungspotenzial durch die Ausarbeitung des *hinge region*-Bindungsmotivs und die Durchführung von Fragmentwachstum und Fusionsansätzen.

Zukünftige Studien sollten sich auf die Erweiterung der Fragmentbibliothek sowie die Entwicklung weiterer Linkersysteme und anderer stabiler C($sp^3$)−X-Strukturen konzentrieren. Die sich ständig erweiternde Bibliothek könnte weiterhin nach zusätzlichen Bindungsfragmenten durchsucht werden, die auf therapeutisch relevante Proteine abzielen. Die gefundenen Treffer können einer Leitstrukturoptimierung unterzogen werden.

Im zweiten Teil (Abschnitt 3.2) wurde ein PDB-Dekorations-Scan durchgeführt und als zweckdienliches Instrument für die Suche nach vielversprechenden, potenziellen Halogenbindungen etabliert. Hierzu wurden aromatische $C_{ar}$−H-Bindungen ohne Linker-Systeme mit $CF_2Br$-Gruppen substituiert und entlang ihrer $C_{ar}$−$CF_2Br$-Achse rotiert. Ergebnisse ohne oder mit nur geringen Kollisionswerten und innerhalb definierter XB-Akzeptor- und XB-Donor-Abständen und -Winkeln wurden erfasst und analysiert. Hierbei zeigte sich, dass die Protein-Rückgrat addressierenden Treffer mit dem natürlichen Vorkommen der Aminosäuren in Proteinen korrelieren, mit Ausnahme des Rückgrat-Sauertsoffatoms der Aminosäure Glycin. Die erhöhte Trefferrate von Glycin kann mit der fehlenden Seitenkette erklärt werden, was eine weniger gehinderte Addressierung des Rückgrats ermöglicht.

Anhand der gefunden Resultate wurde von uns ein in Position 5 $CF_2Br$-dekoriertes Indazol sowie davon abgeleitet ein Benzisoxazol und ein Imidazo[1,5-*a*]pyridin als Modellmoleküle mit dem Ziel ausgewählt, ein Rückgrat-Sauerstoff in den Proteinkinasen JNK1 und JNK3 zu adressieren ($CF_2Br\cdots O_{S193}$ in JNK3). Bei der Präparation zeigten sich unterschiedliche Grenzen der synthetischen Zugänglichkeit. Grundsätzlich ließen sich $CF_2Br$-tragende Indazole und Benzisoxazole herstellen. Im Gegensatz zu Benzisoxazol war das finale Indazolprodukt jedoch nach der Entfernung von Boc-Schutzgruppen chemisch nicht stabil. Imidazo[1,5-*a*]pyridin mit $CF_2Br$-Gruppe war synthetisch nicht realisierbar, da die $C_2FH$ nicht bromierbar war.

Die analogen Vergleichssubstanzen mit $CF_2H$- und $CF_3$-Gruppe wurden erfolgreich für alle drei Verbindungsklassen hergestellt und an JNK1 und JNK3 mittels STD-NMR und ITC getestet. Hierbei zeigte sich, dass Benzisoxazole keine ausreichend gute Bindungsaffinitäten besitzen, um an die jeweiligen Proteine zu binden (ebenso wenig das $CF_2Br$-tragende Benzisoxazol). Mit einem $K_d$ von 12 μM bindet das $CF_2H$-tragende Indazol von allen Vergleichssubstanzen mit größter Affinität an JNK3. An JNK3 zeigten $CF_2H$-tragende Indazole / imidazo[1,5-*a*]pyridine ($K_d$ = 12 μM / 109 μM) im Vergleich zu den Molekülen mit $CF_3$ Gruppe ($K_d$ = 100 μM / >1000 μM) eine signifikant bessere Bindung. In der Proteinkristallstruktur von JNK3 in Komplex mit der $CF_2H$-Indazol-Verbindung **51a** zeigte sich, dass das Indazol, wie im PDB-Scan gefunden, an die *hinge region* der Kinase bindet. Die $CF_2H$-Gruppe ist in Richtung des S193-Sauerstoffatoms gerichtet und mit einem $C_H\cdots O$-Abstand von 5.3 bis 6.0 Å böte die Kristallstruktur, wie im ursprünglichen Design geplant, genug Raum für ein Halogen.

Im dritten Teil (Abschnitt 3.3) wurden Fmoc-geschützte Phenylalanin-, Lysin- und 2,4-Diaminobuttersäure-Derivate hergestellt und in Peptidsequenzen integriert. Diese wurden wurden anschließend mittels kompetitiven Fluoreszenzpolarisationsassays (FP-Assay) an MDM2 und MDM4, wichtige Negativ-Regulatoren des Tumorsupressors p53, getestet. Die Synthese von Phenylalanin-Derivaten mit $CF_2Br$-Ethern in *meta*- und *para*-Position des aromatischen Rings erfolgte ausgehend von den entsprechenden Kresol-Derivaten. Die Syntheseroute beinhaltet zwei wichtige Schritte: Erstens, die Herstellung der $OCF_2Br$-Gruppe ausgehend von einer $OCF_2CO_2H$-Gruppe mittels einer radikalischen, decarboxylierenden Halogenierungsreaktion. Und zweitens, die Synthese der Aminosäure-Funktion an der Methylgruppe über ein Acetamidomalonsäure-diethylester-Intermediat.

Die Amin-Funktion der Fmoc-geschützten Lysin- und 2,4-Diaminobuttersäure-Seitenketten wurden unter Bildung eines Amides in einer lediglich einstufigen Synthese acetyliert ($R-NHCOCY_2X$; Y = H, X = H oder Y = F, X = H, F, Br, I).

Insbesondere die FP-Messungen mit acetylierten Lysin- und Diaminobuttersäure-Derivaten (Nle- bzw. Abu-Derivate im Dreibuchstaben-Code) ergaben interessante Resultate: Lys24Nle(εNHCOCF$_2$X) in $^{17\text{-}28}$p53-abgeleiteten Peptiden zeigten bei Messungen an MDM4 eine für Halogenbindungen typische Abnahme des $K_i$-Wertes von X = F > Cl > Br ($K_i$ = 202 nM > 112 nM > 82 nM gegenüber $K_i$ = 307 nM beim $^{17\text{-}28}$p53-Wildtyp). Die um zwei $CH_2$-Einheiten kürzere Seitenkette der Lys24Abu(εNHCOCF$_2$X)-Referenzpeptide zeigte keine solch eindeutige Tendenz, was ein Indiz dafür ist, dass die kürzere Variante bei der Bindung an MDM4 kein Akzeptoratom für die Halogenbindung findet.

Da wir keine Kristallstruktur erhielten, näherten wir uns mittels *in silico*-Methoden einer möglichen Hypothese des Bindungsmodus der Peptide an MDM4. Hierzu wurden zufällige Konformere der Seitenkette von Nle(εNHCOCF$_2$Br) erzeugt und in die Position 24 der p53-Sequenz der bekannten MDM4-Proteinkristallstrukturen 2Z5T (Zebrafisch) und 3DAB (human) integriert. Anschließend wurden die jeweils erzeugten Sessions frei QM-optimiert. Nach Auskonvergierung zeigten 49 % der gefundenen Interaktionen einen intra- oder intermolekularen XB-Kontakt. Die Ergebnisse deuten auf das unprotonierte Nδ in His51 (Zebrafisch) / His54 (human) als wahrscheinlichsten XB-Akzeptor in MDM4 hin. Die weit zu überbrückende Distanz vom Cα zu diesem Akzeptoratom erklärt ebenso, warum die Messungen der Diaminobuttersäure-Derivate mit kürzerer Seitenkette schlechtere $K_i$-Werte ohne die für Halogenbindungen typische Tendenz ergaben, da der XB-Donor Nδ nicht erreicht wird.

Zusammenfassend lässt sich sagen, dass die in dieser Dissertation durchgeführten Studien gezeigt haben, dass $CF_2X$-Gruppen ein nützliches zusätzliches Werkzeug beim Design von Wirkstoff-Molekülen sein können. Die räumliche Struktur dieser Gruppe in

Kombination mit verschiedenen Linker-System ermöglicht neue Interaktion mit Zielproteinen, die einhergehenend mit verbesserten molekularen Eigenschaften zu höheren Affinitäten führen können.

# 5 Methods

## 5.1 Stability Assays

### 5.1.1 Glutathione Stability Assay

The glutathione stability assay was performed according to a modified protocol by Keeley *et al.* (2019).[281] 225 µL of PBS buffer (pH 7.4), 12.5 µL of ACN, 250 µL of GSH solution (10 mM in PBS buffer containing 10 % (v/v) ACN), and 6.25 µL of indoprofen or ketoprofen (8 mM in ACN) as internal standard were added into an HPLC vial. The assay was started by adding of fragment solution (20 mM in ACN) to give a final concentration of 250 µM fragment, 5 mM GSH, and 100 µM internal standard in 500 µL of PBS containing 10 % (v/v) ACN. The final mixture was incubated at 37 °C and processed by injection of 5 µL into an analytical HPLC after different time intervals.

Analytical HPLC was performed on an UltiMate 3000 HPLC system (Thermo Fisher Scientific Inc, Waltham, MA, USA) equipped with a ReproSil-XR 120 C18 column (5 µm, 120 Å, 4.6 × 150 mm, Dr. Maisch GmbH, Ammerbuch-Entringen, Germany) and a flow rate of 1 mL $min^{-1}$ using eluent A1 (0.01 M potassium phosphat buffer, pH 2.3) and eluent B1 (MeOH). Eluent B1 increases linearly from 10 % to 85 % over 9 min, the gradient was retained for 4 min at 85 % eluent B1, then back to the initial condition over 1 min and retained for 4 min. The column temperature was kept at 25 °C. Absorption was detected at 218 nm, 254 nm and 280 nm. Chromatograms were analyzed with Chromeleon v7.2.10 (Thermo Fisher Scientific Inc, Waltham, MA, USA).

The values of the area under the curve were determined by integrating the HPLC spectra and normalized relative to the internal standard.

### 5.1.2 Microsomal Stability Assay

Samples were measured in triplicates and incubated at 37 °C. Each incubation had a total volume of 600 µL: 540 µL of potassium phosphate buffer (100 mM, pH 7.4), 36 µL of NADPH regenerating system (1.3 mM $NADP^+$, 3.3 mM isocitrate, 0.4 U $mL^{-1}$ isocitrate dehydrogenase, 3.3 mM $MgCl_2$), 21 µL of microsomes pooled from human liver (10 mg $mL^{-1}$), and 3 µL of substance standard solution (1 mg $mL^{-1}$ for targets, 0.1 mg $mL^{-1}$ for positive controls). Testosterone, diclofenac, and propranolol were used as positive controls for different cytochrome P450 enzymes and heat-inactivated microsomes (45 min, 60 °C) with testosterone as negative control. In addition, a mixture of all substances and a blank control of microsomes without substances were measured. Samples were taken at 0, 5, 15, 30, 45, 60, 120, and 300 min. For this purpose, 50 µL was quenched in 150 µL of ice-cold MeOH. Samples were centrifuged and supernatants were analyzed using HPLC-MS.

The LC-MS system used and the parameters for the evaluation of the microsomal stability assay are described in the Appendix A.1 on page 229.

## 5.2 Turbidimetric Solubility Assay

Turbidimetric solubility assay was performed in 50 mM HEPES (pH 7.4) and 100 mM NaCl at 25 °C. The 100 mM fragment stocks in DMSO were diluted by a factor of 4/5 in a 96-well plate. By adding buffer, the assay was started. The final conditions were 200 µL and 5% (v/v) DMSO. The measurement was done with the CLARIOstar (BMG Labtech, Ortenberg, Germany) over approximately 1 h at 600–800 nm. Before each implemented kinetic cycle of 115 s, the plate was shaken in double orbital at 300 rpm for 60 s.

## 5.3 Small Molecule Crystals

Small molecule crystals were grown by using vapor diffusion or solvent evaporation. About 5 mg of **6a**–**e** was placed in the inner tube and dissolved in 0.4 mL acetone. 2 mL of chloroform as antisolvent was placed in the outer container, then the outer container was sealed to induce the equilibration of the two liquids via vapor diffusion at room temperature. About 5 mg of **7a**–**e** was placed in an HPLC vial. 0.8 mL of *n*-hexane was added as an antisolvent, and then DCM was added dropwise until the solid was dissolved. The vial was sealed with a septum and evaporation was allowed through a cannula at room temperature. All crystals were grown within 7 d. The crystals were analyzed using the STOE IPDS 2T diffractometer (STOE & Cie GmbH, Darmstadt, Germany). The final crystal structures are deposited in the CCDC database with the deposit numbers 2248877, and 2232102–2232110 (Appendix A.7.1 on page 255 ff.).

## 5.4 Expression and Purification of Proteins

### 5.4.1 Preparation of Buffers and Other Solutions

Buffers were calculated by using the buffer calculator tool from Rob J. Beynon, taking into account the temperature correction and Debye-Hueckel correction for ionic strength (http://phbuffers.org/BuffferCalc/Buffer.html). All buffers were sterile filtered using a 0.22 µm filter and stored at 4 °C. Reducing agents such as β-ME were added immediately before use.

Kanamycin and ampicillin stocks were prepared at 100 mg mL$^{-1}$ in *dd*$H_2O$ and sterile filtered using a 0.22 µm syringe filter. Chloramphenicol stocks were prepared at 34 mg mL$^{-1}$ in ethanol. All stock solutions were stored at −20 °C.

### 5.4.2 Media Preparation

The media components (Table 23) were dissolved in 1 L *dd*$H_2O$, the pH was adjusted to 7.0, and the media were autoclaved at 121 °C for 20 min. Media for plates were supplemented with 1.5 g agar per 100 mL media solution before autoclaving.

**Table 23:** Recipes for media preparation.

| Component | LB-Medium (1 L) | 2xYT-Medium (1 L) |
|---|---|---|
| tryptone | 15 g | 16 g |
| yeast extract | 5 g | 10 g |
| NaCl | 10 g | 5 g |

### 5.4.3 SDS-PAGE

The loading buffer was prepared as a 5-fold stock solution (250 mM Bis-Tris at pH 6.8, 5 % (v/v) DTT, 30 % (v/v) glycerol, 10 % (v/v) SDS, 0.02 % (v/v) bromophenol blue). The running buffer was also prepared as a 5-fold stock solution (52.3 g MOPS, 30.3 g Tris base, 1.46 g EDTA, 12.5 ml 20 % (v/v) SDS). The SDS-PAGE gel consisted of the components described in the following Table 24:

**Table 24:** Recipes for SDS-Page gel preparation.

| Component | Stacking gel | Seperating gel |
|---|---|---|
| 1.25 mM Bis-Tris buffer 3.5x (pH 6.6) | 11.4 mL | 14.3 mL |
| Polyacrylamide 40 (29:1) | 5.3 mL | 16.7 mL |
| *dd*$H_2O$ | 23.3 mL | 19.0 mL |
| TEMED | 30 µL | 40 µL |
| APS (10 %) | 150 µL | 200 µL |
| bromophenol blue | 2 mg | |

For protein monitoring, a 20 µL sample was taken and mixed with 5 µL sample buffer, then heated to 95 °C for 2 min. The gel was loaded with 10 µL of denaturated protein sample mix and Blue Prestained Protein Standard (Broad Range, 11–190 kDa; New England BioLabs, Ipswich, MA, USA) was used as a molecular weight marker. The electrophoresis was performed at 200 V and 100 mA. Finally, the gel was stained with InstantBlue™ solution (Expedeon AG, Heidelberg, Germany) for at least 30 min, with two subsequent water wash steps.

### 5.4.4 JNK1 and JNK3

JNK1 (2–364) and JNK3 (39–402): The pET24a_HLT_JNK3 construct was transformed into BL21(DE3)pLysS cells (Novagen) or the pET24a_HLT_JNK1 construct was transformed into BL21-CodonPlus-RIL cells (Agilent Technologies, Inc., Santa Clara, CA, USA) and incubated at 37 °C overnight on LB medium plates with kanamycin (50 µg mL$^{-1}$) and chloramphenicol (37 µg mL$^{-1}$). Cells were transferred with LB medium and the same antibiotics into a 9-fold volume of the same media and grown to an $OD_{600}$ = 1.0 at 37 °C and 180 rpm as a pre-culture. Ten mL of this culture was used to inoculate 6 L of 2xYT containing the antibiotics. These main cultures were grown at 37 °C and 200 rpm until an $OD_{600}$ = 0.5, then the temperature was reduced to 20 °C and IPTG was added to final concentration of 0.8 mM. The expression lasted for 16–18 h. Cultures were centrifuged at 4 °C, 4000 rpm for 30 min in a J6-MI centrifuge (Beckman-Coulter, Brea, CA, USA). The pellet was resuspended with ice-cold lysis buffer (50 mM TRIS, 500 mM NaCl, 10 mM imidazole and 5 mM β-ME, pH of 7.4). After adding DNase and RNase, the suspension was lysed by sonication. The suspension was centrifuged at 4 °C and 18 500 rpm for 1 h in an Avanti J-30-I (Beckman-Coulter, Brea, CA, USA). The supernatant was sterile filtered (0.22 µM filter, rapid-FILTERMAX, TTP®, Trasadingen, Switzerland) and loaded onto a Nickel-NTA column (HisTrap FF, GE Healthcare, Chicago, IL, USA) equilibrated with lysis buffer. The column was washed with 5 CV of lysis buffer. The protein was eluted with 30 % elution buffer (50 mM TRIS, 500 mM NaCl, 300 mM imidazole and 5 mM β-ME, pH of 7.4). His-tag was cleaved with 1 mg mL$^{-1}$ TEV protease per 10 mL protein sample while dialyzing with regenerated cellulose sleeve (ZelluTrans/Roth, Dialysiermembran T1, MWCO = 3500 Da; Carl Roth, Karlsruhe, Germany) in 5 L lysis buffer without imidazole overnight while stirring at 4 °C. The His-tag and His-tagged TEV were removed using a subsequent nickel column run. After protein concentration using a Vivaspin® Turbo 15 (MWCO = 30 kDa; Sartorius, Göttingen, Germany), the protein was loaded onto a size-exclusion gel filtration column (HiLoad 26/60 Superdex 75 prep grade, GE Healthcare, Chicago, IL, USA) equilibrated with SEC buffer (50 mM HEPES, 100 mM NaCl, 2 mM $MgCl_2$, pH of 7.0). The collected fractions were concentrated to approximately 50 µM, flash-frozen in liquid nitrogen and aliquots were stored at −80 °C. The purity of the protein was monitored by SDS-PAGE after each purification step.

### 5.4.5 MDM2

MDM2 (2–125): Expression and purification were mainly adopted from the literature and modified.[282] The pminiRSET/pRESTa/pGEX-2T_GST_MDM2 construct was transformed into *E. coli* Rosetta BL21(DE3)pLysS cells (Novagen, Merck KGaA, Darmstadt, Germany) and incubated at 37 °C overnight on LB medium plates with ampicillin (50 µg mL$^{-1}$) and chloramphenicol (37 µg mL$^{-1}$). Cells were transferred with LB medium and the same

antibiotics into a 9-fold volume of the same media and grown to an $OD_{600}$ = 1.0 at 37 °C and 180 rpm as a pre-culture. 20 mL of this culture was used to inoculate 4 L of 2xYT containing the antibiotics. These main cultures were grown at 37 °C and 220 rpm until an $OD_{600}$ = 0.4, then the temperature was reduced to 25 °C and IPTG was added to final concentration of 0.5 mM. The expression lasted for 16 h. Cultures were centrifuged at 4 °C, 4000 rpm for 30 min in a J6-MI centrifuge (Beckman-Coulter, Brea, CA, USA). The pellet was resuspended with ice-cold lysis buffer (50 mM TRIS, 500 mM NaCl, 5 mM DTT, 1 mM EDTA, 0.1 % (v/v) Triton X-100, 50 µM PMSF, pH of 8.0). After adding DNase and RNase, the suspension was lysed by sonication. The suspension was centrifuged at 4 °C and 18 500 rpm for 1 h in an Avanti J-30-I (Beckman-Coulter, Brea, CA, USA). The supernatant was sterile filtered (0.22 µM filter, rapid-FILTERMAX, TTP®, Trasadingen, Switzerland) and loaded onto a GST-affinity column (GE XK 1, Amintra Glutathione Resin, Expedeon, Heidelberg, Germany) equilibrated with elution buffer (50 mM TRIS, 500 mM NaCl, 5 mM DTT, 1 mM EDTA, pH of 8.0). The column was washed with 5 CV of elution buffer. The protein was eluted with elution buffer containing 10 mM reduced glutathione using a linear gradient elution from 0 % elution buffer to 100 % in 15 min. The fractions were pooled and thrombin-digested at pH 8.0 and 4 °C (250 units high active thrombin per 40 mL) overnight. After protein concentration using a Vivaspin® Turbo 15 (MWCO = 5 kDa; Sartorius, Göttingen, Germany), the protein was loaded onto a size-exclusion gel filtration column (HiLoad 26/60 Superdex 75 prep grade, GE Healthcare, Chicago, IL, USA) equilibrated with SEC buffer (5 mM TRIS, 50 mM NaCl, 5 mM β-ME, pH of 8.0). The fractions collected were concentrated to approximately 60 µM, then 10 % (v/v) glycerol was added, the mixture was flash-frozen in liquid nitrogen and aliquots were stored at −80 °C. The purity of the protein was monitored by SDS-PAGE after each purification step. The protein mass was confirmed by ESI-MS and the protein concentration was calculated via UV-spectroscopy using the molar extinction coefficient 10 430 $M^{-1}$ $cm^{-1}$ at 280 nM from the ProtParam program on the EXPASY server.

### 5.4.6 MDM4

MDM4 (16–116, C17S): The Expression and purification were mainly adopted from the literature and modified.[248,283] The pET24a(+)_HLT_MDM4 construct was transformed into *E. coli* Rosetta BL 21 (DE3) pLysS cells (Novagen, Merck KGaA, Darmstadt, Germany) and incubated at 37 °C overnight on LB medium plates with kanamycin (50 µg $mL^{-1}$) and chloramphenicol (37 µg $mL^{-1}$). Cells were transferred with LB medium and the same antibiotics into a 9-fold volume of the same media and grown to an $OD_{600}$ = 1.0 at 37 °C and 180 rpm as a pre-culture. Ten mL of this culture was used to inoculate 6 L of 2xYT containing the antibiotics. These main cultures were grown at 37 °C and 220 rpm until an $OD_{600}$ = 0.6, then the temperature was reduced to 20 °C and IPTG was added to final concentration of 1.0 mM. The expression lasted for 16 h. Cultures were centrifuged at 4 °C,

4000 rpm for 30 min in a J6-MI centrifuge (Beckman-Coulter, Brea, CA, USA). The pellet was resuspended with ice-cold lysis buffer (50 mM sodium phosphate, 300 mM NaCl, 10 mM imidazole, 5 mM β-ME, pH of 8.0). After adding DNase and RNase, the suspension was lysed by sonication. The suspension was centrifuged at 4 °C and 18 500 rpm for 1 h in an Avanti J-30-I (Beckman-Coulter, Brea, CA, USA). The supernatant was sterile filtered (0.22 µM filter, rapid-FILTERMAX, TTP®, Trasadingen, Switzerland) and loaded onto a Nickel-NTA column (HisTrap FF, GE Healthcare, Chicago, IL, USA) equilibrated with lysis buffer. The column was washed with 5 CV of lysis buffer. The Protein was eluted with elution buffer (50 mM sodium phosphate, 300 mM NaCl, 250 mM imidazole, 5 mM β-ME, pH of 8.0) using a linear gradient elution from 0 % elution buffer to 100 % in 15 min. His-tag were cleaved with 1 mg $mL^{-1}$ TEV protease per 5 mL protein sample while dialyzing with regenerated cellulose sleeve (ZelluTrans/Roth, Dialysiermembran T1, MWCO = 3500 Da; Carl Roth, Karlsruhe, Germany) in 5 L lysis buffer without imidazole overnight on stirrer at 4 °C. The His-tag and His-tagged TEV were removed using a reverse nickel column run. After protein concentration using a Vivaspin® Turbo 15 (MWCO = 5 kDa; Sartorius, Göttingen, Germany), the protein was loaded onto a size-exclusion gel filtration column (HiLoad 26/60 Superdex 75 prep grade, GE Healthcare, Chicago, IL, USA) equilibrated with SEC buffer (25 mM sodium phosphate, 150 KCl, 5 mM β-ME, pH of 7.2). The collected fractions were concentrated to approximately 50 µM, then 10 % (v/v) glycerol was added, the mixture was flash-frozen in liquid nitrogen and aliquots were stored at −80 °C. The purity of the protein was monitored by SDS-PAGE after each purification step. The protein mass was confirmed by ESI-MS and the protein concentration was calculated via UV-spectroscopy using the molar extinction coefficient 7450 $M^{-1}$ $cm^{-1}$ at 280 nM from the ProtParam program on the EXPASY server.

## 5.5 Biophysical Evaluation Methods

### 5.5.1 Saturation-Transfer Difference NMR Assay

JNK1 or JNK3 was buffer exchanged to 100 mM sodium phosphate, 250 mM NaCl, and 2 mM $MgCl_2$ with a pH of 7.0 at 25 °C using a desalting column (HiPrep™ 26/10 Desalting; Cytiva, Marlborough, MA, USA). The samples contained final concentrations of 20 µM protein, 10 % (v/v) DMSO-$d_6$, and 1 mM of the fragments. NMR spectra were acquired with a Bruker Avance III HDX 700 spectrometer (Bruker Corporation, Billerica, MA, USA), equipped with a 5 mm Prodigy TCI cryo probe head. $^1$H NMR experiment with 1 k scans and water suppression through presaturation was performed. The STD experiments adapted the pulse sequence published by Mayer *et al.*[284,285] The on-resonance frequency, which was determined from the $^1$H NMR spectra of the protein, was between 0.5–0.6 ppm. 40 ppm was used as the off-resonance frequency. For an interleaved acquisition of the on- and off-resonance, a pseudo-2D scheme was applied. The saturation was done by Gaussian

pulses with a length of 50 ms and 60 dB of attenuation, done with an interpulse delay of 1 ms leading to an excitation bandwidth of about 4 Hz. The screening was done with 16 scans of on- and off-resonance scans each, with a 3 s saturation time. A $^{1}$H NMR experiment was performed for each compound to act as a reference spectrum in the STD experiments. NMR experiments were carried out at 25 °C. Spectra were processed and analyzed with TopSpin v4.0.8 (Bruker Corporation, Billerica, MA, USA) and were reported as chemical shifts (δ) in parts per million (ppm) relative to the solvent peak.

### 5.5.2 Isothermal Titration Calorimetry

JNK1 or JNK3 was buffer exchanged to 50 mM HEPES, 100 mM NaCl, 2 mM $MgCl_2$, and 1 mM TCEP with a pH of 7.4 at 25 °C using a desalting column (HiPrep™ 26/10 Desalting; Cytiva, Marlborough, MA, USA). The protein solution was usually concentrated to 60–120 µM and DMSO was added to a final concentration of 5 % (v/v). The fragments were dissolved in DMSO to give a 300 mM stock solution, which was further diluted with buffer and DMSO to yield a 1.5–5 mM solution, also containing 5 % (v/v) DMSO. Depending on the binding strenght the fragment concentrations varried. A MicroCal iTC200 instrument (Malvern Panalytical Ltd, Malvern, UK) was used, with the measuring cell set at 25 °C, while the cooling jacket was set at 15 °C. The measurement was performed by using a needle stirring speed of 1000 rpm and a reference heat rate of 10 µcal s$^{-1}$. Experiments were aborted, when the measuring cell was unable to reach a heat rate greater than 9.0 µcal s$^{-1}$ during equilibration. After an initial delay of 120 s following a temperature equilibration, a first injection of 0.5 µL was done over 2 s. 19 injections of 2.0 µL were performed over 4 s every 120 s.[286]

Based on the results of the ITC measurements, the ligand efficiency (LE) was calculated using the following equation:[287,288]

$$LE = -\frac{\Delta G}{HA} = -log\,(K_d)\,\frac{1.4}{HA} \tag{8}$$

### 5.5.3 Fluorescence Polarization Assay

Peptide stock solutions (800 µM) of fluorescence-labeled probe and test peptides were prepared in DMSO and stored at −20 °C. The buffer of a thawed MDM2 or MDM4 protein solution was exchanged using a desalting column (HiPrep™ 26/10 Desalting; Cytiva, Marlborough, MA, USA). FP assay buffer (pH 7.2 at 25 °C) contained 25 mM potassium phosphate, 150 mM ionic strenght (NaCl), 5 mM DTT. The protein was concentrated with Vivaspin® Turbo 4 or 15 (MWCO = 5 kDa; Sartorius, Göttingen, Germany) at 4 °C and

4000 rpm where appropriate. BSA (0.2 mg $mL^{-1}$) was added just before the FP measurement. All FP experiments were performed using a CLARIOstar plate reader (emission filter: 530 nM, excitation filter: 482 nM, and dichroic mirror: 504 nM. BMG Labtech, Ortenberg, Germany) with black non-binding polystyrene 96-well microplates (GBO, Frickenhausen, Germany).

$K_d$ values of the fluorescence probe (FAM-LTFEHYWAQLTS-$CONH_2$) against MDM2 and MDM4 were determined by direct titration. 11-step serial dilutions of protein were prepared in FP assay buffer. To obtain the final protein concentration with 5 % (v/v) DMSO, 190 µL of the dilutions were mixed in a 96-well plate with 5 µL DMSO and 5 µL of 800 nM fluorescence-labeled probe (final concentration: 20 nM) in DMSO. A 12th measurement point contained only DMSO instead of probe. Each protein concentration was measured as quadruplicate. After 30 min incubation at 25 °C, measurements were taken 3 times at 10 min intervals and the results were averaged. This series of measurements was repeated at least three times to determine reliable $K_d$ values and protein concentrations in a range of 50–70 % of detected FP signal for competitive FP assay. It is recommended to re-determine these values for each protein batch.

For the competitive FP assay, 11-step serial dilutions of test peptide were prepared in DMSO. To obtain the final test peptide concentration with 5 % (v/v) DMSO, 5 µL of the dilutions were mixed in a 96-well plate with 5 µL of 800 nM fluorescence-labeled probe (final concentration: 20 nM) in DMSO and 190 µL protein solution (protein concentration determined during direct titration experiment) in FP assay buffer. A 12th measurement point contained only DMSO instead of test peptide. For experiments with 10 % (v/v) DMSO instead of 5 % (v/v) DMSO, the protein solution was reduced to 180 µL and additional 10 µL DMSO was added. Each test peptide concentration of the competitive assay was measured as quadruplicate and each series of measurements was repeated at least three times analogous to direct titration to determine reliable $[IC]_{50}$ values.

All normalized fluorescence polarization measurements were fitted with four parameter logistic regression (4PL) in OriginPro 2020 (OriginLab, Northampton, MA, USA) using the following equation,

$$y = \frac{A_1 - A_2}{1 + \left(\frac{x}{x_0}\right)^p} + A_2 \tag{9}$$

where $A_1$ is the minimum value and $A_2$ is the maximum value that can be obtained, $x_0$ is the point of inflection and $p$ is the Hill's slope of the curve. As reported previously (see Section 3.3.6.1 on page 93), the inhibition constant $K_i$ was determined using Equation 10 on the next page,

$$K_i = \frac{[I]_{50}}{\left(\frac{[L]_{50}}{K_d} + \frac{[P]_{50}}{K_d} + 1\right)} \tag{10}$$

where $[I]_{50}$ denotes the concentration of the free inhibitor at 50 % inhibition, $[L]_{50}$ is the concentration of the free labeled ligand at 50 % inhibition, $[P]_{50}$ is the concentration of the free protein at 0 % inhibition, and $K_d$ is the dissociation constant of the protein-ligand complex. $[I]_{50}$, $[L]_{50}$ and $[P]_{50}$ were determined as described in literature.[257]

### 5.5.4 Circular Dichroism Spectroscopy

CD measurements were performed on a Jasco J-720 (Jasco, Easton, MD, USA) at 20 °C using a quartz flow cell with a 2 mm path length. Peptides were dissolved in PBS (pH 7.4) at a concentration of 150 µM. Spectra were recorded at 50 nm min$^{-1}$ with a bandwidth of 2 nm and averaged over 2–10 scans. The PBS baseline was subtracted from each spectrum. As reported previously (see Section 3.3.6.2 on page 94), the mean residue weight ellipticity $[\theta]$ was calculated using the following equation,

$$[\theta] = \frac{\theta \cdot \frac{M}{n}}{\frac{m}{V} \cdot l \cdot 10} \tag{11}$$

where $\theta$ is the measured ellipticity in mdeg, $M$ is the molar mass in g mol$^{-1}$, $n$ is the number of amino acid residues in the peptide, $m$ is the dissolved mass in g, $V$ is the volume of the solvent in cm$^3$, and $l$ is the path length in cm. To determine the relative helicity, a maximum helicity value is required, which can be calculated by the following Equation 12,

$$[\theta]_{max} = \frac{-44000 + 250T}{1 - \frac{k}{n}} \tag{12}$$

where $[\theta]_{max}$ is the maximum helicity, $T$ is the temperature in °C, $k$ is a finite length correction parameter with $k = 4$ and $n$ is the number of amino acid residues in the peptide. The relative helicity in % was determined with the mean residue weight ellipticity $[\theta]_{obs,215}$ at wavelength $\lambda = 215$ nm calculated as described in Equation 11 and $[\theta]_{max}$ using Equation 13,

$$Helicity\% = \frac{[\theta]_{obs,215}}{[\theta]_{max}} \cdot 100 \tag{13}$$

## 5.6 Crystallization of JNK3

### 5.6.1 Crystallization and Soaking Procedure

Crystallization was performed as previously described.[24] JNK3 crystals were obtained by the sitting drop vapor diffusion method in MRC Maxi 48-well plates (Swissci) with 200 µL reservoir. Protein in SEC buffer (50 mM HEPES, 100 mM NaCl, 2 mM $MgCl_2$, 5 % (v/v) glycerol, pH of 7.0) was thawed and concentrated to 7–9 mg $mL^{-1}$. The protein solution was supplemented with 1 mM AMP-PCP, 0.4 mM Zwittergent 3-14 and 10 % (v/v) ethylene glycol. The reservoir solution (100 mM BisTris with a pH of 6.0–6.5, 27 % (v/v) PEG-3350 and 200 mM NaCl) was added into the plate reservoir, and a 2 µL protein drop was mixed with 2 µL reservoir solution. Then, the plate was sealed. After one day, rectangular cuboidal crystals grew and reached a sufficient size within one week. For cryo protection, the previously described condition was supplemented with an additional 20 % (v/v) glycerol and contained 5 mM fragment with no more than 5 % (v/v) DMSO. Fragments were soaked for 24 h and then frozen in liquid nitrogen. Data were collected at the Swiss Light Source in Switzerland at the Beamline Xo6SA (PXI).

### 5.6.2 Data Reduction and Refinement

Data reduction was performed using XDS (version Feb 5, 2021).[289] To obtain initial phases, PDB 4X21, was used as a 937 search model for molecular replacement using PHASER[290] as part of the CCP4 suit (v7.1)[291]. Multiple rounds of manual model building in COOT (v0.9.5)[292] and refinement using PHENIX (v1.19.2)[293] were performed. AceDRG[294] was used to create restraints for the compound **30**. The final model is deposited with the accession number 8BZP (Table 12 on page 57). Not deposited in the PDB is the crystal structure JNK3 in complex with Fragment **51a** (Table 15 on page 75).

## 5.7 Computational Methods

### 5.7.1 QPLogP and QPLogS calculations

LogS and logP values (denoted QPLogS and QPLogPo/w) were calculated using the QikProp module of Schrodinger suite version 2021-1.[195] Molecules were protonated and preprocessed using Schrodingers' LigPrep module with default parameters.[196] All calculations were then carried out using the default parameters and the normal processing mode of QikProp.

### 5.7.2 MP2 Geometry Optimizations and Single Point Calculations

Geometry optimizations and single point calculations were carried out using TURBOMOLE 7.4.1.[295] MP2 calculations were done in combination with the resolution of identity (RI) technique and the frozen core approximation.[280,296–298] The frozen core orbitals were defined using default settings by which all orbitals possessing energies below −3.0 au were considered core orbitals. The SCF convergence criterion was increased to $10^{-8}$ hartree for all calculations.

Throughout this study, we mainly used MP2-calculations combined with a triple-ζ basis set (def2-TZVPP).[280] For comparison purposes, a quadruple-ζ basis set (def2-QZVPP)[299] was used for selected interaction geometries. Furthermore, selected single points were counterpoise corrected using the procedure of Boys and Bernardi[21] to correct for basis set superposition errors (BSSE). Additional single point calculations were performed using the hybrid functional M06-2X[300] in combination with Grimme's dispersion correction (D3)[277]. When necessary, hydrogen atoms were added before starting the optimization using Protonate 3D in MOE 2018.0101.[301]

### 5.7.3 Sphercial Scan

The fragment (chlorodifluoromethoxy)benzene was derived from asciminib in the crystal structure 5MO4. Hydrogen atoms were added using the Protonate3D feature of the MOE at default settings. Next, the fragment was freely optimized using MP2/TZVPP. Using a custom Python/PyMOL script, 500 evenly distributed points on a sphere with the radius of 3.27 Å (identical with the distance between the chlorine atom in asciminib and the backbone oxygen of L448 in the crystal structure) were generated around the oxygen of the MP2/TZVPP-optimized backbone model system *N*-methylacetamide. For each of these points, a complex of (chlorodifluoromethoxy)benzene and *N*-methylacetamide was generated using the following procedure: The fragment was translated by placing the chlorine atom at the coordinates of this data point. Next, the fragment was rotated around the coordinates of the chlorine atom to obtain an optimal σ-hole angle of 180° between the fragment and the oxygen of *N*-methylacetamide. In a final step, the fragment was rotated around its C−Cl bond in steps of 60° to obtain six geometries per data point. In total, 3000 complexes were generated and single point calculations on the MP2/TZVPP level of theory were performed. The six complex formation energies of each data point were averaged and colored according to the supplied color scheme by using PyMOL.

### 5.7.4 Potential Energy Surfaces

Model molecules with the general formula Ph−Y−$CF_2$X (X = H, Cl, Br, I) were geometry-optimized using the MP2/TZVPP-level of theory. Starting from these geometry-optimized molecules, further geometries were generated by rotation along their rotatable axes (φ, ψ) with an increment of 10° of each step. For each newly generated geometry single point energies were calculated using MP2/TZVPP. Contour maps of potential energy surfaces (PESs) with ΔE in kJ $mol^{-1}$ as a function of dihedral angles φ and ψ were generated for amide (Y = NHCO) and ether (Y = O) derivatives, each with 1296 geometries (36 × 36). All PES plots were generated using OriginPro 2020 (OriginLab, Northampton, MA, USA).[302]

### 5.7.5 Electrostatic Potential and $V_{max}$ Calculations

Molecules were geometry-optimized using the MP2/TZVPP-level of theory. For conformers A and B of ligand **30**, heavy atoms were kept frozen during optimization. Electrostatic potentials and electron densities for all geometry-optimized molecules were calculated by using MP2/TZVPP on a regular 3D-grid. The size of the 3D-grid was adapted to the size of the respective molecule. Point density was kept uniform. The $V_{max}$ values were derived from a similar 3D-grid calculation surrounding the halogen atom and extracted at an isodensity level of 0.02 au. The ESP isosurface depictions of the model compounds were prepared with MOLCAD.[2,199] Negative ESP isosurfaces at an energy of −0.01 au are colored in dark blue and at an energy of −0.005 au in cyan. Positive ESP isosurfaces at 0.01 au are colored in red and at an energy of 0.005 au in orange. The isosurfaces at approximately 0.000 au, indicating the boundaries for the transition between negative and positive ESPs, are shown as gray surfaces. Cyan, orange and gray surfaces were kept transparent and a clipping plane was applied to all surfaces for better visibility.

### 5.7.6 Distance Scans

Molecules were optimized using the MP2/TZVPP-level of theory. For the evaluation of the small molecule crystals, heavy atoms of the molecules were kept frozen during optimization. Geometries shown in Figure 20 on page 52 were altered in steps of 0.1 Å along the $C_X$−X vectors of the respective halogen bond donating molecule. In the systematic approach, the freely geometry-optimized model molecules (Ph−X, Ph−O−$CF_2$X, and Ph−NHCO−$CF_2$X) and *N*-methylacetamide were oriented toward each other using the same protocol to avoid arbitrary differences: The $C_X$−X···O angle is equal to 180°, the X···O=C angle is equal to 120° (with X = H, Cl, Br, I), and the dihedral angle N−C=O···X is equal to 90°. The distances were varied with an increment of 0.1 Å of each step. Distances X···O (X = H, Cl, Br, I) ranged from 1.5 to 5.0 Å.

### 5.7.7 Structural Depictions

Structural depictions of calculated molecules were prepared using PyMOL 2.3.3.[303] The depictions of the small molecule crystal structures were prepared with Mercury (v.2020.2.0).[304]

### 5.7.8 Interaction Vectors and Pseudo-Interaction Points

Data used for this visualization were taken from the potential energy surface scans described above. Interaction vectors and pseudointeraction points were visualized using a custom Python/PyMOL-script. Interaction vectors were generated using CYLINDER and CONE objects and colored according to the provided energy scale. The direction of the vector was taken from the respective $C_X-X$ bond. Vector length was set to 2 Å. Only vectors within $\Delta\varphi, \Delta\psi = \pm 90°$ of the geometry-optimized molecule are shown. The energy threshold was set to 20 kJ $mol^{-1}$ with respect to the geometry-optimized minimum. Pseudointeraction points were generated by elongation of the $C_X-X$ vector by 3 Å. Then, these points were combined into one PyMOL object. The "vdw radius" of each point was altered to 0.2 Å and a surface was drawn. Surface quality was set to 3.

### 5.7.9 Conformational Energy Calculations

Hydrogen atoms were added to conformers A and B of compound **30** using the Protonate3D feature of MOE 2018.0101[301] and, subsequently, optimized using MP2/TZVPP. Heavy atoms were kept frozen during optimization. The difference in the conformational energy was derived from these optimized structures.

### 5.7.10 PDB Database Screening

Section 3.2.1: Ligands in 538 UNIProt IDs (all kinases, MDM2, MDM4, HIV-1 protease and SARS-CoV-2 main protease) were analyzed for putative new halogen bonds. Aromatic carbon positions of ligands were decorated with $CF_2Br$ groups. The attached substituents were rotated along the rotatable bond in steps of 5°. Severe clashes with the surroundings were filtered out. Hits with a putative halogen bond angle of >150° and an interaction distance of 2.5–4.5 Å were saved as PSE files. This was done using a custom PyMOL/Python script. The data was then evaluated manually.

Section 3.3.3: Peptides bound to HIV-1 protease, MDM2, and MDM4 were analyzed for putative new halogen bonds. For this, aromatic carbon positions of peptide amino acids were decorated with $CF_2Br$ or $OCF_2Br$ groups. The attached substituents were rotated along all rotatable bonds in steps of 5°. Severe clashes with the surroundings were filtered out.

Hits with a putative halogen bond angle of >160° and an interaction distance of <4 Å were saved as PSE files. This was done using a custom PyMOL/Python script. The data was then sighted manually.

### 5.7.11 Generation of Conformers

The side chain of Lys24 in chain P (starting at the Cα atom) in the crystal structure of 2Z5T was modified into the bromodifluoroacetylated variant and protonated using the Protonate 3D feature of Molecular Operating Environment(MOE) 2018.0101 at default settings. Then, a conformational search of this modified side chain was conducted using the Conformational Search feature of MOE at default settings, resulting in 162 conformers.

### 5.7.12 Binding Site Representation

In two crystal structures (PDB IDs: 2Z5T and 3DAB), the surroundings of Lys24 were carefully selected and used as an interaction site for the modified lysine. The interaction site consists of:

Peptide residues in 2Z5T and 3DAB: Phe19 (C, O, Cα), Ser20 (full), Asp21 (full), Leu22 (side chain removed), Trp23 (full), Lys24 (full), Leu25 (N, Cα).

Protein residues in 2Z5T: Met50 (C, O, Cα), His51 (full), Tyr52 (side chain removed), Leu53 (side chain removed), Gly54 (full), Gln55 (full), Tyr56 (side chain removed), Ile57 (side chain removed), Met58 (full), Val59 (N, Cα).

Protein residues in 3DAB: Met53 (C, O, Cα), His54 (full), Tyr55 (side chain removed), Leu56 (side chain removed), Gly57 (full), Gln58 (full), Tyr59 (side chain removed), Ile60 (side chain removed), Met61 (full), Val62 (N, Cα).

Next, the interaction site representation was protonated using MOE and the Protonate 3D feature at default settings.

### 5.7.13 Generation of Interaction Site Variants Using the Conformers

Using a custom Python script, the interaction site representations were altered using the previously generated conformers of the modified lysine side chain as follows: The positions of the Cα and Cβ atoms of Lys24 were used to match the modified conformers, thus replacing the natural side chain. For each conformer, 12 variations of the interaction site were generated by rotating the modified side chain around the Cα and Cβ bond in steps of 30 ° Next, generated interaction site variants resulting in severe clashes between the modified lysine side chain and the remaining peptide residues or the protein were removed. This resulted in 450 interaction site variants for 2Z5T and 420 for 3DAB.

### 5.7.14 Quantum Mechanical Calculations

Optimization of the remaining interaction site variants was performed using TPSS-D3/def-SV(P)[277–280] within TURBOMOLE 7.4.1.[295] Heavy atoms of the protein and peptide backbone were kept frozen during optimization. The convergence criterion was set to $10^{-6}$. Due to the high atom number (115 heavy atoms, 108 hydrogen atoms), $scfdamp was altered to: start=5.000 step=0.050 min=0.500. Multipole accelerated RI-J was activated ($marij). For 2Z5T, 247 converged structures were obtained and for 3DAB 304 structures.

## 5.8 Author Contributions

Prof. Dr. Frank M. Böckler envisioned the research. All experimental methods, data analysis and reprocessing, unless otherwise stated below, were planned and performed by Sebastian Vaas. Based on the preliminary work and ideas of Sebastian Vaas, the following contributions were made by other participants.

Experimental part: Dr. Dieter Schollmeyer performed X-ray measurements and data refinement of small molecule crystal structures. Sebastian Vaas performed the microsomal stability assay and Dr. Bernhard Drotleff, Matthias Olfert and Prof. Dr. Michael Lämmerhofer conducted and analyzed the respective MS measurements. Sebastian Vaas prepared and analyzed the STD NMR samples and Dr. Markus Kramer set up the STD NMR experiments. Sebastian Vaas performed and analyzed the ITC experiments, Janosch Rheinganz and Jason Stahlecker conducted supplemental ITC measurements. Janosch Rheinganz conducted the turbidimetric solubility assay. Theresa Klett prepared MDM2 and MDM4 by heterologous expression, Sebastian Vaas and Jason Stahlecker prepared JNK3, Sebastian Vaas and Marcel Dammann prepared JNK1. Sebastian Vaas and Jason Stahlecker conducted the JNK3 protein crystallization experiments. Prof. Dr. Thilo Stehle granted access to the SLS beamline. Jason Stahlecker performed protein data reduction and structure refinement.

Computational part: Dr. Markus O. Zimmermann performed all QM calculations with respect to: observed interactions in small molecular crystals, conformational analysis, potential interaction space, tuning, strength and geometry dependence of XB interactions, electrostatic potentials of compounds and $V_{max}$ values. Dr. Markus O. Zimmermann performed also the PDB decoration scans and all peptide-related *in silico* calculations. Marc U. Engelhardt calculated logP / logS values and distance scans of **7a**,**c**–**e** crystals. Prof. Dr. Frank M. Böckler generated the ESP plots and analyzed the logP / logS and solubility data in Section 3.1.6.

# 6 Synthesis

## 6.1 General Chemical Methods

### 6.1.1 General Remarks

Chemicals were purchased from Abcr, Acros, Activate Scientific, Alfa Aesar, BLDpharm, Carbolution, Fisher, Fluorochem, Iris Biotech, Sigma-Aldrich and used as received. Reactions were monitored by thin-layer chromatography (TLC) carried out on Merck Kieselgel 60 F254 plates (Merck KGaA, Darmstadt, Germany) or by analytical HPLC. Purity of all synthesized final test compounds and peptides was >95 %, as determined by HPLC analysis, unless otherwise stated.

### 6.1.2 Analytical HPLC

Analytical RP-HPLC was performed on an UltiMate 3000 HPLC system (Thermo Fisher Scientific Inc, Waltham, MA, USA) equipped with a ReproSil-XR 120 C18 column (5 µm, 120 Å, 4.6 × 150 mm, Dr. Maisch GmbH, Ammerbuch-Entringen, Germany) and a flow rate of 1 mL $min^{-1}$ using 0.01 M potassium phosphat buffer (pH 2.3) as eluent A1 and MeOH as eluent B1. Absorptions were detected at 218 nm, 254 nm and 280 nm. Chromatograms were analyzed with Chromeleon v7.2.10 (Thermo Fisher Scientific Inc, Waltham, MA, USA).

### 6.1.3 Semi-preparative HPLC

Semi-preparative purifications were performed on a PuriFlash 4250 system (Interchim, Montluçon, France) equipped with a ReproSil-XR 120 C18 column (5 µm, 120 Å, 30 × 250 mm, Dr. Maisch GmbH, Ammerbuch-Entringen, Germany) and a linear gradient elution with a mobile phase composed of eluent A2 (99.9 % (v/v) $H_2O$ and 0.1 % (v/v) TFA) and eluent B2 (80 % (v/v) ACN, 19.9 % (v/v) $H_2O$, and 0.1 % (v/v) TFA) at a flow rate of 30 mL $min^{-1}$. Absorption was detected at 218 nm. Collected fractions were lyophilized.

### 6.1.4 Flash Column Chromatography

Purifications using reversed-phase column chromatography were carried out on a PuriFlash 4250 system (Interchim, Montluçon, France) equipped with a C18 column (puriFlash® C18-HP 15 µm). Collected aqueous fractions were lyophilized. Silica gel column chromatography was performed on a PuriFlash XS520Plus system (Interchim, Montluçon, France) with silica gel 60 for column chromatography (particle size: 0.025–0.04 mm and 0.04–0.063 mm; Machery-Nagel, Düren, Germany). Organic solvents were removed under reduced pressure.

### 6.1.5 Mass Spectroscopy

Mass spectrometry measurements were performed on AmaZon SL (Bruker Corporation, Billerica, MA, USA) using positive or negative electrospray ionization (ESI) or MSD 5977 (Agilent Technologies, Inc., Santa Clara, CA, USA) using electron ionization (EI) and high-resolution mass spectrometry measurements were recorded on a maXis 4G (Bruker Corporation, Billerica, MA, USA) using positive electrospray ionization (HR-ESI-TOF) coupled with an UltiMate 3000 HPLC system (Thermo Fisher Scientific Inc, Waltham, MA, USA). GC-MS were performed with 5977B MSD / 8890 GC system (Agilent Technologies, Inc., Santa Clara, CA, USA) using electron ionization (EI). Data were analyzed using Bruker Compass DataAnalysis 4.4.

### 6.1.6 NMR Spectroscopy

NMR spectra were acquired primarily with a Bruker Avance III HDX 400 spectrometer, but also with Bruker Avance III HD 300 XWB, Bruker Avance III HDX 600 and Bruker Avance III HDX 700 spectrometers (Bruker Corporation, Billerica, MA, USA). $^{1}$H, $^{13}$C and $^{19}$F NMR spectra were reported as chemical shifts ($\delta$) in parts per million (ppm) in relation to tetramethylsilane (TMS) and were calibrated using the residual peak of the used solvent or, in case of $^{19}$F NMR spectra, using the reference peak of $C_6F_6$ (163.0 ppm) or TFA (76.0 ppm). Coupling constants ($J$) were reported in units of hertz (Hz). The following abbreviations were used to describe multiplicities: s (singlet), d (doublet), q (quartet), m (multiplet) and bs (broad singlet). NMR spectra were analyzed with MestReNova v5.3.1 (Mestrelab Research S.L., Santiago de Compostela, Spain) or TopSpin v4.0.8 (Bruker Corporation, Billerica, MA, USA).

## 6.2 Peptide Synthesis

### 6.2.1 Solid-Phase Peptide Synthesis

All peptides were synthesized with free *N*-terminus and amidated *C*-terminus by SPPS using the Fmoc strategy. The automated SPPS was carried out on a MultiSynTech Syro I peptide synthesizer (Biotage). The peptide synthesis was performed on a 50 µM scale and all reagents were dissolved in DMF. Rink amide resin (TentaGel® HL RAM, particle size: 75 µm, capacity: 0.38 mmol $g^{-1}$, Rapp Polymere, Tübingen, Germany) was used as solid support and the following purchased Fmoc-protected standard amino acids were used as building blocks for peptide synthesis: Fmoc-L-Ala-OH, Fmoc-L-Asp(O*t*-Bu)-OH, Fmoc-L-Glu(O*t*-Bu)-OH, Fmoc-L-Leu-OH, Fmoc-L-Lys(Boc)-OH, Fmoc-L-Phe-OH, Fmoc-L-Pro-OH, Fmoc-L-Ser(*t*-Bu)-OH, Fmoc-L-Thr(*t*-Bu)-OH, Fmoc-L-Trp(Boc)-OH, Fmoc-L-Tyr(*t*-Bu)-OH.

Purchased Fmoc-protected non-standard amino acid: Fmoc-L-Phe(*m*-$OCH_3$)-OH, Fmoc-L-Phe(*m*-$OCF_3$)-OH, Fmoc-L-Dab(Boc)-OH, Fmoc-L-Nle(εNH$COCH_3$)-OH (**82a**), Fmoc-L-Nle-(εNH$COCF_3$)-OH (**82c**), Fmoc-L-Nle(ε$N_3$)-OH, Fmoc-D-Pra-OH.

Synthesized Fmoc-protected non-standard amino acids: Fmoc-L-Phe(*p*-$OCF_2$Br)-OH (**80**), Fmoc-L-Phe(*m*-$OCF_2$Br)-OH (**81**), Fmoc-L-Nle(εNH$COCF_2$H)-OH (**82b**), Fmoc-L-Nle(εNH$COCF_2$Cl)-OH (**82d**), Fmoc-L-Nle(εNH$COCF_2$Br)-OH (**82e**), Fmoc-L-Abu(εNH$COCH_3$)-OH (**83a**), Fmoc-L-Abu(εNH$COCF_2$H)-OH (**83b**), Fmoc-L-Abu(εNH$COCF_3$)-OH (**83c**), Fmoc-L-Abu(εNH$COCF_2$Cl)-OH (**83d**), Fmoc-L-Abu(εNH$COCF_3$Br)-OH (**83e**) (synthesis procedures: see Section 6.3.7 on page 182).

Each cycle included three reaction steps: coupling, capping, and deprotection of the Fmoc protecting group. Each reactor was loaded with resin (132 mg, 1 eq) and swollen with DMF. The first cycle started with an additional deprotection step. The coupling was done with HBTU (4.4 eq) as coupling reagent, NMM (39 mM) as base and standard amino acid (4.5 eq) for 40 min or with non-standard amino acid (1.5 eq) for 2 h, followed by capping reaction with a solution of 5 % (v/v) acetic anhydrid and 6 % (v/v) lutidine for 15 min. The Fmoc group was removed by 40 % (v/v) piperidine for 3 min. After each coupling, capping and Fmoc deprotection, the resin was washed 6 times with DMF, and after synthesis, resins were additionally washed several times with ethanol and DCM, then dried *in vacuo*. Cleavage solution (670 mg phenol, 450 µL TIPS, 450 µL $H_2O$ in 9 mL TFA) was used to cleave the acid-labile rink amide linker and the protecting groups of the amino acid side chains by shaking for 2 h at room temperature. The resin was washed with DCM and the combined fractions were concentrated *in vacuo*. The remaining peptide solution was precipitated twice in $Et_2O$ at −80 °C and centrifuged for 15 min at 4000 × g. The peptide was dissolved in ACN and $H_2O$, then lyophilized. The lyophilized crude peptide was purified using semi-preparative HPLC (see Section 6.1.3 on page 133). The collected fractions were freeze-dried.

The molecular masses were determined by HR-ESI mass spectrometry (Bruker maXis 4G, Bruker Corporation, Billerica, MA, USA). The purity of all synthesized test peptides was >95 % as determined by analytical HPLC analysis (see Section 6.1.2 on page 133).

### 6.2.2 Triazole-Stapled Peptides: Peptide Cyclization via CuAAC

Peptide cyclization was performed using an optimized copper(I)-catalyzed alkyne-azide cycloaddition protocol (Section 3.3.5.2 on page 88). Lyophilized linear peptide, $CuSO_4 \cdot 5\,H_2O$ (1 eq), TBTA (1 eq) and $NaHCO_3$ (5 eq) were dissolved in ACN / $H_2O$ (2:1) resulting in a final peptide concentration of 8 mg $mL^{-1}$. Sodium L-ascorbate (2 eq) dissolved in $H_2O$ (1–2 mL) was added slowly. The reaction was shaken at room temperature and was completed within 30 min as shown by analytical HPLC. Triazole-stapled peptides had retention times approx. 2 min shorter then their linear precursor. The reaction mixture was purified by direct injection into a semi-preparative HPLC. If necessary, the solution was filtered with an RC syringe filter before injection.

## 6.3 Synthesis Protocols

### 6.3.1 General Procedures

Deviations from the General Procedures are noted in the respective synthesis protocols.

**General Procedure A (4d, 63 and 64)**

To a solution of an appropriate carboxylic acid (5 mmol, 1 eq) in DCM (10 mL) was added a catalytic amount of DMF (0.5 mmol, 0.1 eq) and oxalyl chloride (7.5 mmol, 2 M in DCM, 1.5 eq) at 0 °C. The reaction mixture was stirred at room temperature for 3 h, then concentrated *in vacuo*. The crude acyl chloride was added $BrCCl_3$ (15 mL), DMAP (1.25 mmol, 0.25 eq) and sodium-*N*-hydroxy-2-thiopyridone (6 mmol, 1.2 eq). The reaction mixture was refluxed at 120 °C for 2 h under argon atmosphere, then concentrated *in vacuo*. The crude product was purified by silica gel column chromatography.

**General Procedure B (5d,e, 10, 13 and 37)**

To a solution of an appropriate nitrobenzene (1 mmol, 1 eq) in EtOH (7 mL) was added $SnCl_2 \cdot 2\,H_2O$ (5 mmol, 5 eq) and conc. HCl (1 mL). The reaction mixture was stirred at room temperature for 16 h under argon atmosphere. To the reaction mixture was added sat. $NaHCO_3$ (80 mL), then extracted with EtOAc ($3 \times 40$ mL). The combined organic layers were washed with brine, dried over $Na_2SO_4$, and concentrated *in vacuo* to provide the title compound. The title compound can be used with and without purification by silica gel column chromatography.

**General Procedure C (18a–e)**

To a solution of **17a** (0.5 mmol, 1 eq) was added an appropriate amine (0.5 mmol, 1 eq or 0.55 mmol, 1.1 eq), $HOBt \cdot H_2O$ (0.55 mmol, 1.1 eq), $EDCI \cdot HCl$ (0.75 mmol, 1.5 eq), DMAP (0.05 mmol, 0.1 eq) and DIPEA (2 mmol, 4 eq) in THF (5 mL). The mixture was stirred at 45 °C for 48 h. After cooling to room temperature, $H_2O$ (50 mL) was added and the mixture was extracted with EtOAc ($3 \times 20$ mL). The combined organic layers were washed with brine, dried over $Na_2SO_4$ and concentrated *in vacuo*. The crude product was purified by silica gel column chromatography.

**General Procedure D (7a–d, 23, 24, 28, 29, 30, 32, 41, 42 and 45)**

An appropriate aniline (5 mmol, 1 eq) was dissolved in dry THF (25 mL) and the solution was cooled to 0 °C. After 10 min, NMM (5–11 mmol, 1.0–2.2 eq) followed by an appropriate acetic anhydride (5.0–7.5 mmol, 1.0–1.5 eq) in dry THF (12 mL) were added to the solution. The reaction mixture was allowed to warm up to room temperature overnight. The stirred

reaction mixture was quenched with MeOH after 18 h and the solvent was removed under reduced pressure. The crude product was dissolved in EtOAc (50 mL) and washed with 1 M HCl (3 × 30 mL), $H_2O$ (30 mL) and brine (30 mL). The organic phase was dried over $Na_2SO_4$ and the solvent was removed *in vacuo*. The crude product was purified by silica gel column chromatography or by reversed-phase chromatography.

**General Procedure E (6a–e, 12, 13 and 38)**

To a solution of an appropriate aniline (1 mmol, 1 eq) in 10 % acetic acid (12 mL) was added potassium cyanate (5 mmol, 5 eq) at 0 °C, then the reaction mixture was stirred at room temperature for 3 h. The reaction mixture was filtered off, washed with $H_2O$ and dried at 60 °C. The crude product was purified by silica gel column chromatography to provide the title compound.

**General Procedure F (20a–e)**

An appropriate THP-protected asciminib derivative **18a–e** (1 eq) was dissolved in dry DCM and TFA (40 eq) was added at 0 °C. The reaction mixture was stirred at room temperature for 4 h. After completion of the reaction, sat. aq. $NaHCO_3$ and EtOAc were added and the organic layer was washed three times with sat. aq. $NaHCO_3$, once with brine and dried over $Na_2SO_4$. The organic solvent was removed under reduced pressure and the crude product was purified by silica gel column chromatography.

**General Procedure G (20a–e)**

To a solution of **17b** (3 mmol, 1 eq) in dry DCM (15 mL) was added DMF (0.3 mmol, 0.1 eq) and oxalyl chloride (2 M in DCM, 4.5 mmol, 1.5 eq) at 0 °C. After 15 min stirring at 0 °C, the reaction mixture was stirred at room temperature for 3 h, then concentrated *in vacuo*. Dry THF (20 mL) was added to the crude acyl chloride, followed by $Et_3N$ (9 mol, 3 eq) and dropwise addition of an appropriate amine (3 mmol, 1 eq) at 0 °C. The reaction mixture was stirred at room temperature for 16 h. After completion of the reaction, the solvent was removed under reduced pressure to obtain the crude intermediate product **19a–e**. The residue was dissolved in DCM, then washed with 1 M HCl. The organic phase was concentrated *in vacuo* to 5–10 mL, TFA (9.25 mL, 40 eq) was added and the mixture was stirred at room temperature for another 3 h. The solvent was removed under reduced pressure and the residue was dissolved in EtOAc (150 mL), washed with a sat. solution of $K_2CO_3$ (2 × 50 mL) and brine (50 mL), dried over $Na_2SO_4$ and the solvent was evaporated off under reduced pressure to give a residue which was purified by silica gel column chromatography to afford the title compound.

**General Procedure H (25 and 31)**

An appropriate aniline (5 mmol, 1 eq) and **1b** (7.5 mmol, 1.5 eq) were suspended in dry DCM (35 mL) under argon atmosphere and the mixture was cooled to 0 °C. After 10 min, T3P (≥50 wt % solution in EtOAc, 7.5 mmol, 1.5 eq) and DIPEA (10 mmol, 2 eq) were added to the suspension. The reaction mixture was stirred at room temperature for 1 h, then diluted with $H_2O$ and extracted with $CHCl_3$ (3 × 40 mL). The organic phase was washed with $H_2O$ (3 × 30 mL) and brine (30 mL), dried over $Na_2SO_4$ and the solvent was removed *in vacuo*. The crude product was purified by silica gel column chromatography or by reversed-phase chromatography.

**General Procedure I (26, 35, 39, 40, 43 and 44)**

An appropriate aniline (5 mmol, 1 eq) was dissolved in dry DCM (25 mL) and the solution was cooled to 0 °C. After 10 min, $Et_3N$ (5–11 mmol, 1.0–2.2 eq) followed by an appropriate acetic anhydride (5.0–7.5 mmol, 1.0–1.5 eq) in dry DCM (12 mL) were added to the solution. The reaction mixture was allowed to warm up to room temperature overnight. The stirred reaction mixture was quenched with MeOH after 18 h and the solvent was removed under reduced pressure. The crude product was dissolved in EtOAc (50 mL) and washed with 1 M HCl (3 × 30 mL), $H_2O$ (30 mL) and brine (30 mL). The organic phase was dried over $Na_2SO_4$ and the solvent was removed *in vacuo*. The crude product was purified by silica gel column chromatography or by reversed-phase chromatography.

**General Procedure J (47 and 48)**

A stirred solution of an appropriate aldehyde (10 mmol, 1 eq) in dry DCM (50 mL) was cooled to −10 °C under argon atmosphere. DAST (12 mmol, 1.2 eq) was added dropwise. The reaction mixture was allowed to warm up overnight. After 18 h, $H_2O$ was poured to the reaction mixture. The organic phase was seperated and the aq. phase was extracted twice with EtOAc. The combined organic phases were washed with brine, dried over $Na_2SO_4$ and the solvent was removed *in vacuo*. The crude product was purified by silica gel column chromatography.

**General Procedure K (54d and 55d)**

A suspension of an appropriate carboxylic acid (5 mmol, 1 eq) and DBDMH (5 mmol, 1 eq or 15 mmol, 3 eq) in degassed $CCl_4$ (100 mL) was stirred under argon atmosphere and illuminated by a 300 W sun lamp for 3–10 d. The reaction was monitored via HPLC. After completion of reaction, the mixture was filtered, diluted with DCM and then washed with

20 % $Na_2S_2O_3$ solution (80 mL) and brine. The organic layer was dried over $Na_2SO_4$ and the solvent was removed *in vacuo*. The crude product was purified by silica gel column chromatography.

**General Procedure L (60 and 61)**

An appropriate cresol (10 mmol, 1 eq) was dissolved in dry 1,4-dioxane (30 mL) under argon atmosphere, then NaH (60 % dispersion in mineral oil; 11 mmol, 1.1 eq) was added. After 30 min stirring at room temperature, **1a** (11 mmol, 1.1 eq) was added and the mixture was stirred at 60 °C until no more cresol can be observed with TLC (approximately 5 to 6 h). The reaction mixture was cooled down to room temperature, then $Et_2O$ was added and the mixture was extracted three times with sat. $NaHCO_3$. $Et_2O$ was added to the combined aq. phases, then the biphasic mixture was acidified with conc. HCl at 0 °C to pH = 1. The mixture was extracted three times with $Et_2O$, the combined organic phases were washed with brine and dried over $Na_2SO_4$. After removing the solvent, 1,4-dioxane is still present. The purity was determined using $^1$H NMR and the crude product was used without further purification for the next synthesis step.

**General Procedure M (66–69)**

In an oven dried two-necked flask, an appropriate methylbenzene (10 mmol, 1 eq) was dissolved in dry benzene or $CCl_4$ (30 mL) under argon atmosphere, then NBS (11 mmol, 1.1 eq) and ABCN (3 mmol, 0.3 eq) were added. The suspension was refluxed for 8 h. Afterwards, the mixture was cooled down to room temperature and the solid succinimide was filtered off. The filtrate was concentrated *in vacuo* and the crude product was used without purification for the next synthesis step.

**General Procedure N (71, 72, 73 and 74)**

The crude bromomethylbenzene from General Procedure **M** (10 mmol, 1 eq), diethyl-acetamidomalonate (10 mmol, 1 eq), $K_2CO_3$ (20 mmol, 2 eq) and KI (10 mmol, 1 eq) were dissolved in dry ACN (60 mL) under argon atmosphere. The suspension was refluxed for 18 h. After that, the mixture was cooled down to room temperature and filtered. The solvent was removed *in vacuo* and the crude product was purified by silica gel column chromatography.

**General Procedure O (82b,d,e and 83a–e)**

To a suspension of an appropriate Fmoc-protected amino acid (10 mmol, 1 eq) and NMM (30 mmol, 3 eq) in dry THF (70 mL) were added dropwise the required anhydride (12 mmol, 1.2 eq) at 0 °C under argon atmosphere. The reaction mixture was stirred at 0 °C for 30 min,

then additional anhydride was added dropwise at 0 °C until the suspension became a clear solution without any precipitate and the resulting red-brown solution was stirred at room temperature for 2 h. The reaction mixture was quenched by addition of MeOH and concentrated under reduced pressure. The residue was dissolved in EtOAc and washed twice with 10 % HCl, then with $H_2O$ and brine. The solvent was removed *in vacuo* and the crude product was purified by reversed-phase column chromatography.

### 6.3.2 Reagents

**Potassium 2-bromo-2,2-difluoroacetate (1a)**

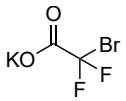


Potassium hydroxide (31.4 g, 619 mmol, 1.0 eq) was dissolved in MeOH (500 mL) at 0 °C, then ethyl bromodifluoroacetate (132 g, 650 mmol, 1.05 eq) was added. The mixture was allowed to warm up to room temperature and stirred for 72 h. The solvent was removed *in vacuo* to provide the title compound **1a** (130 g, 98.6 %) as a white solid.

ESI-MS (*m/z*): $[M-K]^-$ 173.0 / 175.0 (1:1); $^{19}$F NMR (376 MHz, DMSO-$d_6$): δ –47.77 (s, 2F).

**Potassium 2,2-difluoro-2-iodo-acetate (1b)**

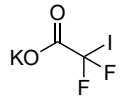


Potassium hydroxide (1.02 g, 18.2 mmol, 1.0 eq) was dissolved in MeOH (18 mL) at 0 °C, then ethyl difluoroiodoacetate (5.0 g, 20 mmol, 1.1 eq) was added. After stirring at 0 °C for 30 min, the mixture was warmed to room temperature and stirred for 48 h. The solvent was removed *in vacuo* to provide the title compound **1b** (4.17 g, 80.2 %) as a yellow solid.

ESI-MS (*m/z*): $[M-K]^-$ 220.9; $^{19}$F NMR (376 MHz, DMSO-$d_6$): δ –52.47 (s, 2F).

### 6.3.3 Fragments with Ether and Acetamide Moiety

**2,2-Difluoro-2-(4-nitrophenoxy)acetic acid (3)**

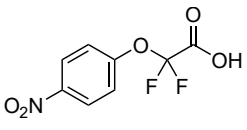


**Method A:** To a suspension of $K_2CO_3$ (10.4 g, 75.0 mmol, 2.5 eq) in a solution of 4-nitrophenol (4.17 g, 30.0 mmol, 1.0 eq) in DMF (60 mL) was slowly added ethyl bromodifluoroacetate (5.77 mL, 45.0 mmol, 1.58 g $cm^{-3}$, 1.5 eq) at room temperature. The reaction mixture was stirred at room temperature for 13 h under argon atmosphere. The reaction mixture was poured on to $H_2O$, extracted with $Et_2O$ (3 × 100 mL), dried over $Na_2SO_4$ and concentrated *in vacuo*. The crude product was purified by silica gel column chromatography (eluent: PE 40/60 / EtOAc 96:4) to provide a mixture of intermediate product **2** and **4a** (3.38 g) as a yellow oil and colorless crystalline solid. As further side product, **4d** (375 mg, 4.7 %; GC-MS (EI): $[M]^+$ 266.9 / 268.9) could be isolated as a yellow oil.

To a solution of **2** and **4a** (3.38 g) in $Et_2O$ (13 mL) was added 6 M aq. NaOH (13 mL). The reaction mixture was stirred at room temperature for 3 h before diluting with $Et_2O$. The reaction mixture was extracted with sat. $NaHCO_3$ (3 × 60 mL). The combined aq. layers were acidified to pH 1 and extracted with $Et_2O$ (3 × 60 mL), then the combined organic phases were washed with brine, dried over $Na_2SO_4$ and concentrated *in vacuo*. Products were purified by washing with *n*-pentane to provide the title compound **3** (1.05 g, 15.0 %) as a pale-yellow crystalline solid.

From the first organic phase compound **4a** could be isolated. After washing with brine, drying over $Na_2SO_4$ and concentration *in vacuo*, the side product was purified by silica gel column chromatography (eluent: PE 40/60 / EtOAc 96:4) to obtain **4a** (1.63 g, 28.8 %; GC-MS (EI; *m/z*): $[M]^+$ 189.1) as a colorless crystalline solid.

**Method B:** To a solution/suspension of 4-nitrophenol (1.0 g, 7.19 mmol, 1.0 eq) in 1,4-dioxane under argon atmosphere was added NaH (60 % dispersion in mineral oil; 316 mg, 7.91 mmol, 1.1 eq) at room temperature and stirred for 30 min. **1a** (1.68 g, 7.91 mmol, 1.1 eq) was added and the reaction mixture was stirred for 20 h at 80 °C. After completion, the reaction mixture turns from red to yellow/colorless. At room temperature EtOAc was added and the mixture was extracted with sat. $NaHCO_3$ (3 × 20 mL). To the combined aq. layers were added EtOAc and the biphasic mixture was adjusted to pH 1 with HCl. The mixture was extracted with EtOAc (3 × 20 mL). The combined organic layers were washed with brine, dried over $Na_2SO_4$ and concentrated *in vacuo* to provides the title compound **3** (185 mg, 9.5 %) as a pale-yellow crystalline solid.

ESI-MS (*m/z*): $[M-H]^-$ 232.0; $^1$H NMR (400 MHz, DMSO-$d_6$): δ 13.92 (bs, 1H), 8.35–8.27 (m, 2H), 7.49 (d, $J$ = 9.2 Hz, 2H); $^{13}$C NMR (101 MHz, DMSO-$d_6$): δ 160.0 (t, $J$ = 38.2 Hz), 154.1, 145.0, 125.9, 121.3, 114.1 (t, $J$ = 275.1 Hz); $^{19}$F NMR (376 MHz, DMSO-$d_6$): δ –77.29 (s, 2F).

**1-(Bromodifluoromethoxy)-4-nitrobenzene (4d)**

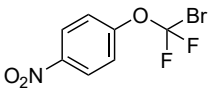


The title compound was prepared following General Procedure **A** using **3** (109 mg, 0.468 mmol, 1.0 eq), DMF (3.6 µL, 0.047 mmol, 0.95 g cm$^{-3}$, 0.1 eq) and oxalyl chloride (350 µL, 0.701 mmol, 2 M in DCM, 1.5 eq) in DCM (1.5 mL). After the first reaction step and concentration of the reaction mixture, $BrCCl_3$ (3 mL), DMAP (14.3 mg, 0.117 mmol, 0.25 eq) and sodium-*N*-hydroxy-2-thiopyridone (83.6 mg, 0.562 mmol, 1.2 eq) were added for the second reaction step. The crude product was purified by silica gel column chromatography (eluent: *n*-hexane / EtOAc 97:3) to provide the title compound **4d** (39.8 mg, 31.7 %) as a yellow oil.

GC-MS (EI) (*m/z*): $[M]^+$ 266.9 / 268.9 (1:1); $^1$H NMR (400 MHz, $CDCl_3$): δ 8.31–8.26 (m, 1H), 7.86–7.81 (m, 2H); $^{13}$C NMR (101 MHz, $CDCl_3$): δ 136.2, 135.0, 124.3, 117.8, 114.2 (t, $J$ = 329.0 Hz); $^{19}$F NMR (376 MHz, $CDCl_3$): δ –23.10 (s, 2F).

**1-(Difluoroiodomethoxy)-4-nitrobenzene (4e)**

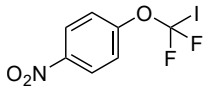


To a solution of **3** (975 mg, 4.18 mmol, 1.0 eq) in dry DCM (6 mL) was added DMF (32.3 µL, 0.418 mmol, 0.95 g cm$^{-3}$, 0.1 eq) and oxalyl chloride (3.14 mL, 2 M in DCM, 6.27 mmol, 1.5 eq) at 0 °C. The reaction mixture was stirred at room temperature for 3 h, then concentrated *in vacuo*. Dry toluene (13.0 mL), $CHI_3$ (3.29 g, 8.36 mmol, 2.0 eq), DMAP (127.7 mg, 1.05 mmol, 0.25 eq) and sodium-*N*-hydroxy-2-thiopyridone (748.5 mg, 5.02 mmol, 1.2 eq) was added to the crude acyl chloride. The reaction mixture was refluxed at 120 °C for 2 h under argon atmosphere, then concentrated *in vacuo*. The crude product was purified by silica gel column chromatography (eluent: PE 40/60 / EtOAc 97:3) to provide the title compound **4e** (357.8 mg, 27.2 %) as a pale-yellow solid.

EI-MS (*m/z*): $[M-I]^+$ 188.1, $[M-OCF_2I]^+$ 122.1; $^1$H NMR (400 MHz, $CDCl_3$): δ 8.32 (m, 2H), 7.39 (m, 2H); $^{13}$C NMR (101 MHz, $CDCl_3$): δ 156.0, 146.0, 125.8, 121.8, 84.6 (t, $J$ = 329.8 Hz); $^{19}$F NMR (376 MHz, $CDCl_3$): δ –6.33 (s, 2F).

**4-(Bromodifluoromethoxy)aniline (5d)**

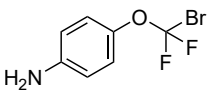

The title compound was prepared following General Procedure **B** using **4d** (380 mg, 1.42 mmol, 1.0 eq), $SnCl_2 \cdot 2\,H_2O$ (1.60 g, 7.09 mmol, 5.0 eq) in EtOH (7 mL) and conc. HCl (1 mL). The crude product was purified by silica gel column chromatography (eluent: PE 40/60 / EtOAc 75:25) to provide the title compound **5d** (281 mg, 83.3 %) as a dark-brown oil.

ESI-MS (*m/z*): $[M+H]^+$ 238.03 / 240.03 (1:1); $^1$H NMR (400 MHz, DMSO-$d_6$): δ 6.98–6.93 (m, 2H), 6.62–6.56 (m, 2H), 5.31 (s, 2H); $^{13}$C NMR (101 MHz, DMSO-$d_6$): δ 148.1, 140.3 (t, $J$ = 1.9 Hz), 122.1, 115.6 (t, $J$ = 305.1 Hz), 114.1; $^{19}$F NMR (376 MHz, DMSO-$d_6$): δ –16.00 (s, 2F).

**4-(Difluoroiodomethoxy)aniline (5e)**

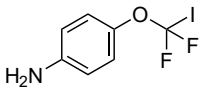

The title compound was prepared following General Procedure **B** using **4e** (225.2 mg, 0.72 mmol, 1.0 eq), $SnCl_2 \cdot 2\,H_2O$ (806.5 mg, 3.57 mmol, 5.0 eq) in EtOH (7 mL) and conc. HCl (1 mL) to provide the crude title compound (210.7 mg, 103.4 %) as yellow oil. The crude product **5e** was used without further purification.

ESI-MS (*m/z*): $[M+H]^+$ 286.13.

**1-(4-(Difluoromethoxy)phenyl)urea (6a)**

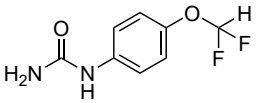

The title compound was prepared following General Procedure **E** using **5a** (390 mg, 2.45 mmol, 1.0 eq) and potassium cyanate (994 mg, 12.25 mmol, 5.0 eq) in 10 % acetic acid (20 mL). The crude product was purified by silica gel column chromatography (eluent: DCM / MeOH 94:6) to provide the title compound **6a** (789.9 mg, 79.7 %) as a white solid.

ESI-MS (*m/z*): $[M+H]^+$ 203.35; $^1$H NMR (400 MHz, DMSO-$d_6$): δ 8.59 (bs, 1H), 7.43 (m, 2H), 7.06 (d, $J$ = 1.8 Hz, 2H), 7.05 (t, $J$ = 74.6 Hz, 1H), 5.86 (bs, 2H); $^{13}$C NMR (101 MHz, DMSO-$d_6$): δ 156.1, 144.8 (t, $J$ = 3.1 Hz), 138.1, 119.7, 119.2, 119.0, 116.7 (t, $J$ = 257.4 Hz); $^{19}$F NMR (376 MHz, DMSO-$d_6$ -162.59): δ –81.52 (d, $J$ = 74.7 Hz, 2F).

**1-(4-(Trifluoromethoxy)phenyl)urea (6b)**

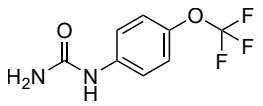

The title compound was prepared following General Procedure **E** using **5b** (381.7 µL, 1.31 g cm$^{-3}$, 2.16 mmol, 1.0 eq) and potassium cyanate (874.0 mg, 10.77 mmol, 5.0 eq) in 10 % acetic acid (15 mL). The crude product was purified by silica gel column chromatography (eluent: DCM / MeOH 98:2) to provide the title compound **6b** (448.6 mg, 94.6 %) as a white solid.

ESI-MS (*m/z*): $[M+H]^+$ 221.14; $^1$H NMR (400 MHz, DMSO-$d_6$): δ 8.73 (bs, 1H), 7.50 (m, 2H), 7.20 (d, $J$ = 8.2 Hz, 2H), 5.92 (bs, 2H); $^{13}$C NMR (101 MHz, DMSO-$d_6$): δ 155.9, 142.1 (dd, $J$ = 3.5, 1.6 Hz), 139.9, 121.5, 120.2 (dd, $J$ = 506.8, 258.1 Hz), 118.8; $^{19}$F NMR (376 MHz, DMSO-$d_6$): δ –57.25 (s, 2F).

**1-(4-(Chlorodifluoromethoxy)phenyl)urea (6c)**

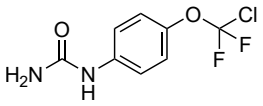

The title compound was prepared following General Procedure **E** using **5c** (113.1 mg, 0.58 mmol, 1.0 eq) and potassium cyanate (237.0 mg, 2.92 mmol, 5.0 eq) in 10 % acetic acid (10 mL). The crude product was purified by silica gel column chromatography (eluent: DCM / MeOH 97:3) to provide the title compound **6c** (103.6 mg, 75.0 %) as a white solid.

ESI-MS (*m/z*): $[M-H]^-$ 235.28 / 237.28 (3:1); $^1$H NMR (400 MHz, DMSO-$d_6$): δ 8.73 (bs, 1H), 7.49 (m, 2H), 7.20 (d, $J$ = 9.1 Hz, 2H), 5.91 (bs, 2H); $^{13}$C NMR (101 MHz, DMSO-$d_6$): δ 155.8, 143.2 (t, $J$ = 1.9 Hz), 139.9, 125.1 (t, $J$ = 286.4 Hz), 121.9, 118.7; $^{19}$F NMR (376 MHz, DMSO-$d_6$): δ –25.14 (s, 2F).

**1-(4-(Bromoodifluoromethoxy)phenyl)urea (6d)**

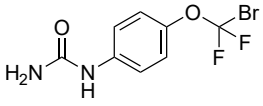

The title compound was prepared following General Procedure **E** using **5d** (177.5 mg, 0.75 mmol, 1.0 eq) and potassium cyanate (302.5 mg, 3.73 mmol, 5.0 eq) in 10 % acetic acid (10 mL). The crude product was purified by silica gel column chromatography (eluent: DCM / MeOH 96:4) to provide the title compound **6d** (125.2 mg, 59.7 %) as a white solid.

ESI-MS (*m/z*): $[M-H]^-$ 279.16 / 281.16 (1:1); $^1$H NMR (400 MHz, DMSO-$d_6$): δ 8.73 (bs, 1H), 7.50 (m, 2H), 7.18 (d, *J* = 9.0 Hz, 2H), 5.92 (bs, 2H); $^{13}$C NMR (101 MHz, DMSO-$d_6$): δ 155.9, 143.9 (t, *J* = 1.9 Hz), 139.9, 121.7, 118.7, 115.0 (t, *J* = 306.1 Hz); $^{19}$F NMR (376 MHz, DMSO-$d_6$): δ –16.30 (s, 2F).

**1-(4-(Difluoroiodomethoxy)phenyl)urea (6e)**

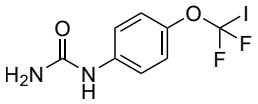

The title compound was prepared following General Procedure **E** using crude **5e** (210.7 mg, 0.72 mmol, 1.0 eq) and potassium cyanate (290.0 mg, 3.58 mmol, 5.0 eq) in 10 % acetic acid (10 mL). The crude product was purified by silica gel column chromatography (eluent: DCM / MeOH 97:3) to provide the title compound **6e** (130.1 mg, 55.5 % over 2 steps) as a white solid.

ESI-MS (*m/z*): $[M+H]^+$ 329.25; $^1$H NMR (400 MHz, DMSO-$d_6$): δ 8.71 (bs, 1H), 7.48 (m, 2H), 7.11 (d, *J* = 9.0 Hz, 2H), 5.91 (bs, 2H); $^{13}$C NMR (101 MHz, DMSO-$d_6$): δ 155.9, 145.4 (t, *J* = 2.2 Hz), 139.6, 121.7, 118.8, 89.4 (t, *J* = 324.6 Hz); $^{19}$F NMR (376 MHz, DMSO-$d_6$): δ –8.26 (s, 2F).

***N*-(Benzo[*d*][1,3]dioxol-5-yl)-2,2-difluoroacetamide (7a)**

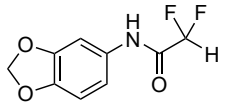

The title compound was prepared following General Procedure **D** using benzo[*d*][1,3]dioxol-5-amine (411.4 mg, 3.0 mmol, 1.0 eq) and NMM (0.33 mL, 3.0 mmol, 1.0 eq) in 10 mL dry THF followed by addition of 2,2-difluoroacetic anhydride (1.4 mL, 3.3 mmol, 1.1 eq) in 10 mL dry THF. The crude product was purified by silica gel column chromatography (eluent: DCM / MeOH 98:2) to provide the title compound **7a** (456.2 mg, 70.7 %).

ESI-MS (*m/z*): $[M+Na]^+$ 237.98; $^1$H NMR (400 MHz, $CDCl_3$): δ 7.87 (bs, 1H), 7.24 (d, *J* = 2.1 Hz, 1H), 6.88 (dd, *J* = 8.3, 2.2 Hz, 1H), 6.77 (d, *J* = 8.3 Hz, 1H), 6.00 (t, *J* = 54.4 Hz, 1H), 5.98 (s, 2H); $^{13}$C NMR (101 MHz, $CDCl_3$): δ 160.3 (t, *J* = 24.3 Hz), 148.2, 145.6, 129.8, 113.9, 108.7 (t, *J* = 254.0 Hz), 108.4, 103.0, 101.7; $^{19}$F NMR (376 MHz, $CDCl_3$): δ –126.86 (dd, *J* = 54.4, 2.4 Hz, 2F).

**_N_-(Benzo[_d_][1,3]dioxol-5-yl)-2,2,2-trifluoroacetamide (7b)**

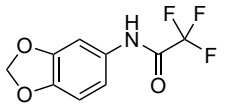

The title compound was prepared following General Procedure **D** using benzo[*d*][1,3]dioxol-5-amine (500 mg, 3.65 mmol, 1.0 eq) and NMM (0.41 mL, 3.65 mmol, 1.0 eq) in 20 mL dry THF followed by addition of 2,2,2-trifluoroacetic anhydride (1.11 mL, 4.01 mmol, 1.1 eq) in 15 mL dry THF. The crude product was purified by silica gel column chromatography (eluent: DCM) to provide the title compound **7b** (626.5 mg, 73.7 %).

ESI-MS (*m/z*): $[M+Na]^+$ 255.98; $^1$H NMR (400 MHz, $CDCl_3$): δ 7.86 (s, 1H), 7.21 (d, *J* = 2.2 Hz, 1H), 6.88 (dd, *J* = 8.3, 2.2 Hz, 1H), 6.79 (d, *J* = 8.3 Hz, 1H), 5.99 (s, 2H); $^{13}$C NMR (101 MHz, $CDCl_3$): δ 154.9 (dd, *J* = 74.2, 36.9 Hz), 148.3, 146.1, 129.1, 115.9 (q, *J* = 288.5 Hz), 114.3, 108.5, 103.1, 101.9; $^{19}$F NMR (376 MHz, $CDCl_3$): δ –76.94 (d, *J* = 1.0 Hz, 3F).

**_N_-(Benzo[_d_][1,3]dioxol-5-yl)-2-chloro-2,2-difluoroacetamide (7c)**

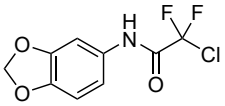

The title compound was prepared following General Procedure **D** using benzo[*d*][1,3]dioxol-5-amine (822.8 mg, 6.0 mmol, 1.0 eq) and NMM (0.66 mL, 6.0 mmol, 1.0 eq) in 20 mL dry THF followed by addition of 2-chloro-2,2-difluoroacetic anhydride (2.8 mL, 6.6 mmol, 1.1 eq) in 15 mL dry THF. The crude product was purified by silica gel column chromatography (eluent: DCM) to provide the title compound **7c** (1.03 g, 69.0 %).

ESI-MS (*m/z*): $[M-H]^-$ 248.08; $^1$H NMR (400 MHz, $CDCl_3$): δ 7.81 (bs, 1H), 7.22 (d, *J* = 2.2 Hz, 1H), 6.89 (dd, *J* = 8.3, 2.2 Hz, 1H), 6.79 (d, *J* = 8.3 Hz, 1H), 5.99 (s, 2H); $^{13}$C NMR (101 MHz, $CDCl_3$): δ 156.9 (t, *J* = 29.9 Hz), 148.3, 146.0, 129.4, 119.2 (t, *J* = 303.1 Hz), 114.2, 108.4, 103.1, 101.8; $^{19}$F NMR (376 MHz, $CDCl_3$): δ –63.97 (s, 2F).

**_N_-(Benzo[_d_][1,3]dioxol-5-yl)-2-bromo-2,2-difluoroacetamide (7d)**

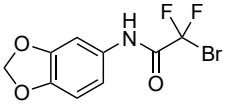

The title compound was prepared following General Procedure **D** using benzo[*d*][1,3]dioxol-5-amine (822.8 mg, 6.0 mmol, 1.0 eq) and NMM (0.66 mL, 6.0 mmol, 1.0 eq) in 20 mL dry THF followed by addition of 2-bromo-2,2-difluoroacetic anhydride (3.6 mL, 6.6 mmol, 1.1 eq) in 15 mL dry THF. The crude product was purified by silica gel column chromatography (eluent: DCM) to provide the title compound **7d** (1.38 g, 78.0 %).

ESI-MS (*m/z*): $[M-H]^-$ 316.01 / 318.01; $^1$H NMR (400 MHz, $CDCl_3$): δ 7.76 (bs, 1H), 7.22 (d, *J* = 2.1 Hz, 1H), 6.89 (dd, *J* = 8.3, 2.1 Hz, 1H), 6.79 (d, *J* = 8.3 Hz, 1H), 5.99 (s, 2H); $^{13}$C NMR (101 MHz, $CDCl_3$): δ 157.5 (t, *J* = 27.8 Hz), 148.3, 145.9, 129.4, 114.1, 111.7 (t, *J* = 317.3 Hz), 108.4, 103.0, 101.8; $^{19}$F NMR (376 MHz, $CDCl_3$): δ –60.47 (s, 2F).

**_N_-(Benzo[_d_][1,3]dioxol-5-yl)-2,2-difluoro-2-iodoacetamide (7e)**

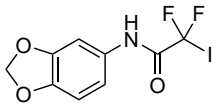

**Method A:** Benzo[*d*][1,3]dioxol-5-amine (274 mg, 2 mmol, 1 eq), **1b** (520 mg, 2 mmol, 1 eq), EDCI (575 mg, 3 mmol, 1.5 eq), HOBt · $H_2O$ (337 mg, 2.2 mmol, 1.1 eq), DMAP (25 mg, 0.2 mmol, 0.1 eq) and DIPEA (1.37 mL, 8 mmol, 0.76 g cm$^{-3}$, 4 eq) were dissolved in dry THF (40 mL) under argon atmosphere. The reaction mixture was stirred for 24 h. Afterwards, the reaction was quenched with MeOH and the solvent was removed under reduced pressure. The crude product was dissolved in EtOAc (50 mL) and washed with 1 M HCl (3 × 30 mL), $H_2O$ (30 mL) and Brine (30 mL). The organic phase was dried over $Na_2SO_4$ and the solvent was removed *in vacuo*. The crude product was purified by silica gel column chromatography (eluent: DCM) to provide the title compound **7e** (136.4 mg, 20.0 %).

**Method B:** Benzo[*d*][1,3]dioxol-5-amine (500 mg, 3.65 mmol, 1.0 eq) and **1b** (1.90 g, 7.29 mmol, 2 eq) were dissolved in dry DMF (10 mL) under argon atmosphere and the mixture was cooled to 0 °C. After 10 min, T3P (≥50 wt % solution in EtOAc, 3,26 mL, 5.47 mmol, 1.5 eq) and DIPEA (1.91 mL, 10.9 mmol, 3 eq) were added to the solution. The reaction mixture was stirred at room temperature for 5 h, then diluted with sat. $NaHCO_3$ and extracted with EtOAc (3 × 40 mL). The organic phase was washed with $H_2O$ (3 × 30 mL) and brine (30 mL), dried over $Na_2SO_4$ and the solvent was removed *in vacuo*. The crude product was purified by silica gel column chromatography (eluent: DCM) to provide the title compound **7e** (296.9 mg, 23.9 %).

ESI-MS (*m/z*): $[M+Na]^+$ 363.86; $^1$H NMR (400 MHz, $CDCl_3$): δ 7.69 (bs, 1H), 7.23 (d, *J* = 2.1 Hz, 1H), 6.88 (dd, *J* = 8.4, 2.2 Hz, 1H), 6.79 (d, *J* = 8.3 Hz, 1H), 5.99 (s, 2H); $^{13}$C NMR (101 MHz, $CDCl_3$): δ 158.8 (t, *J* = 24.7 Hz), 148.3, 145.9, 129.4, 114.1, 108.5, 103.0, 101.8, 90.76 (t, *J* = 324.6 Hz); $^{19}$F NMR (376 MHz, $CDCl_3$): δ –57.99 (d, *J* = 2.0 Hz, 2F).

**(Bromodifluoromethyl)(4-nitrophenyl)sulfane (8)**

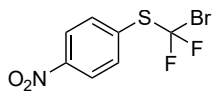


To a solution of 1,2-bis(4-nitrophenyl)disulfane (3.08 g, 10.0 mmol, 1.0 eq) in DMF (200 mL) and $H_2O$ (10 mL) were added $Na_2HPO_4$ (2.12 g, 15.0 mmol, 1.5 eq) and $Na_2S_2O_4$ (82.5 % pure, 3.17 g, 15.0 mmol, 1.5 eq) dissolved in $H_2O$ (40 mL) at 0 °C, then $CF_2Br_2$ (2.75 mL, 30.0 mmol, 2.31 g $cm^{-3}$, 3.0 eq) was added. The reaction mixture was allowed to warm up to room temperature and stirred for 18 h. $H_2O$ (400 mL) was poured to the reaction mixture and extracted with EtOAc (3 × 150 mL). The combined organic phases were washed with $H_2O$ (100 mL) and brine (100 mL), dried over $Na_2SO_4$ and the solvent was removed *in vacuo*. The crude product was purified by silica gel column chromatography (eluent: DCM) and by reversed-phase column chromatography (C18, eluent: $H_2O$ / ACN) to provide the title compound **8** (1.32 g, 46.4 %) as pale-yellow crystals.

EI-MS (*m/z*): $[M+H]^+$ 283.0 / 285.0; $^1$H NMR (400 MHz, $CDCl_3$): δ 8.31–8.23 (m, 2H), 7.86–7.78 (m, 2H); $^{13}$C NMR (101 MHz, $CDCl_3$): δ 149.4, 136.4, 135.1, 124.5, 124.3, 117.9 (t, $J$ = 339.1 Hz); $^{19}$F NMR (376 MHz, $CDCl_3$): δ –23.10 (s, 2F).

**4,4'-Disulfanediyldianiline (9)**

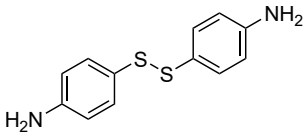


4-Aminothiophenol (626.0 mg, 5.00 mmol, 1.0 eq) and DMSO (177.6 µL, 2.50 mmol, 0.5 eq) were stirred at room temperature for 24 h. After completion of the reaction, DMS was removed *in vacuo* and EtOH (1.25 mL) was added to the residue. The mixture was stirred at 0 °C for 30 min, then the precipitate was filtered and washed with cold EtOH. The crude product **9** (304 mg, 49.0 %) was used without further purification.

ESI-MS (*m/z*): $[M+H]^+$ 249.10; $^1$H NMR (400 MHz, DMSO-$d_6$): δ 7.17–6.95 (m, 4H), 6.61–6.39 (m, 4H), 5.57–5.39 (bs, 4H); $^{13}$C NMR (101 MHz, DMSO-$d_6$): δ 150.0, 134.4, 120.8, 114.2.

**4-((Bromodifluoromethyl)thio)aniline (10)**

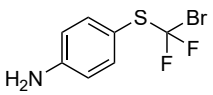

**Method A:** To a solution of 4,4'-disulfanediyldianiline **9** (1.24 g, 5.0 mmol, 1.0 eq) in DMF (75 mL) and $H_2O$ (5 mL) were added $Na_2HPO_4$ (1.06 g, 7.5 mmol, 1.5 eq) and $Na_2S_2O_4$ (82.5 % pure, 1.58 g, 7.5 mmol, 1.5 eq) dissolved in $H_2O$ (20 mL) at 0 °C, then $CF_2Br_2$ (1.37 mL, 15.0 mmol, 2.31 g cm$^{-3}$, 3.0 eq) was added. The reaction mixture was allowed to warm up to room temperature and stirred for 18 h. $H_2O$ (200 mL) was poured to the reaction mixture and extracted with EtOAc (3 × 100 mL). The combined organic phases were washed with $H_2O$ (100 mL) and brine (100 mL), dried over $Na_2SO_4$ and the solvent was removed *in vacuo*. The crude product was purified by silica gel column chromatography (eluent: *n*-hexane / EtOAc 80:20) to provide the title compound **10** (657 mg, 51.7 %) as a pale-yellow solid.

**Method B:** The title compound was prepared following General Procedure **B** using **8** (150 mg, 0.528 mmol, 1.0 eq), $SnCl_2 \cdot 2\,H_2O$ (596 g, 2.64 mmol, 5.0 eq) in EtOH (7 mL) and conc. HCl (1 mL). The crude product was purified by silica gel column chromatography (eluent: DCM / *n*-hexane 85:15) to provide the title compound **10** (106 mg, 79.3 %) as a pale-yellow solid.

ESI-MS (*m/z*): $[M+H]^+$ 253.93 / 255.93 (1:1); $^1$H NMR (400 MHz, $CDCl_3$): δ 7.44–7.38 (m, 2H), 6.69–6.63 (m, 2H), 3.95 (bs, 2H); $^{13}$C NMR (101 MHz, $CDCl_3$): δ 149.4, 138.5, 120.5 (t, $J$ = 338.3 Hz), 115.4, 114.6; $^{19}$F NMR (376 MHz, $CDCl_3$): δ –24.60 (s, 2F).

**1-((Bromodifluoromethyl)sulfonyl)-4-nitrobenzene (11)**

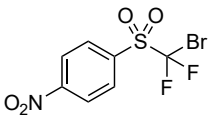

To a solution of **8** (100 mg, 0.352 mmol, 1.0 eq) in dry DCM (5 mL) was added mCPBA (260 mg, 1.06 mmol, 3.0 eq) at 0 °C. The reaction mixture was stirred at room temperature for 18 h, then the solvent was evaporated off *in vacuo*. The residue was dissolved in EtOAc (40 mL), washed with 10 % aq. NaOH (3 × 10 mL), brine (10 mL), dried over $Na_2SO_4$ and the solvent was concentrated *in vacuo*. The crude product was purified by silica gel column chromatography (eluent: *n*-hexane / EtOAc 95:5) to provide the title compound **11** (101.9 mg, 91.6 %) as a white crystalline solid.

EI-MS (*m/z*): $[M-CF_2Br]^+$ 186.0, $[CF_2Br]^+$ 128.9 / 130.9 (1:1); $^1$H NMR (400 MHz, $CDCl_3$): δ 8.53–8.44 (m, 2H), 8.30–8.21 (m, 2H); $^{13}$C NMR (101 MHz, $CDCl_3$): δ 152.5, 136.1, 133.0, 124.9, 124.5 (d, $J$ = 84.4 Hz), 120.6 (t, $J$ = 348.5 Hz); $^{19}$F NMR (376 MHz, $CDCl_3$): δ –58.68 (s, 2F).

**1-(4-((Bromodifluoromethyl)thio)phenyl)urea (12)**

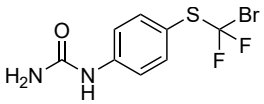

The title compound was prepared following General Procedure **E** using **10** (35.3 mg, 0.139 mmol, 1.0 eq) and potassium cyanate (56.3 mg, 0.695 mmol, 5.0 eq) in 10 % acetic acid (3 mL) to provide the title compound **12** (1.5 mg, 3.6 %) as a white solid.

ESI-MS (*m/z*): $[M+H]^+$ 296.82 / 298.81 (1:1); $^1$H NMR (400 MHz, DMSO-$d_6$): δ 8.92 (s, 1H), 7.60–7.48 (m, 4H), 6.03 (s, 2H); $^{13}$C NMR (101 MHz, DMSO-$d_6$): 155.6, 143.9, 137.3, 119.7 (t, $J$ = 336.0 Hz), 118.2, 116.4; $^{19}$F NMR (376 MHz, DMSO-$d_6$): δ –24.59 (s, 2F).

**1-(4-((Bromodifluoromethyl)sulfonyl)phenyl)urea (13)**

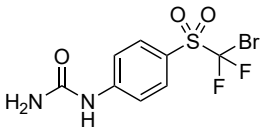

The title compound was prepared first following General Procedure **B** using **8** (117.6 mg, 0.372 mmol, 1.0 eq), $SnCl_2 \cdot 2\,H_2O$ (420 mg, 1.86 mmol, 5.0 eq) in EtOH (8 mL) and conc. HCl (1 mL). The crude product was used without further purification for second reaction step following General Procedure **E** using potassium cyanate (874.0 mg, 10.77 mmol, 50 eq) in 25 % acetic acid (12 mL). The crude product was purified by silica gel column chromatography (eluent: DCM / MeOH 98:2) to provide the title compound **13** (28.9 mg, 23.6 %) as a resinous yellow solid.

ESI-MS (*m/z*): $[M+H]^+$ 326.99 / 328.99 (1:1); $^1$H NMR (400 MHz, DMSO-$d_6$): δ 9.43 (s, 1H), 7.88 (d, $J$ = 9.0 Hz, 2H), 7.83–7.74 (m, 2H), 6.27 (s, 2H); $^{13}$C NMR (101 MHz, DMSO-$d_6$): δ 155.2, 148.8, 132.7, 120.6 (t, $J$ = 345.0 Hz), 118.1, 117.7; $^{19}$F NMR (376 MHz, DMSO-$d_6$): δ –60.54 (s, 2F).

### 6.3.4 Asciminib Derivatives

**Methyl (*R*)-5-bromo-6-(3-hydroxypyrrolidin-1-yl)nicotinate (15)**

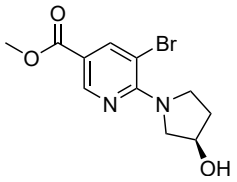


DIPEA (2.78 mL, 16.0 mmol, 0.76 g $cm^{-3}$, 4.0 eq) was added to a solution of methyl 5-bromo-6-chloronicotinate (**14**) (1.0 g, 3.99 mmol, 1.0 eq) and (*R*)-pyrrolidin-3-ol hydrochloride (641 mg, 5.19 mmol, 1.3 eq) in 25 mL isopropyl alcohol and the reaction mixture was stirred at 70 °C for 14 h. After cooling at room temperature, the solvent was evaporated off under reduced pressure and the residue was dissolved in EtOAc. The organic phase was washed with $H_2O$ and brine, dried over $Na_2SO_4$ and the solvent was concentrated *in vacuo*. The crude product was purified by silica gel column chromatography (eluent: PE 40/60 and EtOAc 50:50) to provide the title compound **15** (1.15 g, 96.0 %) as a yellow oil.

ESI-MS (*m/z*): $[M+H]^+$ 301.27 / 303.27 (1:1); $^1$H NMR (400 MHz, DMSO-$d_6$): δ 8.55 (d, *J* = 1.9 Hz, 1H), 8.10 (d, *J* = 1.9 Hz, 1H), 4.99 (d, *J* = 3.3 Hz, 1H), 4.34 (bs, 1H), 3.89–3.82 (m, 2H), 3.79 (s, 3H), 3.75–3.69 (m, 2H), 3.58 (d, *J* = 11.7 Hz, 1H), 1.97–1.83 (m, 2H); $^{13}$C NMR (101 MHz, DMSO-$d_6$): δ 164.4, 156.5, 148.0, 142.7, 115.4, 101.1, 68.8, 58.5, 51.8, 48.1, 33.1.

**Methyl 6-((*R*)-3-hydroxypyrrolidin-1-yl)-5-(1-(tetrahydro-2*H*-pyran-2-yl)-1*H*-pyrazol-5-yl)nicotinate (16a)**

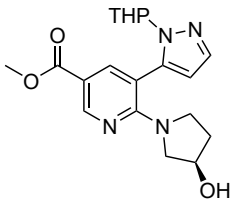


**Preparation of 16a for Synthesis of 16b:** A mixture of **15** (5.60 g, 18.7 mmol, 1.0 eq), 1-(tetrahydro-2*H*-pyran-2-yl)-1*H*-pyrazole-5-boronic acid pinacol ester (6.75 g, 24.3 mmol, 1.3 eq), $K_3PO_4$ (11.9 g, 56.0 mmol, 3.0 eq), $Pd(PPh_3)_2Cl_2$ (655 mg, 0.933 mmol, 0.05 eq) in toluene (125 mL) was stirred at 95 °C for 16 h. Additional 1-(tetrahydro-2*H*-pyran-2-yl)-1*H*-pyrazole-5-boronic acid pinacol ester (2.60 g, 9.33 mmol, 0.5 eq), $K_3PO_4$ (3.96 g, 18.7 mmol, 1.0 eq), $Pd(PPh_3)_2Cl_2$ (131 mg, 0.187 mmol, 0.01 eq) were added and the reaction mixture was stirred for further 20 h at 95 °C. After cooling the mixture to room temperature, the solution was washed with $H_2O$ (100 mL), 5 % $NaHCO_3$ solution (100 mL), brine (100 mL) and the solvent was evaporated off under reduced pressure. The crude product was purified by silica gel column chromatography (eluent: PE 40/60 and EtOAc) to provide the title compound **16a** (5.51 g, 79.3 %).

**Preparation of 16a for Synthesis of 17a:** A mixture of **15** (2.90 g, 9.67 mmol, 1.0 eq), 1-(tetrahydro-2*H*-pyran-2-yl)-1*H*-pyrazole-5-boronic acid pinacol ester (3.50 g, 12.6 mmol, 1.3 eq), $K_3PO_4$ (6.16 g, 29.0 mmol, 3.0 eq), $Pd(PPh_3)_2Cl_2$ (339 mg, 0.483 mmol, 0.05 eq) in toluene (55 mL) was stirred for 22 h at 95 °C. After cooling the mixture to room temperature, the solution was washed with $H_2O$ (10 mL), 5 % $NaHCO_3$ solution (10 mL) and the solvent was evaporated off under reduced pressure to give a residue **16a** which was used without further purifications in the next step.

ESI-MS (*m/z*): $[M+H]^+$ 373.40; $^1$H NMR (400 MHz, DMSO-$d_6$): δ 8.70 (t, *J* = 2.1 Hz, 1H), 7.85 (br. s, 1H), 7.58 (d, *J* = 1.6 Hz, 1H), 6.36 (br. s, 1H), 5.04 (d, *J* = 8.7 Hz, 1H), 4.86 (dd, *J* = 17.9, 3.0 Hz, 1H), 4.24–4.11 (m, 1H), 3.94–3.74 (m, 1H), 3.78 (s, 3H), 3.49–3.06 (m, 5H), 2.37–2.20 (m, 1H), 1.93 (dd, *J* = 18.5, 14.9 Hz, 1H), 1.75 (ddd, *J* = 17.6, 15.0, 9.4 Hz, 3H), 1.63–1.38 (m, 3H); $^{13}$C NMR (101 MHz, DMSO-$d_6$): δ 165.3 (d, *J* = 1.2 Hz), 157.5 (d, *J* = 4.2 Hz), 150.3, 141.0 (d, *J* = 4.5 Hz), 140.2, 138.7, 112.8, 108.7, 107.8, 83.8, 68.6 (d, *J* = 23.4 Hz), 66.6, 55.7 (d, *J* = 169.1 Hz), 51.6, 46.6 (d, *J* = 40.7 Hz), 32.9 (d, *J* = 24.7 Hz), 28.9, 24.6, 22.1 (d, *J* = 7.2 Hz).

**Methyl 5-(1-(tetrahydro-2*H*-pyran-2-yl)-1*H*-pyrazol-5-yl)-6-((3*R*)-3-((tetrahydro-2*H*-pyran-2-yl)oxy)pyrrolidin-1-yl)nicotinate (16b)**

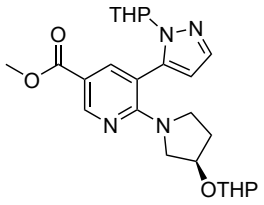


DHP (6.69 mL, 74.0 mmol, 5.0 eq) and PTSA·$H_2O$ (141 mg, 0.737 mmol, 0.05 eq) were added to a solution of **16a** (5.51 g, 14.8 mmol, 1.0 eq) in dry DCM (30 mL) and stirred at 40 °C for 48 h. The reaction mixture was washed with sat. $NaHCO_3$ (10 mL), $H_2O$ (10 mL) and brine (10 mL), dried over $Na_2SO_4$ and the solvent was concentrated *in vacuo*. The crude product was purified by silica gel column chromatography (eluent: PE 40/60 / EtOAc 50:50 to 40:60) to provide the title compound **16b** (5.95 g, 88.1 %) as a yellow foam.

ESI-MS (*m/z*): $[M+H]^+$ 457.21; $^1$H NMR (700 MHz, DMSO-$d_6$): δ 8.75–8.60 (m, 1H), 7.99–7.54 (m, 2H), 6.55–6.37 (m, 1H), 4.76–4.53 (m, 1H), 4.32–4.20 (m, 1H), 3.97–3.84 (m, 1H), 3.79 (s, 3H), 3.77–3.56 (m, 2H), 3.44–3.10 (m, 5H), 2.16–2.06 (m, 1H), 1.97–41.79 (m, 4H), 1.72–21.60 (m, 2H), 1.60–1.31 (m, 8H); $^{13}$C NMR (176 MHz, DMSO-$d_6$): δ 165.4, 157.4, 149.0, 139.9, 129.7, 113.2, 113.1, 106.9, 97.1, 86.7, 83.8, 74.6, 66.8, 61.8, 55.0, 51.6, 47.1, 31.4, 30.5, 29.8, 24.9, 24.6, 22.0, 19.3.

**6-((*R*)-3-Hydroxypyrrolidin-1-yl)-5-(1-(tetrahydro-2*H*-pyran-2-yl)-1*H*-pyrazol-5-yl)nicotinic acid (17a)**

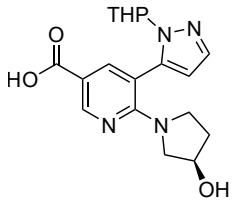


To a solution of crude **16a** (9.67 mmol, 1.0 eq) in MeOH (18 mL) was added NaOH (619 mg, 15.5 mmol, 1.6 eq) in $H_2O$ (6 mL). The reaction mixture was stirred for 19 h at room temperature. The organic solvent was removed under reduced pressure. The resulting aqueous residue was diluted with brine (20 mL) and washed with $Et_2O$ (2 × 20 mL). The combined organic layers were reextracted once with $H_2O$. The combined aqueous layers were cooled to 0 °C, $Et_2O$ (80 mL) was added, the pH was adjusted with 10 % HCl to 4.0 – 4.5 and the aqueous phase was extracted three times with $Et_2O$. The three last extracted organic layers were combined, dried over $Na_2SO_4$ and the solvent was removed *in vacuo* to provide the title compound **17a** (2.65 g, 76.5 % over 2 steps) as a pale-yellow foam.

ESI-MS (*m/z*): $[M+H]^+$ 359.36; $^1$H NMR (400 MHz, $CDCl_3$): δ 8.87–8.83 (m, 1H), 7.90 (s, 1H), 7.62 (d, *J* = 1.7 Hz, 1H), 6.83 (bs, 1H), 6.31 (s, 1H), 5.08–4.78 (m, 1H), 4.38 (s, 1H), 3.99 (dd, *J* = 38.6, 9.9 Hz, 1H), 3.60–3.13 (m, 5H), 2.56–2.27 (m, 1H), 2.06–1.42 (m, 8H); $^{13}$C NMR (101 MHz, $CDCl_3$): δ 170.3, 158.4, 152.1, 142.4, 140.8, 139.9, 113.5, 108.8, 108.2, 84.6, 70.6, 68.3, 57.0, 46.8, 33.6, 30.1, 24.9, 22.9.

**5-(1-(Tetrahydro-2*H*-pyran-2-yl)-1*H*-pyrazol-5-yl)-6-((3*R*)-3-((tetrahydro-2*H*-pyran-2-yl)oxy)pyrrolidin-1-yl)nicotinic acid (17b)**

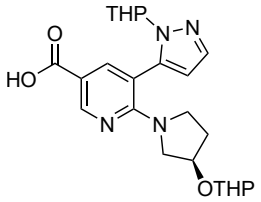


To a solution of crude **16b** (5.56 g, 12.2 mmol, 1.0 eq) in MeOH (11 mL) was added NaOH (779 mg, 19.5 mmol, 1.6 eq) in $H_2O$ (7.5 mL). The reaction mixture was stirred for 16 h at room temperature. The organic solvent was removed under reduced pressure. The resulting aqueous residue was diluted with brine (20 mL) and washed with $Et_2O$ (2 × 20 mL). The combined organic layers were reextracted with $H_2O$ (20 mL). The combined aqueous layers were cooled to 0 °C, $Et_2O$ (80 mL) was added, the pH was adjusted with 10 % HCl to 4.0 – 4.5 and the aqueous phase was extracted three times with $Et_2O$. The three last extracted organic layers were combined, washed with brine, dried over $Na_2SO_4$ and the solvent was removed *in vacuo* to provide the title compound **17b** (5.25 g, 97.4 %) as a white foam.

ESI-MS (*m/z*): $[M+H]^+$ 443.19; $^1$H NMR (700 MHz, DMSO-$d_6$): δ 12.56 (s, 1H), 8.78–8.56 (m, 1H), 8.01–7.46 (m, 2H), 6.50–6.37 (m, 1H), 4.77–4.51 (m, 1H), 4.32–4.17 (m, 1H), 4.01–3.56 (m, 3H), 3.47–3.13 (m, 6H), 2.35–2.03 (m, 1H), 2.03–1.74 (m, 4H), 1.74–1.58 (m, 2H), 1.58–1.28 (m, 8H); $^{13}$C NMR (176 MHz, DMSO-$d_6$): δ 166.5, 157.4, 149.18, 140.30, 129.7, 114.2, 113.1, 106.9, 97.1, 86.6, 83.8, 74.6, 66.8, 61.8, 55.0, 47.1, 31.4, 30.5, 29.8, 25.0, 24.6, 22.0, 19.2.

**_N_-(4-(Difluoromethoxy)phenyl)-6-((_R_)-3-hydroxypyrrolidin-1-yl)-5-(1-(tetrahydro-2_H_-pyran-2-yl)-1_H_-pyrazol-5-yl)nicotinamide (18a)**

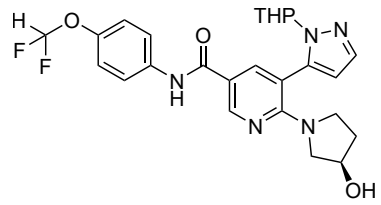


The title compound was prepared following General Procedure **C** using **17a** (200.0 mg, 0.558 mmol, 1.0 eq), **5a** (76.0 µL, 0.614 mmol, 1.29 g cm$^{-3}$, 1.1 eq), HOBt·$H_2O$ (94.0 mg, 0.614 mmol, 1.1 eq), EDCI·HCl (161 mg, 0.837 mmol, 1.5 eq), DMAP (6.8 mg, 0.056 mmol, 0.1 eq) and DIPEA (389 µL, 2.23 mmol, 0.76 g cm$^{-3}$, 4.0 eq) in THF (6 mL). The crude product was purified by silica gel column chromatography (eluent: DCM / MeOH 99:03 to 98:05) to provide the title compound **18a** (185.6 mg, 66.6 %) as a yellow solid.

ESI-MS (*m/z*): $[M+H]^+$ 500.48; $^1$H NMR (400 MHz, DMSO-$d_6$): δ 10.09 (s, 1H), 8.81 (t, *J* = 2.5 Hz, 1H), 8.02 (s, 1H), 7.78 (d, *J* = 8.8 Hz, 2H), 7.61 (d, *J* = 1.4 Hz, 1H), 7.16 (t, *J* = 74.3 Hz, 1H), 7.16 (d, *J* = 8.9 Hz, 2H), 6.41 (d, *J* = 14.1 Hz, 1H), 5.05 (s, 1H), 4.85 (dd, *J* = 6.2, 3.3 Hz, 1H), 4.19 (dd, *J* = 7.1, 3.4 1Hz, 1H), 3.83 (dd, *J* = 34.4, 10.7 Hz, 1H), 3.51–3.37 (m, 1H), 3.40–3.06 (m, 4H), 2.30 (dt, *J* = 13.0, 6.8 Hz, 1H), 1.99–1.66 (m, 4H), 1.63–1.36 (m, 3H); $^{13}$C NMR (101 MHz, DMSO-$d_6$): δ 163.6, 157.0, 149.0, 146.4, 140.7, 139.8, 138.7, 136.6, 121.7, 121.6, 119.3, 116.5 (t, *J* = 257.6 Hz), 108.7, 108.5, 83.8, 68.7, 66.7, 56.6, 46.5, 33.0, 29.0, 24.6, 22.1; $^{19}$F NMR (376 MHz, DMSO-$d_6$): δ –81.46 (dd, *J* = 74.3, 1.7 Hz, 2F).

**6-((_R_)-3-Hydroxypyrrolidin-1-yl)-5-(1-(tetrahydro-2_H_-pyran-2-yl)-1_H_-pyrazol-5-yl)-_N_-(4-(tri-fluoromethoxy)phenyl)nicotinamide (18b)**

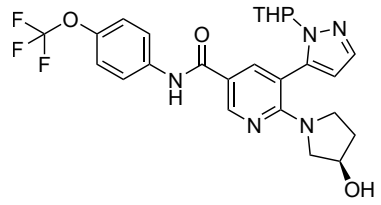


The title compound was prepared following General Procedure **C** using **17a** (200.0 mg, 0.558 mmol, 1.0 eq), **5b** (83.0 µL, 0.614 mmol, 1.31 g cm$^{-3}$, 1.1 eq), HOBt·$H_2O$ (94.0 mg, 0.614 mmol, 1.1 eq), EDCI·HCl (161 mg, 0.837 mmol, 1.5 eq), DMAP (6.8 mg, 0.056 mmol, 0.1 eq) and DIPEA (389 µL, 2.23 mmol, 0.76 g cm$^{-3}$, 4.0 eq) in THF (6 mL). The crude product was purified by silica

gel column chromatography (eluent: DCM / MeOH 99:03 to 98:05) to provide the title compound **18b** (134.3 mg, 46.5 %) as a yellow solid.

ESI-MS (*m/z*): $[M+H]^+$ 518.47; $^1$H NMR (400 MHz, DMSO-$d_6$): δ 10.19 (s, 1H), 8.92–8.78 (m, 1H), 8.03 (s, 1H), 7.86 (d, *J* = 8.8 Hz, 2H), 7.61 (d, *J* = 1.4 Hz, 1H), 7.33 (d, *J* = 8.7 Hz, 2H), 6.52–6.27 (m, 1H), 5.05 (bs, 1H), 4.92–4.77 (m, 1H), 4.20 (dd, *J* = 7.6, 3.7 Hz, 1H), 3.84 (dd, *J* = 32.8, 8.9 Hz, 1H), 3.56–3.04 (m, 5H), 2.40–2.19 (m, 1H), 2.02–1.62 (m, 4H), 1.62–1.28 (m, 3H); $^{13}$C NMR (101 MHz, DMSO-$d_6$): δ 164.2, 157.5, 149.6, 144.1, 141.1, 140.3, 139.1, 139.0, 122.0, 122.0, 121.9, 119.4, 109.1, 109.0, 84.3, 69.2, 67.2, 57.1, 46.9, 33.5, 29.5, 25.0, 22.6; $^{19}$F NMR (376 MHz, DMSO-$d_6$): δ –57.04 (s, 3F).

**_N_-(4-(Chlorodifluoromethoxy)phenyl)-6-((_R_)-3-hydroxypyrrolidin-1-yl)-5-(1-(tetrahydro-2_H_-pyran-2-yl)-1_H_-pyrazol-5-yl)nicotinamide (18c)**

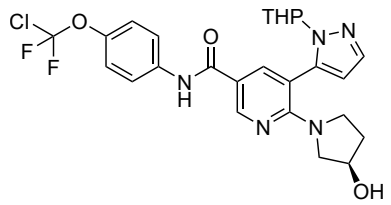


The title compound was prepared following General Procedure **C** using **17a** (200.0 mg, 0.558 mmol, 1.0 eq), **5c** (118.8 mg, 0.614 mmol, 1.1 eq), HOBt·$H_2O$ (94.0 mg, 0.614 mmol, 1.1 eq), EDCI·HCl (161 mg, 0.837 mmol, 1.5 eq), DMAP (6.8 mg, 0.056 mmol, 0.1 eq) and DIPEA (389 µL, 2.23 mmol, 0.76 g cm$^{-3}$, 4.0 eq) in THF (6 mL). The crude product was purified by silica gel column chromatography (eluent: DCM / MeOH 99:03 to 98:05) to provide the title compound **18c** (91.3 mg, 30.6 %) as a yellow solid.

ESI-MS (*m/z*): $[M+H]^+$ 534.17 / 536.16 (3:1); $^1$H NMR (400 MHz, $CDCl_3$): δ 9.14 (s, 1H), 8.45 (s, 1H), 8.23 (s, 1H), 8.06 (d, *J* = 8.9 Hz, 2H), 8.00 (s, 1H), 7.60 (s, 2H), 6.68 (s, 1H), 5.41 (d, *J* = 10.1 Hz, 1H), 4.77 (s, 1H), 4.48–4.24 (m,1H), 4.06–3.49 (m, 6H), 2.88–1.78 (m, 8H); $^{13}$C NMR (101 MHz, $CDCl_3$): δ 164.2, 157.7, 148.6, 146.4, 140.8, 140.7, 139.9, 137.0, 125.4 (t, *J* = 288.7 Hz, 1H), 122.4, 121.5, 121.5, 108.9, 108.7, 84.7, 70.5, 68.2, 57.1, 46.7, 33.7, 30.0, 24.9, 22.8; $^{19}$F NMR (376 MHz, $CDCl_3$): δ –25.67 (s, 2F).

**_N_-(4-(Bromodifluoromethoxy)phenyl)-6-((_R_)-3-hydroxypyrrolidin-1-yl)-5-(1-(tetrahydro-2_H_-pyran-2-yl)-1_H_-pyrazol-5-yl)nicotinamide (18d)**

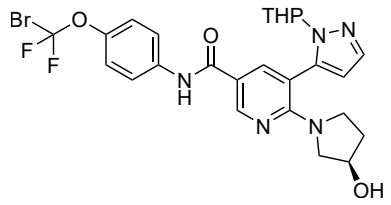

The title compound was prepared following General Procedure **C** using **17a** (362.7 mg, 1.01 mmol, 1.0 eq), crude **5d** (288.5 mg, 1.01 mmol, 1.0 eq), HOBt·$H_2O$ (170.5 mg, 1.11 mmol, 1.1 eq), EDCI·HCl (291 mg, 1.52 mmol, 1.5 eq), DMAP (12.4 mg, 0.101 mmol, 0.1 eq) and DIPEA (705 µL, 4.05 mmol, 0.76 g $cm^{-3}$, 4.0 eq) in THF (9 mL). The crude product was purified by silica gel column chromatography (eluent: DCM / MeOH 99:03 to 98:05) to provide the title compound **18d** (157.0 mg, 26.8 %) as a yellow solid.

ESI-MS (*m/z*): $[M+H]^+$ 578.11 / 580.11 (1:1); $^1$H NMR (400 MHz, $CDCl_3$): δ 8.74 (s, 1H), 8.15 (s, 1H), 7.84 (s, 1H), 7.67 (d, *J* = 9.0 Hz, 2H), 7.65–7.56 (m, 1H), 7.20 (d, *J* = 8.6 Hz, 2H), 6.28 (s, 1H), 5.06–4.79 (m, 1H), 4.37 (s, 1H), 3.97 (dd, *J* = 42.2, 9.9 Hz, 1H), 3.56–3.11 (m, 5H), 2.49–2.30 (m, 2H), 2.09–1.42 (m, 7H); $^{13}$C NMR (101 MHz, $CDCl_3$): δ 164.2, 157.8, 148.7, 147.0, 140.8, 139.9, 139.8, 137.1, 122.2, 121.5, 121.4, 114.9 (t, *J* = 308.6 Hz), 108.9, 108.7, 84.7, 70.5, 68.2, 57.1, 46.7, 33.8, 30.0, 24.9, 22.8; $^{19}$F NMR (376 MHz, $CDCl_3$): δ –15.72 (d, *J* = 3.1 Hz, 2F).

**_N_-(4-(Difluoroiodomethoxy)phenyl)-6-((_R_)-3-hydroxypyrrolidin-1-yl)-5-(1-(tetrahydro-2_H_-pyran-2-yl)-1_H_-pyrazol-5-yl)nicotinamide (18e)**

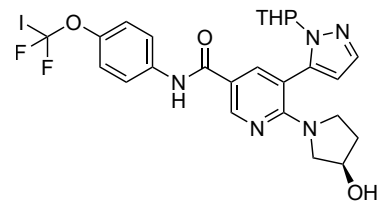

The title compound was prepared following General Procedure **C** using **17a** (90.3 mg, 0.252 mmol, 1.0 eq), crude **5e** (71.8 mg, 0.252 mmol, 1.0 eq), HOBt·$H_2O$ (42.4 mg, 0.277 mmol, 1.1 eq), EDCI·HCl (72.2 mg, 0.378 mmol, 1.5 eq), DMAP (3.1 mg, 0.025 mmol, 0.1 eq) and DIPEA (176 µL, 1.01 mmol, 0.76 g $cm^{-3}$, 4.0 eq) in THF (5 mL). The crude product was purified by silica gel column chromatography (eluent: DCM / MeOH 99:03 to 98:05) to provide the title compound **18e** (48.0 mg, 30.5 %) as a yellow solid.

ESI-MS (*m/z*): $[M+H]^+$ 626.11; $^1$H NMR (400 MHz, $CDCl_3$): δ 8.89–8.61 (m, 1H), 7.91–7.76 (m, 2H), 7.73–7.54 (m, 3H), 7.23–7.09 (m, 2H), 6.32 (s, 1H), 5.00 (dd, *J* = 20.9, 8.7 Hz, 1H), 4.39 (s, 1H), 4.01 (dd, *J* = 41.6, 11.0 Hz, 1H), 3.52–3.17 (m, 5H), 2.04–1.41 (m, 9H); $^{13}$C NMR (101 MHz, $CDCl_3$): δ 164.0, 157.8, 148.3, 147.5, 140.8, 139.9, 137.0, 135.9, 122.3, 121.8 (t, *J* = 50.6 Hz), 121.3, 120.6, 108.9, 108.8, 84.6, 70.6, 68.3, 57.0, 46.7, 33.9, 29.8, 24.9, 22.8; $^{19}$F NMR (376 MHz, $CDCl_3$): δ –3.46 (d, *J* = 4.0 Hz, 1H).

**(*R*)-*N*-(4-(Difluoromethoxy)phenyl)-6-(3-hydroxypyrrolidin-1-yl)-5-(1*H*-pyrazol-5-yl)-nicotinamide (20a)**

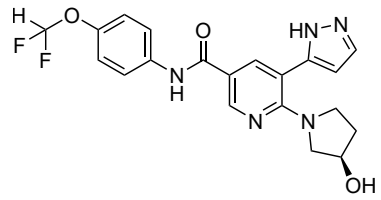

**Method A:** The title compound was prepared following General Procedure **F** using **18a** (148.1 mg, 0.296 mmol, 1.0 eq) and TFA (914 µL, 11.9 mmol, 1.48 g cm$^{-3}$, 40.0 eq) in DCM (6.5 mL). The crude product was purified by silica gel column chromatography (eluent: DCM / MeOH 99:01 to 98:05) to provide the title compound **20a** (62.2 mg, 50.8 %) as a white solid.

**Method B:** The title compound was prepared following General Procedure **G** using **17b** (500 mg, 1.13 mmol, 1.0 eq), DMF (7.8 µL, 0.113 mmol, 0.95 g cm$^{-3}$, 0.1 eq), oxalyl chloride (847 µL, 1.70 mmol, 2 M in DCM, 1.5 eq) in dry DCM (6 mL), **5a** (140 µL, 1.13 mmol, 1.29 g cm$^{-3}$, 1.0 eq), $Et_3N$ (470 µL, 3.39 mmol, 0.73 g cm$^{-3}$, 3.0 eq) in dry THF (8 mL) and TFA (3.48 mL, 45.2 mmol, 1.48 g cm$^{-3}$, 40 eq) in dry DCM (6 mL). The crude product was purified by silica gel column chromatography (eluent: DCM / MeOH 99:01 to 98:05) to provide the title compound **20a** (325.0 mg, 69.2 %) as a white solid.

ESI-MS (*m/z*): $[M+H]^+$ 416.11; HR-ESI-MS (*m/z*): $[M+H]^+_{theor.}$ 416.15287, found 416.15341, rel. Δm 1.30 ppm; $^1$H NMR (700 MHz, DMSO-$d_6$): δ 13.02 (d, *J* = 130.5 Hz, 1H), 10.09 (s, 1H), 8.74 (s, 1H), 8.04 (s, 1H), 7.83–7.72 (m, 2H), 7.16 (s, 2H), 7.16 (t, *J* = 74.4 Hz, 1H), 6.38 (s, 1H), 4.85 (s, 1H), 4.20 (s, 1H), 3.44 (dt, *J* = 9.8, 7.4 Hz, 1H), 3.31–3.21 (m, 2H), 2.94 (d, *J* = 11.6 Hz, 1H), 1.86–1.80 (m, 1H), 1.76–1.70 (m, 1H); $^{13}$C NMR (176 MHz, DMSO-$d_6$): δ 164.0, 157.2, 149.2, 147.6, 146.3, 138.8, 136.7, 128.9, 121.6, 119.3, 117.5, 116.5 (t, *J* = 257.5 Hz), 113.5, 106.1, 68.8, 57.4, 46.9, 33.0; $^{19}$F NMR (659 MHz, DMSO-$d_6$): δ –81.87 (d, *J* = 74.4 Hz, 2F).

**(*R*)-6-(3-Hydroxypyrrolidin-1-yl)-5-(1*H*-pyrazol-5-yl)-*N*-(4-(trifluoromethoxy)phenyl)nicotinamide (20b)**

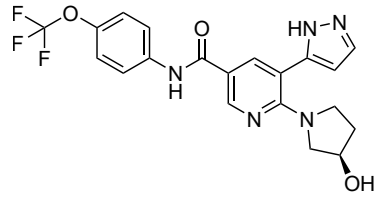

**Method A:** The title compound was prepared following General Procedure **F** using **18b** (47.5 mg, 0.092 mmol, 1.0 eq) and TFA (283 µL, 3.67 mmol, 1.48 g cm$^{-3}$, 40.0 eq) in DCM (6.5 mL). The crude product was purified by silica gel column chromatography (eluent: DCM / MeOH 99:01 to 98:06) to provide the title compound **20b** (13.5 mg, 33.9 %) as a white solid.

**Method B:** The title compound was prepared following General Procedure **G** using **17b** (300 mg, 0.678 mmol, 1.0 eq), DMF (5.2 µL, 0.068 mmol, 0.95 g cm$^{-3}$, 0.1 eq), oxalyl chloride (509 µL, 1.02 mmol, 2 M in DCM, 1.5 eq) in dry DCM (4 mL), **5b** (91.7 µL, 0.678 mmol, 1.31 g cm$^{-3}$, 1.0 eq), $Et_3N$ (282 µL, 2.03 mmol, 0.73 g cm$^{-3}$, 3.0 eq) in dry THF (6 mL) and TFA (2.09 mL, 27.1 mmol, 1.48 g cm$^{-3}$, 40 eq) in dry DCM (8 mL). The crude product was purified by silica gel column chromatography (eluent: DCM / MeOH 99:01 to 98:06) to provide the title compound **20b** (86.9 mg, 29.6 %) as a white solid.

ESI-MS (*m/z*): $[M+H]^+$ 434.10; HR-ESI-MS (*m/z*): $[M+H]^+_{theor.}$ 434.14345, found 434.14412, rel. Δm 1.54 ppm; $^1$H NMR (700 MHz, DMSO-$d_6$): δ 13.02 (d, *J* = 131.9 Hz, 1H), 10.18 (s, 1H), 8.75 (d, *J* = 31.2 Hz, 1H), 8.04 (d, *J* = 15.3 Hz, 1H), 7.87 (d, *J* = 9.1 Hz, 2H), 7.68 (d, *J* = 194.6 Hz, 1H), 7.33 (d, *J* = 8.6 Hz, 2H), 6.38 (d, *J* = 17.3 Hz, 1H), 4.86 (d, *J* = 35.7 Hz, 1H), 4.20 (s, 1H), 3.44 (dd, *J* = 17.0, 9.4 Hz, 1H), 3.28 (d, *J* = 11.1 Hz, 2H), 2.95 (d, *J* = 11.7 Hz, 1H), 1.85–1.72 (m, 2H); $^{13}$C NMR (176 MHz, DMSO-$d_6$): δ 164.2, 157.3, 149.2, 147.6, 143.6, 128.9, 121.5, 121.4, 120.9, 119.4, 117.3, 113.5, 108.9, 106.0, 68.8, 57.4, 46.9, 33.0; $^{19}$F NMR (659 MHz, DMSO-$d_6$): δ –57.43 (s, 3F).

**(*R*)-*N*-(4-(Chlorodifluoromethoxy)phenyl)-6-(3-hydroxypyrrolidin-1-yl)-5-(1*H*-pyrazol-5-yl)-nicotinamide (20c)**

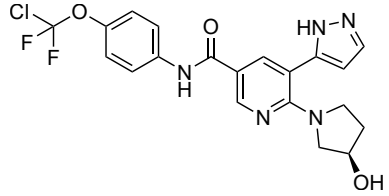


**Method A:** The title compound was prepared following General Procedure **F** using **18c** (60.0 mg, 0.112 mmol, 1.0 eq) and TFA (346 µL, 4.50 mmol, 1.48 g cm$^{-3}$, 40.0 eq) in DCM (2.5 mL). The crude product was purified by silica gel column chromatography (eluent: DCM / MeOH 99:01 to 98:05) to provide the title compound **20c** (15.5 mg, 30.8 %) as a white solid.

**Method B:** The title compound was prepared following General Procedure **G** using **17b** (500 mg, 1.13 mmol, 1.0 eq), DMF (7.8 µL, 0.113 mmol, 0.95 g cm$^{-3}$, 0.1 eq), oxalyl chloride (847 µL, 1.70 mmol, 2 M in DCM, 1.5 eq) in dry DCM (6 mL), **5c** (219 mg, 1.13 mmol, 1.0 eq), $Et_3N$ (470 µL, 3.39 mmol, 0.73 g cm$^{-3}$, 3.0 eq) in dry THF (8 mL) and TFA (3.48 mL, 45.2 mmol, 1.48 g cm$^{-3}$, 40 eq) in dry DCM (6 mL). The crude product was purified by silica gel column chromatography (eluent: DCM / MeOH 99:01 to 98:05) to provide the title compound **20c** (99.9 mg, 19.7 %) as a white solid.

ESI-MS (*m/z*): $[M+H]^+$ 450.08 / 452.07 (3:1); HR-ESI-MS (*m/z*): $[M+H]^+_{theor.}$ 450.11390, found 450.11470, rel. Δm 1.77 ppm; $^1$H NMR (700 MHz, DMSO-$d_6$): δ 13.01 (d, *J* = 130.6 Hz, 1H), 10.19 (s, 1H), 8.76 (d, *J* = 31.8 Hz, 1H), 8.04 (d, *J* = 14.6 Hz, 1H), 7.87 (d, *J* = 9.0 Hz, 2H), 7.68 (d, *J* = 194.5 Hz, 1H), 7.32 (d, *J* = 8.6 Hz, 2H), 6.38 (d, *J* = 18.3 Hz, 1H), 4.85 (t, *J* = 19.0 Hz, 1H), 4.20 (s, 1H), 3.44 (dd, *J* = 17.0, 9.5 Hz, 1H), 3.27 (dd, *J* = 26.5, 15.5 Hz, 2H), 2.95 (d, *J* = 11.7 Hz, 1H), 1.89–1.78 (m, 1H), 1.73 (d, *J* = 3.2 Hz, 1H); $^{13}$C NMR (176 MHz, DMSO-$d_6$): δ 164.2, 157.3, 149.2, 147.6, 144.7, 138.8, 138.7, 128.9, 125.0 (t, *J* = 286.8 Hz), 121.8, 121.4, 117.3, 113.5, 106.6, 106.0, 68.8, 57.4, 46.9 33.0; $^{19}$F NMR (659 MHz, DMSO-$d_6$): δ –25.13 (s, 2F).

**(*R*)-*N*-(4-(Bromodifluoromethoxy)phenyl)-6-(3-hydroxypyrrolidin-1-yl)-5-(1*H*-pyrazol-5-yl)-nicotinamide (20d)**

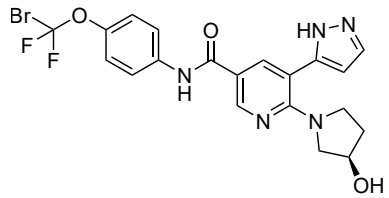


**Method A:** The title compound was prepared following General Procedure **F** using **18d** (128.7 mg, 0.223 mmol, 1.0 eq) and TFA (686 µL, 8.90 mmol, 1.48 g cm$^{-3}$, 40.0 eq) in DCM (5.0 mL). The crude product was purified by silica gel column chromatography (eluent: DCM / MeOH 99:01 to 98:05) to provide the title compound **20d** (56.5 mg, 51.3 %) as a white solid.

**Method B:** The title compound was prepared following General Procedure **G** using **17b** (1.34 g, 3.03 mmol, 1.0 eq), DMF (23.3 µL, 0.303 mmol, 0.95 g cm$^{-3}$, 0.1 eq), oxalyl chloride (2.27 mL, 4.54 mmol, 2 M in DCM, 1.5 eq) in dry DCM (15 mL), **5d** (721 mg, 3.03 mmol, 1.0 eq), $Et_3N$ (1.26 mL, 9.08 mmol, 0.73 g cm$^{-3}$, 3.0 eq) in dry THF (20 mL) and TFA (9.33 mL, 121 mmol, 1.48 g cm$^{-3}$, 40 eq) in dry DCM (20 mL). The crude product was purified by silica gel column chromatography (eluent: DCM / MeOH 99:01 to 98:05) to provide the title compound **20d** (589.8 mg, 39.4 %) as a white solid.

ESI-MS (*m/z*): $[M+H]^+$ 494.05 / 496.05 (1:1); HR-ESI-MS (*m/z*): $[M+H]^+_{theor.}$ 494.06381, found 494.06338, rel. Δm 0.86 ppm; $^1$H NMR (700 MHz, DMSO-$d_6$): δ 13.02 (d, *J* = 130.2 Hz, 1H), 10.19 (s, 1H), 8.74 (s, 1H), 8.04 (s, 1H), 7.89–7.86 (m, 2H), 7.69 (d, *J* = 192.0 Hz, 1H), 7.31 (d, *J* = 8.8 Hz, 2H), 6.39 (s, 1H), 4.84 (s, 1H), 4.20 (s, 1H), 3.51-3.39 (m, 1H), 3.30 (dd, *J* = 26.7, 18.6 Hz, 2H), 2.95 (d, *J* = 11.7 Hz, 1H), 1.83 (dd, *J* = 8.3, 4.0 Hz, 1H), 1.74 (s, 1H); $^{13}$C NMR (176 MHz, DMSO-$d_6$): δ 164.2, 157.2, 149.2, 147.6, 145.5, 138.8, 138.6, 128.9, 121.6, 121.4, 117.4, 114.8 (t, *J* = 306.5 Hz), 113.6, 106.6, 106.0, 68.8, 57.5, 46.9 33.0; $^{19}$F NMR (659 MHz, DMSO-$d_6$): δ –16.39 (s, 2F).

**(*R*)-*N*-(4-(Difluoroiodomethoxy)phenyl)-6-(3-hydroxypyrrolidin-1-yl)-5-(1*H*-pyrazol-5-yl)nicotinamide (20e)**

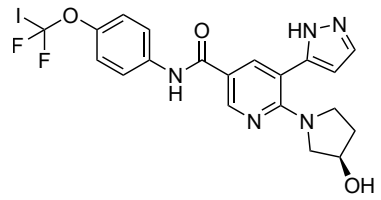

**Method A:** The title compound was prepared following General Procedure **F** using **18e** (41.0 mg, 0.066 mmol, 1.0 eq) and TFA (202 µL, 2.62 mmol, 1.48 g cm$^{-3}$, 40.0 eq) in DCM (1.5 mL). The crude product was purified by silica gel column chromatography (eluent: DCM / MeOH 99:01 to 98:05) to provide the title compound **20e** (15.3 mg, 43.1 %) as a white solid.

**Method B:** The title compound was prepared following General Procedure **G** using **17b** (564 mg, 1.28 mmol, 1.0 eq), DMF (9.8 µL, 0.128 mmol, 0.95 g cm$^{-3}$, 0.1 eq), oxalyl chloride (956 µL, 1.91 mmol, 2 M in DCM, 1.5 eq) in dry DCM (6.5 mL), **5e** (363 mg, 1.28 mmol, 1.0 eq), $Et_3N$ (530 mL, 3.83 mmol, 0.73 g cm$^{-3}$, 3.0 eq) in dry THF (8 mL) and TFA (3.93 mL, 51.0 mmol, 1.48 g cm$^{-3}$, 40 eq) in dry DCM (8 mL). The crude product was purified by silica gel column chromatography (eluent: DCM / MeOH 99:01 to 98:05) to provide the title compound **20e** (78.0 mg, 10.3 %) as a white solid.

ESI-MS (*m/z*): $[M+H]^+$ 542.03; HR-ESI-MS (*m/z*): $[M+H]^+_{theor.}$ 542.04952, found 542.05050, rel. Δm 1.81 ppm; $^1$H NMR (700 MHz, DMSO-$d_6$): δ 13.03 (d, *J* = 134.8 Hz, 1H), 10.19 (s, 1H), 8.74 (s, 1H), 8.03 (s, 1H), 7.86 (d, *J* = 9.1 Hz, 2H), 7.68 (d, *J* = 191.4 Hz, 1H), 7.24 (d, *J* = 8.8 Hz, 2H), 6.39 (s, 1H), 4.84 (s, 1H), 4.20 (s, 1H), 3.44 (dd, *J* = 17.1, 9.9 Hz, 1H), 3.32–3.21 (m, 2H), 2.95 (d, *J* = 11.6 Hz, 1H), 1.89–1.78 (m, 1H), 1.73 (s, 1H); $^{13}$C NMR (176 MHz, DMSO-$d_6$): δ 164.2, 157.2, 149.2, 147.5, 146.9, 138.8, 138.3, 128.9, 121.6, 121.3, 117.4, 113.6, 106.0, 89.0 (t, *J* = 325.1 Hz), 68.8, 57.4, 46.9 33.0; $^{19}$F NMR (659 MHz, DMSO-$d_6$): δ –8.52 (s, 2F).

### 6.3.5 Fragment Library

**2-Chloro-2,2-difluoro-1-(imidazo[1,2-*a*]pyridin-3-yl)ethan-1-one (21)**

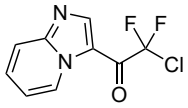

Imidazole[1,2-*a*]pyridine (1.0 g, 8.46 mmol, 1.0 eq) and 2-chloro-2,2-difluoroacetic anhydride (3.90 mL, 27.9 mmol, 1.74 g cm$^{-3}$, 3.3 eq) were dissolved in DCE (20 mL) under argon atmosphere. The reaction mixture was refluxed for 48 h. Afterwards, the mixture was cooled down to room temperature and concentrated under reduced pressure. The crude product was dissolved in EtOAc (100 mL) and washed with 1 M HCl (3 × 50 mL), $H_2O$ (50 mL) and Brine (50 mL). The organic phase was dried over $Na_2SO_4$ and the solvent was removed *in vacuo*. The crude product was purified by silica gel column chromatography (eluent: DCM / MeOH 99:1) to provide the title compound **21** (1.89 g, 96.9 %).

ESI-MS (*m/z*): $[M+H]^+$ 230.97 / 232.97 (3:1); $^1$H NMR (400 MHz, DMSO-$d_6$): δ 9.51 (dt, *J* = 6.8, 1.1 Hz, 1H), 8.70 (t, *J* = 2.3 Hz, 1H), 8.02 (dt, *J* = 8.9, 1.1 Hz, 1H), 7.94–7.82 (m, 1H), 7.49 (td, *J* = 6.9, 1.2 Hz, 1H); $^{13}$C NMR (101 MHz, DMSO-$d_6$): δ 169.8 (t, *J* = 30.3 Hz), 160.0 (t, *J* = 30.9 Hz), 149.8, 146.7 (t, *J* = 6.3 Hz), 132.6, 129.1, 120.1 (t, *J* = 303.3 Hz), 117.9, 117.5; $^{19}$F NMR (376 MHz, DMSO-$d_6$): δ –60.45 (t, *J* = 2.0 Hz, 2F).

***N*-(2-(1*H*-Indol-3-yl)ethyl)-2-chloro-2,2-difluoroacetamide (22)**

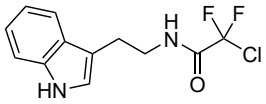

2-(1*H*-Indol-3-yl)ethan-1-amine (1 g, 6.24 mmol, 1.0 eq) was dissolved in dry DCM (25 mL) and the solution was cooled to 0 °C. After 10 min, pyridine (0.60 mL, 7.79 mmol, 1.2 eq) followed by 2-chloro-2,2-difluoroacetic anhydride (1.74 mL, 12.5 mmol, 1.74 g cm$^{-3}$, 1.2 eq) in dry DCM (20 mL) were added to solution. The reaction mixture was allowed to warm up to room temperature overnight. The stirred reaction mixture was quenched with MeOH after 18 h. The solvent was removed under reduced pressure. The crude product was dissolved in EtOAc (100 mL) and washed with 1 M HCl (3 × 50 mL), $H_2O$ (50 mL) and Brine (50 mL). The organic phase was dried over $Na_2SO_4$ and the solvent was removed *in vacuo*. The crude product was purified by silica gel column chromatography (eluent: *n*-hexane / EtOAc 80:20 to 65:35) to provide the title compound **22** (1.16 g, 68.2 %).

ESI-MS (*m/z*): $[M+Na]^+$ 295.00 / 296.99 (3:1); $^1$H NMR (400 MHz, DMSO-$d_6$): δ 10.84 (s, 1H), 9.38 (t, *J* = 5.3 Hz, 1H), 7.54 (d, *J* = 7.9 Hz, 1H), 7.34 (dt, *J* = 8.1, 0.8 Hz, 1H), 7.16 (d, *J* = 2.3 Hz, 1H), 7.07 (ddd, *J* = 8.1, 7.1, 1.1 Hz, 1H), 6.99 (ddd, *J* = 7.9, 7.0, 1.0 Hz, 1H), 3.45 (dd, *J* = 13.5, 7.2 Hz, 2H), 2.92 (t, *J* = 7.4 Hz, 2H); $^{13}$C NMR (101 MHz, DMSO-$d_6$): δ 158.5 (t, *J* = 29.4 Hz), 136.2, 127.1, 122.8, 121.0, 119.2 (t, *J* = 302.6 Hz, 1H), 118.3, 118.1, 111.4, 111.0, 40.3, 24.2; $^{19}$F NMR (376 MHz, DMSO-$d_6$): δ –63.08 (s, 2F).

**2-Chloro-2,2-difluoro-*N*-(1,3,4-thiadiazol-2-yl)acetamide (23)**

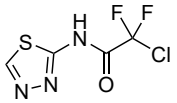

The title compound was prepared following General Procedure **D** using 1,3,4-thiadiazol-2-amine (607 mg, 6.0 mmol, 1 eq) and NMM (1.45 mL, 13.2 mmol, 0.92 g cm$^{-3}$, 2.2 eq) in 30 mL dry THF followed by addition of 2-chloro-2,2-difluoroacetic anhydride (0.92 mL, 6.6 mmol, 1.74 g cm$^{-3}$, 1.1 eq) in 15 mL dry THF. The crude product was purified by silica gel column chromatography (eluent: DCM / MeOH 99:1 to 90:10) to provide the title compound **23** (308.0 mg, 24.0 %).

ESI-MS (*m/z*): $[M-H]^-$ 211.99; $^1$H NMR (400 MHz, DMSO-$d_6$): δ 9.18 (s, 1H); $^{13}$C NMR (101 MHz, DMSO-$d_6$): δ 168.5 (t, *J* = 50.8 Hz), 149.1, 143.3, 119.9 (t, *J* = 300.8 Hz); $^{19}$F NMR (376 MHz, DMSO-$d_6$): δ –62.65 (s, 2F).

**2-Bromo-2,2-difluoro-*N*-(1,3,4-thiadiazol-2-yl)acetamide (24)**

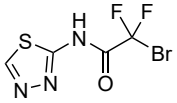

The title compound was prepared following General Procedure **D** using 1,3,4-thiadiazol-2-amine (607 mg, 6.0 mmol, 1 eq) and NMM (1.45 mL, 13.2 mmol, 0.92 g cm$^{-3}$, 2.2 eq) in 30 mL dry THF followed by addition of 2-bromo-2,2-difluoroacetic anhydride (1.86 g, 7.2 mmol, 1.2 eq) in 15 mL dry THF. The crude product was purified by silica gel column chromatography (eluent: DCM / MeOH 99:1 to 90:10) to provide the title compound **24** (883.8 mg, 57.1 %).

ESI-MS (*m/z*): $[M+H]^+$ 257.95 / 259.94 (1:1); $^1$H NMR (400 MHz, DMSO-$d_6$): δ 9.18 (s, 1H); $^{13}$C NMR (101 MHz, DMSO-$d_6$): δ 165.9 (t, *J* = 24.4 Hz), 149.0, 143.5, 112.8 (t, *J* = 313.4 Hz); $^{19}$F NMR (376 MHz, DMSO-$d_6$): δ –69.86 (s, 2F).

**2,2-Difluoro-2-iodo-*N*-(1,3,4-thiadiazol-2-yl)acetamide (25)**

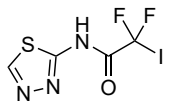

The title compound was prepared following General Procedure **H** using 1,3,4-thiadiazol-2-amine (610 mg, 6.03 mmol, 1.0 eq), **1b** (2.35 g, 9.05 mmol, 1.5 eq), T3P (≥50 wt % solution in EtOAc, 5.38 mL, 9.05 mmol, 1.07 g cm$^{-3}$, 1.5 eq) and DIPEA (2.05 mL, 12.1 mmol, 0.76 g cm$^{-3}$, 2 eq) in dry DCM (60 mL). The crude product was purified by silica gel column chromatography (eluent: DCM / MeOH 99:1 to 90:10) to provide the title compound **25** (372.2 mg, 20.2 %).

ESI-MS (*m/z*): $[M+H]^+$ 305.99; $^1$H NMR (400 MHz, DMSO-$d_6$): δ 9.17 (s, 1H); $^{13}$C NMR (101 MHz, DMSO-$d_6$): δ 166.6, 149.0, 92.5 (t, $J$ = 318.2 Hz); $^{19}$F NMR (376 MHz, DMSO-$d_6$): δ –60.41 (s, 2F).

**Methyl 3-(2-chloro-2,2-difluoroacetamido)-4-methylthiophene-2-carboxylate (26)**

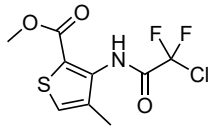

The title compound was prepared following General Procedure **I** using methyl 3-amino-4-methylthiophene-2-carboxylate (1.0 g, 5.84 mmol, 1 eq) and $Et_3N$ (1.78 mL, 12.8 mmol, 0.73 g cm$^{-3}$, 2.2 eq) in 30 mL dry DCM followed by addition of 2-chloro-2,2-difluoroacetic anhydride (1.62 mL, 8.47 mmol, 1.74 g cm$^{-3}$, 1.45 eq) in 15 mL dry DCM. The crude product was purified by silica gel column chromatography (eluent: *n*-hexane / EtOAc 90:10 to 70:30) to provide the title compound **26** (1.53 g, 92.2 %).

ESI-MS (*m/z*): $[M+Na]^+$ 305.94 / 307.93 (3:1); $^1$H NMR (400 MHz, $CDCl_3$): δ 9.65 (s, 1H), 7.21 (d, $J$ = 0.6 Hz, 1H), 3.90 (s, 3H), 2.24 (d, $J$ = 0.9 Hz, 3H); $^{13}$C NMR (101 MHz, $CDCl_3$): δ 163.5, 157.1 (t, $J$ = 30.9 Hz), 139.4, 135.5, 128.4, 119.2, 119.0 (t, $J$ = 303.1 Hz), 52.5, 15.6; $^{19}$F NMR (376 MHz, $CDCl_3$): δ –64.17 (s, 2F).

**2-Chloro-*N*-(3,4-dihydroxyphenyl)-2,2-difluoroacetamide (27)**

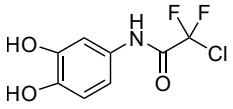

A solution of **7c** (483 mg, 1.94 mmol, 1 eq) in dry DCM (70 mL) under argon atmosphere was cooled to 0 °C. After 10 min, boron tribromide (1.47 g, 0.56 mL, 2.64 g cm$^{-3}$, 3 eq) was added slowly through a cooled-down syringe. The reaction mixture was allowed to warm up to room temperature overnight. The stirred reaction mixture was quenched with MeOH after 18 h and the solvent was removed under reduced pressure. The crude product was purified by silica gel

column chromatography (eluent: DCM / MeOH 99:1 to 90:10) and reversed-phase chromatography (C18, eluent: $H_2O$ and ACN) to provide the title compound **27** (110 mg, 24 %).

ESI-MS (*m/z*): $[M-H]^-$ 234.04 / 236.05 (3:1); $^1$H NMR (400 MHz, DMSO-$d_6$): δ 10.74 (s, 1H), 9.15 (s, 1H), 8.93 (s, 1H), 7.16 (d, *J* = 2.5 Hz, 1H), 6.90 (dd, *J* = 8.6, 2.5 Hz, 1H), 6.71 (d, *J* = 8.5 Hz, 1H); $^{13}$C NMR (101 MHz, DMSO-$d_6$): δ 156.3 (t, *J* = 29.7 Hz), 145.1, 143.2, 128.1, 118.9 (t, *J* = 303.2 Hz), 115.3, 112.3, 109.3; $^{19}$F NMR (376 MHz, DMSO-$d_6$): δ –62.74 (s, 2F).

**Ethyl 5-(2-chloro-2,2-difluoroacetamido)-1-methyl-1*H*-pyrazole-4-carboxylate (28)**

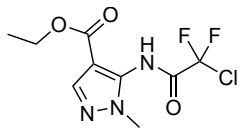

The title compound was prepared following General Procedure **D** using 5-amino-1-methyl-1*H*-pyrazole-4-carboxylate (1.0 g, 5.91 mmol, 1 eq) and NMM (1.43 mL, 13.0 mmol, 0.92 g cm$^{-3}$, 2.2 eq) in 30 mL dry THF followed by addition of 2-chloro-2,2-difluoroacetic anhydride (0.93 mL, 6.50 mmol, 1.74 g cm$^{-3}$, 1.1 eq) in 15 mL dry THF. The crude product was purified by silica gel column chromatography (eluent: DCM / MeOH 99:1 to 90:10) to provide the title compound **28** (1.23 g, 73.9 %).

ESI-MS (*m/z*): $[M+H]^+$ 282.02 / 284.01 (3:1); $^1$H NMR (400 MHz, DMSO-$d_6$): δ 11.56 (s, 1H), 7.92 (s, 1H), 4.18 (q, *J* = 7.1 Hz, 2H), 3.70 (s, 3H), 1.23 (t, *J* = 7.1 Hz, 3H); $^{13}$C NMR (101 MHz, DMSO-$d_6$): δ 161.2, 157.9 (t, *J* = 31.4 Hz), 140.0, 135.2, 118.4 (t, *J* = 302.0 Hz), 108.5, 59.8, 35.8, 14.1; $^{19}$F NMR (376 MHz, DMSO-$d_6$): δ –63.67 (s, 2F).

**2-Chloro-2,2-difluoro-*N*-(5-(pyridin-4-yl)-1,3,4-thiadiazol-2-yl)acetamide (29)**

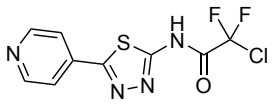

The title compound was prepared following General Procedure **D** using 5-(pyridin-4-yl)-1,3,4-thiadiazol-2-amine (500 mg, 2.81 mmol, 1 eq) and NMM (0.68 mL, 6.17 mmol, 0.92 g cm$^{-3}$, 2.2 eq) in 14 mL dry THF followed by addition of 2-chloro-2,2-difluoroacetic anhydride (0.47 mL, 3.37 mmol, 1.74 g cm$^{-3}$, 1.2 eq) in 7 mL dry THF. The crude product was purified by silica gel column chromatography (eluent: DCM / MeOH 99:1 to 90:10) and reversed-phase chromatography (C18, eluent: $H_2O$ and ACN) to provide the title compound **29** (462 mg, 56.6 %).

ESI-MS (*m/z*): $[M+H]^+$ 291.09 / 293.09 (3:1); $^1$H NMR (400 MHz, DMSO-$d_6$): δ 8.80 (d, *J* = 5.8 Hz, 2H), 8.03 (dd, *J* = 4.8, 1.5 Hz, 2H); $^{13}$C NMR (101 MHz, DMSO-$d_6$): δ 169.0, 164.6 (t, *J* = 29.6 Hz), 157.4, 149.2, 138.5, 121.2, 120.0 (t, *J* = 300.9 Hz); $^{19}$F NMR (376 MHz, DMSO-$d_6$): δ –62.35 (s, 2F).

**2-Bromo-2,2-difluoro-*N*-(5-(pyridin-4-yl)-1,3,4-thiadiazol-2-yl)acetamide (30)**

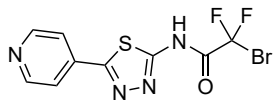

The title compound was prepared following General Procedure **D** using 5-(pyridin-4-yl)-1,3,4-thiadiazol-2-amine (407 mg, 2.28 mmol, 1 eq) and NMM (0.55 mL, 5.02 mmol, 0.92 g cm$^{-3}$, 2.2 eq) in 12 mL dry THF followed by addition of 2-bromo-2,2-difluoroacetic anhydride (908 mg, 2.74 mmol, 1.2 eq) in 6 mL dry THF. The crude product was purified by silica gel column chromatography (eluent: DCM / MeOH 99:1 to 90:10) and reversed-phase chromatography (C18, eluent: $H_2O$ and ACN) to provide the title compound **30** (484 mg, 63.2 %).

ESI-MS (*m/z*): $[M+H]^+$ 335.07 / 337.07 (1:1); $^1$H NMR (400 MHz, DMSO-$d_6$): δ 8.80 (dd, *J* = 4.7, 1.6 Hz, 2H), 8.02 (dd, *J* = 4.7, 1.6 Hz, 2H); $^{13}$C NMR (101 MHz, DMSO-$d_6$): δ 168.4, 165.2 (t, *J* = 27.2 Hz), 157.6, 149.4, 138.2, 121.1, 112.9 (t, *J* = 313.5 Hz); $^{19}$F NMR (376 MHz, DMSO-$d_6$): δ –59.59 (s, 2F).

**2,2-Difluoro-2-iodo-*N*-(5-(pyridin-4-yl)-1,3,4-thiadiazol-2-yl)acetamide (31)**

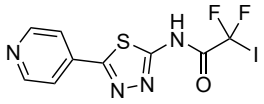

The title compound was prepared following General Procedure **H** using 5-(pyridin-4-yl)-1,3,4-thiadiazol-2-amine (425 mg, 2.38 mmol, 1.0 eq), **1b** (928 mg, 3.57 mmol, 1.5 eq), T3P (≥50,wt % solution in EtOAc, 2.13 mL, 3.57 mmol, 1.07 g cm$^{-3}$, 1.5 eq) and DIPEA (810 µL, 4.76,mmol, 0.76 g cm$^{-3}$, 2 eq) in dry DCM (25 mL). The crude product was purified by silica gel column chromatography (eluent: DCM / MeOH 99:1 to 90:10) and reversed-phase chromatography (C18, eluent: $H_2O$ / ACN) to provide the title compound **31** (184.6 mg, 20.3 %).

ESI-MS (*m/z*): $[M+H]^+$ 383.04; $^1$H NMR (400 MHz, DMSO-$d_6$): δ 8.78 (d, *J* = 5.9 Hz, 2H), 7.97 (dd, *J* = 4.6, 1.6 Hz, 2H); $^{13}$C NMR (101 MHz, DMSO-$d_6$): δ 166.1 (t, *J* = 25.3 Hz), 166.0, 158.4, 150.1, 137.4, 120.9, 92.2 (t, *J* = 317.4 Hz); $^{19}$F NMR (376 MHz, DMSO-$d_6$): δ –60.74 (s, 2F).

**2-Chloro-*N*-(1-(4-chlorophenyl)-4-cyano-1*H*-pyrazol-5-yl)-2,2-difluoroacetamide (32)**

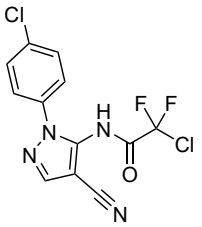

The title compound was prepared following General Procedure **D** using 5-amino-1-(4-chlorophenyl)-1*H*-pyrazole-4-carbonitrile (498 mg, 2.28 mmol, 1 eq) and NMM (0.55 mL, 5.02 mmol, 0.92 g cm$^{-3}$, 2.2 eq) in 15 mL dry THF followed by addition of 2-chloro-2,2-difluoroacetic anhydride (0.53 mL, 3.82 mmol, 1.74 g cm$^{-3}$, 1.6 eq) in 8 mL dry THF. The crude product was purified by silica gel column chromatography (eluent: DCM / MeOH 99:1) to provide the title compound **32** (271 mg, 35.9 %).

**Remark:** The substance was very difficult to purify due to its very poor solubility properties and was only suitable as a test substance to a limited extent.

ESI-MS (*m/z*): $[M-H]^-$ 329.19 / 331.18 (3:1); $^1$H NMR (400 MHz, DMSO-$d_6$): δ 13.86 (bs, 1H), 8.48 (d, *J* = 2.8 Hz, 1H), 8.05 (dd, *J* = 8.8, 1.5 Hz, 2H), 7.67 (d, *J* = 8.9 Hz, 2H); $^{19}$F NMR (376 MHz, DMSO-$d_6$): δ –57.73 (s, 2F).

**2-((Bromodifluoromethyl)thio)-4-methylthiazole (33)**

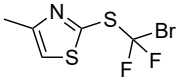

To a solution of 4-methylthiazole-2-thiol (1.0 g, 7.62 mmol, 1.0 eq) in dry DMF (8 mL) was added NaH (60 % dispersion in mineral oil; 457 mg, 11.4 mmol, 1.5 eq) at 0 °C. The reaction mixture was stirred at room temperature for 1 h, then $CF_2Br_2$ was added at 0 °C and the mixture was stirred further 3 h at 0 °C. The remaining NaH was quenched with $H_2O$ (200 mL) and the mixture was extracted with $Et_2O$ (3 × 80 mL). The combined organic layers were washed with $H_2O$ (50 mL), brine (50 mL), dried over $Na_2SO_4$ and concentrated *in vacuo*. The crude product was purified by silica gel column chromatography (eluent: DCM with 0.4 % MeOH) to provide the title compound **33** (1.48 g, 74.8 %) as a yellow crystalline solid.

EI-MS (*m/z*): $[M]^+$ 258.9 / 260.9 (1:1); $^1$H NMR (400 MHz, $CDCl_3$): δ 7.22 (dd, *J* = 1.8, 0.9 Hz, 1H), 2.52 (d, *J* = 0.9 Hz, 3H); $^{13}$C NMR (101 MHz, $CDCl_3$): δ 155.9, 150.3, 122.0 (d, *J* = 6.4 Hz), 117.3 (t, *J* = 341.5 Hz), 17.4 (d, *J* = 8.9 Hz); $^{19}$F NMR (376 MHz, $CDCl_3$): δ –23.82 (s, 2F).

**2-((Bromodifluoromethyl)sulfonyl)-4-methylthiazole (34)**

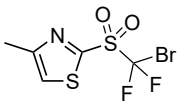

To a solution of **33** (951 mg, 3.66 mmol, 1.0 eq) in dry DCM (15 mL) was added mCPBA (2.70 g, 11.0 mmol, 3.0 eq) at 0 °C. The reaction mixture was stirred at room temperature for 22 h, then the solvent was removed *in vacuo*. The residue was dissolved in EtOAc (100 mL), washed with sat. $NaHCO_3$ ($3 \times 30$ mL), brine (30 mL), dried over $Na_2SO_4$ and the solvent was concentrated *in vacuo*. The crude product was purified by silica gel column chromatography (eluent: DCM with 0.2 % MeOH) to provide the title compound **34** (578 mg, 54.1 %) as a yellow oil.

ESI-MS (*m/z*): $[M+H]^+$ 291.90 / 293.90 (1:1); $^1$H NMR (400 MHz, DMSO-$d_6$): δ 8.32 (d, $J$ = 0.8 Hz, 1H), 2.55 (d, $J$ = 0.8 Hz, 3H); $^{13}$C NMR (101 MHz, DMSO-$d_6$): δ 157.7, 152.1, 129.5, 119.6 (t, $J$ = 345.8 Hz), 16.6; $^{19}$F NMR (376 MHz, DMSO-$d_6$): δ –59.26 (s, 2F).

**2-Bromo-2,2-difluoro-*N*-(thiazol-2-yl)acetamide (35)**

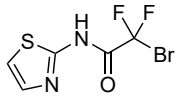

The title compound was prepared following General Procedure **I** using 2-aminothiazole (500 mg, 4.99 mmol, 1 eq) and $Et_3N$ (1.52 mL, 11.0 mmol, 0.73 g cm$^{-3}$, 2.2 eq) in 25 mL dry DCM followed by addition of 2-bromo-2,2-difluoroacetic anhydride (1.82 g, 5.49 mmol, 1.1 eq) in 12 mL dry DCM. The crude product was purified by silica gel column chromatography (eluent: DCM / MeOH 95:5) to provide the title compound **35** (1.02 g, 79.5 %).

ESI-MS (*m/z*): $[M+H]^+$ 256.89 / 258.89 (1:1); $^1$H NMR (400 MHz, $CDCl_3$): δ 13.75 (bs, 1H), 7.56 (d, $J$ = 4.1 Hz, 1H), 7.10 (d, $J$ = 4.1 Hz, 1H); $^{13}$C NMR (101 MHz, $CDCl_3$): δ 164.5, 162.1 (t, $J$ = 28.8 Hz), 132.4, 114.4, 111.8 (t, $J$ = 314.8 Hz); $^{19}$F NMR (376 MHz, $CDCl_3$): δ –61.29 (s, 2F).

**2-Bromo-2,2-difluoro-*N*-(4-nitrophenyl)acetamide (36)**

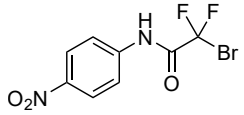

4-Nitroaniline (500 mg, 3.62 mmol, 1 eq) was dissolved in dry DCM (15 mL) and the solution was cooled to 0 °C. After 10 min, $Et_3N$ (1.10 mL, 7.96 mmol, 0.73 g cm$^{-3}$, 2.2 eq) followed by 2-bromo-2,2-difluoroacetic anhydride (1.32 g, 3.98 mmol, 1.1 eq) in dry DCM (8 mL) were added to the solution. The reaction mixture was allowed to warm up to room temperature overnight. The stirred reaction mixture was quenched with crushed ice and an off-white precipitate was formed, which was filtered using vacuum-filtration. The residue was washed with $H_2O$

and dried at 60 °C. The crude product was purified by silica gel column chromatography (eluent: DCM) to provide the title compound **36** (870 mg, 81.4 %).

ESI-MS (*m/z*): $[M+H]^+$ 292.95 / 294.95 (1:1); $^1$H NMR (400 MHz, DMSO-$d_6$): δ 11.59 (s, 1H), 8.35–8.22 (m, 2H), 8.02–7.90 (m, 2H); $^{13}$C NMR (101 MHz, DMSO-$d_6$): δ 158.8 (t, $J$ = 28.6 Hz), 144.4, 143.2, 125.3, 121.4, 111.1 (t, $J$ = 315.0 Hz); $^{19}$F NMR (376 MHz, DMSO-$d_6$): δ –61.03 (s, 2F).

**_N_-(4-Aminophenyl)-2-bromo-2,2-difluoroacetamide (37)**

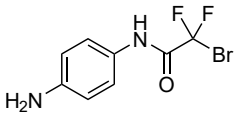

The title compound was prepared following General Procedure **B** using **36** (200 mg, 0.678 mmol, 1.0 eq) and $SnCl_2 \cdot 2\,H_2O$ (765 mg, 3.39 mmol, 5.0 eq) in EtOH (7 mL) and conc. HCl (1 mL). The crude product was purified by silica gel column chromatography (eluent: DCM / MeOH 95:05) to provide the title compound **37** (134 mg, 74.5 %) as an orange solid.

ESI-MS (*m/z*): $[M+H]^+$ 264.98 / 266.98 (1:1); $^1$H NMR (400 MHz, DMSO-$d_6$): δ 10.60 (s, 1H), 7.31–7.21 (m, 2H), 6.58–6.51 (m, 2H), 5.11 (s, 1H); $^{13}$C NMR (101 MHz, DMSO-$d_6$): δ 157.1 (t, $J$ = 26.9 Hz), 146.6, 125.0, 122.5, 113.61, 111.7 (t, $J$ = 315.7 Hz); $^{19}$F NMR (376 MHz, DMSO-$d_6$): δ –59.44 (s, 2F).

**2-Bromo-2,2-difluoro-_N_-(4-ureidophenyl)acetamide (38)**

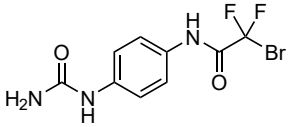

The title compound was prepared following General Procedure **E** using **37** (100 mg, 0.377 mmol, 1.0 eq) and potassium cyanate (153 mg, 1.89 mmol, 5.0 eq) in 10 % acetic acid (3 mL). The crude product was purified by silica gel column chromatography (eluent: DCM / MeOH 90:10 to 70:30) to provide the title compound **38** (56.6 mg, 48.7 %) as a white solid.

ESI-MS (*m/z*): $[M+H]^+$ 308.05 / 310.05 (1:1); $^1$H NMR (400 MHz, DMSO-$d_6$): δ 10.87 (s, 1H), 8.57 (s, 1H), 7.53–7.47 (m, 2H), 7.43–7.38 (m, 2H), 5.84 (s, 2H); $^{13}$C NMR (101 MHz, DMSO-$d_6$): δ 158.3–156.9 (m, 1C), 155.9, 138.1, 129.8, 121.6, 117.9, 111.4 (t, $J$ = 294.9 Hz); $^{19}$F NMR (376 MHz, DMSO-$d_6$): δ –59.87 (s, 2F).

**2-Bromo-*N*-(4-chloropyrimidin-2-yl)-2,2-difluoroacetamide (39)**

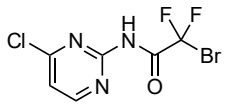

The title compound was prepared following General Procedure **I** using 4-chloropyrimidin-2-amine (300 mg, 2.3 mmol, 1 eq) and $Et_3N$ (485 µL, 3.5 mmol, 0.73 g cm$^{-3}$, 1.5 eq) in 10 mL dry DCM followed by addition of 2-bromo-2,2-difluoroacetic anhydride (846 mg, 2.55 mmol, 1.1 eq). The crude product was purified by silica gel column chromatography (eluent: DCM / MeOH 95:5 to 85:10) to provide the title compound **39** (158 mg, 24.0 %).

ESI-MS (*m/z*): $[M+H]^+$ 287.89; $^1$H NMR (400 MHz, DMSO-$d_6$): δ 12.28 (s, 1H), 8.78 (d, $J$ = 5.3 Hz, 1H), 7.57 (d, $J$ = 5.3 Hz, 1H); $^{13}$C NMR (101 MHz, DMSO-$d_6$): δ 160.6, 157.8–157.1, 156.4, 118.7, 110.4 (t, $J$ = 315.4 Hz); $^{19}$F NMR (376 MHz, DMSO-$d_6$): δ –61.76 (s, 2F).

***N*-(4-((1*H*-1,2,4-Triazol-1-yl)methyl)phenyl)-2-bromo-2,2-difluoroacetamide (40)**

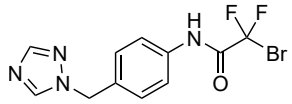

The title compound was prepared following General Procedure **I** using 4-((1*H*-1,2,4-triazol-1-yl)methyl)aniline hydrochloride (500 mg, 2.37 mmol, 1 eq) and $Et_3N$ (1.32 g, 9 mmol, 0.73 g cm$^{-3}$, 3.3 eq) in 20 mL dry DCM followed by addition of 2-bromo-2,2-difluoroacetic anhydride (2.28 g, 6.87 mmol, 1.45 eq) in 15 mL dry DCM. The crude product was purified by silica gel column chromatography (eluent: DCM / MeOH 97:3 to 90:10, with 0.1 % TFA) to provide the title compound **40** (632 mg, 92.2 %).

ESI-MS (*m/z*): $[M+H]^+$ 330.97 / 332.96 (1:1); $^1$H NMR (400 MHz, DMSO-$d_6$): δ 11.08 (s, 1H), 8.65 (s, 1H), 7.98 (s, 1H), 7.69–7.58 (m, 2H), 7.32 (d, $J$ = 8.6 Hz, 2H), 5.40 (s, 2H); $^{13}$C NMR (101 MHz, DMSO-$d_6$): δ 157.9 (t, $J$ = 27.7 Hz), 151.7, 144.2, 136.2, 133.3, 128.6, 121.1, 111.1 (t, $J$ = 315.4 Hz), 51.6; $^{19}$F NMR (376 MHz, DMSO-$d_6$): δ –63.08 (s, 2F).

**2-Bromo-2,2-difluoro-1-(4-(furan-2-carbonyl)piperazin-1-yl)ethan-1-one (41)**

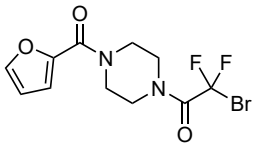

The title compound was prepared following General Procedure **D** using furan-2-yl(piperazin-1-yl)methanone (1.08 g, 6.0 mmol, 1 eq) and NMM (1.45 mL, 13.2 mmol, 0.92 g cm$^{-3}$, 2.2 eq) in 30 mL dry THF followed by addition of 2-bromo-2,2-difluoroacetic anhydride (2.19 g, 6.6 mmol, 1.1 eq) in 15 mL dry THF. The crude product was purified by silica gel column chromatography (eluent: *n*-hexane / EtOAc 60:40) to provide the title compound **41** (1.93 g, 95.4 %).

ESI-MS (*m/z*): $[M+H]^+$ 336.98 / 338.98 (1:1); $^1$H NMR (400 MHz, DMSO-$d_6$): δ 7.87 (dd, *J* = 1.8, 0.8 Hz, 1H), 7.06 (dd, *J* = 3.5, 0.8 Hz, 1H), 6.65–6.64 (m, 1H), 3.89–3.52 (m, 8H); $^{13}$C NMR (101 MHz, DMSO-$d_6$): δ 158.5, 157.3 (t, *J* = 26.3 Hz), 146.6, 145.0, 116.1, 111.4, 110.4 (t, *J* = 311.9 Hz), 46.0, 43.2; $^{19}$F NMR (376 MHz, DMSO-$d_6$): δ –55.60 (s, 2F).

**_N_-(Benzo[_c_][1,2,5]thiadiazol-4-yl)-2-bromo-2,2-difluoroacetamide (42)**

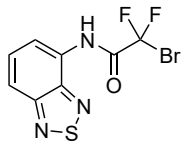

The title compound was prepared following General Procedure **I** using benzo[*c*][1,2,5]thiadiazol-4-amine (498 mg, 3.29 mmol, 1 eq) and $Et_3N$ (1.01 mL, 7.24 mmol, 0.73 g cm$^{-3}$, 2.2 eq) in 15 mL dry DCM followed by addition of 2-bromo-2,2-difluoroacetic anhydride (1.20 g, 3.62 mmol, 1.1 eq) in 8 mL dry DCM. The crude product was purified by silica gel column chromatography (eluent: *n*-hexane / EtOAc 95:5 to 85:15) to provide the title compound **42** (683 mg, 67.4 %).

ESI-MS (*m/z*): $[M-H]^-$ 306.07 / 308.06 (1:1); $^1$H NMR (400 MHz, $CDCl_3$): δ 9.14 (s, 1H), 8.46 (d, *J* = 7.4 Hz, 1H), 7.82 (dd, *J* = 8.9, 0.8 Hz, 1H), 7.66 (dd, *J* = 8.9, 7.5 Hz, 1H); $^{13}$C NMR (101 MHz, $CDCl_3$): δ 157.7 (t, *J* = 28.6 Hz), 154.8, 147.7, 130.7, 127.6, 118.2, 116.6, 111.2 (t, *J* = 316.6 Hz); $^{19}$F NMR (376 MHz, $CDCl_3$): δ –60.72 (s, 2F).

**Ethyl 2-(2-bromo-2,2-difluoroacetamido)-4,5,6,7-tetrahydrobenzo[_b_]thiophene-3-carboxylate (43)**

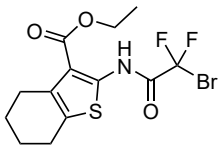

The title compound was prepared following General Procedure **I** using ethyl 2-amino-4,5,6,7-tetrahydrobenzo[*b*]-thiophene-3-carboxylate (500 mg, 2.22 mmol, 1 eq) and $Et_3N$ (0.68 mL, 4.88 mmol, 0.73 g cm$^{-3}$, 2.2 eq) in 15 mL dry DCM followed by addition of 2-bromo-2,2-difluoroacetic anhydride (810 mg, 2.44 mmol, 1.1 eq) in 8 mL dry DCM. The crude product was purified by silica gel column chromatography (eluent: DCM) to provide the title compound **43** (635 mg, 74.8 %).

ESI-MS (*m/z*): $[M+Na]^+$ 404.08 / 406.08 (1:1); $^1$H NMR (400 MHz, $CDCl_3$): δ 12.22 (s, 1H), 4.37 (q, *J* = 7.1 Hz, 2H), 2.82–2.77 (m, 2H), 2.71–2.67 (m, 2H), 1.88–1.74 (m, 5H), 1.40 (t, *J* = 7.1 Hz, 3H); $^{13}$C NMR (101 MHz, $CDCl_3$): δ 166.5, 156.4 (t, *J* = 29.0 Hz), 144.3, 132.1, 129.5, 114.8, 111.2 (t, *J* = 315.6 Hz), 61.3, 26.4, 24.6, 23.0, 22.8, 14.4; $^{19}$F NMR (376 MHz, $CDCl_3$): δ –60.51 (s, 2F).

**2-Bromo-2,2-difluoro-*N*-(5-(4-nitrophenyl)-1,3,4-oxadiazol-2-yl)acetamide (44)**

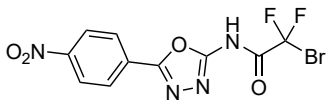

The title compound was prepared following General Procedure **I** using 5-(4-nitrophenyl)-1,3,4-oxadiazol-2-amine (500 mg, 2.43 mmol, 1 eq) and $Et_3N$ (0.74 mL, 5.35 mmol, 0.73 g cm$^{-3}$, 2.2 eq) in 15 mL dry DCM followed by addition of 2-bromo-2,2-difluoroacetic anhydride (891 mg, 2.68 mmol, 1.1 eq) in 8 mL dry DCM. The crude product was purified by silica gel column chromatography (eluent: DCM / MeOH 97:3 to 90:10) to provide the title compound **44** (837 mg, 94.9 %).

ESI-MS (*m/z*): $[M-H]^-$ 360.95 / 362.94 (1:1); $^1$H NMR (400 MHz, DMSO-$d_6$): δ 8.92 (s, 1H), 8.39–8.34 (m, 2H), 8.14–8.09 (m, 2H); $^{13}$C NMR (101 MHz, DMSO-$d_6$): δ 167.9, 157.6, 148.4, 131.0, 126.7, 125.0, 116.5 (t, $J$ = 318.0 Hz); $^{19}$F NMR (376 MHz, DMSO-$d_6$): δ –54.79 (s, 2F).

**2-Bromo-2,2-difluoro-*N*-(4-fluorophenyl)acetamide (45)**

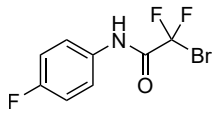

The title compound was prepared following General Procedure **D** using 4-fluoroaniline (620 mg, 5.58 mmol, 1 eq) and NMM (0.92 mL, 8.37 mmol, 0.92 g cm$^{-3}$, 1.5 eq) in 20 mL dry THF followed by addition of 2-bromo-2,2-difluoroacetic anhydride (2.22 g, 6.70 mmol, 1.2 eq). The crude product was purified by silica gel column chromatography (eluent: *n*-hexane / EtOAc 95:5 to 85:15) to provide the title compound **45** (1.93 g, 92.5 %).

ESI-MS (*m/z*): $[M+H]^+$ 265.95 / 267.95 (1:1); $^1$H NMR (400 MHz, $CDCl_3$): δ 7.85 (bs, 1H), 7.59–7.50 (m, 2H), 7.15–7.05 (m, 2H); $^{13}$C NMR (101 MHz, $CDCl_3$): δ 160.6 (d, $J$ = 246.5 Hz), 157.7 (t, $J$ = 27.8 Hz), 131.3, 122.6 (d, $J$ = 8.3 Hz), 116.4 (d, $J$ = 22.9 Hz), 111.5 (t, $J$ = 316.8 Hz); $^{19}$F NMR (376 MHz, $CDCl_3$): δ –61.91 (d, $J$ = 1.8 Hz, 2F), -116.19 (ddd, $J$ = 14.4, 8.2, 4.6 Hz, 1F).

### 6.3.6 Indazole-based Kinase Inhibitors

**5-(Difluoromethyl)-2-fluorobenzonitrile (47)**

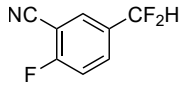

The title compound was prepared following General Procedure **J** using 2-fluoro-5-formylbenzonitrile (3.0 g, 20.1 mmol, 1 eq) and DAST (3.2 mL, 24.1 mmol, 1.2 eq) in dry DCM (100 mL). The crude product was purified by silica gel column chromatography (eluent: *n*-hexane / EtOAc 98:2 to 80:20) to provide the title compound **47** (3.04 g, 88.3 %) as a white crystalline solid.

ES-MS (*m/z*): $[M]^+$ 170.9; $^1$H NMR (300 MHz, $CDCl_3$): δ 7.81–7.75 (m, 2H), 7.34 (td, *J* = 8.4, 0.6 Hz, 1H), 6.67 (t, *J* = 55.9 Hz, 1H); $^{13}$C NMR (75 MHz, $CDCl_3$): δ 164.3 (dt, *J* = 263.1, 1.8 Hz), 132.6 (dt, *J* = 9.2, 5.8 Hz), 131.8 (td, *J* = 23.9, 3.8 Hz), 131.3 (td, *J* = 6.3, 0.8 Hz), 117.4 (d, *J* = 20.4 Hz), 113.1, 112.8 (t, *J* = 240.7 Hz), 102.4 (d, *J* = 16.3 Hz); $^{19}$F NMR (282 MHz, $CDCl_3$): δ –104.05 (t, *J* = 3.1 Hz, 2F), -112.71 (d, *J* = 3.1 Hz, 1F).

**5-(Difluoromethyl)picolinonitrile (48)**

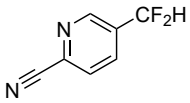

The title compound was prepared following General Procedure **J** using 5-formylpicolinonitrile (1.0 g, 7.57 mmol, 1 eq) and DAST (1.2 mL, 9.09 mmol, 1.2 eq) in dry DCM (20 mL). The crude product was purified by silica gel column chromatography (eluent: *n*-hexane / EtOAc 85:15) to provide the title compound **47** (976.8 g, 83.7 %) as a pale-yellow crystalline solid.

ESI-MS (*m/z*): $[M+H]^+$ 155.03; $^1$H NMR (400 MHz, $CDCl_3$): δ 8.87 (d, *J* = 0.8 Hz, 1H), 8.06–7.95 (m, 1H), 7.82 (dd, *J* = 8.0, 0.6 Hz, 1H), 6.78 (t, *J* = 55.2 Hz, 1H); $^{13}$C NMR (101 MHz, $CDCl_3$): δ 148.7 (t, *J* = 6.5 Hz), 136.1, 134.7 (t, *J* = 5.7 Hz), 133.2 (t, *J* = 23.5 Hz), 128.4, 116.6, 112.3 (t, *J* = 241.5 Hz); $^{19}$F NMR (376 MHz, $CDCl_3$): δ –115.56 (d, *J* = 55.2 Hz, 2F).

***tert*-Butyl ((5-(difluoromethyl)pyridin-2-yl)methyl)carbamate (49)**

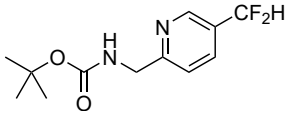

To a solution of **48** (3.95 g, 25.6 mmol, 1 eq), di-*tert*-butyl dicarbonate (11.2 g, 51.3 mmol, 2 eq) and $NiCl_2 \cdot 5\,H_2O$ (610 mg, 2.56 mmol, 0.1 eq) in MeOH (100 mL) was added $NaBH_4$ (6.79 g, 180 mmol, 7 eq) in portions over 30 min at 0 °C (Caution: Gas formation!). The reaction mixture was stirred at 0 °C for 30 min, then for 18 h at room temperature. Diethylenetriamine (5.51 mL, 51.3 mmol, 0.96 g cm$^{-3}$, 2 eq) was added and the mixture was concentrated *in vacuo*. The residue was dissolved in EtOAc and the organic phase was washed with sat. $NaHCO_3$

(2 × 40 mL), brine (40 mL) and dried over $Na_2SO_4$. The solvent was removed under reduced pressure. The crude product **49** (2.74 g, 41.4 %) was used without further purification for the next synthesis step.

ESI-MS (*m/z*): $[M+H]^+$ 259.05.

**(5-(Difluoromethyl)pyridin-2-yl)methanamine (50a)**

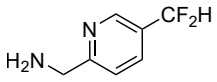

To a solution of **49** (2.72 g, 10.5 mmol) in DCM (60 mL) was added a solution of TFA (5 mL) and DCM (10 mL) at 0 °C. The reaction mixture was stirred at 0 °C for 30 min, then for 24 h at room temperature. $H_2O$ (200 mL) was poured to the mixture at 0 °C, followed by addition of 10 % NaOH (80 mL). The biphasic mixture was extracted with DCM (3 × 100 mL) and EtOAc (3 × 100 mL). The combined organic layers were dried over $Na_2SO_4$ and the solvent was removed *in vacuo*. The crude product **50a** (1.06 g, 63.5 %) was used without further purification for the next synthesis step.

ESI-MS (*m/z*): $[M+H]^+$ 159.07.

**5-(Difluoromethyl)-1*H*-indazol-3-amine (51a)**

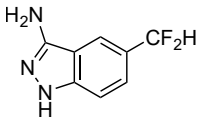

A solution of **47** (530 mg, 3.1 mmol, 1 eq) and hydrazine hydrate (602 µL, 12.4 mmol, 4 eq) in EtOH (120 mL) was refluxed at 90 °C for 4 h. After cooling down to room temperature, the solvent was removed under reduced pressure. The residue was dissolved in a biphasic mixture of EtOAc and $H_2O$. The organic phase was seperated and the aq. phase was extracted twice with ethyle acetate. The combined organic phases were washed with brine, dried over $Na_2SO_4$ and the solvent was removed *in vacuo*. The crude product was purified by silica gel column chromatography (eluent: DCM / MeOH 80:20 to 0:100) to provide the title compound **51a** (456 mg, 80.4 %) as a pale-brown solid.

ESI-MS (*m/z*): $[M+H]^+$ 184.2; $^1$H NMR (300 MHz, DMSO-$d_6$): δ 11.66 (s, 1H), 7.96 (s, 1H), 7.40–7.31 (m, 2H), 7.03 (t, $J$ = 56.4 Hz, 1H), 5.52 (s, 2H); $^{13}$C NMR (75 MHz, DMSO-$d_6$): δ 150.4, 142.5, 123.9–123.8 (m), 123.8 (t, $J$ = 234.5 Hz), 119.4 (t, $J$ = 7.0 Hz), 116.5 (dt, $J$ = 234.5 Hz), 113.8, 110.3; $^{19}$F NMR (282 MHz, DMSO-$d_6$): δ –105.51 (s, 2F).

**5-(Trifluoromethyl)-1*H*-indazol-3-amine (51b)**

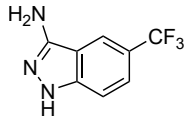

A solution of 2-fluoro-5-(trifluoromethyl)benzonitrile (1.0 mL, 1.83 g, 7.31 mmol, 1 eq) and hydrazine hydrate (1.42 mL, 29.3 mmol, 4 eq) in EtOH (50 mL) was refluxed at 90 °C for 3 h. After cooling down to room temperature, the solvent was removed under reduced pressure. The crude product was purified by silica gel column chromatography (eluent: *n*-hexane / EtOAc 95:05 to 0:100) and reversed-phase chromatography (C18, eluent: $H_2O$ and ACN) to provide the title compound **51b** (975 mg, 66.3 %) as a white solid.

ESI-MS (*m/z*): $[M+H]^+$ 201.9; $^1$H NMR (400 MHz, DMSO-$d_6$): δ 11.84 (s, 1H), 8.21–8.18 (m, 1H), 7.47 (dd, *J* = 8.8, 1.6 Hz, 1H), 7.39 (d, *J* = 8.8 Hz, 1H), 5.66 (s, 2H); $^{13}$C NMR (101 MHz, DMSO-$d_6$): δ 150.2, 142.1, 125.4 (q, *J* = 270.9 Hz), 122.3 (d, *J* = 2.8 Hz), 119.0 (d, *J* = 4.3 Hz), 117.9 (q, *J* = 31.6 Hz), 113.1, 110.3; $^{19}$F NMR (376 MHz, DMSO-$d_6$): δ –58.99 (s, 3F).

**5-(Chlorodifluoromethyl)-1*H*-indazol-3-amine (51c)**

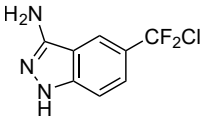

By-product of **51d**. Up to 20 % yield under reflux conditions in conc. HCl from intermediate **54d**, but unstable and not feasible to isolate the pure title compound **51c**.

ESI-MS (*m/z*): $[M+H]^+$ 218.0 / 220.0 (3:1).

**5-(Bromodifluoromethyl)-1*H*-indazol-3-amine (51d)**

Synthetically not accessible from intermediate **54d**.

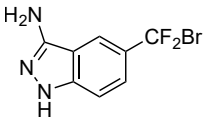

**5-(Difluoromethyl)benzo[*d*]isoxazol-3-amine (52a)**

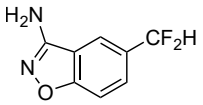

Acetohydroxamic acid (438.7 mg, 5.84 mmol, 1 eq) was added to a suspension of **47** (1.0 g, 5.84 mmol, 1 eq) and *t*-BuOK (655.7 mg, 5.84 mmol, 1 eq) in 10 mL dry DMF. After 18 h, the reaction mixture was concentrated under reduced pressure. The residue was dissolved in EtOAc, washed three times with $H_2O$ and with brine. The organic phase was dried over $Na_2SO_4$ and the solvent was removed *in vacuo*. The crude product was purified by silica gel column chromatography (eluent: *n*-hexane / EtOAc 80:20 to 60:40) to provide the title compound **52a** (471 mg, 43.8 %) as a white crystalline solid.

ESI-MS (*m/z*): $[M+H]^+$ 184.9; $^1$H NMR (300 MHz, DMSO-$d_6$): δ 8.14 (s, 1H), 7.73–7.70 (m, 1H), 7.58 (dd, *J* = 8.7, 0.6 Hz, 1H), 7.15 (t, *J* = 56.0 Hz, 1H), 6.58 (s, 2H); $^{13}$C NMR (75 MHz, DMSO-$d_6$): δ 162.9 (t, *J* = 1.4 Hz), 158.7, 128.3 (t, *J* = 22.6 Hz), 127.7 (t, *J* = 5.8 Hz), 119.9 (t, *J* = 6.4 Hz), 117.1, 114.9 (t, *J* = 235.9 Hz), 110.0; $^{19}$F NMR (282 MHz, DMSO-$d_6$): δ –107.91 (d, *J* = 56.3 Hz, 2F).

**5-(Trifluoromethyl)benzo[*d*]isoxazol-3-amine (52b)**

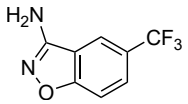

A solution of 2-fluoro-5-(trifluoromethyl)benzonitrile (700.5 mg, 3.70 mmol, 1 eq) in dry DMF (3.5 mL) was added to a suspension of *N*-Hydroxyacetamide (278.1 mg, 3.70 mmol, 1 eq) and *t*-BuOK (655.7 mg, 5.84 mmol, 1 eq) in 6.5 mL dry DMF. After 18 h, the reaction mixture was concentrated under reduced pressure. The crude product was purified by silica gel column chromatography (eluent: *n*-hexane / EtOAc 90:10 to 50:50) to provide the title compound **52b** (295.8 mg, 39.5 %) as a white solid.

ESI-MS (*m/z*): $[M+H]^+$ 203.0; $^1$H NMR (400 MHz, DMSO-$d_6$): δ 8.38–8.33 (m, 1H), 7.86 (dd, *J* = 8.8, 1.5 Hz, 1H), 7.68 (d, *J* = 8.8 Hz, 1H), 6.67 (s, 2H); $^{13}$C NMR (101 MHz, DMSO-$d_6$): δ 163.4, 158.6, 126.8 (d, *J* = 3.1 Hz), 124.4 (q, *J* = 271.8 Hz), 123.1 (q, *J* = 32.0 Hz), 120.2 (d, *J* = 4.1 Hz), 117.3, 110.7; $^{19}$F NMR (376 MHz, DMSO-$d_6$): δ –59.82 (s, 3F).

**5-(Bromodifluoromethyl)benzo[*d*]isoxazol-3-amine (52d)**

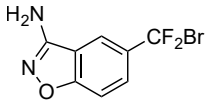

Intermediate **55d** (100 mg, 0.299 mmol) was dissolved in a solution of 4 M HCl in 1,4-dioxane (5 mL) at 0 °C. The reaction mixture was stirred at 0 °C for 30 min, then for 24 h at room temperature. $H_2O$ (12 mL) was poured to the mixture at 0 °C, followed by addition of sat. aq. $NaHCO_3$ solution (until pH > 8). The biphasic mixture was extracted with DCM (3 × 10 mL). The combined organic layers were dried over $Na_2SO_4$ and the solvent was removed *in vacuo*. The crude product was purified by silica gel column chromatography (eluent: *n*-hexane / EtOAc 90:10 to 50:50) to provide the title compound **52d** (35.7 mg, 89.0 %) as a white solid.

ESI-MS (*m/z*): $[M+H]^+$ 263.0 / 265.0 (1:1), $[2M-Br]^+$ 445.1 / 447.1 (1:1); $^1$H NMR (300 MHz, $CDCl_3$): δ 7.86–7.82 (m, 2H), 7.68 (d, *J* = 9.4 Hz, 1H), 1.42 (s, 18H); $^{13}$C NMR (75 MHz, $CDCl_3$): δ 164.8, 155.1, 149.3, 134.9 (t, *J* = 24.3 Hz), 126.9 (t, *J* = 4.5 Hz), 118.5, 111.5; $^{19}$F NMR (282 MHz, $CDCl_3$): δ –43.95 (d, 2F)

**(6-(Difluoromethyl)imidazo[1,5-*a*]pyridin-3-amine (53a)**

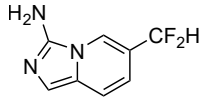

To a solution of crude **50a** (1.04 g, 6.58 mmol, 1 eq) in dry toluene (50 mL) was added $Et_3N$ (1.10 mL, 7.90 mmol, 0.73 g cm$^{-3}$, 1.2 eq), followed by dropwise addition of cyanogen bromide (836 mg, 7.90 mmol, 1.2 eq) in toluene (1.7 mL). The reaction mixture was stirred for 30 min at room temperature, then the solvent was removed *in vacuo*. The residue was purified by reversed-phase chromatography (eluent: $H_2O$ / ACN) to provide the title compound **53a** (920 mg, 76.3 %) as a yellow solid.

ESI-MS (*m/z*): $[M+H]^+$ 184.04; $^1$H NMR (400 MHz, DMSO-$d_6$): δ 8.09 (d, *J* = 0.9 Hz, 1H), 7.34 (d, *J* = 9.5 Hz, 1H), 6.94 (s, 1H), 6.87 (t, *J* = 55.3 Hz, 1H), 6.42 (dd, *J* = 9.5, 0.9 Hz, 1H), 6.08 (s, 2H); $^{13}$C NMR (101 MHz, DMSO-$d_6$): δ 142.8, 125.0, 120.5 (t, *J* = 11.3 Hz), 119.3, 117.2 (t, *J* = 23.1 Hz), 115.9, 114.5 (t, *J* = 234.0 Hz), 110.7 (t, *J* = 3.3 Hz); $^{19}$F NMR (376 MHz, DMSO-$d_6$): δ –110.76 (dd, *J* = 55.3, 2.8 Hz, 2F).

**6-(Trifluoromethyl)imidazo[1,5-*a*]pyridin-3-amine (53b)**

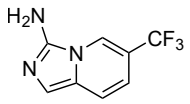

To a solution of (5-(trifluoromethyl)pyridin-2-yl)methanamine **50b** (800 mg, 4.54 mmol, 1 eq) in dry toluene (40 mL) was added $Et_3N$ (756 µL, 5.45 mmol, 0.73 g cm$^{-3}$, 1.2 eq), followed by dropwise addition of cyanogen bromide (577 mg, 5.45 mmol, 1.2 eq) in toluene (10 mL). The reaction mixture was stirred for 36 h at room temperature, then the solvent was removed *in vacuo*. The residue was purified by reversed-phase chromatography (eluent: $H_2O$ / ACN) to provide the title compound **53b** (563 mg, 61.6 %) as a yellow solid.

ESI-MS (*m/z*): $[M+H]^+$ 202.02; $^1$H NMR (400 MHz, $CDCl_3$): δ 7.90–7.83 (m, 1H), 7.33 (d, *J* = 9.6 Hz, 1H), 7.12 (s, 1H), 6.55 (dd, *J* = 9.6, 1.3 Hz, 1H), 4.14 (bs, 2H); $^{13}$C NMR (101 MHz, $CDCl_3$): δ 140.3, 126.8, 123.8 (dd, *J* = 541.2, 270.6 Hz), 119.9, 119.3 (q, *J* = 6.3 Hz), 116.8, 116.1 (dd, *J* = 67.3, 33.7 Hz), 112.0; $^{19}$F NMR (376 MHz, $CDCl_3$): δ –63.75 (s, 3F).

***tert*-Butyl 3-(bis(*tert*-butoxycarbonyl)amino)-5-(difluoromethyl)-1*H*-indazole-1-carboxylate (54a)**

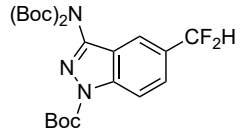

A solution of **51a** (544.0 mg, 2.97 mmol, 1 eq), di-*tert*-butyldicarbonate (2.14 g, 9.80 mmol, 3.3 eq) and DMAP (18 mg, 0.149 mmol, 0.05 eq) in dry THF (50 mL) under argon atmosphere was coold to 0 °C. $Et_3N$ (2.47 mL, 17.8 mmol, 6 eq) was added dropwise. After 15 min, the reaction mixtures was warmed up to room temperature and stirred for 18 h. The solvent was removed under reduced pressure. The residue was dissolved in EtOAc and washed with 2 M HCl (2 × 10 mL), sat. $NaHCO_3$ and Brine. The organic phase was dried over $Na_2SO_4$ and the solvent was removed *in vacuo*. The crude product was purified by silica gel column chromatography (eluent: *n*-hexane / EtOAc 95:05 to 70:30) to provide the title compound **54a** (1.24 g, 86.1 %) as a colorless foam.

ESI-MS (*m/z*): $[M+Na]^+$ 506.6; $^1$H NMR (300 MHz, DMSO-$d_6$): δ 8.25 (d, *J* = 8.8 Hz, 1H), 7.94 (s, 1H), 7.86 (d, *J* = 8.9 Hz, 1H), 7.21 (t, *J* = 55.7 Hz, 1H), 1.66 (s, 9H), 1.39 (s, 18H); $^{13}$C NMR (75 MHz, DMSO-$d_6$): δ 149.8, 147.8, 144.9, 140.8, 130.4 (t, *J* = 22.7 Hz), 126.8 (t, *J* = 4.7 Hz), 120.9, 118.2 (t, *J* = 7.2 Hz), 115.4, 114.6 (t, *J* = 235.9 Hz), 85.7, 83.9, 27.6, 27.3; $^{19}$F NMR (282 MHz, DMSO-$d_6$): δ –108.65 (s, 2F).

**_tert_-Butyl 3-(bis(_tert_-butoxycarbonyl)amino)-5-(bromodifluoromethyl)-1_H_-indazole-1-carboxylate (54d)**

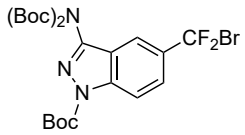


The title compound was prepared following General Procedure **K** using **54a** (2.59 g, 5.36 mmol, 1 eq) and DBDMH (1.53 g, 5.36 mmol, 1 eq) in degassed $CCl_4$ (100 mL). The reaction mixture was illuminated for 4 d. The crude product was purified by silica gel column chromatography (eluent: *n*-hexane / EtOAc 90:10 to 75:25) to provide the title compound **54d** (2.00 g, 66.3 %) as a pale-yellow foam.

ESI-MS (*m/z*): $[M+Na]^+$ 583.9 / 585.9 (1:1); $^1$H NMR (300 MHz, DMSO-$d_6$): δ 8.28 (d, *J* = 8.9 Hz, 1H), 8.10 (s, 1H), 7.96 (dd, *J* = 9.0, 1.5 Hz, 1H), 1.66 (s, 9H), 1.38 (s, 18H); $^{13}$C NMR (75 MHz, DMSO-$d_6$): δ 149.6, 147.7, 145.2, 140.7, 133.2 (t, *J* = 23.7 Hz), 125.8 (t, *J* = 4.6 Hz), 120.7, 116.6, 115.7, 114.5, 86.0, 83.9, 27.6, 27.3; $^{19}$F NMR (282 MHz, DMSO-$d_6$): δ –42.95 (s, 2F).

**_tert_-Butyl (_tert_-butoxycarbonyl)(5-(difluoromethyl)benzo[_d_]isoxazol-3-yl)carbamate (55a)**

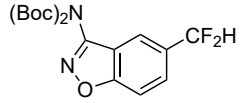


To a solution of **52a** (1.71 g, 9.28 mmol, 1 eq), di-*tert*-butyldicarbonate (4.45 g, 20.4 mmol, 2.2 eq) and DMAP (113 mg, 0.928 mmol, 0.1 eq) in dry THF (50 mL) under argon atmosphere was coold to 0 °C. $Et_3N$ (5.15 mL, 37.1 mmol, 4.4 eq) was added dropwise. After 15 min, the reaction mixtures was warmed up to room temperature and stirred for 18 h. The solvent was removed under reduced pressure. The residue was dissolved in EtOAc and washed with 2 M HCl (2 × 25 mL), sat. $NaHCO_3$ and Brine. The organic phase was dried over $Na_2SO_4$ and the solvent was removed *in vacuo*. The crude product was purified by silica gel column chromatography (eluent: *n*-hexane / EtOAc 98:02 to 80:20) to provide the title compound **55a** (2.90 g, 81.3 %) as a colorless foam.

ESI-MS (*m/z*): $[M+Na]^+$ 406.8; $^1$H NMR (300 MHz, $CDCl_3$): δ 7.74–7.66 (m, 3H), 6.78 (t, *J* = 56.3 Hz, 1H), 1.42 (s, 18H); $^{13}$C NMR (75 MHz, $CDCl_3$): δ 165.1, 154.9, 149.4, 118.9–118.8 (m, 2C), 131.1 (t, *J* = 23.0 Hz), 127.7 (t, *J* = 5.3 Hz), 114.2 (t, *J* = 239.7 Hz), 111.5, 84.9, 27.9; $^{19}$F NMR (282 MHz, $CDCl_3$): δ –110.50 (d, 2F).

**_tert_-Butyl (5-(bromodifluoromethyl)benzo[_d_]isoxazol-3-yl)(_tert_-butoxycarbonyl)carbamate (55d)**

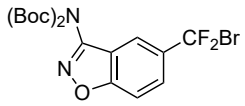


The title compound was prepared following General Procedure **K** using **55a** (2.90 g, 7.55 mmol, 1 eq) and DBDMH (6.47 g, 22.6 mmol, 3 eq) in degassed $CCl_4$ (100 mL). The reaction mixture was illuminated for 10 d. The crude product was purified by silica gel column chromatography (eluent: *n*-hexane / EtOAc 98:2 to 80:20) to provide the title compound **55d** (2.08 g, 59.6 %) as a pale-yellow foam.

ESI-MS (*m/z*): $[M+Na]^+$ 485.0 / 487.0 (1:1); $^1$H NMR (300 MHz, $CDCl_3$): δ 7.86–7.82 (m, 2H), 7.68 (d, *J* = 9.4 Hz, 1H), 1.42 (s, 18H); $^{13}$C NMR (75 MHz, $CDCl_3$): δ 164.8, 155.1, 149.3, 134.9 (t, *J* = 24.3 Hz), 126.9 (t, *J* = 4.5 Hz), 118.5, 111.5, 85.1, 27.8; $^{19}$F NMR (282 MHz, $CDCl_3$): δ –43.95 (d, 2F).

**_tert_-Butyl (_tert_-butoxycarbonyl)(6-(difluoromethyl)imidazo[1,5-_a_]pyridin-3-yl)carbamate (56a)**

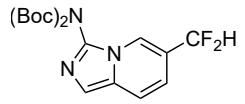


To a solution of **53a** (760 mg, 4.15 mmol, 1 eq), di-*tert*-butyldicarbonat (1.99 g, 9.13 mmol, 2.2 eq) and DMAP (25.3 mg, 0.207 mmol, 0.05 eq) in dry THF (60 mL) under argon atmosphere was coold to 0 °C. $Et_3N$ (2.30 mL, 16.6 mmol, 0.73 g cm$^{-3}$, 4.0 eq) was added dropwise. After 15 min, the reaction mixtures was warmed up to room temperature and stirred for 2.5 h. The solvent was removed under reduced pressure. The residue was dissolved in EtOAc and washed with 2 M HCl (2 × 25 mL), sat. $NaHCO_3$ and Brine. The organic phase was dried over $Na_2SO_4$ and the solvent was removed *in vacuo*. The crude product was purified by silica gel column chromatography (eluent: *n*-hexane / EtOAc 70:30) to provide the title compound **56a** (1.35 g, 85.0 %) as a colorless crystalline solid.

ESI-MS (*m/z*): $[M+Na]^+$ 406.26; $^1$H NMR (400 MHz, $CDCl_3$): δ 7.78 (s, 1H), 7.51 (d, *J* = 9.4 Hz, 1H), 7.46 (d, *J* = 0.7 Hz, 1H), 6.84 (dd, *J* = 9.5, 1.1 Hz, 1H), 6.61 (t, *J* = 55.7 Hz, 1H), 1.37 (s, 18H); $^{13}$C NMR (101 MHz, $CDCl_3$): δ 149.9, 130.8, 129.5, 121.1 (t, *J* = 23.4 Hz), 119.6, 119.2, 118.6 (t, *J* = 10.4 Hz), 115.6 (t, *J* = 3.8 Hz), 113.3 (t, *J* = 239.1 Hz), 84.5, 27.9; $^{19}$F NMR (376 MHz, $CDCl_3$): δ –113.90 (dd, *J* = 55.8, 2.2 Hz, 2F).

### 6.3.7 Amino Acids

**Ethyl 2,2-difluoro-2-(*p*-tolyl)acetate (58)**

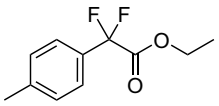

To a solution of 1-iodo-4-methylbenzene (1.0 g, 4.59 mmol, 1 eq) and ethyl bromodifluoroacetate (647 µL, 5.05 mmol, 1.58 g cm$^{-3}$, 1.1 eq) under argon atmosphere was added activated $Cu^0$ powder (874.4 mg, 13.76 mmol, 1 eq). The reaction mixture was stirred at 60 °C for 26 h. The crude mixture was filtered through a pad of diatomaceous earth and washed with $Et_2O$. The organic layer was washed with sat. $NH_4Cl$ (2 × 30 mL) and brine (2 × 30 mL), dried over $Na_2SO_4$ and the solvent was removed *in vacuo*. The crude product was purified by silica gel column chromatography (eluent: PE 40/60 / $Et_2O$ 98:02) to provide the title compound **58** (651.5 mg, 66.3 %) as a colorless oil.

*Activation of copper powder*: $Cu^0$ powder (874.4 mg, 13.76 mmol, <425 µm) was stirred in aq. 6 M HCl (5 mL) for 10 min at room temperature. The solution was decanted and the procedure was repeated with $H_2O$ (5 mL), MeOH (5 mL) and acetone (5 mL). Before use, the $Cu^0$ powder was dried under vacuum for 15 min.

EI-MS (*m/z*): $[M]^+$ 214.01; $^1$H NMR (600 MHz, DMSO-$d_6$): δ 7.47 (d, *J* = 8.2 Hz, 2H), 7.35 (d, *J* = 7.9 Hz, 2H), 4.29 (q, *J* = 7.1 Hz, 2H), 2.35 (s, 3H), 1.21 (t, *J* = 7.9 Hz, 2H); $^{13}$C NMR (151 MHz, $CDCl_3$): δ 169.7 (t, *J* = 36.8 Hz), 142.0, 129.6, 129.1 (t, *J* = 25.7 Hz), 125.6, 113.3 (t, *J* = 252.1 Hz), 21.5; $^{19}$F NMR (565 MHz, $CDCl_3$): δ –105.13 (s, 2F).

**2,2-Difluoro-2-(*p*-tolyl)acetic acid (59)**

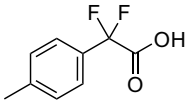

To solution of **58** (5.18 g, 24 mmol, 1 eq) in MeOH (70 mL) was added aq. 1 M $K_2CO_3$ (70 mL). The reaction mixture was stirred at room temperature for 18 h. MeOH was removed *in vacuo*, then the mixture was diluted with $Et_2O$ and the biphasic mixture was extracted three times with sat. $NaHCO_3$. The combined aq. layers were cooled to 0 °C and $Et_2O$ was added. The biphasic mixture was acidified with conc. HCl to pH = 1. After that, the mixture was extracted three times with $Et_2O$, the combined organic phases were washed with brine and dried over $Na_2SO_4$. The solvent was removed *in vacuo* to obtain the title compound **59** (4.37 g, 97.1 %) as a white solid.

ESI-MS (*m/z*): $[M-H]^-$ 185.07; $^1$H NMR (600 MHz, $CDCl_3$): δ 10.80 (s, 1H), 7.51 (d, *J* = 8.2 Hz, 2H), 7.27 (d, *J* = 8.0 Hz, 2H), 2.40 (s, 3H); $^{13}$C NMR (151 MHz, $CDCl_3$): δ 163.4 (t, *J* = 35.0 Hz), 141.5, 129.6, 129.1 (t, *J* = 25.5 Hz), 125.0 (t, *J* = 5.8 Hz), 113.6 (t, *J* = 250.4 Hz), 63.3, 20.8, 13.6; $^{19}$F NMR (565 MHz, $CDCl_3$): δ –101.52 (s, 2F).

**2,2-Difluoro-2-(*p*-tolyloxy)acetic acid (60)**

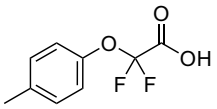

The title compound was prepared following General Procedure **L** using *p*-cresol (500 mg, 4.62 mmol, 1.0 eq), NaH (60 % dispersion in mineral oil; 203 mg, 5.09 mmol, 1.1 eq) and **1a** (1.08 g, 5.09 mmol, 1.1 eq) in dry 1,4-dioxane (15 mL). The title compound **60** (882 mg, 94.3 %) was obtained as a yellow oil.

ESI-MS (*m/z*): $[M-H]^-$ 201.06; $^1$H NMR (600 MHz, DMSO-$d_6$): δ 7.22 (d, $J$ = 8.3 Hz, 2H), 7.10 (d, $J$ = 8.4 Hz, 2H), 3.56 (1,4-dioxane), 2.29 (s, 3H); $^{13}$C NMR (151 MHz, DMSO-$d_6$): δ 160.8 (t, $J$ = 39.6 Hz), 147.0, 135.9, 130.3, 121.2, 114.3 (t, $J$ = 271.2 Hz), 66.4 (1,4-dioxane), 20.3; $^{19}$F NMR (565 MHz, DMSO-$d_6$): δ –76.60 (s, 2F).

**2,2-Difluoro-2-(*m*-tolyloxy)acetic acid (61)**

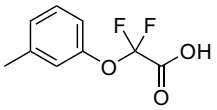

The title compound was prepared following General Procedure **L** using *m*-cresol (20.0 g, 185 mmol, 1.0 eq), NaH (60 % dispersion in mineral oil; 8.13 g, 203 mmol, 1.1 eq) and **1a** (43.3 g, 203 mmol, 1.1 eq) in dry 1,4-dioxane (700 mL). The title compound **61** (31.1 g, 83.4 %) was obtained as a yellow oil.

ESI-MS (*m/z*): $[M-H]^-$ 200.85; $^1$H NMR (400 MHz, DMSO-$d_6$): δ 7.31 (t, $J$ = 7.8 Hz, 1H), 7.17–7.08 (m, 1H), 7.05–7.01 (m, 2H), 2.32 (s, 3H); $^{13}$C NMR (101 MHz, DMSO-$d_6$): δ 160.7 (t, $J$ = 39.5 Hz), 149.2, 139.9, 129.7, 127.1, 121.7, 118.1, 114.2 (t, $J$ = 271.6 Hz), 20.8; $^{19}$F NMR (376 MHz, DMSO-$d_6$): δ –76.08 (s, 2F).

**1-(Bromodifluoromethyl)-4-methylbenzene (62)**

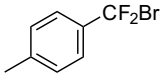

To a solution of **59** (418.5 mg, 2.25 mmol, 1.0 eq) in DCM (2.8 mL) was added a catalytic amount of DMF (17.3 µL, 0.23 mmol, 0.95 g cm$^{-3}$, 0.1 eq) and oxalyl chloride (1.70 mL, 3.37 mmol, 2 M in DCM, 1.5 eq) at 0 °C. The reaction mixture was stirred at room temperature for 3 h, then concentrated *in vacuo*. The crude acyl chloride was added degassed $BrCCl_3$ (7 mL), DMAP (68.7 mg, 0.56 mmol, 0.25 eq) and sodium-*N*-hydroxy-2-thiopyridone (402.2 mg, 2.70 mmol, 1.2 eq). The reaction mixture was stirred under argon atmosphere and illuminated by a 300 W sun lamp for 20 h, then concentrated *in vacuo*. The crude product was purified by silica gel column chromatography (eluent: PE 40/60 / EtOAc 95:5) to provide the title compound **62** (201.9 mg, 40.6 %) as a colorless oil.

EI-MS (*m/z*): $[M]^+$ 218.9 / 220.9 (1:1); $^1$H NMR (400 MHz, $CDCl_3$): δ 7.50 (d, *J* = 8.3 Hz, 2H), 7.25 (d, *J* = 7.9 Hz, 2H), 2.40 (s, 3H); $^{13}$C NMR (101 MHz, $CDCl_3$): δ 141.8, 135.7 (t, *J* = 23.5 Hz), 129.4, 124.4 (t, *J* = 5.1 Hz), 118.8 (t, *J* = 303.5 Hz), 21.5; $^{19}$F NMR (376 MHz, $CDCl_3$): δ –42.57 (s, 2F).

**1-(Bromodifluoromethoxy)-4-methylbenzene (63)**

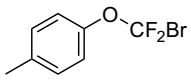


The title compound was prepared following General Procedure **A** using **60** (18.7 g, 92.5 mmol, 1.0 eq), DMF (712 µL, 9.25 mmol, 0.95 g cm$^{-3}$, 0.1 eq) and oxalyl chloride (69.4 mL, 138.7 mmol, 2 M in DCM, 1.5 eq) in DCM (115 mL). After the first reaction step and concentration of the reaction mixture, $BrCCl_3$ (260 mL), DMAP (2.82 g, 23.1 mmol, 0.25 eq) and sodium-*N*-hydroxy-2-thiopyridone (16.6 g, 111.0 mmol, 1.2 eq) were added for the second reaction step. The crude product was purified by silica gel column chromatography (eluent: *n*-hexane / EtOAc 97:3) to provide the title compound **63** (11.2 g, 51.1 %) as a yellow oil.

EI-MS (*m/z*): $[M]^+$ 235.9 / 237.8 (1:1); $^1$H NMR (400 MHz, $CDCl_3$): δ 7.20 (d, *J* = 8.3 Hz, 2H), 7.13 (d, *J* = 8.7 Hz, 2H), 2.37 (s, 3H); $^{13}$C NMR (101 MHz, $CDCl_3$): δ 148.9 (t, *J* = 2.0 Hz), 137.0, 130.3, 121.3, 115.0 (t, *J* = 308.2 Hz), 21.0; $^{19}$F NMR (376 MHz, $CDCl_3$): δ –15.33 (s, 2F).

**1-(Bromodifluoromethoxy)-4-methylbenzene (64)**

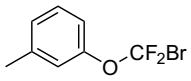


The title compound was prepared following General Procedure **A** using **61** (30.0 g, 148.4 mmol, 1.0 eq), DMF (2.8 mL, 14.8 mmol, 0.95 g cm$^{-3}$, 0.1 eq) and oxalyl chloride (111 mL, 222 mmol, 2 M in DCM, 1.5 eq) in DCM (115 mL). After the first reaction step and concentration of the reaction mixture, $BrCCl_3$ (490 mL), DMAP (4.5 g, 37.1 mmol, 0.25 eq) and sodium-*N*-hydroxy-2-thiopyridone (22.1 g, 148.4 mmol, 1.0 eq) were added for the second reaction step. The crude product was purified by silica gel column chromatography (eluent: *n*-hexane / EtOAc 99:1) to provide the title compound **64** (19.0 g, 53.9 %) as a yellow oil.

EI-MS (*m/z*): $[M]^+$ 236.0 / 238.0 (1:1); $^1$H NMR (400 MHz, $CDCl_3$): δ 7.31–7.26 (m, 1H), 7.14 (d, *J* = 7.5 Hz, 1H), 7.06 (d, *J* = 4.8 Hz, 1H), 2.40 (s, 3H); $^{13}$C NMR (101 MHz, $CDCl_3$): δ 151.0, 140.3, 129.5, 127.9, 122.1, 118.4, 114.7 (t, *J* = 308.4 Hz), 21.5; $^{19}$F NMR (376 MHz, $CDCl_3$): δ –16.37 (s, 2F).

**(Bromodifluoromethyl)(*p*-tolyl)sulfane (65)**

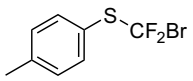


To a solution of 4-methylbenzenethiol (2.0 g, 16.1 mmol, 1.0 eq) in dry DMF (32 mL) was added NaH (60 % dispersion in mineral oil; 966 mg, 24.2 mmol, 1.5 eq) at 0 °C. The reaction mixture was stirred at room temperature for 30 min, then $CF_2Br_2$ was added at 0 °C and the mixture was stirred further 3 h at 0 °C. The remaining NaH was quenched with $H_2O$ (400 mL) and the mixture was extracted with EtOAc (3 × 100 mL). The combined organic layers were washed with brine (100 mL), dried over $Na_2SO_4$ and concentrated *in vacuo*. The crude product was purified by silica gel column chromatography (eluent: PE 40/60 / $Et_2O$ 99:1) to provide the title compound **65** (2.55 g, 62.5 %) as a colorless oil.

EI-MS (*m/z*): $[M]^+$ 251.9 / 253.9 (1:1); $^1$H NMR (400 MHz, $CDCl_3$): δ 7.54 (d, *J* = 8.1 Hz, 2H), 7.24 (d, *J* = 7.9 Hz, 2H), 2.40 (s, 3H); $^{13}$C NMR (101 MHz, $CDCl_3$): δ 141.8, 136.6, 130.4, 123.9, 119.7 (t, *J* = 338.3 Hz), 21.6; $^{19}$F NMR (376 MHz, $CDCl_3$): δ –22.34 (s, 2F).

**1-(Bromodifluoromethyl)-4-(bromomethyl)benzene (66)**

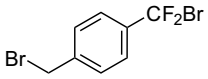


The title compound was prepared following General Procedure **M** using **62** (1.17 g, 5.30 mmol, 1.0 eq), NBS (1.04 g, 5.83 mmol, 1.1 eq) and ABCN (389 mg, 1.59 mmol, 0.3 eq) in $CCl_4$ (15 mL). The crude product **66** was used without further purification for the next synthesis step of **71**.

**1-(Bromodifluoromethoxy)-4-(bromomethyl)benzene (67)**

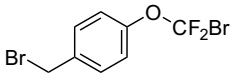


The title compound was prepared following General Procedure **M** using **63** (10.6 g, 44.8 mmol, 1.0 eq), NBS (8.76 g, 49.2 mmol, 1.1 eq) and ABCN (3.28 g, 13.4 mmol, 0.3 eq) in $CCl_4$ (125 mL). The crude product **67** was used without further purification for the next synthesis step of **72**.

**1-(Bromodifluoromethoxy)-3-(bromomethyl)benzene (68)**

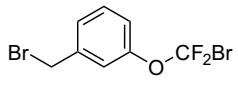


The title compound was prepared following General Procedure **M** using **64** (2.00 g, 8.44 mmol, 1.0 eq), NBS (1.65 g, 9.28 mmol, 1.1 eq) and ABCN (619 mg, 2.53 mmol, 0.3 eq) in benzene (25 mL). The crude product **68** was used without further purification for the next synthesis step of **73**.

**(Bromodifluoromethyl)(4-(bromomethyl)phenyl)sulfane (69)**

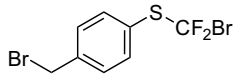


The title compound was prepared following General Procedure **M** using **65** (2.44 g, 9.63 mmol, 1.0 eq), NBS (1.88 g, 10.6 mmol, 1.1 eq) and ABCN (706 mg, 2.89 mmol, 0.3 eq) in $CCl_4$ (27 mL). The crude product **69** was used without further purification for the next synthesis step of **74**.

**Diethyl 2-acetamido-2-(4-(bromodifluoromethyl)benzyl)malonate (71)**

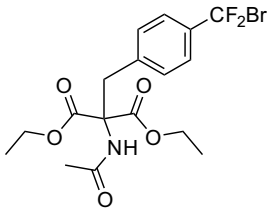


The title compound was prepared following General Procedure **N** using crude **66** (5.30 mmol, 1.0 eq), diethylacetamidomalonate (1.15 g, 5.30 mmol, 1.0 eq), $K_2CO_3$ (1.47 g, 10.6 mmol, 2.0 eq) and KI (880 mg, 5.30 mmol, 1.0 eq) in ACN (30 mL). The crude product was purified by silica gel column chromatography (eluent: PE 40/60 / EtOAc 75:25) to provide the title compound **71** (1.14 g, 49.1 % over 2 steps) as a white solid.

ESI-MS (*m/z*): $[M+Na]^+$ 457.91 / 459.91 (1:1); $^1$H NMR (400 MHz, $CDCl_3$): δ 7.49 (d, *J* = 8.4 Hz, 2H), 7.09 (d, *J* = 8.3 Hz, 2H), 6.55 (s, 1H), 4.41–4.10 (m, 4H), 3.70 (s, 2H), 2.03 (s, 3H), 1.29 (t, *J* = 7.1 Hz, 6H); $^{13}$C NMR (151 MHz, $CDCl_3$): δ 169.4, 167.4, 139.2, 137.2 (t, *J* = 23.8 Hz), 130.2, 124.5 (t, *J* = 5.1 Hz), 118.4 (t, *J* = 303.6 Hz), 67.1, 63.0, 37.7, 23.2, 14.1; $^{19}$F NMR (565 MHz, $CDCl_3$) δ –43.15 (s, 2F).

**Diethyl 2-acetamido-2-(4-(bromodifluoromethoxy)benzyl)malonate (72)**

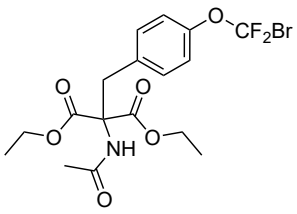

The title compound was prepared following General Procedure **N** using crude **67** (44.8 mmol, 1.0 eq), diethylacetamidomalonate (9.72 g, 44.8 mmol, 1.0 eq), $K_2CO_3$ (12.4 g, 89.5 mmol, 2.0 eq) and KI (7.43 g, 44.8 mmol, 1.0 eq) in ACN (275 mL). The crude product was purified by silica gel column chromatography (eluent: PE 40/60 / EtOAc 75:25) to provide the title compound **72** (8.58 g, 45.1 % over 2 steps) as a white solid.

ESI-MS (*m/z*): $[M+Na]^+$ 473.92 / 475.91 (1:1); $^1$H NMR (600 MHz, $CDCl_3$): δ 7.13 (d, *J* = 8.5 Hz, 2H), 7.04 (d, *J* = 8.6 Hz, 2H), 6.56 (s, 1H), 4.37–4.17 (m, 4H), 3.66 (s, 2H), 2.03 (s, 3H), 1.28 (t, *J* = 7.1 Hz, 6H); $^{13}$C NMR (151 MHz, $CDCl_3$): δ 169.3, 167.5, 150.1 (t, *J* = 1.7 Hz), 134.4, 131.3, 121.3, 114.6 (t, *J* = 308.9 Hz), 67.2, 62.9, 37.3, 23.2, 14.1; $^{19}$F NMR (565 MHz, $CDCl_3$) δ –16.82 (s, 2F).

**Diethyl 2-acetamido-2-(3-(bromodifluoromethoxy)benzyl)malonate (73)**

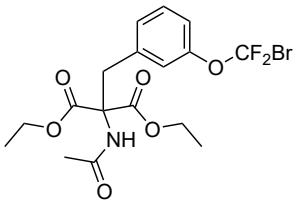

The title compound was prepared following General Procedure **N** using crude **68** (8.44 mmol, 1.0 eq), diethylacetamidomalonate (1.83 g, 8.44 mmol, 1.0 eq), $K_2CO_3$ (2.33 g, 16.9 mmol, 2.0 eq) and KI (1.40 g, 8.44 mmol, 1.0 eq) in ACN (55 mL). The crude product was purified by silica gel column chromatography (eluent: PE 40/60 / EtOAc 75:25) to provide the title compound **73** (2.15 g, 56.2 % over 2 steps) as a pale-yellow solid.

ESI-MS (*m/z*): $[M+Na]^+$ 473.96 / /475.95 (1:1); $^1$H NMR (400 MHz, $CDCl_3$): δ 7.30 (t, *J* = 7.9 Hz, 1H), 7.12 (ddd, *J* = 8.2, 2.2, 0.9 Hz, 1H), 6.97 (d, *J* = 7.7 Hz, 1H), 6.91 (s, 1H), 4.33-4.18 (m, 4H), 3.68 (s, 3H), 2.03 (s, 3H), 1.29 (t, *J* = 7.1 Hz, 6H); $^{13}$C NMR (101 MHz, $CDCl_3$): δ 169.4, 167.4, 150.9, 137.7, 129.7, 128.7, 122.9, 120.3, 114.6 (t, *J* = 308.6 Hz), 67.2, 63.0, 37.6, 23.1, 14.1; $^{19}$F NMR (376 MHz, $CDCl_3$) δ –15.30 (s, 2F).

**Diethyl 2-acetamido-2-(4-((bromodifluoromethyl)thio)benzyl)malonate (74)**

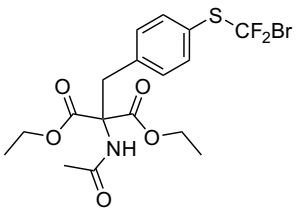

The title compound was prepared following General Procedure **N** using crude **69** (9.63 mmol, 1.0 eq), diethylacetamidomalonate (2.09 g, 9.63 mmol, 1.0 eq), $K_2CO_3$ (2.66 g, 19.2 mmol, 2.0 eq) and KI (1.60 g, 9.63 mmol, 1.0 eq) in ACN (55 mL). The crude product was purified by silica gel column chromatography (eluent: PE 40/60 / EtOAc 90:10) to provide the title compound **74** (3.47 g, 76.9 % over 2 steps) as a pale-yellow solid.

ESI-MS (*m/z*): $[M+Na]^+$ 489.91 / 491.89 (1:1); $^1$H NMR (400 MHz, $CDCl_3$): δ 7.53 (d, *J* = 8.1 Hz, 2H), 7.07 (d, *J* = 8.2 Hz, 2H), 6.55 (s, 1H), 4.30–4.21 (m, 4H), 3.68 (s, 2H), 2.02 (s, 3H), 1.27 (t, *J* = 7.1 Hz, 6H); $^{13}$C NMR (101 MHz, $CDCl_3$): δ 169.3, 167.4, 139.0, 136.3, 131.1, 126.1, 119.2 (t, *J* = 338.4 Hz), 67.1, 63.0, 37.7, 23.1, 14.1; $^{19}$F NMR (376 MHz, $CDCl_3$): δ –23.42 (s, 2F).

**Diethyl 2-acetamido-2-(4-((bromodifluoromethyl)sulfonyl)benzyl)malonate (75)**

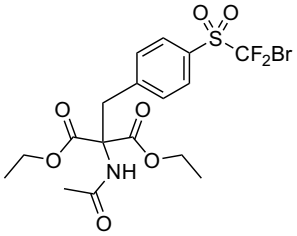

To a solution of **74** (200 mg, 0.427 mmol, 1.0 eq) in dry DCM (5 mL) was added mCPBA (316 mg, 1.82 mmol, 3.0 eq) at 0 °C. The reaction mixture was stirred at room temperature for 18 h, then additional mCBPA (160 mg, 0.92 mmol, 1.5 eq) and dry DCM (2 mL) were added. After further 22 h of stirring, the solvent was removed *in vacuo*. The residue was dissolved in EtOAc (50 mL), washed with sat. $NaHCO_3$ (3 × 15 mL), brine (15 mL), dried over $Na_2SO_4$ and the solvent was concentrated *in vacuo*. The crude product was purified by reversed-phase chromatography (C18, eluent: $H_2O$ / ACN with 0.1 % TFA) and the resulting fractions were freeze-dried to provide the title compound **75** (155.2 mg, 72.6 %) as a white solid.

ESI-MS (*m/z*): $[M+H]^+$ 500.06 / 502.05 (1:1); $^1$H NMR (400 MHz, $CDCl_3$): δ 7.92 (d, *J* = 8.4 Hz, 2H), 7.30 (d, *J* = 8.5 Hz, 2H), 6.56 (s, 1H), 4.40–4.17 (m, 4H), 3.81 (s, 2H), 2.04 (s, 3H), 1.29 (t, *J* = 7.1 Hz, 6H); $^{13}$C NMR (101 MHz, $CDCl_3$): δ 169.6, 167.1, 145.4, 131.4 (s, 2C), 129.0, 121.1 (t, *J* = 348.7 Hz), 66.9, 63.3, 38.0, 23.2, 14.2; $^{19}$F NMR (376 MHz, $CDCl_3$): δ –57.56 (s, 2F).

**2-Acetamido-3-(4-(bromodifluoromethoxy)phenyl)propanoic acid (76)**

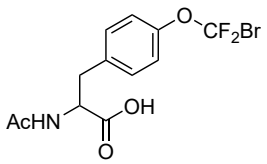


To a solution of **72** (808 mg, 1.79 mmol, 1.0 eq) in MeOH (12 mL) and $H_2O$ (4 mL) was added NaOH (357 g, 8.93 mmol, 40.0 eq) at 0 °C. After 15 min, the reaction mixture stirred at room temperature for 1 h, then at 80 °C for 3 h. MeOH was removed *in vacuo*, then $H_2O$ and $Et_2O$ were added and the biphasic mixture was acidified with HCl to pH = 3–5. After that, the mixture was extracted three times with $Et_2O$, the combined organic layers were washed with brine, dried over $Na_2SO_4$ and the solvent was removed *in vacuo*. The crude product was purified by silica gel column chromatography (eluent: DCM / MeOH 98:02 to 86:14 with 0.1 % TFA) to provide the title compound **76** (362.8 mg, 57.7 %) as a colorless solid.

ESI-MS (*m/z*): $[M-H]^-$ 349.94 / 351.93 (1:1); $^1$H NMR (400 MHz, DMSO-$d_6$): δ 7.88 (s, 1H), 7.33 (d, *J* = 8.3 Hz, 2H), 7.19 (d, *J* = 8.1 Hz, 2H), 4.33 (s, 1H), 3.12 (dd, *J* = 13.6, 4.2 Hz, 1H), 2.87 (dd, *J* = 13.6, 8.5 Hz, 1H), 1.77 (s, 3H); $^{13}$C NMR (101 MHz, DMSO-$d_6$): δ 174.6, 169.0, 148.6, 138.3, 130.9, 120.7, 114.4 (t, *J* = 306.9 Hz), 114.4 (t, *J* = 306.9 Hz), 54.5, 36.6, 22.6; $^{19}$F NMR (376 MHz, DMSO-$d_6$): δ –16.28 (s, 2F).

**2-Acetamido-3-(3-(bromodifluoromethoxy)phenyl)propanoic acid (77)**

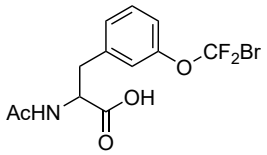


To a solution of **73** (1.82 mg, 4.02 mmol, 1.0 eq) in MeOH (45 mL) and $H_2O$ (15 mL) was added NaOH (357 g, 8.93 mmol, 40.0 eq) at 0 °C. After 15 min, the reaction mixture stirred at room temperature for 4 h. MeOH was removed *in vacuo*, then $H_2O$ and EtOAc were added and the biphasic mixture was acidified at 0 °C with HCl to pH = 3–5. After that, the mixture was extracted three times with EtOAc and the combined organic layers were washed with brine. The solvent was removed *in vacuo* and the crude intermediate was dissolved in THF (45 mL) and $H_2O$ (15 mL). After 3 h stirring at 70 °C, THF was removed *in vacuo* and 1 M HCl (40 mL) was added. The aq. phase was extracted three times with EtOAc. The combined organic layers were washed with brine, dried over $Na_2SO_4$ and the solvent was concentrated *in vacuo* to provide the title compound **77** (1.32 g, 93.3 %) as a pale-yellow solid.

ESI-MS (*m/z*): $[M-H]^-$ 349.99 / 351.99 (1:1); $^1$H NMR (400 MHz, DMSO-$d_6$): δ 8.22 (d, *J* = 8.2 Hz, 1H), 7.42 (t, *J* = 8.0 Hz, 1H), 7.28 (d, *J* = 7.8 Hz, 1H), 7.24–7.13 (m, 2H), 4.43 (ddd, *J* = 9.8, 8.3, 4.8 Hz, 1H), 3.12 (dd, *J* = 13.9, 4.8 Hz, 1H), 2.89 (dd, *J* = 13.9, 9.8 Hz, 1H), 1.77 (s, 3H); $^{13}$C NMR (101 MHz, DMSO-$d_6$): δ 172.9, 169.2, 150.0, 140.4, 129.9, 128.2, 121.9, 119.2, 114.3 (t, *J* = 307.0 Hz, 1H), 53.1, 36.3, 22.3; $^{19}$F NMR (376 MHz, DMSO-$d_6$): δ –16.18 (d, 2F).

**(*S*)-2-Amino-3-(4-(bromodifluoromethoxy)phenyl)propanoic acid TFA salt (78)**

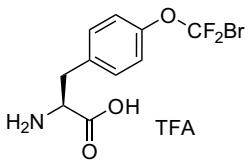


A solution of **76** (1.59 g, 4.15 mmol) and $CoCl_2$ (1.1 mL, 0.1 M) in 0.1 M $K_2HPO_4$ / $KH_2PO_4$ buffer (220 mL) was adjusted to pH 8. Amano Acylase (56.6 mg, ≥30 000 U $g^{-1}$, pH 8.0,2 50 °C (optimum pH and temperature)) was added to the solution and the reaction mixture was stirred for 6 h at room temperature, then the mixture was shock-frozen and freeze-dried. The lyophilized residue was suspended in EtOAc and $H_2O$. The biphasic mixture was adjusted to pH 1 by dropwise addition of conc. HCl at 0 °C. The aq. phase was washed three times with EtOAc, the pH was adjusted to pH 5.6 with $NaHCO_3$ and the aq. layer was freeze-dried. The crude product was purified by reversed-phase chromatography (C18, eluent: $H_2O$ / ACN with 0.1 % TFA) to provide the L-amino acid **78** (194.4 mg, 10.2 %) as a white solid.

HR-ESI-MS (*m/z*): $[M+H]^+_{theor.}$ 309.98849, found 309.98871, rel. Δm 0.72 ppm; $^1$H NMR (400 MHz, DMSO-$d_6$): δ 7.40 (d, *J* = 8.6 Hz, 2H), 7.29 (d, *J* = 8.4 Hz, 2H), 4.09 (t, *J* = 6.4 Hz, 1H), 3.12 (qd, *J* = 14.3, 6.5 Hz, 2H); $^{13}$C NMR (101 MHz, DMSO-$d_6$): δ 170.4, 149.3, 134.9, 131.4, 121.3, 114.3 (t, *J* = 307.2 Hz), 53.4, 35.3; $^{19}$F NMR (376 MHz, DMSO-$d_6$): δ –16.07 (s, 2F).

**(*S*)-2-Amino-3-(3-(bromodifluoromethoxy)phenyl)propanoic acid TFA salt (79)**

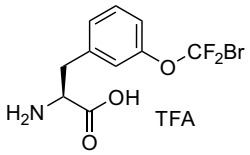


A suspension of **77** in *dd*$H_2O$ (220 mL) was adjusted with 0.1 M NaOH to pH 10 until the reactant was completely dissolved. Amano Acylase (220 mg, ≥30 000 U $g^{-1}$, pH 8.0, 50 °C (optimum pH and temperature)) was added to the solution and the reaction mixture was stirred for 4 h at room temperature. The pH was kept between 7 and 10 during the reaction. The mixture was freeze-dried and the lyophilized product was purified by reversed-phase chromatography (C18, eluent: $H_2O$ / ACN with 0.1 % TFA) to provide the L-amino acid **79** (172.2 mg, 13.0 %) as a white solid.

HR-ESI-MS (*m/z*): $[M+H]^+_{theor.}$ 309.98849, found 309.98824, rel. Δm 0.79 ppm; $^1$H NMR (400 MHz, DMSO-$d_6$): δ 7.46 (t, *J* = 7.8 Hz, 1H), 7.32 (d, *J* = 7.7 Hz, 1H), 7.24 (d, *J* = 9.1 Hz, 2H), 4.01 (t, *J* = 6.4 Hz, 1H), 3.14 (ddd, *J* = 21.1, 14.3, 6.4 Hz, 2H); $^{13}$C NMR (101 MHz, DMSO-$d_6$): δ 170.0, 150.1, 138.4, 130.2, 128.7, 122.3, 119.7, 117.3, 114.2 (t, *J* = 307.3 Hz), 53.4, 35.6; $^{19}$F NMR (376 MHz, DMSO-$d_6$): δ –18.41 (s, 2F).

**(*S*)-2-((((9*H*-Fluoren-9-yl)methoxy)carbonyl)amino)-3-(4-(bromodifluoromethoxy)-phenyl)propanoic acid (80)**

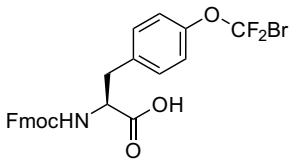


To a solution of **78** (168 mg, 0.396 mmol, 1 eq) in 1,4-dioxane (5 mL) was added at 0 °C a 10 % $Na_2CO_3$ solution (2 mL, 1.89 mmol, 5 eq), followed by Fmoc-Cl (105 mg, 0.405 mmol, 1.1 eq). After stirring 1 h at 0 °C, the reaction mixture was stirred for 3 h at room temperature, then the mixture was concentrated *in vacuo*. DCM and $H_2O$ were added to the residue and the pH was adjusted at 0 °C with conc. HCl to pH 1–2. The biphasic mixture was extracted three times with DCM. The combined organic layers were washed with brine, dried over $Na_2SO_4$ and the solvent was removed *in vacuo*. The crude product was purified by reversed-phase chromatography (C18, eluent: $H_2O$ / ACN with 0.1 % TFA) to provide the title compound **81** (98.0 mg, 46.5 %) as a white solid.

HR-ESI-MS (*m/z*): $[M-H]^-_{theor.}$ 530.04201, found 530.04280, rel. Δm 1.48 ppm; $^1$H NMR (700 MHz, DMSO-$d_6$): δ 12.80 (bs, 1H), 7.88 (d, *J* = 7.5 Hz, 2H), 7.78 (d, *J* = 8.6 Hz, 1H), 7.64 (t, *J* = 6.9 Hz, 2H), 7.43–7.38 (m, 4H), 7.33–7.27 (m, 2H), 7.22 (d, *J* = 8.4 Hz, 2H), 4.24–4.12 (m, 4H), 3.12 (dd, *J* = 13.9, 4.3 Hz, 1H), 2.90 (dd, *J* = 13.8, 10.8 Hz, 1H); $^{13}$C NMR (176 MHz, DMSO-$d_6$): δ 173.6, 156.4, 149.2, 144.2 (d, *J* = 6.5 Hz), 141.2 (d, *J* = 5.0 Hz), 138.0, 131.3, 128.1, 127.5, 125.7 (d, *J* = 7.4 Hz), 121.4, 120.6, 114.8 (t, *J* = 306.9 Hz), 66.1, 55.7, 47.0, 36.2; $^{19}$F NMR (659 MHz, DMSO-$d_6$): δ –15.92 (d, *J* = 7.7 Hz, 2F).

**(*S*)-2-((((9*H*-Fluoren-9-yl)methoxy)carbonyl)amino)-3-(3-(bromodifluoromethoxy)-phenyl)propanoic acid (81)**

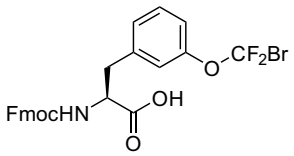


To a solution of **79** (156 mg, 0.368 mmol, 1 eq) in 1,4-dioxane (5 mL) was added at 0 °C a 10 % $Na_2CO_3$ solution (2 mL, 1.89 mmol, 5 eq), followed by Fmoc-Cl (105 mg, 0.405 mmol, 1.1 eq). The reaction mixture was stirred for 4 h at room temperature. $H_2O$ was added and the mixture was washed with $Et_2O$, then EtOAc was added to the aq. layer and the pH was adjusted at 0 °C with conc. HCl to pH 1–2. The biphasic mixture was extracted three times with EtOAc. The combined organic layers were washed with brine, dried over $Na_2SO_4$ and the solvent was removed *in vacuo*. The crude product was purified by reversed-phase chromatography (C18, eluent: $H_2O$ / ACN with 0.1 % TFA) to provide the title compound **81** (176.2 mg, 89.9 %) as a white solid.

HR-ESI-MS (*m/z*): $[M+Na]^+_{theor.}$ 554.03851, found 554.03874, rel. Δm 0.41 ppm; $^1$H NMR (700 MHz, DMSO-$d_6$): δ 12.82 (bs, 1H), 7.88 (d, *J* = 7.6 Hz, 2H), 7.78 (d, *J* = 8.6 Hz, 1H), 7.63 (dd, *J* = 8.9, 8.3 Hz, 2H), 7.45–7.36 (m, 3H), 7.35–7.23 (m, 4H), 7.19 (d, *J* = 8.1 Hz, 1H), 4.24–4.13 (m, 4H), 3.16 (dd, *J* = 13.8, 4.2 Hz, 1H), 2.93 (dd, *J* = 13.8, 10.9 Hz, 1H); $^{13}$C NMR (176 MHz, DMSO-$d_6$): δ 173.5, 156.4, 150.5, 144.2, 141.2, 141.1, 130.4, 128.8, 128.1, 127.5, 125.7 (d, *J* = 11.9 Hz), 122.5, 120.6, 119.7, 114.8 (t, *J* = 307.1 Hz), 66.1, 55.6, 47.0, 36.4; $^{19}$F NMR (659 MHz, DMSO-$d_6$): δ –15.76 (s, 2F).

### $N^2$-(((9*H*-Fluoren-9-yl)methoxy)carbonyl)-$N^6$-(2,2-difluoroacetyl)-L-lysine (82b)

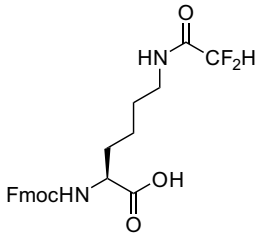


The title compound was prepared following General Procedure **O** using Fmoc-L-Lys-OH (3.0 g, 8.14 mmol, 1 eq), NMM (2.69 mL, 24.4 mmol, 0.92 g cm$^{-3}$, 3 eq) and 2,2-difluoroacetic anhydride (1.70 g, 9.77 mmol, 1.2 eq) in dry THF (60 mL). The crude product was purified by reversed-phase chromatography (eluent: $H_2O$ / ACN with 0.1 % TFA) to provide the title compound **82b** (3.27 g, 89.8 %) as a white solid.

ESI-MS (*m/z*): $[M-H]^-$ 445.19; $^1$H NMR (400 MHz, DMSO-$d_6$): δ 8.78 (t, *J* = 5.3 Hz, 1H), 7.89 (d, *J* = 7.5 Hz, 2H), 7.73 (d, *J* = 7.4 Hz, 2H), 7.63 (d, *J* = 8.0 Hz, 1H), 7.42 (t, *J* = 7.3 Hz, 2H), 7.33 (td, *J* = 7.4, 0.8 Hz, 2H), 6.18 (t, *J* = 53.8 Hz, 1H), 4.29 (d, *J* = 6.6 Hz, 2H), 4.26–4.17 (m, 1H), 3.92 (td, *J* = 9.3, 4.7 Hz, 1H), 3.13 (dd, *J* = 13.0, 6.5 Hz, 2H), 1.81–1.54 (m, 2H), 1.53–1.20 (m, 4H); $^{13}$C NMR (101 MHz, DMSO-$d_6$): δ 174.0, 162.1 (t, *J* = 25.0 Hz), 156.2, 143.9 (d, *J* = 4.2 Hz), 140.8, 127.7, 127.1, 125.3, 120.1, 108.6 (t, *J* = 246.7 Hz, 65.6, 53.8, 46.7, 38.3, 30.4, 28.2, 23.0; $^{19}$F NMR (376 MHz, DMSO-$d_6$): δ –125.68 (d, *J* = 53.8 Hz, 2F).

### $N^2$-(((9*H*-Fluoren-9-yl)methoxy)carbonyl)-$N^6$-(2-chloro-2,2-difluoroacetyl)-L-lysine (82d)

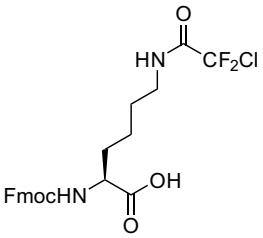


The title compound was prepared following General Procedure **O** using Fmoc-L-Lys-OH (3.0 g, 8.14 mmol, 1 eq), NMM (2.69 mL, 24.4 mmol, 0.92 g cm$^{-3}$, 3 eq) and 2-chloro-2,2-difluoroacetic anhydride (2.37 g, 9.77 mmol, 1.2 eq) in dry THF (60 mL). The crude product was purified by reversed-phase chromatography (eluent: $H_2O$ / ACN with 0.1 % TFA) to provide the title compound **82d** (2.18 g, 55.7 %) as a white solid.

ESI-MS (*m/z*): $[M+Na]^+$ 503.17; $^1$H NMR (400 MHz, DMSO-$d_6$): δ 9.25 (t, *J* = 5.4 Hz, 1H), 7.89 (d, *J* = 7.5 Hz, 2H), 7.73 (d, *J* = 7.4 Hz, 2H), 7.63 (d, *J* = 8.0 Hz, 1H), 7.42 (t, *J* = 7.3 Hz, 2H), 7.33 (td, *J* = 7.4, 1.0 Hz, 2H), 4.39–4.27 (m, 2H), 4.27–4.15 (m, 1H), 3.92 (td, *J* = 9.4, 4.7 Hz, 1H), 3.17 (dd, *J* = 13.3, 6.3 Hz, 2H), 1.81–1.25 (m, 6H); $^{13}$C NMR (101 MHz, DMSO-$d_6$): δ 174.0, 158.6 (t, *J* = 29.4 Hz), 156.2, 143.8 (d, *J* = 4.9 Hz), 140.7, 127.7, 127.1, 125.3, 120.1, 119.1 (t, *J* = 302.6 Hz), 65.6, 53.7, 46.7, 39.2, 30.3, 27.9, 22.9; $^{19}$F NMR (376 MHz, DMSO-$d_6$): δ –62.73 (s, 2F).

### $N^2$-(((9*H*-Fluoren-9-yl)methoxy)carbonyl)-$N^6$-(2-bromo-2,2-difluoroacetyl)-L-lysine (82e)

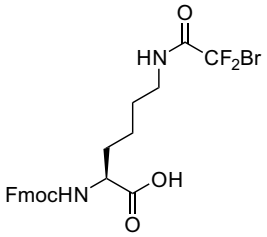


The title compound was prepared following General Procedure **O** using Fmoc-L-Lys-OH (3.0 g, 8.14 mmol, 1 eq), NMM (2.69 mL, 24.4 mmol, 0.92 g cm$^{-3}$, 3 eq) and 2-bromo-2,2-difluoroacetic anhydride (3.24 g, 9.77 mmol, 1.2 eq) in dry THF (60 mL). The crude product was purified by reversed-phase chromatography (eluent: $H_2O$ / ACN with 0.1 % TFA) to provide the title compound **82e** (2.44 g, 57.0 %) as a white solid.

ESI-MS (*m/z*): $[M+H]^+$ 523.10 / 525.10 (1:1); $^1$H NMR (400 MHz, DMSO-$d_6$): δ 9.18 (t, *J* = 5.5 Hz, 1H), 7.89 (d, *J* = 7.5 Hz, 2H), 7.73 (d, *J* = 7.4 Hz, 2H), 7.63 (d, *J* = 8.0 Hz, 1H), 7.42 (t, *J* = 7.5 Hz, 2H), 7.33 (td, *J* = 7.4, 1.0 Hz, 2H), 4.28 (dd, *J* = 9.9, 3.3 Hz, 2H), 4.25–4.18 (m, 1H), 3.92 (td, *J* = 9.4, 4.7 Hz, 1H), 3.16 (dd, *J* = 13.5, 6.3 Hz, 2H), 1.78–1.29 (m, 6H); $^{13}$C NMR (101 MHz, DMSO-$d_6$): δ 173.9, 159.5 (t, *J* = 26.9 Hz), 156.2, 143.8 (d, *J* = 4.9 Hz), 143.8 (d, *J* = 4.9 Hz), 140.7, 127.6, 127.1, 125.3, 120.1, 111.9 (t, *J* = 315.1 Hz), 65.6, 53.7, 46.7, 39.1, 30.3, 27.9, 22.9; $^{19}$F NMR (376 MHz, DMSO-$d_6$): δ –59.92 (s, 2F).

### (*S*)-2-((((9*H*-Fluoren-9-yl)methoxy)carbonyl)amino)-4-acetamidobutanoic acid (83a)

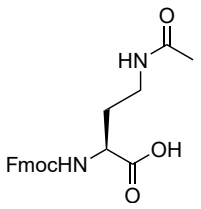


The title compound was prepared following General Procedure **O** using Fmoc-L-Dab-OH (1.0 g, 2.94 mmol, 1 eq), NMM (970 µL, 8.82 mmol, 0.92 g cm$^{-3}$, 3 eq) and acetic anhydride (360 mg, 3.53 mmol, 1.2 eq) in dry THF (20 mL). The crude product was purified by reversed-phase chromatography (eluent: $H_2O$ / ACN with 0.1 % TFA) to provide the title compound **83a** (498.9 mg, 45.0 %) as a white solid.

ESI-MS (*m/z*): $[M-H]^-$ 381.06; $^1$H NMR (400 MHz, DMSO-$d_6$): δ 7.90 (d, *J* = 7.5 Hz, 2H), 7.78 (d, *J* = 8.5 Hz, 1H), 7.71 (d, *J* = 7.4 Hz, 2H), 7.42 (t, *J* = 7.4 Hz, 2H), 7.34 (t, *J* = 7.1 Hz, 2H), 4.48–4.29 (m, 3H), 4.25 (t, *J* = 6.7 Hz, 1H), 3.73 (t, *J* = 10.0 Hz, 1H), 3.40 (td, *J* = 10.9, 7.0 Hz, 1H), 2.37 (s, 1H), 2.28–2.13 (m, 1H), 1.88 (dt, *J* = 22.5, 11.2 Hz, 1H); $^{13}$C NMR (101 MHz, DMSO-$d_6$): δ 173.5, 170.2, 155.8, 143.8, 140.8, 127.6, 127.1, 125.1, 120.1, 65.7, 53.2, 46.6, 40.9, 24.4, 23.7.

**(*S*)-2-((((9*H*-Fluoren-9-yl)methoxy)carbonyl)amino)-4-(2,2-difluoroacetamido)butanoic acid (83b)**

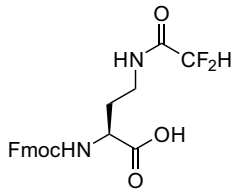


The title compound was prepared following General Procedure **O** using Fmoc-L-Dab-OH (1.0 g, 2.94 mmol, 1 eq), NMM (970 µL, 8.82 mmol, 0.92 g cm$^{-3}$, 3 eq) and 2,2-difluoroacetic anhydride (609 mg, 3.53 mmol, 1.2 eq) in dry THF (20 mL). The crude product was purified by reversed-phase chromatography (eluent: $H_2O$ / ACN with 0.1 % TFA) to provide the title compound **83a** (298.6 mg, 24.6 %) as a white solid.

ESI-MS (*m/z*): $[M+Na]^+$ 441.07; $^1$H NMR (400 MHz, DMSO-$d_6$): δ 12.63 (bs, 1H), 8.83 (t, *J* = 5.2 Hz, 1H), 7.89 (d, *J* = 7.5 Hz, 2H), 7.73 (dd, *J* = 7.7, 4.6 Hz, 3H), 7.41 (dt, *J* = 7.5, 3.7 Hz, 2H), 7.38–7.28 (m, 2H), 6.19 (t, *J* = 53.7 Hz, 1H), 4.33–4.20 (m, 3H), 4.01 (td, *J* = 9.0, 4.7 Hz, 1H), 3.23 (dd, *J* = 12.9, 6.6 Hz, 2H), 1.98 (td, *J* = 12.8, 7.6 Hz, 1H), 1.86–1.73 (m, 1H); $^{13}$C NMR (101 MHz, DMSO-$d_6$): δ 173.6, 162.3 (t, *J* = 25.1 Hz), 156.2, 143.8, 140.7, 127.7, 127.1, 125.3 (d, *J* = 3.3 Hz), 120.1, 108.5 (t, *J* = 246.6 Hz, 65.7, 51.6, 46.7, 35.8, 30.0; $^{19}$F NMR (376 MHz, DMSO-$d_6$): δ –125.76 (d, *J* = 53.7 Hz, 2F).

**(*S*)-2-((((9*H*-Fluoren-9-yl)methoxy)carbonyl)amino)-4-(2,2,2-trifluoroacetamido)butanoic acid (83c)**

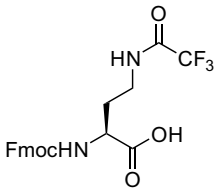


The title compound was prepared following General Procedure **O** using Fmoc-L-Dab-OH (1.0 g, 2.94 mmol, 1 eq), NMM (970 µL, 8.82 mmol, 0.92 g cm$^{-3}$, 3 eq) and 2,2,2-trifluoroacetic anhydride (2.22 g, 10.6 mmol, 1.2 eq) in dry THF (60 mL). The crude product was purified by reversed-phase chromatography (eluent: $H_2O$ / ACN with 0.1 % TFA) to provide the title compound **83c** (273.0 mg, 21.6 %) as a white solid.

ESI-MS (*m/z*): $[M+Na]^+$ 459.05; $^1$H NMR (400 MHz, DMSO-$d_6$): δ 12.73 (bs, 1H), 9.47 (t, *J* = 5.2 Hz, 1H), 7.91 (d, *J* = 7.5 Hz, 2H), 7.75 (d, *J* = 6.7 Hz, 3H), 7.44 (t, *J* = 7.3 Hz, 2H), 7.35 (t, *J* = 7.4 Hz, 2H), 4.36-4.19 (m, 3H), 4.03 (td, *J* = 9.4, 4.7 Hz, 1H), 3.30 (m, 2H), 2.10–1.97 (m, 1H), 1.92–1.77 (m, 1H); $^{13}$C NMR (101 MHz, DMSO-$d_6$): δ 173.4, 156.8–155.6 (m, 2C) 143.8, 140.7, 127.6, 127.1, 125.3 (d, *J* = 4.4 Hz), 120.2-111.6 (m, 2C), 65.7, 51.5, 46.6, 36.4, 29.6; $^{19}$F NMR (376 MHz, DMSO-$d_6$): δ δ -74.76 (s, 3F).

**(*S*)-2-((((9*H*-Fluoren-9-yl)methoxy)carbonyl)amino)-4-(2-chloro-2,2-difluoroacetamido)butanoic acid (83d)**

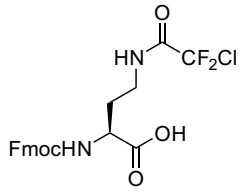


The title compound was prepared following General Procedure **O** using Fmoc-L-Dab-OH (1.0 g, 2.94 mmol, 1 eq), NMM (970 µL, 8.82 mmol, 0.92 g cm$^{-3}$, 3 eq) and 2-chloro-2,2-difluoroacetic anhydride (2.57 g, 10.6 mmol, 1.2 eq) in dry THF (60 mL). The crude product was purified by reversed-phase chromatography (eluent: $H_2O$ / ACN with 0.1 % TFA) to provide the title compound **83d** (306.2 mg, 23.3 %) as a white solid.

ESI-MS (*m/z*): $[M+Na]^+$ 475.03 / 477.02 (3:1); $^1$H NMR (400 MHz, DMSO-$d_6$): δ 12.65 (bs, 1H), 9.29 (t, *J* = 5.3 Hz, 1H), 7.89 (d, *J* = 7.5 Hz, 2H), 7.72 (dd, *J* = 7.8, 3.7 Hz, 3H), 7.42 (t, *J* = 7.3 Hz, 2H), 7.38–7.28 (m, 2H), 4.33–4.18 (m, 3H), 4.01 (td, *J* = 9.4, 4.7 Hz, 1H), 3.27 (dd, *J* = 13.3, 7.3 Hz, 2H), 2.01 (qd, *J* = 7.7, 4.9 Hz, 1H), 1.88–1.74 (m, 1H); $^{13}$C NMR (101 MHz, DMSO-$d_6$): δ 173.4, 158.7 (t, *J* = 29.5 Hz), 156.1, 143.8, 140.7, 127.7, 127.1, 125.3 (d, *J* = 4.3 Hz), 120.1, 119.0 (t, *J* = 302.6 Hz), 65.7, 51.5, 46.6, 36.7, 29.7; $^{19}$F NMR (376 MHz, DMSO-$d_6$): δ –62.72 (s, 2F).

**(*S*)-2-((((9*H*-Fluoren-9-yl)methoxy)carbonyl)amino)-4-(2-bromo-2,2-difluoroacetamido)butanoic acid (83e)**

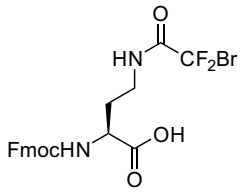


The title compound was prepared following General Procedure **O** using Fmoc-L-Dab-OH (1.0 g, 2.94 mmol, 1 eq), NMM (970 µL, 8.82 mmol, 0.92 g cm$^{-3}$, 3.0 eq) and 2-bromo-2,2-difluoroacetic anhydride (3.51 g, 10.6 mmol, 1.2 eq) in dry THF (60 mL). The crude product was purified by reversed-phase chromatography (eluent: $H_2O$ / ACN with 0.1 % TFA) to provide the title compound **83e** (341.7 mg, 23.7 %) as a white solid.

ESI-MS (*m/z*): $[M+Na]^+$ 518.97 / 520.97 (1:1); $^1$H NMR (400 MHz, DMSO-$d_6$): δ 12.70 (s, 1H), 9.23 (t, *J* = 5.2 Hz, 1H), 7.89 (d, *J* = 7.5 Hz, 2H), 7.73 (dd, *J* = 7.7, 3.9 Hz, 3H), 7.42 (t, *J* = 7.2 Hz, 2H), 7.33 (ddd, *J* = 7.4, 4.4, 1.3 Hz, 2H), 4.37–4.15 (m, 4H), 4.01 (td, *J* = 8.9, 4.7 Hz, 1H), 3.26 (dd, *J* = 12.8, 6.4 Hz, 2H), 2.01 (td, *J* = 12.8, 7.5 Hz, 1H), 1.81 (tt, *J* = 10.1, 5.0 Hz, 1H); $^{13}$C NMR (101 MHz, DMSO-$d_6$): δ 173.5, 159.6 (t, *J* = 27.0 Hz), 156.1, 143.8, 140.7, 127.7, 127.1, 125.3 (d, *J* = 4.4 Hz), 120.1, 111.8 (t, *J* = 314.9 Hz), 65.7, 51.5, 46.6, 36.6, 29.7; $^{19}$F NMR (376 MHz, DMSO-$d_6$): δ –59.97 (s, 2F).

**((9*H*-Fluoren-9-yl)methyl (*S*)-(2-oxopyrrolidin-3-yl)carbamate (84)**

By-product of **83a**–**e**.

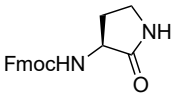


ESI-MS (*m/z*): $[M+Na]^+$ 345.09; $^1$H NMR (400 MHz, DMSO-$d_6$): δ 7.89 (d, *J* = 7.5 Hz, 2H), 7.76 (s, 1H), 7.72 (d, *J* = 7.4 Hz, 2H), 7.57 (d, *J* = 8.7 Hz, 1H), 7.42 (t, *J* = 7.4 Hz, 2H), 7.33 (t, *J* = 7.4 Hz, 1H), 4.34–4.28 (m, 2H), 4.27–4.20 (m, 1H), 4.07 (dd, *J* = 18.6, 9.2 Hz, 1H), 3.19–3.10 (m, 2H), 2.35–2.18 (m, 1H), 1.95–1.74 (m, 1H).; $^{13}$C NMR (101 MHz, DMSO-$d_6$): 174.3, 156.1, 143.9, 140.8, 127.6, 127.1, 125.2, 120.1, 66.6, 51.2, 46.7, 37.8, 27.9.

# 7 References


[1] J. Brickmann, R. J. Marhofer, T. E. Exner, and M. Keil. Molecular graphics – trends and perspectives. *Journal of Molecular Modeling*, 6(2):328–340, 2000. doi: 10.1007/s0089400060328.

[2] J. Brickmann, T. E. Exner, J. Gimmler, P. Lautenschläger, W. Heiden, G. Moeckel, and D. Zahn. MOLCAD II; MOLCAD GmbH: Darmstadt, Germany; http://www.molcad.de.

[3] R. Wilcken, M. O. Zimmermann, A. Lange, A. C. Joerger, and F. M. Boeckler. Principles and applications of halogen bonding in medicinal chemistry and chemical biology. *Journal of Medicinal Chemistry*, 56(4):1363–1388, 2013. doi: 10.1021/jm3012068.

[4] R. Wilcken, M. O. Zimmermann, A. Lange, S. Zahn, and F. M. Boeckler. Using halogen bonds to address the protein backbone: A systematic evaluation. *Journal of Computer-Aided Molecular Design*, 26(8):935–945, 2012. doi: 10.1007/s10822-012-9592-8.

[5] T. Clark, M. Hennemann, J. S. Murray, and P. Politzer. Halogen bonding: The σ-hole. proceedings of "modeling interactions in biomolecules ii", prague, september 5th-9th, 2005. *Journal of Molecular Modeling*, 13(2):291–296, 2007. doi: 10.1007/s00894-006-0130-2.

[6] R. Wilcken, X. Liu, M. O. Zimmermann, T. J. Rutherford, A. R. Fersht, A. C. Joerger, and F. M. Boeckler. Halogen-enriched fragment libraries as leads for drug rescue of mutant p53. *Journal of the American Chemical Society*, 134(15):6810–6818, 2012. doi: 10.1021/ja301056a.

[7] R. Wilcken, G. Wang, F. M. Boeckler, and A. R. Fersht. Kinetic mechanism of p53 oncogenic mutant aggregation and its inhibition. *Proceedings of the National Academy of Sciences of the United States of America*, 109(34):13584–13589, 2012. doi: 10.1073/pnas.1211550109.

[8] A. Lange, J. Heidrich, M. O. Zimmermann, T. E. Exner, and F. M. Boeckler. Scaffold effects on halogen bonding strength. *Journal of Chemical Information and Modeling*, 59(2):885–894, 2019. doi: 10.1021/acs.jcim.8b00621.

[9] M. O. Zimmermann and F. M. Boeckler. Targeting the protein backbone with aryl halides: Systematic comparison of halogen bonding and π···π interactions using N-methylacetamide. *Medicinal Chemistry Communications*, 7(3):500–505, 2016. doi: 10.1039/C5MD00499C.

[10] M. O. Zimmermann, A. Lange, and F. M. Boeckler. Evaluating the potential of halogen bonding in molecular design: Automated scaffold decoration using the new scoring function xbscore. *Journal of Chemical Information and Modeling*, 55(3):687–699, 2015. doi: 10.1021/ci5007118.

[11] M. O. Zimmermann, A. Lange, S. Zahn, T. E. Exner, and F. M. Boeckler. Using surface scans for the evaluation of halogen bonds toward the side chains of aspartate, asparagine, glutamate, and glutamine. *Journal of Chemical Information and Modeling*, 56(7):1373–1383, 2016. doi: 10.1021/acs.jcim.6b00075.

[12] A. Lange, M. O. Zimmermann, R. Wilcken, S. Zahn, and F. M. Boeckler. Targeting histidine side chains in molecular design through nitrogen-halogen bonds. *Journal of Chemical Information and Modeling*, 53(12):3178–3189, 2013. doi: 10.1021/ci4004305.

[13] R. Wilcken, M. O. Zimmermann, A. Lange, S. Zahn, B. Kirchner, and F. M. Boeckler. Addressing methionine in molecular design through directed sulfur-halogen bonds. *Journal of Chemical Theory and Computation*, 7(7):2307–2315, 2011. doi: 10.1021/ct200245e.

[14] T. Steiner. The hydrogen bond in the solid state. *Angewandte Chemie*, 41(1):48–76, 2002. doi: 10.1002/1521-3773(20020104)41:1<48::AID-ANIE48>3.0.CO;2-U.

[15] H. G. Kümmel. A biography of the coupled cluster method. *International Journal of Modern Physics B*, 17(28):5311–5325, 2003. doi: 10.1142/S0217979203020442.

[16] C. Møller and M. S. Plesset. Note on an approximation treatment for many-electron systems. *Physical Review*, 46(7):618–622, 1934. doi: 10.1103/PhysRev.46.618.

[17] J. A. Pople, J. S. Binkley, and R. Seeger. Theoretical models incorporating electron correlation. *International Journal of Quantum Chemistry*, 10(S10):1–19, 1976. doi: 10.1002/qua.560100802.

[18] Y. Lu, T. Shi, Y. Wang, H. Yang, X. Yan, X. Luo, H. Jiang, and W. Zhu. Halogen bonding–a novel interaction for rational drug design? *Journal of Medicinal Chemistry*, 52(9):2854–2862, 2009. doi: 10.1021/jm9000133.

[19] Y. Lu, Y. Wang, and W. Zhu. Nonbonding interactions of organic halogens in biological systems: Implications for drug discovery and biomolecular design. *Physical Chemistry Chemical Physics*, 12(18):4543–4551, 2010. doi: 10.1039/B926326H.

[20] P. Dobes, J. Rezác, J. Fanfrlík, M. Otyepka, and P. Hobza. Semiempirical quantum mechanical method PM6-DH2X describes the geometry and energetics of CK2-inhibitor complexes involving halogen bonds well, while the empirical potential fails. *The Journal of Physical Chemistry B*, 115(26):8581–8589, 2011. doi: 10.1021/jp202149z.

[21] S. F. Boys and F. Bernardi. The calculation of small molecular interactions by the differences of separate total energies. some procedures with reduced errors. *Molecular Physics*, 19(4):553–566, 1970. doi: 10.1080/00268977000101561.

[22] C. B. Aakeroy, D. L. Bryce, G. R. Desiraju, A. Frontera, A. C. Legon, F. Nicotra, K. Rissanen, S. Scheiner, G. Terraneo, P. Metrangolo, and G. Resnati. Definition of the chalcogen bond (IUPAC recommendations 2019). *Pure and Applied Chemistry*, 91(11):1889–1892, 2019. doi: 10.1515/pac-2018-0713.

[23] P. Scilabra, G. Terraneo, and G. Resnati. The chalcogen bond in crystalline solids: A world parallel to halogen bond. *Accounts of Chemical Research*, 52(5):1313–1324, 2019. doi: 10.1021/acs.accounts.9b00037.

[24] A. Lange, M. Günther, F. M. Büttner, M. O. Zimmermann, J. Heidrich, S. Hennig, S. Zahn, C. Schall, A. Sievers-Engler, F. Ansideri, P. Koch, M. Laemmerhofer, T. Stehle, S. A. Laufer, and F. M. Boeckler. Targeting the gatekeeper met146 of c-jun N-terminal kinase 3 induces a bivalent halogen/chalcogen bond. *Journal of the American Chemical Society*, 137(46):14640–14652, 2015. doi: 10.1021/jacs.5b07090.

[25] O. Carugo, G. Resnati, and P. Metrangolo. Chalcogen bonds involving selenium in protein structures. *ACS Chemical Biology*, 16(9):1622–1627, 2021. doi: 10.1021/acschembio.1c00441.

[26] T. Eneqvist, E. Lundberg, A. Karlsson, S. Huang, C. R. A. Santos, D. M. Power, and A. E. Sauer-Eriksson. High resolution crystal structures of piscine transthyretin reveal different binding modes for triiodothyronine and thyroxine. *Protein Structure and Folding*, 279(25):26411–26416, 2004. doi: 10.1074/jbc.M313553200.

[27] F. J. Álvarez-Martínez, E. Barrajón-Catalán, and V. Micol. Tackling antibiotic resistance with compounds of natural origin: A comprehensive review. *Biomedicines*, 8(10), 2020. doi: 10.3390/biomedicines8100405.

[28] N. F. Valadares, L. B. Salum, I. Polikarpov, A. D. Andricopulo, and R. C. Garratt. Role of halogen bonds in thyroid hormone receptor selectivity: Pharmacophore-based 3D-QSSR studies. *Journal of Chemical Information and Modeling*, 49(11):2606–2616, 2009. doi: 10.1021/ci900316e.

[29] C. A. Bayse and E. R. Rafferty. Is halogen bonding the basis for iodothyronine deiodinase activity? *Inorganic Chemistry*, 49(12):5365–5367, 2010. doi: 10.1021/ic100711n.

[30] E. S. Marsan and C. A. Bayse. A halogen bonding perspective on iodothyronine deiodinase activity. *Molecules*, 25(6), 2020. doi: 10.3390/molecules25061328.

[31] G. W. Gribble. Natural organohalogens: A new frontier for medicinal agents? *Journal of Chemical Education*, 81(10):1441, 2004. doi: 10.1021/ed081p1441.

[32] G. W. Gribble. Newly discovered naturally occurring organohalogens. *Archive for Organic Chemistry*, (part i):372–410, 2018.

[33] C. S. Neumann, D. G. Fujimori, and C. T. Walsh. Halogenation strategies in natural product biosynthesis. *Chemistry & Biology*, 15(2):99–109, 2008. doi: 10.1016/j.chembiol.2008.01.006.

[34] M. F. Carvalho and R. S. Oliveira. Natural production of fluorinated compounds and biotechnological prospects of the fluorinase enzyme. *Critical Reviews in Biotechnology*, 37(7):880–897, 2017. doi: 10.1080/07388551.2016.1267109.

[35] L. Wang, X. Zhou, M. Fredimoses, S. Liao, and Y. Liu. Naturally occurring organoiodines. *RSC Advances*, 4(101):57350–57376, 2014. doi: 10.1039/C4RA09833A.

[36] FDA. New drug therapy approvals 2020. 2021. URL https://www.fda.gov/drugs/new-drugs-fda-cders-new-molecular-entities-and-new-therapeutic-biological-products/novel-drug-approvals-2020.

[37] FDA. New drug therapy approvals 2021, 2022. URL https://www.fda.gov/drugs/new-drugs-fda-cders-new-molecular-entities-and-new-therapeutic-biological-products/novel-drug-approvals-2021.

[38] P. Shah and A. D. Westwell. The role of fluorine in medicinal chemistry. *Journal of Enzyme Inhibition and Medicinal Chemistry*, 22(5):527–540, 2007. doi: 10.1080/14756360701425014.

[39] M. Z. Hernandes, S. M. T. Cavalcanti, D. R. M. Moreira, W. F. de Azevedo Junior, and A. C. L. Leite. Halogen atoms in the modern medicinal chemistry: Hints for the drug design. *Current Drug Targets*, 11(3):303–314, 2010. doi: 10.2174/138945010790711996.

[40] W.-Y. Fang, L. Ravindar, K. P. Rakesh, H. M. Manukumar, C. S. Shantharam, N. S. Alharbi, and H.-L. Qin. Synthetic approaches and pharmaceutical applications of chloro-containing molecules for drug discovery: A critical review. *European Journal of Medicinal Chemistry*, 173:117–153, 2019. doi: 10.1016/j.ejmech.2019.03.063.

[41] A. Bondi. Van der waals volumes and radii. *Journal of Physical Chemistry*, 68:441–451, 1964.

[42] N. Shindo, H. Fuchida, M. Sato, K. Watari, T. Shibata, K. Kuwata, C. Miura, K. Okamoto, Y. Hatsuyama, K. Tokunaga, S. Sakamoto, S. Morimoto, Y. Abe, M. Shiroishi, J. M. M. Caaveiro, T. Ueda, T. Tamura, N. Matsunaga, T. Nakao, S. Koyanagi, S. Ohdo,

Y. Yamaguchi, I. Hamachi, M. Ono, and A. Ojida. Selective and reversible modification of kinase cysteines with chlorofluoroacetamides. *Nature Chemical Biology*, 15(3): 250–258, 2019. doi: 10.1038/s41589-018-0204-3.

[43] T. Khotavivattana, S. Verhoog, M. Tredwell, L. Pfeifer, S. Calderwood, K. Wheelhouse, T. Lee Collier, and V. Gouverneur. $^{18}$F-labeling of aryl-$SCF_3$, -$OCF_3$ and -$OCHF_2$ with [$^{18}$F]fluoride. *Angewandte Chemie*, 54(34):9991–9995, 2015. doi: 10.1002/anie.201504665.

[44] A. Haas, M. Spitzer, and M. Lieb. Synthese seitenkettenfluorierter aromatischer verbindungen und deren chemische reaktivität. *Chemische Berichte*, 121(7):1329–1340, 1988. doi: 10.1002/cber.19881210718.

[45] M. R. Kilbourn, M. R. Pavia, and V. E. Gregor. Synthesis of fluorine-18 labeled GABA uptake inhibitors. *International Journal of Radiation Applications and Instrumentation. Part A. Applied Radiation and Isotopes*, 41(9):823–828, 1990. doi: 10.1016/0883-2889(90)90059-P.

[46] M. K. Das and J. Mukherjee. Radiosynthesis of [F-18]fluoxetine as a potential radiotracer for serotonin reuptake sites. *Applied Radiation and Isotopes*, 44(5):835–842, 1993. doi: 10.1016/0969-8043(93)90025-6.

[47] J. He and C. U. Fittman. The photochemical synthesis of α,α,α-bromodifluorotoluene and α,α,α-chlorodifluorotoluene. *Synthetic Communications*, 29(5):855–862, 1999. doi: 10.1080/00397919908086043.

[48] N. Levi, D. Amir, E. Gershonov, and Y. Zafrani. Recent progress on the synthesis of $CF_2H$-containing derivatives. *Synthesis*, 51(24):4549–4567, 2019. doi: 10.1055/s-0039-1690027.

[49] G. Prakash, J. Hu, J. Simon, D. R. Bellew, and G. A. Olah. Preparation of α,α-difluoroalkanesulfonic acids. *Journal of Fluorine Chemistry*, 125(4):595–601, 2004. doi: 10.1016/j.jfluchem.2003.11.031.

[50] A. Dorian, E. J. Landgreen, H. R. Petras, J. J. Shepherd, and F. J. Williams. Iron-catalyzed halogen exchange of trifluoromethyl arenes*. *Chemistry – A European Journal*, 27 (42):10839–10843, 2021. doi: 10.1002/chem.202101324.

[51] V. Muzalevskiy, V. Nenajdenko, A. Shastin, E. Balenkova, and G. Haufe. Application of 1-(3-bromo-3,3-difluoroprop-1-ynyl)benzenes in diels-alder reactions: Synthesis of ortho-$CF_2$Br-substituted biaryls. *Synthesis*, 2008(18):2899–2904, 2008. doi: 10.1055/s-2008-1067221.

[52] S. N. Tverdomed, J. Kolanowski, E. Lork, and G.-V. Röschenthaler. An effective synthetic route to ortho-difluoromethyl arylphosphosphonates: Studies on the reactivity of phosphorus- and fluorine-containing functions. *Tetrahedron*, 67(21): 3887–3903, 2011. doi: 10.1016/j.tet.2011.03.076.

[53] B. Duda, S. N. Tverdomed, B. I. Ionin, and G.-V. Röschenthaler. Fluorinated alkynylphosphonates in C,C-cyclizations: Regioselective formation of polysubstituted fluorinated arylphosphonates. *European Journal of Organic Chemistry*, 2014 (18):3757–3761, 2014. doi: 10.1002/ejoc.201402188.

[54] W. R. Dolbier, C. R. Burkholder, and M. Médebielle. Syntheses of 2-(bromodifluoromethyl)benzoxazole and 5-(bromodifluoromethyl)-1,2,4-oxadiazoles. *Journal of Fluorine Chemistry*, 95(1-2):127–130, 1999. doi: 10.1016/S0022-1139(99)00007-X.

[55] C. R. Burkholder, W. R. Dolbier, and M. Médebielle. The syntheses of nonnucleoside, HIV-1 reverse transcriptase inhibitors containing a $CF_2$ group. *Journal of Fluorine Chemistry*, 102(1-2):369–376, 2000. doi: 10.1016/S0022-1139(99)00314-0.

[56] H. Jiang, L. Sun, S. Yuan, W. Lu, W. Wan, S. Zhu, and J. Hao. A facile one-pot synthesis of 2-fluoroalkyl 1,3-imidazolines and 1,3-oxazolines through imidoyl halide intermediates. *Tetrahedron*, 68(13):2858–2863, 2012. doi: 10.1016/j.tet.2012.01.086.

[57] H. Jiang, L. Yan, M. Xu, W. Lu, Y. Cai, W. Wan, J. Yao, S. Wu, S. Zhu, and J. Hao. Nucleophile-dependent regioselective reaction of (S)-4-benzyl-2-fluoroalkyl-1,3-oxazolines. *The Journal of Organic Chemistry*, 78(9):4261–4269, 2013. doi: 10.1021/jo400073d.

[58] M.-T. Hsieh, S.-C. Kuo, and H.-C. Lin. Solvent- and transition metal catalyst-dependent regioselectivity in the [3+2] cyclocondensation of trifluoromethyl-α,β-ynones with hydrazines: Switchable access to 3- and 5-trifluoromethylpyrazoles. *Advanced Synthesis & Catalysis*, 357(4):683–689, 2015. doi: 10.1002/adsc.201400853.

[59] M. G. Barlow, S. Tajammal, and A. E. Tipping. Fluorinated acetylenes. part 13 [1]. synthesis of 1,6-diphenyl-3,3,4,4-tetrafluorohexa-1,5-diyne. *Journal of Fluorine Chemistry*, 64(1-2):61–71, 1993. doi: 10.1016/S0022-1139(00)80063-9.

[60] G. B. Hammond. Nucleophilic and electrophilic substitutions of difluoropropargyl bromides. *Journal of Fluorine Chemistry*, 127(4-5):476–488, 2006. doi: 10.1016/j.jfluchem.2005.12.024.

[61] C.-P. Zhang, H.-P. Cao, Z.-L. Wang, C.-T. Zhang, Q.-Y. Chen, and J.-C. Xiao. New electrophilic bromodifluoromethylation and pentafluoroethylation reagents. *Synlett*, 2010(07):1089–1092, 2010. doi: 10.1055/s-0029-1219579.

[62] M. Shiosaki and M. Inoue. Bromodifluoromethylation of aromatic grignard reagents with $CF_2Br_2$. *Tetrahedron Letters*, 55(50):6839–6843, 2014. doi: 10.1016/j.tetlet.2014.10.082.

[63] V. V. Levin, A. A. Zemtsov, M. I. Struchkova, and A. D. Dilman. Reactions of organozinc reagents with potassium bromodifluoroacetate. *Journal of Fluorine Chemistry*, 171: 97–101, 2015. doi: 10.1016/j.jfluchem.2014.08.021.

[64] V. V. Levin, A. A. Zemtsov, M. I. Struchkova, and A. D. Dilman. Reactions of difluorocarbene with organozinc reagents. *Organic Letters*, 15(4):917–919, 2013. doi: 10.1021/ol400122k.

[65] W.-Y. Huang. Perfluoroalkylation initiated with sodium dithionite and related reagent systems. *Journal of Fluorine Chemistry*, 58(1):1–8, 1992. doi: 10.1016/S0022-1139(00)82787-6.

[66] W.-Y. Huang and H.-Z. Zhang. The reaction of perfluoroalkanesulfonyl halides viii. A mild method for introducing $BrCF_2$ group to organic molecules. *Chinese Journal of Chemistry*, 10(3):274–277, 1992. doi: 10.1002/cjoc.19920100313.

[67] J. Zhang, X.-H. Xu, and F.-L. Qing. Bromodifluoromethylation of heteroaromatics with sodium bromodifluoromethanesulfinate. *Tetrahedron Letters*, 57(22):2462–2464, 2016. doi: 10.1016/j.tetlet.2016.04.095.

[68] D. H. R. Barton, D. Crich, and W. B. Motherwell. The invention of new radical chain reactions: Part viii. Radical chemistry of thiohydroxamic esters; a new method for the generation of carbon radicals from carboxylic acids. *Tetrahedron*, 41(19): 3901–3924, 1985. doi: 10.1016/S0040-4020(01)97173-X.

[69] S. Verhoog, L. Pfeifer, T. Khotavivattana, S. Calderwood, T. Collier, K. Wheelhouse, M. Tredwell, and V. Gouverneur. Silver-mediated $^{18}$F-labeling of aryl-$CF_3$ and aryl-$CHF_2$ with $^{18}$F-fluoride. *Synlett*, 27(01):25–28, 2015. doi: 10.1055/s-0035-1560592.

[70] L. M. Yagupolskii, D. V. Fedyuk, K. I. Petko, V. I. Troitskaya, V. I. Rudyk, and V. V. Rudyuk. N-trihalomethyl derivatives of benzimidazole, benzotriazole and indazole. *Journal of Fluorine Chemistry*, 106(2):181–187, 2000. doi: 10.1016/S0022-1139(00)00321-3.

[71] G. Bissky, V. I. Staninets, A. A. Kolomeitsev, and G.-V. Röschenthaler. Heteroaryl-N-difluoromethyltrimethylsilanes - versatile sources of heteroaryl-N-difluoromethyl anions in reactions with carbonyl compounds. *Synlett*, 2001(3):374–378, 2001. doi: 10.1055/s-2001-11389.

[72] T. M. Sokolenko, K. I. Petko, and L. M. Yagupolskii. N-trifluoromethylazoles. *Chemistry of Heterocyclic Compounds*, 45(4):430–435, 2009. doi: 10.1007/s10593-009-0289-4.

[73] J. Xu, Y. Cao, J. Zhang, S. Yu, Y. Zou, X. Chai, Q. Wu, D. Zhang, Y. Jiang, and Q. Sun. Design, synthesis and antifungal activities of novel 1,2,4-triazole derivatives. *European Journal of Medicinal Chemistry*, 46(7):3142–3148, 2011. doi: 10.1016/j.ejmech.2011.02.042.

[74] E. C. Truong, P. W. Phuan, A. L. Reggi, L. Ferrera, L. J. V. Galietta, S. E. Levy, A. C. Moises, O. Cil, E. Diez-Cecilia, S. Lee, A. S. Verkman, and M. O. Anderson. Substituted 2-acylaminocycloalkylthiophene-3-carboxylic acid arylamides as inhibitors of the calcium-activated chloride channel transmembrane protein 16a (TMEM16A). *Journal of Medicinal Chemistry*, 60(11):4626–4635, 2017. doi: 10.1021/acs.jmedchem.7b00020.

[75] O. V. Stanko, Y. V. Rassukana, K. A. Zamulko, V. V. Dyakonenko, S. V. Shishkina, and P. P. Onys'ko. Diastereoselective synthesis of polyfluoroalkylated α-aminophosphonic acid derivatives. *Journal of Fluorine Chemistry*, 216:47–56, 2018. doi: 10.1016/j.jfluchem.2018.10.001.

[76] A. A. Wylie, J. Schoepfer, W. Jahnke, S. W. Cowan-Jacob, A. Loo, P. Furet, A. L. Marzinzik, X. Pelle, J. Donovan, W. Zhu, S. Buonamici, A. Q. Hassan, F. Lombardo, V. Iyer, M. Palmer, G. Berellini, S. Dodd, S. Thohan, H. Bitter, S. Branford, D. M. Ross, T. P. Hughes, L. Petruzzelli, K. G. Vanasse, M. Warmuth, F. Hofmann, N. J. Keen, and W. R. Sellers. The allosteric inhibitor ABL001 enables dual targeting of BCR-ABL1. *Nature*, 543(7647):733–737, 2017. doi: 10.1038/nature21702.

[77] J. Schoepfer, W. Jahnke, G. Berellini, S. Buonamici, S. Cotesta, S. W. Cowan-Jacob, S. Dodd, P. Drueckes, D. Fabbro, T. Gabriel, J.-M. Groell, R. M. Grotzfeld, A. Q. Hassan, C. Henry, V. Iyer, D. Jones, F. Lombardo, A. Loo, P. W. Manley, X. Pellé, G. Rummel, B. Salem, M. Warmuth, A. A. Wylie, T. Zoller, A. L. Marzinzik, and P. Furet. Discovery of asciminib (ABL001), an allosteric inhibitor of the tyrosine kinase activity of BCR-ABL1. *Journal of Medicinal Chemistry*, 61(18):8120–8135, 2018. doi: 10.1021/acs.jmedchem.8b01040.

[78] K. Leclercq, A. Matagne, L. Provins, H. Klitgaard, and R. M. Kaminski. Pharmacological profile of the novel antiepileptic drug candidate padsevonil: Characterization in rodent seizure and epilepsy models. *The Journal of Pharmacology and Experimental Therapeutics*, 372(1):11–20, 2020. doi: 10.1124/jpet.119.261222.

[79] A. S. Kiselyov, M. Semenova, V. V. Semenov, and D. Milligan. Inhibitors of VEGF receptors-1 and -2 based on the 2-((pyridin-4-yl)ethyl)pyridine template. *Bioorganic & Medicinal Chemistry Letters*, 16(7):1913–1919, 2006. doi: 10.1016/j.bmcl.2005.12.090.

[80] A. S. Kiselyov, M. Semenova, V. V. Semenov, E. Piatnitski, and S. Ouyang. Hetaryl imidazoles: A novel dual inhibitors of VEGF receptors i and ii. *Bioorganic & Medicinal Chemistry Letters*, 16(5):1440–1444, 2006. doi: 10.1016/j.bmcl.2005.11.033.

[81] Y. Quesnel. 2-oxo-1-pyrrolidinyl imidazothiadiazole derivatives. WO 2011/047860 A1, April 28, 2011.

[82] B. Kenda, P. Michel, and Y. Quesnel. Imidazole derivatives, processes for preparing them and their uses. WO 2005/054188 A1, June 16,2005.

[83] D. Benedetto Tiz, L. Bagnoli, O. Rosati, F. Marini, L. Sancineto, and C. Santi. New halogen-containing drugs approved by FDA in 2021: An overview on their syntheses and pharmaceutical use. *Molecules*, 27(5), 2022. doi: 10.3390/molecules27051643.

[84] V. L. Makitruk, Y. O. Nuzha, K. I. Petko, Y. A. Fialkov, A. S. Shalamai, and L. M. Yagupolskii. 2-amino-6-(trifluoromethoxy)benzothiazole (borizole) and admixtures accompanying it. *Zhurnal Organichnoi ta Farmatsevtichnoi Khimii*, 5(3):28–33, 2007.

[85] L. Fu, A. Wang, B. He, J. Sun, and C. Song. Preparation method for 4-(chlorodifluoromethoxy)aniline. CN 104119238 A, October 29, 2014.

[86] Y. Hagooly, R. Sasson, M. J. Welch, and S. Rozen. Preparation of alkyl and aryl chlorodifluoromethyl ethers using $BrF_3$. *European Journal of Organic Chemistry*, 2008(17):2875–2880, 2008. doi: 10.1002/ejoc.200800231.

[87] M. Mardirossian, M. Rubini, M. F. A. Adamo, M. Scocchi, M. Saviano, A. Tossi, R. Gennaro, and A. Caporale. Natural and synthetic halogenated amino acids-structural and bioactive features in antimicrobial peptides and peptidomimetics. *Molecules*, 26(23), 2021. doi: 10.3390/molecules26237401.

[88] A. Pizzi, C. Pigliacelli, G. Bergamaschi, A. Gori, and P. Metrangolo. Biomimetic engineering of the molecular recognition and self-assembly of peptides and proteins via halogenation. *Coordination Chemistry Reviews*, 411:213242, 2020. doi: 10.1016/j.ccr.2020.213242.

[89] S. Bittner, R. Scherzer, and E. Harlev. The five bromotryptophans. *Amino Acids*, 33(1): 19–42, 2007. doi: 10.1007/s00726-006-0441-8.

[90] M. Strickland and C. L. Willis. Synthesis of halogenated α–amino acids. In A. B. Hughes, editor, *Origins and synthesis of amino acids*, volume 53 of *Amino Acids, Peptides and Proteins in Organic Chemistry*, pages 441–471. Wiley-VCH, Weinheim, 2009. doi: 10.1002/9783527631766.ch10.

[91] L. A. Hardegger, B. Kuhn, B. Spinnler, L. Anselm, R. Ecabert, M. Stihle, B. Gsell, R. Thoma, J. Diez, J. Benz, J.-M. Plancher, G. Hartmann, D. W. Banner, W. Haap, and F. Diederich. Systematic investigation of halogen bonding in protein-ligand interactions. *Angewandte Chemie*, 50(1):314–318, 2011. doi: 10.1002/anie.201006781.

[92] E. Parisini, P. Metrangolo, T. Pilati, G. Resnati, and G. Terraneo. Halogen bonding in halocarbon-protein complexes: A structural survey. *Chemical Society Reviews*, 40(5): 2267–2278, 2011. doi: 10.1039/c0cs00177e.

[93] M. Erak, K. Bellmann-Sickert, S. Els-Heindl, and A. G. Beck-Sickinger. Peptide chemistry toolbox - transforming natural peptides into peptide therapeutics. *Bioorganic & Medicinal Chemistry*, 26(10):2759–2765, 2018. doi: 10.1016/j.bmc.2018.01.012.

[94] Z. Li, H. Zhao, and C. Wan. *Cyclized helical peptides: Synthesis, properties, and therapeutic applications*. Wiley-VCH, Weinheim, 2021.

[95] M. Xie, D. Liu, and Y. Yang. Anti-cancer peptides: Classification, mechanism of action, reconstruction and modification. *Open Biology*, 10(7):200004, 2020. doi: 10.1098/rsob.200004.

[96] H. Amii, S. Kondo, and K. Uneyama. Novel intramolecular rearrangement of 3-bromo-3,3-difluoroalanine schiff bases via radical ipso-substitution at the aromatic ring. *Chemical Communications*, (17):1845–1846, 1998. doi: 10.1039/A803944E.

[97] T. Katagiri, M. Handa, Y. Matsukawa, J. S. Dileep Kumar, and K. Uneyama. Efficient synthesis of an optically pure β-bromo-β,β-difluoroalanine derivative, a general precursor for β,β-difluoroamino acids. *Tetrahedron: Asymmetry*, 12(9):1303–1311, 2001. doi: 10.1016/S0957-4166(01)00237-3.

[98] A. Suzuki, M. Mae, H. Amii, and K. Uneyama. Catalytic route to the synthesis of optically active β,β-difluoroglutamic acid and β,β-difluoroproline derivatives. *Journal of Organic Chemistry*, 69(15):5132–5134, 2004. doi: 10.1021/jo049789c.

[99] Q. Li, C.-H. Ding, X.-H. Li, W. Weissensteiner, and X.-L. Hou. Diastereo- and enantioselective synthesis of fluorinated proline derivatives via copper(i)-catalyzed asymmetric 1,3-dipolar cycloaddition. *Synthesis*, 2012(02):265–271, 2012. doi: 10.1055/s-0031-1289653.

[100] N. A. Tolmachova, I. S. Kondratov, V. G. Dolovanyuk, S. O. Pridma, A. V. Chernykh, C. G. Daniliuc, and G. Haufe. Synthesis of new fluorinated proline analogues from polyfluoroalkyl β-ketoacetals and ethyl isocyanoacetate. *Chemical Communications*, 54(69):9683–9686, 2018. doi: 10.1039/c8cc05912h.

[101] S. Colombel, N. van Hijfte, T. Poisson, E. Leclerc, and X. Pannecoucke. Addition of electrophilic radicals to 2-benzyloxyglycals: Synthesis and functionalization of fluorinated α-c-glycosides and derivatives. *Chemistry – A European Journal*, 19(38): 12778–12787, 2013. doi: 10.1002/chem.201302070.

[102] R. A. Hazlitt, J. P. John, Q.-L. Tran, and D. A. Colby. Optimized synthesis of a pentafluoro-gem-diol and conversion to a $CF_2Br$-glucopyranose through trifluoroacetate-release and halogenation. *Tetrahedron Letters*, 57(17):1906–1908, 2016. doi: 10.1016/j.tetlet.2016.03.064.

[103] C. Mamat, M. Hein, and R. Miethchen. Fluorinated acyclo-C-nucleoside analogues from glycals in two steps. *Carbohydrate Research*, 341(10):1758–1763, 2006. doi: 10.1016/j.carres.2006.01.011.

[104] R. Miethchen, M. Hein, and H. Reinke. A new method for the selective introduction of difluoromethyl and trifluoromethyl groups into sugar moieties. *European Journal of Organic Chemistry*, 1998(5):919–923, 1998. doi: 10.1002/(SICI)1099-0690(199805)1998:5<919::AID-EJOC919>3.0.CO;2-3.

[105] A. Wegert, M. Hein, H. Reinke, N. Hoffmann, and R. Miethchen. Chlorodifluoromethyl-substituted monosaccharide derivatives–radical activation of the carbon-chlorine-bond. *Carbohydrate Research*, 341(16):2641–2652, 2006. doi: 10.1016/j.carres.2006.08.023.

[106] H. Abe, H. Amii, and K. Uneyama. Pd-catalyzed asymmetric hydrogenation of alpha-fluorinated iminoesters in fluorinated alcohol: A new and catalytic enantioselective synthesis of fluoro alpha-amino acid derivatives. *Organic Letters*, 3(3):313–315, 2001. doi: 10.1021/ol0002471.

[107] H. Watanabe, Y. Hashizume, and K. Uneyama. Homologation of trifluoroacetimidoyl iodides by palladium-catalyzed carbonylation. An approach to α-amino perfluoroalkanoic acids. *Tetrahedron Letters*, 33(30):4333–4336, 1992. doi: 10.1016/S0040-4039(00)74253-5.

[108] H. Amii, Y. Kishikawa, K. Kageyama, and K. Uneyama. Palladium-catalyzed tert-butoxycarbonylation of trifluoroacetimidoyl iodides. *Journal of Organic Chemistry*, 65(11):3404–3408, 2000. doi: 10.1021/jo991917n.

[109] F. Fenain, M. Médebielle, M. Rocher, O. Onomura, E. Okada, and D. Shibata. Indium-mediated reduction of β-aminovinyl chloro-difluoromethylated ketones in the presence of heteroaryl aldehydes. *Journal of Fluorine Chemistry*, 128(10):1286–1299, 2007. doi: 10.1016/j.jfluchem.2007.06.001.

[110] I. S. Kondratov, I. I. Gerus, M. V. Furmanova, S. I. Vdovenko, and V. P. Kukhar. Reactions of ethyl triphenylphosphoranylideneacetate with fluorinated β-ketoaldehyde derivatives. *Tetrahedron*, 63(30):7246–7255, 2007. doi: 10.1016/j.tet.2007.04.102.

[111] S. Vaas, M. O. Zimmermann, D. Schollmeyer, J. Stahlecker, M. U. Engelhardt, J. Rheinganz, B. Drotleff, M. Olfert, M. Lämmerhofer, M. Kramer, T. Stehle, and F. M. Boeckler. Principles and applications of $CF_2X$ moieties as unconventional halogen bond donors in medicinal chemistry, chemical biology, and drug discovery. *Journal of Medicinal Chemistry*, 66(15):10202–10225, 2023. doi: 10.1021/acs.jmedchem.3c00634.

[112] G. R. Desiraju, P. S. Ho, L. Kloo, A. C. Legon, R. Marquardt, P. Metrangolo, P. Politzer, G. Resnati, and K. Rissanen. Definition of the halogen bond (IUPAC recommendations 2013). *Pure and Applied Chemistry*, 85(8):1711–1713, 2013. doi: 10.1351/PAC-REC-12-05-10.

[113] D. Bulfield and S. M. Huber. Halogen bonding in organic synthesis and organocatalysis. *Chemistry*, 22(41):14434–14450, 2016. doi: 10.1002/chem.201601844.

[114] R. L. Sutar and S. M. Huber. Catalysis of organic reactions through halogen bonding. *ACS Catalysis*, 9(10):9622–9639, 2019. doi: 10.1021/acscatal.9b02894.

[115] H. Yang and M. W. Wong. Application of halogen bonding to organocatalysis: A theoretical perspective. *Molecules*, 25(5), 2020. doi: 10.3390/molecules25051045.

[116] M. D. Perera and C. B. Aakeröy. Organocatalysis by a multidentate halogen-bond donor: An alternative to hydrogen-bond based catalysis. *New Journal of Chemistry*, 43(21):8311–8314, 2019. doi: 10.1039/C9NJ01404G.

[117] G. Cavallo, P. Metrangolo, R. Milani, T. Pilati, A. Priimagi, G. Resnati, and G. Terraneo. The halogen bond. *Chemical Reviews*, 116(4):2478–2601, 2016. doi: 10.1021/acs.chemrev.5b00484.

[118] M. C. Gullo, L. Baldini, A. Casnati, and L. Marchiò. Halogen bonds direct the solid state architectures of a multivalent iodopropargylcalix[4]arene. *Crystal Growth & Design*, 20(6):3611–3616, 2020. doi: 10.1021/acs.cgd.0c00442.

[119] V. V. Panikkattu, A. S. Huber, A. S. Sinha, B. B. Averkiev, and C. B. Aakeröy. "triply activated" phenyl 3-iodopropiolates: Halogen-bond donors with remarkable σ-hole potentials. *Crystal Growth & Design*, 22(3):1538–1542, 2022. doi: 10.1021/acs.cgd.1c01450.

[120] M. H. Kolář and O. Tabarrini. Halogen bonding in nucleic acid complexes. *Journal of Medicinal Chemistry*, 60(21):8681–8690, 2017. doi: 10.1021/acs.jmedchem.7b00329.

[121] A.-C. C. Carlsson, M. R. Scholfield, R. K. Rowe, M. C. Ford, A. T. Alexander, R. A. Mehl, and P. S. Ho. Increasing enzyme stability and activity through hydrogen bond-enhanced halogen bonds. *Biochemistry*, 57(28):4135–4147, 2018. doi: 10.1021/acs.biochem.8b00603.

[122] S. Peintner and M. Erdélyi. Pushing the limits of characterising a weak halogen bond in solution. *Chemistry*, 28(5):e202103559, 2022. doi: 10.1002/chem.202103559.

[123] K. Mu, Z. Zhu, A. Abula, C. Peng, W. Zhu, and Z. Xu. Halogen bonds exist between noncovalent ligands and natural nucleic acids. *Journal of Medicinal Chemistry*, 65(6):4424–4435, 2022. doi: 10.1021/acs.jmedchem.1c01854.

[124] M. O. Zimmermann, A. Lange, R. Wilcken, M. B. Cieslik, T. E. Exner, A. C. Joerger, P. Koch, and F. M. Boeckler. Halogen-enriched fragment libraries as chemical probes for harnessing halogen bonding in fragment-based lead discovery. *Future Medicinal Chemistry*, 6(6):617–639, 2014. doi: 10.4155/fmc.14.20.

[125] J.-Y. Le Questel, C. Laurence, and J. Graton. Halogen-bond interactions: A crystallographic basicity scale towards iodoorganic compounds. *CrystEngComm*, 15(16):3212, 2013. doi: 10.1039/C2CE26749G.

[126] C. Bissantz, B. Kuhn, and M. Stahl. A medicinal chemist's guide to molecular interactions. *Journal of Medicinal Chemistry*, 53(14):5061–5084, 2010. doi: 10.1021/jm100112j.

[127] A. Bermejo Góme, M. A. C. González, M. Lübcke, M. J. Johansson, M. Schou, and K. J. Szabó. Synthesis of trifluoromethyl moieties by late-stage copper (i) mediated nucleophilic fluorination. *Journal of Fluorine Chemistry*, 194:51–57, 2017. doi: 10.1016/j.jfluchem.2016.12.017.

[128] J.-W. Gu, W.-H. Guo, and X. Zhang. Synthesis of diaryldifluoromethanes by pd-catalyzed difluoroalkylation of arylboronic acids. *Organic Chemistry Frontiers*, 2(1):38–41, 2015. doi: 10.1039/C4QO00246F.

[129] A. Hammadi and C. Crouzel. Synthesis of [18F]-(S)-fluoxetine: A selective serotonine uptake inhibitor. *Journal of Labelled Compounds and Radiopharmaceuticals*, 33(8):703–710, 1993. doi: 10.1002/jlcr.2580330805.

[130] J. Prabhakaran, M. D. Underwood, R. V. Parsey, V. Arango, V. J. Majo, N. R. Simpson, R. van Heertum, J. J. Mann, and J. S. D. Kumar. Synthesis and in vivo evaluation of 18F-4-5-(4-methylphenyl)-3-(trifluoromethyl)-1H-pyrazol-1-ylbenzenesulfonamide as a PET imaging probe for COX-2 expression. *Bioorganic & Medicinal Chemistry*, 15(4): 1802–1807, 2007. doi: 10.1016/j.bmc.2006.11.033.

[131] J. S. Qian and J. J. Wei. Strong halogen bonding of 1,2-diiodoperfluoroethane and 1,6-diiodoperfluorohexane with halide anions revealed by UV-Vis, FT-IR, NMR spectroscopies and crystallography. *Physical Chemistry Chemical Physics*, 13(30):13721–13729, 2011. doi: 10.1039/c1cp20522f.

[132] E. A. L. Gillis, M. Demireva, M. G. Sarwar, M. G. Chudzinski, M. S. Taylor, E. R. Williams, and T. D. Fridgen. Structure and energetics of gas phase halogen-bonding in mono-, bi-, and tri-dentate anion receptors as studied by bird. *Physical Chemistry Chemical Physics*, 15(20):7638–7647, 2013. doi: 10.1039/c3cp00105a.

[133] M. G. Sarwar, B. Dragisic, E. Dimitrijevic, and M. S. Taylor. Halogen bonding between anions and iodoperfluoroorganics: Solution-phase thermodynamics and multidentate-receptor design. *Chemistry – A European Journal*, 19(6):2050–2058, 2013. doi: 10.1002/chem.201202689.

[134] D. Gaspard, K. R. Seddon, P. K. J. Robertson, and H. Q. N. Gunaratne. Halogen-bond mediated efficient storage of extremely volatile perfluoroiodides in ionic liquids. *Chemical Communications*, 55(62):9088–9091, 2019. doi: 10.1039/c9cc04198b.

[135] A. Bruckmann, M. A. Pena, and C. Bolm. Organocatalysis through halogen-bond activation. *Synlett*, (6):900–902, 2008. doi: 10.1055/s-2008-1042935.

[136] S. Dordonne, B. Crousse, D. Bonnet-Delpon, and J. Legros. Fluorous tagging of DABCO through halogen bonding: Recyclable catalyst for the morita-baylis-hillman reaction. *Chemical Communications*, 47(20):5855–5857, 2011. doi: 10.1039/c1cc10869g.

[137] Z. Pan, Z. Fan, B. Lu, and J. Cheng. Halogen-bond-promoted α-C-H amination of ethers for the synthesis of hemiaminal ethers. *Advanced Synthesis & Catalysis*, 360 (9):1761–1767, 2018. doi: 10.1002/adsc.201800006.

[138] F. Sladojevich, E. McNeill, J. Boergel, S.-L. Zheng, and T. Ritter. Condensed-phase, halogen-bonded $CF_3I$ and $C_2F_5I$ adducts for perfluoroalkylation reactions. *Angewandte Chemie*, 54(12):3712–3716, 2015. doi: 10.1002/anie.201410954.

[139] D. A. Smith, L. Brammer, C. A. Hunter, and R. N. Perutz. Metal hydrides form halogen bonds: Measurement of energetics of binding. *Journal of the American Chemical Society*, 136(4):1288–1291, 2014. doi: 10.1021/ja4121499.

[140] H. Takezawa, T. Murase, G. Resnati, P. Metrangolo, and M. Fujita. Halogen-bond-assisted guest inclusion in a synthetic cavity. *Angewandte Chemie*, 54(29):8411–8414, 2015. doi: 10.1002/anie.201500994.

[141] T. Tasnim, C. Ryan, M. L. Christensen, C. J. Fennell, and S. P. Pitre. Radical perfluoroalkylation enabled by a catalytically generated halogen bonding complex and visible light irradiation. *Organic Letters*, 24(1):446–450, 2022. doi: 10.1021/acs.orglett.1c04139.

[142] C. Zhang, H. Zuo, G. Y. Lee, Y. Zou, Q.-D. Dang, K. N. Houk, and D. Niu. Halogen-bond-assisted radical activation of glycosyl donors enables mild and stereoconvergent 1,2-cis-glycosylation. *Nature Chemistry*, 14(6):686–694, 2022. doi: 10.1038/s41557-022-00918-z.

[143] C. B. Aakeroy, T. K. Wijethunga, J. Desper, and C. Moore. Halogen-bond preferences in co-crystal synthesis. *Journal of Chemical Crystallography*, 45(6):267–276, 2015. doi: 10.1007/s10870-015-0596-9.

[144] C. B. Aakeroy, T. K. Wijethunga, J. Desper, and M. Djakovic. Electrostatic potential differences and halogen-bond selectivity. *Crystal Growth & Design*, 16(5):2662–2670, 2016. doi: 10.1021/acs.cgd.5b01770.

[145] C. B. Aakeroy, T. K. Wijethunga, J. Benton, and J. Desper. Stabilizing volatile liquid chemicals using co-crystallization. *Chemical Communications*, 51(12):2425–2428, 2015. doi: 10.1039/c4cc09650a.

[146] C. B. Aakeroy, T. K. Wijethunga, M. A. Haj, J. Desper, and C. Moore. The structural landscape of heteroaryl-2-imidazoles: Competing halogen- and hydrogen-bond interactions. *CrystEngComm*, 16(31):7218–7225, 2014. doi: 10.1039/c4ce00803k.

[147] N. Biot and D. Bonifazi. Programming recognition arrays through double chalcogen-bonding interactions. *Chemistry – A European Journal*, 24(21):5439–5443, 2018. doi: 10.1002/chem.201705428.

[148] A. Carletta, M. Zbacnik, M. van Gysel, M. Vitkovic, N. Tumanov, V. Stilinovic, J. Wouters, and D. Cincic. Playing with isomerism: Cocrystallization of isomeric N-salicylideneaminopyridines with perfluorinated compounds as halogen bond donors and its impact on photochromism. *Crystal Growth & Design*, 18(11):6833–6842, 2018. doi: 10.1021/acs.cgd.8b01064.

[149] A. Crihfield, J. Hartwell, D. Phelps, R. B. Walsh, J. L. Harris, J. F. Payne, W. T. Pennington, and T. W. Hanks. Crystal engineering through halogen bonding. 2. Complexes of diacetylene-linked heterocycles with organic iodides. *Crystal Growth & Design*, 3(3): 313–320, 2003. doi: 10.1021/cg0340042.

[150] R. Puttreddy, F. Topic, A. Valkonen, and K. Rissanen. Halogen-bonded co-crystals of aromatic N-oxides: Polydentate acceptors for halogen and hydrogen bonds. *Crystals*, 7(7):214/1, 2017. doi: 10.3390/cryst7070214.

[151] S. Castro-Fernandez, I. R. Lahoz, A. L. Llamas-Saiz, J. L. Alonso-Gomez, M.-M. Cid, and A. Navarro-Vazquez. Preparation and characterization of a halogen-bonded shape-persistent chiral alleno-acetylenic inclusion complex. *Organic Letters*, 16(4): 1136–1139, 2014. doi: 10.1021/ol403778f.

[152] G. Gattuso, A. Pappalardo, M. F. Parisi, I. Pisagatti, F. Crea, R. Liantonio, P. Metrangolo, W. Navarrini, G. Resnati, T. Pilati, and S. Pappalardo. Dipyridinocalixcrown/diiodoperfluorocarbon binary host systems for CsI: Structural studies and fluorous phase extraction of cesium. *Tetrahedron*, 63(23):4951–4958, 2007. doi: 10.1016/j.tet.2007.03.136.

[153] P. Metrangolo, Y. Carcenac, M. Lahtinen, T. Pilati, K. Rissanen, A. Vij, and G. Resnati. Nonporous organic solids capable of dynamically resolving mixtures of diiodoperfluoroalkanes. *Science (Washington, DC, U. S.)*, 323(5920):1461–1464, 2009. doi: 10.1126/science.1168679.

[154] F. Pan, N. K. Beyeh, R. H. A. Ras, and K. Rissanen. Guest-induced folding of the N-benzyl substituents in an ammonium resorcinarene chloride and the formation of a halogen-bonded dimer of capsules. *Crystal Growth & Design*, 16(12):6729–6733, 2016. doi: 10.1021/acs.cgd.6b01454.

[155] L.-Y. You, S.-G. Chen, X. Zhao, Y. Liu, W.-X. Lan, Y. Zhang, H.-J. Lu, C.-Y. Cao, and Z.-T. Li. CδH···O hydrogen bonding induced triazole foldamers: Efficient halogen bonding receptors for organohalogens. *Angewandte Chemie*, 124(7):1689–1693, 2012. doi: 10.1002/ange.201106996.

[156] R. Bertani, P. Metrangolo, A. Moiana, E. Perez, T. Pilati, G. Resnati, I. Rico-Lattes, and A. Sassi. Supramolecular route to fluorinated coatings: Self-assembly between poly(4-vinylpyridines) and haloperfluorocarbons. *Adv. Mater. (Weinheim, Ger.)*, 14(17):1197–1201, 2002. doi: 10.1002/1521-4095(20020903)14:17<1197::aid-adma1197>3.0.co;2-v.

[157] S. Bi, H. Wang, J. Zhou, S. You, Y. Zhang, X. Shi, Z. Tang, and H. Zhou. Halogen bonding reduces intrinsic traps and enhances charge mobilities in halide perovskite solar cells. *Journal of Materials Chemistry A*, 7(12):6840–6848, 2019. doi: 10.1039/c8ta11835c.

[158] M. T. Messina, P. Metrangolo, W. Navarrini, S. Radice, G. Resnati, and G. Zerbi. Infrared and raman analyses of the halogen-bonded non-covalent adducts formed by α,ω-diiodoperfluoroalkanes with DABCO and other electron donors. *J. Mol. Struct.*, 524: 87–94, 2000. doi: 10.1016/s0022-2860(99)00445-7.

[159] R. Milani, N. Houbenov, F. Fernandez-Palacio, G. Cavallo, A. Luzio, J. Haataja, G. Giancane, M. Saccone, A. Priimagi, P. Metrangolo, and O. Ikkala. Hierarchical self-assembly of halogen-bonded block copolymer complexes into upright cylindrical domains. *Chem*, 2(3):417–426, 2017. doi: 10.1016/j.chempr.2017.02.003.

[160] K. Shou, J. K. Hong, E. S. Wood, J. M. Hook, A. Nelson, Y. Yin, G. G. Andersson, A. Abate, U. Steiner, and C. Neto. Ultralow surface energy self-assembled monolayers of iodo-perfluorinated alkanes on silica driven by halogen bonding. *Nanoscale*, 11(5):2401–2411, 2019. doi: 10.1039/c8nr08195f.

[161] C. M. Widdifield, G. Cavallo, G. A. Facey, T. Pilati, J. Lin, P. Metrangolo, G. Resnati, and D. L. Bryce. Multinuclear solid-state magnetic resonance as a sensitive probe of structural changes upon the occurrence of halogen bonding in co-crystals. *Chemistry – A European Journal*, 19(36):11949–11962, 2013. doi: 10.1002/chem.201300809.

[162] C. M. Wolff, L. Canil, C. Rehermann, N. L. Nguyen, F. Zu, M. Ralaiarisoa, P. Caprioglio, L. Fiedler, M. Stolterfoht, Kogikoski, Sergio, Jr., I. Bald, N. Koch, E. L. Unger, T. Dittrich, A. Abate, and D. Neher. Perfluorinated self-assembled monolayers enhance the stability and efficiency of inverted perovskite solar cells. *ACS Nano*, 14(2):1445–1456, 2020. doi: 10.1021/acsnano.9b03268.

[163] X. Q. Yan, Q. J. Shen, X. R. Zhao, H. Y. Gao, X. Pang, and W. J. Jin. Halogen bonding: A new retention mechanism for the solid phase extraction of perfluorinated iodoalkanes. *Analytica Chimica Acta*, 753:48–56, 2012. doi: 10.1016/j.aca.2012.09.024.

[164] X. Zhu, Y. Lu, C. Peng, J. Hu, H. Liu, and Y. Hu. Halogen bonding interactions between brominated ion pairs and $CO_2$ molecules: Implications for design of new and efficient ionic liquids for $CO_2$ absorption. *The Journal of Physical Chemistry B*, 115(14):3949–3958, 2011. doi: 10.1021/jp111194k.

[165] R. Cabot and C. A. Hunter. Non-covalent interactions between iodo-perfluorocarbons and hydrogen bond acceptors. *Chemical Communications*, (15):2005–2007, 2009. doi: 10.1039/b822284c.

[166] D. Hauchecorne, B. J. van der Veken, W. A. Herrebout, and P. E. Hansen. A $^{19}$F NMR study of C−I···π halogen bonding. *Chemical Physics*, 381(1-3):5–10, 2011. doi: 10.1016/j.chemphys.2010.12.012.

[167] B. Jimmink, D. Sethio, L. Turunen, D. von der Heiden, and M. Erdelyi. Probing halogen bonds by scalar couplings. *Journal of the American Chemical Society*, 143 (28):10695–10699, 2021. doi: 10.1021/jacs.1c04477.

[168] M. T. Messina, P. Metrangolo, W. Panzeri, T. Pilati, and G. Resnati. Intermolecular recognition between hydrocarbon oxygen-donors and perfluorocarbon iodine-acceptors: The shortest O···I non-covalent bond. *Tetrahedron*, 57(40):8543–8550, 2001. doi: 10.1016/s0040-4020(01)00794-3.

[169] M. G. Sarwar, D. Ajami, G. Theodorakopoulos, I. D. Petsalakis, and Rebek, Julius, Jr. Amplified halogen bonding in a small space. *Journal of the American Chemical Society*, 135(37):13672–13675, 2013. doi: 10.1021/ja407815t.

[170] E. Corradi, S. V. Meille, M. T. Messina, P. Metrangolo, and G. Resnati. Perfluorocarbon-hydrocarbon self-assembly, part ix. Halogen bonding versus hydrogen bonding in driving self-assembly processes. *Angewandte Chemie*, 39(10):1782–1786, 2000. doi: 10.1002/(sici)1521-3773(20000515)39:10<1782::aid-anie1782>3.0.co;2-5.

[171] N. Houbenov, R. Milani, M. Poutanen, J. Haataja, V. Dichiarante, J. Sainio, J. Ruokolainen, G. Resnati, P. Metrangolo, and O. Ikkala. Halogen-bonded mesogens direct polymer self-assemblies up to millimetre length scale. *Nature Communications*, 5, 2014. doi: 10.1038/ncomms5043.

[172] M. T. Johnson, Z. Dzolic, M. Cetina, O. F. Wendt, L. Ohrstrom, and K. Rissanen. Neutral organometallic halogen bond acceptors: Halogen bonding in complexes of PCPPdX (X = Cl, Br, I) with iodine ($I_2$), 1,4-diiodotetrafluorobenzene (F4DIBz), and 1,4-diiodooctafluorobutane (F8DIBu). *Crystal Growth & Design*, 12(1):362–368, 2012. doi: 10.1021/cg201170w.

[173] R. Liantonio, P. Metrangolo, T. Pilati, G. Resnati, and A. Stevenazzi. Perfluorocarbon-hydrocarbon self-assembly: First crystalline halogen-bonded complex involving bromoperfluoroalkanes. *Crystal Growth & Design*, 3(5):799–803, 2003. doi: 10.1021/cg034098f.

[174] P. Metrangolo, W. Panzeri, F. Recupero, and G. Resnati. Perfluorocarbon-hydrocarbon self-assembly part 16. $^{19}$F NMR study of the halogen bonding between haloperfluorocarbons and heteroatom containing hydrocarbons. *Journal of Fluorine Chemistry*, 114(1):27–33, 2002.

[175] P. Metrangolo, T. Pilati, G. Resnati, and A. Stevenazzi. Metric engineering of perfluorocarbon-hydrocarbon layered solids driven by the halogen bonding. *Chemical Communications*, (13):1492–1493, 2004. doi: 10.1039/b402305f.

[176] M. Saccone, G. Cavallo, P. Metrangolo, A. Pace, I. Pibiri, T. Pilati, G. Resnati, and G. Terraneo. Halogen bond directionality translates tecton geometry into self-assembled architecture geometry. *CrystEngComm*, 15(16):3102–3105, 2013. doi: 10.1039/c3ce40268a.

[177] P. Cardillo, E. Corradi, A. Lunghi, S. Valdo Meille, T. M. Messina, P. Metrangolo, and G. Resnati. The N···I intermolecular interaction as a general protocol for the formation of perfluorocarbon-hydrocarbon supramolecular architectures. *Tetrahedron*, 56(30): 5535–5550, 2000. doi: 10.1016/s0040-4020(00)00476-2.

[178] A. Casnati, R. Liantonio, P. Metrangolo, G. Resnati, R. Ungaro, and F. Ugozzoli. Molecular and supramolecular homochirality: Enantiopure perfluorocarbon rotamers and halogen-bonded fluorous double helices. *Angewandte Chemie*, 45(12):1915–1918, 2006. doi: 10.1002/anie.200504459.

[179] V. Kumar, T. Pilati, G. Terraneo, F. Meyer, P. Metrangolo, and G. Resnati. Halogen bonded borromean networks by design: Topology invariance and metric tuning in a library of multi-component systems. *Chemical Science*, 8(3):1801–1810, 2017. doi: 10.1039/c6sc04478f.

[180] C.-Z. Liu, S. Koppireddi, H. Wang, D.-W. Zhang, and Z.-T. Li. Halogen bonding directed supramolecular quadruple and double helices from hydrogen-bonded arylamide foldamers. *Angewandte Chemie*, 58(1):226–230, 2019. doi: 10.1002/anie.201811561.

[181] P. Metrangolo, F. Meyer, T. Pilati, D. M. Proserpio, and G. Resnati. Highly interpenetrated supramolecular networks supported by N···I halogen bonding. *Chemistry – A European Journal*, 13(20):5765–5772, 2007. doi: 10.1002/chem.200601653.

[182] F. Pan, N. K. Beyeh, and K. Rissanen. Concerted halogen-bonded networks with N-alkyl ammonium resorcinarene bromides: From dimeric dumbbell to capsular architectures. *Journal of the American Chemical Society*, 137(32):10406–10413, 2015. doi: 10.1021/jacs.5b06590.

[183] F. Topic and K. Rissanen. Systematic construction of ternary cocrystals by orthogonal and robust hydrogen and halogen bonds. *Journal of the American Chemical Society*, 138(20):6610–6616, 2016. doi: 10.1021/jacs.6b02854.

[184] S. Vaas, M. O. Zimmermann, T. Klett, and F. M. Boeckler. Synthesis of amino acids bearing halodifluoromethyl moieties and their application to p53-derived peptides binding to Mdm2/Mdm4. *Drug Design, Development and Therapy*, 17:1247–1274, 2023. doi: 10.2147/DDDT.S406703.

[185] J. Heidrich, T. E. Exner, and F. M. Boeckler. Predicting the magnitude of σ-holes using VmaxPred, a fast and efficient tool supporting the application of halogen bonds in drug discovery. *Journal of Chemical Information and Modeling*, 59(2):636–643, 2019. doi: 10.1021/acs.jcim.8b00622.

[186] C. D. Sessler, M. Rahm, S. Becker, J. M. Goldberg, F. Wang, and S. J. Lippard. $Cf_2h$, a hydrogen bond donor. *Journal of the American Chemical Society*, 139(27):9325–9332, 2017. doi: 10.1021/jacs.7b04457.

[187] Y. Zhou, J. Wang, Z. Gu, S. Wang, W. Zhu, J. L. Aceña, V. A. Soloshonok, K. Izawa, and H. Liu. Next generation of fluorine-containing pharmaceuticals, compounds currently in phase ii-iii clinical trials of major pharmaceutical companies: New structural trends and therapeutic areas. *Chemical Reviews*, 116(2):422–518, 2016. doi: 10.1021/acs.chemrev.5b00392.

[188] Y. Guo and Q.-Y. Chen. The reactions of difluorodiiodomethane with nucleophiles. *Journal of Fluorine Chemistry*, 102(1-2):105–109, 2000. doi: 10.1016/S0022-1139(99)00228-6.

[189] D. J. Burton and Denise M. Wiemers. Synthesis of bromodifluoromethyl phenyl sulfide, sulfoxide and sulfone. *Journal of Fluorine Chemistry*, 18(4):573–582, 1981. doi: 10.1016/S0022-1139(00)82673-1.

[190] T. Ismalaj, Ermal; Billard. An easier and quicker access to (benzenesulfonyl)difluoromethanesulfenamide reagent. *Journal of Fluorine Chemistry*, 203:215–217, 2017. doi: 10.1016/j.jfluchem.2017.07.001.

[191] C. Wakselman, M. Tordeux, J.-L. Clavel, and B. Langlois. Reactions of bromotrifluoromethane and related halides: Synthesis of trifluoromethyl sulphides from disulphides. *Journal of the Chemical Society, Chemical Communications*, page 993, 1991. doi: 10.1039/c39910000993.

[192] M. Breccia, G. Colafigli, E. Scalzulli, and M. Martelli. Asciminib: An investigational agent for the treatment of chronic myeloid leukemia. *Expert Opinion on Investigational Drugs*, 30(8):803–811, 2021. doi: 10.1080/13543784.2021.1941863.

[193] P. Schuld, S. Grzesiek, J. Schlotte, J. M. Habazettl, W. Jahnke, L. Barys, S. W. Cowan-Jacob, A. Loo, A. Wiget, and P. W. Manley. Structural and biochemical studies confirming the mechanism of action of asciminib, an agent specifically targeting the abl myristoyl pocket (STAMP). *Blood*, 136:34–35, 2020. doi: 10.1182/blood-2020-140968.

[194] M. R. McGill and H. Jaeschke. Metabolism and disposition of acetaminophen: Recent advances in relation to hepatotoxicity and diagnosis. *Pharmaceutical Research*, 30: 2174–2187, 2013. doi: 10.1007/s11095-013-1007-6.

[195] Schrödinger Release 2021-1: QikProp, Schrödinger, LLC, New York, NY, 2021.

[196] Schrödinger Release 2021-1: LigPrep, Schrödinger, LLC, New York, NY, 2021.

[197] A. Leo, C. Hansch, and D. Elkins. Partition coefficients and their uses. *Chemical Reviews*, 71(6):525–616, 1971. doi: 10.1021/cr60274a001.

[198] Y. Kwon. *Handbook of Essential Pharmacokinetics, Pharmacodynamics and Drug Metabolism for Industrial Scientists*. Springer eBook Collection. Springer US Imprint Springer, New York, NY, 1st 2002 edition, 2002. doi: 10.1007/b112416.

[199] E. P. Gillis, K. J. Eastman, M. D. Hill, D. J. Donnelly, and N. A. Meanwell. Applications of fluorine in medicinal chemistry. *Journal of Medicinal Chemistry*, 58(21):8315–8359, 2015. doi: 10.1021/acs.jmedchem.5b00258.

[200] N. A. Meanwell. Fluorine and fluorinated motifs in the design and application of bioisosteres for drug design. *Journal of Medicinal Chemistry*, 61(14):5822–5880, 2018. doi: 10.1021/acs.jmedchem.7b01788.

[201] M. R. Bauer, R. N. Jones, M. G. J. Baud, R. Wilcken, F. M. Boeckler, A. R. Fersht, A. C. Joerger, and J. Spencer. Harnessing fluorine-sulfur contacts and multipolar interactions for the design of p53 mutant Y220C rescue drugs. *ACS Chemical Biology*, 11(8): 2265–2274, 2016. doi: 10.1021/acschembio.6b00315.

[202] S. Kozuch and J. M. L. Martin. Halogen bonds: Benchmarks and theoretical analysis. *Journal of Chemical Theory and Computation*, 9(4):1918–1931, 2013. doi: 10.1021/ct 301064t.

[203] M. Kolář, J. Hostaš, and P. Hobza. The strength and directionality of a halogen bond are co-determined by the magnitude and size of the σ-hole. *Physical Chemistry Chemical Physics*, 16(21):9987–9996, 2014. doi: 10.1039/C3CP55188A.

[204] M. H. Kolář and P. Hobza. Computer modeling of halogen bonds and other σ-hole interactions. *Chemical Reviews*, 116(9):5155–5187, 2016. doi: 10.1021/acs.chemrev.5b 00560.

[205] P. Politzer, P. Lane, M. C. Concha, Y. Ma, and J. S. Murray. An overview of halogen bonding. *Journal of Molecular Modeling*, 13(2):305–311, 2007. doi: 10.1007/ s00894-006-0154-7.

[206] P. Politzer, J. S. Murray, and T. Clark. Halogen bonding: An electrostatically-driven highly directional noncovalent interaction. *Physical Chemistry Chemical Physics*, 12 (28):7748–7757, 2010. doi: 10.1039/C004189K.

[207] K. E. Riley, J. S. Murray, J. Fanfrlík, J. Rezáč, R. J. Solá, M. C. Concha, F. M. Ramos, and P. Politzer. Halogen bond tunability i: The effects of aromatic fluorine substitution on the strengths of halogen-bonding interactions involving chlorine, bromine, and iodine. *Journal of Molecular Modeling*, 17(12):3309–3318, 2011. doi: 10.1007/s00894-011-1015-6.

[208] K. E. Riley, J. S. Murray, J. Fanfrlík, J. Rezáč, R. J. Solá, M. C. Concha, F. M. Ramos, and P. Politzer. Halogen bond tunability ii: The varying roles of electrostatic and dispersion contributions to attraction in halogen bonds. *Journal of Molecular Modeling*, 19 (11):4651–4659, 2013. doi: 10.1007/s00894-012-1428-x.

[209] K. E. Riley and P. Hobza. Strength and character of halogen bonds in protein–ligand complexes. *Crystal Growth & Design*, 11(10):4272–4278, 2011. doi: 10.1021/cg200882f.

[210] K. E. Riley and P. Hobza. The relative roles of electrostatics and dispersion in the stabilization of halogen bonds. *Physical Chemistry Chemical Physics*, 15(41):17742–17751, 2013. doi: 10.1039/C3CP52768A.

[211] J. Heidrich, L. E. Sperl, and F. M. Boeckler. Embracing the diversity of halogen bonding motifs in fragment-based drug discovery-construction of a diversity-optimized halogen-enriched fragment library. *Frontiers in Chemistry*, 7:9, 2019. doi: 10.3389/fchem.2019.00009.

[212] M. Dammann, M. Kramer, M. O. Zimmermann, and F. M. Boeckler. Quadruple target evaluation of diversity-optimized halogen-enriched fragments (heflibs) reveals substantial ligand efficiency for AP2-associated protein kinase 1 (AAK1). *Frontiers in Chemistry*, 9:815567, 2021. doi: 10.3389/fchem.2021.815567.

[213] J. Stahlecker, T. Klett, M. Schwer, S. Jaag, M. Dammann, L. N. Ernst, M. B. Braun, M. O. Zimmermann, M. Kramer, M. Lämmerhofer, T. Stehle, M. Coles, and F. M. Boeckler. Revisiting a challenging p53 binding site: A diversity-optimized HEFLib reveals diverse binding modes in T-p53C-Y220C. *RSC Medicinal Chemistry*, 13(12):1575–1586, 2022. doi: 10.1039/D2MD00246A.

[214] M. Dammann, J. Stahlecker, M. O. Zimmermann, T. Klett, K. Rotzinger, M. Kramer, M. Coles, T. Stehle, and F. M. Boeckler. Screening of a halogen-enriched fragment library leads to unconventional binding modes. *Journal of Medicinal Chemistry*, 65 (21):14539–14552, 2022. doi: 10.1021/acs.jmedchem.2c00951.

[215] F. Ansideri, M. Dammann, F. M. Boeckler, and P. Koch. Fluorescence polarization-based competition binding assay for c-jun N-terminal kinases 1 and 2. *Analytical Biochemistry*, 532:26–28, 2017. doi: 10.1016/j.ab.2017.05.022.

[216] B. R. Beno, K.-S. Yeung, M. D. Bartberger, L. D. Pennington, and N. A. Meanwell. A survey of the role of noncovalent sulfur interactions in drug design. *Journal of Medicinal Chemistry*, 58(11):4383–4438, 2015. doi: 10.1021/jm501853m.

[217] Y. Nagao, T. Hirata, S. Goto, S. Sano, A. Kakehi, K. Iizuka, and M. Shiro. Intramolecular nonbonded S···O interaction recognized in (acylimino)thiadiazoline derivatives as angiotensin ii receptor antagonists and related compounds. *Journal of the American Chemical Society*, 120(13):3104–3110, 1998. doi: 10.1021/ja973109o.

[218] L. P. Kozlowski. Proteome-pI 2.0: Proteome isoelectric point database update. *Nucleic Acids Research*, 50(D1):D1535–D1540, 2022. doi: 10.1093/nar/gkab944.

[219] K. Amaning, M. Lowinski, F. Vallee, V. Steier, C. Marcireau, A. Ugolini, C. Delorme, F. Foucalt, G. McCort, N. Derimay, C. Andouche, S. Vougier, S. Llopart, N. Halland, and A. Rak. The use of virtual screening and differential scanning fluorimetry for the rapid identification of fragments active against MEK1. *Bioorganic & Medicinal Chemistry Letters*, 23(12):3620–3626, 2013. doi: 10.1016/j.bmcl.2013.04.003.

[220] P. G. Wyatt, A. J. Woodhead, V. Berdini, J. A. Boulstridge, M. G. Carr, D. M. Cross, D. J. Davis, L. A. Devine, T. R. Early, R. E. Feltell, E. J. Lewis, R. L. McMenamin, E. F. Navarro, M. A. O'Brien, M. O'Reilly, M. Reule, G. Saxty, L. C. A. Seavers, D.-M. Smith, M. S. Squires, G. Trewartha, M. T. Walker, and A. J.-A. Woolford. Identification of N-(4-piperidinyl)-4-(2,6-dichlorobenzoylamino)-1H-pyrazole-3-carboxamide (AT7519), a novel cyclin dependent kinase inhibitor using fragment-based x-ray crystallography and structure based drug design. *Journal of Medicinal Chemistry*, 51(16):4986–4999, 2008. doi: 10.1021/jm800382h.

[221] T. Kamenecka, J. Habel, D. Duckett, W. Chen, Y. Y. Ling, B. Frackowiak, R. Jiang, Y. Shin, X. Song, and P. LoGrasso. Structure-activity relationships and X-ray structures describing the selectivity of aminopyrazole inhibitors for c-jun N-terminal kinase 3 (JNK3) over p38. *The Journal of Biological Chemistry*, 284(19):12853–12861, 2009. doi: 10.1074/jbc.M809430200.

[222] R. Jain, M. Mathur, J. Lan, A. Costales, G. Atallah, S. Ramurthy, S. Subramanian, L. Setti, P. Feucht, B. Warne, L. Doyle, S. Basham, A. B. Jefferson, M. Lindvall, B. A. Appleton, and C. M. Shafer. Discovery of potent and selective rsk inhibitors as biological probes. *Journal of Medicinal Chemistry*, 58(17):6766–6783, 2015. doi: 10.1021/acs.jmedchem.5b00450.

[223] D. Lesuisse, G. Dutruc-Rosset, G. Tiraboschi, M. K. Dreyer, S. Maignan, A. Chevalier, F. Halley, P. Bertrand, M.-C. Burgevin, D. Quarteronet, and T. Rooney. Rational design of potent GSK3beta inhibitors with selectivity for Cdk1 and Cdk2. *Bioorganic & Medicinal Chemistry Letters*, 20(6):1985–1989, 2010. doi: 10.1016/j.bmcl.2010.01.114.

[224] H.-L. Wang, V. J. Cee, F. Chavez, B. A. Lanman, A. B. Reed, B. Wu, N. Guerrero, J. R. Lipford, C. Sastri, J. Winston, K. L. Andrews, X. Huang, M. R. Lee, C. Mohr, Y. Xu, Y. Zhou, and A. S. Tasker. The discovery of novel 3-(pyrazin-2-yl)-1H-indazoles as potent pan-Pim kinase inhibitors. *Bioorganic & Medicinal Chemistry Letters*, 25(4): 834–840, 2015. doi: 10.1016/j.bmcl.2014.12.068.

[225] W. J. Middleton. New fluorinating reagents. Dialkylaminosulfur fluorides. *The Journal of Organic Chemistry*, 40(5):574–578, 1975. doi: 10.1021/jo00893a007.

[226] K. Lukin, M. C. Hsu, D. Fernando, and M. R. Leanna. New practical synthesis of indazoles via condensation of o-fluorobenzaldehydes and their O-methyloximes with hydrazine. *The Journal of Organic Chemistry*, 71(21):8166–8172, 2006. doi: 10.1021/jo0613784.

[227] P. A. Procopiou, J. W. Barrett, N. P. Barton, M. Begg, D. Clapham, R. C. Copley, A. J. Ford, R. H. Graves, D. A. Hall, A. P. Hancock, et al. Synthesis and structure–activity relationships of indazole arylsulfonamides as allosteric CC-chemokine receptor 4 (CCR4) antagonists. *Journal of Medicinal Chemistry*, 56(5):1946–1960, 2013. doi: 10.1021/jm301572h.

[228] M. G. Palermo. Novel one-pot cyclization of ortho substituted benzonitriles to 3-amino-1,2-benzisoxazoles. *Tetrahedron Letters*, 37(17):2885–2886, 1996. doi: 10.1016/0040-4039(96)00425-X.

[229] B. Gallagher, J. Van Veldhuizen, X. Wu, H. Deng, I. Sucholeiki, M. Hochguertel, H. Bluhm, and A. Taveras. Heterobicyclic metalloprotease inhibitors. US 2007/0155737 A1, July 5, 2007.

[230] U. Heinelt, A. Hofmeister, and J. Czech. WO2008/014888A3: Imino-imidazo-pyridine derivatives having antithrombotic activity. 2008.

[231] F. Shibahara, Y. Dohke, and T. Murai. Palladium-catalyzed C-H bond direct alkynylation of 5-membered heteroarenes: A well-defined synthetic route to azole derivatives containing two different alkynyl groups. *The Journal of Organic Chemistry*, 77(12): 5381–5388, 2012. doi: 10.1021/jo3008385.

[232] F. Bellina, M. Lessi, G. Marianetti, and A. Panattoni. Highly regioselective C-5 alkynylation of imidazoles by one-pot sequential bromination and sonogashira cross coupling. *Tetrahedron Letters*, 56(25):3855–3857, 2015. doi: 10.1016/j.tetlet.2015.04.094.

[233] M. R. Scholfield, M. C. Ford, A.-C. C. Carlsson, H. Butta, R. A. Mehl, and P. S. Ho. Structure-energy relationships of halogen bonds in proteins. *Biochemistry*, 56(22): 2794–2802, 2017. doi: 10.1021/acs.biochem.7b00022.

[234] M. Erdélyi. Halogen bonding in solution. *Chemical Society Reviews*, 41(9):3547–3557, 2012. doi: 10.1039/C2CS15292D.

[235] E. Danelius, H. Andersson, P. Jarvoll, K. Lood, J. Gräfenstein, and M. Erdélyi. Halogen bonding: A powerful tool for modulation of peptide conformation. *Biochemistry*, 56 (25):3265–3272, 2017. doi: 10.1021/acs.biochem.7b00429.

[236] M. Erdélyi. Application of the halogen bond in protein systems. *Biochemistry*, 56(22): 2759–2761, 2017. doi: 10.1021/acs.biochem.7b00371.

[237] A. Bertolani, L. Pirrie, L. Stefan, N. Houbenov, J. S. Haataja, L. Catalano, G. Terraneo, G. Giancane, L. Valli, R. Milani, O. Ikkala, G. Resnati, and P. Metrangolo. Supramolecular amplification of amyloid self-assembly by iodination. *Nature Communications*, 6:7574, 2015. doi: 10.1038/ncomms8574.

[238] A. Pizzi, V. Dichiarante, G. Terraneo, and P. Metrangolo. Crystallographic insights into the self-assembly of KLVFF amyloid-beta peptides. *Biopolymers*, 110(5):e23088, 2017. doi: 10.1002/bip.23088.

[239] A. Pizzi, L. Lascialfari, N. Demitri, A. Bertolani, D. Maiolo, E. Carretti, and P. Metrangolo. Halogen bonding modulates hydrogel formation from fmoc amino acids. *CrystEngComm*, 19(14):1870–1874, 2017. doi: 10.1039/C7CE00031F.

[240] A. Pizzi, N. Demitri, G. Terraneo, and P. Metrangolo. Halogen bonding at the wet interfaces of an amyloid peptide structure. *CrystEngComm*, 20(36):5321–5326, 2018. doi: 10.1039/C8CE01205A.

[241] A. Pizzi, L. Catalano, N. Demitri, V. Dichiarante, G. Terraneo, and P. Metrangolo. Halogen bonding as a key interaction in the self–assembly of iodinated diphenylalanine peptides. *Peptide Science*, 112(1), 2020. doi: 10.1002/pep2.24127.

[242] G. Bergamaschi, L. Lascialfari, A. Pizzi, M. I. Martinez Espinoza, N. Demitri, A. Milani, A. Gori, and P. Metrangolo. A halogen bond-donor amino acid for organocatalysis in water. *Chemical Communications*, 54(76):10718–10721, 2018. doi: 10.1039/c8cc06010j.

[243] A. Marchetti, A. Pizzi, G. Bergamaschi, N. Demitri, U. Stollberg, U. Diederichsen, C. Pigliacelli, and P. Metrangolo. Fibril structure demonstrates the role of iodine labelling on a pentapeptide self-assembly. *Chemistry*, 28(14):e202104089, 2022. doi: 10.1002/chem.202104089.

[244] W. Li, F. Separovic, N. M. O'Brien-Simpson, and J. D. Wade. Chemically modified and conjugated antimicrobial peptides against superbugs. *Chemical Society Reviews*, 50 (8):4932–4973, 2021. doi: 10.1039/d0cs01026j.

[245] A. C. Joerger and A. R. Fersht. Structural biology of the tumor suppressor p53. *Annual Review of Biochemistry*, 77(1):557–582, 2008. doi: 10.1146/annurev.biochem.77.060806.091238.

[246] D. G. Kirsch and M. B. Kastan. Tumor-suppressor p53: Implications for tumor development and prognosis. *Journal of Clinical Oncology*, 16(9):3158–3168, 1998. doi: 10.1200/JCO.1998.16.9.3158.

[247] F. M. Boeckler, A. C. Joerger, G. Jaggi, T. J. Rutherford, D. B. Veprintsev, and A. R. Fersht. Targeted rescue of a destabilized mutant of p53 by an in silico screened drug. *Proceedings of the National Academy of Sciences of the United States of America*, 105 (30):10360–10365, 2008. doi: 10.1073/pnas.0805326105.

[248] S. M. Vogel, M. R. Bauer, A. C. Joerger, R. Wilcken, T. Brandt, D. B. Veprintsev, T. J. Rutherford, A. R. Fersht, and F. M. Boeckler. Lithocholic acid is an endogenous inhibitor of MDM4 and MDM2. *Proceedings of the National Academy of Sciences of the United States of America*, 109(42):16906–16910, 2012. doi: 10.1073/pnas.1215060109.

[249] R. Wilcken, M. O. Zimmermann, M. R. Bauer, T. J. Rutherford, A. R. Fersht, A. C. Joerger, and F. M. Boeckler. Experimental and theoretical evaluation of the ethynyl moiety as a halogen bioisostere. *ACS Chemical Biology*, 10(12):2725–2732, 2015. doi: 10.1021/acschembio.5b00515.

[250] A. C. Joerger, M. R. Bauer, R. Wilcken, M. G. J. Baud, H. Harbrecht, T. E. Exner, F. M. Boeckler, J. Spencer, and A. R. Fersht. Exploiting transient protein states for the design of small-molecule stabilizers of mutant p53. *Structure*, 23(12):2246–2255, 2015. doi: 10.1016/j.str.2015.10.016.

[251] S. Bell, C. Klein, L. Müller, S. Hansen, and J. Buchner. p53 contains large unstructured regions in its native state. *Journal of Molecular Biology*, 322(5):917–927, 2002. doi: 10.1016/S0022-2836(02)00848-3.

[252] R. Dawson, L. Müller, A. Dehner, C. Klein, H. Kessler, and J. Buchner. The N-terminal domain of p53 is natively unfolded. *Journal of Molecular Biology*, 332(5):1131–1141, 2003. doi: 10.1016/j.jmb.2003.08.008.

[253] P. H. Kussie, S. Gorina, V. Marechal, B. Elenbaas, J. Moreau, A. J. Levine, and N. P. Pavletich. Structure of the MDM2 oncoprotein bound to the p53 tumor suppressor transactivation domain. *Science*, 274(5289):948–953, 1996. doi: 10.1126/science.274.5289.948.

[254] G. M. Popowicz, A. Czarna, and T. A. Holak. Structure of the human Mdmx protein bound to the p53 tumor suppressor transactivation domain. *Cell Cycle*, 7(15):2441–2443, 2008. doi: 10.4161/cc.6365.

[255] M. Pazgier, M. Liu, G. Zou, W. Yuan, C. Li, C. Li, J. Li, J. Monbo, D. Zella, S. G. Tarasov, and W. Lu. Structural basis for high-affinity peptide inhibition of p53 interactions with MDM2 and MDMX. *Proceedings of the National Academy of Sciences of the United States of America*, 106(12):4665–4670, 2009. doi: 10.1073/pnas.0900947106.

[256] C. Li, M. Pazgier, C. Li, W. Yuan, M. Liu, G. Wei, W.-Y. Lu, and W. Lu. Systematic mutational analysis of peptide inhibition of the p53-MDM2/MDMX interactions. *Journal of Molecular Biology*, 398(2):200–213, 2010. doi: 10.1016/j.jmb.2010.03.005.

[257] Z. Nikolovska-Coleska, R. Wang, X. Fang, H. Pan, Y. Tomita, P. Li, P. P. Roller, K. Krajewski, N. G. Saito, J. A. Stuckey, and S. Wang. Development and optimization of a binding assay for the XIAP BIR3 domain using fluorescence polarization. *Analytical Biochemistry*, 332(2):261–273, 2004. doi: 10.1016/j.ab.2004.05.055.

[258] A. Czarna, G. M. Popowicz, A. Pecak, S. Wolf, G. Dubin, and T. A. Holak. High affinity interaction of the p53 peptide-analogue with human Mdm2 and Mdmx. *Cell Cycle*, 8 (8):1176–1184, 2009. doi: 10.4161/cc.8.8.8185.

[259] I. T. Weber, J. Wu, J. Adomat, R. W. Harrison, A. R. Kimmel, E. M. Wondrak, and J. M. Louis. Crystallographic analysis of human immunodeficiency virus 1 protease with an analog of the conserved CA-p2 substrate – interactions with frequently occurring glutamic acid residue at p2' position of substrates. *European Journal of Biochemistry*, 249(2):523–530, 1997. doi: 10.1111/j.1432-1033.1997.00523.x.

[260] J. H. Jung, S. Bae, J. Y. Lee, S. R. Woo, H. J. Cha, Y. Yoon, K.-S. Suh, S.-J. Lee, I.-C. Park, Y.-W. Jin, K.-H. Lee, S. An, and J. H. Lee. E3 ubiquitin ligase Hades negatively regulates the exonuclear function of p53. *Cell Death and Differentiation*, 18(12):1865–1875, 2011. doi: 10.1038/cdd.2011.57.

[261] Y. A. Zhan, H. Wu, A. T. Powell, G. W. Daughdrill, and F. M. Ytreberg. Impact of the K24N mutation on the transactivation domain of p53 and its binding to murine double-minute clone 2. *Proteins*, 81(10):1738–1747, 2013. doi: 10.1002/prot.24310.

[262] S. Mizuta, I. S. R. Stenhagen, M. O'Duill, J. Wolstenhulme, A. K. Kirjavainen, S. J. Forsback, M. Tredwell, G. Sandford, P. R. Moore, M. Huiban, S. K. Luthra, J. Passchier, O. Solin, and V. Gouverneur. Catalytic decarboxylative fluorination for the synthesis of tri- and difluoromethyl arenes. *Organic Letters*, 15(11):2648–2651, 2013. doi: 10.1021/ol4009377.

[263] Y.-S. Wang, X. Fang, H.-Y. Chen, B. Wu, Z. U. Wang, C. Hilty, and W. R. Liu. Genetic incorporation of twelve meta-substituted phenylalanine derivatives using a single pyrrolysyl-tRNA synthetase mutant. *ACS Chemical Biology*, 8(2):405–415, 2013. doi: 10.1021/cb300512r.

[264] R. B. Merrifield. Solid phase peptide synthesis. i. The synthesis of a tetrapeptide. *Journal of the American Chemical Society*, 85(14):2149–2154, 1963. doi: 10.1021/ja00897a025.

[265] J. M. Palomo. Solid-phase peptide synthesis: An overview focused on the preparation of biologically relevant peptides. *RSC Advances*, 4(62):32658–32672, 2014. doi: 10.1039/C4RA02458C.

[266] V. Mäde, S. Els-Heindl, and A. G. Beck-Sickinger. Automated solid-phase peptide synthesis to obtain therapeutic peptides. *Beilstein Journal of Organic Chemistry*, 10:1197–1212, 2014. doi: 10.3762/bjoc.10.118.

[267] D. A. Pearson, M. Blanchette, M. L. Baker, and C. A. Guindon. Trialkylsilanes as scavengers for the trifluoroacetic acid deblocking of protecting groups in peptide synthesis. *Tetrahedron Letters*, 30(21):2739–2742, 1989. doi: 10.1016/S0040-4039(00)99113-5.

[268] S. Cantel, A. C. Le Isaad, M. Scrima, J. J. Levy, R. D. DiMarchi, P. Rovero, J. A. Halperin, A. M. D'Ursi, A. M. Papini, and M. Chorev. Synthesis and conformational analysis of a cyclic peptide obtained via i to i+4 intramolecular side-chain to side-chain azide-alkyne 1,3-dipolar cycloaddition. *The Journal of Organic Chemistry*, 73(15):5663–5674, 2008. doi: 10.1021/jo800142s.

[269] S. A. Kawamoto, A. Coleska, X. Ran, H. Yi, C.-Y. Yang, and S. Wang. Design of triazole-stapled BCL9 α-helical peptides to target the β-catenin/B-cell CLL/lymphoma 9 (BCL9) protein-protein interaction. *Journal of Medicinal Chemistry*, 55(3):1137–1146, 2012. doi: 10.1021/jm201125d.

[270] T. R. Chan, R. Hilgraf, K. B. Sharpless, and V. V. Fokin. Polytriazoles as copper(i)-stabilizing ligands in catalysis. *Organic Letters*, 6(17):2853–2855, 2004. doi: 10.1021/ol0493094.

[271] T. J. Burke, K. R. Loniello, J. A. Beebe, and K. M. Ervin. Development and application of fluorescence polarization assays in drug discovery. *Combinatorial Chemistry & High Throughput Screening*, 6(3):183–194, 2003. doi: 10.2174/138620703106298365.

[272] N. J. Moerke. Fluorescence polarization (FP) assays for monitoring peptide-protein or nucleic acid-protein binding. *Current Protocols in Chemical Biology*, 1(1):1–15, 2009. doi: 10.1002/9780470559277.ch090102.

[273] P. Luo and R. L. Baldwin. Mechanism of helix induction by trifluoroethanol: A framework for extrapolating the helix-forming properties of peptides from trifluoroethanol/water mixtures back to water. *Biochemistry*, 36(27):8413–8421, 1997. doi: 10.1021/bi9707133.

[274] C. A. Rohl and R. L. Baldwin. Deciphering rules of helix stability in peptides. *Methods in Enzymology*, 295:1–26, 1998. doi: 10.1016/S0076-6879(98)95032-7.

[275] N. E. Shepherd, H. N. Hoang, G. Abbenante, and D. P. Fairlie. Single turn peptide alpha helices with exceptional stability in water. *Journal of the American Chemical Society*, 127(9):2974–2983, 2005. doi: 10.1021/ja0456003.

[276] G. M. Popowicz, A. Czarna, U. Rothweiler, A. Szwagierczak, M. Krajewski, L. Weber, and T. A. Holak. Molecular basis for the inhibition of p53 by Mdmx. *Cell Cycle*, 6(19):2386–2392, 2007. doi: 10.4161/cc.6.19.4740.

[277] S. Grimme, J. Antony, S. Ehrlich, and H. Krieg. A consistent and accurate ab initio parametrization of density functional dispersion correction (dft-d) for the 94 elements H–Pu. *The Journal of Chemical Physics*, 132(15):154104, 2010. doi: 10.1063/1.3382344.

[278] A. Schäfer, H. Horn, and R. Ahlrichs. Fully optimized contracted gaussian basis sets for atoms Li to Kr. *The Journal of Chemical Physics*, 97(4):2571–2577, 1992. doi: 10.1063/1.463096.

[279] J. Tao, J. P. Perdew, V. N. Staroverov, and G. E. Scuseria. Climbing the density functional ladder: Nonempirical meta-generalized gradient approximation designed for molecules and solids. *Physical Review Letters*, 91(14):146401, 2003. doi: 10.1103/PhysRevLett.91.146401.

[280] F. Weigend and R. Ahlrichs. Balanced basis sets of split valence, triple zeta valence and quadruple zeta valence quality for H to Rn: Design and assessment of accuracy. *Physical Chemistry Chemical Physics*, 7(18):3297–3305, 2005. doi: 10.1039/B508541A.

[281] A. Keeley, P. Ábrányi-Balogh, and G. M. Keserű. Design and characterization of a heterocyclic electrophilic fragment library for the discovery of cysteine-targeted covalent inhibitors. *Medicinal Chemistry Communications*, 10(2):263–267, 2019. doi: 10.1039/c8md00327k.

[282] O. Schon, A. Friedler, M. Bycroft, S. M. Freund, and A. R. Fersht. Molecular mechanism of the interaction between MDM2 and p53. *Journal of Molecular Biology*, 323(3): 491–501, 2002. doi: 10.1016/S0022-2836(02)00852-5.

[283] N. Sánchez-Puig, D. B. Veprintsev, and A. R. Fersht. Binding of natively unfolded HIF-1α ODD domain to p53. *Molecular Cell*, 17(1):11–21, 2005. doi: 10.1016/j.molcel .2004.11.019.

[284] M. Mayer and B. Meyer. Characterization of ligand binding by saturation transfer difference NMR spectroscopy. *Angewandte Chemie*, 38(12):1784–1788, 1999. doi: 10.1002/(SICI)1521-3773(19990614)38:12<1784::AID-ANIE1784>3.0.CO;2-Q.

[285] M. Mayer and B. Meyer. Group epitope mapping by saturation transfer difference NMR to identify segments of a ligand in direct contact with a protein receptor. *Journal of the American Chemical Society*, 123(25):6108–6117, 2001. doi: 10.1021/ja0100120.

[286] E. Rühmann, M. Betz, M. Fricke, A. Heine, M. Schäfer, and G. Klebe. Thermodynamic signatures of fragment binding: Validation of direct versus displacement ITC titrations. *Biochimica et Biophysica Acta*, 1850(4):647–656, 2015. doi: 10.1016/j.bbagen.2014.12.007.

[287] A. L. Hopkins, C. R. Groom, and A. Alex. Ligand efficiency: A useful metric for lead selection. *Drug Discovery Today*, 9(10):430–431, 2004. doi: 10.1016/S1359-6446(04) 03069-7.

[288] S. Schultes, C. de Graaf, E. E. J. Haaksma, I. J. P. de Esch, R. Leurs, and O. Krämer. Ligand efficiency as a guide in fragment hit selection and optimization. *Drug Discovery Today: Technologies*, 7(3):e147–202, 2010. doi: 10.1016/j.ddtec.2010.11.003.

[289] W. Kabsch. Xds. *Acta Crystallographica Section D: Biological Crystallography*, 66(2): 125–132, 2010. doi: 10.1107/S0907444909047337.

[290] A. J. McCoy, R. W. Grosse-Kunstleve, P. D. Adams, M. D. Winn, L. C. Storoni, and R. J. Read. Phaser crystallographic software. *Journal of Applied Crystallography*, 40(4): 658–674, 2007. doi: 10.1107/S0021889807021206.

[291] M. D. Winn, C. C. Ballard, K. D. Cowtan, E. J. Dodson, P. Emsley, P. R. Evans, R. M. Keegan, E. B. Krissinel, A. G. W. Leslie, A. McCoy, S. J. McNicholas, G. N. Murshudov, N. S. Pannu, E. A. Potterton, H. R. Powell, R. J. Read, A. Vagin, and K. S. Wilson. Overview of the CCP4 suite and current developments. *Acta Crystallographica Section D: Biological Crystallography*, 67(4):235–242, 2011. doi: 10.1107/S0907444910045749.

[292] P. Emsley, B. Lohkamp, W. G. Scott, and K. Cowtan. Features and development of coot. *Acta Crystallographica Section D: Biological Crystallography*, 66(4):486–501, 2010. doi: 10.1107/S0907444910007493.

[293] P. V. Afonine, R. W. Grosse-Kunstleve, V. B. Chen, J. J. Headd, N. W. Moriarty, J. S. Richardson, D. C. Richardson, A. Urzhumtsev, P. H. Zwart, and P. D. Adams. phenix.model_vs_data: High-level tool for the calculation of crystallographic model and data statistics. *Journal of Applied Crystallography*, 43(4):669–676, 2010. doi: 10.1107/S0021889810015608.

[294] F. Long, R. A. Nicholls, P. Emsley, S. Graæulis, A. Merkys, A. Vaitkus, and G. N. Murshudov. AceDRG: A stereochemical description generator for ligands. *Acta Crystallographica Section D: Structural Biology*, 73(2):112–122, 2017. doi: 10.1107/S2059798317000067.

[295] TURBOMOLE V7.4.1 2019, a development of University of Karlsruhe and Forschungszentrum Karlsruhe GmbH, 1989–2007, TURBOMOLE GmbH; 2007. Available from http://www.turbomole.com. Accessed April 3, 2023.

[296] F. Weigend, M. Häser, H. Patzelt, and R. Ahlrichs. RI-MP2: Optimized auxiliary basis sets and demonstration of efficiency. *Chemical Physics Letters*, 294(1-3):143–152, 1998. doi: 10.1016/S0009-2614(98)00862-8.

[297] C. Hättig. Optimization of auxiliary basis sets for RI-MP2 and RI-CC2 calculations: Core–valence and quintuple-ζ basis sets for H to Ar and QZVPP basis sets for Li to Kr. *Physical Chemistry Chemical Physics*, 7(1):59–66, 2005. doi: 10.1039/B415208E.

[298] M. Feyereisen and G. Fitzgerald. Use of approximate integrals in ab initio theory. An application in mp2 energy calculations. *Chemical Physics Letters*, (208):359–363, 1993. doi: 10.1016/0009-2614(93)87156-W.

[299] F. Weigend, F. Furche, and R. Ahlrichs. Gaussian basis sets of quadruple zeta valence quality for atoms H–Kr. *The Journal of Chemical Physics*, 119(24):12753–12762, 2003. doi: 10.1063/1.1627293.

[300] Y. Zhao and D. G. Truhlar. The M06 suite of density functionals for main group thermochemistry, thermochemical kinetics, noncovalent interactions, excited states, and transition elements: Two new functionals and systematic testing of four M06-class functionals and 12 other functionals. *Theoretical Chemistry Accounts*, 120(1–3): 215–241, 2007. doi: 10.1007/s00214-007-0310-x.

[301] Molecular Operating Environment (MOE), 2018.0101 Chemical Computing Group ULC, 1010 Sherbooke St. West, Suite #910, Montreal, QC, Canada, H3A 2R7, 2023.

[302] OriginPro, Version 2020. OriginLab Corporation, Northampton, MA, USA.

[303] The PyMOL Molecular Graphics System, Version 1.2r3pre, Schrödinger, LLC.

[304] C. F. Macrae, I. Sovago, S. J. Cottrell, P. T. A. Galek, P. McCabe, E. Pidcock, M. Platings, G. P. Shields, J. S. Stevens, M. Towler, and P. A. Wood. Mercury 4.0: From visualization to analysis, design and prediction. *Journal of Applied Crystallography*, 53(1):226–235, 2020. doi: 10.1107/S1600576719014092.

# A Appendix

## A.1 Evaluation of the Microsomal Stability Assay

**HPLC-system:**

Agilent 1290 Infinity series UHPLC system: thermostated column compartment, binary pump (Agilent Technologies, Santa Clara, USA). PAL HTC-xt autosampler (CTC Analytics AG, Zwingen, Switzerland).

Column (compounds **6a**–**e**): Kinetex C18, 2.6 µm, 50 × 2.1 mm; mobile phases: eluent A3: $H_2O$ + 0.1 % FA; eluent B3: ACN + 0.1 % FA; flow rate: 0.35 mL $min^{-1}$; gradient: 5 to 50 % B3 in 4 min, 50 to 98 % B3 in 0.1 min, 98 % B3 for 0.4 min, 98 to 5 % B3 in 0.1 min, 5 % B3 for 1.4 min; column temperature: 30 °C; injection volume: 5 µL.

Column (compounds **7a**–**d**): Waters Acquity UPLC CSH C18, 1.7 µm, 100 × 2.1 mm; mobile phases: eluent A4: $H_2O$ + 0.1 % FA; eluent B4: ACN + 0.1 % FA; flow rate: 0.5 mL $min^{-1}$; gradient: 20 to 100 % B4 in 5 min, 100 % B4 for 1.9 min, 100 to 20 % B4 in 0.1 min, 20 % B4 for 2 min; column temperature: 60 °C; injection volume: 5 µL.

**MS-system:**

Sciex TripleTOF 5600+ system with DuoSpray source (electrospray-ionization); Sciex (Framingham, MA, USA).

MS-settings: Source gas 1: 50 psi, source gas 2: 40 psi, curtain gas: 30 psi, temperature: 600 °C, ion-spray voltage floating: 5500 V.

TOF-MS: accumulation time: 250 ms, scan range: *m/z* 30–1000, declustering potential: 80 V, collision energy: 5 V; IDA-experiments: accumulation time: 100 ms, declustering potential: 80 V, collision energy: 15 V.

**Data evaluation (software):**

MetabolitePilot 1.5, Peakview 2.2, Multiquant 3.0.

## A.2 LogP and Solubility

**Table A1:** List of compounds with calculated or measured properties.

| Entry | X | Structure | MW (g mol$^{-1}$) | SMILES | QPlogP$^{o/w}$ | QPlogS | QPlogS predicted solubility (mM) | Tubidimetric MIS (mM) | Tubidimetric MFS (mM) | JNK1 STD NMR | JNK1 $K_D$ (µM) | JNK3 STD NMR | JNK3 $K_D$ (µM) |
|---|---|---|---|---|---|---|---|---|---|---|---|---|---|
| 6a | H |  | 202.2 | FC(OC1=CC=C(NC(N)=O)C=C1)(F)[H] | 0.838 | -1.334 | 46.34 | 5.0 | 5.0 | N/A | N/A | N/A | N/A |
| 6b | F |  | 220.2 | FC(OC1=CC=C(NC(N)=O)C=C1)(F)F | 1.015 | -1.55 | 28.18 | 3.2 | 2.6 | N/A | N/A | N/A | N/A |
| 6c | Cl |  | 236.6 | FC(OC1=CC=C(NC(N)=O)C=C1)(F)Cl | 1.302 | -1.984 | 10.38 | 4.0 | 4.0 | N/A | N/A | N/A | N/A |
| 6d | Br |  | 281.1 | FC(OC1=CC=C(NC(N)=O)C=C1)(F)Br | 1.384 | -1.987 | 10.30 | 5.0 | 5.0 | N/A | N/A | N/A | N/A |
| 6e | I |  | 328.1 | FC(OC1=CC=C(NC(N)=O)C=C1)(F)I | 1.465 | -2.109 | 7.78 | 3.2 | 2.0 | N/A | N/A | N/A | N/A |
| 7a | H |  | 215.2 | O=C(C(F)(F)[H])NC1=CC(OCO2)=C2C=C1 | 1.636 | -2.18 | 6.61 | 5.0 | 5.0 | N/A | N/A | N/A | N/A |
| 7b | F |  | 233.1 | O=C(C(F)(F)F)NC1=CC(OCO2)=C2C=C1 | 1.882 | -2.428 | 3.73 | 5.0 | 4.0 | N/A | N/A | N/A | N/A |
| 7c | Cl |  | 249.6 | O=C(C(F)(F)Cl)NC1=CC(OCO2)=C2C=C1 | 2.174 | -2.822 | 1.51 | 5.0 | 5.0 | + | N/A | + | >1000 |
| 7d | Br |  | 294.1 | O=C(C(F)(F)Br)NC1=CC(OCO2)=C2C=C1 | 2.249 | -2.719 | 1.91 | 5.0 | 5.0 | – | >1000 | + | >1000 |
| 7e | I |  | 341.1 | O=C(C(F)(F)I)NC1=CC(OCO2)=C2C=C1 | 2.318 | -2.787 | 1.63 | 3.2 | 2.0 | – | N/A | + | N/A |
| 14[a] | Cl |  | 230.6 | O=C(C1=CN=C2N1C=CC=C2)C(F)(F)Cl | 2.149 | -2.389 | 4.08 | 4.0 | 4.0 | – | >1000 | + | >1000 |
| 15 | Cl |  | 272.7 | O=C(C(F)(F)Cl)NCCC1=CNC2=C1C=CC=C2 | 2.823 | -3.637 | 0.23 | 4.0 | 4.0 | – | N/A | – | N/A |
| 16 | Cl |  | 213.6 | O=C(C(F)(F)Cl)NC1=NN=CS1 | 1.118 | -2.426 | 3.75 | 5.0 | 5.0 | + | 186 ±0.3 | + | 243 ± 3 |
| 17 | Br |  | 258.0 | O=C(C(F)(F)Br)NC1=NN=CS1 | 1.222 | -2.445 | 3.59 | 5.0 | 5.0 | + | 193 ± 15 | N/A | 248 ± 70 |
| 18 | I |  | 305.0 | O=C(C(F)(F)I)NC1=NN=CS1 | 1.309 | -2.55 | 2.82 | 5.0 | 5.0 | + | 104 ± 17 | N/A | 186 ± 86 |
| 19 | Cl |  | 283.7 | O=C(C(F)(F)Cl)NC1=C(C(OC)=O)SC=C1C | 2.943 | -3.896 | 0.13 | 4.0 | 5.0 | – | N/A | – | N/A |
| 20 | Cl |  | 237.6 | O=C(C(F)(F)Cl)NC1=CC(O)=C(O)C=C1 | 1.201 | -2.661 | 2.18 | 5.0 | 5.0 | – | N/A | – | N/A |
| 21 | Cl |  | 281.6 | O=C(C(F)(F)Cl)NC1=C(C(OCC)=O)C=NN1C | 2.412 | -3.651 | 0.22 | 5.0 | 5.0 | – | N/A | – | N/A |
| 22 | Cl |  | 290.7 | O=C(C(F)(F)Cl)NC1=NN=C(C2=CC=NC=C2)S1 | 1.856 | -3.885 | 0.13 | 5.0 | 5.0 | + | 20 ± 3 | + | 23 ± 4 |
| 23 | Br |  | 335.1 | O=C(C(F)(F)Br)NC1=NN=C(C2=CC=NC=C2)S1 | 1.946 | -3.847 | 0.14 | 5.0 | 5.0 | + | 15 ± 2 | N/A | 17 ± 2 |
| 24 | I |  | 382.1 | O=C(C(F)(F)I)NC1=NN=C(C2=CC=NC=C2)S1 | 2.033 | -3.952 | 0.11 | 5.0 | 5.0 | + | 10 ± 0.3 | N/A | 13 ± 5 |
| 25 | Br |  | 257.1 | O=C(NC1=NC=CS1)C(F)(Br)F | 1.803 | -2.674 | 2.12 | 5.0 | 5.0 | + | >1000 | + | >1000 |
| 28 | Br |  | 308.1 | O=C(C(F)(F)Br)NC1=CC=C(NC(N)=O)C=C1 | 0.61 | -2.238 | 5.78 | 5.0 | 5.0 | – | N/A | – | N/A |
| 29 | Br |  | 331.1 | O=C(C(F)(F)Br)NC1=CC=C(CN2C=NC=N2)C=C1 | 2.486 | -3.799 | 0.16 | 5.0 | 5.0 | – | N/A | – | N/A |
| 30 | Br |  | 337.1 | O=C(C(F)(F)Br)N1CCN(C(C2=CC=CO2)=O)CC1 | 0.964 | -1.274 | 53.21 | 5.0 | 5.0 | – | N/A | – | N/A |
| 31 | Br |  | 308.1 | O=C(C(F)(F)Br)NC1=CC=CC2=NSN=C21 | 2.141 | -3.351 | 0.45 | 1.3 | 0.7 | – | N/A | – | N/A |
| 32 | Br |  | 382.2 | O=C(C(F)(F)Br)NC1=C(C(OCC)=O)C(CCCC2)=C2S1 | 4.242 | -5.988 | 0.00 | 0.8 | 0.5 | – | N/A | – | N/A |
| 33 | Br | 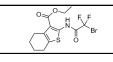 | 363.1 | O=C(C(F)(F)Br)NC(O1)=NN=C1C(C=C2)=CC=C2[N+]([O-])=O | 1.576 | -3.97 | 0.11 | 5.0 | 5.0 | – | N/A | + | N/A |
| 34 | Br |  | 268.0 | FC1=CC=C(NC(C(F)(F)Br)=O)C=C1 | 2.886 | -3.421 | 0.38 | 4.0 | 3.2 | – | N/A | – | N/A |
| 35[b] | N/A |  | 178.2 | NC1=NN=C(C2=CC=NC=C2)S1 | 0.476 | -1.833 | 14.69 | 5.0 | 5.0 | N/A | 162 ± 20 | N/A | N/A |

## A.3 STD NMR Spectra

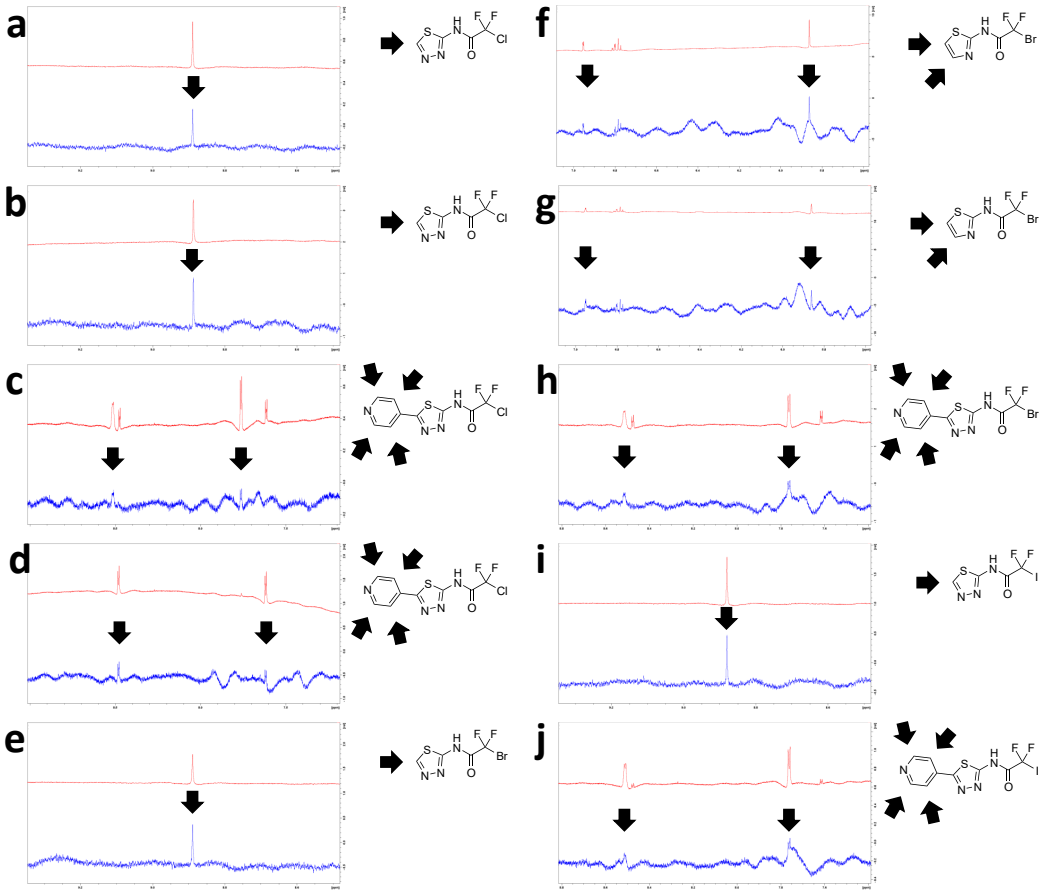


**Figure A1:** STD spectra (blue) and $^{1}$H NMR spectra (red). The arrows in the spectra highlight the STD signal and the corresponding proton in the structure. JNK1 with fragment **23** (a), **24** (e), **25** (i), **29** (c), **30** (h), **31** (i), and **35** (f). JNK3 with fragment **23** (b), **29** (d), and **35** (g).

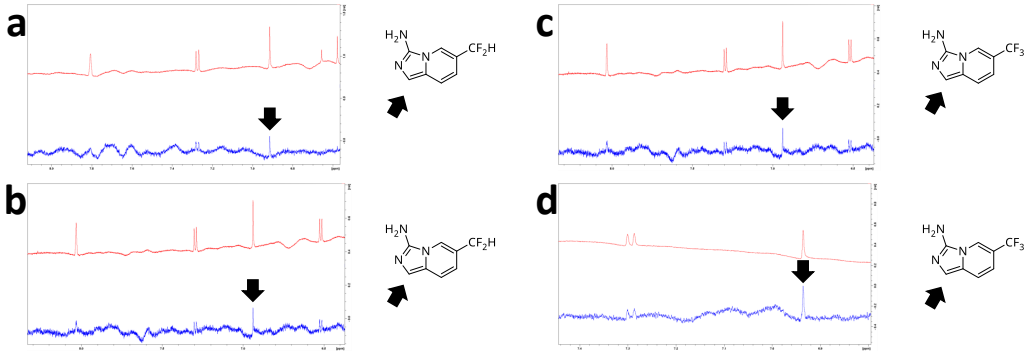


**Figure A2:** STD spectra (blue) and $^{1}$H NMR spectra (red). The arrows in the spectra highlight the STD signal and the corresponding proton in the structure. JNK1 with fragment **53a** (a) and **53b** (c). JNK3 with fragment **53a** (b) and **53b** (d)

.

## A.4 ITC Data

**Table A2:** Affinity fitting data for all ITC measurements of Section 3.1.10.

| Protein | Figure | Cmpd No. | Cmpd Conc. (mM) | Prot. Conc. (µM) | N | N_SD | $K_a$ ($M^{-1}$) | $K_a$_SD ($M^{-1}$) | ΔH (cal $mol^{-1}$) | ΔH_SD (cal $mol^{-1}$) | ΔS (cal $mol^{-1}K^{-1}$) |
|---|---|---|---|---|---|---|---|---|---|---|---|
| JNK1 | A3a | **23** | 5 | 80.92 | 1 | 0 | 5370 | 145 | –1215 | 113.9 | –23.7 |
| JNK1 | A3b | **23** | 5 | 83.37 | 1 | 0 | 5390 | 98.6 | –11070 | 85.15 | –20.1 |
| JNK1 | A3c | **24** | 5 | 76.93 | 1 | 0 | 5800 | 371 | –11630 | 249.7 | –21.8 |
| JNK1 | A3d | **24** | 5 | 76.93 | 1 | 0 | 4910 | 416 | –12760 | 385.5 | –25.9 |
| JNK1 | A3e | **24** | 5 | 83.37 | 1 | 0 | 4920 | 179 | –12230 | 192.0 | –24.1 |
| JNK1 | A3f | **25** | 5 | 83.37 | 1 | 0 | 8250 | 266 | –14550 | 140.3 | –30.9 |
| JNK1 | A3g | **25** | 5 | 80.92 | 1 | 0 | 11400 | 542 | –12700 | 207.4 | –24.0 |
| JNK1 | A4a | **29** | 2 | 77.85 | 1 | 0 | 59700 | 7000 | –6701 | 184.5 | –0.624 |
| JNK1 | A4b | **29** | 2 | 77.85 | 1 | 0 | 53900 | 4250 | –7328 | 139.5 | –2.93 |
| JNK1 | A4c | **29** | 5 | 83.37 | 1 | 0 | 43100 | 3600 | –8176 | 168.9 | –6.22 |
| JNK1 | A4d | **30** | 5 | 77.85 | 1 | 0 | 57600 | 5070 | –6551 | 132.8 | –0.185 |
| JNK1 | A4e | **30** | 2 | 77.85 | 0.93 | 0.34 | 71800 | 7830 | –8613 | 449.9 | –6.67 |
| JNK1 | A4f | **30** | 5 | 83.37 | 1.41 | 0.02 | 78500 | 5730 | –5967 | 132.1 | 2.38 |
| JNK1 | A4g | **31** | 5 | 80.92 | 0.89 | 0 | 105000 | 3750 | –8979 | 66.5 | –7.09 |
| JNK1 | A4h | **31** | 2 | 77.85 | 0.99 | 0.02 | 99900 | 7280 | –8327 | 221.8 | –5.05 |
| JNK1 | A4i | **31** | 5 | 83.27 | 1 | 0 | 95700 | 12300 | –10910 | 284.0 | –13.8 |
| JNK3 | A5a | **23** | 5 | 89.60 | 1 | 0 | 4170 | 438 | –5572 | 283.3 | –2.12 |
| JNK3 | A5b | **23** | 5 | 107.3 | 0.86 | 0.35 | 4070 | 729 | –6158 | 2754 | –4.14 |
| JNK3 | A5c | **24** | 5 | 75.03 | 1 | 0 | 5620 | 486 | –5213 | 208.7 | –0.328 |
| JNK3 | A5d | **24** | 5 | 107.3 | 1.07 | 0.42 | 3140 | 460 | –5748 | 2486 | –3.28 |
| JNK3 | A5e | **25** | 2 | 75.03 | 0.59 | 0.14 | 18300 | 3720 | –5046 | 1394 | 2.58 |
| JNK3 | A5f | **25** | 5 | 107.3 | 0.31 | 0.19 | 4400 | 440 | –23080 | 14990 | –60.7 |
| JNK3 | A5g | **25** | 5 | 95.00 | 0.25 | 0.27 | 3630 | 382 | –34460 | 37830 | –99.3 |
| JNK3 | A6a | **29** | 5 | 158.75 | 1.29 | 0.03 | 44100 | 6300 | –1143 | 39.2 | 17.4 |
| JNK3 | A6b | **29** | 5 | 75.03 | 1.48 | 0.10 | 54200 | 14800 | –2275 | 204.3 | 14.0 |
| JNK3 | A6c | **29** | 5 | 89.88 | 0.84 | 0.08 | 34700 | 6150 | –3593 | 411.5 | 8.72 |
| JNK3 | A6d | **30** | 5 | 75.03 | 1 | 0 | 64900 | 7100 | –3164 | 77.5 | 11.4 |
| JNK3 | A6e | **30** | 5 | 89.88 | 1 | 0 | 58400 | 5140 | –3574 | 68.14 | 9.82 |
| JNK3 | A6f | **30** | 5 | 89.88 | 1 | 0.02 | 52500 | 4080 | –3475 | 108.8 | 9.94 |
| JNK3 | A6g | **31** | 1.5 | 75.03 | 0.76 | 0.11 | 52700 | 15200 | –7156 | 1352 | 2.40 |
| JNK3 | A6h | **31** | 1.5 | 89.88 | 0.90 | 0.02 | 82200 | 7638 | –5364 | 139.0 | 4.50 |
| JNK3 | A6i | **31** | 5 | 95.00 | 1.21 | 0.02 | 154000 | 21700 | –3742 | 93.5 | 11.2 |
| JNK1 | A7a | **46**[1] | 5 | 77.85 | 1 | 0 | 7060 | 287 | –7332 | 93.26 | –6.98 |
| JNK1 | A7b | **46**[1] | 5 | 77.85 | 1 | 0 | 5490 | 445 | –6444 | 242.0 | -4.50 |

[1] 5-(Pyridin-4-yl)-1,3,4-thiadiazol-2-amine (**46**): Educt of compounds **29**, **30** and **31**.

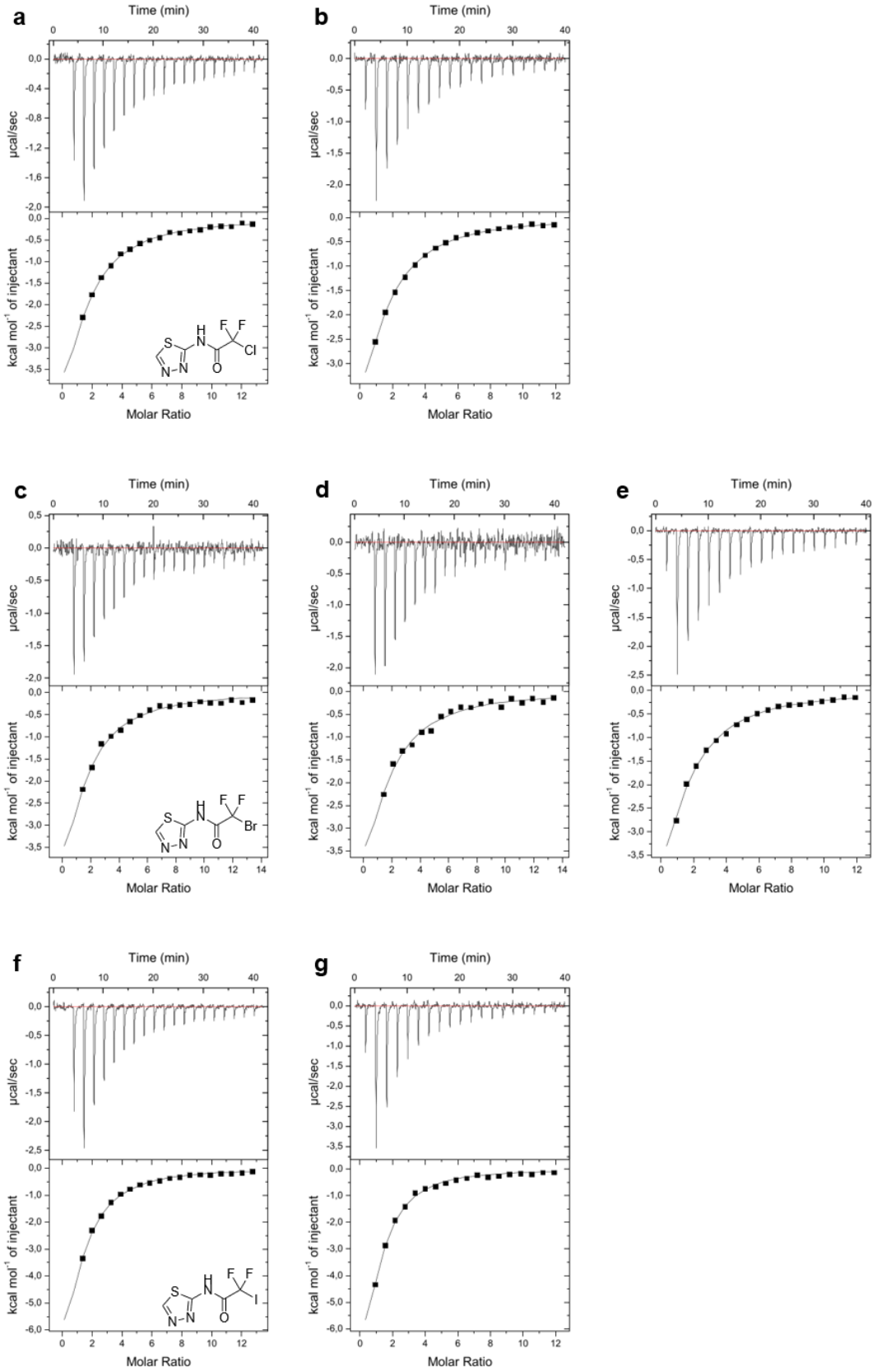


**Figure A3:** Thermograms of JNK1 with fragments **23** (a, b), **24** (c-e), and **25** (f, g).

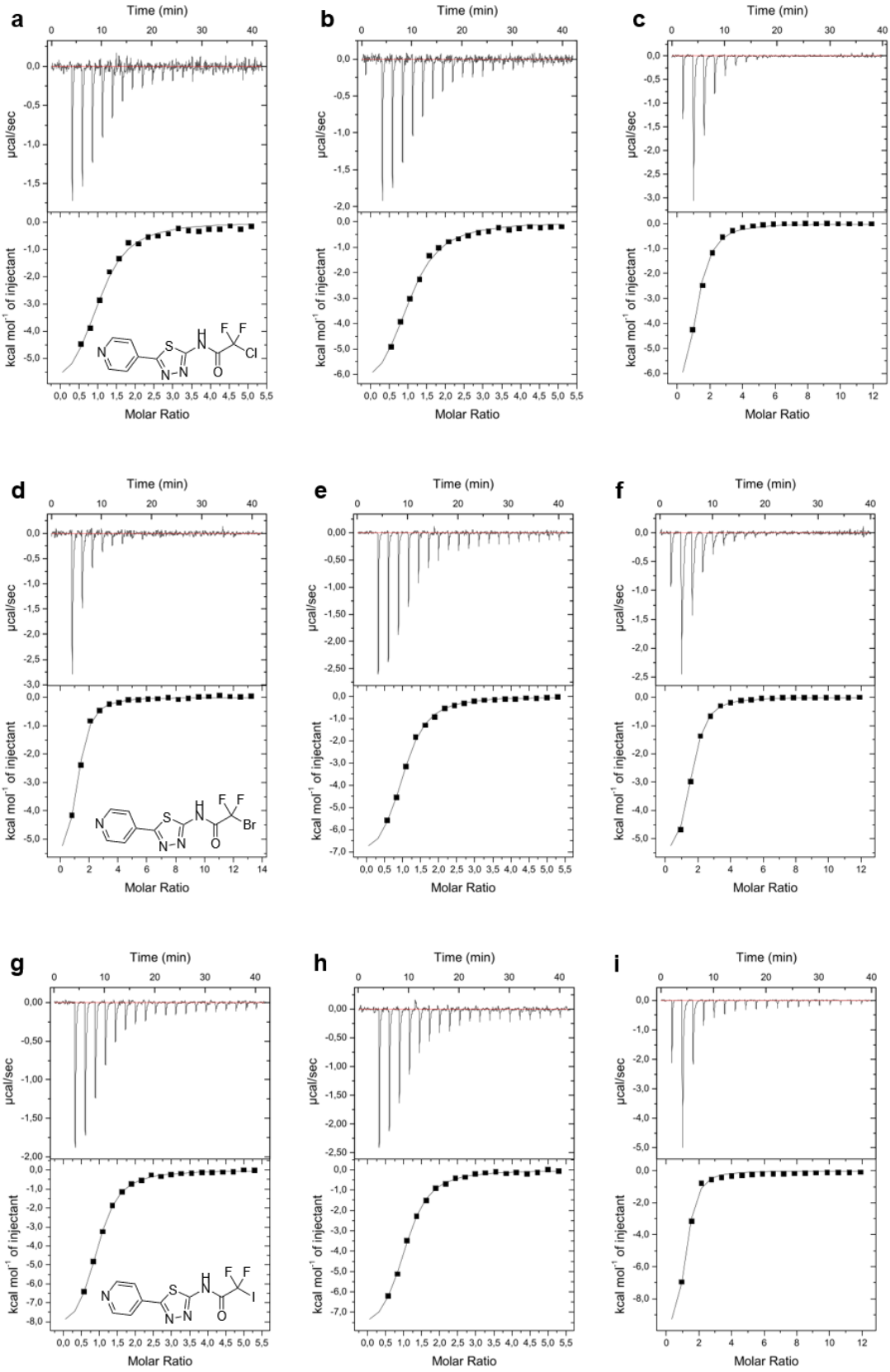


**Figure A4:** Thermograms of JNK1 with fragments **29** (a-c), **30** (d-f), and **31** (g-i).

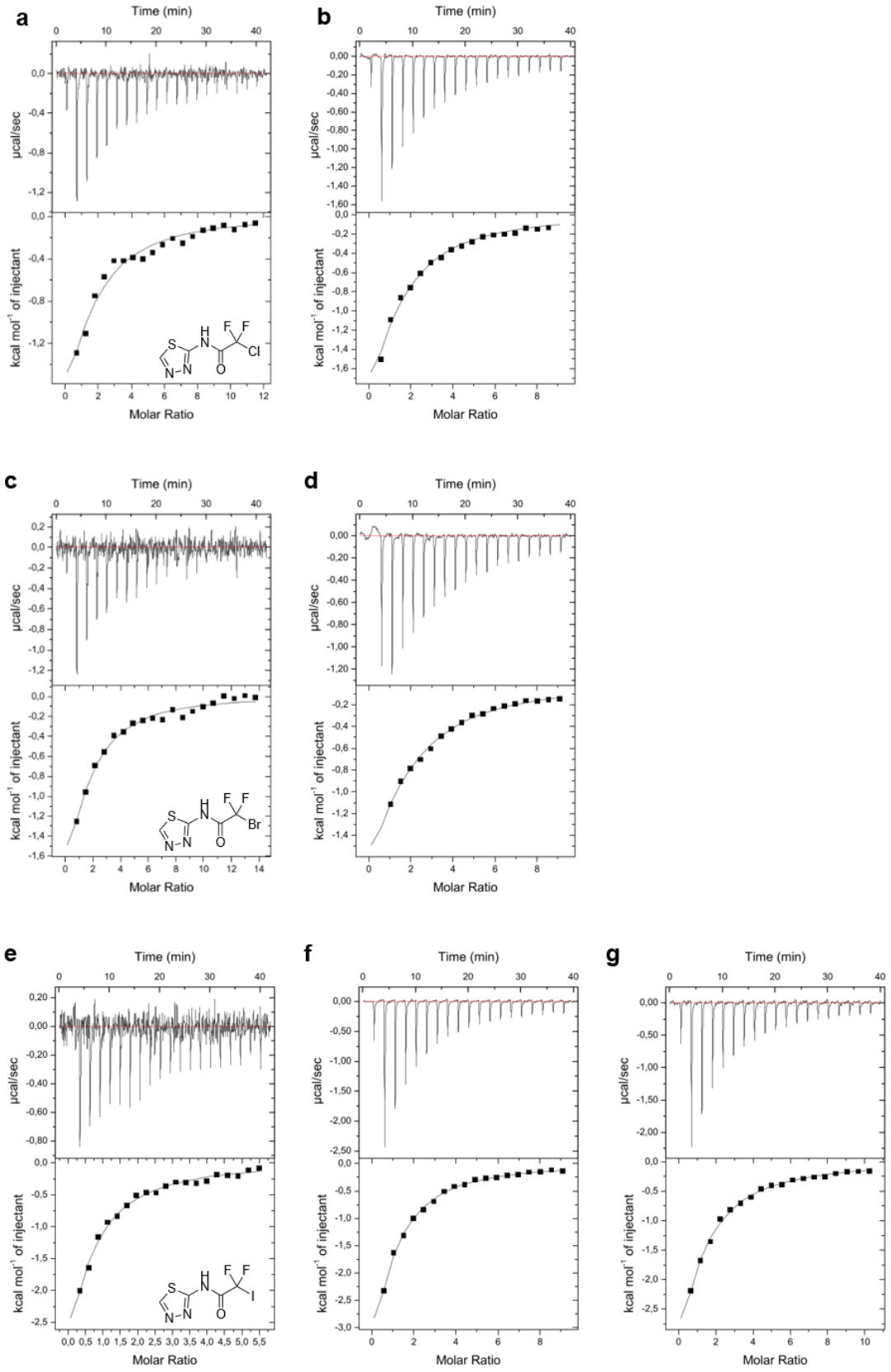


**Figure A5:** TThermograms of JNK3 with fragments **23** (a, b), **24** (c, d), and **25** (e-g).

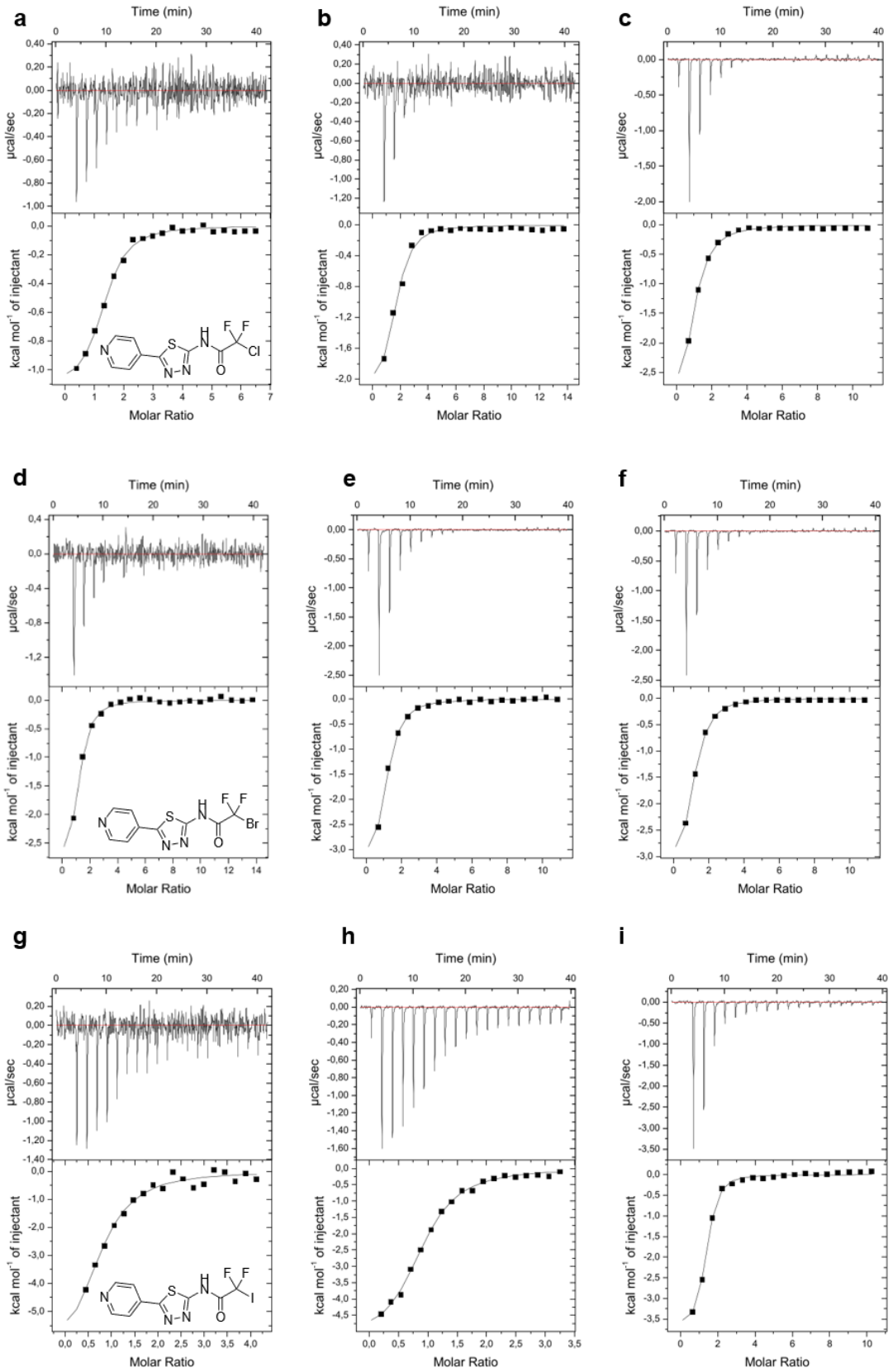


**Figure A6:** Thermograms of JNK3 with fragments **29** (a-c), **30** (d-f), and **31** (g-i).

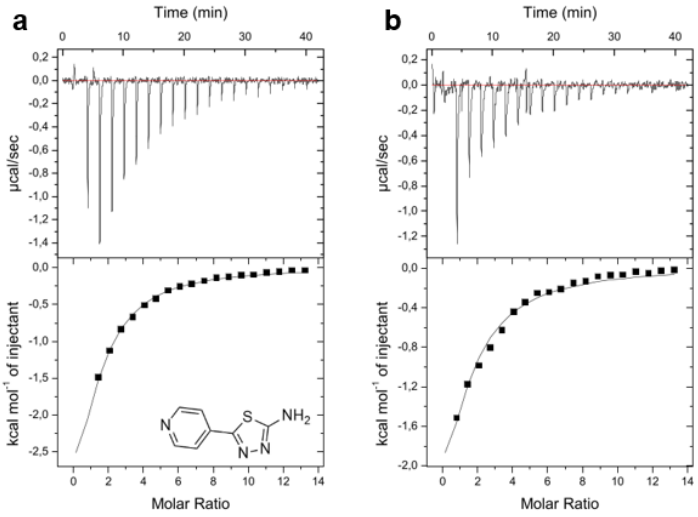


**Figure A7:** Thermograms of JNK1 with 5-(pyridin-4-yl)-1,3,4-thiadiazol-2-amine **46** (a, b); educt of **29**, **30** and **31**.

**Table A3:** Affinity fitting data for all ITC measurements of Section 3.2.4.

| Protein | Figure | Cmpd No. | Cmpd Conc. (mM) | Prot. Conc. (μM) | N | N_SD | $K_a$ ($M^{-1}$) | $K_a$_SD ($M^{-1}$) | ΔH (cal $mol^{-1}$) | ΔH_SD (cal $mol^{-1}$) | ΔS (cal $mol^{-1}K^{-1}$) |
|---|---|---|---|---|---|---|---|---|---|---|---|
| JNK1 | A8a | **51a** | 5 | 76.93 | 0.59 | 0.05 | 17000 | 5740 | –6203 | 2856 | –1.45 |
| JNK1 | A8b | **51a** | 5 | 95.19 | 1.59 | 0.08 | 19800 | 1680 | –5449 | 355 | 1.39 |
| JNK1 | A8c | **51a** | 5 | 92.62 | 0.87 | 0.09 | 10400 | 698 | –10750 | 1200 | –17.7 |
| JNK1 | A8d | **53a** | 5 | 95.19 | 2.10 | 0.10 | 19000 | 2160 | –3114 | 195.8 | 9.13 |
| JNK1 | A8e | **53a** | 5 | 95.19 | 1.80 | 0.22 | 13200 | 2490 | –3565 | 555.6 | 6.89 |
| JNK1 | A8f | **53a** | 5 | 92.62 | 0.62 | 0.27 | 6840 | 1030 | –1193 | 5620.1 | –22.5 |
| JNK1 | A9a | **51b** | 5 | 76.93 | 1.64 | 0.28 | 23200 | 6060 | –3413 | 781.2 | 8.53 |
| JNK1 | A9b | **51b** | 5 | 95.19 | 1.09 | 0.10 | 13600 | 1610 | –6940 | 754.1 | –4.36 |
| JNK1 | A9c | **51b** | 5 | 92.62 | 1.02 | 0.09 | 15200 | 1440 | –7073 | 740.9 | –4.58 |
| JNK1 | A9d | **53b** | 5 | 95.19 | 1.68 | 0.30 | 15400 | 4360 | –3336 | 773.5 | 7.97 |
| JNK1 | A9e | **53b** | 5 | 95.19 | 2.00 | 0.18 | 16100 | 2890 | –2987 | 348.1 | 9.23 |
| JNK1 | A9f | **53b** | 5 | 92.62 | 1.32 | 0.16 | 8740 | 994 | –5986 | 1109 | –2.04 |
| JNK3 | A10a | **51a** | 1.5 | 89.60 | 0.59 | 0.05 | 85400 | 24400 | –2104 | 220.7 | 15.5 |
| JNK3 | A10b | **53a** | 5 | 93.74 | 1.60 | 0.20 | 9960 | 1860 | –2135 | 323.2 | 11.1 |
| JNK3 | A10c | **51b** | 5 | 158.75 | 0.70 | 0.15 | 9190 | 1980 | –1881 | 460.5 | 11.8 |

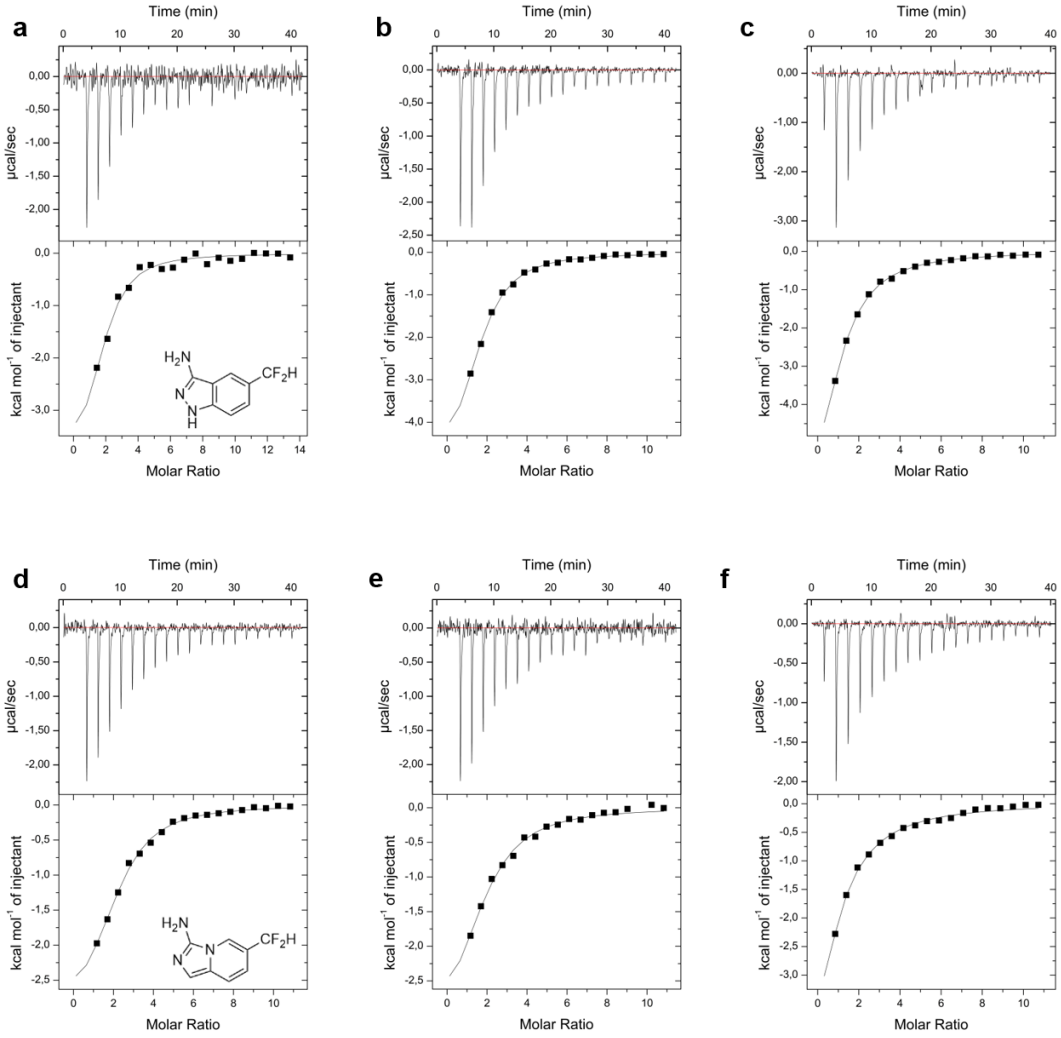


**Figure A8:** Thermograms of JNK1 with fragments **51a** (a-c) and **53a** (d-f).

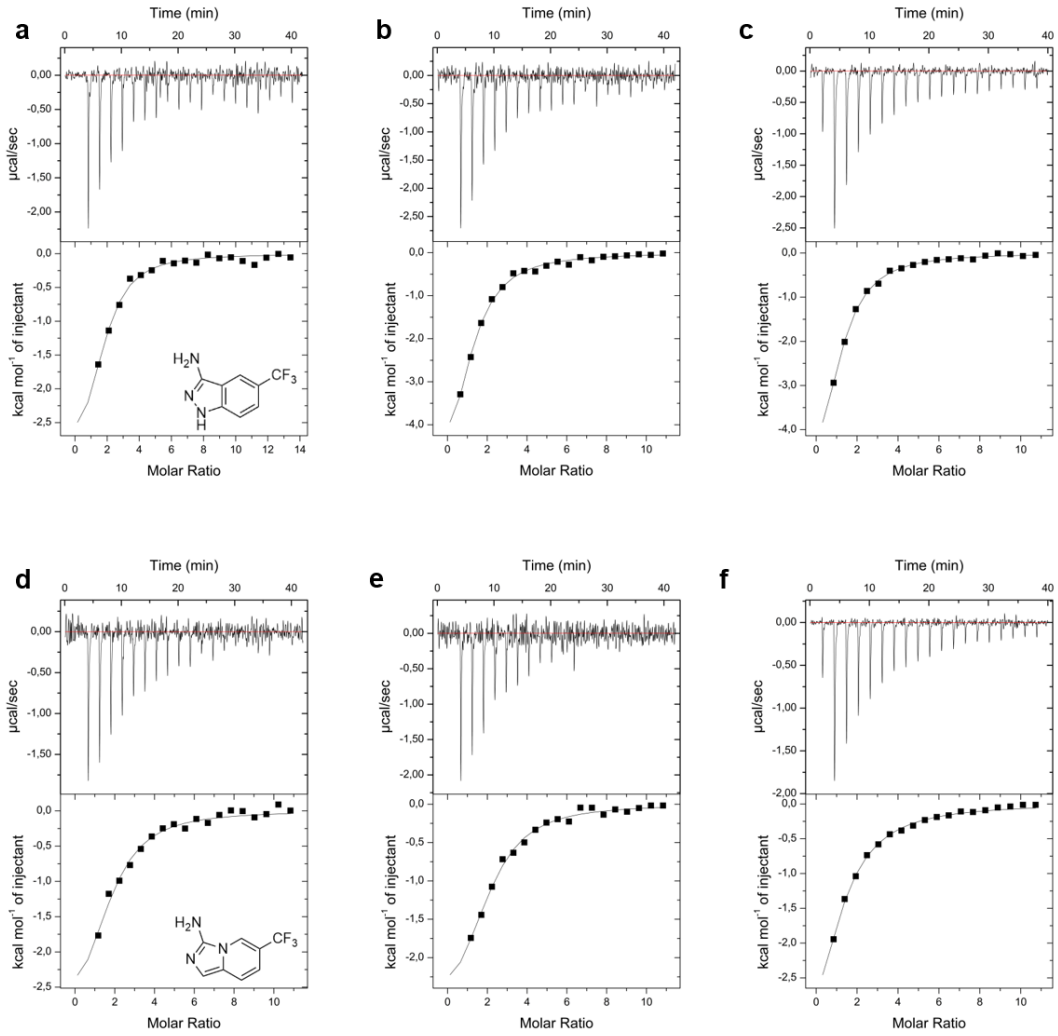


**Figure A9:** Thermograms of JNK1 with fragments **51b** (a-c) and **53b** (d-f).

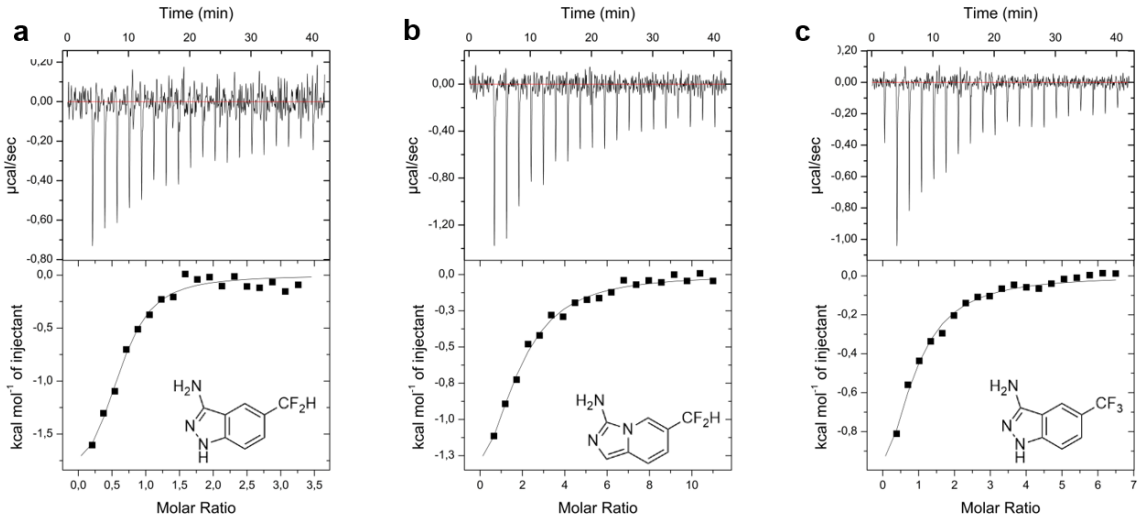


**Figure A10:** Thermograms of JNK3 with fragments **51a** (a), **53a** (b), and **51b** (c).

## A.5 PDB Scan

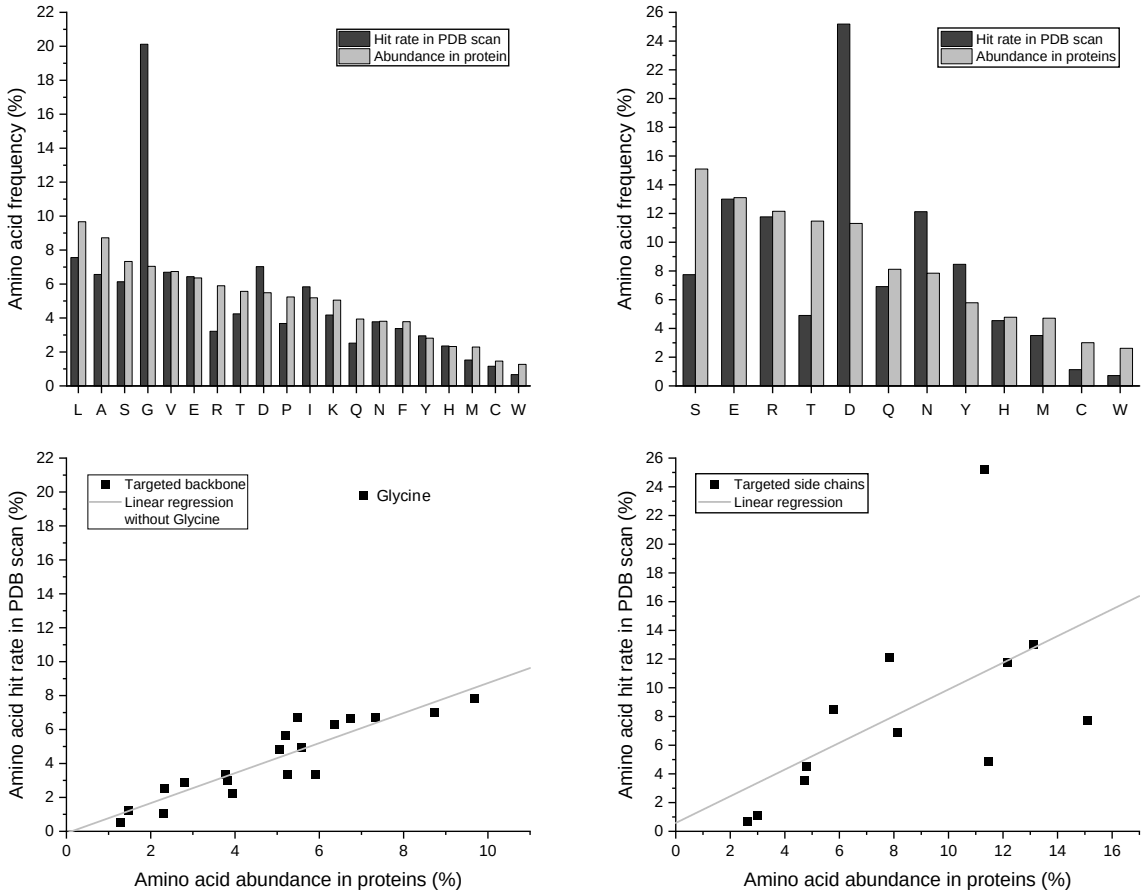


**(a)** Protein backbone.

**(b)** Protein side chain.

**Figure A11:** Correlation between targeted halogen bonding acceptor heteroatoms of protein backbones and abundance of amino acids in proteins. Number of targeted backbone amino acids n = 3017 (backbone N: n = 1357 and backbone O: n = 1662); number of targeted protein side chains n = 1938 and sum of targeted acceptor atoms n = 4955. **(a)** Comparison between halogen acceptor amino acids in protein backbone and abundance in proteins ($\rho$ = 0.92). **(b)** Comparison between halogen acceptor side chains of amino acids and amino acid abundance in proteins. Abundance in proteins normalized to 100 % ($\rho$ = 0.57).

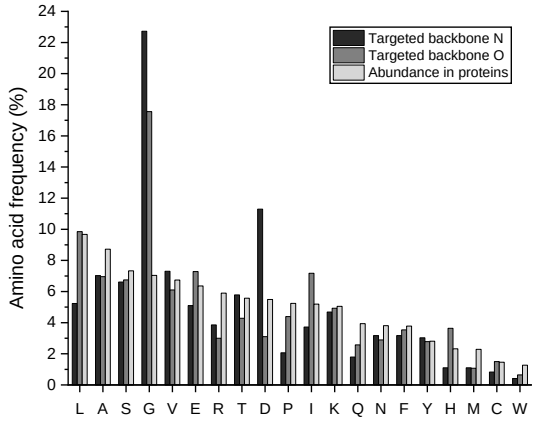


**(a)** Targeted protein backbone N and O, and amino acid abundance in proteins.

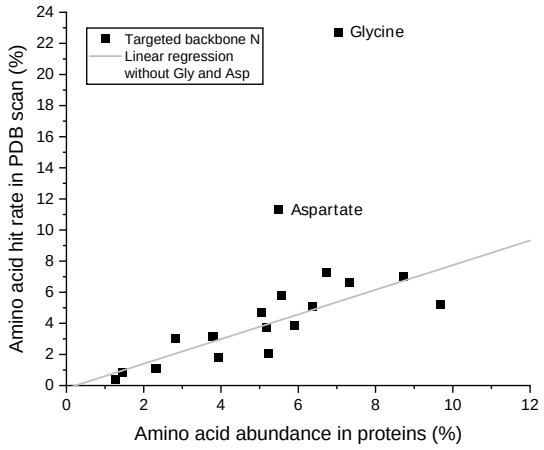


**(b)** Protein backbone N.

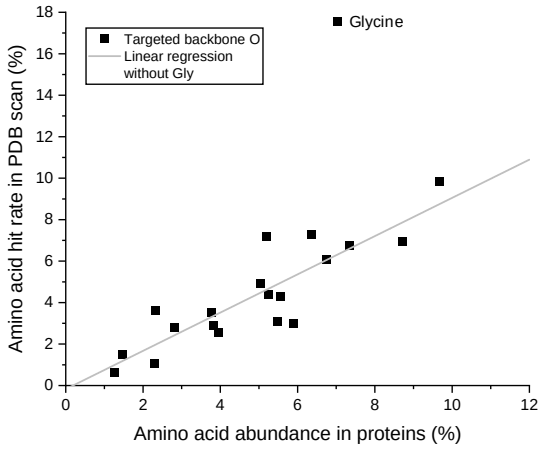


**(c)** Protein backbone O.

**Figure A12:** Correlation between targeted halogen bonding acceptor heteroatoms of protein backbones with a σ-hole angle ≥150° and abundance of amino acids in proteins. Number of targeted backbone amino acids n = 1660 (backbone N: n = 726 and backbone O: n = 934). **(a)** Comparison of the amino acid frequency of targeted protein backbone N, targeted protein backbone O, and the abundance of amino acids in proteins. **(b)** Comparison between halogen acceptor N in protein backbone and abundance in proteins (ρ = 0.86). **(c)** Comparison between halogen acceptor O in protein backbone and amino acid abundance in proteins (ρ = 0.88).

## A.6 Peptides bearing $CF_2X$ Moieties

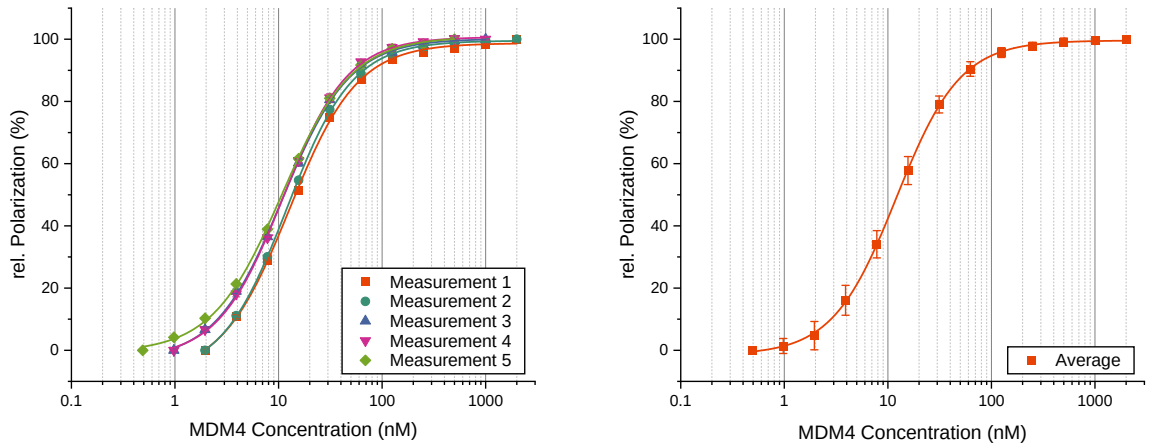


**(a)** MDM4 Titration Measurements.

**(b)** Average of MDM4 Titration.

**Figure A13:** Exemplary MDM4 titrations towards 20 nM fluorescent probe to determine the required protein concentration ranging from 60 % to 80 % of the fluorescence polarization signal for the competitive fluorescence polarization assay experiments. The determined protein concentration for the experiments around 75% of the signal: 30 nM MDM4 protein.

**Table A4:** Individual fluorescence polarization measurement data of **TPV-3**, **TPV-4**, **TPV-5** with MDM2 and MDM4 (Table 20 on page 97).

| | | | | $IC_{50}$ ± SD (nM) | | | | $K_i$ ± SD (nM) | | | | |
|---|---|---|---|---|---|---|---|---|---|---|---|---|
| Protein | DMSO | Peptide | Xaa6 | 1 | 2 | 3 | Mean | 1 | 2 | 3 | Mean | Ratio |
| MDM2 | 5 % | **TPV-3** | F(*m*-$OCF_2Br$) | 741 ± 25 | 752 ± 51 | 717 ± 57 | 736 ± 15 | 218 | 222 | 211 | 217 ± 4 | 1.00 |
| | | **TPV-4** | F(*m*-$OCF_3$) | 832 ± 30 | 770 ± 31 | 825 ± 46 | 809 ± 28 | 246 | 227 | 244 | 258 ± 8 | 1.19 |
| | | **TPV-5** | F(*m*-$OCH_3$) | 676 ± 23 | 646 ± 6 | 706 ± 15 | 676 ± 24 | 199 | 190 | 208 | 199 ± 7 | 0.92 |
| | 10 % | **TPV-3** | F(*m*-$OCF_2Br$) | 598 ± 18 | 572 ± 12 | 587 ± 16 | 586 ± 11 | 175 | 167 | 172 | 171 ± 3 | 0.79 |
| | | **TPV-4** | F(*m*-$OCF_3$) | 647 ± 52 | 646 ± 22 | 643 ± 37 | 646 ± 2 | 190 | 189 | 189 | 189 ± 1 | 0.87 |
| | | **TPV-5** | F(*m*-$OCH_3$) | 619 ± 12 | 635 ± 5 | 651 ± 19 | 635 ± 13 | 181 | 186 | 191 | 186 ± 4 | 0.86 |
| MDM4 | 5 % | **TPV-3** | F(*m*-$OCF_2Br$) | 249 ± 4 | 270 ± 3 | 254 ± 7 | 258 ± 9 | 79 | 87 | 81 | 82 ± 3 | 1.00 |
| | | **TPV-4** | F(*m*-$OCF_3$) | 242 ± 5 | 243 ± 7 | 228 ± 5 | 237 ± 7 | 76 | 77 | 71 | 75 ± 3 | 0.91 |
| | | **TPV-5** | F(*m*-$OCH_3$) | 233 ± 9 | 218 ± 7 | 235 ± 7 | 229 ± 7 | 73 | 67 | 74 | 71 ± 3 | 0.87 |
| | 10 % | **TPV-3** | F(*m*-$OCF_2Br$) | 207 ± 6 | 213 ± 8 | 211 ± 4 | 211 ± 3 | 63 | 66 | 65 | 65 ± 1 | 0.78 |
| | | **TPV-4** | F(*m*-$OCF_3$) | 205 ± 8 | 206 ± 6 | 197 ± 4 | 203 ± 4 | 62 | 63 | 59 | 62 ± 2 | 0.75 |
| | | **TPV-5** | F(*m*-$OCH_3$) | 191 ± 4 | 179 ± 13 | 189 ± 18 | 186 ± 5 | 57 | 53 | 56 | 55 ± 2 | 0.67 |

**Table A5:** Individual $IC_{50}$ value determinations (Table 21 on page 99).

| | | $IC_{50}$ ± SD (nM) | | | |
|---|---|---|---|---|---|
| Peptide | Xaa24 | 1 | 2 | 3 | Mean |
| **$^{17-28}$p53** | Lys | 1160 ± 46 | 1136 ± 60 | 1226 ± 15 | 1173 ± 39 |
| **TPV-6** | Nle(εNHCOCH$_3$) | 1790 ± 72 | 2084 ± 67 | 1927 ± 60 | 1927 ± 47 |
| **TPV-7** | Nle(εNHCOCF$_2$H) | 1439 ± 74 | 1330 ± 38 | 1270 ± 27 | 1347 ± 38 |
| **TPV-8** | Nle(εNHCOCF$_3$) | 794 ± 29 | 733 ± 22 | 811 ± 29 | 779 ± 24 |
| **TPV-9** | Nle(εNHCOCF$_2$Cl) | 415 ± 9 | 444 ± 8 | 463 ± 12 | 440 ± 8 |
| **TPV-10** | Nle(εNHCOCF$_2$Br) | 311 ± 11 | 337 ± 8 | 331 ± 12 | 326 ± 9 |
| **TPV-11** | Dab | 1964 ± 88 | 1999 ± 42 | 1740 ± 84 | 1897 ± 48 |
| **TPV-12** | Abu(γNHCOCH$_3$) | 2069 ± 111 | 1799 ± 71 | 1768 ± 66 | 1874 ± 53 |
| **TPV-13** | Abu(γNHCOCF$_2$H) | 2034 ± 81 | 2131 ± 67 | 2126 ± 98 | 2096 ± 55 |
| **TPV-14** | Abu(γNHCOCF$_3$) | 2627 ± 101 | 2409 ± 91 | 2325 ± 86 | 2447 ± 70 |
| **TPV-15** | Abu(γNHCOCF$_2$Cl) | 2283 ± 102 | 1946 ± 82 | 2349 ± 85 | 2176 ± 65 |
| **TPV-16** | Abu(γNHCOCF$_2$Br) | 1602 ± 69 | 1622 ± 66 | 1609 ± 37 | 1611 ± 30 |

**Table A6:** Individual $K_i$ value calculations (Table 21 on page 99).

| | | $K_i$ ± SD (nM) | | | | |
|---|---|---|---|---|---|---|
| Peptide | Xaa24 | 1 | 2 | 3 | Mean | ratio |
| **$^{17-28}$p53** | Lys | 303 | 297 | 321 | 307 ± 10 | 1.00 |
| **TPV-6** | Nle(εNHCOCH$_3$) | 471 | 549 | 507 | 509 ± 32 | 1.66 |
| **TPV-7** | Nle(εNHCOCF$_2$H) | 377 | 348 | 332 | 353 ± 19 | 1.15 |
| **TPV-8** | Nle(εNHCOCF$_3$) | 206 | 190 | 210 | 202 ± 9 | 0.66 |
| **TPV-9** | Nle(εNHCOCF$_2$Cl) | 105 | 113 | 118 | 112 ± 5 | 0.37 |
| **TPV-10** | Nle(εNHCOCF$_2$Br) | 77.6 | 84.5 | 82.9 | 81.7 ± 3 | 0.27 |
| **TPV-11** | Dab | 517 | 526 | 457 | 500 ± 30 | 1.63 |
| **TPV-12** | Abu(γNHCOCH$_3$) | 545 | 473 | 465 | 494 ± 36 | 1.61 |
| **TPV-13** | Abu(γNHCOCF$_2$H) | 535 | 561 | 560 | 552 ± 12 | 1.80 |
| **TPV-14** | Abu(γNHCOCF$_3$) | 693 | 635 | 613 | 647 ± 34 | 2.11 |
| **TPV-15** | Abu(γNHCOCF$_2$Cl) | 601 | 512 | 619 | 577 ± 47 | 1.88 |
| **TPV-16** | Abu(γNHCOCF$_2$Br) | 421 | 426 | 422 | 423 ± 2 | 1.38 |

**Table A7:** XB results from geometry optimization using TPSS(D3)/SV(P) of p53 peptide with bromodifluoroacetylated Lys24 side chain (PDB ID: 2Z5T). The parameters for a positive XB match were a distance of <4 Å and an angle of >160°. Fused_92_red_240.pdb (#33) already starts with the XB. Matches with concurrent interaction of at least one fluorine atom are highlighted in blue. Matches with concurrent H···O(amide) contact are highlighted in green.

| # | System | Distance (Å) | Angle (°) | Peptide / Protein | ID | Atom | Atom and amino acid |
|---|---|---|---|---|---|---|---|
| 1 | fused_2_rot_300.pdb | 3.00 | 164.16 | peptide | 98 | O | SC O of Ser20 |
| 2 | fused_31_rot_300.pdb | 3.01 | 163.38 | peptide | 98 | O | |
| 3 | fused_106_rot_180.pdb | 2.93 | 161.68 | peptide | 105 | O | SC O of Asp21 |
| 4 | fused_44_rot_330.pdb | 2.72 | 171.82 | peptide | 105 | O | |
| 5 | fused_72_rot_300.pdb | 2.91 | 162.24 | peptide | 105 | O | |
| 6 | fused_19_rot_0.pdb | 2.67 | 176.64 | peptide | 106 | O | SC O of Asp21 |
| 7 | fused_20_rot_180.pdb | 3.00 | 169.64 | peptide | 106 | O | |
| 8 | fused_4_rot_210.pdb | 2.64 | 173.25 | peptide | 106 | O | |
| 9 | fused_77_rot_300.pdb | 2.97 | 164.83 | peptide | 106 | O | |
| 10 | fused_77_rot_330.pdb | 2.97 | 164.72 | peptide | 106 | O | |
| 11 | fused_78_rot_240.pdb | 2.71 | 179.15 | peptide | 106 | O | |
| 12 | fused_83_rot_270.pdb | 3.15 | 161.62 | peptide | 106 | O | |
| 13 | fused_75_rot_240.pdb | 3.37 | 171.65 | peptide | 130 | N | Prot N of Trp23 |
| 14 | fused_103_rot_240.pdb | 2.95 | 160.34 | peptide | 199 | O | BB O of Ser20 |
| 15 | fused_37_rot_240.pdb | 3.03 | 175.58 | peptide | 199 | O | |
| 16 | fused_12_rot_210.pdb | 2.88 | 173.67 | peptide | 204 | O | BB O of Asp21 |
| 17 | fused_12_rot_240.pdb | 2.87 | 173.55 | peptide | 204 | O | |
| 18 | fused_1_rot_210.pdb | 2.87 | 173.83 | peptide | 204 | O | |
| 19 | fused_1_rot_240.pdb | 2.88 | 173.78 | peptide | 204 | O | |
| 20 | fused_101_rot_0.pdb | 2.86 | 165.91 | peptide | 219 | O | BB O of Lys24 |
| 21 | fused_101_rot_330.pdb | 2.87 | 165.93 | peptide | 219 | O | |
| 22 | fused_94_rot_0.pdb | 2.89 | 166.06 | peptide | 219 | O | |
| 23 | fused_99_rot_330.pdb | 2.88 | 165.71 | peptide | 219 | O | |
| 24 | fused_112_rot_240.pdb | 3.09 | 164.62 | protein | 27 | N | Unprot SC N of |
| 25 | fused_131_rot_240.pdb | 2.85 | 167.36 | protein | 27 | N | His51 |
| 26 | fused_31_rot_270.pdb | 3.03 | 165.75 | protein | 27 | N | |
| 27 | fused_47_rot_240.pdb | 2.97 | 170.58 | protein | 27 | N | |
| 28 | fused_57_rot_330.pdb | 2.79 | 173.00 | protein | 27 | N | |
| 29 | fused_62_rot_240.pdb | 2.80 | 166.68 | protein | 27 | N | |

*Continued on next page*

**Table A7:** *Continued from previous page*

| # | System | Distance (Å) | Angle (°) | Peptide / Protein | ID | Atom | Atom and amino acid |
|---|---|---|---|---|---|---|---|
| 30 | fused_66_rot_330.pdb | 2.88 | 174.49 | protein | 27 | N | |
| 31 | fused_67_rot_240.pdb | 2.89 | 172.65 | protein | 27 | N | |
| 32 | fused_75_rot_270.pdb | 3.08 | 168.83 | protein | 27 | N | |
| 33 | fused_92_rot_240.pdb | 2.82 | 174.29 | protein | 27 | N | |
| 34 | fused_77_rot_240.pdb | 3.11 | 175.51 | protein | 52 | O | SC O of Gln55 |
| 35 | fused_131_rot_300.pdb | 2.86 | 171.26 | protein | 153 | O | BB O of His51 |
| 36 | fused_159_rot_240.pdb | 3.98 | 160.67 | protein | 170 | N | BB N of Gln55 |

**Table A8:** XB results from geometry optimization using TPSS(D3)/SV(P) of p53 peptide with bromodifluoroacetylated Lys24 side chain (PDB ID: 3DAB). The parameters for a positive XB match were a distance of <4 Å and an angle of >160°. Matches with concurrent interaction of at least one fluorine atom are highlighted in blue. Matches with concurrent H···O(amide) contact are highlighted in green.

| # | System | Distance (Å) | Angle (°) | Peptide / Protein | ID | Atom | Atom and amino acid |
|---|---|---|---|---|---|---|---|
| 1 | fused_27_rot_210.pdb | 2.72 | 170.45 | peptide | 84 | O | SC O of |
| 2 | fused_27_rot_330.pdb | 2.70 | 161.25 | peptide | 84 | O | Asp21 |
| 3 | fused_77_rot_180.pdb | 2.72 | 170.09 | peptide | 84 | O | |
| 4 | fused_81_rot_180.pdb | 2.86 | 163.21 | peptide | 84 | O | |
| 5 | fused_81_rot_210.pdb | 2.86 | 163.22 | peptide | 84 | O | |
| 6 | fused_11_rot_270.pdb | 2.69 | 176.68 | peptide | 85 | O | |
| 7 | fused_18_rot_270.pdb | 2.72 | 173.10 | peptide | 85 | O | |
| 8 | fused_18_rot_300.pdb | 2.71 | 173.24 | peptide | 85 | O | |
| 9 | fused_19_rot_0.pdb | 2.68 | 175.62 | peptide | 85 | O | |
| 10 | fused_19_rot_330.pdb | 2.68 | 175.63 | peptide | 85 | O | |
| 11 | fused_20_rot_180.pdb | 2.69 | 170.88 | peptide | 85 | O | |
| 12 | fused_20_rot_210.pdb | 2.69 | 170.92 | peptide | 85 | O | |
| 13 | fused_23_rot_210.pdb | 2.89 | 169.36 | peptide | 85 | O | |
| 14 | fused_23_rot_240.pdb | 2.90 | 167.52 | peptide | 85 | O | |
| 15 | fused_24_rot_330.pdb | 2.74 | 170.05 | peptide | 85 | O | |
| 16 | fused_27_rot_0.pdb | 2.74 | 161.10 | peptide | 85 | O | |
| 17 | fused_28_rot_180.pdb | 2.72 | 175.89 | peptide | 85 | O | |

*Continued on next page*

**Table A8:** *Continued from previous page*

| # | System | Distance (Å) | Angle (°) | Peptide / Protein | ID | Atom | Atom and amino acid |
|---|---|---|---|---|---|---|---|
| 18 | fused_28_rot_210.pdb | 2.73 | 175.53 | peptide | 85 | O | |
| 19 | fused_33_rot_210.pdb | 2.73 | 162.01 | peptide | 85 | O | |
| 20 | fused_3_rot_0.pdb | 2.64 | 172.93 | peptide | 85 | O | |
| 21 | fused_4_rot_180.pdb | 2.70 | 168.69 | peptide | 85 | O | |
| 22 | fused_77_rot_300.pdb | 2.65 | 179.56 | peptide | 85 | O | |
| 23 | fused_77_rot_330.pdb | 2.74 | 161.06 | peptide | 85 | O | |
| 24 | fused_78_rot_210.pdb | 2.72 | 175.81 | peptide | 85 | O | |
| 25 | fused_78_rot_240.pdb | 2.73 | 175.75 | peptide | 85 | O | |
| 26 | fused_26_rot_240.pdb | 3.24 | 160.78 | peptide | 97 | N | SC N of Trp23 |
| 27 | fused_103_rot_240.pdb | 2.76 | 162.81 | peptide | 166 | O | BB O of Ser20 |
| 28 | fused_135_rot_330.pdb | 2.97 | 163.90 | peptide | 171 | O | BB O of Asp21 |
| 29 | fused_1_rot_210.pdb | 2.83 | 177.04 | peptide | 171 | O | |
| 30 | fused_1_rot_240.pdb | 2.73 | 173.17 | peptide | 171 | O | |
| 31 | fused_1_rot_270.pdb | 2.83 | 178.50 | peptide | 171 | O | |
| 32 | fused_1_rot_300.pdb | 2.83 | 178.51 | peptide | 171 | O | |
| 33 | fused_68_rot_300.pdb | 2.98 | 163.84 | peptide | 171 | O | |
| 34 | fused_70_rot_300.pdb | 2.78 | 164.53 | peptide | 171 | O | |
| 35 | fused_82_rot_0.pdb | 2.90 | 164.36 | peptide | 171 | O | |
| 36 | fused_97_rot_330.pdb | 3.01 | 163.66 | peptide | 171 | O | |
| 37 | fused_101_rot_0.pdb | 3.12 | 165.82 | peptide | 186 | O | BB O of Lys24 |
| 38 | fused_101_rot_330.pdb | 3.17 | 165.51 | peptide | 186 | O | |
| 39 | fused_90_rot_0.pdb | 3.15 | 165.71 | peptide | 186 | O | |
| 40 | fused_94_rot_0.pdb | 3.06 | 165.71 | peptide | 186 | O | |
| 41 | fused_99_rot_330.pdb | 3.16 | 165.72 | peptide | 186 | O | |
| 42 | fused_14_rot_330.pdb | 3.13 | 164.02 | protein | 27 | N | SC N of His54 |
| 43 | fused_156_rot_240.pdb | 2.82 | 169.21 | protein | 27 | N | |
| 44 | fused_31_rot_240.pdb | 2.91 | 173.08 | protein | 27 | N | |
| 45 | fused_56_rot_240.pdb | 2.94 | 170.21 | protein | 27 | N | |
| 46 | fused_66_rot_330.pdb | 2.87 | 174.62 | protein | 27 | N | |
| 47 | fused_88_rot_270.pdb | 2.91 | 171.40 | protein | 27 | N | |
| 48 | fused_8_rot_270.pdb | 2.94 | 170.16 | protein | 27 | N | |
| 49 | fused_9_rot_240.pdb | 3.22 | 161.77 | protein | 27 | N | |
| 50 | fused_112_rot_240.pdb | 3.40 | 166.86 | protein | 45 | N | SC N of Gln58 |

*Continued on next page*

**Table A8:** *Continued from previous page*

| # | System | Distance (Å) | Angle (°) | Peptide / Protein | ID | Atom | Atom and amino acid |
|---|---|---|---|---|---|---|---|
| 51 | fused_136_rot_330.pdb | 3.03 | 174.28 | protein | 46 | O | SC O of Gln58 |
| 52 | fused_9_rot_330.pdb | 2.95 | 160.12 | protein | 46 | O | |
| 53 | fused_26_rot_270.pdb | 3.91 | 161.09 | protein | 116 | O | BB O of Met53 |
| 54 | fused_60_rot_270.pdb | 3.04 | 168.03 | protein | 120 | O | BB O of His54 |

**Table A9:** Other acetyl amide interaction results from geometry optimization using TPSS(D3)/SV(P) of p53 peptide with bromodifluoroacetylated Lys24 side chain (PDB ID: 2Z5T). Matches with an XB-positive result are highlighted in yellow.

| # | System | Peptide donor/acceptor | Distance (Å) | Angle (°) |
|---|---|---|---|---|
| | **unpolar** | | <3.0 Å | >150° |
| 1 | fused_100_rot_210.pdb | F | 2.56 | 157.61 |
| 2 | fused_103_rot_240.pdb | F | 2.29 | 158.30 |
| 3 | fused_104_rot_240.pdb | F | 2.99 | 151.90 |
| 4 | fused_104_rot_240.pdb | F | 2.50 | 158.72 |
| 5 | fused_106_rot_210.pdb | F | 2.84 | 168.99 |
| 6 | fused_125_rot_300.pdb | F | 2.85 | 158.92 |
| 7 | fused_158_rot_0.pdb | F | 2.68 | 164.16 |
| 8 | fused_15_rot_240.pdb | F | 2.86 | 154.06 |
| 9 | fused_15_rot_270.pdb | F | 2.88 | 154.72 |
| 10 | fused_16_rot_270.pdb | F | 2.86 | 151.71 |
| 11 | fused_17_rot_300.pdb | F | 2.51 | 151.15 |
| 12 | fused_1_rot_0.pdb | F | 2.50 | 166.98 |
| 13 | fused_2_rot_300.pdb | F | 2.98 | 152.99 |
| 14 | fused_30_rot_240.pdb | F | 2.75 | 153.82 |
| 15 | fused_30_rot_270.pdb | F | 2.93 | 156.24 |
| 16 | fused_31_rot_300.pdb | F | 2.39 | 158.15 |
| 17 | fused_40_rot_330.pdb | F | 2.44 | 175.36 |
| 18 | fused_59_rot_0.pdb | F | 2.74 | 155.40 |
| 19 | fused_63_rot_330.pdb | F | 2.38 | 152.15 |
| 20 | fused_73_rot_270.pdb | F | 2.76 | 153.44 |
| 21 | fused_75_rot_270.pdb | F | 2.43 | 156.48 |

*Continued on next page*

**Table A9:** *Continued from previous page*

| # | System | Peptide donor/acceptor | Distance (Å) | Angle (°) |
|---|---|---|---|---|
| 22 | fused_7_rot_330.pdb | F | 2.74 | 162.97 |
| 23 | fused_87_rot_0.pdb | F | 2.38 | 151.83 |
| 24 | fused_87_rot_330.pdb | F | 2.38 | 151.64 |
| 25 | fused_89_rot_210.pdb | F | 2.90 | 156.15 |
| 26 | fused_92_rot_240.pdb | F | 2.30 | 170.07 |
| 27 | fused_93_rot_240.pdb | F | 2.97 | 166.51 |
| 28 | fused_93_rot_240.pdb | F | 2.56 | 157.75 |
| 29 | fused_9_rot_330.pdb | F | 2.83 | 165.29 |
| | **polar** | | <3.0 Å | >150° |
| 1 | used_106_rot_180.pdb | F | 2.03 | 162.49 |
| 2 | fused_17_rot_210.pdb | F | 2.70 | 150.61 |
| 3 | fused_90_rot_180.pdb | F | 1.98 | 163.97 |
| 4 | fused_9_rot_210.pdb | F | 2.68 | 150.79 |
| | **amide O** | | <3.5 Å | >150° |
| 1 | fused_125_rot_300.pdb | O | 1.93 | 168.35 |
| 2 | fused_12_rot_0.pdb | O | 1.76 | 171.05 |
| 3 | fused_131_rot_300.pdb | O | 1.89 | 172.27 |
| 4 | fused_156_rot_180.pdb | O | 1.76 | 162.67 |
| 5 | fused_156_rot_210.pdb | O | 1.75 | 174.46 |
| 6 | fused_156_rot_240.pdb | O | 1.74 | 175.96 |
| 7 | fused_15_rot_240.pdb | O | 1.78 | 171.45 |
| 8 | fused_15_rot_270.pdb | O | 1.78 | 170.80 |
| 9 | fused_161_rot_240.pdb | O | 1.85 | 170.88 |
| 10 | fused_161_rot_270.pdb | O | 1.85 | 170.96 |
| 11 | fused_19_rot_270.pdb | O | 1.90 | 172.88 |
| 12 | fused_20_rot_180.pdb | O | 1.79 | 179.67 |
| 13 | fused_20_rot_210.pdb | O | 1.88 | 161.94 |
| 14 | fused_20_rot_240.pdb | O | 2.00 | 160.77 |
| 15 | fused_21_rot_0.pdb | O | 1.70 | 174.79 |
| 16 | fused_21_rot_330.pdb | O | 1.81 | 164.25 |
| 17 | fused_23_rot_240.pdb | O | 1.90 | 172.20 |
| 18 | fused_24_rot_240.pdb | O | 1.80 | 165.02 |
| 19 | fused_27_rot_0.pdb | O | 1.74 | 179.59 |
| 20 | fused_43_rot_240.pdb | O | 1.79 | 170.55 |
| 21 | fused_44_rot_330.pdb | O | 1.71 | 168.76 |

*Continued on next page*

**Table A9:** *Continued from previous page*

| # | System | Peptide donor/acceptor | Distance (Å) | Angle (°) |
|---|---|---|---|---|
| 22 | fused_69_rot_300.pdb | O | 1.78 | 167.79 |
| 23 | fused_77_rot_300.pdb | O | 1.80 | 162.89 |
| 24 | fused_77_rot_330.pdb | O | 1.78 | 162.15 |
| 25 | fused_7_rot_0.pdb | O | 1.73 | 173.70 |
| | **amide NH** | | <3.5 Å | >150° |
| 1 | fused_101_rot_300.pdb | NH | 2.06 | 152.64 |
| 2 | fused_151_rot_240.pdb | NH | 1.92 | 152.76 |
| 3 | fused_151_rot_270.pdb | NH | 1.97 | 155.42 |
| 4 | fused_28_rot_210.pdb | NH | 2.06 | 152.89 |
| 5 | fused_78_rot_270.pdb | NH | 2.06 | 152.71 |

**Table A10:** Other acetyl amide interaction results from geometry optimization using TPSS(D3)/SV(P) of p53 peptide with bromodifluoroacetylated Lys24 side chain (PDB ID: 3DAB). Matches with an XB-positive result are highlighted in yellow.

| # | System | Peptide donor/acceptor | Distance (Å) | Angle (°) |
|---|---|---|---|---|
| | **F** | | <3.0 Å | >150° |
| 1 | fused_100_rot_180.pdb | F | 2.48 | 156.11 |
| 2 | fused_100_rot_180.pdb | F | 2.47 | 176.76 |
| 3 | fused_101_rot_120.pdb | F | 2.92 | 163.38 |
| 4 | fused_103_rot_240.pdb | F | 2.84 | 173.65 |
| 5 | fused_10_rot_300.pdb | F | 2.82 | 158.22 |
| 6 | fused_112_rot_240.pdb | F | 2.7 | 175.99 |
| 7 | fused_123_rot_300.pdb | F | 2.7 | 161.74 |
| 8 | fused_127_rot_330.pdb | F | 2.3 | 165.43 |
| 9 | fused_12_rot_300.pdb | F | 2.58 | 155.29 |
| 10 | fused_134_rot_240.pdb | F | 2.77 | 167.66 |
| 11 | fused_136_rot_330.pdb | F | 2.76 | 156.2 |
| 12 | fused_13_rot_300.pdb | F | 2.85 | 156.4 |
| 13 | fused_152_rot_0.pdb | F | 2.31 | 166.12 |
| 14 | fused_153_rot_0.pdb | F | 2.27 | 166.94 |
| 15 | fused_153_rot_330.pdb | F | 2.28 | 167.62 |
| 16 | fused_156_rot_180.pdb | F | 2.44 | 170.6 |

*Continued on next page*

**Table A10:** *Continued from previous page*

| # | System | Peptide donor/acceptor | Distance (Å) | Angle (°) |
|---|---|---|---|---|
| 17 | fused_156_rot_210.pdb | F | 2.44 | 169.51 |
| 18 | fused_158_rot_0.pdb | F | 2.69 | 160.86 |
| 19 | fused_158_rot_330.pdb | F | 2.7 | 160.8 |
| 20 | fused_161_rot_180.pdb | F | 2.41 | 160.7 |
| 21 | fused_161_rot_270.pdb | F | 2.48 | 163.76 |
| 22 | fused_17_rot_240.pdb | F | 2.82 | 159.97 |
| 23 | fused_1_rot_0.pdb | F | 2.52 | 167.39 |
| 24 | fused_1_rot_330.pdb | F | 2.5 | 171.2 |
| 25 | fused_30_rot_240.pdb | F | 2.84 | 167.28 |
| 26 | fused_30_rot_270.pdb | F | 2.84 | 165.06 |
| 27 | fused_37_rot_210.pdb | F | 2.57 | 168.36 |
| 28 | fused_43_rot_210.pdb | F | 2.58 | 153.98 |
| 29 | fused_47_rot_270.pdb | F | 2.85 | 169.61 |
| 30 | fused_51_rot_0.pdb | F | 2.31 | 177.37 |
| 31 | fused_51_rot_300.pdb | F | 2.3 | 178.64 |
| 32 | fused_51_rot_330.pdb | F | 2.32 | 177.04 |
| 33 | fused_53_rot_240.pdb | F | 2.53 | 155.31 |
| 34 | fused_53_rot_270.pdb | F | 2.45 | 166.08 |
| 35 | fused_61_rot_330.pdb | F | 2.53 | 156.32 |
| 36 | fused_63_rot_330.pdb | F | 2.74 | 153.93 |
| 37 | fused_64_rot_240.pdb | F | 2.36 | 154.61 |
| 38 | fused_72_rot_300.pdb | F | 2.67 | 156.04 |
| 39 | fused_73_rot_240.pdb | F | 2.85 | 165.72 |
| 40 | fused_73_rot_270.pdb | F | 2.81 | 172.34 |
| 41 | fused_78_rot_180.pdb | F | 2.75 | 172.97 |
| 42 | fused_79_rot_0.pdb | F | 2.43 | 153.64 |
| 43 | fused_81_rot_180.pdb | F | 2.4 | 154.26 |
| 44 | fused_81_rot_210.pdb | F | 2.4 | 154.26 |
| 45 | fused_88_rot_330.pdb | F | 2.61 | 156.27 |
| 46 | fused_89_rot_0.pdb | F | 2.57 | 163.07 |
| 47 | fused_89_rot_210.pdb | F | 2.7 | 157.72 |
| 48 | fused_89_rot_330.pdb | F | 2.58 | 172.3 |
| 49 | fused_90_rot_120.pdb | F | 2.96 | 162.03 |
| 50 | fused_93_rot_240.pdb | F | 2.85 | 156.38 |
| | **amide NH** | | <3.5 Å | >150° |
| 1 | fused_119_rot_300.pdb | NH | 2.03 | 157.07 |

*Continued on next page*

**Table A10:** *Continued from previous page*

| # | System | Peptide donor/acceptor | Distance (Å) | Angle (°) |
|---|---|---|---|---|
| 2 | fused_28_rot_240.pdb | NH | 2.02 | 158.16 |
| 3 | fused_78_rot_300.pdb | NH | 2.02 | 158.18 |

## A.7 Small Molecule Crystal Data

### A.7.1 1-(4-(Difluoromethoxy)phenyl)urea (6a)

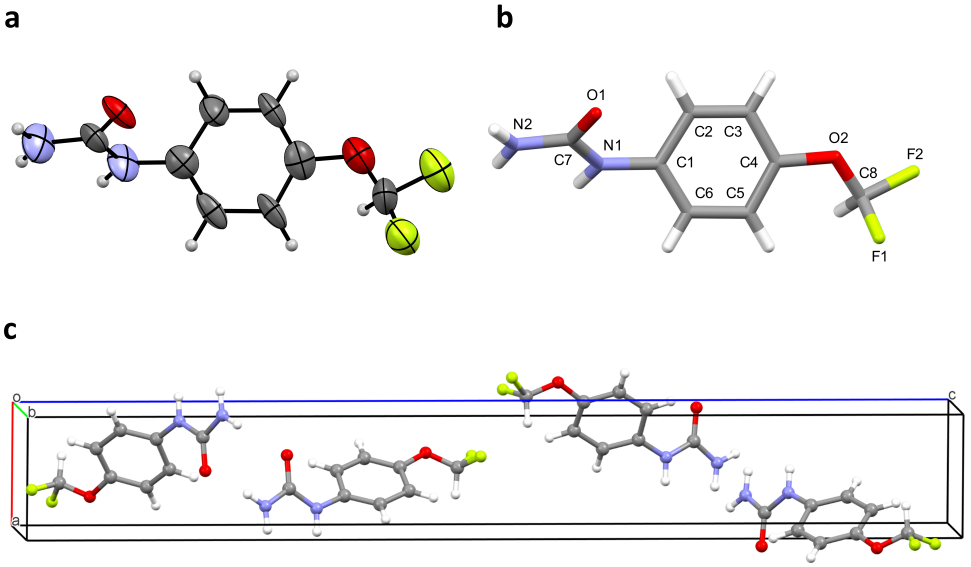


**Figure A14:** Data for **6a**. **(a)** ORTEP depicted at the 50 % probability level; **(b)** atom numbering; **(c)** crystal cell with cell axes.

**Table A11:** Crystal and refinement data for **6a**

| | |
|---|---|
| Substance code | SV153 (**6a**) |
| CCDC ID | 2248877 |
| Total formular | $C_8H_8F_2N_2O_2$ |
| Molecular formula | $C_8H_8F_2N_2O_2$ |
| Formula weight | 202.16 |
| Temperature | 120(2) K |
| Wavelength, type of radiation | 0.71073 Å, MoKα |
| Diffractometer | STOE IPDS 2T |
| Crystal system | Orthorhombic |
| Space group, number | $P2_12_12_1$, (19) |
| Lattice constant | a = 4.5833(5) Å |
| | b = 5.3595(8) Å |
| | c = 34.717(4) Å |
| Volume | 852.80(19) $Å^3$ |
| Number of reflexes and | 9126 |

*Continued on next page*

**Table A11:** *Continued from previous page*

| | |
|---|---|
| Measuring range for lattice constants | $2.35° \leq \Theta \leq 28.34°$ |
| Z | 4 |
| Density (calculated) | $1.575\,mg\,m^{-3}$ |
| Absorption coefficient | $0.143\,mm^{-1}$ |
| Method of absorption correction | None |
| F(000) | 416 |
| Crystal size, shape and color | $0.100 \times 0.400 \times 0.600\,mm^3$, colorless plate |
| Theta range of measurement | 2.347 to 28.122° |
| Index area | $-5 \leq h \leq 6$, $-7 \leq k \leq 7$, $-45 \leq l \leq 45$ |
| Number of reflexes: | |
| measured | 4266 |
| independent | 1894 [$R_{int} = 0.1182$] |
| observed [$I>2\sigma(I)$] | 1342 |
| Completeness at $\Theta_{max} = 25.2°$ | 92.8 % |
| Refinement method | Full-matrix least-squares on $F^2$ |
| Reflexes / Restraints / Parameters | 1894 / 0 / 128 |
| Goodness of fit for $F^2$ | 3.591 |
| Final R values [$I>2\sigma(I)$] | R1 = 0.2040, wR2 = 0.5013 |
| R value (all data) | R1 = 0.2394, wR2 = 0.5228 |
| Absolute structure parameter | 4.5(10) |
| Maximum and minimum of the diff. Map | 1.037 and $-1.008\,eÅ^{-3}$ |
| Remarks | Crystals with poor quality, only usable as synthesis evidence |

### A.7.2 1-(4-(Trifluoromethoxy)phenyl)urea (6b)

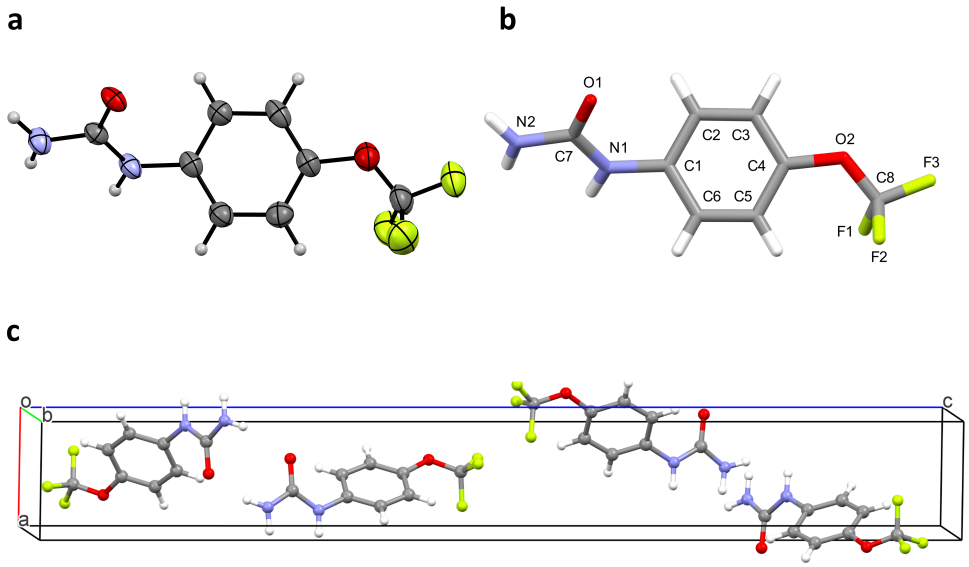


**Figure A15:** Data for **6b**. **(a)** ORTEP depicted at the 50 % probability level; **(b)** atom numbering; **(c)** crystal cell with cell axes.

**Table A12:** Crystal and refinement data for **6b**

| | |
|---|---|
| Substance code | SV158 (**6b**) |
| CCDC ID | 2232102 |
| Total formular | $C_8H_7F_3N_2O_2$ |
| Molecular formula | $C_8H_7F_3N_2O_2$ |
| Formula weight | 220.16 |
| Temperature | 120(2) K |
| Wavelength, type of radiation | 0.71073 Å, MoKα |
| Diffractometer | STOE IPDS 2T |
| Crystal system | Orthorhombic |
| Space group, number | $P2_12_12_1$, (19) |
| Lattice constant | a = 4.6027(3) Å |
| | b = 5.3114(4) Å |
| | c = 36.096(4) Å |
| Volume | 882.43(14) $Å^3$ |
| Number of reflexes and | 8594 |
| Measuring range for lattice constants | $2.26° \leq \Theta \leq 28.35°$ |

*Continued on next page*

**Table A12:** *Continued from previous page*

| | |
|---|---|
| Z | 4 |
| Density (calculated) | 1.657 mg $m^{-3}$ |
| Absorption coefficient | 0.161 $mm^{-1}$ |
| Method of absorption correction | Integration |
| Max. und min. transmission | 0.9959 and 0.9619 |
| F(000) | 448 |
| Crystal size, shape and color | 0.020 x 0.150 x 0.450 $mm^3$, colorless needle |
| Theta range of measurement | 3.386 to 27.977° |
| Index area | $-5 \leq h \leq 6$, $-6 \leq k \leq 6$, $-46 \leq l \leq 47$ |
| Number of reflexes: | |
| measured | 6240 |
| independent | 2078 [$R_{int}$ = 0.0571] |
| observed [I>2σ(I)] | 1431 |
| Completeness at $\Theta_{max}$ = 25.2° | 99.8 % |
| Refinement method | Full-matrix least-squares on $F^2$ |
| Reflexes / Restraints / Parameters | 2078 / 0 / 145 |
| Goodness of fit for $F^2$ | 1.109 |
| Final R values [I>2σ(I)] | R1 = 0.0963, wR2 = 0.2455 |
| R value (all data) | R1 = 0.1416, wR2 = 0.2795 |
| Absolute structure parameter | 3.3(10) |
| Maximum and minimum of the diff. Map | 0.613 and −0.441 e$Å^{-3}$ |
| Remarks | NH's localized and refined |

### A.7.3 1-(4-(Chlorodifluoromethoxy)phenyl)urea (6c)

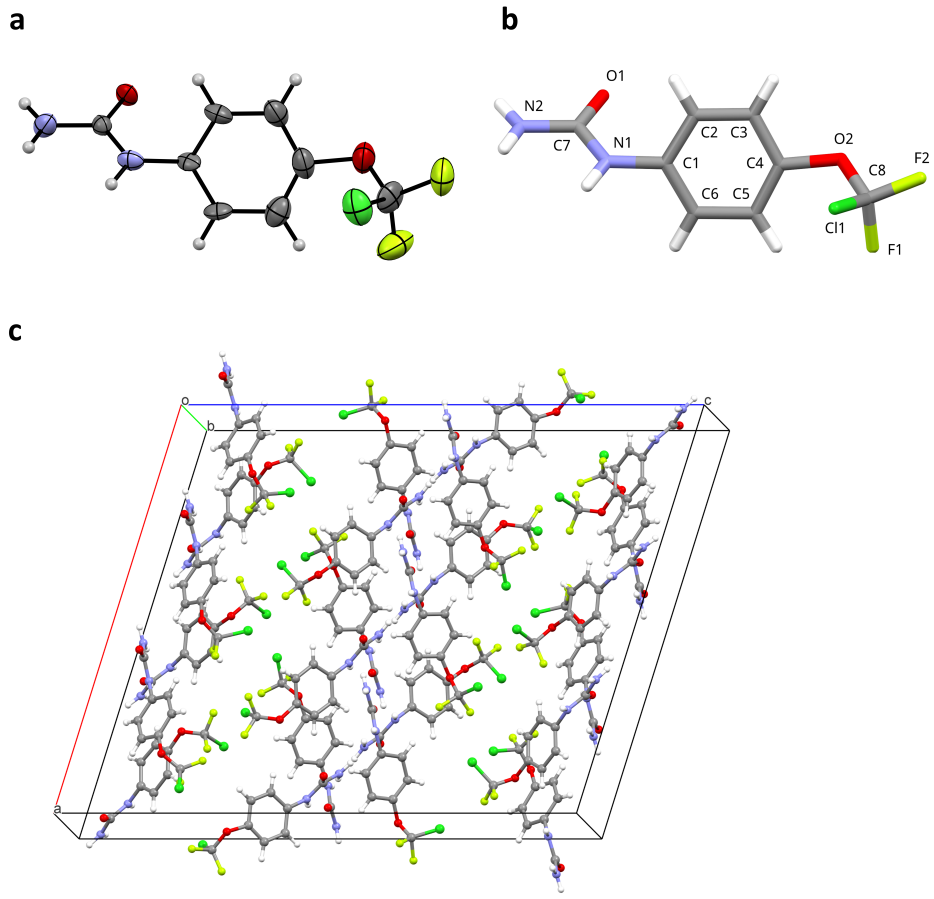


**Figure A16:** Data for **6c**. **(a)** ORTEP depicted at the 50 % probability level; **(b)** atom numbering; **(c)** crystal cell with cell axes.

**Table A13:** Crystal and refinement data for **6c**

| | |
|---|---|
| Substance code | SV155 (**6c**) |
| CCDC ID | 2232103 |
| Total formular | $C_8H_7ClF_2N_2O_2$ |
| Molecular formula | $C_8H_7ClF_2N_2O_2$ |
| Formula weight | 236.61 |
| Temperature | 120(2) K |
| Wavelength, type of radiation | 0.71073 Å, MoKα |
| Diffractometer | STOE IPDS 2T |
| Crystal system | Monoclinic |

*Continued on next page*

**Table A13:** *Continued from previous page*

| | |
|---|---|
| Space group, number | $P2_1/n$, (14) |
| Lattice constant | a = 23.504(3) Å |
| | b = 9.0214(6) Å; β = 106.046(8)° |
| | c = 28.905(3) Å |
| Volume | 5890.1(10) $Å^3$ |
| Number of reflexes and | 4451 |
| Measuring range for lattice constants | $2.47° \leq \Theta \leq 28.46°$ |
| Z | 24 |
| Density (calculated) | 1.601 mg $m^{-3}$ |
| Absorption coefficient | 0.400 $mm^{-1}$ |
| Method of absorption correction | Integration |
| Max. und min. transmission | 0.9702 and 0.8793 |
| F(000) | 2880 |
| Crystal size, shape and color | 0.060 x 0.260 x 0.900 $mm^3$, colorless needle |
| Theta range of measurement | 2.374 to 28.143° |
| Index area | $-30 \leq h \leq 31$, $-11 \leq k \leq 11$, $-38 \leq l \leq 37$ |
| Number of reflexes: | |
| measured | 34022 |
| independent | 34022 |
| observed [I>2σ(I)] | 16632 |
| Completeness at $\Theta_{max} = 25.2°$ | 93.7 % |
| Refinement method | Full-matrix least-squares on $F^2$ |
| Reflexes / Restraints / Parameters | 34022 / 7 / 812 |
| Goodness of fit for $F^2$ | 1.873 |
| Final R values [I>2σ(I)] | R1 = 0.1884, wR2 = 0.4877 |
| R value (all data) | R1 = 0.2890, wR2 = 0.5531 |
| Maximum and minimum of the diff. Map | 3.470 and −1.224 e$Å^{-3}$ |
| Remarks | Structure contains 6 independent molecules whose conformation differs slightly. Crystals are twinned. |

### A.7.4 1-(4-(Bromoodifluoromethoxy)phenyl)urea (6d)

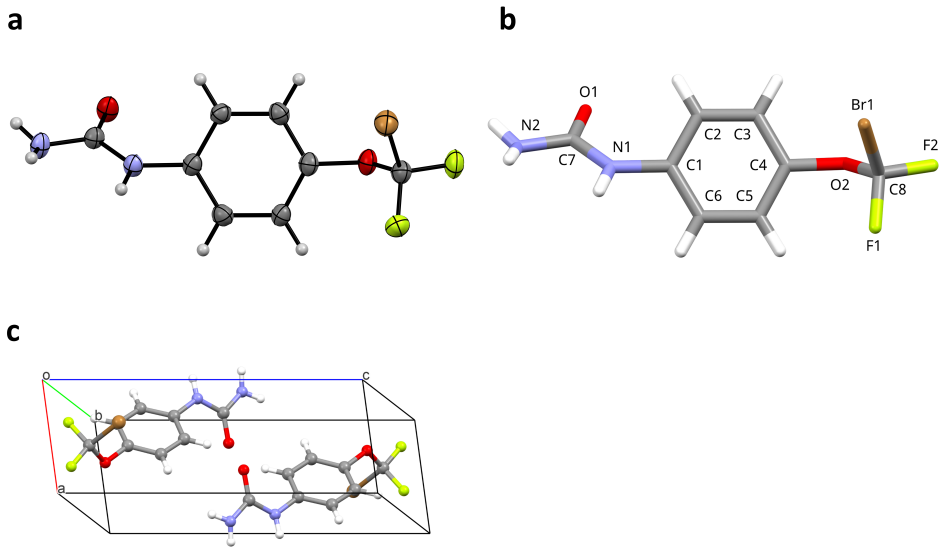


**Figure A17:** Data for **6d**. **(a)** ORTEP depicted at the 50 % probability level; **(b)** atom numbering; **(c)** crystal cell with cell axes.

**Table A14:** Crystal and refinement data for **6d**

| | |
|---|---|
| Substance code | SV154 (**6d**) |
| CCDC ID | 2232104 |
| Total formular | $C_8H_7BrF_2N_2O_2$ |
| Molecular formula | $C_8H_7BrF_2N_2O_2$ |
| Formula weight | 281.07 |
| Temperature | 120(2) K |
| Wavelength, type of radiation | 0.71073 Å, MoKα |
| Diffractometer | STOE IPDS 2T |
| Crystal system | Triclinic |
| Space group, number | $P\bar{1}$, (2) |
| Lattice constant | a = 4.6143(4) Å; α = 75.698(7)° |
| | b = 8.5484(7) Å; β = 82.322(7)° |
| | c = 12.9250(12) Å; γ = 77.166(7)° |
| Volume | 480.01(8) $Å^3$ |
| Number of reflexes and | 6677 |
| Measuring range for lattice constants | $2.51° \leq \Theta \leq 28.44°$ |

*Continued on next page*

**Table A14:** *Continued from previous page*

| | |
|---|---|
| Z | 2 |
| Density (calculated) | 1.945 mg m$^{-3}$ |
| Absorption coefficient | 4.293 mm$^{-1}$ |
| Method of absorption correction | Integration |
| Max. und min. transmission | 0.5917 and 0.3698 |
| F(000) | 276 |
| Crystal size, shape and color | 0.160 x 0.160 x 0.300 mm$^3$, colorless needle |
| Theta range of measurement | 2.508 to 27.902° |
| Index area | $-6 \leq h \leq 6$, $-11 \leq k \leq 11$, $-16 \leq l \leq 16$ |
| Number of reflexes: | |
| measured | 4142 |
| independent | 2262 [$R_{int}$ = 0.0321] |
| observed [I>2σ(I)] | 2025 |
| Completeness at $\Theta_{max}$ = 25.2° | 99.7 % |
| Refinement method | Full-matrix least-squares on $F^2$ |
| Reflexes / Restraints / Parameters | 2262 / 3 / 147 |
| Goodness of fit for $F^2$ | 1.085 |
| Final R values [I>2σ(I)] | R1 = 0.0407, wR2 = 0.1074 |
| R value (all data) | R1 = 0.0471, wR2 = 0.1163 |
| Maximum and minimum of the diff. Map | 0.672 and −1.111 eÅ$^{-3}$ |
| Remarks | NH's localized and refined isotropically |

### A.7.5 1-(4-(Difluoroiodomethoxy)phenyl)urea (6e)

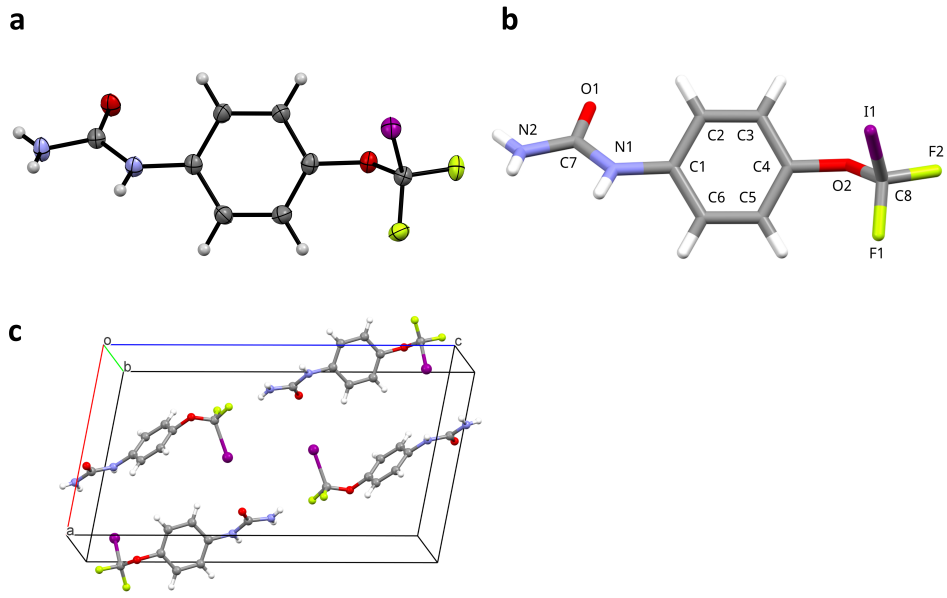


**Figure A18:** Data for **6e**. **(a)** ORTEP depicted at the 50 % probability level; **(b)** atom numbering; **(c)** crystal cell with cell axes.

**Table A15:** Crystal and refinement data for **6e**

| | |
|---|---|
| Substance code | SV157 (**6e**) |
| CCDC ID | 2232105 |
| Total formular | $C_8H_7F_2IN_2O_2$ |
| Molecular formula | $C_8H_7F_2IN_2O_2$ |
| Formula weight | 328.06 |
| Temperature | 120(2) K |
| Wavelength, type of radiation | 0.71073 Å, MoKα |
| Diffractometer | STOE IPDS 2T |
| Crystal system | Monoclinic |
| Space group, number | $P2_1/n$, (14) |
| Lattice constant | a = 11.0114(19) Å |
| | b = 4.6009(5) Å; β = 96.097(14)° |
| | c = 19.813(3) Å |
| Volume | 998.1(3) $Å^3$ |
| Number of reflexes and | 11256 |
| Measuring range for lattice constants | $2.63° \leq \Theta \leq 28.54°$ |

*Continued on next page*

**Table A15:** *Continued from previous page*

| | |
|---|---|
| Z | 4 |
| Density (calculated) | 2.183 mg $m^{-3}$ |
| Absorption coefficient | 3.220 $mm^{-1}$ |
| Method of absorption correction | Integration |
| Max. und min. transmission | 0.8193 and 0.1617 |
| F(000) | 624 |
| Crystal size, shape and color | 0.050 x 0.360 x 1.120 $mm^3$, colorless plate |
| Theta range of measurement | 3.444 to 27.925° |
| Index area | $-14 \leq h \leq 14$, $-6 \leq k \leq 6$, $-25 \leq l \leq 26$ |
| Number of reflexes: | |
| measured | 7031 |
| independent | 7031 |
| observed [I>2σ(I)] | 6682 |
| Completeness at $\Theta_{max}$ = 25.2° | 98.3 % |
| Refinement method | Full-matrix least-squares on $F^2$ |
| Reflexes / Restraints / Parameters | 7031 / 0 / 148 |
| Goodness of fit for $F^2$ | 1.135 |
| Final R values [I>2σ(I)] | R1 = 0.0400, wR2 = 0.1268 |
| R value (all data) | R1 = 0.0414, wR2 = 0.1295 |
| Maximum and minimum of the diff. Map | 0.911 and −1.117 e$Å^{-3}$ |
| Remarks | Crystals are twinned, NH's localized and refined isotropically |

### A.7.6 *N*-(Benzo[*d*][1,3]dioxol-5-yl)-2,2-difluoroacetamide (7a)

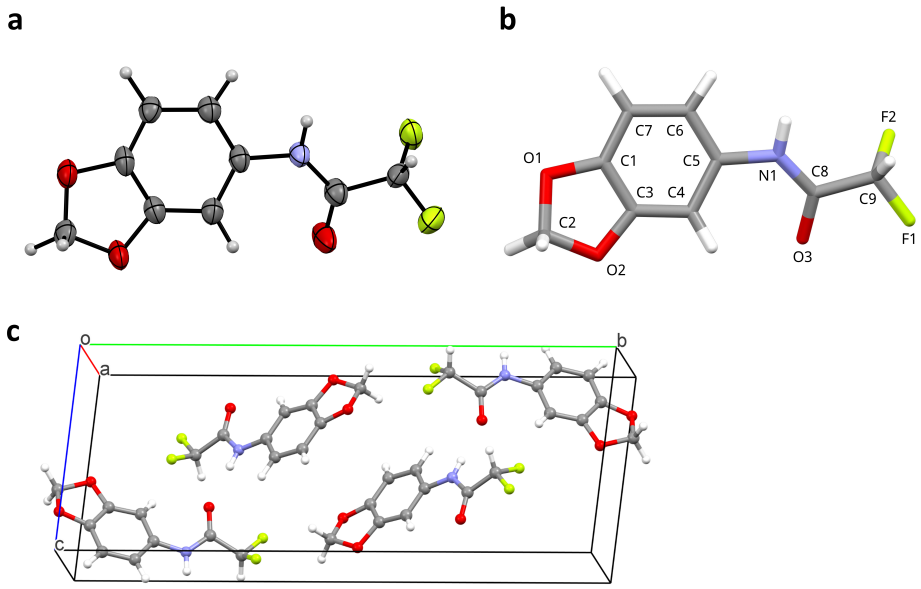


**Figure A19:** Data for **7a**. **(a)** ORTEP depicted at the 50 % probability level; **(b)** atom numbering; **(c)** crystal cell with cell axes.

**Table A16:** Crystal and refinement data for **7a**

| | |
|---|---|
| Substance code | SV-5-1-019 (**7a**) |
| CCDC ID | 2232106 |
| Total formular | $C_9H_7F_2NO_3$ |
| Molecular formula | $C_9H_7F_2NO_3$ |
| Formula weight | 215.16 |
| Temperature | 120(2) K |
| Wavelength, type of radiation | 0.71073 Å, MoKα |
| Diffractometer | STOE IPDS 2T |
| Crystal system | Triclinic |
| Space group, number | $P\bar{1}$, (2) |
| Lattice constant | a = 4.0665(5) Å; α = 90.793(9)° |
| | b = 22.496(3) Å; β = 100.066(9)° |
| | c = 9.5787(10) Å; γ = 89.197(10)° |
| Volume | 862.62(18) Å$^3$ |
| Number of reflexes and | 14 047 |
| Measuring range for lattice constants | 2.35° ≤ Θ ≤ 28.23° |

*Continued on next page*

**Table A16:** *Continued from previous page*

| | |
|---|---|
| Z | 4 |
| Density (calculated) | 1.657 mg $m^{-3}$ |
| Absorption coefficient | 0.152 $mm^{-1}$ |
| Method of absorption correction | Integration |
| Max. und min. transmission | 0.9874 and 0.9635 |
| F(000) | 440 |
| Crystal size, shape and color | 0.090 x 0.150 x 0.290 $mm^3$, colorless needle |
| Theta range of measurement | 2.717 to 27.498° |
| Index area | $-4 \leq h \leq 5$, $-29 \leq k \leq 29$, $-12 \leq l \leq 12$ |
| Number of reflexes: | |
| measured | 8111 |
| independent | 3858 [$R_{int}$ = 0.0447] |
| observed [I>2σ(I)] | 2668 |
| Completeness at $\Theta_{max}$ = 25.2° | 97.1 % |
| Refinement method | Full-matrix least-squares on $F^2$ |
| Reflexes / Restraints / Parameters | 3858 / 0 / 314 |
| Goodness of fit for $F^2$ | 1.047 |
| Final R values [I>2σ(I)] | R1 = 0.0905, wR2 = 0.2011 |
| R value (all data) | R1 = 0.1322, wR2 = 0.2342 |
| Maximum and minimum of the diff. Map | 0.435 and −0.428 e$Å^{-3}$ |
| Remarks | Crystals are twinned, structure contains two independent molecules A and B, but their geometry is identical. |

### A.7.7 *N*-(Benzo[*d*][1,3]dioxol-5-yl)-2,2,2-trifluoroacetamide (7b)

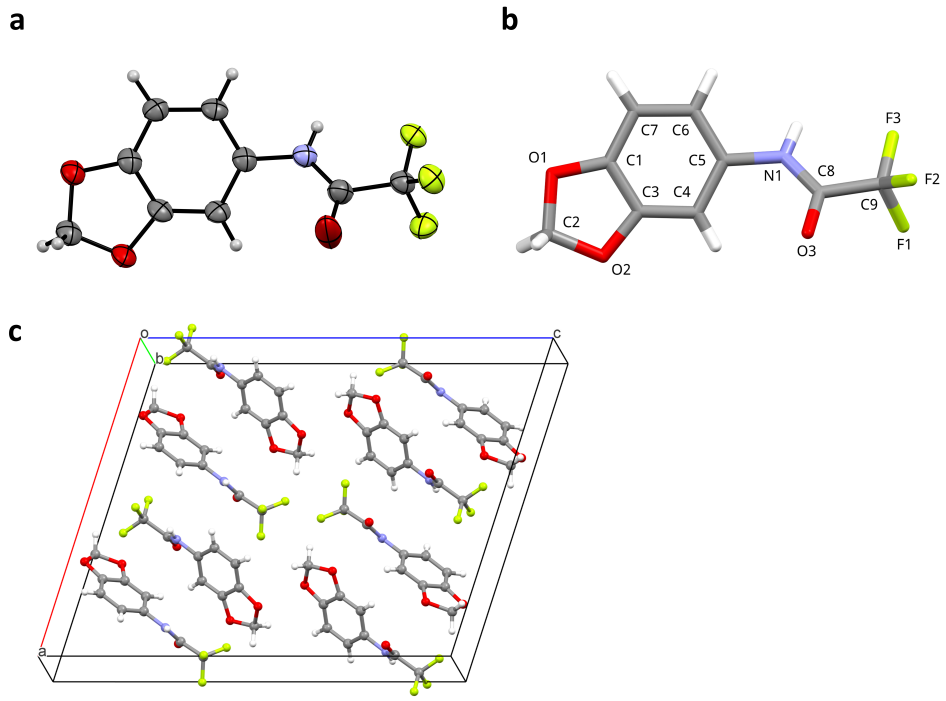


**Figure A20:** Data for **7b**. **(a)** ORTEP depicted at the 50 % probability level; **(b)** atom numbering; **(c)** crystal cell with cell axes..

**Table A17:** Crystal and refinement data for **7b**

| | |
|---|---|
| Substance code | SV-5-2-019 (**7b**) |
| CCDC ID | 2232107 |
| Total formular | $C_4H_2F_3NO_3$ |
| Molecular formula | $C_4H_2F_3NO_3$ |
| Formula weight | 249.60 |
| Temperature | 120(2) K |
| Wavelength, type of radiation | 0.71073 Å, MoKα |
| Diffractometer | STOE IPDS 2T |
| Crystal system | Monoclinic |
| Space group, number | C6/c, (15) |
| Lattice constant | a = 17.2930(18) Å |
| | b = 5.0327(3) Å; β = 105.299(8)° |
| | c = 21.184(2) Å |
| Volume | 1778(3) $Å^3$ |

*Continued on next page*

**Table A17:** *Continued from previous page*

| | |
|---|---|
| Number of reflexes and | 11 514 |
| Measuring range for lattice constants | $3.54° \leq \Theta \leq 28.41°$ |
| Z | 8 |
| Density (calculated) | $1.742\,mg\,m^{-3}$ |
| Absorption coefficient | $0.170\,mm^{-1}$ |
| Method of absorption correction | Integration |
| Max. und min. transmission | 0.9904 and 0.9059 |
| F(000) | 944 |
| Crystal size, shape and color | $0.060 \times 0.070 \times 1.200\,mm^3$, colorless needle |
| Theta range of measurement | 3.538 to 27.985° |
| Index area | $-22 \leq h \leq 22, -6 \leq k \leq 6, -27 \leq l \leq 27$ |
| Number of reflexes: | |
| measured | 7840 |
| independent | 2118 [$R_{int} = 0.1150$] |
| observed [$I>2\sigma(I)$] | 1570 |
| Completeness at $\Theta_{max} = 25.2°$ | 99.8 % |
| Refinement method | Full-matrix least-squares on $F^2$ |
| Reflexes / Restraints / Parameters | 2118 / 80 / 168 |
| Goodness of fit for $F^2$ | 1.112 |
| Final R values [$I>2\sigma(I)$] | R1 = 0.0649, wR2 = 0.1566 |
| R value (all data) | R1 = 0.0944, wR2 = 0.1829 |
| Maximum and minimum of the diff. Map | 0.314 and $-0.321\,eÅ^{-3}$ |
| Remarks | H atoms localized and refined |

### A.7.8 *N*-(Benzo[*d*][1,3]dioxol-5-yl)-2-chloro-2,2-difluoroacetamide (7c)

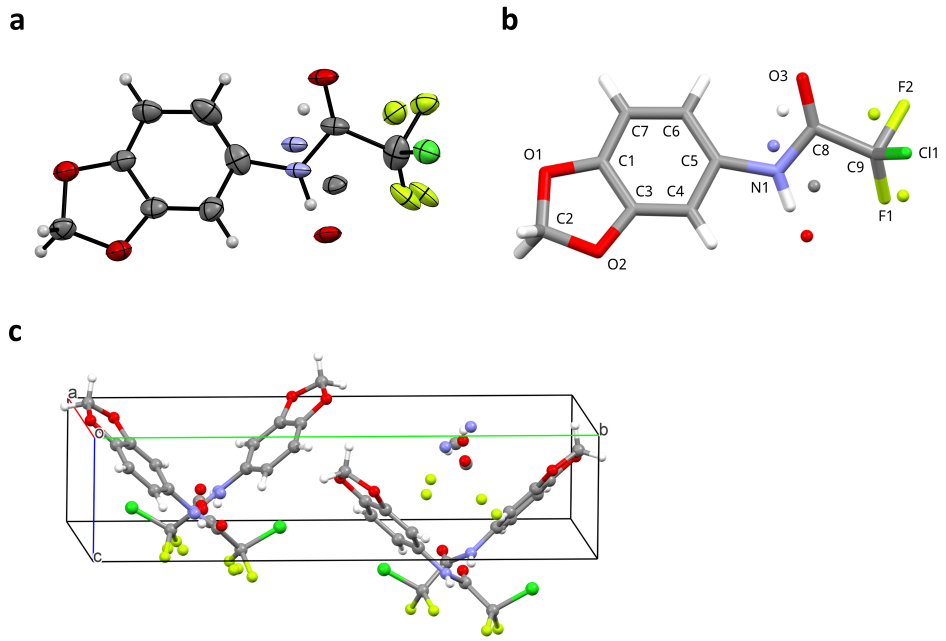


**Figure A21:** Data for **7c**. **(a)** ORTEP depicted at the 50 % probability level; **(b)** atom numbering; **(c)** crystal cell with cell axes.

**Table A18:** Crystal and refinement data for **7c**

| | |
|---|---|
| Substance code | SV-5-3-019 (**7c**) |
| CCDC ID | 2232108 |
| Total formular | $C_9H_6ClF_2NO_3$ |
| Molecular formula | $C_9H_6ClF_2NO_3$ |
| Formula weight | 249.60 |
| Temperature | 120(2) K |
| Wavelength, type of radiation | 0.71073 Å, MoKα |
| Diffractometer | STOE IPDS 2T |
| Crystal system | Orthorhombic |
| Space group, number | $Pna2_1$, (33) |
| Lattice constant | a = 9.9559(6) Å |
| | b = 19.6251(17) Å |
| | c = 4.8437(3) Å |
| Volume | 946.39(12) $Å^3$ |

*Continued on next page*

**Table A18:** *Continued from previous page*

| | |
|---|---|
| Number of reflexes and | 15 039 |
| Measuring range for lattice constants | $2.29° \leq \Theta \leq 28.38°$ |
| Z | 4 |
| Density (calculated) | $1.752\,mg\,m^{-3}$ |
| Absorption coefficient | $0.425\,mm^{-1}$ |
| Method of absorption correction | Integration |
| Max. und min. transmission | 0.9875 and 0.8614 |
| F(000) | 504 |
| Crystal size, shape and color | $0.030 \times 0.360 \times 0.370\,mm^3$, colorless plate |
| Theta range of measurement | 2.915 to 28.135° |
| Index area | $-13 \leq h \leq 13$, $-26 \leq k \leq 25$, $-5 \leq l \leq 6$ |
| Number of reflexes: | |
| measured | 6164 |
| independent | 2200 [$R_{int} = 0.0528$] |
| observed [$I>2\sigma(I)$] | 1946 |
| Completeness at $\Theta_{max} = 25.2°$ | 99.8 % |
| Refinement method | Full-matrix least-squares on $F^2$ |
| Reflexes / Restraints / Parameters | 2200 / 80 / 184 |
| Goodness of fit for $F^2$ | 1.046 |
| Final R values [$I>2\sigma(I)$] | R1 = 0.0686, wR2 = 0.1737 |
| R value (all data) | R1 = 0.0787, wR2 = 0.1870 |
| Maximum and minimum of the diff. Map | $0.550$ and $-0.463\,eÅ^{-3}$ |
| Remarks | $NHCOCF_2$ is misordered (flip by 180°) isomorphic to the Br compound (**7d**) |

### A.7.9 *N*-(Benzo[*d*][1,3]dioxol-5-yl)-2-bromo-2,2-difluoroacetamide (7d)

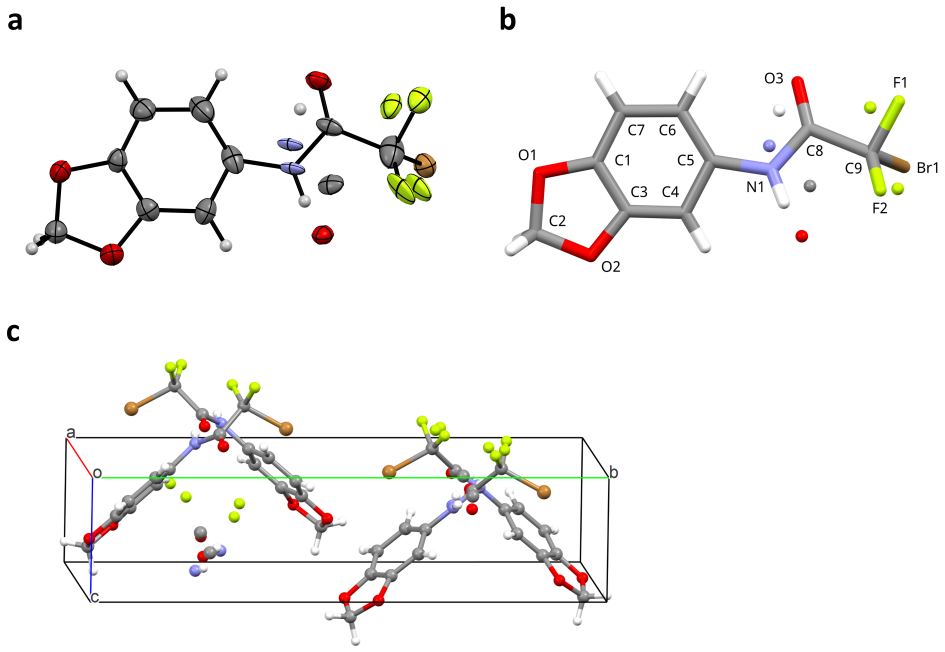


**Figure A22:** Data for **7d**. **(a)** ORTEP depicted at the 50 % probability level; **(b)** atom numbering; **(c)** crystal cell with cell axes.

**Table A19:** Crystal and refinement data for **7d**

| | |
|---|---|
| Substance code | SV-5-4-019 (**7d**) |
| CCDC ID | 2232109 |
| Total formular | $C_6H_6BrF_2NO_3$ |
| Molecular formula | $C_6H_6BrF_2NO_3$ |
| Formula weight | 294.06 |
| Temperature | 120(2) K |
| Wavelength, type of radiation | 0.71073 Å, MoKα |
| Diffractometer | STOE IPDS 2T |
| Crystal system | Orthorhombic |
| Space group, number | $Pna2_1$, (33) |
| Lattice constant | a = 9.9445(6) Å |
| | b = 20.1455(13) Å |
| | c = 4.8798(4) Å |
| Volume | 977.60(12) $Å^3$ |

*Continued on next page*

**Table A19:** *Continued from previous page*

| | |
|---|---|
| Number of reflexes and | 13 553 |
| Measuring range for lattice constants | $2.88° \leq \Theta \leq 28.38°$ |
| Z | 4 |
| Density (calculated) | $1.998\,mg\,m^{-3}$ |
| Absorption coefficient | $4.226\,mm^{-1}$ |
| Method of absorption correction | Integration |
| Max. und min. transmission | 0.9034 and 0.4367 |
| F(000) | 576 |
| Crystal size, shape and color | $0.020 \times 0.150 \times 0.270\,mm^3$, colorless plate |
| Theta range of measurement | 2.878 to 28.042° |
| Index area | $-12 \leq h \leq 13$, $-26 \leq k \leq 22$, $-6 \leq l \leq 6$ |
| Number of reflexes: | |
| measured | 5908 |
| independent | 2349 [$R_{int} = 0.0330$] |
| observed [$I>2\sigma(I)$] | 2055 |
| Completeness at $\Theta_{max} = 25.2°$ | 99.8 % |
| Refinement method | Full-matrix least-squares on $F^2$ |
| Reflexes / Restraints / Parameters | 2349 / 80 / 184 |
| Goodness of fit for $F^2$ | 1.077 |
| Final R values [$I>2\sigma(I)$] | R1 = 0.0505, wR2 = 0.1160 |
| R value (all data) | R1 = 0.0626, wR2 = 0.1274 |
| Maximum and minimum of the diff. Map | $0.556$ and $-0.634\,eÅ^{-3}$ |
| Remarks | $NHCOCF_2$ is misordered (flip by 180°) isomorphic to the Cl compound (**7c**) |

### A.7.10 *N*-(Benzo[*d*][1,3]dioxol-5-yl)-2,2-difluoro-2-iodoacetamide (7e)

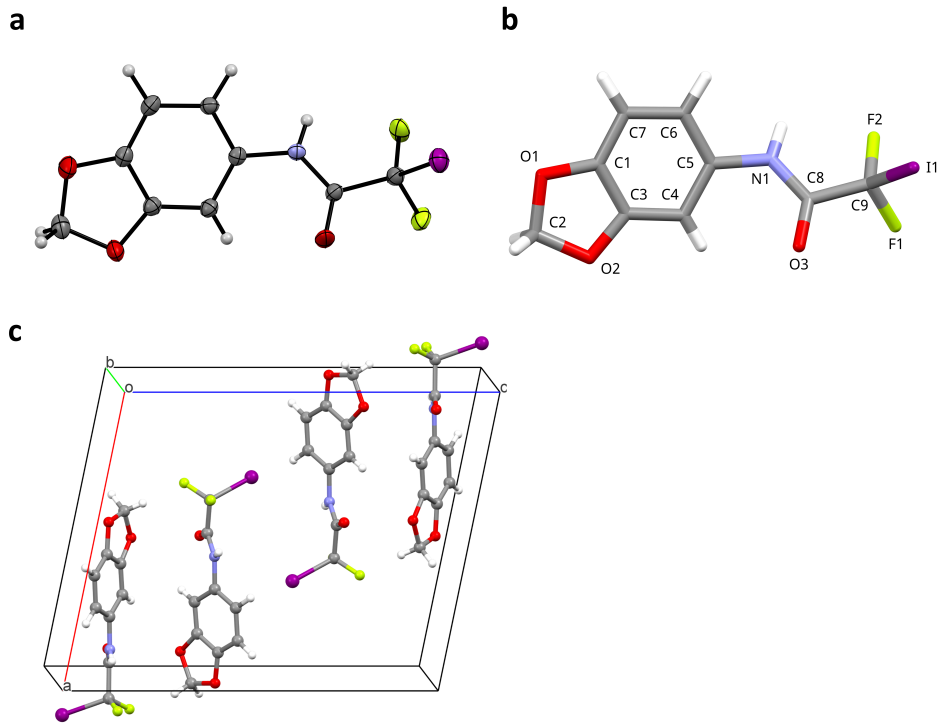


**Figure A23:** Data for **7e**. **(a)** ORTEP depicted at the 50 % probability level; **(b)** atom numbering; **(c)** crystal cell with cell axes.

**Table A20:** Crystal and refinement data for **7e**

| | |
|---|---|
| Substance code | SV-5-5-019 (**7e**) |
| CCDC ID | 2232110 |
| Total formular | $C_4H_2F_2INO_3$ |
| Molecular formula | $C_4H_2F_2INO_3$ |
| Formula weight | 341.05 |
| Temperature | 120(2) K |
| Wavelength, type of radiation | 0.71073 Å, MoKα |
| Diffractometer | STOE IPDS 2T |
| Crystal system | Monoclinic |
| Space group, number | $P2_1/n$, (14) |
| Lattice constant | a = 13.1540(7) Å |
| | b = 5.0645(2) Å; β = 99.687(4)° |
| | c = 16.1653(8) Å |
| Volume | 1061.55(9) Å$^3$ |

*Continued on next page*

**Table A20:** *Continued from previous page*

| | |
|---|---|
| Number of reflexes and | 7927 |
| Measuring range for lattice constants | $3.70° \leq \Theta \leq 28.38°$ |
| Z | 4 |
| Density (calculated) | $2.134\,mg\,m^{-3}$ |
| Absorption coefficient | $3.036\,mm^{-1}$ |
| Method of absorption correction | Integration |
| Max. und min. transmission | 0.7719 and 0.2661 |
| F(000) | 648 |
| Crystal size, shape and color | $0.090 \times 0.130 \times 0.730\,mm^3$, colorless needle |
| Theta range of measurement | 3.703 to 27.906° |
| Index area | $-17 \leq h \leq 12, -6 \leq k \leq 6, -21 \leq l \leq 21$ |
| Number of reflexes: | |
| measured | 5008 |
| independent | 2512 [$R_{int} = 0.0343$] |
| observed [$I>2\sigma(I)$] | 2168 |
| Completeness at $\Theta_{max} = 25.2°$ | 99.1 % |
| Refinement method | Full-matrix least-squares on $F^2$ |
| Reflexes / Restraints / Parameters | 2512 / 0 / 163 |
| Goodness of fit for $F^2$ | 1.081 |
| Final R values [$I>2\sigma(I)$] | R1 = 0.0410, wR2 = 0.1012 |
| R value (all data) | R1 = 0.0490, wR2 = 0.1080 |
| Maximum and minimum of the diff. Map | 1.187 and $-0.800\,eÅ^{-3}$ |
| Remarks | H atoms localized and their position refined |

### A.7.11 Hydrogen Bonds in Crystal Structures of 6b–e and 7a–e

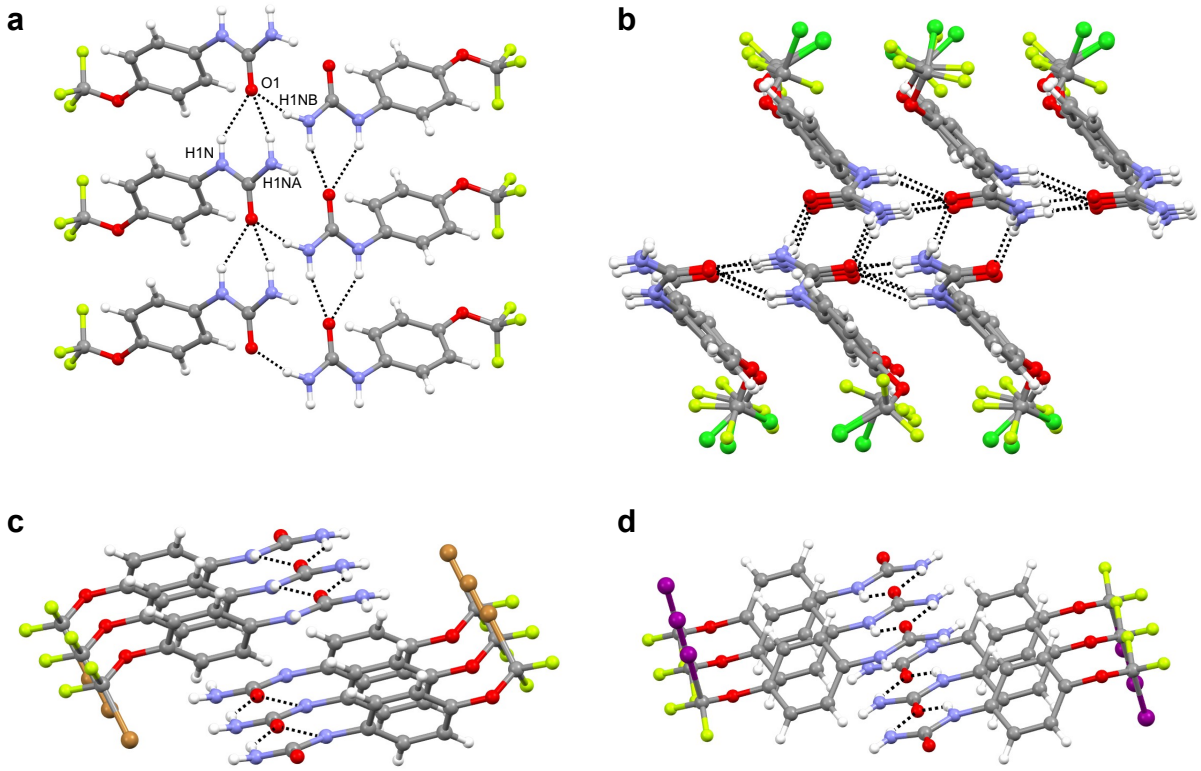


**Figure A24:** Overview of HB interactions and parallel-displaced π-πstacking of **6b**–**e**. Numbering of all urea groups is analogous. **(a)** Crystal structure of **6b** (H1N···O1, 2.16 Å; H1NA···O1, 1.98 Å; H1NB···O1, 2.18 Å); view along *b* axis. **(b)** Crystal structure of **6c** (NH···O, 2.0–2.3 Å); view along *a* axis. **(c)** Crystal structure of **6d** (H1N···O1, 2.19 Å; H2NB···O1, 2.11 Å). **(d)** Crystal structure of **6e** (H1N···O1, 2.12 Å; H1NB···O1, 2.09 Å).

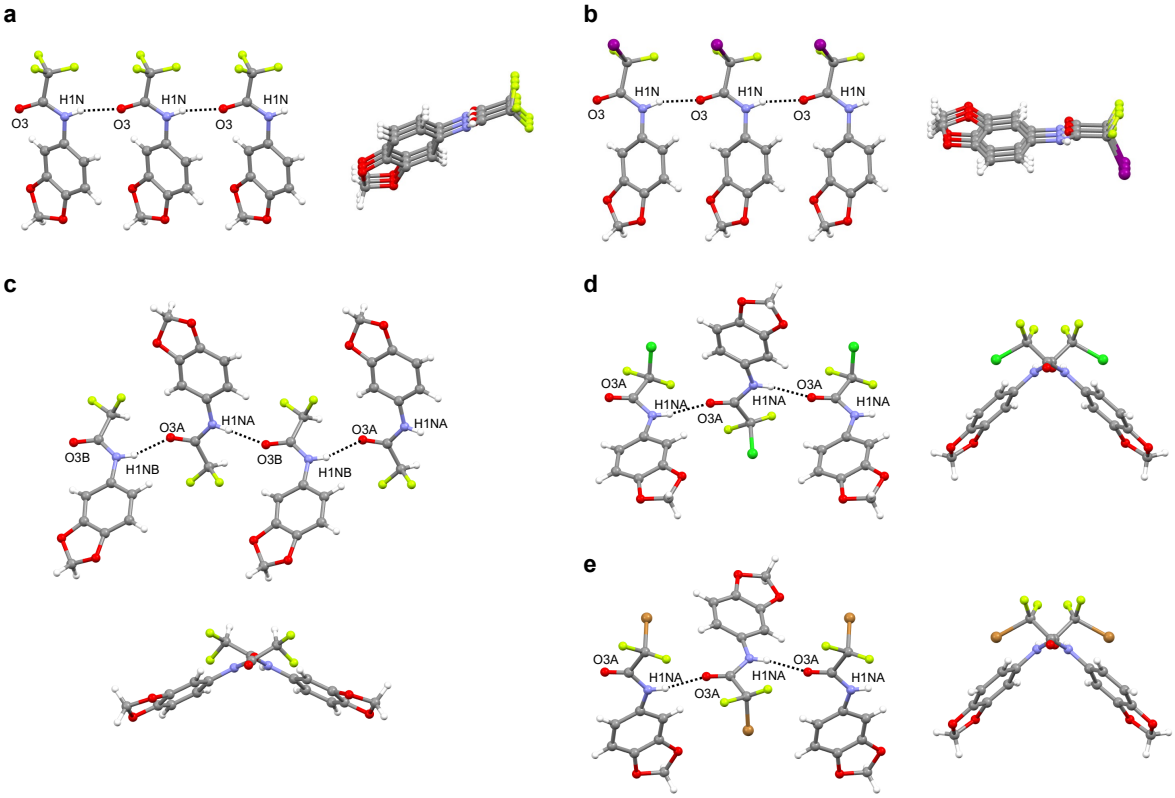


**Figure A25:** Overview of HB interactions. **(a)** Crystal structure of **7b** (H1N···O3, 2.02 Å). The viewing angle of the right depiction is slightly tilted. **(b)** Crystal structure of **7e** (H1N···O3, 2.04 Å). The viewing angle of the right depiction is slightly tilted. **(c)** Crystal structure of **7a** (H1NA···O3B, 1.99 Å; H2NB···O3A, 2.96 Å). **(d)** Crystal structure of **7c** (molecule A; H1NA···O3A, 2.02 Å). **(e)** Crystal structure of **7d** (molecule A; H1NA···O3A, 2.04 Å).

### A.7.12 Halogen Bonds in Crystal Structure 6c

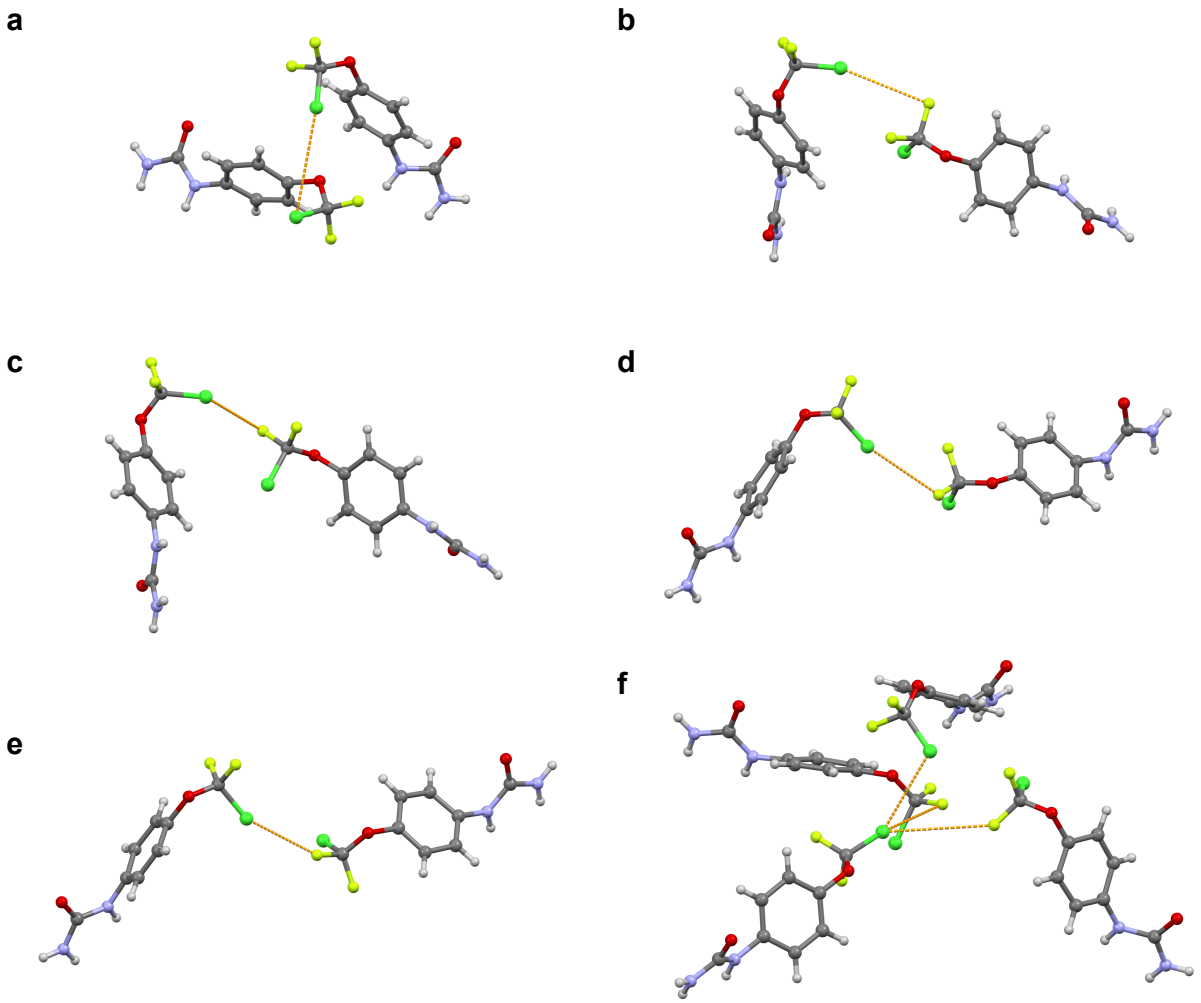


**Figure A26:** All Cl···F and Cl···Cl contacts in crystal structure **6c**. **(a)** Cl1A···Cl1B. **(b)** Cl1B···F2A. **(c)** Cl1C···F2A. **(d)** Cl1D···F1D. **(e)** Cl1E···F1B. **(f)** Cl1F···Cl1C, Cl1F···F2B, Cl1F···F2E. Angles C−X···B and distances X···B are stated in Table A21 on the following page.

**Table A21:** All Cl···F and Cl···Cl contacts in crystal structure **6c** shown in Figure A26 on the preceding page.

| XB donor | XB acceptor | C−X···B angle (°) | X···B distance (Å) |
|---|---|---|---|
| Cl1A | Cl1B | 140.6(5) | 4.281(8) |
| Cl1B | F2A | 158.1(6) | 3.59(1) |
| Cl1C | F2B | 166.2(6) | 3.60(1) |
| Cl1D | F1D | 166.5(6) | 3.35(1) |
| Cl1E | F1B | 158.1(6) | 3.14(1) |
| Cl1F | Cl1C | 145.5(6) | 3.524(9) |
| Cl1F | F2B | 146.8(6) | 4.13(1) |
| Cl1F | F2E | 142.2(6) | 3.48(1) |